Molecular mechanisms of
RASopathy-associated hypertrophic cardiomyopathy

Inaugural-Dissertation

zur Erlangung des Doktorgrades
der Mathematisch-Naturwissenschaftlichen Fakultät
der Heinrich-Heine-Universität Düsseldorf

vorgelegt von

Marcel Buchholzer

aus Gummersbach

Düsseldorf, Mai 2020

aus dem Institut für Biochemie & Molekularbiologie II
der Medizinischen Fakultät der Heinrich-Heine-Universität Düsseldorf

Gedruckt mit der Genehmigung der Mathematisch-Naturwissenschaftlichen
Fakultät der Heinrich-Heine-Universität Düsseldorf

Berichterstatter:

1. Prof. Dr. Reza Ahmadian

2. Prof. Dr. Axel Gödecke

Tag der mündlichen Prüfung:

06.08.2020

"Everything Not Saved Will Be Lost"

– Nintendo 'Quit Screen' Message

Summary

Dysregulation of MAPK pathway components is frequently associated with carcinogenesis and developmental disorders. The Noonan syndrome (NS), one group of these disorders, is characterized by dysmorphic facial features, skeletal anomalies, and intellectual and developmental disabilities. NS is caused by germline mutations of genes related to MAPK pathway components, such as *RAF1,* which cause a gain-of-function of the pathway. A special feature of NS patients with *RAF1* mutations is the high occurrence of a hypertrophic cardiomyopathy (HCM), which is defined by an increased left ventricular wall thickness. In this doctoral study, we established a protocol for the differentiation of iPSC lines (wild-type RAF1 and patient-derived RAF1^{S257L}) to highly pure, ventricular and contractile 3-dimensional cardiac bodies (CBs). This cell model system enabled us to investigate the mechanistic basis of cardiac hypertrophy induced by NS-associated RAF1^{S257L}. We observed hypertrophic features in RAF1^{S257L} CBs, such as cell size enlargement, re-expression of fetal genes, a switch of myosin heavy chain beta to alpha, and an impaired calcium transient. Most remarkably, RAF1^{S257L} CBs and the corresponding heart biopsy samples from the RAF1^{S257L} patient revealed a lack of the I-band, the flexible region of the sarcomeres. These features were revertible upon treatment with a MEK inhibitor. Signal transduction processes were investigated in further projects related to the RHO GTPases, CDC42 and RAC1. A gain-of-function variant of CDC42 (R186C), causing a previously unrecognized and distinctive hematological/autoinflammatory disorder, revealed an impaired cytosol/membrane shuttling due to an extraction inhibition by the GDP dissociation inhibitor (GDI) This resulted in an enhanced localization at the Golgi apparatus. Other issues dealt with the positive effect of RAC1 signal suppression in a tumor relevant surrounding. We discovered a small molecule inhibitor against VAV3, a RAC activator and a critical component of BCR-ABL pathway. Most strikingly, administration of this inhibitor to a BCR-ABL leukemia model resulted in a significant decrease in leukemic burden. Finally, we provided novel evidence that inhibition of RAC signaling by lovastatin mediats radioprotective potency on primary lung cells and rodent lung tissue following fractionated irradiation. This radioprotective effects of statins on normal tissue might be useful in the clinic to widen the therapeutic window of radiotherapy.

Zusammenfassung

Eine Dysregulation der MAPK-Signalwegkomponenten ist häufig mit einer Karzinogenese und auftretenden Entwicklungsstörungen verbunden. Das Noonan-Syndrom (NS), eine Gruppe dieser Störungen, ist durch dysmorphe Gesichtsmerkmale, Skelettanomalien sowie Geistes- und Entwicklungsstörungen gekennzeichnet. NS wird durch Keimbahnmutationen in Genen von MAPK-Signalwegkomponenten wie *RAF1* ausgelöst, was zu einem *gain-of-function* des Signalwegs führt. Eine Besonderheit bei NS-Patienten mit *RAF1*-Mutationen ist das verstärkte Auftreten einer hypertrophen Kardiomyopathie, die durch eine erhöhte Wandstärke des linken Ventrikels definiert ist. In dieser Doktorarbeit wurde ein Protokoll entwickelt um iPSC-Linien (Wildtyp-RAF1 und vom Patienten stammende RAF1^{S257L}) zu reinen, ventrikulären und kontraktilen dreidimensionalen Cardiac Bodies (CBs) zu differenzieren. Dieses Zellmodell ermöglichte uns die Untersuchung, der mechanistischen Grundlagen der NS-assoziierten RAF1^{S257L} induzierte Herzhypertrophie. Wir beobachteten in RAF1^{S257L} CBs hypertrophe Merkmale wie Zellvergrößerung, die erneute Expression fetaler Gene, einen Expressionswechsel der schweren Myosin Ketten von Beta zu Alpha und eine Beeinträchtigung der Calciumtransienten. Bemerkenswerterweise zeigte sich in RAF1^{S257L}-CBs und den entsprechenden Herzbiopsien des RAF1^{S257L}-Patienten ein fehlendes I-Band, die flexible Region der Sarkomere. Die meisten der genannten Merkmale waren nach Behandlung mit einem MEK-Inhibitor umkehrbar. Außerdem wurden in weiteren Teilprojekten die Signaltransduktionsprozesse im Zusammenhang mit den RHO-GTPasen CDC42 und RAC1 untersucht. Eine Variante von CDC42 (R186C), die eine zuvor nicht beschriebene hämatologische/autoinflammatorische Störung verursachte, zeigte einen gestörten Zytosol/Membran-Transport, der auf eine Extraktions-Hemmung durch den GDP dissociation inhibitor (GDI) zurückgeführt werde konnte und zu einer erhöhten Lokalisierung am Golgi-Apparat führte. Andere Themen befassten sich mit dem positiven Effekt der RAC1-Signalunterdrückung in einem tumorrelevanten Zellmilieu. Wir entdeckten einen kleinen Inhibitor gegen VAV3, einen RAC-Aktivator und eine kritische Komponente des BCR-ABL-Signalwegs. Am auffälligsten ist, dass die Verabreichung dieses Inhibitors in einem BCR-ABL-Leukämiemodell zu einer signifikanten Verringerung der Leukämiebelastung führte. Schließlich lieferten wir neue Beweise dafür, dass die Hemmung der RAC-Signalübertragung durch Lovastatin nach fraktionierter Bestrahlung, eine Strahlenschutzwirkung auf primäre Lungenzellen und Nagetier-Lungengewebe verursachte. Diese Strahlenschutzwirkung von Statinen auf normales Gewebe könnte in der Klinik nützlich sein, um das therapeutische Fenster der Strahlentherapie zu erweitern.

Table of Content

I.   List of abbreviations

aa	Amino acid
ANP	A-type natriuretic peptide
ATM	Ataxia telangiectasia mutated
ATP	Adenosine triphosphate
BNP	B-type natriuretic peptide
CaMK	Calmodulin dependent kinase
CDC42	Cell division cycle protein 42 homolog
CFC	Cardio-facio-cutaneous syndrome
CM-AVM	Capillary malformation–arteriovenous malformation syndrome
CR	Conserved region
CRIB	Cdc42/Rac interactive binding
CRD	Cysteine rich domain
CS	Costello syndrome
DAG	Diacylglycerol
DNA	Deoxyribonucleic acid
DSB	Double strand break
e.g.	Exempli gratia, for example
ER	Endoplasmic reticulum
ERK	Extracellular regulated kinase
ESC	Embryonic stem cell
FGF	Fibroblast growth factor
FL	Full length
GAP	GTPase-activating protein
GDI	GDP dissociation inhibitor
GDP	Guanosine diphosphate
GEF	Guanine-nucleotide-exchange factor
GPCR	G-protein coupled receptors
GRD	GAP-related domain
GSK3β	Glycogen synthase kinase 3 beta
GTP	Guanosine triphosphate
GTPases	Guanosine triphosphatases
Hh	Hedgehog
HMG-CoA	β-Hydroxy β-methylglutaryl-CoA
HRAS	Harvey rat sarcoma
HVR	Hyper variable region
IL	Interleukin
IODVA	Inhibitor of oncogene driven VAV3 activation
IP3	Inositol-1,4,5-trisphosphate
iPSC	Induced pluripotent stem cell
IR	Ionizing radiation
kDa	Kilo Dalton
KRAS	Kirsten rat sarcoma
KSR	Kinase suppressor of Ras
LATS1	Large tumor suppressor kinase 1
MLP	Muscle LIM protein
MAPK	Mitogen-activated protein kinase
MEK	MAPK/ERK kinase
MEKi	MEK inhibitor
MRAS	Muscle rat sarcoma
NF1	Neurofibromatosis type 1

NFAT	Nuclear factor of activated T-cells
NP	Natural product
NS	Noonan syndrome
NSML	Noonan syndrome with multiple lentigines
PKA	Protein kinase A
PAK	p21-activated kinase
PD	Pull-down
PKA	Protein kinase C
PLB	Phospholamban
PP	Protein phosphatase
PTM	Posttranslational modifications
RAC	RAS-related C3 botulinum toxin substrate
RAF	Rapidly accelerated fibrosarcoma
RAS	Rat sarcoma
RBD	RNA binding domain
RHO	RAS homologue
RKIP	RAF kinase inhibitor protein
ROCK	Rho-associated coiled-coil kinase
RTK	Receptor tyrosine kinase
SERCA	Sarcoplasmic/endoplasmic reticulum calcium ATPase
SOS	Son of Sevenless
SR	Sarcoplasmic reticulum
TGFβ	Transforming growth factor-β
WB	Western blotting
WT	Wild type

II.   Amino acid abbraviation

Amino Acid	Three letter code	One letter code
Alanine	Ala	A
Arginine	Arg	R
Asparagine	Asn	N
Aspartic acid	Asp	D
Cysteine	Cys	C
Glutamine	Gln	Q
Glutamic acid	Glu	E
Glycine	Gly	G
Histidine	His	H
Isoleucine	Ile	I
Leucine	Leu	L
Lysine	Lys	K
Methionine	Met	M
Phenylalanine	Phe	F
Proline	Pro	P
Serine	Ser	S
Threonine	Thr	T
Tryptophan	Trp	W
Tyrosine	Tyr	Y
Valine	Val	V

III.List of figures

Chapter I

General introduction

1 The human heart

The human heart is the contractile center of the circulatory system whose main task is to pump blood through the pulmonary system and peripheral organs. Therefore, the heart is responsible for the transport of nutrients and oxygen as well as the removal of metabolic end products. Furthermore, it plays a major role in the distribution of hormones and immune cells, defending the body against infections [1,2]. In humans, the heart is divided into four distinct chambers, the right atrium and the affiliated ventricle that pumps blood through the lungs, and the left atrium and its affiliated ventricle that pumps blood through the peripheral organs [3]. In the healthy heart, valves separate each atrium and ventricle, as well as the exit of each ventricle. The contractility of the heart is achieved by the myocardium, striated muscles that represent the main tissue of the heart wall. It is composed of cardiomyocytes which serve as the cellular contracting subunits [4].

1.1 Structure and function of cardiomyocytes

Cardiomyocytes, also known as the contracting cells in the myocardium, enable the hearts function as a pumping organ. Compared to other cell types, cardiomyocytes own special features. After formation and differentiation of the fetal heart cardiomyocytes lose their ability to proliferate. A second DNA synthesis phase occurring directly after birth is associated with a karyokinesis without cytokinesis, resulting in binucleation of most cardiomyocytes [5,6]. Postnatal, the heart size is therefore not regulated by an increase in cell number but almost exclusively by an increase in cardiomyocyte size, a process which is referred to as hypertrophy [7]. This physiological hypertrophy results in a size increase of approximately 8-fold within the first 20 years of life [8]. Even if there is more occurring evidence that some cardiomyocytes still maintain their ability to proliferate, this small number is almost negligible in consideration of heart regeneration [9]. Due to that, hypertrophy of cardiomyocytes after injury, long lasting hemodynamic stress, or as a result of genetic alteration often results in a pathological state involving cardiomyocytes death and fibrotic remodeling of the heart [10].

The ability to contract is triggered by action potentials which originate from the sinoatrial node, located in the right atrium of the heart. This electrical impulse is precisely orchestrated from cell to cell to guarantee a properly organized contraction of the whole organ [11]. The contraction of single cardiomyocytes is accurately regulated by a defined set of ion channels and ion exchangers which control the Ca^{2+} influx from the extracellular space as well as from the sarcoplasmic reticulum (SR) [12]. The action potential is initiated by depolarization of the sarcolemma, the cell membrane of myocytes, which results in opening of voltage dependent L-type Ca^{2+} channels. The influx of Ca^{2+}, activates in turn the Ca^{2+}-induced Ca^{2+} release from the SR which is controlled by ryanodine receptors (RyR). On a molecular level the muscular contractility is the result of a reversible interaction of the two proteins actin and myosin [13].
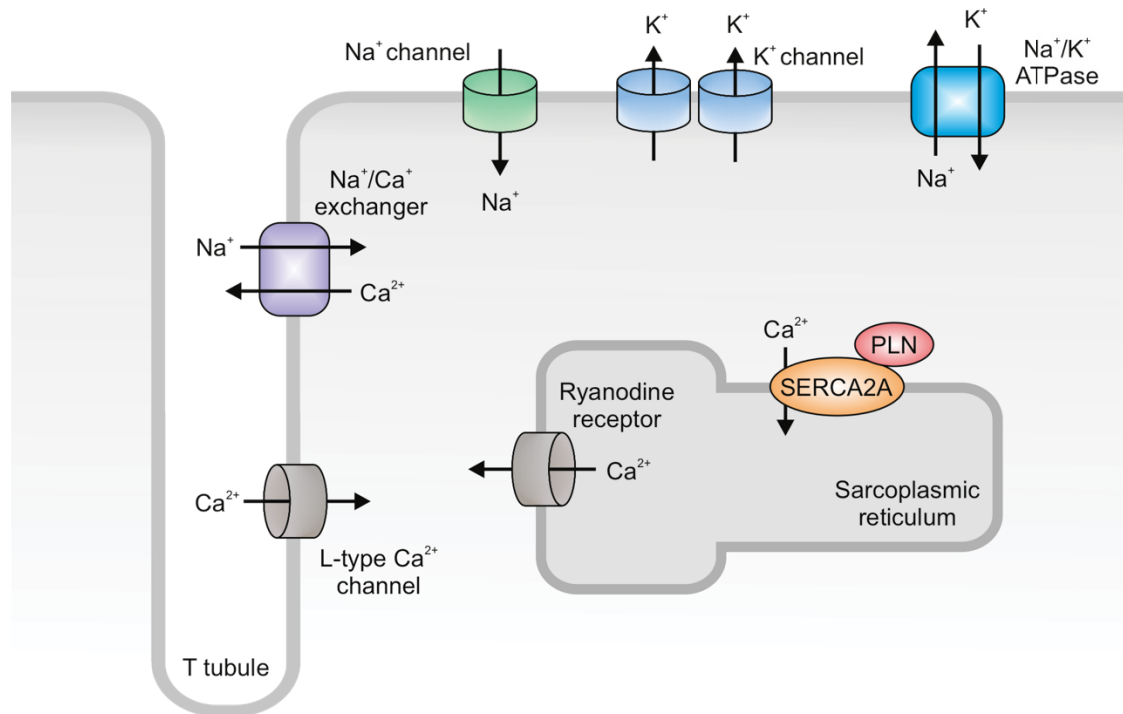
Figure 1: Calcium cycling in cardiomyocytes.
Depolarization of the sarcolemma by rapid sodium influx results in opening of voltage-dependent L-type Ca^{2+} channels. Extracellular Ca^{2+} influx causes calcium-induced calcium release from the SR via the ryanodine receptor. The increase in free intracellular Ca^{2+} enables myocyte contraction. Ca^{2+}-activated kinases phosphorylate phospholamban (PLN), therefore relieving its repression on SERCA2A, which rapidly re-imports Ca^{2+} into the SR. This leads to decreased levels of intracellular Ca^{2+}. The Na+/Ca2+ exchangers help restoring the initial Ca^{2+} concentration resulting in relaxation of the sarcomeres. (Figure adapted from Baskin, *et al.* [14])

Every cardiomyocyte contains numerous tubular myofibrils which are composed of repeating sections of sarcomeres. These sarcomeres are limited by the so-called Z disc. Titin, a 3400 kDa large protein is furthermore contributing in stability of the sarcomeres [15]. One single titin molecule is stretched from each Z-disc to the middle of the sarcomeres which is usually referred to as M line. The regions containing myosin filaments are called A band (*anisotropic* when viewed with polarized light) and appears darker under the microscope. In contrast, regions that are lacking myosin and only contain actin are called I bands (*isotropic*) (Figure 2) [16-18]. The globular end of the myosin heads can bind to actin and bend, leading to sarcomere shortening due to actin-myosin filament sliding [19]. This cycle requires the hydrolysis of adenosine triphosphate (ATP) as a main source of energy for the contraction. The increase in cytosolic Ca^{2+} furthermore serve as important regulator of myosin-binding to filamentous actin by interacting with troponin and tropomyosin, therefore exposing myosin-binding sites [20]. Cytosolic Ca^{2+} is mainly removed by two mechanisms. Re-uptake of Ca^{2+} into the SR is achieved in an active manner by the sarcoplasmic/endoplasmic reticulum calcium ATPase (SERCA) which can be negatively regulated by phosphorylated phospholamban (PLN) [21]. Furthermore, Ca^{2+} is exported by a Na^+/Ca^{2+} exchangers, guaranteeing a repolarization of the cardiomyocyte resulting in the relaxation of the cell [22].
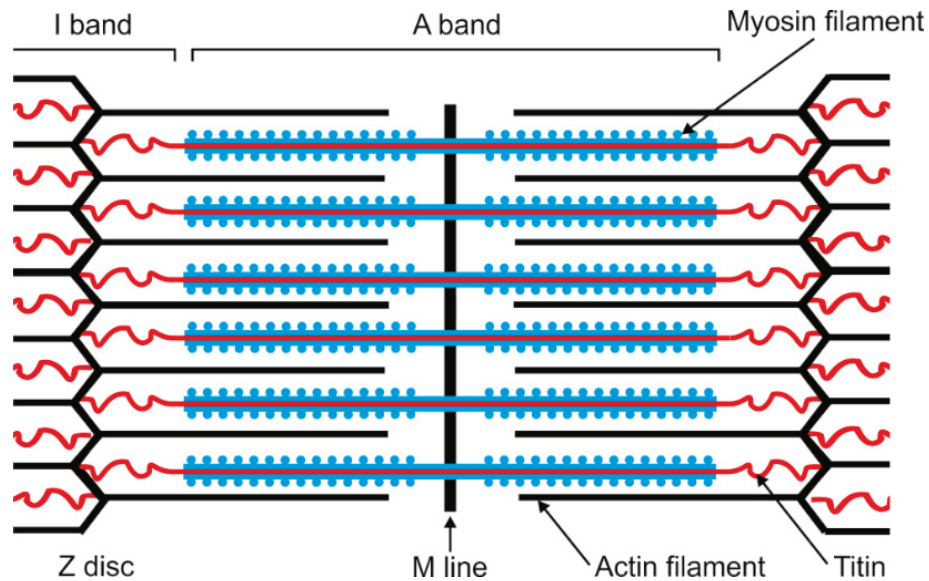
3

Figure 2: Schematic illustration of a human sarcomere.
Sarcomeres are repeating units between two Z discs. The Z discs are surrounded by the I band (for isotropic) which is the zone of thin actin filaments that do not contain thick myosin filaments. The A band (for anisotropic) contains thin and thick filaments. In the middle of each sarcomere is the M line (for middle). Titin, the biggest known protein, functions as a molecular spring, therefore guaranteeing the elasticity of the sarcomeres. It extends from the Z-line of the sarcomere to the M-band, where it interacts with the thick filaments.

2   Stem cells

Stem cells are a special cell population which can be found biologically conserved in a majority of multicellular organisms. Stem cells are usually characterized by two special abilities, which separate them from any other cell type. The ability to continuously proliferate, called self-renewal, and the ability to differentiate into different cell lineages that is called potency [23]. The introduction of embryonic stem cells (ESCs) into medical research paved the way for a new variety of possible experimental applications [24]. The first human ESCs were successfully isolated from the inner cell mass of a human blastocyst in 1998. Due to their high telomerase activity, these cells can be cultured for several passages without losing their karyotype and their specific stem cell characteristics [25]. Self-renewal of stem cells is defined as the capability to perform cell division and generating daughter cells that are identical to the mother cell and remain the same developmental potential [26]. Potency is described as the potential to differentiate into any available mature cell type. Nevertheless, the level of potency differs between the human stem cells, reaching from totipotent stem cells which can differentiate into embryonic and extraembryonic cell types up to unipotent stem cells which are solely able to produce one cell type but still have the property of self-renewal [27,28].

2.1   Induced pluripotent stem cells

Although the use of ESCs enabled a huge variety of experimental applications, problems like cell derivation as well as ethical issues made it difficult for the community to work with ESCs [29].

Therefore, the discovery of induced pluripotent stem cells (iPSCs) was seen as a breakthrough in creating an alternative to ESCs. Retroviral transduction of the four transcriptional factors OCT3/4, SOX2, c-MYC and KLF4 into human adult fibroblasts resulted in generation of pluripotent stem cells [30]. Pluripotent cells are characterized by their ability to differentiate into any cells that are derived from the three germ layers (ectoderm, mesoderm and endoderm) [31,32]. With the introduction of iPSCs, existing problems like efficiency, but also ethical and immunological issues were solved. Although iPSCs still reveal certain differences to ESCs in their expression and epigenetics, they share the characteristics of self-renewal and pluripotency as well as their morphology and the physiological properties of ESCs [33,34].

In the last decades, human stem cells were widely used as a model to study cellular processes like differentiation and tissue development. Furthermore, stem cells have a huge impact on biomedical research regarding the identification of target genes for new drugs or toxicity assays [26]. Nevertheless, the biggest impact of iPSCs on biomedical science is their usage in cell-based therapies and regenerative medicine. Human iPSCs are widely used to generate human disease models *in vitro* either to investigate the molecular mechanism of the diseases or for drug-screening against proteins of interest. Disease modeling starts with the isolation of patient-specific cells harboring disease-deriving somatic mutations, followed by their reprogramming to iPSCs. These cells are afterwards differentiated into the disease-relevant cell types which can be used for further investigation [35,36]. Moreover, iPSC-derived cells are frequently used to study their application as a replacement of disease-involved cells, for example in the treatment of macular degeneration or cardiac ischemia, where they replace fibrotic tissue [37,38]

3 Mitogen-activated protein kinase (MAPK) pathway signaling

Mitogen-activated protein kinases (MAPK) are usually components of a three kinase regulatory cascade, being key components in intracellular signal transduction of external stimuli and thereby, controlling multiple cellular processes including growth, proliferation, differentiation, motility, stress response, survival and apoptosis [39,40]. Within the cascade MAPKs are phosphorylated and activated by upstream MAPK kinases (MAPKK) which catalyze the phosphorylation of MAPKs on both tyrosine and threonine residues [41]. MAPKKs in turn are phosphorylated and activated by MAPKK kinases (MAPKKK). The signal transduction is controlled by guanosine-5'-triphosphate (GTP) binding proteins and specific kinases that might be considered as MAPKKK kinases (MAPKKKK) [42]. The variety of MAPK responses is regulated by spatio-temporal activation of the different cascades in response to different stimuli [39].

4   RAS superfamily at a glance

The members of the RAS superfamily proto-oncogenes were introduced in the 1960s by the discovery of two viruses causing tumors in rats. The sarcoma-causing viral genes were names after their discoverers Jennifer Harvey and Werner Kirsten, from this time on as Harvey rat sarcoma (HRAS) and Kirsten rat sarcoma (KRAS) [43,44]. Two decades later, the first activated human form of HRAS has been identified in bladder cancer, showing a genetic alteration in amino acid (aa) residue 12 [45-47]. Until today, more than 150 homologous proteins were discovered, collectively termed as RAS superfamily proteins. All of its members are small (21-25 kDa) GTP binding proteins which hydrolyze GTP and therefore cycle between an active, GTP-bound and an inactive, GDP-bound state (Figure 3) [48,49]. Structurally, RAS family GTPases share a conserved 20 kDa G domain which is involved in GTP binding as well as in GTP hydrolysis [48]. Furthermore, these GTPases carry an additional C-terminal hypervariable region (HVR) that can be posttranslationally modified and is important for membrane interaction [50]. Functionally, the RAS superfamily is divided into five major families, named RAS, RHO, RAB, ARF and RAN according to their sequence, structure and their functional similarities [51,52]. The members of the RAS superfamily are essential for signal transduction by sensing extracellular signals trough their corresponding receptors which are afterwards transmitted to their downstream substrates. Therefore, they regulate a huge variety of cellular functions including gene expression, metabolism, cell cycle progression, proliferation, survival, differentiation, vesicular transport, cytoskeleton organization, migration, cell motility, endocytosis, contraction and nuclear transport [53-55]. Furthermore, somatic and germline mutations in genes that are associated to the members of the RAS family or their modulators are frequently correlated with the progression of cancer and developmental diseases [56-59].

4.1   Structural properties of RAS GTPases

All RAS proteins share a nearly identical tertiary structure, which is composed of six β-sheets surrounded by α-helices [60]. All members of the RAS superfamily share a central GTP/GDP-binding domain, shortly called G-domain, which is important for the nucleotide binding as well as their hydrolysis [49]. Furthermore, they share five conserved GDP/GTP-binding (G) motifs along their sequence [61]. G1, or also called P-loop (^{10}GxxxxGKS/T^{17}; HRAS numbering), is able to bind the beta and gamma phosphates resulting in high affinity binding of the nucleotides [49,62]. Codon 12 and codon 13 in G1 are the most frequently mutated RAS codons in human tumors, resulting in a reduced intrinsic GTPase activity or an insensitivity against GTPase-activating proteins (GAP). Therefore, RAS is locked in a constant hyperactive state [58,63]. G2 and G3, also referred to as switch I and switch II, are dynamic regions that sense the state of the bound nucleotide and serve furthermore as main interaction site for RAS regulators and RAS effectors. The main conformational changes upon nucleotide exchange in

RAS are basically confined to the switch regions [49,64]. Moreover, switch II comprises the critical catalytic amino acid Q61. Similar to G12, mutations of Q61 significantly reduce the intrinsic hydrolysis rate and prevent the GAP-mediated inactivation [65]. Finally, G4 and G5 are crucial to determine the nucleotide specificity of RAS [66].

In the active state RAS proteins are located at the plasma membrane where they can physically interact with their regulators and effectors. The association of RAS proteins with the cellular lipid membrane is mediated through posttranslational modifications (PTM) and distinct motifs at their C-terminal end, which is referred to as hyper variable region (HVR) [67,68]. Almost all RAS proteins serve as substrates for isoprenyl-transferring enzymes, which covalently link farnesyl or geranylgeranyl moieties to the cysteine residue of the very C-terminal CAAX motif (C, cysteine; A, aliphatic amino acid; X, any amino acid) [69]. After prenylation of the RAS proteins, the AAX residues get proteolytically cleaved by the endopeptidase RCE1 and the terminal isoprenylcysteine gets methylated [70].

4.2 RAS family GTPases

RAS is a family of ubiquitously expressed small GTPase, involved in intracellular signal transduction, therefore regulating various cellular processes including proliferation and differentiation, cell growth and survival [71,72]. Of its approximately 40 members, HRAS, NRAS and KRAS4B are the best investigated RAS paralogues. The family members became scientifically interesting because of their critical role in oncogenesis [73]. The best investigated RAS signaling pathway is RAS activation by SOS1 which is triggered through dimerization of the epidermal growth factor receptor (EGFR). Active RAS then consequently binds and phosphorylates the members of the rapidly accelerated fibrosarcoma (RAF) paralogues resulting in their activation.

4.3 RHO family GTPases

RAS Homologue (RHO) GTPases are a subfamily of the RAS superfamily with 20 classical members identified in humans. They are key regulators of several cellular functions, especially in the regulation of the cytoskeletal structure and dynamics [74]. Like RAS family proteins, RHO GTPases cycle between an inactive GDP-bound and an active GTP-bound state. RHOA, RAC1 and CDC42 are the best characterized members of the RHO family. Although the RHO members are strongly homologous in their amino acid composition, stimulation of the single members results in different cellular outcomes. Whereas RHOA regulates the assembly of contractile actin myosin filaments (also called stress fibers), RAC1 and CDC42 regulate actin polymerization to form peripheral lamellipodial and filopodial protrusions, respectively [75,76]. Furthermore, all three GTPase members can promote integrin engagement with the extracellular matrix, therefore playing a critical role in cell migration [77].

4.4 Regulation of small GTPases

The members of the RAS and RHO family GTPases can cycle between an active, GTP-bound and an inactive, GDP-bound state, as discussed before. Nucleotide exchange and GTP hydrolysis are tightly regulated by two classes of regulators, called guanine-nucleotide-exchange factors (GEFs) and GTPase-activating proteins (GAPs), respectively [78,79]. RHO GEFs promote the exchange of GDP to GTP therby activating the GTPase whereas RHO GAPs negatively regulate RAS activity by enhancing its intrinsic GTPase activity. RHO GTPases comprise a third class of regulators which are determined as GDP dissociation inhibitors (GDIs) [80]. GDIs inhibit the GTPase cycle by sequestering GDP bound RHO GTPases from the membrane [81].
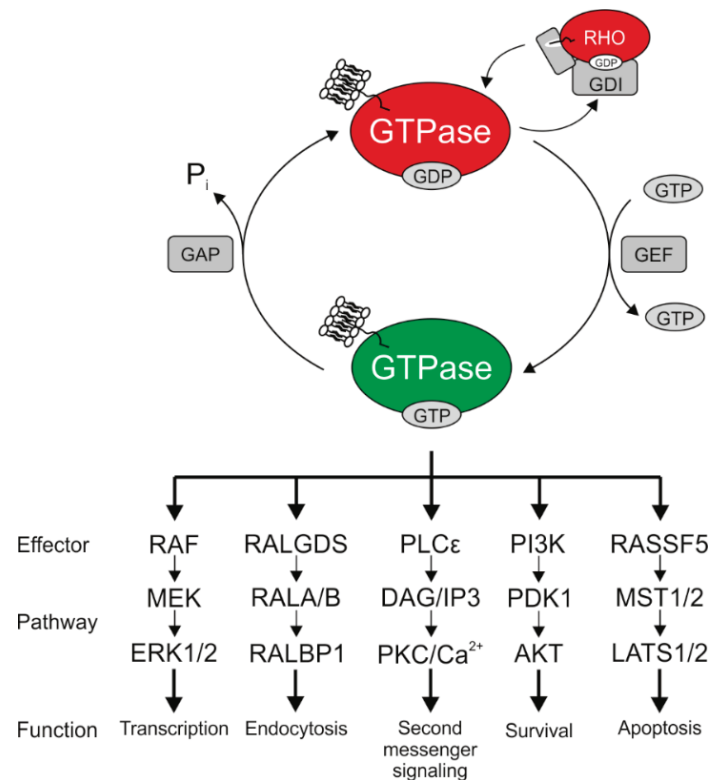
Figure 3: Schematic illustration of GTPase regulation and RAS downstream pathways.
RAS proteins cycle between an inactive GDP and an active GTP-bound state. The transition between these states is mainly regulated by two main regulatory proteins called GEFs and GAPs. Whereas GEFs accelerate the exchange of GDP to GTP, GAPs enhance their intrinsic GTPase activity. GTPases are only able to transduce a signal in the GTP-bound state while they are located at the membrane by posttranslational modifications. Effector proteins of active RAS and the downstream targets are visualized below the cycle. RAS, rat sarcoma; GEF, guanine nucleotide exchange factor; GAP, GTPase-activating protein; RALGDS, guanine nucleotide dissociation stimulator; RALBP1, RALA binding protein 1; PLCε, Phospholipase C ε; DAG, diacylglycerol; IP3, inositol trisphosphate; PKC, protein kinase C; RASSF5, RAS-association domain family; MST, mammalian sterile 20-like kinase; LATS, large tumor suppressor kinase.

4.4.1 GAPs

The complexity of cellular events explains the urgent need of enzymes like GAPs. Most cellular events can be activated within a fraction of a second up to seconds upon *e.g.* ligand interaction with membrane bound receptors. The fact that most of the known GTPases share a rather slow intrinsic GTP hydrolysis rate results in an accumulation of active GTPases after stimulation. Since GAPs negatively regulate RAS activity, enhancing its intrinsic GTPase activity by several orders of magnitude, they are needed to terminate the initial signal transduction [78,82]. Therefore, GAP proteins coordinate many processes in cells by either shutting down the main cascade or opposing signaling pathways to provide stability of main cascade transmission [83].

4.4.2 GEFs

GEFs are able to bind specifically their affiliated RAS protein, accelerate the exchange of GDP for GTP, and thus activate the GTPase. The most common mechanism to accelerate the exchange is a reduction of the affinity to the bound GDP by several orders of magnitude [84]. The much higher intracellular concentration of GTP results from the formation of an active GTP-bound complex, which is in turn able to bind tightly to effector proteins. This results in conformational changes of the effector and in signal transduction controlling a variety of cellular functions [85,86]. The Rho GEFs from the diffuse B-cell lymphoma family (Dbl) consist of 74 members existing in humans [79]. A question of great interest is why the necessity of such a large number of GEFs exists for the relative low number of GTPases.

4.4.3 GDIs

The RHO family of GTPases holds another class of regulators, which are called GDIs. In contrast to the high number of GAPs and GEFs [78,79], there are only three genes in the human genome encoding GDIs [80]. Whereas GDI1 is ubiquitously expressed, GDI2 is mainly expressed in the hematopoietic tissue and GDI3 in human cerebral, lung and pancreatic tissue [87-89]. RHO GDIs main task is to sequester GDP-bound RHO GTPases from the membrane, therefore protecting them against both degradation and unspecific activation by RHO GEFs [90,91].

5 RAF proto-oncogene serine/threonine-protein kinase

The RAF Ser/Thr kinases link the RAS family proteins with the MEK/ERK pathway to control multiple biochemical processes, such as proliferation, differentiation, and survival [92]. The first RAF member was discovered 1983 by identification of the viral oncogene *v-raf* from the transforming murine retrovirus 3611-MSV [93]. Shortly afterwards, its first cellular homologue CRAF [94,95] was discovered, followed by identification of its paralogues ARAF [96] and BRAF [97].

Activation of RAF kinases is a multistep process initialized by RAF recruitment from the cytosol to the plasma membrane, followed by binding to GTP-bound RAS proteins [98-100]. Thereafter, the RAF paralogues form homo- or heterodimer, resulting in the transphosphorylation of their kinase domains [101]. Once activated, the RAF kinases are the main link in the RAS-MAPK pathway, ultimately resulting in the activation of multiple other pathways [102,103]. Dysregulation of all three RAF paralogues was shown to be associated with carcinogenesis and occurrence of developmental disorders, e.g. Noonan syndrome (NS) [104-108].

5.1   RAF domain organization

All three human RAF paralogues share three conserved regions (CR) (Figure 4) [109,110]. CR1 consist out of a RAS-binding domain (RBD) and a cysteine-rich domain (CRD), which are essential for the interaction with active RAS proteins as well as with the plasma membrane, respectively [111,112]. CRAF RBD consists of 5 β-sheets, interrupted by an α-helix, followed by two additional α-helices [113]. Amino acid alignment as well as structural determination of all human RAF paralogues revealed a high structural identity in the RBD [114]. Due to a high electrostatic complementary in their interaction surface, RAF RBD is able to bind the switch I region of RAS proteins [112,115]. Genetic studies and mutational analysis of the interaction site highlighted Arg59, Gln66, Lys84, and Arg89 (CRAF numbering) to have a particular contribution to the high binding affinity between RAS and RAF [116-119]. Beside interacting with active RAS proteins, RAF RBD was found to be involved in membrane association of the RAF kinases. Five residues (Lys28, Arg52 Lys66, Arg68, and Lys69) in ARAF were shown to be engaged in lipid binding. Interestingly, named amino acids were found to be mutated in human cancer [118,120-122].
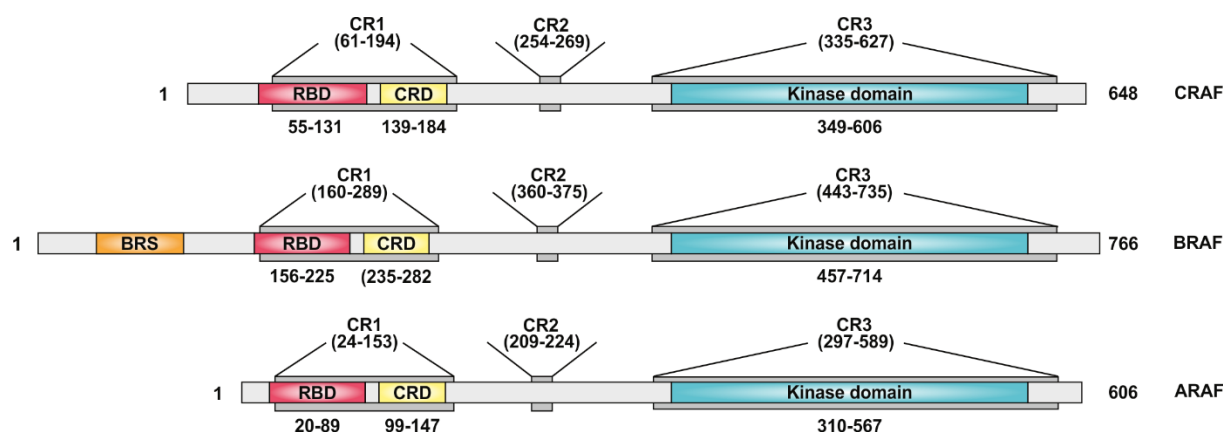
Figure 4: Schematic illustration of RAF serine/threonine-protein kinase domain organization.
RAF paralogue domain organization, highlighting the evolutionary conserved regions (CR) as well as their domains. ARAF is the shortest paralogue, followed by CRAF. BRAF contains an additional N-terminal domain which is called BRAF-specific (BRS) domain. In the first conserved region, all RAFs share a Ras-binding domain (RBD) and a cysteine-rich domain (CRD). CR2 is described as a flexible linker between the first and the third conserved region which contains a regulatory multi-phosphorylation site. CR3 is composed out of the kinase domain.

The second domain in the CR1 is the CRD, which is connected to the RBD through a short linker fragment [123]. It is composed of two functional zinc-binding motifs which enable interaction with membrane lipids, like phosphatidic acid and phosphatidylserine [124,125]. Membrane interaction occurs mainly through its residues 143-160 (CRAF counting) which are highly conserved among different species [114]. Whether the CRD also directly interacts with RAS is still not fully deciphered [126-129]. However, CRD interaction with plasma membrane lipids stabilizes the RAS-RAF complex, therefore facilitating RAF activation. Mutational analysis of the zinc finger region revealed a diminished CRD association with phosphatidylserine-containing liposomes and a diminished HRAS-dependent activation [130,131].

CR2 is a small Ser/Thr-rich region and mainly important as multi-phosphorylation site, therefore negatively regulating RAF kinase function [132,133]. The region linking CR1 with CR3, is structurally disordered and therefore confers high structural flexibility to the kinase structure [134], which ensures signal transduction of the kinase domain to its substrates [135].

CR3 is located in the C-terminus of the protein and mainly consists of the catalytic kinase domain [136]. Like other kinase domains it contains two lobes which can open or close the catalytic cleft [135]. The opened cleft is able to bind ATP with an antiparallel β-sheet in its small lobe, whereas the α-helical large lobe binds protein substrates in its closed form [135,137]. Although the RAF paralogue kinase domains are highly conserved, they still differ in their kinase activity. BRAF was shown to have the highest activity for MEK activation, followed by CRAF and then ARAF [138]. Nevertheless, regarding RAF dimerization, a BRAF/CRAF heterodimer represents the most effective form for MEK phosphorylation among all possible hetero- and homodimers [139]. Unlike the other paralogues, BRAF carries an additional BRAF-specific region (BRS) in the N-terminus which forms an α-hairpin consisting of two antiparallel α-helices that are connected by a short turn. BRS was shown to be important for the dimerization with scaffolding proteins like the kinase suppressor of Ras (KSR) [140].

5.2 Regulation of the RAF kinase activity

In unstimulated quiescent cells, RAF kinases exist in a cytosolic autoinhibited form [141] in which the N-terminal region inhibits the kinase domain [142,143]. This conformation is stabilized by binding of two 14-3-3 proteins to two phosphorylation sites with a consensus sequence RSXpSXP (pS, phosphor-serine; X, any amino acid; R, arginine; P, proline) [144-146]. The first site is located in CR2 (pS259 of CRAF, pS365 of BRAF and pS214 of ARAF) and the other behind CR3 (pS621 of CRAF, pS729 of BRAF, pS582 of ARAF) [147-150]. This simultaneous interaction results in a conformational change, maintaining RAF in its inactive state (Figure 5) [146].

Activation of the RAF paralogues starts by the interaction with GTP-RAS [98,99], which is a critical step towards translocation to the plasma membrane [124]. RBD and CRD collectively enable the

interaction with RAS and the membrane phospholipids [151,152]. Furthermore, it was shown that also the kinase domain transiently interacts with the membrane, which may lead to further modulation of RAF function [153]. As the only member of the RAF kinases, BRAF was supposed to not exclusively be activated by RAS but furthermore also by Ras-related protein Rap-1A [154,155].
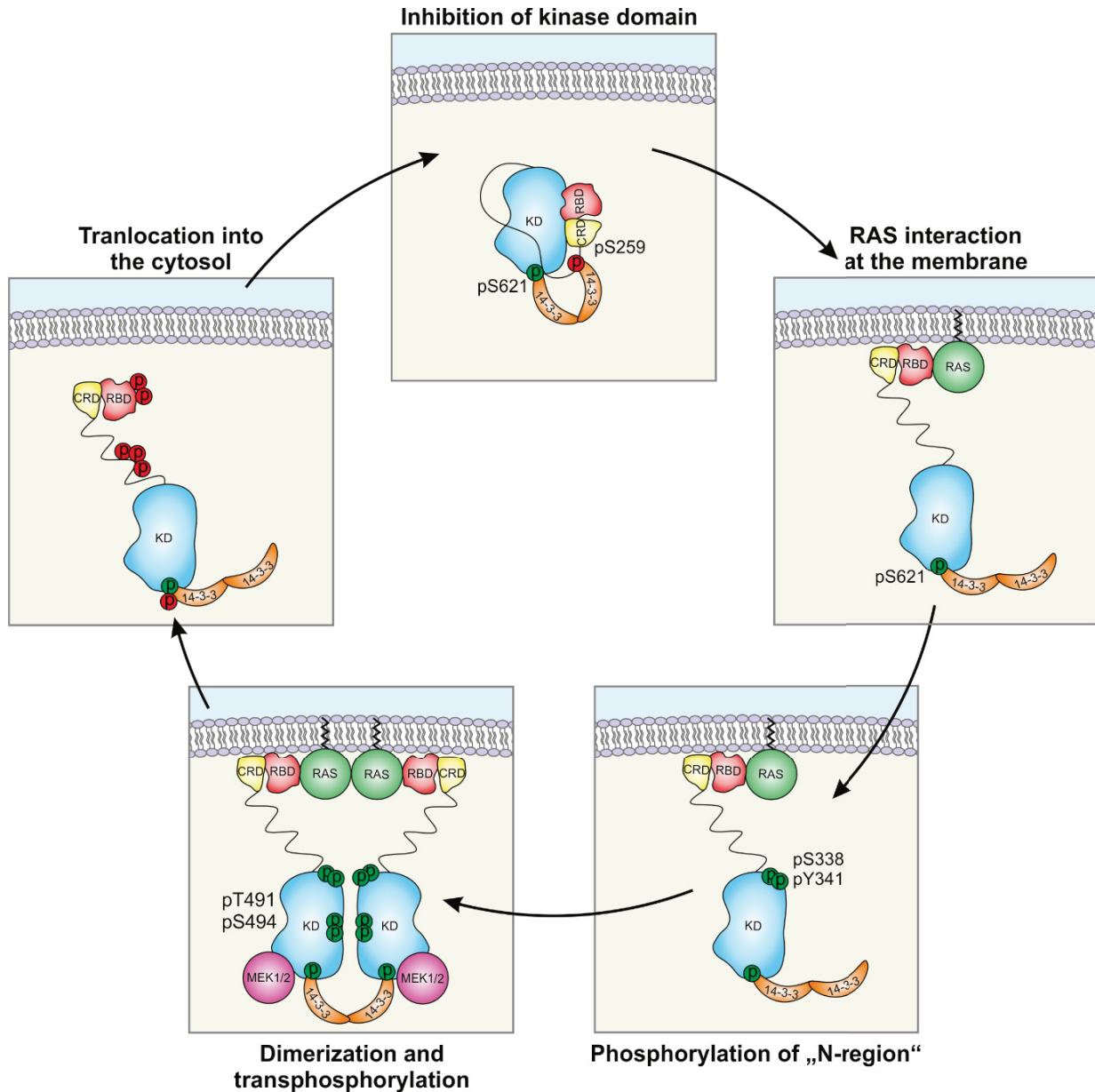
Figure 5: Regulation of CRAF kinase activity.
Activation of RAF starts by interaction with GTP-bound RAS and its translocation to the plasma membrane, which is followed by 14-3-3 dissociation and dephosphorylation of the negative regulatory site in the CR2 (pS259) by PP2A or a complex consisting of MRAS, SHOC2, and the dimeric PP1 phosphatase. Afterwards the N-region gets phosphorylated at the tyrosine residues by members of the SRC family and at the serine residues by members of the PAK and PKC families. Emerging negative electrostatic potential results in release of the autoinhibition and formation of RAF dimers. This consequently leads to transphosphorylation of the activation segment. Activated RAF dimers transmit the signal towards MEK1/2 which in turn phosphorylate ERK1/2. After signal transduction dephosphorylation at S388 by PP5 and RKIP interaction with the N-region interfere with MEK binding. ERK phosphorylates RAF in a negative feedback regulation at six different sites (S29/S43/S289/S296/S301/S642). Finally, PKA, AKT and LATS1 rephosphorylate RAF at S259 therefore recycling RA Finto its autoinhibited state.

Membrane translocation and RAS-association are followed by 14-3-3 dissociation and dephosphorylation of the negative regulatory site in the CR2 (pS259 of CRAF, pS365 of BRAF and pS214 of ARAF) [156,157]. Currently, there are two proposed mechanisms for the dephosphorylation. In the first scenario, a heterotrimeric PP2A phosphatase was proposed to dephosphorylate RAF using a yet unclear mechanism [158-160]. The second mechanism employs a complex consisting of MRAS, SHOC2, and the dimeric PP1 phosphatase, therefore facilitating the dephosphorylation of the inhibitory CR2 phosphorylation site and 14-3-3 dissociation [161-163].

All of the previous named actions induce a conformational change which results in activation of the kinase domain. Afterwards, the RAF kinases have to be further phosphorylated on three more sites, the negatively charged regulatory region (N-region), the activation segment and the C-terminal 14-3-3 binding site [110]. The N-region is a 4-amino acid sequence motif in the N-terminus of CR3 which slightly differs between the paralogues (^{338}SSYY^{341} for CRAF, ^{446}SGYY^{449} for BRAF and ^{299}SGYY^{302} for ARAF) [164,165]. Members of the SRC family kinases are responsible for the phosphorylation of the tyrosine residues in the N-region of CRAF and ARAF. Phosphorylation of the serine residues at site I is achieved by members of the PAK and PKC families [166,167]. Further phosphorylation is required in the activation segment which is defined as two distinct residues in the kinase domain (ARAF: T452 and T455, BRAF: T599 and S602, CRAF: T491 and S494) [168-170]. The emerging negative electrostatic potential finally results in the release of the autoinhibition [142], enabling the formation of RAF dimers [167,171-173]. RAF kinases form homodimers and heterodimers, which influence their substrate specificity and catalytic efficiency [138,174]. RAF paralogues mainly dimerize through the N-terminal lobes of their kinase domains [175,176]. Activating phosphorylation and the subsequent dimerization are required for stable formation and increased local concentration of membrane-bound RAS-RAF complexes into so-called nanoclusters [177,178]. Activated RAF dimers transmit the signal downstream to MEK1 and MEK2 by phosphorylation of S218/S222 and S222/S226, respectively [179], which in turn phosphorylate ERK1/2 [180,181].

After signal transduction, the hyperphosphorylated RAF will be inactivated and translocated into the cytoplasm in a multistep process. Dephosphorylation at S388 by protein phosphatase 5 (PP5) and RAF kinase inhibitor protein (RKIP) interaction with the phosphorylated N-region interfere with MEK signaling and -binding, respectively [182,183]. Furthermore, CRAF was found to be phosphorylated by ERK in a negative feedback regulation at six different sites, at the N-terminus (S29 and S43), between CR2 and CR3 (S289/S296/S301) and at the C-terminus (S642) [184,185]. These phosphorylations interfere with RAS-RAF interaction and RAF dimerization.

RAF paralogues are rephosphorylated at the CR2 (pS259 of CRAF, pS365 of BRAF and pS214 of ARAF) in a final step, that ensures 14-3-3 interaction, therefore recycling RAF into their presignaling

autoinhibited state. The main cellular kinases for CR2 phosphorylation are Protein kinase A (PKA) and AKT, however also the large tumor suppressor kinase 1 (LATS1) was identified to phosphorylate CR2 in a MST/Hippo-dependent manner [186-189].

6 RAS/MAPK pathway dysfunction in human diseases

RAS GTPases control the majority of signaling networks in the MAPK pathways which collectively include several cellular fates. Only the RAS-MEK-ERK axis mediates early and late developmental processes which finally control morphological determination as well as organogenesis, growth and synaptic plasticity [190]. Therefore, it is not surprising that dysregulation of MAPK components results in drastic effects not only on carcinogenesis but also on human development. Compared to somatic mutations which usually result in the formation of tumors, germline mutations were found to increase the signal intensity to a lesser extent and, therefore, facilitate the formation of developmental diseases [58,191].

6.1 The RASopathies

Dysregulation of MAPK pathway regulators was frequently found to correlate with the occurrence of developmental disorders. A clinically defined class of developmental disorders, characterized by autosomal dominant *de novo* germline mutations of genes encoding components of the MAPK pathway, was found to cause a subset of developmental disorders collectively named RASopathies. Most RASopathy phenotypes are characterized by developmental disorders like facial dysmorphism, skeletal abnormalities, neurocognitive impairment, cardiac malformations and an increased risk of cancer [104-106,192].

Neurofibromatosis type 1 (NF1) (gene encoding NF1) was the first described disease caused by a MAPK pathway alteration [193]. Since then, various diseases were identified to result from genetic alterations, like the NS (genes encoding KRAS4B, NRAS, RRAS1/3, RIT1, SOS1, SOS2, RASGAP1M, CRAF, CBL) [194], the NS with multiple lentigines (NSML) (genes encoding BRAF, CRAF, SHP2) [195,196], the capillary malformation–arteriovenous malformation syndrome (CM-AVM) (gene encoding p120RASGAP) [197], the Costello syndrome (CS) (genes encoding HRAS1, HRAS2) [198], the cardio-facio-cutaneous syndrome (CFC) (genes encoding KRAS4B, BRAF, ERK1/2) [199] and the Legius syndrome (gene encoding SPRED1) [200].

6.1.1 Noonan syndrome

The NS is an autosomal dominant disorder with a prevalence of approximately 1 in 1000–2500 [201]. Noonan syndrome individuals show a distinct dysmorphic phenotype which is characterized by low-set ears, short webbed neck, paired with skeletal anomalies, and intellectual and developmental disabilities. Furthermore, cardiovascular impairments, like congenital heart defects and hypertrophic

cardiomyopathy as well as an increased risk of developing cancer are accompanied with NS [202]. The affected genes in NS all cause gain-of-function mutations of components of the RAS-MAPK pathway, such as *PTPN11, SOS1, SOS2, KRAS, NRAS, RAF1, SHOC2, CDC42, RIT1, RRAS2, LZTR-1, PPP1CB* and *CBL* (Figure 6) [203-206]. Although the phenotype is homologous for different genetic alterations, the occurrence differs. With around 50 % of all cases, the most frequent mutated gene is *PTPN11*, followed by SOS1 mutations with 15 % prevalence [207,208]. *KRAS* and *NRAS* mutations are a rare cause of NS which increase the RAS-MAPK signaling through reduction of the GTPase function [209,210].
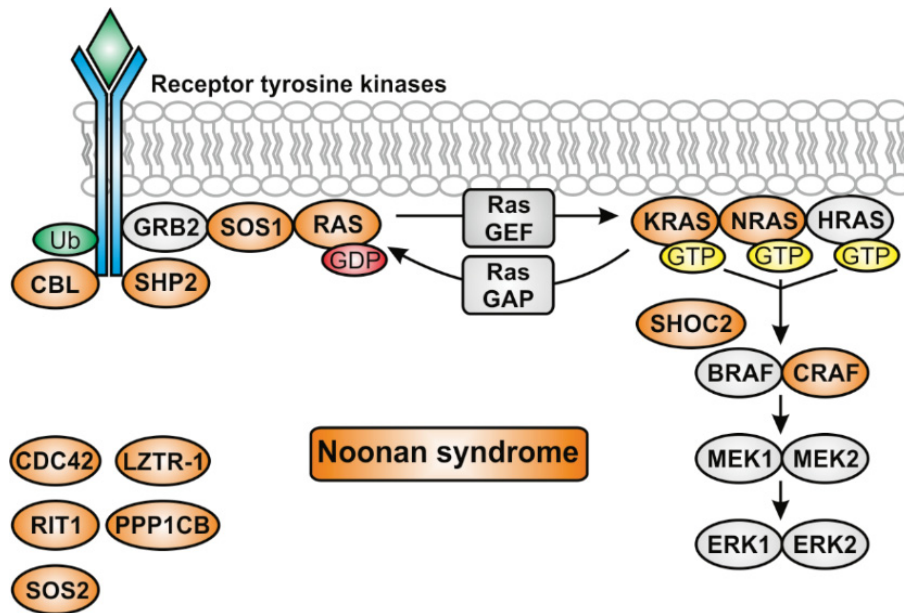
Figure 6: Schematic view of the RAS-MAPK pathway and affected genes in NS.
Ligand interaction with receptor tyrosine kinases results in recruitment of SOS1 to the membrane, which acts as a RAS GEF, that activates RAS. Active RAS transduces its signal towards the members of the RAF family. Subsequently, RAF phosphorylates MEK1/2 which in turn phosphorylate ERK1/2. NS is an autosomal dominant disorder characterized by germline mutations in genes encoding proteins involved in the RAS-MAPK pathway (affected genes are colored in orange).

6.2 Pathomechanism of RAF kinases

Most of the described CRAF mutations resulting in NS are flanking the negative regulation site (S259) which is important for 14-3-3 interaction, therefore controlling its autoinhibition. Fourteen different RAF1 missense mutations were described. Eight of these mutations are located in the flanking region of S259 (R256S, S257L, S259F, T260R, P261A, P261S/L, V263A). Another four mutations were found in the activation segment of the kinase domain (D486N/G, T491I/R) and two more in the very C-terminal part of CR3 (S612T, L613V) [196,211]. A special outcome in NS *RAF1* mutations is the high frequency to from a hypertrophic cardiomyopathy (HCM) which is defined by structural and functional abnormalities of the ventricular myocardium resulting in increased wall thickness of the left ventricle [190,212]. As the molecular cause of the HCM in RASopathy subjects hyperactivation of different MAPK pathways was hypothesized, which was experimentally proven in different cellular models

[196,211,213]. Similar to mutations in regulatory regions, the C-terminal L613V mutation was also shown to increase RAS-MAPK pathway signaling in a mouse model, consequently resulting in HCM. Inhibition of the RAF downstream target MEK was partially able to rescue this phenotype [104]. Other data indicates that Yorkie (Fly homologue to human YAP), a transcriptional co-activator in the Hippo pathway, which is important in organ development, is required for a CRAF-induced HCM. Cardiac-specific knock down of Yorkie rescued the CRAF-mediated HCM phenotype [214].

6.2.1 Hypertrophic cardiomyopathy

Hypertrophic cardiomyopathy is a common cardiovascular disease which is present in approximately 0.2 % of the general population and is defined by structural abnormalities of the ventricular myocardium. This results in a non-dilated thickening of the left ventricle which was shown to be an important cause for contractile dysfunction, pulmonary valve stenosis, atrial fibrillation and finally heart failures resulting in the death of affected individuals [215,216]. To date, 12 genes encoding sarcomeric components have been found to be implicated in the development of hypertrophic cardiomyopathy. Most of them are located in the genes encoding myosin-binding protein C (*MYBPC3*) and the β myosin heavy chain (*MYH7*) [217]. Furthermore, mutations of genes not directly encoding sarcomeric proteins, like certain members of the RASopathy family, were also found to impact the development of HCM [218]. Although the occurrence of HCM in RASopathies is rather low (20–30%), a higher frequency of HCM (≈ 70 %) was identified in individuals with pathogenic variants of *RAF1* and *RIT1* [106,219].

Whereas HCM that is caused by alterations in sarcomeric compounds usually manifests at age 8 years on average, NS-associated HCM occurs much earlier in life with the median being 5 months [106]. Furthermore, NS individuals diagnosed with HCM show a 70 % chance of survival 15 years after diagnosis. The main cause of death for NS-associated HCM is a congestive heart failure [220].

Independent of the mutation, stimuli that result in the development of a cardiac hypertrophy can be divided into biomechanical and stretch-sensitive mechanisms, associated with the release of hormones, cytokines, chemokines, and peptide growth factors. These signals are further processed by cardiomyocytes through membrane-integrated RTKs, G-protein coupled receptors (GPCR), and gp130-linked receptors. Signal transduction of these receptors results in hypertrophic growth due to changes in gene expression and altered protein homeostasis [221,222].

Activation of GPCR signaling is mainly initiated by angiotensin II, endothelin-1 and α-adrenergic catecholamines (e.g. noradrenaline and adrenaline). Upon activation, the $G_{\alpha q/11}$ subunit of the heterotrimeric G proteins stimulates the activation of membrane-bound phospholipase Cβ (PLCβ), consequently inducing the generation of diacylglycerol (DAG) and the production of inositol-1,4,5-trisphosphate (IP3) [223]. Generated IP3 is able to bind to its receptors which are located in the

membrane of the endoplasmic reticulum (ER), thereby triggering the release of internal Ca^{2+} storage into the cytosol. Increased Ca^{2+} can interact with the calcium-binding proteins calcineurin and calmodulin dependent kinase (CaMK), inducing hypertrophic signaling in two different manners. Upon interaction, calcineurin dephosphorylates NFAT, resulting in NFAT translocation into the nucleus followed by the activation of pro-hypertrophic gene expression [224]. Ca^{2+} mediated activation of CaMK causes phosphorylation of HDAC5, a suppressor of hypertrophic gene transcription, and initiates its nuclear export [225].

HCM is accompanied by increased workload of the heart due to hemodynamic overload [226]. Cardiomyocytes use different mechanisms to detect mechanical stress through an internal sensory apparatus. Proteins involved in sensing mechanical alterations are integrins, that link the cytoskeleton to the extracellular matrix [227] as well as the small LIM-domain protein MLP (muscle LIM protein) that is located in the Z-disc within each sarcomere [228]. These mechanisms are crucial in the regulation of GTPases, like Ras and Rho and in inactivation of GSK3β [229].

MAPK signaling in the heart can be initiated by GPCRs, RTKs, transforming growth factor-β (TGFβ), gp130-linked receptors as well as by stress stimuli such as stretch. Stimulation of those MAPKs finally results in the phosphorylation of MAPKs including ERK, JNK and p38 which in turn activate numerous transcription factors [221].

The changes in gene expression caused by alterations in cardiomyocyte workload are typically involved in re-expression of a fetal gene program and go along with higher levels of stress markers like atrial natriuretic factor (ANF) and B-type natriuretic peptide (BNP) as well as alterations in proteins regulating calcium transience [230]. Ongoing hypertrophy is therefore often associated with drastic downregulation of the sarcoplasmic/endoplasmic reticulum calcium ATPase (SERCA2a), which consequently results in prolonged action potential duration in the cardiomyocytes [231].

So far, medical therapy for NS associated HCM usually consists of Beta-blockers, disopyramide or calcium channel blockers [232].

7   Aims of the Thesis

The signal transduction cascades of small GTPases of the RAS and RHO families play important roles in diverse cellular processes, such as proliferation, adhesion, migration, and differentiation. Therefore, it is not surprising that any pathway dysregulation contributes to the progression of numerous diseases, such as cardiovascular diseases, developmental and neurological disorders, and cancer. CRAF is the best-investigated RAS effector linking the signals to its downstream targets MEK1/2, integral components of the MAPK pathway. *RAF1* gain-of-function mutations are frequently associated with NS, an autosomal dominant developmental syndrome caused by germline mutations in genes encoding components of the RAS/MAPK pathway, which is accompanied by a severe HCM. Furthermore, several missense mutations in CDC42 were identified in patients with NS-like disease pattern which, moreover, resulted in the identification of a novel disorder, termed NOCARH syndrome, characterized by neonatal onset of pancytopenia, autoinflammation, rash, and episodes of HLH. RAC1, a close relative to CDC42, is involved in cell migration by regulating actin cytoskeleton reorganization and thus, in tumor invasion and metastasis. We were able to identify and characterize RAC1 suppression in the treatment of BCR-ABL caused leukemia and in cell viability after fractionated irradiation of the lung.

This thesis aimed at investigating the molecular mechanisms of dysregulated proteins and understanding the progression of the underlying diseases. It includes following functional and mechanistic analyzes: (i) Physiological and biochemical characterization of the *RAF1* missense-mutation towards understanding NS pathogenesis accompanied by HCM; (ii) investigating the molecular mechanism of NOCARH syndrome; (iii) identifying how RAC1 suppression benefits therapeutic approaches in distinct human diseases.

Chapter II

Structural snapshot of RAF kinase interactions

Graphical abstract
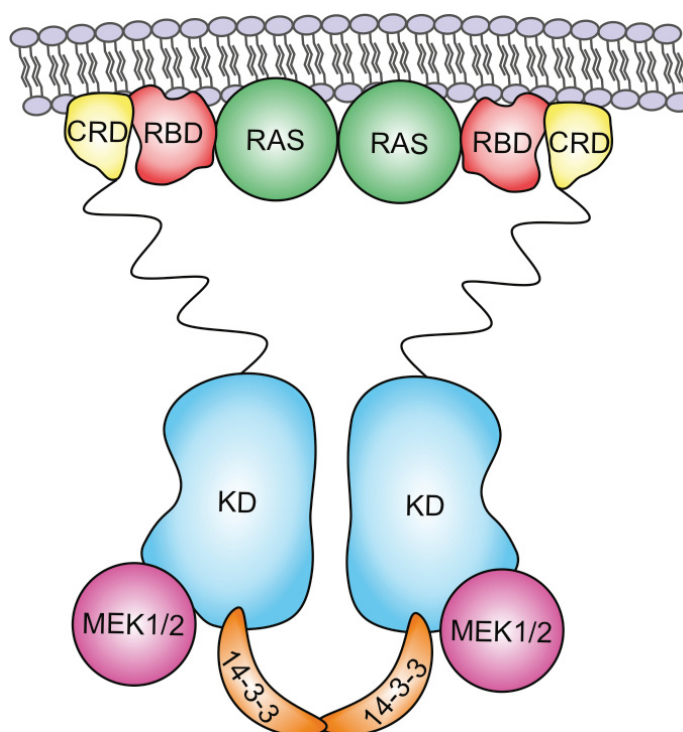
Status: Published in Biochemical Society Transactions, October 31th 2018

Impact factor: 4.316

Own proportion to this work: 35 %

Preparation of Figure 1, writing the manuscript, reference management, discussion.

PORTLAND PRESS

Review Article

Structural snapshots of RAF kinase interactions

Soheila Rezaei Adariani, Marcel Buchholzer, Mohammad Akbarzadeh, Saeideh Nakhaei-Rad, Radovan Dvorsky and Mohammad Reza Ahmadian

Institute of Biochemistry and Molecular Biology II, Medical Faculty, Heinrich-Heine University, Düsseldorf, Germany

Correspondence: Mohammad Reza Ahmadian (reza.ahmadian@hhu.de)

RAF (rapidly accelerated fibrosarcoma) Ser/Thr kinases (ARAF, BRAF, and CRAF) link the RAS (rat sarcoma) protein family with the MAPK (mitogen-activated protein kinase) pathway and control cell growth, differentiation, development, aging, and tumorigenesis. Their activity is specifically modulated by protein–protein interactions, post-translational modifications, and conformational changes in specific spatiotemporal patterns via various upstream regulators, including the kinases, phosphatase, GTPases, and scaffold and modulator proteins. Dephosphorylation of Ser-259 (CRAF numbering) and dissociation of 14-3-3 release the RAF regulatory domains RAS-binding domain and cysteine-rich domain for interaction with RAS-GTP and membrane lipids. This, in turn, results in RAF phosphorylation at Ser-621 and 14-3-3 reassociation, followed by its dimerization and ultimately substrate binding and phosphorylation. This review focuses on structural understanding of how distinct binding partners trigger a cascade of molecular events that induces RAF kinase activation.

Introduction

The discovery of the viral oncogene *v-raf* from the transforming murine retrovirus 3611-MSV in 1983 [1] paved the way for the discovery of a cellular homolog CRAF in 1985 [2] and soon after its paralogs ARAF [3] and BRAF [4]. Evolutionary conservation across different species, including worms (Lin-45) [5] and flies (Draf) [6], unequivocally indicates the biological importance of RAF (rapidly accelerated fibrosarcoma) kinases (Figure 1). Lin-45 encodes a BRAF ortholog that is necessary for larval viability, fertility, and induction of vulval cell fates [7]. Draf plays an important role in early embryogenesis [6]. The three human RAF paralogs regulate a large number of biochemical processes, including survival, proliferation, differentiation, stress responses, and apoptosis [8–13]. RAF kinases constitute a small family of serine/threonine kinases, which control evolutionarily conserved pathways and have essential roles during development [14–16]. Thus, it is not surprising that their dysregulation is associated with progression of a variety of human cancers [16–19], pathogenesis of developmental disorders including Noonan, LEOPARD, and cardiofaciocutaneous syndromes [20,21], and cardiovascular diseases, such as pulmonary arterial hypertension and heart failure [22].

Works from many laboratories have shown that RAF kinases are integral elements of the RAS–MAPK pathway, which is involved in different signaling pathways [22–27]. Activation of RAF kinases at the plasma membrane by RAS [1,28–32], together with the identification of their substrates MEK1/2 (MAPK/ERK kinase 1/2) [33] has provided the missing link between growth factor signals and MAPK cascade activation [34]. The activities of RAF kinases toward MEK differ widely, with BRAF being the strongest MEK activator, followed by CRAF and ARAF [35–37]. These proteins obviously underlay different regulatory mechanisms, including binding to membrane-associated RAS proteins, phosphorylation, and dephosphorylation along with homodimerization and heterodimerization [34,35,38–41]. These and other events collectively result in RAF kinase activation [42].

Despite the long history, investigations of the fundamental mechanisms of RAF kinase activation have substantially lagged far behind the development of kinase inhibitors and inhibitor technologies. In this review, we summarize emerging mechanistic insights gained from structural, biochemical, and
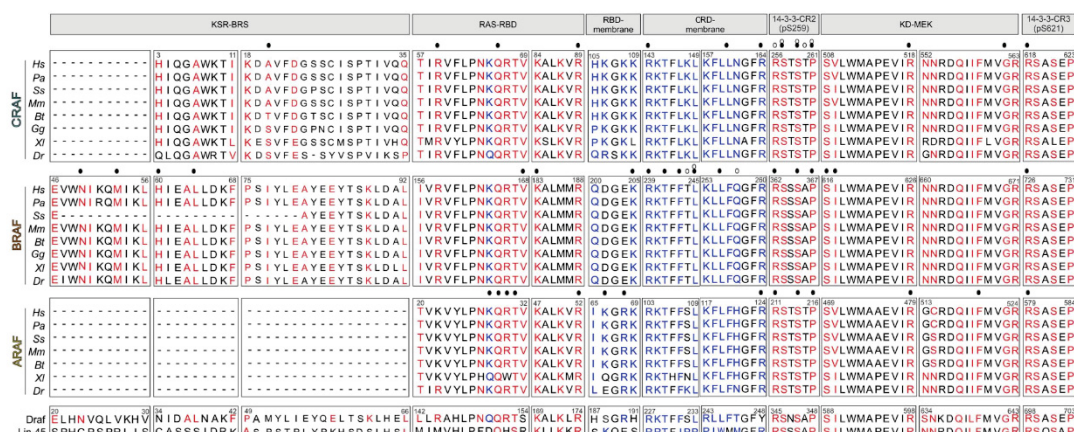
1393

Figure 1. Evolutionary conservation of RAF family members.

Multiple amino acid sequence alignment of RAF family members from different organisms (*Hs*, *Homo sapiens*; *Pa*, *Pongo abelii*; *Ss*, *Sus scrofa*; *Mm*, *Mus musculus*; *Bt*, *Bos taurus*; *Gg*, *Gallus gallus*; *Xl*, *Xenopus laevis*; *Dr*, *Danio rerio*; *Dm*, *Drosophila melanogaster*; *Ca*, *Caenorhabditis elegans*) illustrates selected regions extracted from this figure. Red amino acids are involved in protein interaction, whereas blue amino acids contact membranes.

computational studies on functional interaction networks. Human RAF paralogs share evolutionarily conserved regions (Figure 1), which are functionally split into a regulatory N-terminal half, comprising a RAS-binding domain, a cysteine-rich domain, and a serine/threonine-rich region and a catalytic C-terminal half representing the kinase domain (Figure 2A). In the following, we will discuss the structure–function relationships of individual domains and motifs and their interactions with membrane lipids, RAS, 14-3-3, MEK1/2, and KSR1/2 (kinase suppressor of RAS 1/2).

RAS-binding domains

Signal transduction implies physical association of RAS proteins with their effectors and activation of individual signaling pathways. Effectors specifically interact with the active, GTP-bound form of RAS proteins. These interactions occur usually in response to extracellular signals and link them to downstream signaling pathways in all eukaryotes [26,43]. Effectors act as protein or lipid kinases, phospholipase, GEFs (guanine nucleotide exchange), GAPs (GTPase-activating proteins), and scaffold proteins [44–47]. There are two major groups of effectors: one contains RAS-binding domains (RBDs) and the other RAS association (RA) domains [48,49]. Mining in the UniProt database led us to the identification of 118 distinct human proteins containing RBDs and RA domains (Rezaei Adariani, Dvorsky, et al. unpublished data). Notably, both types of domains utilize critical determinants for the interaction with different RAS proteins, particularly the intermolecular β-sheets (see next section) [50]. Structural studies have provided deep insights into the binding modes and interaction specificities [51–53]. Detailed analysis of 16 RAS structures in complex with different RBD and RA-domain effectors has revealed that, in spite of low sequence similarity, their mode of interaction is well conserved [50]. Yet, the precise mechanism through which effector association with RAS proteins results in their activation is still unclear. It is, however, generally accepted that RAS proteins participate directly in the activation of their downstream effectors and do not simply mediate their recruitment to specific sites at the membrane [54].

A striking feature of RAS proteins is the plethora of possible interactions with a large number of effectors. Notably, RAS proteins change their conformation mainly at two highly mobile regions, designated as switch I (aa 30–40) and switch II (aa 60–68) [53,55]. Mainly in the GTP-bound form, the switch regions of the RAS proteins provide a platform for the association with effector proteins, especially through their RBDs or RA domains. This interaction appears to be a prerequisite for effector activation [49,50,56–58]. However, CRAF RBD and RALGDS (Ral guanine nucleotide dissociation stimulator)-RA domains share a similar ubiquitin-like fold and contact the switch I region via a similar binding mode. In contrast, PI3Kα (phosphoinositide 3-kinase α)-RBD, RASSF5 (RAS association domain-containing protein 5)-RA, and PLCε (phosphatidylinositol

Figure 2. Structural fingerprints for RAF kinase interactions with RAS and the membrane lipids.
Critical residues involved in protein interaction and membrane binding are depicted in red and blue, respectively. CR encompassing amino acids are shown at the upper panel. (**A**) Domain organization of RAF kinases with the typical conserved regions (CR1, CR2, and CR3) along with the functional domains, including the RBD, the CRD, and the kinase domain (KD). (**B**) Overlaid RBD structures of the RAF paralogs and the amino acids interacting with RAS and the membrane. BRAF RBD exhibits negative charges in positions 202 and 204. RAF RBD encompassing amino acids are boxed. (**C**) CRD structure of CRAF and the membrane-binding amino acids. RAF CRD encompassing amino acids are boxed. (**D**) 14-3-3 δ/ζ structure in complex with the CR2 peptide of CRAF along with interacting amino acids of CRAF and 14-3-3 paralogs. (**E**) Overlaid structures of CRAF and BRAF kinase domains' along with MEK-binding amino acids. (**F**) CC-SAM domain of KSR1 in complex with RBS domain of BRAF.

4,5-bisphosphate phosphodiesterase epsilon)-RA domains do not share sequence and structural similarity, but commonly associate with the switch regions, especially switch I [59–63].

RAF–RBD interactions with RAS proteins

Major studies were carried out in the late 1980s and 1990s with regard to RAS interaction with its effectors (reviewed in refs [52,64–69]). An interaction study of CRAF association with RRAS1 led to the identification of the first RBD (aa 51–131) [70]. Soon after CRAF binding to HRAS was reported to be GTP-dependent [28–31,71]. Within a year, the sites of interaction between HRAS and CRAF were determined [72] along with quantitative analysis of the binding affinity between them [73]. All of this occurred before the first structure revealed the CRAF RBD structure and its mode of binding to a RAS family member, RAP1A (RAS-related protein 1A) [74]. CRAF RBD consists of a five-strand mixed β-sheet (β1– β5) with an interrupted α-helix (α1) and two additional 3_{10}-helices (α2 and α3) (Figure 2B). Consistent with an earlier NMR determination [51], the RBD of CRAF has an ubiquitin fold (β1, β2, α1, β3, β4, α2, and β5). The β-strands are nearly identical with ubiquitin-like protein and α-helices are packed diagonally against a part of the β-sheet. To date, several RBD structures of all three human RAF paralogs have been determined (Table 1). Superposition of all three RBD structures revealed a high structural identity (Figure 2B).

1395

Table 1 Structures related to RAF kinases

Proteins and their complexes	PBD ID	Resolution (Å)	References
BRS			
BRAF-KSR1	5VYK	1.75	[75]
RBD			
RAP1A-GppNHp-CRAF RBD[1]	1C1Y	2.2	[59]
RAP1A(E30D/K31E)-GDP-CRAF RB(A85K/N71R)	3KUC	1.92	[76]
RAS-GDP-CRAF RBD(A85K)	3KUD	2.15	[76]
BRAF RBD	3NY5	1.99	Unpublished data
HRAS-GppNHp-CRAF RBD	4G0N	2.45	[77]
HRAS(Q61L)-GppNHp-CRAF RBD	4G3X	3.25	[77]
KRAS-GppNHp-ARAF RBD	2MSE	NMR	[54]
BRAF RBD	5J17	NMR	[58]
BRAF RBD-Rigosertib	5J18	NMR	[58]
BRAF RBD	5J2R	NMR	[58]
ARAF RBD	1WXM	NMR	Unpublished data
CRD			
CRAF CRD	1FAQ, 1FAR	NMR	[78]
CR2			
14-3-3-CRAF CR2	3CU8, 3NKX	2.4	[79]
14-3-3γ-CRAF CR2	3IQV	1.2	[79]
14-3-3γ-CRAF CR2	3O8I	2.0	[79]
14-3-3-CRAF CR2(S233/S259)	4FJ3	1.95	[80]
14-3-3-CRAF CR2-CN-A	4IHL	2.2	[81]
14-3-3γ-CRAF-CR2(S233/S259)	4IEA	1.7	[81]
14-3-3γ-CRAF CR2	3IQJ	1.15	[79]
Kinase domain[2]			
CRAF KD	3OMV	4	[79]
BRAF KD(V599E)	1UWJ	3.5	[82]
BRAF–MEK1	4MNE	2.84	[83]

[1]GppNHp is a non-hydrolyzable GTP analog.
[2]A large number of kinase structures in complex with small molecules are not included.

RAF RBDs bind to the switch I region (also known as the effector loop) of the RAS proteins by forming an intermolecular, antiparallel β-sheet (β1 and β2 of the RBD and β2 and β3 of RAS), which establishes a high degree of electrostatic complementarity across the binding interface [53,77,84,85]. RAF RBDs are mainly positively charged, whereas switch I regions of RAS proteins bear mainly negative charges. Among the 10 RAS-binding residues of RAF RBD (Figure 2B, red residues), Arg-59, Gln-66, Lys-84, and Arg-89 (CRAF numbering) contribute to the high binding affinity between RAS and RAF [86]. Genetic studies on *Drosophila melanogaster* have shown that Arg-89 is strongly involved in the RAS–RAF interaction both *in vivo* and *in vitro*. Its substitution for leucine (R89L) abolishes RAS association and consequently activation of CRAF [87]. The R89T mutation has been reported in breast cancer [88]. This mutation may impair RAS–CRAF interaction, since a conservative substitution of Arg-89 for lysine (R89K) disabled CRAF RBD binding to HRAS [89]. Collectively, a search in cancer databases showed that among the 10 RAS-binding in RAF paralogs, seven residues are mutated in human cancer (Supplementary Table S1).

Arg-59 represents a point of RAF paralog discrimination as ARAF, in contrast with BRAF and CRAF, contains a lysine (Lys-22) instead of arginine (Figure 1). CRAF(R59K) loses its proper binding to HRAS, whereas

1396

ARAF(K22R) gains a higher affinity for HRAS [90]. The substitution of the conserved Gln-66 among three RAF paralogs for histidine in CRAF and for proline in ARAF (aa 29) has been reported in breast and colorectal carcinoma [91,92]. Lys-84, which is conserved in all species (Figure 1), is responsible for effector specificity and favors the complex formation of CRAF with HRAS in preference to RAP1A. Its substitution for alanine strongly reduces its binding affinity to RAS proteins [86,93]. An interesting observation is that A85K mutation tremendously increases CRAF binding not only to GTP-bound HRAS [87] but also to GDP-bound HRAS [94].

Membrane association of RAF RBDs

Cellular membranes play a critical role in the localization and orientation of protein complexes and in fine-tuning of protein functions [95]. As outlined above, the activity of RAS and RAF paralogs is regulated through different parameters, including membrane association. Analysis of dynamic interactions between KRAS4B and lipid bilayer membrane has revealed that association of ARAF RBD with active KRAS4B not only reorients KRAS4B at the membrane surface but also facilitates membrane binding of ARAF RBD itself [54]. This is in agreement with previous observation that disrupted RAS-association of ARAF full-length disturbs its membrane localization when substituting Arg-52 for leucine (as well as R89L in CRAF) [96,97]. Four basic residues, Lys-28, Lys-66, Arg-68, and Lys-69 (ARAF numbering), are engaged in lipid binding, two of which are identical in RAF kinases, while the other two are variable (Figure 2B). Notably, mutations of Lys-28, Arg-52, Lys-66, Arg-68, and Lys-69 in ARAF have been reported in human cancer [88,98–100]. BRAF strikingly contains acidic residues at positions equivalent to Lys-66 and Arg-68 (not only in human but also in other species; Figure 1), which most probably repel membrane lipids. BRAF and CRAF studies have shown that they significantly differ regarding their interactions with HRAS [101]. BRAF binds RAS with higher affinities and does not discriminate between farnesylated and nonfarnesylated HRAS when compared with CRAF. The farnesyl moiety of HRAS has been reported to promote CRAF CRD (cysteine-rich domain) association with HRAS (see the next section).

Cysteine-rich domain

The second domain following RBD in the conserved region 1 (CR1) is a CRD (also called cysteine-rich region or C-kinase homologous domain 1), which is connected through a short flexible linker [102,103]. CRD shows high conservation among different species (Figure 1) and appears to bind membrane lipids via residues 143–160 (Figure 2C), which are conserved among different species (Figure 1). Point mutations of Arg-143 to tryptophan, glutamine, or leucine in CRAF and the equivalent Arg-239 in BRAF to glutamine have been identified in breast and lung carcinoma as well as in melanoma [88,104]. Substitution of Arg-103 and Lys-104 in ARAF CRD (Arg-143 and Lys-144 in CRAF, respectively) for alanine has been shown to disrupt ARAF membrane binding and results in its localization in the cytosol [97]. Two very recent computational studies have analyzed dynamic interaction of KRAS4B with the CRAF RBD–CRD tandem at anionic membranes and proposed how the RAF–RAS complex is regulated at the membrane interface [103,105]. Accordingly, RAF association with the membrane starts with direct binding of RBD to GTP-bound RAS followed by CRD association to the phosphatidylserine-containing liposomes. CRD–membrane interaction is stabilized, in addition to basic residues, by four highly conserved hydrophobic amino acids, Thr-145, Leu-147, Leu-149, Phe-158 Leu-159, Leu160, and Asp-161 (Figure 1). Numerous studies have reported that CRD also binds RAS with low affinity [56,101,105–116]. This may lead to a competitive mechanism between membrane binding of CRAF CRD and its association with KRAS4B [103]. Unlike others reports, these two studies have shown that CRD is in the vicinity, but does contact RAS and/or its farnesyl moiety [103,105]. Membrane binding of CRD stabilizes RAS–RAF interaction and, thus, facilitates RAF activation. Farnesylation and carboxymethylation of Cys-186 of HRAS together with hydrophobic amino acids of CRAF CRD have been suggested to strengthen HRAS–CRAF interaction [116]. CRDs contain two functional zinc-binding motifs and bind membrane lipids such as phosphatidic acid and phosphatidylserine [58,117–119]. Substitution of two invariant zinc-binding cysteines for serines (C165S/C168S) [96,120] and three basic residues for alanine (Agr-143, Lys-144, and Lys-148) (Figure 2C) diminishes HRAS-dependent activation of CRAF and CRD association with phosphatidylserine-containing liposomes [121].

Several studies have previously shown that CRAF CRD undergoes direct interaction with HRAS, which appears to be enhanced by the farnesyl moiety if using farnesylated RAS [57,101,103,105,107,113,116]. In contrast with RAF RBD, which binds to GTP-bound RAS, HRAS–CRAF CRD interaction is outside the switch regions of HRAS and thus independent of its nucleotide-bound state. This interaction is compromised if

Leu-149 and Phe-151 in CRAF CRD were substituted for threonine and glutamine (L149T/F151Q), respectively [113]. L149F substitution in BRAF (L245F) has been detected in melanoma and cardiofaciocutaneous syndrome (NSEuroNet database) (COSMIC database) [122], which may potentiate BRAF CRD interaction with RAS and/or membrane.

RAS–RAF interactions at the membrane interface

Cellular membranes play a critical role in the localization and orientation of protein complexes and in fine-tuning of protein functions [95]. As outlined above, the diversity of RAS and RAF paralogs is regulated through different parameters, including membrane association. For example, orientation of the RAS G domain on the membrane (for more details, see refs [54,123–130]) and intrinsic membrane-binding site of RAF, such as CRD of RAF (see above). In addition, NMR measurements of nanodisc-tethered complexes of isotopically labeled KRAS4B-GTP with ARAF RBD have recently shown that ARAF RBD directly contacts the anionic membrane surface, while KRAS4B-GTP adopts a new semi-exposed orientation intermediate between the exposed and occluded orientations [54]. The only residue of the KRAS4B G domain contacting the membrane is R41, which is conserved in numerous RAS proteins. ARAF residues engaged in membrane binding (Lys-66, Arg-68, and Lys-69; Figure 1B) are highly conserved in ARAF and CRAF proteins from different organisms except *Xenopous laevis* and *Caenorhabditis elegans* (Figure 1). These basic residues remarkably are acidic in BRAF proteins, suggesting distinct mechanistic differences between the RAF paralogs. In contrast, membrane-binding residues of RAF CRD are conserved within various species, which may stabilize RAS–RAF interaction and thus facilitates RAF activation.

Serine/threonine-rich region

This very short region, also called conserved region 2 (CR2; Figure 2A), is a central module in negative regulation of RAF function. Its phosphorylation at Ser-259 (CRAF numbering) followed by 14-3-3 binding locks RAF kinases in a so-called autoinhibited state [131] that blocks both RAS binding and RAF kinase activity [132,133]. CR2 is the substrate of PKA (protein kinase A) and PKB (protein kinase B)/AKTs [134–136]. Gain-of-function mutations in this region are associated with the development of tumors and RASopathies [137,138]. Point mutations in CR2, including R256S, S257L, S259F, and T260R, cause cancer or are associated with developmental disorders (Supplementary Table S2), e.g. hypertrophic cardiomyopathy in Noonan syndrome [79,137–139].

Phosphorylation of RAF paralogs at Ser-259 (CRAF numbering) leads to the association of 14-3-3 proteins and the stabilization of RAF paralogs in their inactive state [79,88,137–143]. 14-3-3 proteins are ubiquitous adaptor proteins, which serve as scaffold proteins in many cellular functions [79,144]. In humans, seven distinct genes encode for nine paralogs (α, β, γ, δ, ε, η, σ, τ, and ζ), which adopt a homo-/heterodimeric [145,146], W-like structure with the two concave surfaces facing the same side of the molecule, whereby the dimer forms a binding groove [147]. They selectively bind peptide motifs, such as RSXpSXP (single amino acids code; pS, phosphor-serine; X, any amino acid); arginine, serine, and proline residues, which are important for high-affinity interactions [148]. This motif is identical in RAF kinases (Figures 1 and 2D) regardless of the binding sites. Phosphorylated serines in CRAF, including Ser-259 and Ser-621, already identified in 1993 [149] are key phosphorylation sites in two distinct motifs in the RAF kinases (Figure 2D) [144]. In contrast to pSer-259, an inhibitory 14-3-3-binding site [79,131,133], 14-3-3 association with pSer-621 in a conserved region (CR3) stabilizes the active state of the RAF kinases [147]. All 14-3-3 paralogs are able to modulate RAF kinase function due to invariant RAF-binding residues and similar tertiary structure of all 14-3-3 proteins (Figure 2D).

Catalytic kinase domain

The molecular mechanism for the RAF activation in the cell involves a series of complex processes that lead to conformational changes, dimerization, and ultimately activation of the kinase domain [150]. The latter constitutes a major part of CR3, which has all known signatures of protein kinases [151], including the two lobes moving relative to each other and consequently opening or closing the catalytic cleft. In an open form, the small lobe with an antiparallel β-sheet structure binds and orients ATP. In the closed form, the α-helical large lobe binds the protein substrates, such as ubiquitously expressed MEK1/2 (Figure 2E). As RAF dimerization is a key step in pathway activation, the RAF kinases activate MEK1/2 by phosphorylating them at two serines (Ser-218/Ser-222 in MEK1) in the catalytic domain [151,152]. An inspection of amino acid sequences of RAF

kinases from different organisms showed identical MEK-binding residues (Figure 1) [153]. However, it is known that RAF kinases differ in their kinase activities. BRAF followed by CRAF and ARAF exhibits the highest MEK activation [35,36]. This can be attributed to dimerization-induced allosteric regulation of protein kinases [41]. RAF kinases form both homodimers and heterodimers, which is crucial for substrate recognition, catalytic efficiency, and substrate specificity [35]. The CRAF/BRAF heterodimers represent the most effective form for MEK phosphorylation when compared with any form of monomers or homodimers [38]. The structure of BRAF kinase domain and MEK1 is insensitive to BRAF dimerization but sensitive to the active conformation of the BRAF kinase and MEK1 phosphorylation, which in turn leads to destabilization of the RAF–MEK1 heterotetrameric complex [83].

Approximately 200 BRAF mutations have been identified in human tumors (see Supplementary Table S1). Based on their mechanism of activation, they can be categorized into three groups corresponding to their sensitivity to inhibitors. Group one mutations (e.g. V600E/K/D/R) signal as monomers and have been suggested to act in a RAS-independent manner [154,155]. Therefore, they are sensitive to BRAF monomer inhibitors. Group 2 mutations (e.g. K601E or G469A, R509H) signal as constitutive dimers and are RAS-independent; hence, they are resistant to RAF inhibitor vemurafenib and may be sensitive to novel MEK inhibitors or RAF dimer inhibitors [154,156]. However, group three mutations have impaired kinase activity (D594G/N) or have low kinase activity (G466V/E). This group is RAS-dependent, and by increasing their binding to RAS or activation of receptors activate ERK (extracellular signal-regulated kinase) signaling [155].

Scaffolding RAF kinases by KSR1/2

Scaffolding proteins play an essential role in regulating the MAPK pathway activity [157–159]. MAPK scaffold proteins especially are dynamic entities that (i) directly interact with multiple components of the MAPK signaling complex, (ii) consolidate or sequester protein interactions to physically insulate the MAPK pathway to specific cellular locations, and (iii) regulate signal strength and stimulus-specific responses to efficiently transmit MAPK signals in a spatiotemporal manner and narrow its actions [157,160,161]. Scaffold proteins regulating MAPK signaling include KSR1/2 [162–164], MORG1 [165], MP1 [166], paxillin [167], β-arrestin [168], MEKK1 [169], and FHL1 [170]. KSR1/2, which belongs to the best characterized MAPK scaffold proteins, controls the signaling strength and duration of the RAF/MEK/ERK complex at the plasma membrane [157,159].

KSR1/2 are pseudokinases homologous to RAF kinases but lack the ability to interact with RAS proteins [83,171]. KSR co-ordinates the assembly of a multiprotein complex containing RAF, MEK, and ERK and facilitates signal transduction from RAS to ERK [172]. Nguyen et al. [173] did not observe that KSR binds to CRAF or BRAF *in vivo*. However, Lavoie et al. have shown that the selective heterodimerization of BRAF with KSR1 directly binds to a BRAF-specific region (BRS) at the N-terminus of BRAF through the coiled-coil/sterile α-motif (CC-SAM). BRS (∼60 aa) forms an α-hairpin which consists of two antiparallel α-helices connected by a short turn (Figure 2F) [75].

In BRAF, I666R mutation disabled binding to MEK1 as well as prevented MEK1 phosphorylation, and in KSR1, W831R mutation abolished MEK1 binding [75]. The crystal structure of the KSR2 kinase domain bound to MEK1 through activation segments and C-lope αG helix reveals that residues Ser-218 and Ser-222 are located at the heterodimer interface and are masked by KSR2, making them inaccessible for RAF phosphorylation [174]. Isolated MEK1–BRAF–14-3-3 complexes proved the stable BRAF–MEK1 interaction in the presence of 14-3-3 [83]. Interestingly, MEK promotes, independently of its catalytic function, BRAF-KSR1/2 heterodimerization and allosterically activates BRAF [75]. A recent study has shown that a direct binding of tumor suppressor DIRAS3 with KSR1 interferes with RAS-induced cell transformation. DIRAS3 either enhances homodimerization of KSR1 or recruits KSR1 to the RAS–CRAF complex and thereby sequesters CRAF from binding to BRAF [175].

Conclusions

Emerging evidence indicates that sequential RAS binding of the two N-terminal RAF domains, first by RBD and then followed by CRD at the membrane, induces a conformational change in RAF and results in the release of the C-terminal kinase domain. This mechanism requires additional functions, including dimerization [35,95,160,161,176–180]. Lipid membranes act not only as a platform for the assembly of protein complexes but also as a scaffold to stabilize protein–protein interactions and potentiate the signal transduction [35,36,54]. Future analysis of protein interaction networks along with the network reconstitution at liposomes using purified proteins will provide further mechanistic insights into RAS-mediated RAF activation.

RAF kinases are known to regulate, in addition to MEK1/2, also adenylyl cyclase, ASK1, calcineurin, CDC25, DMPK, MST2, MYPT, Rb, ROCK, troponin T, and vimentin, thereby controlling different processes, such as proliferation, differentiation, apoptosis, and contraction and motility, respectively [13,14,181–183]. However, the mechanisms how RAF kinases regulate these proteins still need to be addressed in greater detail in a cell-type-specific manner.

Abbreviations

BRS, BRAF-specific region; CC-SAM, coiled-coil/sterile α-motif; CR2, conserved region 2; CRD, cyteine-rich domain; ERK, extracellular signal-regulated kinase; MAPK, mitogen-activated protein kinase; MEK, MAPK/ERK kinase; RA domain, RAS association domain; RAF, rapidly accelerated fibrosarcoma; RAP, RAS-related protein; RAS, rat sarcoma; RASSF, RAS association domain family proteins; RHEB, RAS homolog enriched in brain; RBD, RAS-binding domain; KSR, kinase suppressor of RAS.

Funding

Acknowledgements

Competing Interests

The Authors declare that there are no competing interests associated with the manuscript.

References

1   Rapp, U.R., Goldsborough, M.D., Mark, G.E., Bonner, T.I., Groffen, J., Reynolds, Jr, F.H. et al. (1983) Structure and biological activity of v-raf, a unique oncogene transduced by a retrovirus. *Proc. Natl Acad. Sci. U.S.A.* **80**, 4218–4222 https://doi.org/10.1073/pnas.80.14.4218

2   Bonner, T.I., Kerby, S.B., Sutrave, P., Gunnell, M.A., Mark, G. and Rapp, U.R. (1985) Structure and biological activity of human homologs of the raf/mil oncogene. *Mol. Cell. Biol.* **5**, 1400–1407 https://doi.org/10.1128/MCB.5.6.1400

3   Huleihel, M., Goldsborough, M., Cleveland, J., Gunnell, M., Bonner, T. and Rapp, U.R. (1986) Characterization of murine A-raf, a new oncogene related to the v-raf oncogene. *Mol. Cell. Biol.* **6**, 2655–2662 https://doi.org/10.1128/MCB.6.7.2655

4   Ikawa, S., Fukui, M., Ueyama, Y., Tamaoki, N., Yamamoto, T. and Toyoshima, K. (1988) B-raf, a new member of the raf family, is activated by DNA rearrangement. *Mol. Cell. Biol.* **8**, 2651–2654 https://doi.org/10.1128/MCB.8.6.2651

5   Han, M., Golden, A., Han, Y. and Sternberg, P.W. (1993) *C. elegans* lin-45 raf gene participates in let-60 ras-stimulated vulval differentiation. *Nature* **363**, 133–140 https://doi.org/10.1038/363133a0

6   Mark, G.E., MacIntyre, R.J., Digan, M.E., Ambrosio, L. and Perrimon, N. (1987) *Drosophila melanogaster* homologs of the raf oncogene. *Mol. Cell. Biol.* **7**, 2134–2140 https://doi.org/10.1128/MCB.7.6.2134

7   Hsu, V., Zobel, C.L., Lambie, E.J., Schedl, T. and Kornfeld, K. (2002) *Caenorhabditis elegans* lin-45 raf is essential for larval viability, fertility and the induction of vulval cell fates. *Genetics* **160**, 481–492 PMID:11861555

8   Morrison, D.K. (1990) The Raf-1 kinase as a transducer of mitogenic signals. *Cancer Cells* **2**, 377–382 PMID:2150916

9   Avruch, J., Khokhlatchev, A., Kyriakis, J.M., Luo, Z., Tzivion, G., Vavvas, D. et al. (2001) Ras activation of the Raf kinase: tyrosine kinase recruitment of the MAP kinase cascade. *Recent Prog. Horm. Res.* **56**, 127–155 https://doi.org/10.1210/rp.56.1.127

10 Wellbrock, C., Karasarides, M. and Marais, R. (2004) The RAF proteins take centre stage. *Nat. Rev. Mol. Cell Biol.* **5**, 875–885 https://doi.org/10.1038/nrm1498

11 Leicht, D.T., Balan, V., Kaplun, A., Singh-Gupta, V., Kaplun, L., Dobson, M. et al. (2007) Raf kinases: function, regulation and role in human cancer. *Biochim. Biophys. Acta* **1773**, 1196–1212 https://doi.org/10.1016/j.bbamcr.2007.05.001

12 Osborne, J.K., Zaganjor, E. and Cobb, M.H. (2012) Signal control through Raf: in sickness and in health. *Cell Res.* **22**, 14–22 https://doi.org/10.1038/cr.2011.193

13 Desideri, E., Cavallo, A.L. and Baccarini, M. (2015) Alike but different: RAF paralogs and their signaling outputs. *Cell* **161**, 967–970 https://doi.org/10.1016/j.cell.2015.04.045

14 Niault, T.S. and Baccarini, M. (2010) Targets of Raf in tumorigenesis. *Carcinogenesis* **31**, 1165–1174 https://doi.org/10.1093/carcin/bgp337

15 Sanges, C., Scheuermann, C., Zahedi, R.P., Sickmann, A., Lamberti, A., Migliaccio, N. et al. (2012) Raf kinases mediate the phosphorylation of eukaryotic translation elongation factor 1A and regulate its stability in eukaryotic cells. *Cell Death Dis.* **3**, e276 https://doi.org/10.1038/cddis.2012.16

PORTLAND
PRESS

16 An, S., Yang, Y., Ward, R., Liu, Y., Guo, X.-X. and Xu, T.-R. (2015) A-Raf: a new star of the family of raf kinases. *Crit. Rev. Biochem. Mol. Biol.* **50**, 520–531 https://doi.org/10.3109/10409238.2015.1102858

17 Downward, J. (2003) Targeting RAS signalling pathways in cancer therapy. *Nat. Rev. Cancer* **3**, 11–22 https://doi.org/10.1038/nrc969

18 Maurer, G., Tarkowski, B. and Baccarini, M. (2011) Raf kinases in cancer-roles and therapeutic opportunities. *Oncogene* **30**, 3477–3488 https://doi.org/10.1038/onc.2011.160

19 Roring, M. and Brummer, T. (2012) Aberrant B-Raf signaling in human cancer — 10 years from bench to bedside. *Crit. Rev. Oncog.* **17**, 97–121 https://doi.org/10.1615/CritRevOncog.v17.i1.70

20 Allanson, J.E., Annerén, G., Aoki, Y., Armour, C.M., Bondeson, M.-L., Cave, H. et al. (2011) Cardio-facio-cutaneous syndrome: does genotype predict phenotype? *Am. J. Med. Genet. C Semin. Med. Genet.* **157**, 129–135 https://doi.org/10.1002/ajmg.c.30295

21 Tartaglia, M., Gelb, B.D. and Zenker, M. (2011) Noonan syndrome and clinically related disorders. *Best Pract. Res. Clin. Endocrinol. Metab.* **25**, 161–179 https://doi.org/10.1016/j.beem.2010.09.002

22 Vandamme, D., Herrero, A., Al-Mulla, F. and Kolch, W. (2014) Regulation of the MAPK pathway by raf kinase inhibitory protein. *Crit. Rev. Oncogenesis* **19**, 405–415 https://doi.org/10.1615/CritRevOncog.2014011922

23 Morrison, D.K. and Cutler, R.E. (1997) The complexity of Raf-1 regulation. *Curr. Opin. Cell Biol.* **9**, 174–179 https://doi.org/10.1016/S0955-0674(97)80060-9

24 Dhillon, A.S., Hagan, S., Rath, O. and Kolch, W. (2007) MAP kinase signalling pathways in cancer. *Oncogene* **26**, 3279–3290 https://doi.org/10.1038/sj.onc.1210421

25 Roberts, P.J. and Der, C.J. (2007) Targeting the Raf-MEK-ERK mitogen-activated protein kinase cascade for the treatment of cancer. *Oncogene* **26**, 3291–3310 https://doi.org/10.1038/sj.onc.1210422

26 Karnoub, A.E. and Weinberg, R.A. (2008) Ras oncogenes: split personalities. *Nat. Rev. Mol. Cell Biol.* **9**, 517–531 https://doi.org/10.1038/nrm2438

27 Rauch, N., Rukhlenko, O.S., Kolch, W. and Kholodenko, B.N. (2016) MAPK kinase signalling dynamics regulate cell fate decisions and drug resistance. *Curr. Opin. Struct. Biol.* **41**, 151–158 https://doi.org/10.1016/j.sbi.2016.07.019

28 Zhang, X.-F., Settleman, J., Kyriakis, J.M., Takeuchi-Suzuki, E., Elledge, S.J., Marshall, M.S. et al. (1993) Normal and oncogenic p21ras proteins bind to the amino-terminal regulatory domain of c-Raf-1. *Nature* **364**, 308–313 https://doi.org/10.1038/364308a0

29 Vojtek, A.B., Hollenberg, S.M. and Cooper, J.A. (1993) Mammalian Ras interacts directly with the serine/threonine kinase Raf. *Cell* **74**, 205–214 https://doi.org/10.1016/0092-8674(93)90307-C

30 Moodie, S.A., Willumsen, B.M., Weber, M.J. and Wolfman, A. (1993) Complexes of Ras.GTP with Raf-1 and mitogen-activated protein kinase. *Science* **260**, 1658–1661 https://doi.org/10.1126/science.8503013

31 Warne, P.H., Viciana, P.R. and Downward, J. (1993) Direct interaction of Ras and the amino-terminal region of Raf-1 in vitro. *Nature* **364**, 352–355 https://doi.org/10.1038/364352a0

32 Van Aelst, L., Barr, M., Marcus, S., Polverino, A. and Wigler, M. (1993) Complex formation between RAS and RAF and other protein kinases. *Proc. Natl Acad. Sci. U.S.A.* **90**, 6213–6217 https://doi.org/10.1073/pnas.90.13.6213

33 Kyriakis, J.M., App, H., Zhang, X.-F., Banerjee, P., Brautigan, D.L., Rapp, U.R. et al. (1992) Raf-1 activates MAP kinase-kinase. *Nature* **358**, 417–421 https://doi.org/10.1038/358417a0

34 Matallanas, D., Birtwistle, M., Romano, D., Zebisch, A., Rauch, J., von Kriegsheim, A. et al. (2011) Raf family kinases: old dogs have learned new tricks. *Genes Cancer* **2**, 232–260 https://doi.org/10.1177/1947601911407323

35 Baljuls, A., Kholodenko, B.N. and Kolch, W. (2013) It takes two to tango — signalling by dimeric Raf kinases. *Mol. Biosyst.* **9**, 551–558 https://doi.org/10.1039/C2MB25393C

36 Marais, R., Light, Y., Paterson, H.F., Mason, C.S. and Marshall, C.J. (1997) Differential regulation of Raf-1, A-Raf, and B-Raf by oncogenic ras and tyrosine kinases. *J. Biol. Chem.* **272**, 4378–4383 https://doi.org/10.1074/jbc.272.7.4378

37 Leicht, D.T., Balan, V., Zhu, J., Kaplun, A., Bronisz, A., Rana, A. et al. (2013) MEK-1 activates C-Raf through a Ras-independent mechanism. *Biochim. Biophys. Acta* **1833**, 976–986 https://doi.org/10.1016/j.bbamcr.2013.01.015

38 Rushworth, L.K., Hindley, A.D., O'Neill, E. and Kolch, W. (2006) Regulation and role of Raf-1/B-Raf heterodimerization. *Mol. Cell. Biol.* **26**, 2262–2272 https://doi.org/10.1128/MCB.26.6.2262-2272.2006

39 Rodriguez-Viciana, P., Oses-Prieto, J., Burlingame, A., Fried, M. and McCormick, F. (2006) A phosphatase holoenzyme comprised of Shoc2/Sur8 and the catalytic subunit of PP1 functions as an M-Ras effector to modulate Raf activity. *Mol. Cell* **22**, 217–230 https://doi.org/10.1016/j.molcel.2006.03.027

40 Freeman, A.K., Ritt, D.A. and Morrison, D.K. (2013) The importance of Raf dimerization in cell signaling. *Small GTPases* **4**, 180–185 https://doi.org/10.4161/sgtp.26117

41 Lavoie, H., Li, J.J., Thevakumaran, N., Therrien, M. and Sicheri, F. (2014) Dimerization-induced allostery in protein kinase regulation. *Trends Biochem. Sci.* **39**, 475–486 https://doi.org/10.1016/j.tibs.2014.08.004

42 Lavoie, H. and Therrien, M. (2015) Regulation of RAF protein kinases in ERK signalling. *Nat. Rev. Mol. Cell Biol.* **16**, 281–298 https://doi.org/10.1038/nrm3979

43 Gutierrez-Erlandsson, S., Herrero-Vidal, P., Fernandez-Alfara, M., Hernandez-Garcia, S., Gonzalo-Flores, S., Mudarra-Rubio, A. et al. (2013) R-RAS2 overexpression in tumors of the human central nervous system. *Mol. Cancer* **12**, 127 https://doi.org/10.1186/1476-4598-12-127

44 Herrmann, C. (2003) Ras-effector interactions: after one decade. *Curr. Opin. Struct. Biol.* **13**, 122–129 https://doi.org/10.1016/S0959-440X(02)00007-6

45 Castellano, E. and Downward, J. (2010) Role of RAS in the regulation of PI 3-kinase. *Curr. Top. Microbiol. Immunol.* **346**, 143–169 PMID:20563706

46 Rajalingam, K., Schreck, R., Rapp, U.R. and Albert, S. (2007) Ras oncogenes and their downstream targets. *Biochim. Biophys. Acta* **1773**, 1177–1195 https://doi.org/10.1016/j.bbamcr.2007.01.012

47 Nakhaei-Rad, S., Haghighi, F., Nouri, P., Rezaei Adariani, S., Lissy, J., Kazemein Jasemi, N.S. et al. (2018) Structural fingerprints, interactions, and signaling networks of RAS family proteins beyond RAS isoforms. *Crit. Rev. Biochem. Mol. Biol.* **53**, 130–156 https://doi.org/10.1080/10409238.2018.1431605

48 Repasky, G.A., Chenette, E.J. and Der, C.J. (2004) Renewing the conspiracy theory debate: does Raf function alone to mediate Ras oncogenesis? *Trends Cell Biol.* **14**, 639–647 https://doi.org/10.1016/j.tcb.2004.09.014

1401

49   Wohlgemuth, S., Kiel, C., Krämer, A., Serrano, L., Wittinghofer, F. and Herrmann, C. (2005) Recognizing and defining true Ras binding domains I: biochemical analysis. *J. Mol. Biol.* **348**, 741–758 https://doi.org/10.1016/j.jmb.2005.02.048

50   Nakhaeizadeh, H., Amin, E., Nakhaei-Rad, S., Dvorsky, R. and Ahmadian, M.R. (2016) The RAS-effector interface: isoform-specific differences in the effector binding regions. *PLoS ONE* **11**, e0167145 https://doi.org/10.1371/journal.pone.0167145

51   Patel, M. and Côté, J.-F. (2013) Ras GTPases' interaction with effector domains: breaking the families' barrier. *Commun. Integr. Biol.* **6**, e24298 https://doi.org/10.4161/cib.24298

52   Herrmann, C. and Nassar, N. (1996) Ras and its effectors. *Prog. Biophys. Mol. Biol.* **66**, 1–41 https://doi.org/10.1016/S0079-6107(96)00015-6

53   Mott, H.R. and Owen, D. (2015) Structures of Ras superfamily effector complexes: what have we learnt in two decades? *Crit. Rev. Biochem. Mol. Biol.* **50**, 85–133 https://doi.org/10.3109/10409238.2014.999191

54   Mazhab-Jafari, M.T., Marshall, C.B., Smith, M.J., Gasmi-Seabrook, G.M., Stathopulos, P.B., Inagaki, F. et al. (2015) Oncogenic and RASopathy-associated K-RAS mutations relieve membrane-dependent occlusion of the effector-binding site. *Proc. Natl Acad. Sci. U.S.A.* **112**, 6625–6630 https://doi.org/10.1073/pnas.1419895112

55   Vetter, I.R. and Wittinghofer, A. (2001) The guanine nucleotide-binding switch in three dimensions. *Science* **294**, 1299–1304 https://doi.org/10.1126/science.1062023

56   Drugan, J.K., Khosravi-Far, R., White, M.A., Der, C.J., Sung, Y.-J., Hwang, Y.-W. et al. (1996) Ras interaction with two distinct binding domains in Raf-1 5 be required for Ras transformation. *J. Biol. Chem.* **271**, 233–237 https://doi.org/10.1074/jbc.271.1.233

57   Thapar, R., Williams, J.G. and Campbell, S.L. (2004) NMR characterization of full-length farnesylated and non-farnesylated H-Ras and its implications for Raf activation. *J. Mol. Biol.* **343**, 1391–1408 https://doi.org/10.1016/j.jmb.2004.08.106

58   Athuluri-Divakar, S.K., Vasquez-Del Carpio, R., Dutta, K., Baker, S.J., Cosenza, S.C., Basu, I. et al. (2016) A small molecule RAS-mimetic disrupts RAS association with effector proteins to block signaling. *Cell* **165**, 643–655 https://doi.org/10.1016/j.cell.2016.03.045

59   Nassar, N., Horn, G., Herrmann, C., Scherer, A., McCormick, F. and Wittinghofer, A. (1995) The 2.2 A crystal structure of the Ras-binding domain of the serine/threonine kinase c-Raf1 in complex with Rap1A and a GTP analogue. *Nature* **375**, 554–560 https://doi.org/10.1038/375554a0

60   Huang, L., Hofer, F., Martin, G.S. and Kim, S.-H. (1998) Structural basis for the interaction of Ras with RalGDS. *Nat. Struct. Biol.* **5**, 422–426 https://doi.org/10.1038/nsb0698-422

61   Stieglitz, B., Bee, C., Schwarz, D., Yildiz, O., Moshnikova, A., Khokhlatchev, A. et al. (2008) Novel type of Ras effector interaction established between tumour suppressor NORE1A and Ras switch II. *EMBO J.* **27**, 1995–2005 https://doi.org/10.1038/emboj.2008.125

62   Pacold, M.E., Suire, S., Perisic, O., Lara-Gonzalez, S., Davis, C.T., Walker, E.H. et al. (2000) Crystal structure and functional analysis of Ras binding to its effector phosphoinositide 3-kinase gamma. *Cell* **103**, 931–943 https://doi.org/10.1016/S0092-8674(00)00196-3

63   Bunney, T.D., Harris, R., Gandarillas, N.L., Josephs, M.B., Roe, S.M., Sorli, S.C. et al. (2006) Structural and mechanistic insights into ras association domains of phospholipase C epsilon. *Mol. Cell* **21**, 495–507 https://doi.org/10.1016/j.molcel.2006.01.008

64   Marshall, M.S. (1993) The effector interactions of p21ras. *Trends Biochem. Sci.* **18**, 250–254 https://doi.org/10.1016/0968-0004(93)90175-M

65   Wittinghofer, A. and Herrmann, C. (1995) Ras-effector interactions, the problem of specificity. *FEBS Lett.* **369**, 52–56 https://doi.org/10.1016/0014-5793(95)00667-X

66   Marshall, C.J. (1996) Ras effectors. *Curr. Opin. Cell Biol.* **8**, 197–204 https://doi.org/10.1016/S0955-0674(96)80066-4

67   Wittinghofer, A. and Nassar, N. (1996) How Ras-related proteins talk to their effectors. *Trends Biochem. Sci.* **21**, 488–491 https://doi.org/10.1016/S0968-0004(96)10064-5

68   Wittinghofer, A. (1998) Signal transduction via Ras. *Biol. Chem.* **379**, 933–937 PMID:9792425

69   Corbett, K.D. and Alber, T. (2001) The many faces of Ras: recognition of small GTP-binding proteins. *Trends Biochem. Sci.* **26**, 710–716 https://doi.org/10.1016/S0968-0004(01)01974-0

70   Spaargaren, M., Martin, G.A., McCormick, F., Fernandez-Sarabia, M.J. and Bischoff, J.R. (1994) The Ras-related protein R-ras interacts directly with Raf-1 in a GTP-dependent manner. *Biochem. J.* **300**, 303–307 https://doi.org/10.1042/bj3000303

71   Koide, H., Satoh, T., Nakafuku, M. and Kaziro, Y. (1993) GTP-dependent association of Raf-1 with Ha-Ras: identification of Raf as a target downstream of Ras in mammalian cells. *Proc. Natl Acad. Sci. U.S.A.* **90**, 8683–8686 https://doi.org/10.1073/pnas.90.18.8683

72   Barnard, D., Diaz, B., Hettich, L., Chuang, E., Zhang, X.F., Avruch, J. et al. (1995) Identification of the sites of interaction between c-Raf-1 and Ras-GTP. *Oncogene* **10**, 1283–1290 PMID:7731678

73   Herrmann, C., Martin, G.A. and Wittinghofer, A. (1995) Quantitative analysis of the complex between p21 and the ras-binding domain of the human raf-1 protein kinase. *J. Biol. Chem.* **270**, 2901–2905 https://doi.org/10.1074/jbc.270.7.2901

74   Nassar, N., Horn, G., Herrmann, C., Block, C., Janknecht, R. and Wittinghofer, A. (1996) Ras/Rap effector specificity determined by charge reversal. *Nat. Struct. Biol.* **3**, 723–729 https://doi.org/10.1038/nsb0896-723

75   Lavoie, H., Sahmi, M., Maisonneuve, P., Marullo, S.A., Thevakumaran, N., Jin, T. et al. (2018) MEK drives BRAF activation through allosteric control of KSR proteins. *Nature* **554**, 549–553 https://doi.org/10.1038/nature25478

76   Filchtinski, D., Sharabi, O., Rüppel, A., Vetter, I.R., Herrmann, C. and Shifman, J.M. (2010) What makes Ras an efficient molecular switch: a computational, biophysical, and structural study of Ras-GDP interactions with mutants of Raf. *J Mol Biol.* **399**, 422–435 https://doi.org/10.1016/j.jmb.2010.03.046

77   Fetics, S.K., Guterres, H., Kearney, B.M., Buhrman, G., Ma, B., Nussinov, R. et al. (2015) Allosteric effects of the oncogenic RasQ61L mutant on Raf-RBD. *Structure* **23**, 505–516 https://doi.org/10.1016/j.str.2014.12.017

78   Mott, H.R., Carpenter, J.W., Zhong, S., Ghosh, S., Bell, R.M. and Campbell, S.L. (1996) The solution structure of the Raf-1 cysteine-rich domain: a novel ras and phospholipid binding site. *Proc. Natl Acad. Sci.* **93**, 8312–8317 https://doi.org/10.1073/pnas.93.16.8312

79   Molzan, M., Schumacher, B., Ottmann, C., Baljuls, A., Polzien, L., Weyand, M. et al. (2010) Impaired binding of 14-3-3 to C-RAF in Noonan syndrome suggests new approaches in diseases with increased Ras signaling. *Mol. Cell. Biol.* **30**, 4698–4711 https://doi.org/10.1128/MCB.01636-09

80   Molzan, M. and Ottmann, C. (2012) Synergistic binding of the phosphorylated S233-and S259-binding sites of C-RAF to one 14-3-3ζ dimer. *J. Mol. Biol.* **423**, 486–495 https://doi.org/10.1016/j.jmb.2012.08.009

81   Molzan, M., Kasper, S., Röglin, L., Skwarczynska, M., Sassa, T., Inoue, T. et al. (2013) Stabilization of physical RAF/14-3-3 interaction by cotylenin A as treatment strategy for RAS mutant cancers. *ACS Chem. Biol.* **8**, 1869–1875 https://doi.org/10.1021/cb4003464

1402

PORTLAND
PRESS

82 Wan, P.T., Garnett, M.J., Roe, S.M., Lee, S., Niculescu-Duvaz, D., Good, V.M. et al. (2004) Mechanism of activation of the RAF-ERK signaling pathway by oncogenic mutations of B-RAF. *Cell* **116**, 855–867 https://doi.org/10.1016/S0092-8674(04)00215-6

83 Haling, J.R., Sudhamsu, J., Yen, I., Sideris, S., Sandoval, W., Phung, W. et al. (2014) Structure of the BRAF-MEK complex reveals a kinase activity independent role for BRAF in MAPK signaling. *Cancer Cell* **26**, 402–413 https://doi.org/10.1016/j.ccr.2014.07.007

84 Sprang, S.R. (1995) How Ras works: structure of a Rap-Raf complex. *Structure* **3**, 641–643 https://doi.org/10.1016/S0969-2126(01)00198-8

85 Erijman, A. and Shifman, J.M. (2016) RAS/effector interactions from structural and biophysical perspective. *Mini-Rev. Med. Chem.* **16**, 370–375 https://doi.org/10.2174/1389557515666151001141838

86 Block, C., Janknecht, R., Herrmann, C., Nassar, N. and Wittinghofer, A. (1996) Quantitative structure-activity analysis correlating Ras/Raf interaction in vitro to Raf activation in vivo. *Nat. Struct. Biol.* **3**, 244–251 https://doi.org/10.1038/nsb0396-244

87 Fridman, M., Maruta, H., Gonez, J., Walker, F., Treutlein, H., Zeng, J. et al. (2000) Point mutants of c-raf-1 RBD with elevated binding to v-Ha-Ras. *J. Biol. Chem.* **275**, 30363–30371 https://doi.org/10.1074/jbc.M003193200

88 Zehir, A., Benayed, R., Shah, R.H., Syed, A., Middha, S., Kim, H.R. et al. (2017) Mutational landscape of metastatic cancer revealed from prospective clinical sequencing of 10,000 patients. *Nat. Med.* **23**, 703 https://doi.org/10.1038/nm.4333

89 Zeng, J., Fridman, M., Maruta, H., Treutlein, H.R. and Simonson, T. (1999) Protein-protein recognition: an experimental and computational study of the R89K mutation in Raf and its effect on Ras binding. *Protein Sci.* **8**, 50–64 https://doi.org/10.1110/ps.8.1.50

90 Weber, C.K., Slupsky, J.R., Herrmann, C., Schuler, M., Rapp, U.R. and Block, C. (2000) Mitogenic signaling of Ras is regulated by differential interaction with Raf isozymes. *Oncogene* **19**, 169–176 https://doi.org/10.1038/sj.onc.1203261

91 Lim, B., Mun, J., Kim, J.-H., Kim, C.W., Roh, S.A., Cho, D.-H. et al. (2015) Genome-wide mutation profiles of colorectal tumors and associated liver metastases at the exome and transcriptome levels. *Oncotarget* **6**, 22179

92 Lefebvre, C., Bachelot, T., Filleron, T., Pedrero, M., Campone, M., Soria, J.-C. et al. (2016) Mutational profile of metastatic breast cancers: a retrospective analysis. *PLoS Med.* **13**, e1002201 https://doi.org/10.1371/journal.pmed.1002201

93 Terada, T., Ito, Y., Shirouzu, M., Tateno, M., Hashimoto, K., Kigawa, T. et al. (1999) Nuclear magnetic resonance and molecular dynamics studies on the interactions of the Ras-binding domain of Raf-1 with wild-type and mutant Ras proteins. *J. Mol. Biol.* **286**, 219–232 https://doi.org/10.1006/jmbi.1998.2472

94 Kiel, C., Filchtinski, D., Spoerner, M., Schreiber, G., Kalbitzer, H.R. and Herrmann, C. (2009) Improved binding of raf to Ras.GDP is correlated with biological activity. *J. Biol. Chem.* **284**, 31893–31902 https://doi.org/10.1074/jbc.M109.031153

95 Chavan, T.S., Muratcioglu, S., Marszalek, R., Jang, H., Keskin, O., Gursoy, A. et al. (2015) Plasma membrane regulates Ras signaling networks. *Cell Logist.* **5**, e1136374 https://doi.org/10.1080/21592799.2015.1136374

96 Bondeva, T., Balla, A., Várnai, P. and Balla, T. (2002) Structural determinants of Ras-Raf interaction analyzed in live cells. *Mol. Biol. Cell.* **13**, 2323–2333 https://doi.org/10.1091/mbc.e02-01-0019

97 Nekhoroshkova, E., Albert, S., Becker, M. and Rapp, U.R. (2009) A-RAF kinase functions in ARF6 regulated endocytic membrane traffic. *PLoS ONE* **4**, e4647 https://doi.org/10.1371/journal.pone.0004647

98 Giannakis, M., Mu, X.J., Shukla, S.A., Qian, Z.R., Cohen, O., Nishihara, R. et al. (2016) Genomic correlates of immune-cell infiltrates in colorectal carcinoma. *Cell Rep.* **15**, 857–865 https://doi.org/10.1016/j.celrep.2016.03.075

99 George, J., Lim, J.S., Jang, S.J., Cun, Y., Ozretić, L., Kong, G. et al. (2015) Comprehensive genomic profiles of small cell lung cancer. *Nature* **524**, 47 https://doi.org/10.1038/nature14664

100 Mouradov, D., Sloggett, C., Jorissen, R.N., Love, C.G., Li, S., Burgess, A.W. et al. (2014) Colorectal cancer cell lines are representative models of the main molecular subtypes of primary cancer. *Cancer Res.* **74**, 3238–3247 https://doi.org/10.1158/0008-5472.CAN-14-0013

101 Fischer, A., Hekman, M., Kuhlmann, J., Rubio, I., Wiese, S. and Rapp, U.R. (2007) B- and C-RAF display essential differences in their binding to Ras: the isotype-specific N terminus of B-RAF facilitates Ras binding. *J. Biol. Chem.* **282**, 26503–26516 https://doi.org/10.1074/jbc.M607458200

102 Chuang, E., Barnard, D., Hettich, L., Zhang, X.F., Avruch, J. and Marshall, M.S. (1994) Critical binding and regulatory interactions between Ras and Raf occur through a small, stable N-terminal domain of Raf and specific Ras effector residues. *Mol. Cell. Biol.* **14**, 5318–5325 https://doi.org/10.1128/MCB.14.8.5318

103 Li, Z.-L., Prakash, P. and Buck, M. (2018) A 'Tug of War' maintains a dynamic protein-membrane complex: molecular dynamics simulations of C-Raf RBD-CRD bound to K-Ras4B at an anionic membrane. *ACS Cent. Sci.* **4**, 298–305 https://doi.org/10.1021/acscentsci.7b00593

104 Abaan, O.D., Polley, E.C., Davis, S.R., Zhu, Y.J., Bilke, S., Walker, R.L. et al. (2013) The exomes of the NCI-60 panel: a genomic resource for cancer biology and systems pharmacology. *Cancer Res.* **73**, 4372–4382 https://doi.org/10.1158/0008-5472.CAN-12-3342

105 Li, S., Jang, H., Zhang, J. and Nussinov, R. (2018) Raf-1 cysteine-Rich domain increases the affinity of K-Ras/Raf at the membrane, promoting MAPK signaling. *Structure* **26**, 513–525.e2 https://doi.org/10.1016/j.str.2018.01.011

106 Brtva, T.R., Drugan, J.K., Ghosh, S., Terrell, R.S., Campbell-Burk, S., Bell, R.M. et al. (1995) Two distinct Raf domains mediate interaction with Ras. *J. Biol. Chem.* **270**, 9809–9812 https://doi.org/10.1074/jbc.270.17.9809

107 Hu, C.-D., Kariya, K.-, Tamada, M., Akasaka, K., Shirouzu, M., Yokoyama, S. et al. (1995) Cysteine-rich region of Raf-1 interacts with activator domain of post-translationally modified Ha-Ras. *J. Biol. Chem.* **270**, 30274–30277 https://doi.org/10.1074/jbc.270.51.30274

108 Hu, C.-D., Kariya, K.-i., Kotani, G., Shirouzu, M., Yokoyama, S. and Kataoka, T. (1997) Coassociation of Rap1A and Ha-Ras with Raf-1 N-terminal region interferes with ras-dependent activation of Raf-1. *J. Biol. Chem.* **272**, 11702–11705 https://doi.org/10.1074/jbc.272.18.11702

109 Roy, S., Lane, A., Yan, J., McPherson, R. and Hancock, J.F. (1997) Activity of plasma membrane-recruited Raf-1 is regulated by Ras via the Raf zinc finger. *J. Biol. Chem.* **272**, 20139–20145 https://doi.org/10.1074/jbc.272.32.20139

110 Luo, Z., Diaz, B., Marshall, M.S. and Avruch, J. (1997) An intact Raf zinc finger is required for optimal binding to processed Ras and for ras-dependent Raf activation in situ. *Mol. Cell. Biol.* **17**, 46–53 https://doi.org/10.1128/MCB.17.1.46

111 Daub, M., Jöckel, J., Quack, T., Weber, C.K., Schmitz, F., Rapp, U.R. et al. (1998) The RafC1 cysteine-rich domain contains multiple distinct regulatory epitopes which control Ras-dependent Raf activation. *Mol. Cell. Biol.* **18**, 6698–6710 https://doi.org/10.1128/MCB.18.11.6698

112 Okada, T., Hu, C.-D., Jin, T.-G., Kariya, K.-i., Yamawaki-Kataoka, Y. and Kataoka, T. (1999) The strength of interaction at the Raf cysteine-rich domain is a critical determinant of response of Raf to Ras family small GTPases. *Mol. Cell. Biol.* **19**, 6057–6064 https://doi.org/10.1128/MCB.19.9.6057

1403

113 Williams, J.G., Drugan, J.K., Yi, G.-S., Clark, G.J., Der, C.J. and Campbell, S.L. (2000) Elucidation of binding determinants and functional consequences of Ras/Raf-cysteine-rich domain interactions. *J. Biol. Chem.* **275**, 22172–22179 https://doi.org/10.1074/jbc.M000397200

114 Chan, E.Y., Stang, S.L., Bottorff, D.A. and Stone, J.C. (2002) Mutations in conserved regions 1, 2, and 3 of Raf-1 that activate transforming activity. *Mol. Carcinog.* **33**, 189–197 https://doi.org/10.1002/mc.10031

115 Hibino, K., Shibata, T., Yanagida, T. and Sako, Y. (2011) Activation kinetics of RAF protein in the ternary complex of RAF, RAS-GTP, and kinase on the plasma membrane of living cells: single-molecule imaging analysis. *J. Biol. Chem.* **286**, 36460–36468 https://doi.org/10.1074/jbc.M111.262675

116 Ke, H., Matsumoto, S., Murashima, Y., Taniguchi-Tamura, H., Miyamoto, R., Yoshikawa, Y. et al. (2017) Structural basis for intramolecular interaction of post-translationally modified H-Ras*GTP prepared by protein ligation. *FEBS Lett.* **591**, 2470–2481 https://doi.org/10.1002/1873-3468.12759

117 Ghosh, S., Xie, W.Q., Quest, A.F., Mabrouk, G.M., Strum, J.C. and Bell, R.M. (1994) The cysteine-rich region of raf-1 kinase contains zinc, translocates to liposomes, and is adjacent to a segment that binds GTP-ras. *J. Biol. Chem.* **269**, 10000–10007

118 Hekman, M., Hamm, H., Villar, A.V., Bader, B., Kuhlmann, J., Nickel, J. et al. (2002) Associations of B- and C-Raf with cholesterol, phosphatidylserine, and lipid second messengers: preferential binding of Raf to artificial lipid rafts. *J. Biol. Chem.* **277**, 24090–24102 https://doi.org/10.1074/jbc.M200576200

119 Ghosh, S., Strum, J.C., Sciorra, V.A., Daniel, L. and Bell, R.M. (1996) Raf-1 kinase possesses distinct binding domains for phosphatidylserine and phosphatidic acid. Phosphatidic acid regulates the translocation of Raf-1 in 12-*O*-tetradecanoylphorbol-13-acetate-stimulated Madin-Darby canine kidney cells. *J. Biol. Chem.* **271**, 8472–8480 https://doi.org/10.1074/jbc.271.14.8472

120 Zang, M., Waelde, C.A., Xiang, X., Rana, A., Wen, R. and Luo, Z. (2001) Microtubule integrity regulates Pak leading to Ras-independent activation of Raf-1. Insights into mechanisms of Raf-1 activation. *J. Biol. Chem.* **276**, 25157–25165 https://doi.org/10.1074/jbc.M100152200

121 Improta-Brears, T., Ghosh, S. and Bell, R.M. (1999) Mutational analysis of Raf-1 cysteine rich domain: requirement for a cluster of basic aminoacids for interaction with phosphatidylserine. *Mol. Cell. Biochem.* **198**, 171–178 https://doi.org/10.1023/A:1006981411691

122 Sarkozy, A., Carta, C., Moretti, S., Zampino, G., Digilio, M.C., Pantaleoni, F. et al. (2009) Germline *BRAF* mutations in Noonan, LEOPARD, and cardiofaciocutaneous syndromes: molecular diversity and associated phenotypic spectrum. *Hum. Mutat.* **30**, 695–702 https://doi.org/10.1002/humu.20955

123 Abankwa, D., Gorfe, A.A. and Hancock, J.F. (2007) Ras nanoclusters: molecular structure and assembly. *Semin. Cell Dev. Biol.* **18**, 599–607 https://doi.org/10.1016/j.semcdb.2007.08.003

124 Abankwa, D., Gorfe, A.A., Inder, K. and Hancock, J.F. (2010) Ras membrane orientation and nanodomain localization generate isoform diversity. *Proc. Natl Acad. Sci. U.S.A.* **107**, 1130–1135 https://doi.org/10.1073/pnas.0903907107

125 Cirstea, I.C., Kutsche, K., Dvorsky, R., Gremer, L., Carta, C., Horn, D. et al. (2010) A restricted spectrum of NRAS mutations causes Noonan syndrome. *Nat. Genet.* **42**, 27–29 https://doi.org/10.1038/ng.497

126 Zhou, Y. and Hancock, J.F. (2018) Deciphering lipid codes: K-Ras as a paradigm. *Traffic* **19**, 157–165 https://doi.org/10.1111/tra.12541

127 Kapoor, S., Triola, G., Vetter, I.R., Erlkamp, M., Waldmann, H. and Winter, R. (2012) Revealing conformational substates of lipidated N-Ras protein by pressure modulation. *Proc. Natl Acad. Sci. U.S.A.* **109**, 460–465 https://doi.org/10.1073/pnas.1110553109

128 Vogel, A., Nikolaus, J., Weise, K., Triola, G., Waldmann, H., Winter, R. et al. (2014) Interaction of the human N-Ras protein with lipid raft model membranes of varying degrees of complexity. *Biol. Chem.* **395**, 779–789 https://doi.org/10.1515/hsz-2013-0294

129 Sperlich, B., Kapoor, S., Waldmann, H., Winter, R. and Weise, K. (2016) Regulation of K-Ras4B membrane binding by calmodulin. *Biophys. J.* **111**, 113–122 https://doi.org/10.1016/j.bpj.2016.05.042

130 Erwin, N., Patra, S., Dwivedi, M., Weise, K. and Winter, R. (2017) Influence of isoform-specific Ras lipidation motifs on protein partitioning and dynamics in model membrane systems of various complexity. *Biol. Chem.* **398**, 290–263 https://doi.org/10.1515/hsz-2016-0289

131 Dumaz, N. and Marais, R. (2003) Protein kinase A blocks Raf-1 activity by stimulating 14-3-3 binding and blocking Raf-1 interaction with Ras. *J. Biol. Chem.* **278**, 29819–29823 https://doi.org/10.1074/jbc.C300182200

132 Sendoh, H., Hu, C.-D., Wu, D., Song, C., Yamawaki-Kataoka, Y., Kotani, J. et al. (2000) Role of Raf-1 conserved region 2 in regulation of Ras-dependent Raf-1 activation. *Biochem. Biophys. Res. Commun.* **271**, 596–602 https://doi.org/10.1006/bbrc.2000.2674

133 Dhillon, A.S., Meikle, S., Yazici, Z., Eulitz, M. and Kolch, W. (2002) Regulation of Raf-1 activation and signalling by dephosphorylation. *EMBO J.* **21**, 64–71 https://doi.org/10.1093/emboj/21.1.64

134 Dhillon, A.S., Pollock, C., Steen, H., Shaw, P.E., Mischak, H. and Kolch, W. (2002) Cyclic AMP-dependent kinase regulates Raf-1 kinase mainly by phosphorylation of serine 259. *Mol. Cell. Biol.* **22**, 3237–3246 https://doi.org/10.1128/MCB.22.10.3237-3246.2002

135 Zimmermann, S. and Moelling, K. (1999) Phosphorylation and regulation of Raf by Akt (protein kinase B). *Science* **286**, 1741–1744 https://doi.org/10.1126/science.286.5445.1741

136 Rommel, C., Clarke, B.A., Zimmermann, S., Nunez, L., Rossman, R., Reid, K. et al. (1999) Differentiation stage-specific inhibition of the Raf-MEK-ERK pathway by Akt. *Science* **286**, 1738–1741 https://doi.org/10.1126/science.286.5445.1738

137 Pandit, B., Sarkozy, A., Pennacchio, L.A., Carta, C., Oishi, K., Martinelli, S. et al. (2007) Gain-of-function RAF1 mutations cause Noonan and LEOPARD syndromes with hypertrophic cardiomyopathy. *Nat. Genet.* **39**, 1007–1012 https://doi.org/10.1038/ng2073

138 Razzaque, M.A., Nishizawa, T., Komoike, Y., Yagi, H., Furutani, M., Amo, R. et al. (2007) Germline gain-of-function mutations in RAF1 cause Noonan syndrome. *Nat. Genet.* **39**, 1013–1017 https://doi.org/10.1038/ng2078

139 Kobayashi, T., Aoki, Y., Niihori, T., Cavé, H., Verloes, A., Okamoto, N. et al. (2010) Molecular and clinical analysis of *RAF1* in Noonan syndrome and related disorders: dephosphorylation of serine 259 as the essential mechanism for mutant activation. *Hum. Mutat.* **31**, 284–294 https://doi.org/10.1002/humu.21187

140 Hodis, E., Watson, I.R., Kryukov, G.V., Arold, S.T., Imielinski, M., Theurillat, J.-P. et al. (2012) A landscape of driver mutations in melanoma. *Cell* **150**, 251–263 https://doi.org/10.1016/j.cell.2012.06.024

141 Martin, D., Abba, M.C., Molinolo, A.A., Vitale-Cross, L., Wang, Z., Zaida, M. et al. (2014) The head and neck cancer cell oncogenome: a platform for the development of precision molecular therapies. *Oncotarget* **5**, 8906–8923 PMID:25275298

142 Shi, J., Hua, X., Zhu, B., Ravichandran, S., Wang, M., Nguyen, C. et al. (2016) Somatic genomics and clinical features of lung adenocarcinoma: a retrospective study. *PLoS Med.* **13**, e1002162 https://doi.org/10.1371/journal.pmed.1002162

1404

PORTLAND
PRESS

143 Imielinski, M., Greulich, H., Kaplan, B., Araujo, L., Amann, J., Horn, L. et al. (2014) Oncogenic and sorafenib-sensitive ARAF mutations in lung adenocarcinoma. *J. Clin. Invest.* **124**, 1582–1586 https://doi.org/10.1172/JCI72763

144 Stevers, L.M., Sijbesma, E., Botta, M., MacKintosh, C., Obsil, T., Landrieu, I. et al. (2018) Modulators of 14-3-3 protein-protein interactions. *J. Med. Chem.* **61**, 3755–3778 https://doi.org/10.1021/acs.jmedchem.7b00574

145 Yaffe, M.B., Rittinger, K., Volinia, S., Caron, P.R., Aitken, A., Leffers, H. et al. (1997) The structural basis for 14-3-3:phosphopeptide binding specificity. *Cell* **91**, 961–971 https://doi.org/10.1016/S0092-8674(00)80487-0

146 Shen, Y.H., Godlewski, J., Bronisz, A., Zhu, J., Comb, M.J., Avruch, J. et al. (2003) Significance of 14-3-3 self-dimerization for phosphorylation-dependent target binding. *Mol. Biol. Cell* **14**, 4721–4733 https://doi.org/10.1091/mbc.e02-12-0821

147 Tzivion, G. and Avruch, J. (2002) 14-3-3 proteins: active cofactors in cellular regulation by serine/threonine phosphorylation. *J. Biol. Chem.* **277**, 3061–3064 https://doi.org/10.1074/jbc.R100059200

148 Muslin, A.J., Tanner, J.W., Allen, P.M. and Shaw, A.S. (1996) Interaction of 14-3-3 with signaling proteins is mediated by the recognition of phosphoserine. *Cell* **84**, 889–897 https://doi.org/10.1016/S0092-8674(00)81067-X

149 Morrison, D.K., Heidecker, G., Rapp, U.R. and Copeland, T.D. (1993) Identification of the major phosphorylation sites of the Raf-1 kinase. *J. Biol. Chem.* **268**, 17309–17316 PMID:8349614

150 Roskoski, R.J. (2010) RAF protein-serine/threonine kinases: structure and regulation. *Biochem. Biophys. Res. Commun.* **399**, 313–317 https://doi.org/10.1016/j.bbrc.2010.07.092

151 Alessi, D.R., Saito, Y., Campbell, D.G., Cohen, P., Sithanandam, G., Rapp, U. et al. (1994) Identification of the sites in MAP kinase kinase-1 phosphorylated by p74raf-1. *EMBO J.* **13**, 1610–1619 PMID:8157000

152 Roskoski, R.J. (2012) MEK1/2 dual-specificity protein kinases: structure and regulation. *Biochem. Biophys. Res. Commun.* **417**, 5–10 https://doi.org/10.1016/j.bbrc.2011.11.145

153 Hatzivassiliou, G., Song, K., Yen, I., Brandhuber, B.J., Anderson, D.J., Alvarado, R. et al. (2010) RAF inhibitors prime wild-type RAF to activate the MAPK pathway and enhance growth. *Nature* **464**, 431–400 https://doi.org/10.1038/nature08833

154 Yao, Z., Torres, N.M., Tao, A., Gao, Y., Luo, L., Li, Q. et al. (2015) BRAF mutants evade ERK-dependent feedback by different mechanisms that determine their sensitivity to pharmacologic inhibition. *Cancer Cell* **28**, 370–383 https://doi.org/10.1016/j.ccell.2015.08.001

155 Yao, Z., Yaeger, R., Rodrik-Outmezguine, V.S., Tao, A., Torres, N.M., Chang, M.T. et al. (2017) Tumours with class 3 BRAF mutants are sensitive to the inhibition of activated RAS. *Nature* **548**, 234 https://doi.org/10.1038/nature23291

156 Karoulia, Z., Wu, Y., Ahmed, T.A., Xin, Q., Bollard, J., Krepler, C. et al. (2016) An integrated model of RAF inhibitor action predicts inhibitor activity against oncogenic BRAF signaling. *Cancer Cell* **30**, 485–498 https://doi.org/10.1016/j.ccell.2016.06.024

157 Brown, M.D. and Sacks, D.B. (2009) Protein scaffolds in MAP kinase signalling. *Cell. Signal.* **21**, 462–469 https://doi.org/10.1016/j.cellsig.2008.11.013

158 Morrison, D.K. and Davis, R.J. (2003) Regulation of MAP kinase signaling modules by scaffold proteins in mammals. *Ann. Rev. Cell Dev. Biol.* **19**, 91–118 https://doi.org/10.1146/annurev.cellbio.19.111401.091942

159 Liang, Y. and Sheikh, F. (2016) Scaffold proteins regulating extracellular regulated kinase function in cardiac hypertrophy and disease. *Front. Pharmacol.* **7**, 37 https://doi.org/10.3389/fphar.2016.00037

160 Shaul, Y.D. and Seger, R. (2007) The MEK/ERK cascade: from signaling specificity to diverse functions. *Biochim. Biophys. Acta* **1773**, 1213–1226 https://doi.org/10.1016/j.bbamcr.2006.10.005

161 Wortzel, I. and Seger, R. (2011) The ERK cascade: distinct functions within various subcellular organelles. *Genes Cancer* **2**, 195–209 https://doi.org/10.1177/1947601911407328

162 Kornfeld, K., Hom, D.B. and Horvitz, H.R. (1995) The ksr-1 gene encodes a novel protein kinase involved in Ras-mediated signaling in *C. elegans. Cell* **83**, 903–913 https://doi.org/10.1016/0092-8674(95)90206-6

163 Sundaram, M. and Han, M. (1995) The *C. elegans* ksr-1 gene encodes a novel Raf-related kinase involved in Ras-mediated signal transduction. *Cell* **83**, 889–901 https://doi.org/10.1016/0092-8674(95)90205-8

164 Therrien, M., Chang, H.C., Solomon, N.M., Karim, F.D., Wassarman, D.A. and Rubin, G.M. (1995) KSR, a novel protein kinase required for RAS signal transduction. *Cell* **83**, 879–888 https://doi.org/10.1016/0092-8674(95)90204-X

165 Vomastek, T., Schaeffer, H.-J., Tarcsafalvi, A., Smolkin, M.E., Bissonette, E.A. and Weber, M.J. (2004) Modular construction of a signaling scaffold: MORG1 interacts with components of the ERK cascade and links ERK signaling to specific agonists. *Proc. Natl Acad. Sci. U.S.A.* **101**, 6981–6986 https://doi.org/10.1073/pnas.0305894101

166 Schaeffer, H.J., Catling, A.D., Eblen, S.T., Collier, L.S., Krauss, A. and Weber, M.J. (1998) MP1: a MEK binding partner that enhances enzymatic activation of the MAP kinase cascade. *Science* **281**, 1668–1671 https://doi.org/10.1126/science.281.5383.1668

167 Ishibe, S., Joly, D., Zhu, X. and Cantley, L.G. (2003) Phosphorylation-dependent paxillin-ERK association mediates hepatocyte growth factor-stimulated epithelial morphogenesis. *Mol. Cell* **12**, 1275–1285 https://doi.org/10.1016/S1097-2765(03)00406-4

168 McDonald, P.H., Chow, C.-W., Miller, W.E., Laporte, S.A., Field, M.E., Lin, F.-T. et al. (2000) β-Arrestin 2: a receptor-regulated MAPK scaffold for the activation of JNK3. *Science* **290**, 1574–1577 https://doi.org/10.1126/science.290.5496.1574

169 Karandikar, M., Xu, S. and Cobb, M.H. (2000) MEKK1 binds raf-1 and the ERK2 cascade components. *J. Biol. Chem.* **275**, 40120–40127 https://doi.org/10.1074/jbc.M005926200

170 Sheikh, F., Raskin, A., Chu, P.-H., Lange, S., Domenighetti, A.A., Zheng, M. et al. (2008) An FHL1-containing complex within the cardiomyocyte sarcomere mediates hypertrophic biomechanical stress responses in mice. *J. Clin. Invest.* **118**, 3870–3880 https://doi.org/10.1172/JCI34472

171 Roy, F., Laberge, G., Douziech, M., Ferland-McCollough, D. and Therrien, M. (2002) KSR is a scaffold required for activation of the ERK/MAPK module. *Genes Dev.* **16**, 427–438 https://doi.org/10.1101/gad.962902

172 Ritt, D.A., Daar, I.O. and Morrison, D.K. (2006) KSR regulation of the Raf-MEK-ERK cascade. *Methods Enzymol.* **407**, 224–237 https://doi.org/10.1016/S0076-6879(05)07019-9

173 Nguyen, A., Burack, W.R., Stock, J.L., Kortum, R., Chaika, O.V., Afkarian, M. et al. (2002) Kinase suppressor of Ras (KSR) is a scaffold which facilitates mitogen-activated protein kinase activation in vivo. *Mol. Cell. Biol.* **22**, 3035–3045 https://doi.org/10.1128/MCB.22.9.3035-3045.2002

174 Brennan, D.F., Dar, A.C., Hertz, N.T., Chao, W.C., Burlingame, A.L., Shokat, K.M. et al. (2011) A Raf-induced allosteric transition of KSR stimulates phosphorylation of MEK. *Nature* **472**, 366 https://doi.org/10.1038/nature09860

175 Baljuls, A., Dobrzyński, M., Rauch, J., Rauch, N. and Kolch, W. (2016) Stabilization of C-RAF:KSR1 complex by DiRas3 reduces availability of C-RAF for dimerization with B-RAF. *Cell Signal.* **28**, 1451–1462 https://doi.org/10.1016/j.cellsig.2016.06.019

176 Li, W., Melnick, M. and Perrimon, N. (1998) Dual function of Ras in Raf activation. *Development* **125**, 4999–5008 PMID: 9811584

177 Anderson, D.H. (2006) Role of lipids in the MAPK signaling pathway. *Prog. Lipid Res.* **45**, 102–119 https://doi.org/10.1016/j.plipres.2005.12.003

178 Yoon, S. and Seger, R. (2006) The extracellular signal-regulated kinase: multiple substrates regulate diverse cellular functions. *Growth Factors* **24**, 21–44 https://doi.org/10.1080/02699050500284218

179 Cseh, B., Doma, E. and Baccarini, M. (2014) 'RAF' neighborhood: protein-protein interaction in the Raf/Mek/Erk pathway. *FEBS Lett.* **588**, 2398–2406 https://doi.org/10.1016/j.febslet.2014.06.025

180 Blaževitš, O., Mideksa, Y.G., Šolman, M., Ligabue, A., Ariotti, N., Nakhaeizadeh, H. et al. (2016) Galectin-1 dimers can scaffold Raf-effectors to increase H-ras nanoclustering. *Sci. Rep.* **6**, 24165 https://doi.org/10.1038/srep24165

181 Chen, J., Fujii, K., Zhang, L., Roberts, T. and Fu, H. (2001) Raf-1 promotes cell survival by antagonizing apoptosis signal-regulating kinase 1 through a MEK-ERK independent mechanism. *Proc. Natl Acad. Sci. U.S.A.* **98**, 7783–7788 https://doi.org/10.1073/pnas.141224398

182 Romano, D., Nguyen, L.K., Matallanas, D., Halasz, M., Doherty, C., Kholodenko, B.N. et al. (2014) Protein interaction switches coordinate Raf-1 and MST2/Hippo signalling. *Nat. Cell Biol.* **16**, 673–684 https://doi.org/10.1038/ncb2986

183 Varga, A., Ehrenreiter, K., Aschenbrenner, B., Kocieniewski, P., Kochanczyk, M., Lipniacki, T. et al. (2017) RAF1/BRAF dimerization integrates the signal from RAS to ERK and ROKalpha. *Sci. Signal.* **10**, eaai8482 https://doi.org/10.1126/scisignal.aai8482

1406

Chapter III

Induced pluripotent stem cell-derived cardiac bodies reveal aberrant sarcomeric structure and calcium regulation concomitantly promote hypertrophic cardiomyopathy in RAF1-associated Noonan syndrome

Graphical abstract
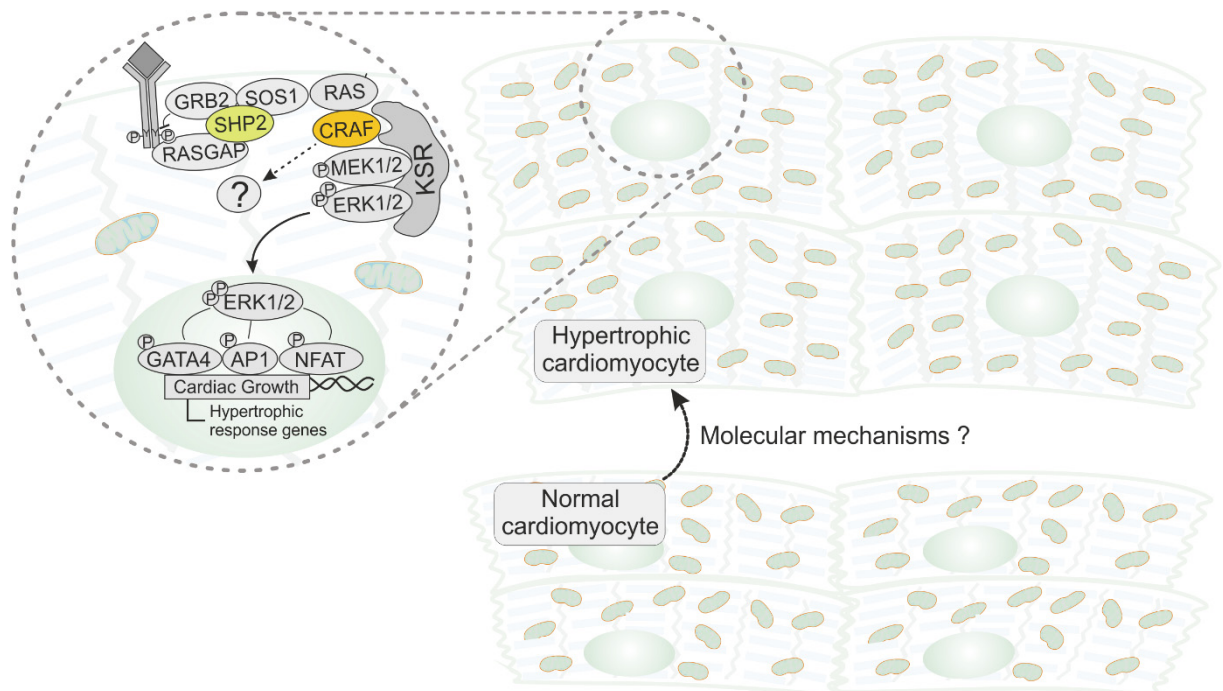
Status:	In preparation
Impact factor:	none
Own proportion to this work:	25 %

iPSC culture, cardiac differentiation, western blotting, RT-PCR, contraction rates, Ca^{2+} measurements, sample preparation, microscopy, figure preparation, writing the manuscript, discussion.

Induced pluripotent stem cell-derived cardiac bodies reveal aberrant sarcomeric structure and calcium regulation concomitantly promote hypertrophic cardiomyopathy in RAF1-associated Noonan syndrome

Contribution Institutions:

Institute of Biochemistry and Molecular Biology II, Medical Faculty of the Heinrich Heine University, Düsseldorf, Germany: Saeideh Nakhaei-Rad, Marcel Buchholzer, Fereshteh Haghighi, Farhad Bazgir, Roland P. Piekorz, Mohammad R. Ahmadian

Department of Thoracic and Cardiovascular Surgery, University Medical Center Göttingen, 37075 Göttingen, Germany: Julia Dahlmann, Fereshteh Haghighi, George Kensah

Institute of Human Genetics, Otto von Guericke-University, Magdeburg, Germany: Martin Zenker

Institute of Biochemistry and Molecular Biology I, Medical Faculty of the Heinrich Heine University, Düsseldorf, Germany: Andrea Borchardt, Ruchika Anand, Andreas Reichert

Institute of Pharmacology and Clinical Pharmacology, Medical Faculty of the Heinrich Heine University, Düsseldorf, Germany: Annette Vera Kronenbitter, Joachim Schmitt

Institute of Cardiovascular Physiology, Medical Faculty of the Heinrich Heine University, Düsseldorf, Germany: Martina Krüger, Sebastian Kötter, Axel Gödecke

Institute of Neuropathology, Justus Liebig University Giessen, Giessen, Germany: Anne Schänzer

Department of Child Neurology, Justus Liebig University Giessen, 35392 Giessen, Germany: Andreas Hahn

Summary

Noonan syndrome (NS) is characterized by gain-of-function mutations in genes encoding components of the RAS-MAPK signaling pathway. Among them, NS patients with c.770C>T (p.Ser257Leu) mutation in *RAF1* frequently suffer from pathological hypertrophic cardiomyopathy (HCM). To comprehensively study the mechanistic link between this gain-of-function mutation of *RAF1* and HCM, induced pluripotent stem cells (iPSCs), derived from fibroblasts of a NS patient with RAF1^{S257L}, were differentiated up to 47-days to three-dimensional (3D) cardiac bodies (CBs). A comparison of highly pure, non-proliferating RAF1^{WT} and RAF1^{S257L} CBs clearly revealed HCM characteristics in RAF1^{S257L} CBs, including expression of fetal genes, increased expression of sarcomere structural proteins and a MYH6-to-MYH7 switch. RAF1^{S257L} cardiomyocytes exhibited elevated ERK and p38 activities, abnormal sarcomere structure, upregulation of the PLN/SERCA2 ratio, decreased calcium transient and cardiac contractility. Most remarkably, electron micrographs of Z-disc area visualized the lack of I-bands in both RAF1^{S257L} CBs and heart biopsy of the patient as compared to RAF1^{WT} CBs. This phenotype RAF1S257L CBs was reverted in the presence of the MEK inhibitor PD0325901. Collectively, our findings uncovered, for the first time, a direct link between RASopathy gene mutation and sarcomeric dysfunction.

Introduction

Germline mutations of RAS-MAPK signaling components result in a set of developmental disorders, collectively referred to as RASopathies. They are characterized by craniofacial dysmorphology, delayed growth, neurocognitive impairment, and mild to severe hypertrophic cardiomyopathy (HCM) [1,2]. HCM is diagnosed in 80% of patients suffering from Noonan syndrome with multiple lentigines (NSML, formerly known as LEOPARD syndrome with *PTPN11* and *RAF1* mutations), 65% in Costello syndrome (*HRAS* mutation), 40% in Cardio-Facio-Cutaneous syndrome (*BRAF* mutations) and 20% in Noonan syndrome (NS; *RAF1>PTPN11>RIT1* mutations) [2]. Notably, more than 90% of NS individuals with *RAF1* mutations clusters are associated with pathological HCM, although the overall frequency of HCM in NS syndrome is only about 20% [3,4]. *RAF1* mutations that are associated with cardiac hypertrophy, including flanking residues of Ser259 (Ser-257, Ser-256 and Ser-621), are adjacent to 14-3-3 binding sites [3]. Impairment of 14-3-3 association with RAF1^{S257L} renders p-Ser-259 accessible for phosphatases [5,6]. Therefore, the heterozygous p.Ser257Leu variant confers functional enhancement (gain-of-function) to RAF1^{S257L} activity due to impaired autoinhibition of RAF1 [7,8]. Most functional studies on RAF1 activity focused on its role in the MAPK pathway in tumor cells [9]. Very few studies have so far described distinct RAF1 activities in cardiomyocytes (CMs) and identified RAF1 as a hub of cardiac-specific signaling network of ERK5 and calcineurin-NFAT [10-12].

CMs represent highly specialized cells in both cytoarchitecture and functions. The functional unit of CMs, the sarcomere, is composed of thin and thick myofilaments, divided into Z-disk, I-band, A-band and M-line regions [13]. Mammalian CM proliferation rates and regenerative capacity decrease drastically shortly after birth [14]. In response to certain external stimuli and stress conditions they grow by increasing their size rather than increasing in number. This phenomenon is known as a hypertrophy [7,15]. HCM is characterized by increase in cardiomyocyte size, return to the fetal gene program, change in the amplitudes of the calcium (Ca^{2+}) transient, higher force generation and energy consumption, increased protein synthesis and changes in the organization of the sarcomeric structure [16]. At the organ level, HCM is manifested as an increase in left ventricular wall thickness, resulting in diastolic dysfunction, an increased risk of heart failure, stroke and cardiac arrhythmia. HCM is the most common cause of sudden death in young people (Maron and Maron, 2013).

Patient-specific pluripotent stem cell-derived cardiomyocytes (iPSC) have been utilized as human HCM model of several genetic diseases and drug screening [17-20]. They recapitulate several HCM features at cellular levels, including increased in cell size, aberrant calcium transients, reactivation of fetal gene program and arrhythmia [11,12,20-22]. This model enabled us to move one step forward towards understanding the cellular and molecular mechanism of the HCM induction via different driver mutations.

In this study, we generated two different three-dimensional (3D) human cardiac cell models, cardiac bodies (CBs) and bioartificial cardiac tissues (BCTs) to elucidate the molecular mechanism of RAF1-induced HCM. To this end, two patient-derived iPSC lines carrying RAF1 c.770C>T (p.Ser257Leu) and one iPSC wild-type control were used. Aberrant molecular mechanisms of generated WT and RAF1^{S257L} CBs as well as BCTs were investigated regarding sarcomeric structures, contractile behavior, Ca^{2+} handling and intracellular signaling pathways downstream of hyperactive RAF1. The treatment of the RAF1^{S257L} CBs with MEK inhibitor (PD0325901) rescued observed HCM phenotype derived from RAF1 mutation in RAF1^{S257L}. Our data are in part comparable to obtained data from the cardiac tissue biopsy of the RAF1 c.770C>T individual.

Material and methods

Generation and cultivation of human iPSCs

Dermal fibroblasts were obtained with the institutional ethics approval and under informed consent of the parents from a 5-year-old female who was diagnosed with progressive HCM and c.770C>T single point mutation in Exon 7 of RAF1. Human iPSC generation and cultivation was performed as previously described [23]. In brief, human iPSCs were generated from patient fibroblasts and human foreskin fibroblasts (HFF, purchased from ATCC), respectively, using a cocktail of non-integrating episomal reprogramming vectors obtained from Addgene (pCE-hSK #41814, pCE-hOct3/4 #41813, pCE-hUL #41855, pCE-mp53DD #41856, pCXB-EBNA1 #41857 [23,24]. Established human iPSCs were cultivated as colonies on mitotically inactivated murine embryonic fibroblasts (γMEFs in iPSC-medium (DMEM/F12 + GlutaMAX supplemented with 20% (v/v) knockout serum replacement, 0.1 mM 2-mercaptoethanol (Sigma), 1% (v/v) non-essential amino acid stock (Supplier) and 25 ng/ml FGF-2 (Peprotech) or as feeder-free monolayers in Geltrex coated cell culture flasks in γMEF conditioned iPSC-medium incl. 100 ng/mL FGF-2 (CM+/100) and passaged every 3-4 days. Generated iPSC cell lines in our lab were plasmid-integration free as tested by PCR.

Tri-lineage differentiation of iPSCs

To induce differentiation of iPSCs into all germ layers, iPSC-colonies were detached from feeder layers using 0.4% (w/v) type IV collagenase and resuspended in differentiation medium consisting of IMDM + GlutaMAX supplemented with 20% (v/v) fetal calf serum, 1 mL L-Glutamine, 0.1 mM 2-mercaptoethanol and 1% non-essential amino acid stock (Thermo Scientific). Colonies were maintained for 7 days in suspension culture on 1% (w/v) agarose/IMDM coated 12-well plates to form 3D embryoid bodies (EBs). Subsequently, about 15-20 EBs were plated on 6-well plates coated with 0.1% (w/v) gelatin. After 24 days, EBs were harvested for qRT-PCR and replated for IF, respectively.

Karyotype analysis

After treatment of undifferentiated human iPSCs with a final concentration of 0.1 µg/mL Colcemid (Invitrogen) for 2 h, cells were detached with trypsin/EDTA (0.05/0.02%, Biochrom). After centrifugation, the pellet was resuspended in hypotonic solution (0.32% KCl with 0.2% (v/v) fetal calf serum) and incubated for 15 min at 37°C. Cells were fixed in ice-cold methanol/acetic acid, 3:1. G-banding was performed according to Seabright [25]. Karyograms were imaged using the IKAROS software of MetaSystems (Altlußheim, Germany). The chromosome arrangement was done according to Hamta et al [26].

Cardiac differentiation of iPSCs

Cardiac differentiation was performed in 3D suspension culture after aggregate formation in agarose microwells modified from Lian et al. and Dahlmann et al [27,28]. For differentiation in 3D suspension culture, agarose microwells (AMW) were generated from AggreWellTM400Ex plates (Stem Cell Technologies) containing 4700 microslots per AMW in a 6-well format [27]. For each AMW, 5×10^6 undifferentiated iPSCs were seeded in 3 mL CM+/100 supplemented with ROCK inhibitor Y-27632 (Selleckchem #S1049). iPSCs formed uniform aggregates during 24 h on AMW, which were harvested and transferred to suspension culture in 15 cm dishes and placed on an orbital shaker at 60 rpm. Suspension aggregates were cultivated for further 3 days in CM+/100 before the start of cardiac differentiation. Differentiation was induced with the exchange of medium to RMPI 1640 supplemented with 1% (v/v) B27 without insulin (RB$^-$, Thermo Scientific#A18956-01). GSK-3 inhibitor CHIR99021 (Selleckchem#S1263) was added at 6 µM for the first 24 h of differentiation, thereafter differentiations were kept in RB$^-$ without small molecule inhibitors until day 3 (d3) before the WNT inhibitor IWR-1 (4 µM, Sigma#I0161) was added for 48 h. First contracting CBs were observed between late d5 and d7. From d7-d10, cardiac bodies were cultivated with RPMI 1640 supplemented with 1% (v/v) B27 with insulin (RB$^+$, Thermo Scientific#17504-044). Afterwards, a metabolic selection was performed for 10 days (until d20) to eliminate all non-cardiomyocytes in RPMI minus Glucose (Thermo Scientific#11879-020) supplemented with human Albumin (Sigma#A0237), Sodium DL-Lactate (Sigma#L4263), L-Ascorbic acid-2-Phosphate (Sigma#A8960). From d20 - d40, CBs were kept in RB$^+$ medium. To induce hypertrophy in WT CBs they were treated with 100 µM L-Phenylephrine (TCI Chemical#P0395, India) for 7 days. MEK inhibitor treatment of RAF1^{S257L} CBs was performed as following; at d12 of differentiation the RAF1^{S257L} CBs were continuously treated with 0.2 µM PD0325901 (Sigma#PZ0162) until d24 (for younger CBs) and 47 of differentiation (for older CBs), respectively.

Reverse transcriptase polymerase chain reaction

Cells were lysed using TRIzol™ (Ambion, Life Technologies, Germany) and the total RNA was extracted via phenol-chloroform extraction. Remaining genomic DNA contaminations were removed

using the DNA-free™ DNA Removal Kit (Ambion, Life Technologies, Germany). DNase-treated RNA was transcribed into complementary DNA (cDNA) using the ImProm-II™ reverse transcription system (Promega, Germany). Quantitative real-time reverse transcriptase polymerase chain reaction (qPCR) was performed using SYBR Green (Life Technologies, Germany). Primer sequences are listed in Supplementary Table S1. The $2^{-\Delta\Delta Ct}$ method was employed for estimating the relative mRNA expression levels and $2^{-\Delta Ct}$ for mRNA levels. Among 6 different housekeeping genes that we tested HPRT1 showed the minimal variation among different cell lines and conditions therefore, it was used for normalization in our qPCR analysis.

Flow cytometry

For flow cytometric analysis, CBs were dissociated into single cells by incubation with Versene (EDTA-Solution, Thermo Scientific #15040066) for 10 min in a Thermomixer at 37°C. Thereafter, TrypLE (Thermo Scientific) was added and incubate for additional 10 min at 37°C and 1200 rpm until the cellular aggregates have dissolved. Cells were fixed in 4% paraformaldehyde (PFA; Merck) for 10 min on ice and permeabilized with 90% ice-cold methanol for 20 min followed by a blocking step with 1.5% BSA and 2.5% goat or donkey serum diluted in PBS for 1 h, at 4°C. Cells were stained with primary antibodies included Anti-OCT3/4 (1:1000; Santa Cruz, #sc-5279), Anti-cardiac troponin t (1:200, Invitrogen, #MA5-12960), Anti-Tra-1-60 (1:100; Abcam, #ab16288) and Anti-Myosin light chain 2 V (1:100, Synaptic Systems, #310111), Anti-SSEA4 (1:70; DSHB, #MC-813-70) overnight at 4°C. Secondary antibodies (Alexa Fluor 488-conjugated goat anti-mouse IgG and Alexa Fluor 488-conjugated donkey anti-rabbit IgG; Life Technologies) were used at a dilution of 1:2000 for one hour at room temperature. Samples were collected with FACScanto (BD PharMingen) and analyzed with FlowJo Software (Treestar, Ashland, OR).

Immunoblotting

To extract the total protein, CBs were washed with PBS prior to the cell lysis (lysis buffer; 50 mM Tris-HCl pH 7.5, 100 mM NaCl, 2 mM $MgCl_2$, 1% Triton X100, 10% glycerol, 20 mM beta-glycerolphosphate, 1 mM Ortho-Na_3VO_4, EDTA-free protease inhibitor (Roche, Germany)). To further disrupt the cellular aggregates a sonicator with 70% power was used prior to an incubation in a rotor in 4°C for 30 min. Protein concentrations were determined with Bradford assay (Bio-Rad). Equal amounts of cell lysates (10-50 µg), were subjected to Sodium dodecyl sulfate polyacrylamide gel electrophoresis (SDS-PAGE). Following electrophoresis, the proteins were transferred to a nitrocellulose membrane by electroblotting and probed with primary antibodies overnight at 4°C. All antibodies from Santa Cruz were diluted 1:200 in 5% non-fat milk (Merck, Germany)/TBST (Tris-buffered saline, 0.05% Tween 20), remaining antibodies were diluted 1:1000. The following antibodies were applied for immunoblotting: mouse Anti-γ-tubulin (WB:1:2000, Sigma-Aldrich, # T5326), rabbit

Anti-phospho-ERK1/2 (WB:1:1000, T202/T204, # 9106), Anti-rabbit phospho-AKT (S473, WB:1:1000# 4060 and T308, #2965), Anti-phospho-YAP (WB 1:1000; Ser 127; Cell Signaling, #4911), Anti-YAP (WB 1:1000; Cell Signaling, # 4912), Anti-JNK (WB 1:1000; Cell Signaling, # 9252), Anti-phospho-JNK (WB 1:1000; Thr183/Tyr185; Cell Signaling, # 9251), Anti-S6K (WB 1:1000; Cell Signaling, # 2708), Anti-phospho-S6K (WB 1:1000; Thr389; Cell Signaling, # 9205), Anti-phospho-p38 (WB 1:1000; Thr180/Tyr182; Cell Signaling, #9211) and Anti-p38 (WB 1:1000; Cell Signaling, # 8690), Anti-OCT3/4 (WB: 1:1000; Santa Cruz, #sc-5279), Anti-alpha-actinin (WB 1:1000, Sigma, # A7811), Anti-cardiac troponin t (WB:1000, Invitrogen, #MA5-12960), Anti-Myosin light chain 2 V (Synaptic Systems, # 310111), Anti-ATP2A2/SERCA2 (WB 1:1000; Cell Signaling, # 4388), Anti-RAF1 (WB 1:1000; Abcam, #AB181115), Anti-phospho-RAF1 (WB 1:1000; S259, Abcam, #ab173539). Secondary antibodies against rabbit (IRDye 800CW Donkey) and mouse (IRDye 800CW Donkey) were purchased from LI-COR Biosciences. Western blots were developed with LI COR Odyssey FX (LI-COR) and quantification of signals was performed by densitometry of scanned signals with the aid of Image Studio (version 5.2, LI-COR).

Immunocytochemistry

Immunostaining was performed as described previously [29]. The procedure for the single-cell suspensions of CBs was described in the flow cytometry section. Briefly, cells were washed twice with ice-cold PBS containing magnesium/calcium and fixed with 4% PFA (Merck) for 20 min at room temperature. To permeabilize the cell membranes, cells were incubated in 0.25% Triton X-100/PBS for 5 min. Blocking was performed with 3% bovine serum albumin (BSA, Merck) and 2% goat serum diluted in PBS containing 0.25% Triton X-100 for 1 h at room temperature. Incubation with primary antibodies was performed overnight. Cells were washed 3-times for 10 min with PBS and incubated with secondary antibodies for 2 h at room temperature. Slides were washed 3-times and ProLong® Gold antifade mountant (4',6-diamidino-2-phenylindole) (Life Technologies) was applied to mount the coverslips. Primary antibodies included Anti-OCT3/4 (1:1000; Santa Cruz, #sc-5279), Anti-TRA-1-60 (1:100; Abcam, #ab16288), Anti-SSEA4 (1:70; Hybridoma Bank, MC-813-70), Anti-TUBB3 (1:100; Thermo Scientific, #MA1-118), Anti-Nkx2.5 (1:200; Santa Cruz Biotechnology, #sc-14033), Anti-Sox17 (1:200; R&D Systems, #AF1924), Anti-alpha-actinin (1:200, Sigma, # A7811), Anti-cardiac troponin T (1:200, Invitrogen, #MA5-12960), Anti-RAF1 (1:250; Abcam, #AB181115). Secondary antibodies included Alexa488-conjugated goat anti-rabbit IgG (Invitrogen, #A11034), Alexa546-conjugated goat anti-mouse IgG (Invitrogen, #A11003), Alexa633-conjugated goat anti-rabbit IgG (#A4671), and Alexa488-conjugated goat anti-mouse IgG (Invitrogen, #A11029) (all from Life Technologies). Confocal images were obtained using an LSM 510-Meta microscope (Zeiss, Jena, Germany).

Immunohistochemistry

From formalin fixed tissue, 3 µm sections were stained with H&E and Masson trichrome (Trichrome II Blue staining kid at Nexus Special Stainer; Roche). Immunohistochemical analysis was performed on cryosections and paraffin sections using a Bench Mark XT automatic staining platform (Ventana, Heidelberg, Germany) with the following primary antibodies: mouse monoclonal anti-desmin (M076029-2, Agilent, 1:1000, Santa Clara, US); anti-troponin I (Ab47003 1:2000, Abcam) anti-SMA (M0851 1:2000, Clone 1A4, DAKO). The sections were examined using a Nikon Eclipse 80i equipped with a DS-Fi1 camera.

Transmission electron microscopy (TEM)

Cardiac bodies were fixed with 6% glutaraldehyde/0.4 M phosphate buffered saline (PBS) and were processed with a Leica EM TP tissue processor with 1%-osmium-tetroxide and embedded in resin. For electron microscopy, ultrathin sections were contrasted with 3% lead citrate trihydrate with a Leica EM AC20 (Ultrastain kit II) and were examined using a Zeiss EM 109 transmission electron microscope equipped with a Slowscan-2K-CCD-digital camera (2K-wide-angle Sharp: eye).

Measurement of Ca^{2+} cycling in cardiac bodies

iPSC-derived CBs were dissociated and grown on gelatin coated cover slips for up to 7 days before loading with the fluorescent Ca^{2+} indicator fura-2 by adding 1 µg Fura-2-AM/mL cell medium. After 15 min incubation at 37°C, cells were washed in prewarmed medium (37°C). A dual excitation (340 nm and 380 nm) fluorescence imaging recording system was used to measure Ca^{2+} transients of paced (0.5 Hz) and spontaneously beating cells (HyperSwitch Myocyte System, IonOptix Corp., Milton, MA, USA). Data were acquired as the ratio of measurements at 340 and 380 nm and analyzed using IonWizard software (Version 6.4, Ion Optix Corp).

Results

Reprogramming of human fibroblast towards iPSCs and their pluripotency properties

Fibroblasts were obtained from dermal biopsies of a female with NS and heterozygous *RAF1 c.770C>T* mutation (Fig. 1A). Reprogramming of fibroblasts to iPSCs was performed using a cocktail of the transcription factors *OCT3/4*, *SOX2*, *L-MYC*, *TRP53* and *EBNA-1* as previously described [24]. The iPSC-RAF1 colonies were positive for pluripotency markers of alkaline phosphatase (Fig. 1B, C and S1), OCT4, TRA1-60 and SSEA4 (Fig. 1F and S1). A karyogram confirmed the stable chromosomal integrity of the iPSC and sequencing verified the presence of the *RAF1 c.770C>T* mutation in iPSC (Fig. 1D and E). Spontaneous embryoid body (EB) formation and random differentiation confirmed the tri-lineage differentiation potential of iPSCs. (Fig. 1G, H and S1).

Cardiac differentiation of patient-specific iPSCs in dynamic suspension culture

The iPSC cell lines were differentiated using a 3D differentiation method including Wnt signaling modulation as described previously [27,28]. iPSC suspension culture iPSCwas used to form 3D EBs (Fig. 2A) which were further differentiated by supplementing small molecule inhibitors of GSK3β (24h) and Wnt (48h) at d0 and d3, respectively (Fig. 2B). Five to seven days after induction of cardiac differentiation, CBs started to contract spontaneously (Sup. Video. 1). At d10 of differentiation, a metabolic selection was performed by converting the source sugar from glucose to lactate therefore taking advantages of the unique cardiomyocytes metabolic pathways and energy sources. This step led to elimination of non-cardiac myocytes and thus to more homogeneous population of CBs (Fig. 2B). Analyzed cells were negative for pluripotency markers at RNA and protein levels (data are not shown) and positive for cardiac markers (Figs. 2C and D). Generated CBs at d40 of differentiation were 95% cardiac troponin T (cTnT) positive and 94% MLC2v positive (Fig. 2C). Immunohistochemistry of cryosections of CBs revealed homogenous populations of cTnT and α-actinin positive cells, in the core as well as in the peripheral cells of the CBs (Fig. 2D). Since hypertrophy is a hallmark of non-proliferating cells, it was of major importance to have cardiomyocytes which do not enter cell cycle in response to external stimuli. Therefore, CBs at d40 were dissociated and cardiomyocytes were seeded adherent (2D; hereafter abbreviated as CMs) on coverslips for 7 days and stained after for phospho-histone 3 (p-H3), a mitotic marker. Our data showed that cardiomyocytes at d47 were p-H3 negative. As a positive control, proliferative iPSCs were treated for 12-hours with 100 nM Nocadazole (NA) to be arrested in mitosis (Fig. 2E and S2A and B). Cell cycle analysis indicated that NA treated iPSC rendered at G2/M phase and stained positive for p-H3 (Fig. S2B and C). Moreover, dissociated cardiomyocytes at d40 were treated with 100 μM L-phenylephrine (PE), an α-adrenergic agonist, for 7 days. Cells were p-H3 negative but increased in size (Fig. S2C, D and E), which is consistent with its pro-hypertrophic activity. Collectively, iPSC-derived CBs possess all important properties of fully differentiated cardiomyocytes, including the expression of cardiac markers, a contractile behavior and the loss of proliferation.

Impact of RAF1^{S257L} mutation in the ultra sarcomeric structure and cardiac architecture of cardiomyocytes

Familial HCM is known to be a disease which is, among other things affecting the sarcomeric architecture. To understand if this is also the case for syndromic HCM, we investigated first the impact of the RAF1^{S257L} mutation on the sarcomeric structure and organization. CBs at d40 were dissociated and single CMs were cultured for 7 days on coverslips. CM-RAF1^{S257L} displayed more disorganized myofibrils compared to the WT (Fig. 3A) which was further confirmed in the electron microscopic (EM) images at higher resolution. Furthermore, RAF1^{S257L} CBs did not develop I-bands (Fig. 3C). Most

interestingly, desmin and troponin staining of the patient derived cardiac tissue (CT)-RAF1^{S257L} exhibited the same sarcomeric disorganization and absence of the I-bands like iPSC-derived CB/CM along with thickened Z-disks (Figs. 3B and 3D). To examine the influence of abundance MAPK signaling on observed phenotype, we treated the RAF1^{S257L} CBs in early stages of the development (d12) with 0.2 μM of MEK inhibitor PD0325901 until d40. Remarkably, ultra-structure analysis indicated the reappearance of the missing I-bands around the Z-disk in the MEKi treated cell population. These data indicate, for the first time, that a RAF-mediated signaling pathway regulates the integrity of the sarcomeric structures.

Next, we addressed the question, whether the higher activity of RAF-MAPK in RAF1^{S257L} CBs modulate the sarcomeric components expression. In comparison with WT CBs, RAF1^{S257L} CBs strikingly exhibited higher levels of MYH7 and MYL2 but lower levels of titin, MYH6, MYL7 and α-SMA (Fig. 3G). We tested HCM marker of MYH7-to-MYH6 ratio in two different maturation time points of younger (d24) and older mutant cells (d47). Notably, we observed a significant increase in MYH7-to-MYH6 ratio in both, younger (d24) and older mutant cells (d47) (Fig. 3H). However, PD0325901 treatment was only able to significantly reduce this ratio in the older RAF1^{S257L} CBs. Therefore, we postulated that the advanced organization of the sarcomeric structure via MEKi treatment is rather due to the sarcomeric/cytoplasmic function of MAPK than to its nuclear function. This also explains the need of a longer period of MEKi treatment. According to the observed data, we suggest that an aberrant RAF-MAPK signaling can affect the sarcomeric components in their expression and structure.

Alternated calcium transients and contractile behavior of RAF1^{S257L} CBs/CMs

Given the fact that we obtained a functional role of RAF1 in the organization of the sarcomeric architecture, we next aimed to investigate whether this also effects the contractility of the RAF1^{S257L} CBs. Interestingly, RAF1^{S257L} CBs contract 1.6-fold slower than WT CBs (Fig. 4A; Video S3 and S4). In parallel, we compared the contraction rate of WT CBs treated with PE. In contrast to RAF1^{S257L} CBs, WT CBs +PE contracted 1.5-fold faster than WT CBs -PE (Fig. S3A). Next, the contractility of CBs in the presence of MEKi PD0325901 was determined using CBs at d24 (younger CBs) versus d47 (older CBs). Both CBs d24 and d47 exhibited reduced contraction rates. However, MEKi treatment significantly increased the contraction rate in the older CBs (Fig. 4A).

Affected contractility of RAF1^{S257L} CBs can be attributed to aberrant calcium handling properties, which are known to be one of the main characteristics of a maladaptive hypertrophy [20,30]. To measure intracellular calcium transients, CMs were seeded on Geltrax-coated coverslips and supplemented at d47 with fura-2, a fluorescent Ca^{2+} indicator. Calcium transients were significantly reduced in RAF1^{S257L} CMs as compared to WT CMs (0.04 versus 0.079, p=0.03) (Fig. 4B-F). On the contrary, WT CM +PE exhibited an increased calcium transient in comparison to WT CM -PE (Fig. S3A). These data are consistent with opposing contraction rates of RAF1^{S257L} CMs and WT CMs +PE clearly

point to distinct mechanism of the hypertrophy induction mediated by RAF1 versus PE (Fig. 4A and S1A, B and C).

We next investigated the molecular basis of the decreased contractility and aberrant calcium handling. Ca^{2+} influx into the cardiomyocytes through L-type calcium channels (LTCCs) triggers additional Ca^{2+} release from the sarcoplasmic reticulum (SR) by activating the ryanodine receptor type-2 (RyR2). Diastole or relaxation occurs when Ca^{2+} is transported into the SR by the sarco/endoplasmic reticulum Ca^{2+}-ATPase (SERCA2a) and into the extracellular space by the Na^+/Ca^{2+} exchanger (NCX), respectively [31]. Phospholamban (PLN) inhibits SERCA if not phosphorylated by PKA or CAMKII, respectively [32]. First, we analyzed the expression of the components regulating/maintaining intracellular calcium transients using WT CBs and RAF1^{S257L} CBs at d24 and d47. RAF1^{S257L} CBs at d24 showed a significant decrease in expression of PLN, SERCA2, RYR, calcium voltage-gated channel alpha (CACNA) subunits 1C and 1D, whereas SERCA2a and CACNA1D were significantly reduced in RAF1^{S257L} CBs at d47 (Fig. 4G). Expression of SERCA2a and its negative regulator PLN, two proteins which are strongly regulating the calcium flux into the SR lumen, were affected in RAF1^{S257L} CBs at d24 and d47 (Fig. 4G). Consistently, PLN/SERCA ratio was remarkably increased in both RAF1^{S257L} CBs, which was reversed to the levels of WT CBs upon MEKi treatment (Fig. 4H). Collected data suggests that the HCM causing RAF1^{S257L} mutation reduces the contractile function by changing the calcium transients. Furthermore, our data reveled higher levels of active PLN (PLN/p-PLN) to SERCA in RAF1^{S257L} CBs, which most likely results in a decreased Ca^{2+} reuptake into the SR and therefore a prolonged contraction of the RAF1^{S257L} CBs. Our data further demonstrated lower RNA levels of PLN and SERCA in RAF1^{S257L} CBs. The fact that PLN levels but not SERCA levels increased after MEKi treatment indicates the selective importance of MEK-ERK signaling in the regulation of PLN expression.

RAF1^{S257L} CBs displayed fluctuation in various signaling pathways

Ser-257 is flanking the regulatory Ser-259 which interacts, when phosphorylated, with a 14-3-3 isoform and therefore stabilizes RAF1 in its inactive form [8]. Ser-257 substitution to Leu resulted in reduced phosphorylation of Ser-259 up to 50% (Fig. 5C), which has been proposed to contribute to a higher overall activity of RAF1 as well as a shift of binding affinity of RAF for MST1/2 to MEK1/2 [33]. The canonical MAPK pathway is one of the most studied pathways downstream of RAF1. However, activation of other RAF1 substrates in addition to MEK1/2 may control pathways related to HCM (Fig. 5A). Analysis of RAF1^{S257L} CBs showed a significantly higher level of p-ERK as compared to WT CBs, which completely abrogated in the presence of 0.2 µM MEKi (Fig. 5B and C). In addition, we observed increased levels of p-p38/p38 and decreased p-YAP/YAP in RAF1^{S257L} CBs, where MEKi treatment was able to partially rescue these changes (Fig. 5B and C). The PI3K-AKT-S6K and JNK axis did not show remarkable different activity between the RAF1^{S257L} CBs and WT CBs (Fig. 5B and C). To check the activity

of RAF1-AC-PKA in mutant CBs, we candidate cTnI as a substrate of PKA [34]. In RAF1^{S257L} CBs, we detected elevated levels of both p-cTnI and total cTnI. The atrial natriuretic peptide and the brain natriuretic peptide (ANP [gene; NPPA] and BNP [gene; NPPB]) are two clinical biomarkers for heart failure which are upregulated during hypertrophy because of a return to the fetal gene program, which was shown to be activated via calcineurin-Nuclear factor of activated T‑cells (NFAT) and Myocyte Enhancer Factor 2 (MEF2) [35,36]. The quantitate PCR of the NPPA and NPPB showed upregulation of NPPB in RAF1^{S257L} CBs (Fig. 5D) which MEKi treatment of CBs had reduced the NPPB levels more than 10 folds.

Discussion

The main purpose of this study was to investigate the mechanistic basis of cardiac hypertrophy induced by RAF1^{S257L}. Therefore, a protocol for the differentiation of highly pure, ventricular and contractile iPSC-derived cardiac bodies (CBs) was established.

Downstream signaling activities of the RAF1^{S257L} in cardiac myocytes

Regulation of the HCM response genes via MAPK

RAF1^{S257L} CBs exhibited an approximately 50% reduced inhibitory phosphorylation of RAF1 at Ser-259 which is consistence with previous reports [3,4,12]. The best studied RAF1 substrates are MEK1/2 that in turn phosphorylate ERK1/2. Accordingly, high p-ERK1/2 levels detected in RAF1^{S257L} CBs, also observed in previous studies [10,12], were completely abolished in the presence of MEKi. This was accompanied with a partial reversion of the observed phenotype in cardiac myocytes. The MAPK pathway seems not only to be crucial for normal heart development but may act as central node of almost all hypertrophy agents stimulating adoptive and maladaptive hypertrophy [37,38]. How MEK-ERK regulates the HCM, remains an open question. Upon activation, ERK1/2 phosphorylates and regulates the activity of a wide range of substrates in the cytoplasm and nucleus. In cardiomyocytes, ERK1/2 phosphorylates cardiac specific transcription factor of GATA4 at Ser-105 and enhance its transcriptional DNA-binding activity. GATA4 is critical for the expression of structural and cardiac hypertrophy response genes, such as *NPPA*, *NPPB*, β-*myosin heavy chain* (*Myh7*), *troponin I* (*Tnni3*), and *α-skeletal Actin* (*Acta1*) [39-43]. The expression analysis in RAF1^{S257L} CBs elucidate upregulation of *NPPB* and *MYH7* at RNA levels and cTnI only at protein levels. This may explain the mechanism of HCM induction via RAF1-MAPK-GATA4.

Calcineurin-NFAT signaling is another critical parameter for cardiac hypertrophy. Growing number of evidences, indicates positive cooperation among calcium regulated signaling of calcineurin-NFAT and MAPK in modulation of hypertrophy response genes [42,44]. Obtained data showed that RAF1^{S257L} regulates the prominent NFAT target gene of *NPPB* whereas RAF1^{S257L} CB + MEKi had 10-fold lower *NPPB*

levels. Previous studies revealed that hypertrophy induction via calcineurin-NFAT can be attenuated by ERK inhibitors. Moreover, calcineurin-NFAT/RAF-MAPK are found in the same signalosome in cardiac cells [10,42,44]. It has been proposed that ERK regulates NFAT activity *via* AP1 phosphorylation or p90 ribosomal S6 kinase type 3 (RSK3) [44,45]. Besides NFAT, GATA4 and RSK3, other ERK substrates, such as ELK1, MSK1, c-MYC and NFκB, are activated by ERK1/2 in cardiomyocytes [30,45-48]. We interpreted the observed expression changes of *NPPB, MYH7, MLY2, cTnI, SERCA2* and *LTCC* due to the co-occupation of the hypertrophy response genes promotors via transcription factors of GATA4, AP1, MEF2, NFAT and NFkB [41,43,49].

Regulation of the calcium handling and contraction via MAPK

One characteristic of the maladaptive hypertrophy is an abnormal calcium handling and consequently contractile defects [20,30]. Our functional analysis of the RAF1^{S257L} CBs revealed slower contraction rate in comparison to RAF1^{WT} CBs. Early treatment of RAF1^{S257L} CBs with MEKi from d12-d40 significantly ameliorated contractile dysfunction, whereas a shorter treatment (d12-d24) did not show any effect. Notably, MYH6-to-MYH7 switch also altered the contractile behavior of CBs, since MYH7 is known as a slower isoform and MYH6 faster isoform of myosin heavy chain [50]. In this regard, RAF1^{S257L} CBs exhibited higher levels of MYH7 leading to a depressed contractility, whereas WT CBs +PE contracted faster due to higher levels of MYH6 (See Fig. 4A and S3C).

Here, RAF1^{S257L} CBs also showed a reduced intracellular Ca^{2+} transient that most likely affects excitation-contraction coupling and cardiac contractile force [15]. Similarly, an impact on intracellular Ca^{2+} transient has been previously reported in iPSC-derived cardiac myocytes with gain of function mutations in BRAF and MRAS [22,51]. In contrast, a recent study that compare the idiopathic HCM and RAF1^{S257L} associated HCM, has shown that idiopathic CBs but not RAF1^{S257L} CBs exhibited significant alternations in calcium handling [11]. Small changes in intracellular Ca^{2+} concentration also affect the activity of Ca^{2+}-dependent phosphatases and kinases, including PKC, CaMKII and calcineurin. In this regard, observed reduced Ca^{2+} handling in RAF1^{S257L} CBs may be due to altered expression of calcium regulatory proteins, such as *SERCA2A*, *PLN* and *LTCC*. Evaluated levels of PLN/SERCA ratio, which inhibits SERCA2 pump and decreases cardiac contractility [52], contributes to HCM phenotype [32,53]. Previous studies have shown that RAS-MAPK pathway regulates *SERCA2A*, *PLN* and *LTCC* expression that are downregulated during hypertrophy and heart failure [49,53,54]. MEKi treatment of RAF1^{S257L} CBs did not restore SERAC2a expression but led to a significant upregulation of PLN and to a significant downregulation of BNP to levels close to that of WT CBs. This suggests that PLN and BNP expression but not SERCA2A may be under transcriptional control of ERK1/2. Interestingly, an increase in BNP, which is known as a HCM biomarker, leads to decrease in SERCA2A expression [55].

Cytosolic ERK target on regulation of the HCM

Sarcomeric signaling

A remarkable and unprecedented finding in the present study are the impaired I-bands in both RAF1[S257L] CBs and the heart biopsy samples from the corresponding patient with heterozygous *RAF1 p.Ser257Leu* variant. The I-band segment of titin, a lighter region of the sarcomere, acts as a molecular spring that develops tension when sarcomeres are stretched. It represents a regulatory node that integrates and perhaps coordinates diverse signaling events [56]. Most interestingly, this phenotype was completely rescued upon MEK inhibition. The underlying molecular mechanism that may explain is the MAPK assembly alongside the N2B region of titin in I-band area by scaffold protein four-and-a-half LIM domain 1 (FHL-1) [57,58]. N2B phosphorylation by ERK2 regulates the titin stiffness and thus, pressure overload-mediated cardiac hypertrophy [57,59]. Consistently, we detected RAF1 largely localized alongside the sarcomeres of RAF1[S257L] CMs.

Feedback and feedforward loops

Signal transduction analysis indicated that inhibition of MEK not only affected the ERK activity but also other critical factors in cardiomyocytes. This includes upregulation of *NPPB*, *MYH7-to-MYH6* ratio and phosphorylation p38, cTnI and YAP. Notably, ERK controls in addition to a wide range of transcription factors (see above) various upstream kinases (*e.g.*, RAF1, MEK1/2) and regulators (*e.g.*, SOS1) of the MAPK pathway dependent on the cellular context [60]. Moreover, ERK phosphorylates RKIP (RAF kinase inhibitor protein) and releases it from RAF1 and therefore activates the MAPK-cascade [34]. Therefore, MEK inhibition affects also the activity of the upstream components, including RAF1, which in turn results in activity changes of other RAF substrates and their pathways, including MST1/2-LATS1/2-YAP-CTGF, AC-cAMP-PKA-cTnI/PLN/MYH-7 and ASK1-JNK/p38-NFAT/MEF-NPPB (see Fig. 6) [61].

The activity of alternative RAF1-dependent pathways in HCM

RAF1-MST1/2-LATS1/2-YAP

Activated RAF1 binds to MST2 (also called STK3) and inhibits MST1/2-LATS1/2 pathway [33,62]. As a consequence, YAP translocates into the nucleus, associates with TEAD and regulates transcription of mitogenic factors, *CTGF*, *miR-206*, c-*MYC* and *NOTCH2*. Accordingly, higher amounts of YAP, detected in RAF1[S257L] CBs, was significantly reduced upon MEKi treatment. *MST1/2-LATS1/2*-YAP axis is critical for heart development, growth, regeneration and pathogenesis. It regulates proliferation in neonatal heart and growth and survival in adult heart [63-65]. YAP-miR206-FoxP1 axis regulates hypertrophy and survival of cardiomyocyte through upregulation of fetal genes, *e.g.*, *MYH7*, *NPPB* and *NPPB* [66].

RAF1-AC6-cAMP-PKA-cTnI

Another substrate of RAF1 is adenylyl cyclase type 6 (AC6) that generates cAMP [67,68]. cAMP-activated PKA, in turn, regulates sarcomeric and calcium transient regulators, such as cTnI. Phosphorylated cTnI (p-cTnI) increases the rate of cardiac muscle contractility [69]. Notably, HCM-associated cTnI mutations abolish phosphorylation of cTnI by PKA [70]. As shown in this study, RAF1^{S257L} CBs revealed elevated levels of both cTnI and p-cTnI. MEKi treatment significantly reduced the amounts of p-cTnI but not total cTnI, strongly suggesting that RAF1 is in cardiomyocytes not only upstream MEK1/2 and MST2 but also AC6.

MAPK networks in RAF1-associated HCM

Other MAPKs among ERK1/2, such as p38, JNK, and ERK5, appear to be involved in cardiac development, function, and diseases [37,71]. We next investigated the activity of other MAPKs in RAF1^{S257L} CBs. Data indicated a higher activating phosphorylation of p38 but not JNK in RAF1^{S257L} CBs. This was reduced upon MEKi treatment to the threshold levels of RAF1^{WT} CBs. The molecular mechanism which underlies p38 activation via RAF1^{S257L} in cardiac cells is unclear. We proposed that elevated levels of p38 in mutant cells could be a compensatory response of the cells to reduce the effects of the sustained ERK activity in an unknown ERK-dependent or ERK-independent positive feed-back regulation of the p38. One possible mechanism would be the positive regulation of the HDAC class I by ERK which deacetylates and inhibits the dual-specificity phosphatase 1 (dusp1). Acetylated DUSP1 bind with more affinity to p38 and dephosphorylates it. Therefore, the inhibition of DUPS1 by ERK-HDAC-DUSP1 axis results in accumulation of more p-p38 on the mutant cells (Fig. 6). Consistently, our results showed that MEKi can reduce the levels of the p38 that could be due to inhibition of the ERK-HDAC and more acetylated DUSP1 that target p-p38 among the MAPKs [72,73]. Based on previous studies, ERK is introduced as a negative regulator of p38, however, our data revealed a novel crosstalk between two set of MAPKs of ERK and p38 in cardiomyocytes that endogenously expressed hyperactive RAF^{S257L}. However, the precise mechanism of the MAPK crosstalk in cardiac myocytes needs further investigations.

Collectively, in this study we identified new aspects of RAF1 function in iPSC-derived cardiomyocytes which resemble the observed phenotype from the corresponding patient, specially the ultra-structure of the sarcomeres. The S257L mutation in RAF1-CBs modulate the RAF1 dependent signaling networking and cardiac specific proteins and functions, such as reactivation of fetal gene program, contraction rate, calcium transient and the sarcomeric structures. However, in this study we were not able to cover the activity of the all known RAF1 substrate which critical on cardiac function and contractions including troponin T, DMPK, ROCK, MYPT and calcineurin {9,10,12,74-78}. Therefore, further studies are needed to uncover the RAF1 signaling towards these components as well.

References

1. Rauen, K.A. The RASopathies. *Annual Review of Genomics and Human Genetics* **2013**, *14*, 355-369, doi:10.1146/annurev-genom-091212-153523.

2. Calcagni, G.; Adorisio, R.; Martinelli, S.; Grutter, G.; Baban, A.; Versacci, P.; Digilio, M.C.; Drago, F.; Gelb, B.D.; Tartaglia, M., et al. Clinical Presentation and Natural History of Hypertrophic Cardiomyopathy in RASopathies. *Heart Fail Clin* **2018**, *14*, 225-235, doi:10.1016/j.hfc.2017.12.005.

3. Pandit, B.; Sarkozy, A.; Pennacchio, L.A.; Carta, C.; Oishi, K.; Martinelli, S.; Pogna, E.A.; Schackwitz, W.; Ustaszewska, A.; Landstrom, A., et al. Gain-of-function RAF1 mutations cause Noonan and LEOPARD syndromes with hypertrophic cardiomyopathy. *Nature Genetics* **2007**, *39*, 1007-1012, doi:10.1038/ng2073.

4. Razzaque, M.A.; Nishizawa, T.; Komoike, Y.; Yagi, H.; Furutani, M.; Amo, R.; Kamisago, M.; Momma, K.; Katayama, H.; Nakagawa, M., et al. Germline gain-of-function mutations in RAF1 cause Noonan syndrome. *Nature Genetics* **2007**, *39*, 1013-1017, doi:10.1038/ng2078.

5. Light, Y.; Paterson, H.; Marais, R. 14-3-3 Antagonizes Ras-Mediated Raf-1 Recruitment to the Plasma Membrane To Maintain Signaling Fidelity. *Molecular and Cellular Biology* **2002**, *22*, 4984-4996, doi:10.1128/mcb.22.14.4984-4996.2002.

6. Molzan, M.; Schumacher, B.; Ottmann, C.; Baljuls, A.; Polzien, L.; Weyand, M.; Thiel, P.; Rose, R.; Rose, M.; Kuhenne, P., et al. Impaired Binding of 14-3-3 to C-RAF in Noonan Syndrome Suggests New Approaches in Diseases with Increased Ras Signaling. *Molecular and Cellular Biology* **2010**, *30*, 4698-4711, doi:10.1128/mcb.01636-09.

7. Maron, B.J.; Maron, M.S. Hypertrophic cardiomyopathy. *The Lancet* **2013**, *381*, 242-255, doi:10.1016/s0140-6736(12)60397-3.

8.   Rezaei Adariani, S.; Buchholzer, M.; Akbarzadeh, M.; Nakhaei-Rad, S.; Dvorsky, R.; Ahmadian, M.R. Structural snapshots of RAF kinase interactions. *Biochem Soc Trans* **2018**, *46*, 1393-1406, doi:10.1042/BST20170528.

9.   Desideri, E.; Cavallo, Anna L.; Baccarini, M. Alike but Different: RAF Paralogs and Their Signaling Outputs. *Cell* **2015**, *161*, 967-970, doi:10.1016/j.cell.2015.04.045.

10. Dhandapany, P.S.; Fabris, F.; Tonk, R.; Illaste, A.; Karakikes, I.; Sorourian, M.; Sheng, J.; Hajjar, R.J.; Tartaglia, M.; Sobie, E.A., et al. Cyclosporine attenuates cardiomyocyte hypertrophy induced by RAF1 mutants in Noonan and LEOPARD syndromes. *Journal of Molecular and Cellular Cardiology* **2011**, *51*, 4-15, doi:10.1016/j.yjmcc.2011.03.001.

11. Sakai, T.; Naito, A.T.; Kuramoto, Y.; Ito, M.; Okada, K.; Higo, T.; Nakagawa, A.; Shibamoto, M.; Yamaguchi, T.; Sumida, T., et al. Phenotypic Screening Using Patient-Derived Induced Pluripotent Stem Cells Identified Pyr3 as a Candidate Compound for the Treatment of Infantile Hypertrophic Cardiomyopathy. *International heart journal* **2018**, *59*, 1096-1105, doi:10.1536/ihj.17-730.

12. Jaffre, F.; Miller, C.L.; Schanzer, A.; Evans, T.; Roberts, A.E.; Hahn, A.; Kontaridis, M.I. iPSC-Derived Cardiomyocytes Reveal Aberrant ERK5 and MEK1/2 Signaling Concomitantly Promote Hypertrophic Cardiomyopathy in RAF1-Associated Noonan Syndrome. *Circulation* **2019**, 10.1161/CIRCULATIONAHA.118.037227, doi:10.1161/CIRCULATIONAHA.118.037227.

13. Luther, P.K. The vertebrate muscle Z-disc: sarcomere anchor for structure and signalling. *Journal of Muscle Research and Cell Motility* **2009**, *30*, 171-185, doi:10.1007/s10974-009-9189-6.

14. Porrello, E.R.; Mahmoud, A.I.; Simpson, E.; Hill, J.A.; Richardson, J.A.; Olson, E.N.; Sadek, H.A. Transient regenerative potential of the neonatal mouse heart. *Science* **2011**, *331*, 1078-1080, doi:10.1126/science.1200708.

15. Eisner, D.A.; Caldwell, J.L.; Kistamas, K.; Trafford, A.W. Calcium and Excitation-Contraction Coupling in the Heart. *Circulation research* **2017**, *121*, 181-195, doi:10.1161/circresaha.117.310230.

16. Sun, C.; Kontaridis, M.I. Physiology of cardiac development: from genetics to signaling to therapeutic strategies. *Current Opinion in Physiology* **2018**, *1*, 123-139, doi:10.1016/j.cophys.2017.09.002.

17. Wang, L.; Kryshtal, D.O.; Kim, K.; Parikh, S.; Cadar, A.G.; Bersell, K.R.; He, H.; Pinto, J.R.; Knollmann, B.C. Myofilament Calcium-Buffering Dependent Action Potential Triangulation in Human-Induced Pluripotent Stem Cell Model of Hypertrophic Cardiomyopathy. *J Am Coll Cardiol* **2017**, *70*, 2600-2602, doi:10.1016/j.jacc.2017.09.033.

18. Wang, L.; Kim, K.; Parikh, S.; Cadar, A.G.; Bersell, K.R.; He, H.; Pinto, J.R.; Kryshtal, D.O.; Knollmann, B.C. Hypertrophic cardiomyopathy-linked mutation in troponin T causes myofibrillar disarray and pro-arrhythmic action potential changes in human iPSC cardiomyocytes. *J Mol Cell Cardiol* **2018**, *114*, 320-327, doi:10.1016/j.yjmcc.2017.12.002.

19. Mosqueira, D.; Mannhardt, I.; Bhagwan, J.R.; Lis-Slimak, K.; Katili, P.; Scott, E.; Hassan, M.; Prondzynski, M.; Harmer, S.C.; Tinker, A., et al. CRISPR/Cas9 editing in human pluripotent stem cell-cardiomyocytes highlights arrhythmias, hypocontractility, and energy depletion as potential therapeutic targets for hypertrophic cardiomyopathy. *Eur Heart J* **2018**, *39*, 3879-3892, doi:10.1093/eurheartj/ehy249.

20. Lan, F.; Lee, A.S.; Liang, P.; Sanchez-Freire, V.; Nguyen, P.K.; Wang, L.; Han, L.; Yen, M.; Wang, Y.; Sun, N., et al. Abnormal calcium handling properties underlie familial hypertrophic cardiomyopathy pathology in patient-specific induced pluripotent stem cells. *Cell Stem Cell* **2013**, *12*, 101-113, doi:10.1016/j.stem.2012.10.010.

21. Doyle, M.J.; Lohr, J.L.; Chapman, C.S.; Koyano-Nakagawa, N.; Garry, M.G.; Garry, D.J. Human Induced Pluripotent Stem Cell-Derived Cardiomyocytes as a Model for Heart Development and Congenital Heart Disease. *Stem Cell Rev* **2015**, *11*, 710-727, doi:10.1007/s12015-015-9596-6.

22. Higgins, E.M.; Bos, J.M.; Dotzler, S.M.; Kim, C.J.; Ackerman, M.J. MRAS Variants Cause Cardiomyocyte Hypertrophy in Patient-Specific iPSC-Derived Cardiomyocytes: Additional Evidence for MRAS as a Definitive Noonan Syndrome-Susceptibility Gene. *Circulation. Genomic and precision medicine* **2019**, 10.1161/circgen.119.002648, doi:10.1161/circgen.119.002648.

23. Haghighi, F.; Dahlmann, J.; Nakhaei-Rad, S.; Lang, A.; Kutschka, I.; Zenker, M.; Kensah, G.; Piekorz, R.P.; Ahmadian, M.R. bFGF-mediated pluripotency maintenance in human induced pluripotent stem cells is associated with NRAS-MAPK signaling. *Cell Commun Signal* **2018**, *16*, 96, doi:10.1186/s12964-018-0307-1.

24. Okita, K.; Matsumura, Y.; Sato, Y.; Okada, A.; Morizane, A.; Okamoto, S.; Hong, H.; Nakagawa, M.; Tanabe, K.; Tezuka, K., et al. A more efficient method to generate integration-free human iPS cells. *Nature methods* **2011**, *8*, 409-412, doi:10.1038/nmeth.1591.

25. Seabright, M. A rapid banding technique for human chromosomes. *Lancet (London, England)* **1971**, *2*, 971-972.

26. Hamta, A.; Adamovic, T.; Samuelson, E.; Helou, K.; Behboudi, A.; Levan, G. Chromosome ideograms of the laboratory rat (Rattus norvegicus) based on high-resolution banding, and anchoring of the cytogenetic map to the DNA sequence by FISH in sample chromosomes. *Cytogenetic and genome research* **2006**, *115*, 158-168, doi:10.1159/000095237.

27. Dahlmann, J.; Kensah, G.; Kempf, H.; Skvorc, D.; Gawol, A.; Elliott, D.A.; Drager, G.; Zweigerdt, R.; Martin, U.; Gruh, I. The use of agarose microwells for scalable embryoid body formation and cardiac differentiation of human and murine pluripotent stem cells. *Biomaterials* **2013**, *34*, 2463-2471, doi:10.1016/j.biomaterials.2012.12.024.

28. Lian, X.; Zhang, J.; Azarin, S.M.; Zhu, K.; Hazeltine, L.B.; Bao, X.; Hsiao, C.; Kamp, T.J.; Palecek, S.P. Directed cardiomyocyte differentiation from human pluripotent stem cells by modulating Wnt/beta-catenin signaling under fully defined conditions. *Nat Protoc* **2013**, *8*, 162-175, doi:10.1038/nprot.2012.150.

29. Nakhaei-Rad, S.; Nakhaeizadeh, H.; Kordes, C.; Cirstea, I.C.; Schmick, M.; Dvorsky, R.; Bastiaens, P.I.; Haussinger, D.; Ahmadian, M.R. The Function of Embryonic Stem Cell-expressed RAS (E-RAS), a Unique RAS Family Member, Correlates with Its Additional Motifs and Its Structural Properties. *The Journal of biological chemistry* **2015**, *290*, 15892-15903, doi:10.1074/jbc.M115.640607.

30. Dorn, G.W., 2nd; Force, T. Protein kinase cascades in the regulation of cardiac hypertrophy. *The Journal of clinical investigation* **2005**, *115*, 527-537, doi:10.1172/jci24178.

31. Tham, Y.K.; Bernardo, B.C.; Ooi, J.Y.; Weeks, K.L.; McMullen, J.R. Pathophysiology of cardiac hypertrophy and heart failure: signaling pathways and novel therapeutic targets. *Arch Toxicol* **2015**, *89*, 1401-1438, doi:10.1007/s00204-015-1477-x.

32. Periasamy, M.; Bhupathy, P.; Babu, G.J. Regulation of sarcoplasmic reticulum Ca2+ ATPase pump expression and its relevance to cardiac muscle physiology and pathology. *Cardiovascular Research* **2007**, *77*, 265-273, doi:10.1093/cvr/cvm056.

33. Romano, D.; Nguyen, L.K.; Matallanas, D.; Halasz, M.; Doherty, C.; Kholodenko, B.N.; Kolch, W. Protein interaction switches coordinate Raf-1 and MST2/Hippo signalling. *Nat Cell Biol* **2014**, *16*, 673-684, doi:10.1038/ncb2986.

34. Lorenz, K.; Rosner, M.R.; Brand, T.; Schmitt, J.P. Raf kinase inhibitor protein: lessons of a better way for beta-adrenergic receptor activation in the heart. *J Physiol* **2017**, *595*, 4073-4087, doi:10.1113/JP274064.

35. Kuwahara, K.; Nakao, K. Regulation and significance of atrial and brain natriuretic peptides as cardiac hormones. *Endocrine journal* **2010**, *57*, 555-565, doi:10.1507/endocrj.k10e-150.

36. Li, X.; Lan, Y.; Wang, Y.; Nie, M.; Lu, Y.; Zhao, E. Telmisartan suppresses cardiac hypertrophy by inhibiting cardiomyocyte apoptosis via the NFAT/ANP/BNP signaling pathway. *Molecular medicine reports* **2017**, *15*, 2574-2582, doi:10.3892/mmr.2017.6318.

37. Rose, B.A.; Force, T.; Wang, Y. Mitogen-activated protein kinase signaling in the heart: angels versus demons in a heart-breaking tale. *Physiol Rev* **2010**, *90*, 1507-1546, doi:10.1152/physrev.00054.2009.

38. Gallo, S.; Vitacolonna, A.; Bonzano, A.; Comoglio, P.; Crepaldi, T. ERK: A Key Player in the Pathophysiology of Cardiac Hypertrophy. *International journal of molecular sciences* **2019**, *20*, doi:10.3390/ijms20092164.

39. Bueno, O.F.; De Windt, L.J.; Tymitz, K.M.; Witt, S.A.; Kimball, T.R.; Klevitsky, R.; Hewett, T.E.; Jones, S.P.; Lefer, D.J.; Peng, C.F., et al. The MEK1-ERK1/2 signaling pathway promotes compensated cardiac hypertrophy in transgenic mice. *EMBO J* **2000**, *19*, 6341-6350, doi:10.1093/emboj/19.23.6341.

40. Charron, F.; Paradis, P.; Bronchain, O.; Nemer, G.; Nemer, M. Cooperative interaction between GATA-4 and GATA-6 regulates myocardial gene expression. *Mol Cell Biol* **1999**, *19*, 4355-4365, doi:10.1128/mcb.19.6.4355.

41. He, A.; Kong, S.W.; Ma, Q.; Pu, W.T. Co-occupancy by multiple cardiac transcription factors identifies transcriptional enhancers active in heart. *Proceedings of the National Academy of Sciences of the United States of America* **2011**, *108*, 5632-5637, doi:10.1073/pnas.1016959108.

42. Liu, Y.L.; Huang, C.C.; Chang, C.C.; Chou, C.Y.; Lin, S.Y.; Wang, I.K.; Hsieh, D.J.; Jong, G.P.; Huang, C.Y.; Wang, C.M. Hyperphosphate-Induced Myocardial Hypertrophy through the GATA-4/NFAT-3 Signaling Pathway Is Attenuated by ERK Inhibitor Treatment. *Cardiorenal medicine* **2015**, *5*, 79-88, doi:10.1159/000371454.

43. Dirkx, E.; da Costa Martins, P.A.; De Windt, L.J. Regulation of fetal gene expression in heart failure. *Biochimica et biophysica acta* **2013**, *1832*, 2414-2424, doi:10.1016/j.bbadis.2013.07.023.

44. Sanna, B.; Bueno, O.F.; Dai, Y.S.; Wilkins, B.J.; Molkentin, J.D. Direct and Indirect Interactions between Calcineurin-NFAT and MEK1-Extracellular Signal-Regulated Kinase 1/2 Signaling Pathways Regulate Cardiac Gene Expression and Cellular Growth. *Molecular and Cellular Biology* **2005**, *25*, 865-878, doi:10.1128/mcb.25.3.865-878.2005.

45. Passariello, C.L.; Martinez, E.C.; Thakur, H.; Cesareo, M.; Li, J.; Kapiloff, M.S. RSK3 is required for concentric myocyte hypertrophy in an activated Raf1 model for Noonan syndrome. *J Mol Cell Cardiol* **2016**, *93*, 98-105, doi:10.1016/j.yjmcc.2016.02.020.

46. Markou, T.; Hadzopoulou-Cladaras, M.; Lazou, A. Phenylephrine induces activation of CREB in adult rat cardiac myocytes through MSK1 and PKA signaling pathways. *J Mol Cell Cardiol* **2004**, *37*, 1001-1011, doi:10.1016/j.yjmcc.2004.08.002.

47. Zhong, W.; Mao, S.; Tobis, S.; Angelis, E.; Jordan, M.C.; Roos, K.P.; Fishbein, M.C.; de Alboran, I.M.; MacLellan, W.R. Hypertrophic growth in cardiac myocytes is mediated by Myc through a Cyclin D2-dependent pathway. *Embo j* **2006**, *25*, 3869-3879, doi:10.1038/sj.emboj.7601252.

48. Lorenz, K.; Schmitt, J.P.; Schmitteckert, E.M.; Lohse, M.J. A new type of ERK1/2 autophosphorylation causes cardiac hypertrophy. *Nature Medicine* **2008**, *15*, 75-83, doi:10.1038/nm.1893.

49. Ho, P.D.; Fan, J.S.; Hayes, N.L.; Saada, N.; Palade, P.T.; Glembotski, C.C.; McDonough, P.M. Ras reduces L-type calcium channel current in cardiac myocytes. Corrective effects of L-channels and SERCA2 on [Ca(2+)](i) regulation and cell morphology. *Circulation research* **2001**, *88*, 63-69, doi:10.1161/01.res.88.1.63.

50. Gupta, M.P. Factors controlling cardiac myosin-isoform shift during hypertrophy and heart failure. *Journal of Molecular and Cellular Cardiology* **2007**, *43*, 388-403, doi:10.1016/j.yjmcc.2007.07.045.

51. Josowitz, R.; Mulero-Navarro, S.; Rodriguez, N.A.; Falce, C.; Cohen, N.; Ullian, E.M.; Weiss, L.A.; Rauen, K.A.; Sobie, E.A.; Gelb, B.D. Autonomous and Non-autonomous Defects Underlie Hypertrophic Cardiomyopathy in BRAF-Mutant hiPSC-Derived Cardiomyocytes. *Stem cell reports* **2016**, *7*, 355-369, doi:10.1016/j.stemcr.2016.07.018.

52. MacLennan, D.H.; Kranias, E.G. Phospholamban: a crucial regulator of cardiac contractility. *Nature reviews. Molecular cell biology* **2003**, *4*, 566-577, doi:10.1038/nrm1151.

53. Huang, H.; Joseph, L.C.; Gurin, M.I.; Thorp, E.B.; Morrow, J.P. Extracellular signal-regulated kinase activation during cardiac hypertrophy reduces sarcoplasmic/endoplasmic reticulum calcium ATPase 2 (SERCA2) transcription. *Journal of Molecular and Cellular Cardiology* **2014**, *75*, 58-63, doi:10.1016/j.yjmcc.2014.06.018.

54. Ho, P.D.; Zechner, D.K.; He, H.; Dillmann, W.H.; Glembotski, C.C.; McDonough, P.M. The Raf-MEK-ERK cascade represents a common pathway for alteration of intracellular calcium by Ras and protein kinase C in cardiac myocytes. *J Biol Chem* **1998**, *273*, 21730-21735.

55. Zhai, Y.; Luo, Y.; Wu, P.; Li, D. New insights into SERCA2a gene therapy in heart failure: pay attention to the negative effects of B-type natriuretic peptides. *Journal of medical genetics* **2018**, *55*, 287-296, doi:10.1136/jmedgenet-2017-105120.

56. Krüger, M.; Linke, W.A. The Giant Protein Titin: A Regulatory Node That Integrates Myocyte Signaling Pathways. *Journal of Biological Chemistry* **2011**, *286*, 9905-9912, doi:10.1074/jbc.R110.173260.

57. Sheikh, F.; Raskin, A.; Chu, P.H.; Lange, S.; Domenighetti, A.A.; Zheng, M.; Liang, X.; Zhang, T.; Yajima, T.; Gu, Y., et al. An FHL1-containing complex within the cardiomyocyte sarcomere mediates hypertrophic biomechanical stress responses in mice. *The Journal of clinical investigation* **2008**, *118*, 3870-3880, doi:10.1172/jci34472.

58. Raskin, A.; Lange, S.; Banares, K.; Lyon, R.C.; Zieseniss, A.; Lee, L.K.; Yamazaki, K.G.; Granzier, H.L.; Gregorio, C.C.; McCulloch, A.D., et al. A novel mechanism involving four-and-a-half LIM domain protein-1 and extracellular signal-regulated kinase-2 regulates titin phosphorylation and mechanics. *The Journal of biological chemistry* **2012**, *287*, 29273-29284, doi:10.1074/jbc.M112.372839.

59. Liang, Y.; Bradford, W.H.; Zhang, J.; Sheikh, F. Four and a half LIM domain protein signaling and cardiomyopathy. *Biophysical reviews* **2018**, *10*, 1073-1085, doi:10.1007/s12551-018-0434-3.

60. Shin, S.Y.; Rath, O.; Choo, S.M.; Fee, F.; McFerran, B.; Kolch, W.; Cho, K.H. Positive- and negative-feedback regulations coordinate the dynamic behavior of the Ras-Raf-MEK-ERK signal transduction pathway. *Journal of cell science* **2009**, *122*, 425-435, doi:10.1242/jcs.036319.

61. Matallanas, D.; Birtwistle, M.; Romano, D.; Zebisch, A.; Rauch, J.; von Kriegsheim, A.; Kolch, W. Raf Family Kinases: Old Dogs Have Learned New Tricks. *Genes & Cancer* **2011**, *2*, 232-260, doi:10.1177/1947601911407323.

62. Romano, D.; Matallanas, D.; Weitsman, G.; Preisinger, C.; Ng, T.; Kolch, W. Proapoptotic Kinase MST2 Coordinates Signaling Crosstalk between RASSF1A, Raf-1, and Akt. *Cancer Research* **2010**, *70*, 1195-1203, doi:10.1158/0008-5472.can-09-3147.

63.   Del Re, D.P.; Yang, Y.; Nakano, N.; Cho, J.; Zhai, P.; Yamamoto, T.; Zhang, N.; Yabuta, N.; Nojima, H.; Pan, D., et al. Yes-associated Protein Isoform 1 (Yap1) Promotes Cardiomyocyte Survival and Growth to Protect against Myocardial Ischemic Injury. *Journal of Biological Chemistry* **2012**, *288*, 3977-3988, doi:10.1074/jbc.M112.436311.

64.   von Gise, A.; Lin, Z.; Schlegelmilch, K.; Honor, L.B.; Pan, G.M.; Buck, J.N.; Ma, Q.; Ishiwata, T.; Zhou, B.; Camargo, F.D., et al. YAP1, the nuclear target of Hippo signaling, stimulates heart growth through cardiomyocyte proliferation but not hypertrophy. *Proceedings of the National Academy of Sciences of the United States of America* **2012**, *109*, 2394-2399, doi:10.1073/pnas.1116136109.

65.   Zhou, Q.; Li, L.; Zhao, B.; Guan, K.L. The hippo pathway in heart development, regeneration, and diseases. *Circulation research* **2015**, *116*, 1431-1447, doi:10.1161/circresaha.116.303311.

66.   Yang, Y.; Del Re, D.P.; Nakano, N.; Sciarretta, S.; Zhai, P.; Park, J.; Sayed, D.; Shirakabe, A.; Matsushima, S.; Park, Y., et al. miR-206 Mediates YAP-Induced Cardiac Hypertrophy and Survival. *Circulation research* **2015**, *117*, 891-904, doi:10.1161/circresaha.115.306624.

67.   Beazely, M.A.; Alan, J.K.; Watts, V.J. Protein kinase C and epidermal growth factor stimulation of Raf1 potentiates adenylyl cyclase type 6 activation in intact cells. *Molecular pharmacology* **2005**, *67*, 250-259, doi:10.1124/mol.104.001370.

68.   Llavero, F.; Luque Montoro, M.; Arrazola Sastre, A.; Fernandez-Moreno, D.; Lacerda, H.M.; Parada, L.A.; Lucia, A.; Zugaza, J.L. Epidermal growth factor receptor controls glycogen phosphorylase in T cells through small GTPases of the RAS family. *The Journal of biological chemistry* **2019**, *294*, 4345-4358, doi:10.1074/jbc.RA118.005997.

69.   Solaro, R.J.; Rosevear, P.; Kobayashi, T. The unique functions of cardiac troponin I in the control of cardiac muscle contraction and relaxation. *Biochemical and biophysical research communications* **2008**, *369*, 82-87, doi:10.1016/j.bbrc.2007.12.114.

70.   Cheng, Y.; Regnier, M. Cardiac troponin structure-function and the influence of hypertrophic cardiomyopathy associated mutations on modulation of contractility. *Archives of biochemistry and biophysics* **2016**, *601*, 11-21, doi:10.1016/j.abb.2016.02.004.

71.   Jaffre, F.; Miller, C.L.; Schanzer, A.; Evans, T.; Roberts, A.E.; Hahn, A.; Kontaridis, M.I. Inducible Pluripotent Stem Cell-Derived Cardiomyocytes Reveal Aberrant Extracellular Regulated Kinase 5 and Mitogen-Activated Protein Kinase Kinase 1/2 Signaling Concomitantly Promote Hypertrophic Cardiomyopathy in RAF1-Associated Noonan Syndrome. *Circulation* **2019**, *140*, 207-224, doi:10.1161/circulationaha.118.037227.

72.   Ferguson, B.S.; Harrison, B.C.; Jeong, M.Y.; Reid, B.G.; Wempe, M.F.; Wagner, F.F.; Holson, E.B.; McKinsey, T.A. Signal-dependent repression of DUSP5 by class I HDACs controls nuclear ERK activity and cardiomyocyte hypertrophy. *Proceedings of the National Academy of Sciences of the United States of America* **2013**, *110*, 9806-9811, doi:10.1073/pnas.1301509110.

73.   Habibian, J.; Ferguson, B.S. The Crosstalk between Acetylation and Phosphorylation: Emerging New Roles for HDAC Inhibitors in the Heart. *International journal of molecular sciences* **2018**, *20*, doi:10.3390/ijms20010102.

74.   Shimizu, M.; Wang, W.; Walch, E.T.; Dunne, P.W.; Epstein, H.F. Rac-1 and Raf-1 kinases, components of distinct signaling pathways, activate myotonic dystrophy protein kinase. *FEBS Lett* **2000**, *475*, 273-277.

75.   Broustas, C.G.; Grammatikakis, N.; Eto, M.; Dent, P.; Brautigan, D.L.; Kasid, U. Phosphorylation of the Myosin-binding Subunit of Myosin Phosphatase by Raf-1 and Inhibition of Phosphatase Activity. *Journal of Biological Chemistry* **2001**, *277*, 3053-3059, doi:10.1074/jbc.M106343200.

76.   Kaliman, P.; Llagostera, E. Myotonic dystrophy protein kinase (DMPK) and its role in the pathogenesis of myotonic dystrophy 1. *Cellular Signalling* **2008**, *20*, 1935-1941, doi:10.1016/j.cellsig.2008.05.005.

77.   Pfleiderer, P.; Sumandea, M.P.; Rybin, V.O.; Wang, C.; Steinberg, S.F. Raf-1: a novel cardiac troponin T kinase. *J Muscle Res Cell Motil* **2009**, *30*, 67-72, doi:10.1007/s10974-009-9176-y.

78.   Zhao, Z.; Manser, E. Myotonic dystrophy kinase-related Cdc42-binding kinases (MRCK), the ROCK-like effectors of Cdc42 and Rac1. *Small GTPases* **2015**, *6*, 81-88, doi:10.1080/21541248.2014.1000699.
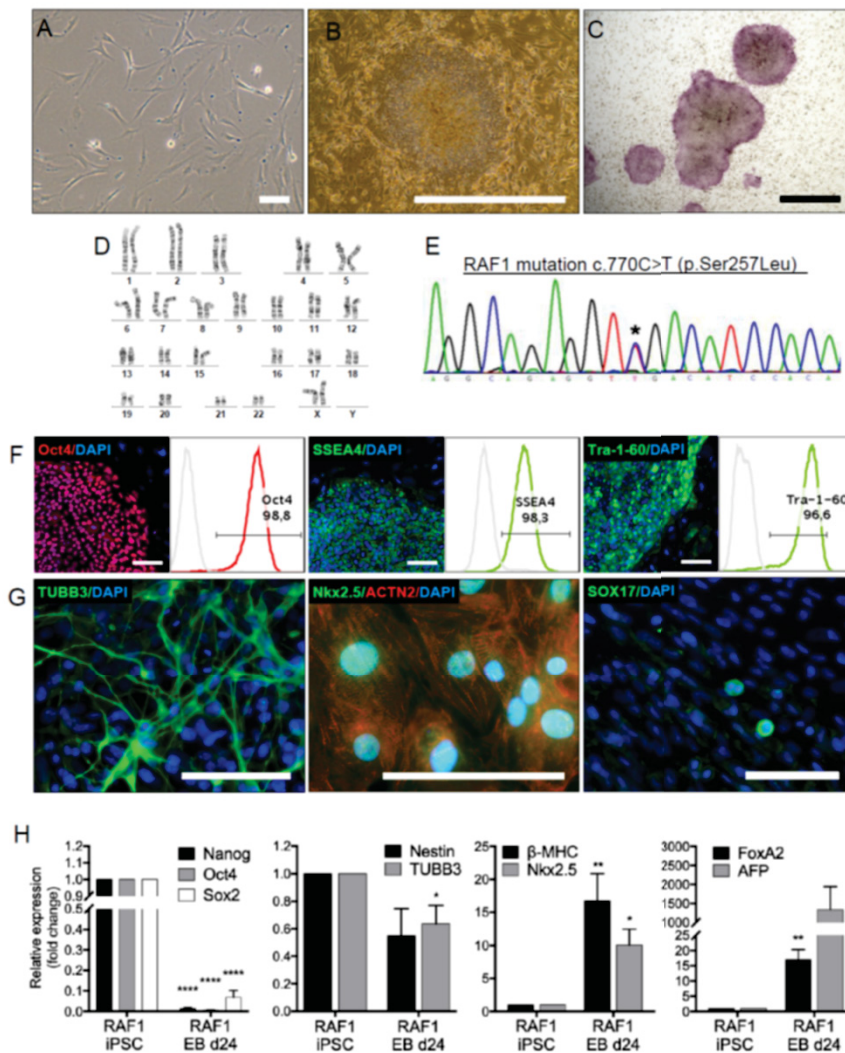
Figure 1: Characterization of iPSC-RAF1^S257L. iPSC-RAF1^S257L reveal a normal karyotype, express pluripotency markers and differentiate into ectodermal, endodermal and mesodermal derivatives *in vitro*. A) RAF1^S257L Patient derived dermal fibroblasts. B) Typical iPSC-RAF1^S257L colony on mitotically inactivated murine feeder cells. C) Colonies stain positive for alkaline phosphatase activity. D) In passage 8 after reprogramming, iPSCs show a normal diploid karyotype. E) Sanger sequencing confirmed the heterozygous RAF1^S257L mutation in iPSCs (asterisk). F) Expression of pluripotency markers Oct4, SSEA4 and Tra-1-60 by immunofluorescence staining and flow cytometry. Gray histograms represent isotype controls. G) Trilineage differentiation of patient iPSCs. Expression of endodermal (TUBB3), mesodermal (Nkx2.5 and sarcomeric α-actinin) and endodermal (SOX17) markers was detected. F) Relative gene expression of pluripotency (NANOG, OCT4, SOX2) and differentiation markers (Nestin, TUBB3, β-myosin heavy chain, Nkx2.5, FoxA2, alpha fetoprotein) of differentiated embryoid bodies on d24 of differentiation relative to undifferentiated iPSCs normalized by beta actin expression. Bar graphs represent mean of three independent samples +/- SEM. $*P < 0.05$, $**P < 0.01$, $***P < 0.001$, $****P < 0.0001$, unpaired t test. Scale bars: A, F, G: 100 μm, B, C: 1000 μm.
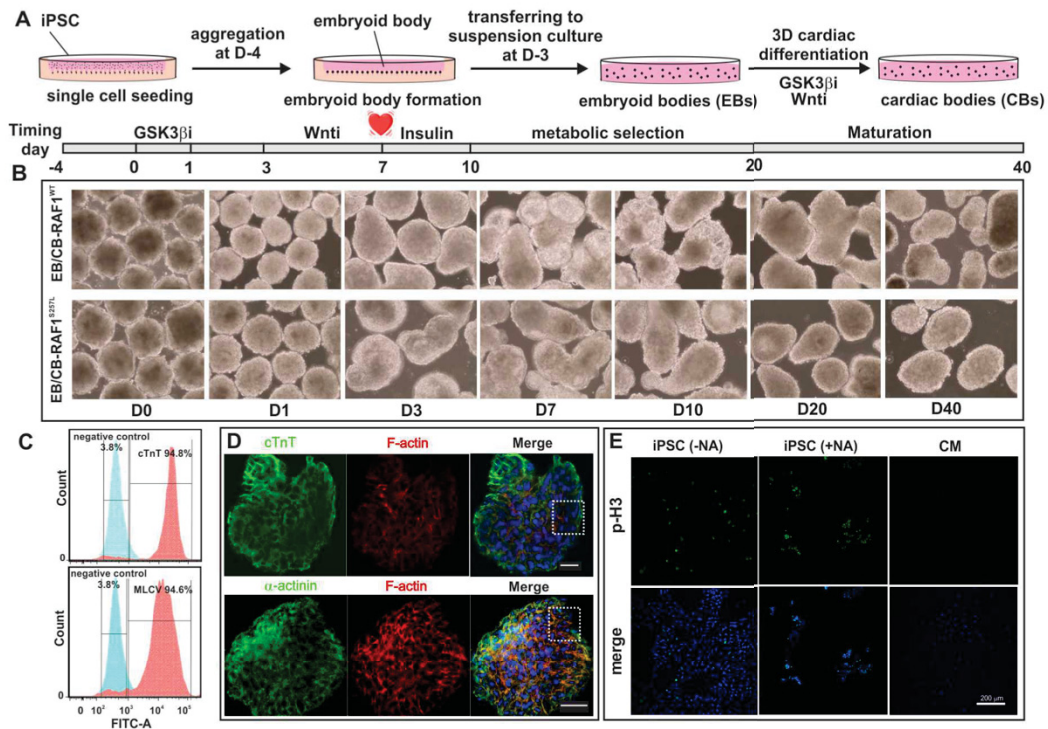
Figure 2: 3D cardiac differentiation of iPSC with Wnt signaling modulation. A) Schematic overview of embryoid body (EB) formation using agarose microwells combined with the stages and timeline of EBs differentiation towards cardiac bodies (CBs). B) Light microscopy pictures of EBs in different stages of cardiac differentiation. C) Flow cytometry of dissociated CBs displays the efficiency of the cardiac differentiation towards ventricular cardiomyocytes by analysis of MLCV2 and cTnT positive cells. D) Representative immunofluorescence staining of a cardiac body for cTnT and α-actinin expression. E) Illustration of mitotic cells stained with p-H3 in iPSC cells and CM. CM show no proliferative behavior compared to iPSCs. Arrested iPSC in mitosis with Nocodazole (NA) used as a positive control.
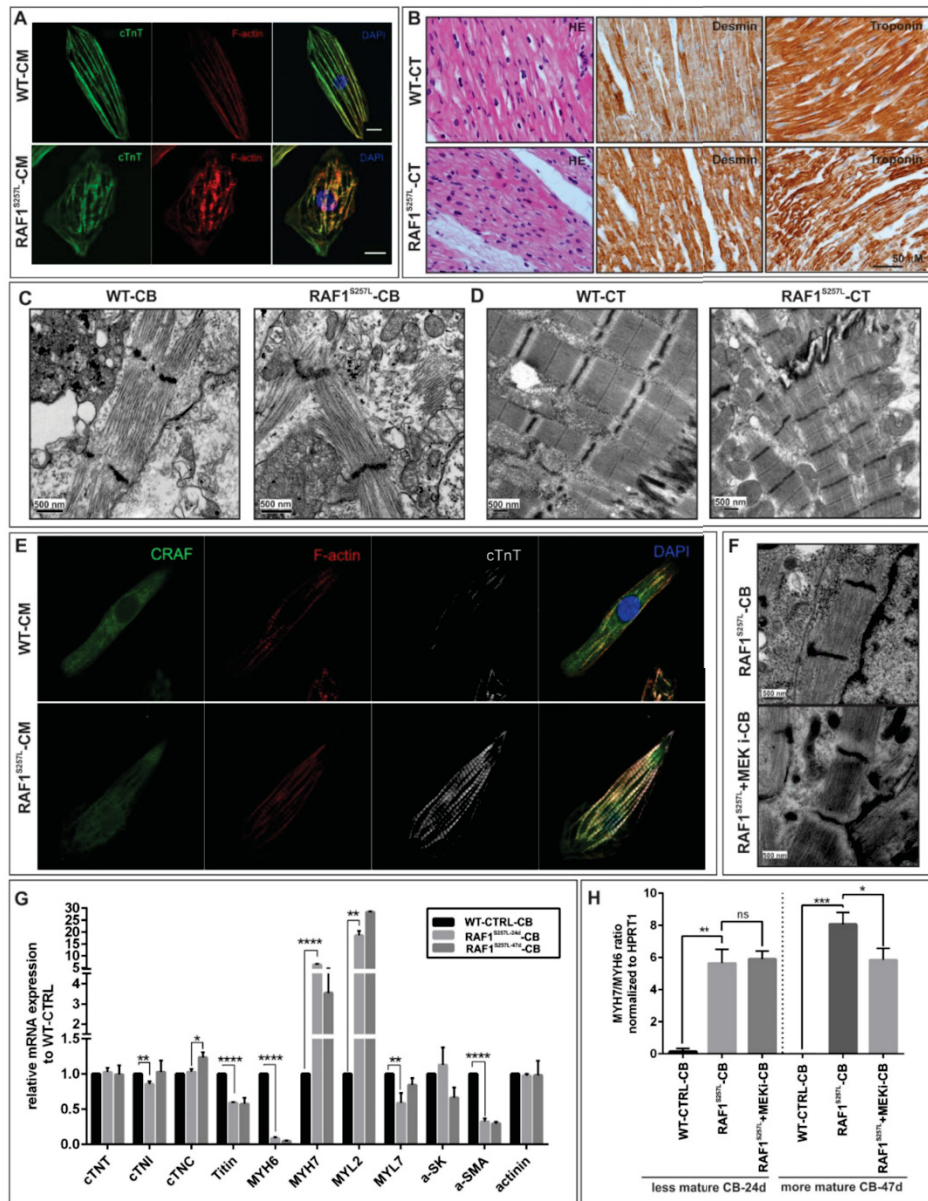
Figure 3: Aberrant RAF1 activity on cytoarchitecture of iPSC-derived cardiomyocytes. A) Dissociated cardiac bodies were seeded on Geltrex coated-coverslips for 7 days and stained with cTnT and F-actin. B) Microscopy analysis NS cardiac tissue (CT) with from the same patients carrying the RAF1 c.770C>T mutation. HE staining shows moderate variation of cardiomyocyte size and nuclei. Desmin and Troponin, represent the microfilament disarray. C) Electron microscopic images of CBs indicating a stronger myofibrillar disarray in CBs derived from RAF1 mutant iPSC than WT cardiac myocytes accompanied with the absence of a clear I-band in mutant cells. D) Electron microscopic images of cardiac tissue (CT) of the NS effected individual (RAF1 c.770C>T). Sarcomeric length is altered due to the RAF mutation. In mostly CT CTRL around 2.2 μm as in the patient between 1.3 – 1.9 μm showing the higher variation. E) Immunocytochemistry of CRAF in WT and RAF1 mutant cardiomyocytes at d90 of differentiation showing its localization at the sarcomere which are stained for F-actin. F) Electron microscopic images from RAF1 mutated CBs treated with 0.2 μM MEK inhibitor from d12 of differentiation. G) Quantitative mRNA expression profiling of sarcomeric molecules in WT CBs, RAF1S257L CBs and RAF1S257L CBs treated with 0.2 μM MEK inhibitor. H) The relative mRNA amount of MYH7 to MYH6 ratio was compared between WT CBs and RAF1S257L CBs at two different maturation phases of d23 and d40. RAF1-CBs were treated with MEK inhibitor from d12 of differentiation. *$P < 0.05$, **$P < 0.01$, ***$P < 0.001$, ****$P < 0.0001$, unpaired 2-tail t-test.

Figure 4: Calcium transients and contraction coupling in RAF mutation CBs. A) Contraction rate of cardiac bodies at d40 of differentiation represented a lower contraction rate of RAF1S257L CBs in comparison with WT CBs. The treatment of the RAF1S257L CBs with 0.2 µM MEKi showed a significant increase in the contraction rate in more mature CBs (>40 Days) but not younger CBs (<24 Days). B) Ca2+ transients are reduced in RAF1-mutant cardiac bodies. Bar graphs display the peak height of the Ca2+ transients. C) the time from offset to 50% of maximum peak height. D) the time from peak to 50% return to baseline. E) as well as the velocities of cytosolic Ca2+ increase and decrease (F). Each data point represents the average of 10 transients obtained from a single cardiac body. 9 wild type and 12 RAF1-mutant cells were analyzed. G) Quantitative transcription profiling of calcium transient regulator molecules in WT CBs and RAF1S257L CBs at d23 (younger) and at d40 (older). H) Relative mRNA ratio of PLN to SERCA2a was compared between WT CBs and RAF1S257L CBs at two different maturation phases of d23 and d40. RAF1S257L CBs were treated with MEK inhibitor from d12 of differentiation. *P < 0.05, **P < 0.01, ***P < 0.001, ****P < 0.0001, unpaired 2-tail t-test.
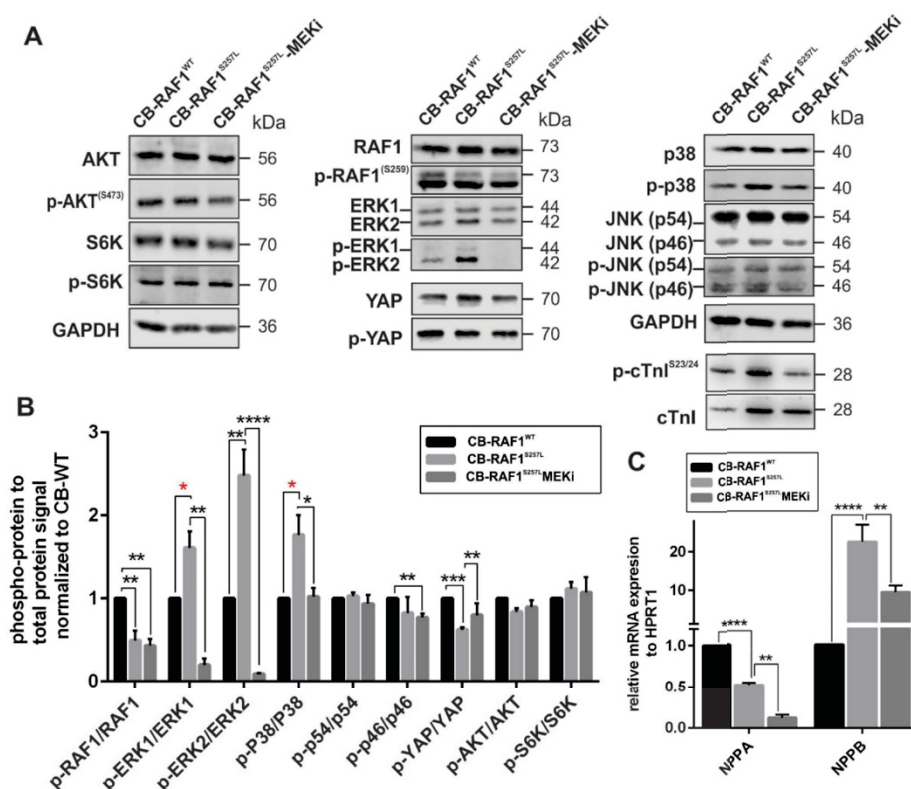
Figure 5: The effect of the RAF1S257L mutation on the selected kinases activity downstream of the RAF. A) Western blots analysis of the signaling molecules, p-AKT/AKT, p-S6K/S6K, p-RAF1S257/RAF1, p-ERK1/2/ERK1/2, p-YAP/ YAP, p-p38/p38, p-JNK/JNK and p-cTnI/cTnI. B) Quantification of western blotting signal intensity of the phospho-proteins normalized to the total protein levels. C) The relative quantitative real-time PCR of the NPPA and NPPB compared to HPRT1. *P < 0.05, **P < 0.01, ***P < 0.001, ****P < 0.0001, unpaired 2-tail t-test.
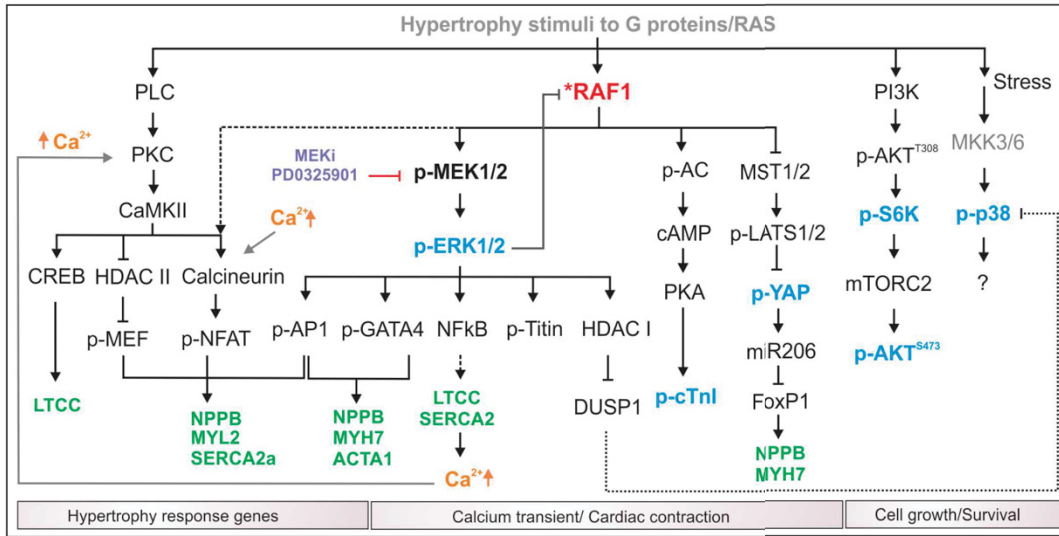
Figure 6: Summary of the proposed cardiac specific RAF1S257L signaling network. The schematic view of the signaling molecules and transcription factors investigated downstream of RAF kinase and hypertrophy stimuli. The blue labeled proteins are investigated at proteins and phosphor-protein analysis in WB and green labeled genes are investigated at RNA levels by qPCR.

Chapter IV

Functional Dysregulation of CDC42 Causes Diverse Developmental Phenotypes

Graphical abstract
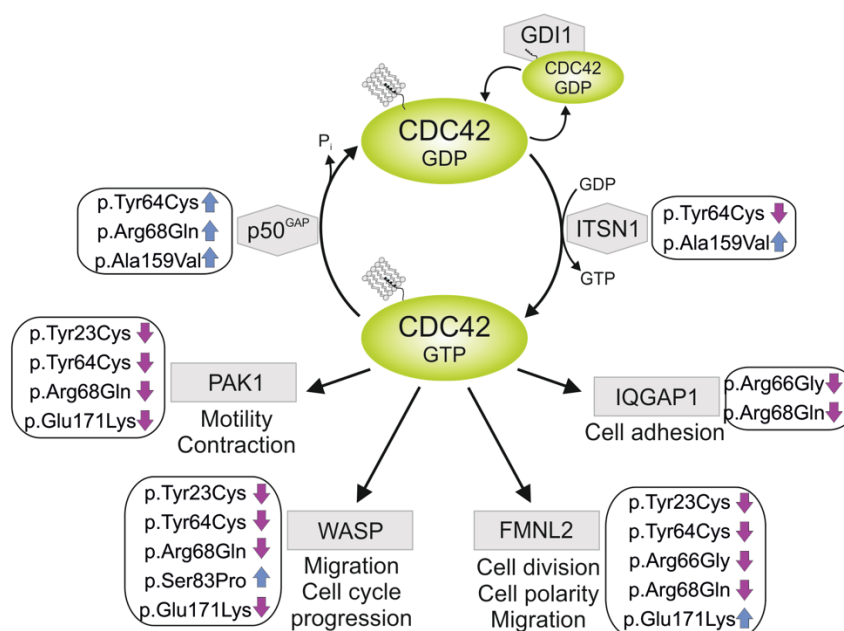
Status:	Published in The American Journal of Human Genetics, January 25th 2018
Impact factor:	9.893
Own proportion to this work:	5 %
	Expression and purification of CDC42 effectors, CDC42 GTP pull down assays, writing the manuscript, discussion.

Functional Dysregulation of CDC42 Causes Diverse Developmental Phenotypes

Simone Martinelli,[1] Oliver H.F. Krumbach,[2,30] Francesca Pantaleoni,[3,30] Simona Coppola,[4,30] Ehsan Amin,[2,31] Luca Pannone,[3] Kazem Nouri,[2,32] Luciapia Farina,[4] Radovan Dvorsky,[2] Francesca Lepri,[3] Marcel Buchholzer,[2] Raphael Konopatzki,[2] Laurence Walsh,[5] Katelyn Payne,[5] Mary Ella Pierpont,[6,7] Samantha Schrier Vergano,[8] Katherine G. Langley,[9] Douglas Larsen,[10] Kelly D. Farwell,[11] Sha Tang,[11] Cameron Mroske,[11] Ivan Gallotta,[12] Elia Di Schiavi,[12] Matteo della Monica,[13] Licia Lugli,[14] Cesare Rossi,[15] Marco Seri,[16] Guido Cocchi,[16] Lindsay Henderson,[9] Berivan Baskin,[9] Mariëlle Alders,[17] Roberto Mendoza-Londono,[18,19,20] Lucie Dupuis,[18] Deborah A. Nickerson,[21] Jessica X. Chong,[22] The University of Washington Center for Mendelian Genomics, Naomi Meeks,[23] Kathleen Brown,[23] Tahnee Causey,[24] Megan T. Cho,[9] Stephanie Demuth,[25] Maria Cristina Digilio,[3] Bruce D. Gelb,[26] Michael J. Bamshad,[21,22] Martin Zenker,[27] Mohammad Reza Ahmadian,[2,33] Raoul C. Hennekam,[28,33] Marco Tartaglia,[3,33,*] and Ghayda M. Mirzaa[22,29,33,*]

Exome sequencing has markedly enhanced the discovery of genes implicated in Mendelian disorders, particularly for individuals in whom a known clinical entity could not be assigned. This has led to the recognition that phenotypic heterogeneity resulting from allelic mutations occurs more commonly than previously appreciated. Here, we report that missense variants in *CDC42*, a gene encoding a small GTPase functioning as an intracellular signaling node, underlie a clinically heterogeneous group of phenotypes characterized by variable growth dysregulation, facial dysmorphism, and neurodevelopmental, immunological, and hematological anomalies, including a phenotype resembling Noonan syndrome, a developmental disorder caused by dysregulated RAS signaling. *In silico*, *in vitro*, and *in vivo* analyses demonstrate that mutations variably perturb CDC42 function by altering the switch between the active and inactive states of the GTPase and/or affecting CDC42 interaction with effectors, and differentially disturb cellular and developmental processes. These findings reveal the remarkably variable impact that dominantly acting *CDC42* mutations have on cell function and development, creating challenges in syndrome definition, and exemplify the importance of functional profiling for syndrome recognition and delineation.

The rate of identification of genes implicated in human disorders has dramatically increased with the use of second-generation sequencing technologies. In particular, exome sequencing has emerged as a feasible and efficient strategy to uncover the molecular basis of Mendelian disorders, particularly for individuals with a rare clinical presentation or for whom a unifying clinical diagnosis is not discerned.[1] Mutations affecting the same gene but resulting in substantial phenotypic differences is a very well-known phenomenon, but the wide use of exome sequencing has led to the recognition that this event occurs much more commonly than previously appreciated.[2–4] In the last few years, it has been recognized that the variable clinical manifestation of allelic mutations can often result from their differential impact on protein function, although the consequences of specific variants

[1]Department of Oncology and Molecular Medicine, Istituto Superiore di Sanità, Rome 00161, Italy; [2]Institute of Biochemistry and Molecular Biology II, Medical Faculty of the Heinrich-Heine University, Düsseldorf 40225, Germany; [3]Genetics and Rare Diseases Research Division, Ospedale Pediatrico Bambino Gesù, IRCCS, Rome 00146, Italy; [4]National Center for Rare Diseases, Istituto Superiore di Sanità, Rome 00161, Italy; [5]Riley Hospital for Children, Indianapolis, IN 46202, USA; [6]Department of Pediatrics, University of Minnesota, Minneapolis, MN 55454, USA; [7]Children's Hospital of Minnesota, Minneapolis, MN 55454, USA; [8]Division of Medical Genetics and Metabolism, Children's Hospital of The King's Daughters, Norfolk, VA 23507, USA; [9]GeneDX, Gaithersburg, MD 20877, USA; [10]Department of Neurology, Washington University, St. Louis, MO 63130, USA; [11]Ambry Genetics, Department of Clinical Genomics, Aliso Viejo, CA 92656, USA; [12]Institute of Biosciences and Bioresources, National Research Council, 80131 Naples, Italy; [13]Genetica Medica, Azienda Ospedaliera Universitaria Meyer, 50139 Florence, Italy; [14]Struttura Complessa di Neonatologia, Policlinico di Modena, 41124 Modena, Italy; [15]Genetica Medica, Policlinico S.Orsola-Malpighi, 40138 Bologna, Italy; [16]Department of Medical and Surgical Sciences, University of Bologna, 40138 Bologna, Italy; [17]Department of Clinical Genetics, Academic Medical Centre, University of Amsterdam, Amsterdam 1105-AZ, the Netherlands; [18]Division of Clinical and Metabolic Genetics, The Hospital for Sick Children, Toronto, ON M5G 1X8, Canada; [19]Genetics and Genome Biology, The Hospital for Sick Children, Toronto, ON M5G 1X8, Canada; [20]Department of Pediatrics, University of Toronto, Toronto, ON M5G 1X8, Canada; [21]Department of Genome Sciences, University of Washington, Seattle, WA 98195, USA; [22]Department of Pediatrics, University of Washington, Seattle, WA 98195, USA; [23]Children's Hospital Colorado, Aurora, CO 80045, USA; [24]Department of Human and Molecular Genetics, Virginia Commonwealth University, Richmond, VA 23284, USA; [25]Praxis für Humangenetik Erfurt, Erfurt 99084, Germany; [26]Mindich Child Health and Development Institute and Departments of Pediatrics, and Genetics and Genomic Sciences, Icahn School of Medicine at Mount Sinai, New York, NY 10029, USA; [27]Institute of Human Genetics, University Hospital Magdeburg, Magdeburg 39120, Germany; [28]Department of Pediatrics, Academic Medical Center, University of Amsterdam, Amsterdam 1105-AZ, the Netherlands; [29]Center for Integrative Brain Research, Seattle Children's Research Institute, Seattle, WA 98101, USA
[30]These authors contributed equally to this work
[31]Present address: Institute of Neural and Sensory Physiology, Medical Faculty of the Heinrich-Heine University, Düsseldorf, Germany
[32]Present address: Department of Pathology and Molecular Medicine, Richardson Laboratory, Queen's University, Kingston, ON K7L 3N6, Canada
[33]These authors contributed equally to this work
*Correspondence: marco.tartaglia@opbg.net (M.T.), gmirzaa@u.washington.edu (G.M.M.)
https://doi.org/10.1016/j.ajhg.2017.12.015.

can be difficult to predict and may require substantial efforts to be fully understood.[5–7] Here, we report that missense mutations in *cell division cycle 42* (*CDC42* [MIM: 116952]), a gene encoding a member of the RAS superfamily of low-molecular-weight GTP/GDP-binding proteins functioning as a major node in intracellular signaling, underlie a clinically heterogeneous group of developmental phenotypes. Our *in silico*, *in vitro*, and *in vivo* dissection of the structural and functional impact of disease-causing mutations documents that they variably perturb CDC42 biochemical behavior and differentially affect cellular and developmental processes, highlighting the variable impact of the functional dysregulation of this GTPase in cell physiology and development. Our findings also exemplify the importance of functional profiling for syndrome recognition and delineation.

A total of 15 subjects from 13 unrelated families were included in the study. Clinical data and DNA samples were collected from the participating families (after written informed consent was obtained) and stored and used under research projects approved by the Review Boards of the participating institutions. Investigators studying the affected individuals described here were connected via the MatchMaker Exchange (MME) network of web-based tools[8] GeneMatcher and MyGene2.[9,10] Nine affected individuals (subjects 1 to 5 and 8 to 11), who exhibited a molecularly unexplained and clinically unrecognized multi-systemic disorder, were investigated by whole-exome sequencing (WES) using DNA samples obtained from either leukocytes or saliva specimens, and a child-parent trio-based strategy. Exome capture was carried out using the SureSelect Clinical Research Exome (Agilent) (subjects 1 and 8), SureSelect Human All Exon v.1, v.3, and v.5 (Agilent) (subjects 2, 10, and 5, respectively), Nextera Exome Enrichment Kit (Illumina) (subject 3), SeqCap EZ VCRome 2.0 (Roche) (subject 4), and SeqCap EZ MedExome v2 (Roche) (subjects 9 and 11) target enrichment kits, and sequencing was performed on a HiSeq 2000 platform (Illumina), using paired-end. WES data processing, sequence alignment to GRCh37, and variant filtering and prioritization by allele frequency, predicted functional impact, and inheritance models were performed as previously described.[11–13] Mean coverage of target regions and average reads depth for individual samples are provided in Table S1. Subjects 12 (simplex case subject) and 13 to 15 (affected members of family 30153) (Figure S1) belonged to a cohort of 235 unrelated individuals with clinical features fitting Noonan syndrome (MIM: 163950) or overlapping with this disorder, followed at three participating genetic centers (Rome, Bologna, and Magdeburg),[14,15] who did not harbor mutations in previously identified genes implicated in RASopathies. Based on the hypothesis that mutations in *CDC42* might be linked causally to Noonan syndrome (or a clinically related RASopathy), the entire *CDC42* coding sequence was analyzed by targeted resequencing, using genomic DNA from blood, skin fibroblasts, hair bulbs, and/or epithelial cells from the oral mucosa. Target enrichment was performed using the Nextera Rapid Capture kit (Illumina), and sequencing was carried out on a NextSeq550 (Illumina) with a 2 × 150 bp paired-end read protocol. Alignment and variant calling were performed with the BWA Enrichment BaseSpace App (Illumina), and VCF output files were annotated using Variant Studio v.2.2 (Illumina). Finally, Sanger sequencing was used to screen the *CDC42* coding exons in subjects 6 and 7, who showed clinical features suggestive for the condition associated with *CDC42* group I mutations (see below).

Overall, nine different missense mutations distributed across the entire *CDC42* coding sequence were identified (Table 1). Two amino acid substitutions affected the N-terminal α helix (residues Ile21 and Tyr23), three involved adjacent residues within the switch II motif (Tyr64, Arg66, and Arg68), two mapped to the fourth β strand (Cys81 and Ser83), and the remaining two were located close to the C terminus (Ala159 and Glu171) (Figure 1A). Four variants were recurrent, and all occurred as a *de novo* event in at least one family. Of note, the c.511G>A substitution (p.Glu171Lys) was shared by the four affected subjects with clinical features resembling Noonan syndrome, occurring *de novo* in subject 12, and co-segregating with the phenotype in family 30153 (subjects 13 to 15), consistent with dominant inheritance. None of these variants had been reported in ExAC/gnomAD, and all were predicted to be pathogenic and met the American College of Medical Genetics (ACMG) criteria to be considered disease causing (Table S2).[19] One variant, c.191A>G (p.Tyr64Cys), had previously been reported in two subjects with syndromic thrombocytopenia (MIM: 616737).[20,21]

CDC42 encodes a small GTPase of the RHO family modulating multiple signaling pathways controlling cell polarity and migration, endocytosis, and cell cycle progression, by cycling between an active (GTP-bound) and an inactive (GDP-bound) state.[22,23] It is characterized by five major highly conserved motifs, G1 to G5, which mediate GTP binding and hydrolysis (G4 and G5), phosphate binding (G1 and G3), and effector binding (G2) (Figure 1A).[24,25] Based on clinical heterogeneity (see below) and location of affected residues, we predicted that the mutations would have a variable functional impact. The structural consequences of the identified disease-causing mutations on CDC42 structure and function were assessed by Pymol molecular viewer (see Web Resources), using available PDB structures. This allowed us to inspect CDC42 interactions with ARHGAP1 (p50^{GAP}/CDC42GAP; PDB: 1grn), ARHGAP18 (MacGAP; PDB: 5c2j), and ITSN1 (PDB: 1ki1) and WAS (WASP; PDB: 1cee), as representatives for CDC42's GTPase activating proteins (GAPs), guanine nucleotide exchange factors (GEFs), and effectors, respectively, and to classify them structurally and functionally into three different groups. A first group of mutations affected the switch II region (p.Tyr64Cys, p.Arg66Gly, and p.Arg68Gln; group I), which mediates CDC42 binding to effectors and regulators (Figures 1B–1D).[25] Tyr64 and

Table 1. List of the Germline CDC42 Missense Mutations Identified in This Study

Exon	Nucleotide Change	Amino Acid Change	Domain	Mutation Group	Subjects	Origin	MetaSVM[a]	CADD phred[a]	REVEL[a]	ACMG
1	c.62T>C	p.Ile21Thr	α1	III	1	de novo	0.3729	27.1	0.901	pathogenic
1	c.68A>G	p.Tyr23Cys	α1	III	2	de novo	0.7752	27.1	0.937	pathogenic
3	c.191A>G	p.Tyr64Cys	switch II	I	3	de novo	0.7976	23.4	0.834	pathogenic
3	c.196A>G	p.Arg66Gly	switch II	I	4, 5	de novo	0.5326	26.9	0.836	pathogenic
3	c.203G>A	p.Arg68Gln	switch II	I	6, 7	de novo	0.6586	26.3	0.827	pathogenic
3	c.242G>T	p.Cys81Phe	β4	II	8	de novo	0.6280	30.0	0.840	pathogenic
3	c.247T>C	p.Ser83Pro	β4	II	9, 10	de novo	0.8283	27.8	0.853	pathogenic
4	c.476C>T	p.Ala159Val	NBP	II	11	de novo	1.0179	34.0	0.916	pathogenic
5	c.511G>A[b]	p.Glu171Lys	CBR	III	12, 13–15	1 de novo, 1 familial	0.0158	24.7	0.768	pathogenic

Nucleotide numbering reflects cDNA numbering with 1 corresponding to the A of the ATG translation initiation codon in the *CDC42* reference sequence (GenBank: NM_001791.3). No variants were reported in the public databases ExAC and GnomAD. All variants were predicted to be "deleterious" by Combined Annotation Dependent Depletion (CADD) v.1.3, Database for Nonsynonymous SNPs' Functional Predictions (dbNSFP) Support Vector Machine (SVM) v.3.0, and REVEL algorithms.[16–18] All changes satisfied the necessary criteria to be classified as pathogenic according to the American College of Medical Genetics guidelines.[19] Abbreviations: NBP, nucleotide binding pocket; CBR, CRIB motif binding region.
[a]Scores > 0 (MetaSVM), > 15 (CADDphred) or > 0.5 (REVEL) predict that the sequence change has a significant impact on protein structure and function.
[b]This change affects transcript variant 1 (GenBank: NM_001791.3) and isoform 1 (GenBank: NP_001782.1), while it does not affect transcript variant 2 (GenBank: NM_044472.2) and isoform 2 (GenBank: NP_426359.1). The two isoforms have the same amino acid length but are characterized by a different C terminus.

Arg66 are located on the surface of CDC42 and directly participate in interactions with regulatory proteins and effectors. These changes were predicted to affect these interactions and, as a consequence, the catalytic activity of the GTPase and/or its capability to transduce signaling. Similarly, Arg68 is embedded in the protein interior and stabilizes the conformation of the switch II region via intramolecular interactions with multiple residues (Ala59, Gln61, and Glu100). The Arg-to-Gln change was assumed to strongly destabilize the switch II loop and the interaction with signaling partners. Group II included substitutions involving residues located within (Ala159) or close to (Cys81 and Ser83) the nucleotide-binding pocket (Figures 1B, 1C, and 1E). Ala159 faces the guanine base and replacement by valine was predicted to promote fast GDP/GTP cycling, favoring a GEF-independent active, GTP-bound state of the protein. A similar hyperactive behavior has been reported in RAS proteins.[26–28] Similarly, Ser83 binds to Gln116, which interacts with the guanine base, predicting indirect perturbation of nucleotide binding properties of CDC42. Cys81 is an invariant residue among RHO GTPases located in proximity of the phosphate-binding loop, and its substitution to phenylalanine was expected to cause favorable hydrophobic interactions with this loop, dislocation of Gly12, and consequently defective GTP hydrolysis. Finally, group III (CRIB mutations) included variants at Ile21, Tyr23, and Glu171, which are exposed residues predicted to affect interactions with effectors containing a CDC42/RAC-interacting binding (CRIB) motif (Figures 1B, 1C, and 1F).[29] Glu171 binds to Lys235 of WAS (WASP, hereafter) and plays a major role in the electrostatic binding network stabilizing the WASP-CDC42 association,[30,31] which was predicted to be disrupted by the Glu-to-Lys change. Tyr23 lies at the CDC42 surface implicated in PAK1 binding and stabilizes proper orientation of helix α5 mediating WASP binding.[32,33] Ile21 is located near the switch I region contributing to the hydrophobic pocket of helix α1 participating in WASP binding.[30] The Ile-to-Thr substitution was predicted to perturb CDC42 binding to signaling partners.

We assessed the effects of the disease-causing mutations on CDC42 GTPase activity, GDP/GTP exchange, and binding to effectors *in vitro*, using recombinant proteins. The p.Tyr23Cys, p.Tyr64Cys, p.Arg66Gly, p.Arg68Gln, p.Ser83Pro, p.Ala159Val, and p.Glu171Lys amino acid substitutions were selected as representative of the three mutation groups that were predicted to perturb differentially CDC42 function. pGEX vectors were used for bacterial overexpression of GST-tagged wild-type and mutant CDC42 proteins, and the GTPase-binding domains (GBD) of WASP (residues 154–321), PAK1 (residues 57–141), FMNL2 (residues 1–379), and IQGAP1 (residues 863–1657) in *E. coli* BL21 (DE3). Proteins were purified after cleavage of the GST tag (Superdex 75 or 200, GE Healthcare).[31] Nucleotide-free and fluorescent nucleotide-bound CDC42 variants were prepared using alkaline phosphatase
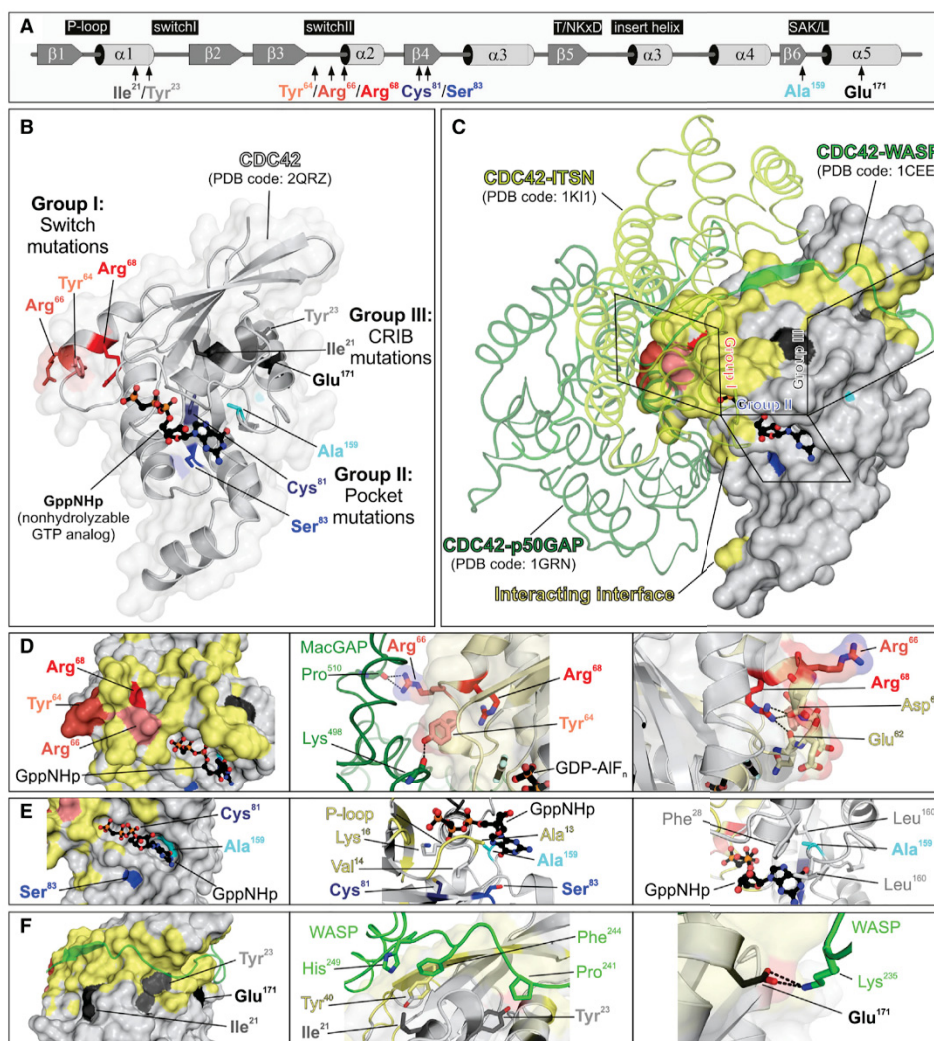
Figure 1. Location of Disease-Causing *CDC42* Mutations and Their Structural Impact

(A) Secondary structure elements (α helices and β strands), conserved motifs critical for tight guanine nucleotide binding and hydrolysis (G1–G5), and position of the identified disease-causing *CDC42* mutations are illustrated.

(B) Variant residues are assigned to three groups according to their position in the context of CDC42 structure (PDB: 2QRZ): group I or switch mutations (Tyr64, Arg66, and Arg68) are part of the switch II loop; group II or pocket mutations (Cys81, Ser83, and Ala159) are located in the vicinity of nucleotide binding pocket; and group III or CRIB mutations (Ile21, Tyr23, and Glu171) are far outside of the major interaction sites of CDC42 with GTP/GDP and involve exposed residues located in or close to regions of the protein mediating binding to effectors containing a CRIB motif.

(C) The position of the mutant residues relative to CDC42 interactions is illustrated by overlaying three different crystal structures of CDC42 in complex with ARHGAP1 (p50^{GAP}) (PDB: 1GRN), ITSN (PDB: 1KI1), and WAS (WASP) (PDB: 1CEE). Residues in reciprocal vicinity up to 4 Å were considered as part of binding interface. Residues of CDC42 mediating these interactions are shown in yellow.

(D) Group I mutations. Tyr64 and Arg66 are solvent-exposed residues and contribute to interactions with regulatory proteins and effectors (left). Interaction of both residues with ARHGAP18 (PDB: 5c2j) is shown as a representative for other interactions such as GEFs and effectors (middle). The disease-causing amino acid changes are predicted to affect this interaction. Arg68 participates in stabilizing the conformation of the switch II region via intramolecular interactions with Glu62 and Asp65 (right). The Arg-to-Gln change is predicted to destabilizes the switch II loop that is crucial for the interaction with signaling partners.

(E) Group II mutations. Cys81, Ser83, and Ala159 are in close vicinity of the phosphates (G1) and guanine base (G5) of bound GTP/GDP. Their substitutions are predicted to directly or indirectly affect the nucleotide binding affinity and to shift the balance between inactive and active CDC42 toward the latter.

(F) Group III mutations. Ile21, Tyr23, and Glu171 are part of a cavity on the CDC42 surface that accommodates the CRIB motif of bound effector proteins (e.g., WASP) (left). Ile21 and Tyr23 are critical for hydrophobic interactions (middle) with these type of proteins, while Glu171 contribute to binding mediating an electrostatic interaction (right).
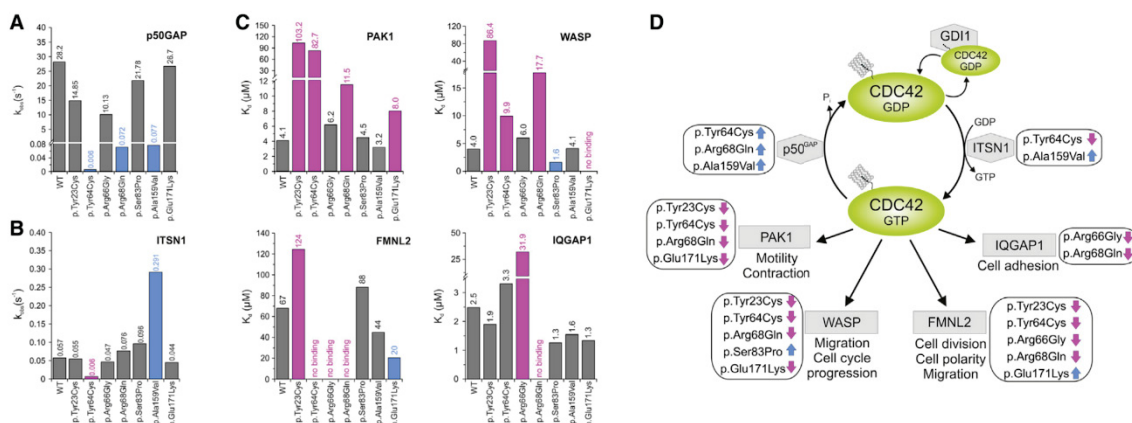
66

Figure 2. Assessment of the GTPase Activity, Nucleotide Exchange, and Binding to Effectors of Disease-Causing CDC42 Mutants

(A) Mean rate constants (k_{obs} values) of p50^{GAP}-stimulated GTP hydrolysis. Grey bars indicate non-significant differences compared to wild-type CDC42; blue bars indicate abolished/impaired GTP hydrolysis, which in turn results in an increased amount of active, GTP-bound CDC42 and thus enhanced signal flow. Data were obtained from >4 independent experiments.

(B) Mean rate constants (k_{obs} values) of the GEF-catalyzed release of labeled GDP (mantGDP). Grey bars indicate non-significant differences compared to wild-type CDC42; blue and magenta bars indicate increased or abolished nucleotide exchange, respectively. The former is predicted to promote enhanced signaling, while the latter blocks CDC42 in its inactive state. Data were obtained from >4 independent experiments.

(C) CDC42 mutants variably affect binding to effectors. Dissociation constants (K_d) obtained for the interaction of CDC42 proteins with PAK1, WASP, IQGAP1, and FMNL2 determined by fluorescence polarization. Data were collected from titration of increasing concentrations of the respective effectors. They were obtained from >4 independent experiments and are illustrated as bar charts. Grey bars indicate non-significant differences compared to wild-type CDC42; blue and magenta bars indicate increased or decreased binding affinity, respectively.

(D) Scheme summarizing the functional dysregulation of disease-causing mutants on downstream signaling pathways and cellular processes. ITSN1 is a specific GEF for CDC42 promoting the active state of the GTPase by catalyzing GDP release. p50^{GAP} negatively controls CDC42 function by stimulating the GTP hydrolysis reaction. CDC42 interaction with PAK1, WASP, FMNL2, and IQGAP1 activates signaling pathways controlling different cellular processes. For each specific function, the blue and magenta arrows indicate the hyperactive or defective behavior, respectively.

(Roche) and phosphodiesterase (Sigma Aldrich) at 4°C.[31,34] First, GTPase activity was measured basally and following ARHGAP1 (p50^{GAP}, hereafter) stimulation by fluorescent experiments using tetramethylrhodamine (tamra-) GTP as substrate with a Hi-Tech Scientific (SF-61) stopped-flow instrument (Figures 2A and S2). The assays documented a variably increased basal GTP hydrolysis for CDC42^{Tyr64Cys}, CDC42^{Arg68Gln}, and CDC42^{Ala159Val}. Each of these mutants, however, exhibited robust GAP insensitivity, showing respectively a 4,700-fold (CDC42^{Tyr64Cys}), 392-fold (CDC42^{Arg68Gln}), and 366-fold (CDC42^{Ala159Val}) reduction in GAP-stimulated GTPase activity, compared to wild-type CDC42. A mildly decreased GAP-stimulated GTP hydrolysis was documented for CDC42^{Tyr23Cys} and CDC42^{Arg66Gly}. By using the same experimental approach, release of methylanthraniloyl (mant-) GDP was used to assess the basal and GEF-catalyzed nucleotide exchange reactions (Figures 2B and S3). The assays documented an increase of GDP release for CDC42^{Ala159Val} and a slightly increased nucleotide exchange for CDC42^{Arg68Gln} and CDC42^{Ser83Pro}. By contrast, p.Tyr64Cys resulted in an almost completely abolished response to GEF. No substantial difference in GDP/GTP exchange behavior was observed for the other mutants. Then, fluorescence experiments were performed by using increasing amounts of the CDC42 interacting domains of WASP, PAK1, FMNL2, and IQGAP1 titrated to CDC42 proteins bound to mant-GppNHp, a non-hydrolyzable GTP analog, to assess the binding of mutants to four major CDC42 effectors and evaluate their ability to transduce signaling (Figures 2C and S4). Experiments were performed using a Fluoromax 4 fluorimeter in polarization mode, and the dissociation constants (K_d) were calculated by fitting the concentration-dependent binding curve using a quadratic ligand binding equation. Interaction with WASP was completely abolished in CDC42^{Glu171Lys} and markedly decreased (21.6-fold) in CDC42^{Tyr23Cys}. Decreased binding, albeit to a milder degree, was documented for CDC42^{Arg68Gln} and CDC42^{Tyr64Cys}, while CDC42^{Ser83Pro} exhibited a slightly increased binding. Binding to PAK1 was impaired for CDC42^{Tyr23Cys} and CDC42^{Tyr64Cys} and reduced for CDC42^{Arg68Gln} and CDC42^{Glu171Lys}. Tyr64 and Arg66 contribute to CDC42 binding to FMNL2;[35] consistently, CDC42^{Tyr64Cys} and CDC42^{Arg66Gly} had impaired FMNL2 binding, with the latter also having defective interaction with IQGAP1. Impaired binding to FMNL2 was also documented for CDC42^{Tyr23Cys} and CDC42^{Arg68Gln}, the latter also exhibiting defective IQGAP1 binding. By contrast, CDC42^{Glu171Lys} showed enhanced FMNL2 binding. Overall, biochemical characterization of CDC42

mutants confirmed the heterogeneous clinical and structural impact of variants demonstrating a stabilized GTP-bound conformation but defective interaction with all tested partners for group I mutations, variable hyperactive behavior for group II mutations, and a diversified binding to effectors for group III mutations (Figure 2D).

CDC42 is a master regulator of cell polarization and controls cell migration and growth.[36,37] The impact of CDC42 mutations on polarized migration was assessed by an *in vitro* wound-healing assay on fibronectin-coated wells (Sigma-Aldrich) (Figures 3A and S5). Monolayers of NIH 3T3 cells (American Type Culture Collection) cultured in high-glucose Dulbecco's modified Eagle's medium (DMEM) supplemented with 10% FCS, 2 mM L-glutamine, and 10 U/mL penicillin/streptomycin (Sigma-Aldrich) were transiently transfected using Fugene 6 (Roche) to express wild-type FLAG-tagged CDC42 isoform 1 (GenBank: NP_001782.1) or each of the p.Tyr23Cys, p.Arg68Gln, p.Ser83Pro, p.Ala159Val, and p.Glu171Lys mutants. 24 hr after transfection, cells were scratched and incubated in low serum medium in the presence of thymidine (Sigma-Aldrich) to inhibit cell proliferation. Cells that had migrated in the wounded area were counted 4 and 7 hr after scratch (four fields per well). Comparable transfection efficiency was verified by western blot analysis of the protein lysates. Only cells expressing group II mutants exhibited enhanced wound closure ability compared to cells expressing wild-type CDC42. Other tested mutants failed to increase migration, suggesting loss of function of this CDC42-mediated process, in line with defective binding of these mutants to WASP, a mediator of polarized migration.[38] Mutants also affected cell proliferation differentially (Figure 3A). CDC42^{Ala159Val} and CDC42^{Ser83Pro} variably enhanced cell growth, while CDC42^{Tyr23Cys} and CDC42^{Arg68Gln} significantly impaired proliferation, indicating a dominant-negative effect.

In *Caenorhabditis elegans*, CDC-42 controls early and late developmental programs (see WormBook in Web Resources), including vulval development,[39–41] a process that is regulated by LET-60/RAS-dependent and -independent signals.[42] To explore the impact of the disease-causing *CDC42* mutations *in vivo*, transgenic lines were generated to conditionally express wild-type CDC-42 or a selected subset of mutations for each mutation group (p.Tyr23Cys, p.Arg68Gln, p.Ser83Pro, p.Ala159Val, and p.Glu171Lys) affecting residues conserved in the nematode ortholog (Figure S6).[43] The wild-type *cdc-42* cDNA (ORF clone R07G3.1; ThermoScientific) was subcloned into the pPD49.83 heat shock-inducible vector (gift of A. Fire, Stanford University School of Medicine), and the generated constructs were injected at 100 ng/μL. The pJM67 plasmid (*pelt-2::NLS::GFP*) (gift from J.D. McGhee, University of Calgary), which drives green fluorescent protein (GFP) expression in intestinal cell nuclei, was used as co-injection marker (30 ng/μL). To analyze vulval induction and morphogenesis, synchronized animals from at least three independent lines for each construct were grown at 20°C

and heat-shocked (90 min at 33°C followed by 30 min at 30°C) at late L2/early L3 larval stages and scored for vulval induction and morphogenesis from late L3 to mid L4 stages. The presence of a protruding vulva (Pvl phenotype), multiple ectopic pseudovulvae (multivulva [Muv] phenotype), and lack of a vulva (vulvaless [Vul] phenotype) was analyzed at the adult stage. Lines were scored in triplicate experiments using a Nikon Eclipse 80i instrument equipped with Nomarski differential interference contrast optics and used for further analyses and crosses. After each cross, the genotype of individual alleles was confirmed by direct sequencing of the appropriate genomic region. Isogenic animals that had lost the transgene were cloned separately and used as controls in each experiment. Overexpression of wild-type CDC-42 at the L2/L3 stage elicited a low-penetrant Muv phenotype, exacerbated the Muv phenotype associated with a *let-60* gain-of-function allele, *let-60(n1046) IV*, and partially rescued the Vul phenotype of animals carrying a hypomorphic *let-23/EGFR* allele, *let-23(sy1) II*, indicating LET-60/RAS signaling hyperactivation (Figures 3B and S7, Table S3). Compared to wild-type CDC-42, group II mutations induced a more severe Muv phenotype and more efficiently rescued the Vul phenotype of *let-23(sy1)* animals, indicative of enhanced signal flow through LET-60. Overexpression of wild-type CDC-42 also engendered aberrant vulva morphogenesis, generating a Pvl phenotype that was mediated, in part, by WSP-1/WASP (Figures 3B and S7, Tables S3 and S4). The same phenotype had previously been reported in *C. elegans* lines expressing the RASopathy-causing SHOC2^{S2G} and RRAS^{G39dup} mutants.[44,45] Like those animals, a variable proportion of CDC-42 hermaphrodites exhibiting Pvl displayed egg-laying defects (Egl phenotype) and accumulation of larvae inside the mother (Bag-of-worms phenotype) (data not shown). Of note, this phenotype was markedly promoted by group II mutations in a WASP-independent manner, indicating a gain-of-function effect of these changes. By contrast, CDC-42^{Tyr23Cys}, CDC-42^{Arg68Gln}, and CDC-42^{Glu171Lys} significantly reduced the Pvl phenotype, supporting a selective hypomorphic behavior. Pvl was not modulated by *wsp-1* RNAi in animals expressing CDC-42^{Tyr23Cys} and CDC-42^{Glu171Lys} and was only slightly reduced in those expressing CDC-42^{Arg68Gln}, consistent with the biochemical data indicating an abolished or strongly reduced binding to WASP of those mutants, respectively. Nomarski observations of L3 and L4 control larvae showed that only P6.p descendants detached from the cuticle generating a single, symmetric invagination; by contrast, a variable proportion of larvae expressing wild-type and mutant CDC-42 displayed asymmetric and/or multiple invaginations (Figure S7), which represent the earliest signs of the Pvl and Muv phenotypes, respectively. Overall, the data indicate that group II mutations upregulate multiple signaling pathways, including LET-60/RAS, while the other variants behave as hypomorphic mutations on WASP-dependent signaling.
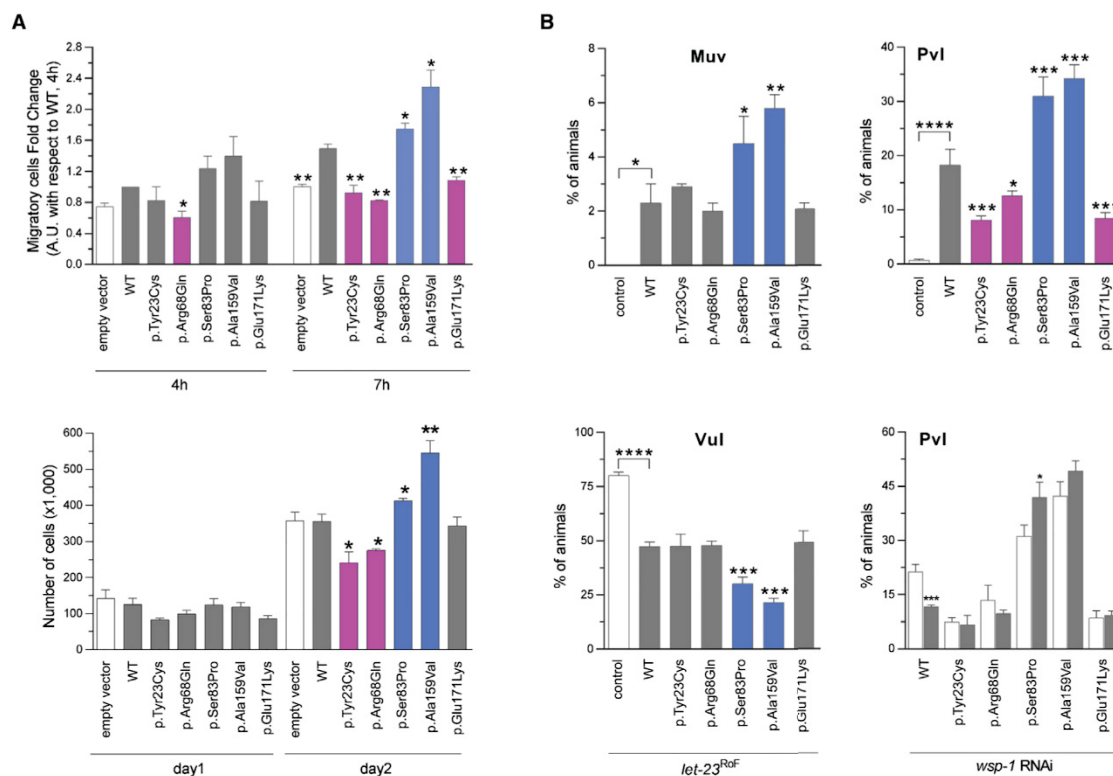
Figure 3. *In Vitro* and *In Vivo* Functional Characterization of *CDC42* Mutations

(A) *CDC42* mutations differentially impact polarized migration and cell proliferation. Wound-healing assays (above) and proliferation assays (below) were performed using NIH 3T3 cells transiently transfected to express wild-type CDC42 or each of the indicated mutants. Mean ± SD densitometry values of three independent experiments are shown. The wound was generated 24 hr after transfection, and migration in the wounded area was evaluated after 4 and 7 hr. Cells expressing exogenous wild-type CDC42 migrate more rapidly into the scratched area than cells transfected with the empty vector (EV). Mutants differentially perturb polarized migration, with CDC42^{Ser83Pro} and CDC42^{Ala159Val} overexpression variably enhancing the wound closure ability of transfected cells compared to the wild-type protein, whereas CDC42^{Tyr23Cys}, CDC42^{Arg68Gln}, and CDC42^{Glu171Lys} fail to do that, supporting a gain-of-function and a loss-of-function effect of these mutants, respectively. Cell proliferation was evaluated in transfected cells at the indicated time points and quantified by manual counting using a Neubauer hemocytometer. The trypan blue dye exclusion test was used to consider viable cells only. While the CDC42^{Ala159Val} and CDC42^{Ser83Pro} mutants variably enhance proliferation compared to cells expressing wild-type CDC42, no effect on proliferation (CDC42^{Glu171Lys}) and reduced proliferation (CDC42^{Tyr23Cys} and CDC42^{Arg68Gln}) is documented for the other mutants, indicating a loss-of-function and a dominant-negative effect, respectively. Asterisks indicate significant differences compared with wild-type CDC42 (*$p < 0.05$; **$p < 0.01$; Student's t test).

(B) Consequences of *CDC-42* expression on vulval development in *C. elegans*. Ectopic expression of wild-type CDC-42 at the L2/L3 stage elicits a multivulva (Muv) phenotype (left, upper panel), and CDC-42 overexpression in a LET-23/EGFR hypomorphic background reduces the penetrance of the vulvaless (Vul) phenotype (left, lower panel). Compared to animals expressing wild-type CDC-42, those expressing CDC-42^{Ser83Pro} and CDC-42^{Ala159Val} show higher prevalence of the Muv phenotype and lower prevalence of the Vul phenotype, indicating a gain-of-function role on LET-60/RAS signaling. Animals expressing the other tested CDC-42 mutants do not significantly differ from those expressing wild-type CDC-42. Ectopic expression of wild-type CDC-42 at the early L3 stage elicits a protruding vulva (Pvl) phenotype (right, upper panel). Animals expressing CDC-42^{Ser83Pro} and CDC-42^{Ala159Val} show a higher prevalence of the phenotype compared to worms expressing wild-type CDC-42, while a less penetrant phenotype was scored for animals expressing CDC-42^{Tyr23Cys}, CDC-42^{Arg68Gln}, or CDC-42^{Glu171Lys} mutants. RNA interference (RNAi) experiments show that the Pvl phenotype associated with overexpression of wild-type CDC-42 is mediated, in part, by WSP-1/WASP (right, lower panel). White and gray bars indicate the penetrance of Pvl in non-interfered and interfered animals, respectively. Error bars indicate SEM of four independent experiments, and asterisks specify significance differences between animals expressing CDC-42 mutants and those expressing wild-type CDC-42 or between interfered and non-interfered nematodes (*$p < 0.05$; **$p < 0.001$; ***$p < 0.0001$; ****$p < 0.00005$; two-tailed Fisher's exact test). Comparisons between worms expressing wild-type CDC-42 and control animals are also shown. RNAi was performed by feeding using HT115 *E. coli* bacteria expressing double stranded *wsp-1* RNA (Ahringer's *C. elegans* RNAi feeding library) and optimized to overcome lethality. As a control of the efficiency of the modified RNAi protocol, *let-60* RNAi experiments were performed on animals carrying the *let-60* gain-of-function allele *n1046* (p.Gly13Glu), and the prevalence of the Muv phenotype was scored at a dissecting microscope (Table S4).

Figure 4. Facial Features of Individuals with Heterozygous *CDC42* Mutations

(A–C) Subject 3 (p.Tyr64Cys) at age 2 years and 6 months (A) and 15 years (B and C) showing upslanted palpebral fissures, smooth philtrum, flaring alae nasi, thin upper vermilion, and wide mouth with widely spaced teeth.

(D) Subject 4 (p.Arg66Gly) at 15 years showing broad forehead and broad nasal bridge with bulbous nasal tip.

(E and F) Subject 6 (p.Arg68Gln) at 24 months (E) and 4 years (F) showing a prominent broad forehead, hypertelorism, long philtrum, and thin upper vermilion.

(G and H) Subject 9 (p.Ser83Pro) at age 2 (G) and 6 (H) years showing prominent forehead, hypertelorism, wide mouth with cupid's bow, thin upper vermilion, and widely spaced teeth.

(I and J) Subject 10 (p.Ser83Pro) at 13 (I) and 32 (J) years showing prominent forehead, wide nasal bridge, ptosis, flared nostrils, and wide mouth with widely spaced teeth.

(K and L) Subject 11 (p.Ala159Val) at 2 years (K) and at 3 years and 7 months (L) showing very broad and prominent forehead, bulbous nasal tip, flared nostrils, cupid's bow, and downturned corners of the mouth.

(M–O) Subject 1 (p.Ile21Thr) at age 3 months (M), 2 years (N), and 10 years (O) showing synophrys, wide palpebral fissures, high and narrow nasal bridge, bulbous nasal tip, wide mouth with downturned corners, and mildly laterally prominent ears.

(P) Subject 2 (p.Tyr23Cys) at 14 years showing wide palpebral fissures, high nasal bridge with elevated nasal tip, short philtrum, and long neck.

(Q) Subject 12 (p.Glu171Lys) at 12 years showing typical facial features of Noonan syndrome, including broad forehead, hypertelorism, low-set ears, bulbous nasal tip, and flared nostrils.

(R) Subject 13 (p.Glu171Lys) showing ptosis, broad neck, and pectus deformity.

Note that individuals fitting the different mutation groups share some facial characteristics, and that intragroup variability is also observed.

The cohort of individuals carrying heterozygous mutations in *CDC42* had an unusually broad spectrum of anomalies. Core clinical features included defective growth, intellectual disability (ID), facial dysmorphism, hearing/vision problems, cardiac malformations, immune, hematologic, and lymphatic abnormalities, and brain malformations (Figures 4 and S8, Tables S5–S7, Supplemental Note). Correlating the functional impact of mutations on clinical phenotypes observed in affected individuals permitted a preliminary analysis of genotype-phenotype relationships (Table 2). Individuals with group I mutations manifested with ID, muscle tone abnormalities, and variable other less common features, including cardiac defects. All individuals within this group had thrombocytopenia, similar to two previously reported individuals.[20,21] Individuals with group II mutations manifested with strikingly dysmorphic facial features: subject 11 (p.Ala159Val) had marked hypertelorism, prominent forehead, bitemporal narrowing, and downslanting palpebral fissures with coarse thick hair, resembling a RASopathy (Figures 4K and 4L). Features within the Noonan syndrome phenotypic spectrum were observed in all affected individuals from two unrelated families carrying the c.511G>A (p.Glu171Lys) change (subjects 12 to 15), with

Table 2. Summary of the Clinical Features of *CDC42* Mutation-Positive Subjects

Mutation group	Group I	Group II	Group III
Number of individuals	5	4	6
Amino acid substitutions	p.Tyr64Cys, p.Arg66Gly, p.Arg68Gln	p.Cys81Phe, p.Ser83Pro, p.Ala159Val	p.Ile21Thr, p.Tyr23Cys, p.Glu171Lys
Growth			
Prenatal – weight at birth $\leq$ 2 SD	1/4	2/4	1/4
Prenatal – OFC at birth $\leq$ 2 SD	1/3	1/2	1/2
Postnatal – weight $\leq$ 2 SD	4/5	2/3	1/4
Postnatal – OFC $\leq$ 2 SD	3/5	2/4	3/4
Postnatal – growth deficiency	3/5	4/4	4/6
Intellectual disability	5/5	4/4	2/6
Seizures	1/4	2/4	1/6
MRI brain anomalies[a]	4/4	4/4	1/2
Tone anomalies	3/4	2/4	2/6
Optic atrophy	1/4	0/4	2/6
Endocrine anomalies	2/4	1/4	1/5
Facial dysmorphism[b]	4/5	4/4	6/6
Pectus deformity	1/5	0/4	4/5
Scoliosis/vertebral anomalies	2/5	1/4	2/6
Camptodacyly	1/5	2/4	1/5
Cardiac anomalies	3/5	2/4	2/5
GU anomalies	2/5	2/4	1/6
Lymphatic anomalies	1/5	1/4	0/6
Recurrent infections	4/5	3/4	1/6
Platelet anomalies (thrombocytopenia, macrothrombocytes)	4/4	1/3	0/5

Abbreviations: OFC, occipito-frontal circumference; SD, standard deviation; GU, genitourinary. Detailed phenotypic description of subjects is reported in the Supplemental Note and Table S5.
[a]For details regarding brain MRI features, see Figure S8 and Table S7.
[b]For details regarding the facial features, see Table S6.

a particularly striking gestalt of this disorder occurring in subject 12 (Figure 4Q). Notably, brain malformations occurred in all groups, and four individuals manifested with cerebellar-posterior fossa abnormalities. Subjects 8 and 11 (with group II mutations) had a large cerebellum with evidence of posterior fossa crowding and cerebellar tonsillar ectopia, features commonly reported in RASopathies.[46] It should be noted that notwithstanding the occurrence of a clinical overlap within each mutation group, intra-group phenotypic variability was observed, which would suggest a specific impact of individual mutations on developmental processes.

While traditionally CDC42 has been functionally linked to remodeling of the actin cytoskeletal architecture,[47] its role in controlling intracellular signaling has recently been broadened.[48] Such complex modulatory function is accomplished by interactions with a wide array of signaling partners functioning in distinct signal cascades. Cdc42 loss of function is embryonic lethal, and its targeted

deletion has been shown to disrupt cell fate decision, differentiation, and function of multiple cell lineages as well as tissue homeostasis.[49] Here, we report that dominantly acting mutations differentially perturb CDC42 function and cause clinically heterogeneous phenotypes affecting development and growth. Group I mutations associated with impaired binding to regulators and effectors cause a syndromic form of thrombocytopenia, while the variably hyperactive group II mutations are associated with a variable developmental disorder characterized by striking dysmorphic features, and one specific amino acid change among the group III mutations, which affects only one of the two CDC42 isoforms and specifically impairs binding to WASP, results in an overall milder clinical phenotype that phenocopies Noonan syndrome.[14]

Noonan syndrome, the most common and clinically variable among the RASopathies, is caused by dysregulated signaling through RAS and the MAPK cascade. This disorder and its clinically related phenotypes result from

heterozygous germline mutations affecting *RAS* genes or genes coding proteins functioning as RAS effectors, regulators of RAS function, or more generally as modulators of RAS-MAPK signaling.[15] More recently, the family of genes implicated in RASopathies has been extended to include *LZTR1* (MIM: 600574), *RIT1* (MIM: 609591), and *RRAS* (MIM: 165090), which encode for signal transducers whose direct link to the RAS and the MAPK cascade had not previously been appreciated.[45,50,51] While it is possible that functional dysregulation of these proteins may impact RAS signaling directly or indirectly, these findings raise also the possibility that other pathways may contribute to disease pathogenesis. The present *in vivo* data provide evidence for enhanced signaling through RAS for group II mutations, indicating that upregulated CDC42 function is able to perturb signal flow through RAS; however, no effect on RAS-mediated signaling was inferred for the p.Glu171Lys change, here identified to be associated with a phenotype resembling Noonan syndrome. While it is possible that the used *in vivo* model failed in providing informative data for the specific effect of CDC42^{Glu171Lys} on RAS signaling, our finding suggests that other processes, including aberrant cytoskeletal rearrangement, may represent a previously unappreciated aspect contributing to disease pathogenesis in Noonan syndrome. Consistent with this possibility, SOS1, SHOC2, and RRAS function has been linked to cell migration and other cellular processes strictly dependent on cytoskeletal rearrangement.[52–54] Further studies are thus required to specifically address the impact of dysregulated CDC42 function on RAS signaling as well as on the cellular and developmental processes that are altered in Noonan syndrome.

Overall, the present work links different classes of dominantly acting mutations of CDC42, a master regulator of actin cytoskeleton and major node in intracellular signaling, to a heterogeneous set of developmental and multi-system phenotypes, demonstrating the critical requirement of proper CDC42 function in a large array of developmental processes. This study also exemplifies current challenges in syndrome delineation in the post-WES era and emphasizes the relevance of functional profiling in syndrome recognition and delineation.

Accession Numbers

ClinVar accession ID for data provided herein are SCV000572034.2 (c.62T>C), SCV000244190.3 (c.68A>G), SCV000577577.2 (c.191A>G), SCV000244118.3 (c.196A>G), SCV000589746.1 (c.242G>T), SCV000678254 (c.203G>A), SCV000678255 (c.247T>C), SCV000678256 (c.476C>T), and SCV000678257 (c.511G>A).

Supplemental Data

Supplemental Data include a supplemental note (clinical data), eight figures, and seven tables and can be found with this article online at https://doi.org/10.1016/j.ajhg.2017.12.015.

Web Resources

CADD, http://cadd.gs.washington.edu/
ClinVar, https://www.ncbi.nlm.nih.gov/clinvar/
dbNSFP, https://sites.google.com/site/jpopgen/dbNSFP
dbSNP, https://www.ncbi.nlm.nih.gov/projects/SNP/
ExAC Browser, http://exac.broadinstitute.org/
GenBank, https://www.ncbi.nlm.nih.gov/genbank/
gnomAD Browser, http://gnomad.broadinstitute.org/
NCBI Gene, https://www.ncbi.nlm.nih.gov/gene
OMIM, http://www.omim.org/
PyMOL, https://pymol.org/2
RCSB Protein Data Bank, http://www.rcsb.org/pdb/home/home.do
REVEL, https://sites.google.com/site/revelgenomics
WormBase, http://www.wormbase.org/
WormBook, http://www.wormbook.org

References

1. Bamshad, M.J., Ng, S.B., Bigham, A.W., Tabor, H.K., Emond, M.J., Nickerson, D.A., and Shendure, J. (2011). Exome sequencing as a tool for Mendelian disease gene discovery. Nat. Rev. Genet. *12*, 745–755.

2. Chong, J.X., Buckingham, K.J., Jhangiani, S.N., Boehm, C., So-breira, N., Smith, J.D., Harrell, T.M., McMillin, M.J., Wiszniewski, W., Gambin, T., et al.; Centers for Mendelian Genomics (2015). The genetic basis of Mendelian phenotypes: discoveries, challenges, and opportunities. Am. J. Hum. Genet. *97*, 199–215.

3. Menke, L.A., van Belzen, M.J., Alders, M., Cristofoli, F., Ehmke, N., Fergelot, P., Foster, A., Gerkes, E.H., Hoffer, M.J., Horn, D., et al.; DDD Study (2016). CREBBP mutations in individuals without Rubinstein-Taybi syndrome phenotype. Am. J. Med. Genet. A. *170*, 2681–2693.

4. Lee, C.S., Fu, H., Baratang, N., Rousseau, J., Kumra, H., Sutton, V.R., Niceta, M., Ciolfi, A., Yamamoto, G., Bertola, D., et al.; Baylor-Hopkins Center for Mendelian Genomics (2017). Mutations in fibronectin cause a subtype of spondylometaphyseal dysplasia with "corner fractures". Am. J. Hum. Genet. *101*, 815–823.

5. Niceta, M., Stellacci, E., Gripp, K.W., Zampino, G., Kousi, M., Anselmi, M., Traversa, A., Ciolfi, A., Stabley, D., Bruselles, A., et al. (2015). Mutations impairing GSK3-mediated MAF phosphorylation cause cataract, deafness, intellectual disability, seizures, and a Down syndrome-like facies. Am. J. Hum. Genet. *96*, 816–825.

6. Reijnders, M.R.F., Ansor, N.M., Kousi, M., Yue, W.W., Tan, P.L., Clarkson, K., Clayton-Smith, J., Corning, K., Jones, J.R., Lam, W.W.K., et al.; Deciphering Developmental Disorders Study (2017). RAC1 missense mutations in developmental disorders with diverse phenotypes. Am. J. Hum. Genet. *101*, 466–477.

7. Martinelli, S., Torreri, P., Tinti, M., Stella, L., Bocchinfuso, G., Flex, E., Grottesi, A., Ceccarini, M., Palleschi, A., Cesareni, G., et al. (2008). Diverse driving forces underlie the invariant occurrence of the T42A, E139D, I282V and T468M SHP2 amino acid substitutions causing Noonan and LEOPARD syndromes. Hum. Mol. Genet. *17*, 2018–2029.

8. Philippakis, A.A., Azzariti, D.R., Beltran, S., Brookes, A.J., Brownstein, C.A., Brudno, M., Brunner, H.G., Buske, O.J., Carey, K., Doll, C., et al. (2015). The Matchmaker Exchange: a platform for rare disease gene discovery. Hum. Mutat. *36*, 915–921.

9. Sobreira, N., Schiettecatte, F., Valle, D., and Hamosh, A. (2015). GeneMatcher: a matching tool for connecting investigators with an interest in the same gene. Hum. Mutat. *36*, 928–930.

10. Chong, J.X., Yu, J.H., Lorentzen, P., Park, K.M., Jamal, S.M., Tabor, H.K., Rauch, A., Saenz, M.S., Boltshauser, E., Patterson, K.E., et al. (2016). Gene discovery for Mendelian conditions via social networking: de novo variants in KDM1A cause developmental delay and distinctive facial features. Genet. Med. *18*, 788–795.

11. Homsy, J., Zaidi, S., Shen, Y., Ware, J.S., Samocha, K.E., Karczewski, K.J., DePalma, S.R., McKean, D., Wakimoto, H., Gorham, J., et al. (2015). De novo mutations in congenital heart disease with neurodevelopmental and other congenital anomalies. Science *350*, 1262–1266.

12. Tanaka, A.J., Cho, M.T., Millan, F., Juusola, J., Retterer, K., Joshi, C., Niyazov, D., Garnica, A., Gratz, E., Deardorff, M., et al. (2015). Mutations in SPATA5 are associated with microcephaly, intellectual disability, seizures, and hearing loss. Am. J. Hum. Genet. *97*, 457–464.

13. Farwell Hagman, K.D., Shinde, D.N., Mroske, C., Smith, E., Radtke, K., Shahmirzadi, L., El-Khechen, D., Powis, Z., Chao, E.C., Alcaraz, W.A., et al. (2017). Candidate-gene criteria for clinical reporting: diagnostic exome sequencing identifies altered candidate genes among 8% of patients with undiagnosed diseases. Genet. Med. *19*, 224–235.

14. Roberts, A.E., Allanson, J.E., Tartaglia, M., and Gelb, B.D. (2013). Noonan syndrome. Lancet *381*, 333–342.

15. Tartaglia, M., and Gelb, B.D. (2010). Disorders of dysregulated signal traffic through the RAS-MAPK pathway: phenotypic spectrum and molecular mechanisms. Ann. N Y Acad. Sci. *1214*, 99–121.

16. Kircher, M., Witten, D.M., Jain, P., O'Roak, B.J., Cooper, G.M., and Shendure, J. (2014). A general framework for estimating the relative pathogenicity of human genetic variants. Nat. Genet. *46*, 310–315.

17. Dong, C., Wei, P., Jian, X., Gibbs, R., Boerwinkle, E., Wang, K., and Liu, X. (2015). Comparison and integration of deleteriousness prediction methods for nonsynonymous SNVs in whole exome sequencing studies. Hum. Mol. Genet. *24*, 2125–2137.

18. Ioannidis, N.M., Rothstein, J.H., Pejaver, V., Middha, S., McDonnell, S.K., Baheti, S., Musolf, A., Li, Q., Holzinger, E., Karyadi, D., et al. (2016). REVEL: an ensemble method for predicting the pathogenicity of rare missense variants. Am. J. Hum. Genet. *99*, 877–885.

19. Richards, S., Aziz, N., Bale, S., Bick, D., Das, S., Gastier-Foster, J., Grody, W.W., Hegde, M., Lyon, E., Spector, E., et al.; ACMG Laboratory Quality Assurance Committee (2015). Standards and guidelines for the interpretation of sequence variants: a joint consensus recommendation of the American College of Medical Genetics and Genomics and the Association for Molecular Pathology. Genet. Med. *17*, 405–424.

20. Takenouchi, T., Kosaki, R., Niizuma, T., Hata, K., and Kosaki, K. (2015). Macrothrombocytopenia and developmental delay with a de novo CDC42 mutation: Yet another locus for thrombocytopenia and developmental delay. Am. J. Med. Genet. A. *167A*, 2822–2825.

21. Takenouchi, T., Okamoto, N., Ida, S., Uehara, T., and Kosaki, K. (2016). Further evidence of a mutation in CDC42 as a cause of a recognizable syndromic form of thrombocytopenia. Am. J. Med. Genet. A. *170A*, 852–855.

22. Etienne-Manneville, S. (2004). Cdc42–the centre of polarity. J. Cell Sci. *117*, 1291–1300.

23. Heasman, S.J., and Ridley, A.J. (2008). Mammalian Rho GTPases: new insights into their functions from in vivo studies. Nat. Rev. Mol. Cell Biol. *9*, 690–701.

24. Colicelli, J. (2004). Human RAS superfamily proteins and related GTPases. Sci. STKE *2004*, RE13.

25. Dvorsky, R., and Ahmadian, M.R. (2004). Always look on the bright site of Rho: structural implications for a conserved intermolecular interface. EMBO Rep. *5*, 1130–1136.

26. Janakiraman, M., Vakiani, E., Zeng, Z., Pratilas, C.A., Taylor, B.S., Chitale, D., Halilovic, E., Wilson, M., Huberman, K., Ricarte Filho, J.C., et al. (2010). Genomic and biological characterization of exon 4 KRAS mutations in human cancer. Cancer Res. *70*, 5901–5911.

27. Gremer, L., Merbitz-Zahradnik, T., Dvorsky, R., Cirstea, I.C., Kratz, C.P., Zenker, M., Wittinghofer, A., and Ahmadian, M.R. (2011). Germline KRAS mutations cause aberrant biochemical and physical properties leading to developmental disorders. Hum. Mutat. *32*, 33–43.

28. Chang, M.T., Asthana, S., Gao, S.P., Lee, B.H., Chapman, J.S., Kandoth, C., Gao, J., Socci, N.D., Solit, D.B., Olshen, A.B.,

73

et al. (2016). Identifying recurrent mutations in cancer reveals widespread lineage diversity and mutational specificity. Nat. Biotechnol. *34*, 155–163.

29. Pirone, D.M., Carter, D.E., and Burbelo, P.D. (2001). Evolutionary expansion of CRIB-containing Cdc42 effector proteins. Trends Genet. *17*, 370–373.

30. Abdul-Manan, N., Aghazadeh, B., Liu, G.A., Majumdar, A., Ouerfelli, O., Siminovitch, K.A., and Rosen, M.K. (1999). Structure of Cdc42 in complex with the GTPase-binding domain of the 'Wiskott-Aldrich syndrome' protein. Nature *399*, 379–383.

31. Hemsath, L., Dvorsky, R., Fiegen, D., Carlier, M.F., and Ahmadian, M.R. (2005). An electrostatic steering mechanism of Cdc42 recognition by Wiskott-Aldrich syndrome proteins. Mol. Cell *20*, 313–324.

32. Morreale, A., Venkatesan, M., Mott, H.R., Owen, D., Nietlispach, D., Lowe, P.N., and Laue, E.D. (2000). Structure of Cdc42 bound to the GTPase binding domain of PAK. Nat. Struct. Biol. *7*, 384–388.

33. Gizachew, D., Guo, W., Chohan, K.K., Sutcliffe, M.J., and Oswald, R.E. (2000). Structure of the complex of Cdc42Hs with a peptide derived from P-21 activated kinase. Biochemistry *39*, 3963–3971.

34. Hemsath, L., and Ahmadian, M.R. (2005). Fluorescence approaches for monitoring interactions of Rho GTPases with nucleotides, regulators, and effectors. Methods *37*, 173–182.

35. Kühn, S., Erdmann, C., Kage, F., Block, J., Schwenkmezger, L., Steffen, A., Rottner, K., and Geyer, M. (2015). The structure of FMNL2-Cdc42 yields insights into the mechanism of lamellipodia and filopodia formation. Nat. Commun. *6*, 7088.

36. Melendez, J., Liu, M., Sampson, L., Akunuru, S., Han, X., Vallance, J., Witte, D., Shroyer, N., and Zheng, Y. (2013). Cdc42 coordinates proliferation, polarity, migration, and differentiation of small intestinal epithelial cells in mice. Gastroenterology *145*, 808–819.

37. Zegers, M.M., and Friedl, P. (2014). Rho GTPases in collective cell migration. Small GTPases *5*, e28997.

38. Beaty, B.T., and Condeelis, J. (2014). Digging a little deeper: the stages of invadopodium formation and maturation. Eur. J. Cell Biol. *93*, 438–444.

39. Welchman, D.P., Mathies, L.D., and Ahringer, J. (2007). Similar requirements for CDC-42 and the PAR-3/PAR-6/PKC-3 complex in diverse cell types. Dev. Biol. *305*, 347–357.

40. Lohmer, L.L., Clay, M.R., Naegeli, K.M., Chi, Q., Ziel, J.W., Hagedorn, E.J., Park, J.E., Jayadev, R., and Sherwood, D.R. (2016). A sensitized screen for genes promoting invadopodia function in vivo: CDC-42 and Rab GDI-1 direct distinct aspects of invadopodia formation. PLoS Genet. *12*, e1005786.

41. Choi, M.S., Yoo, A.S., and Greenwald, I. (2010). sel-11 and cdc-42, two negative modulators of LIN-12/Notch activity in *C. elegans*. PLoS ONE *5*, e11885.

42. Schmid, T., and Hajnal, A. (2015). Signal transduction during *C. elegans* vulval development: a NeverEnding story. Curr. Opin. Genet. Dev. *32*, 1–9.

43. Mello, C.C., Kramer, J.M., Stinchcomb, D., and Ambros, V. (1991). Efficient gene transfer in *C.elegans*: extrachromosomal maintenance and integration of transforming sequences. EMBO J. *10*, 3959–3970.

44. Cordeddu, V., Di Schiavi, E., Pennacchio, L.A., Ma'ayan, A., Sarkozy, A., Fodale, V., Cecchetti, S., Cardinale, A., Martin, J., Schackwitz, W., et al. (2009). Mutation of SHOC2 promotes aberrant protein N-myristoylation and causes Noonan-like syndrome with loose anagen hair. Nat. Genet. *41*, 1022–1026.

45. Flex, E., Jaiswal, M., Pantaleoni, F., Martinelli, S., Strullu, M., Fansa, E.K., Caye, A., De Luca, A., Lepri, F., Dvorsky, R., et al. (2014). Activating mutations in RRAS underlie a phenotype within the RASopathy spectrum and contribute to leukaemogenesis. Hum. Mol. Genet. *23*, 4315–4327.

46. Gripp, K.W., Hopkins, E., Doyle, D., and Dobyns, W.B. (2010). High incidence of progressive postnatal cerebellar enlargement in Costello syndrome: brain overgrowth associated with HRAS mutations as the likely cause of structural brain and spinal cord abnormalities. Am. J. Med. Genet. A. *152A*, 1161–1168.

47. Nobes, C.D., and Hall, A. (1995). Rho, rac and cdc42 GTPases: regulators of actin structures, cell adhesion and motility. Biochem. Soc. Trans. *23*, 456–459.

48. Arias-Romero, L.E., and Chernoff, J. (2013). Targeting Cdc42 in cancer. Expert Opin. Ther. Targets *17*, 1263–1273.

49. Pedersen, E., and Brakebusch, C. (2012). Rho GTPase function in development: how in vivo models change our view. Exp. Cell Res. *318*, 1779–1787.

50. Aoki, Y., Niihori, T., Banjo, T., Okamoto, N., Mizuno, S., Kurosawa, K., Ogata, T., Takada, F., Yano, M., Ando, T., et al. (2013). Gain-of-function mutations in RIT1 cause Noonan syndrome, a RAS/MAPK pathway syndrome. Am. J. Hum. Genet. *93*, 173–180.

51. Yamamoto, G.L., Aguena, M., Gos, M., Hung, C., Pilch, J., Fahiminiya, S., Abramowicz, A., Cristian, I., Buscarilli, M., Naslavsky, M.S., et al. (2015). Rare variants in SOS2 and LZTR1 are associated with Noonan syndrome. J. Med. Genet. *52*, 413–421.

52. Sini, P., Cannas, A., Koleske, A.J., Di Fiore, P.P., and Scita, G. (2004). Abl-dependent tyrosine phosphorylation of Sos-1 mediates growth-factor-induced Rac activation. Nat. Cell Biol. *6*, 268–274.

53. Holly, S.P., Larson, M.K., and Parise, L.V. (2005). The unique N-terminus of R-ras is required for Rac activation and precise regulation of cell migration. Mol. Biol. Cell *16*, 2458–2469.

54. Kaduwal, S., Jeong, W.J., Park, J.C., Lee, K.H., Lee, Y.M., Jeon, S.H., Lim, Y.B., Min, S., and Choi, K.Y. (2015). Sur8/Shoc2 promotes cell motility and metastasis through activation of Ras-PI3K signaling. Oncotarget *6*, 33091–33105.

74

Chapter V

A novel disorder involving dyshematopoiesis, inflammation, and HLH due to aberrant CDC42 function

Graphical abstract
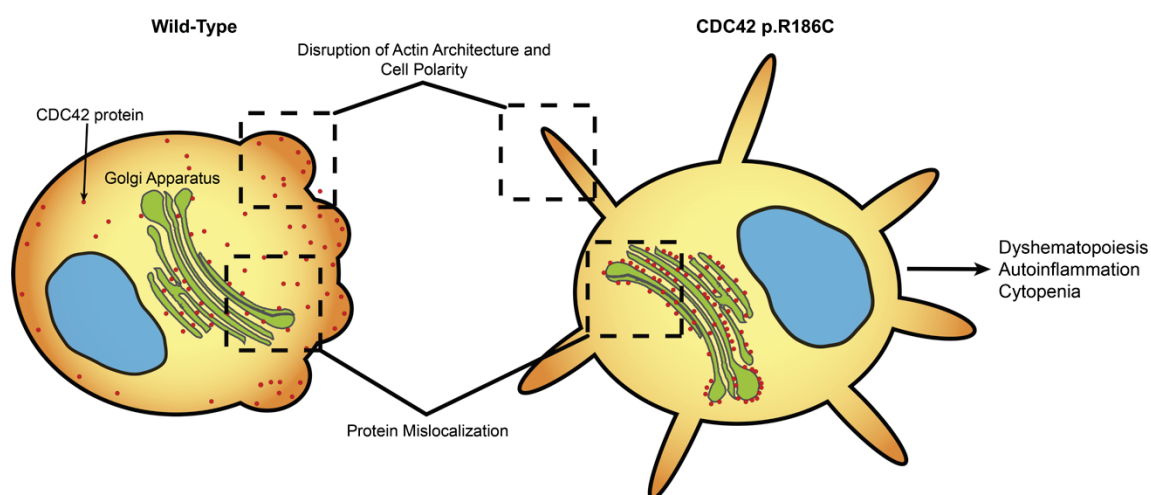
Status:	Published in Journal of Experimental Medicine, October 10th 2019
Impact factor:	10.353
Own proportion to this work:	5 %
	Expression and purification of CDC42 effectors, CDC42 GTP pull down assays, writing the manuscript.

ARTICLE

A novel disorder involving dyshematopoiesis, inflammation, and HLH due to aberrant CDC42 function

Michael T. Lam[1,2,32]*, Simona Coppola[3]*, Oliver H.F. Krumbach[4]*, Giusi Prencipe[5]*, Antonella Insalaco[5]*, Cristina Cifaldi[6,7], Immacolata Brigida[8], Erika Zara[3], Serena Scala[8], Silvia Di Cesare[6,7], Simone Martinelli[9], Martina Di Rocco[9,10], Antonia Pascarella[5], Marcello Niceta[11], Francesca Pantaleoni[11], Andrea Ciolfi[11], Petra Netter[1], Alexandre F. Carisey[1,2], Michael Diehl[12], Mohammad Akbarzadeh[4], Francesca Conti[6], Pietro Merli[13], Anna Pastore[11], Stefano Levi Mortera[11], Serena Camerini[14], Luciapia Farina[3,5], Marcel Buchholzer[4], Luca Pannone[9,11], Tram N. Cao[1], Zeynep H. Coban-Akdemir[15,16], Shalini N. Jhangiani[16,17], Donna M. Muzny[16,17], Richard A. Gibbs[15,16,17], Luca Basso-Ricci[8], Maria Chiriaco[6], Radovan Dvorsky[4], Lorenza Putignani[11], Rita Carsetti[5], Petra Janning[18], Asbjorg Stray-Pedersen[15,19,20], Hans Christian Erichsen[21], AnnaCarin Horne[22,23], Yenan T. Bryceson[24,25], Lamberto Torralba-Raga[24], Kim Ramme[26], Vittorio Rosti[27], Claudia Bracaglia[5], Virginia Messia[5], Paolo Palma[6], Andrea Finocchi[6,7], Franco Locatelli[13,28], Ivan K. Chinn[1,29], James R. Lupski[1,15,16,17], Emily M. Mace[2], Caterina Cancrini[6,7], Alessandro Aiuti[8,30,31], Mohammad R. Ahmadian[4]**, Jordan S. Orange[2,32]**, Fabrizio De Benedetti[5]**, and Marco Tartaglia[11]**

Hemophagocytic lymphohistiocytosis (HLH) is characterized by immune dysregulation due to inadequate restraint of overactivated immune cells and is associated with a variable clinical spectrum having overlap with more common pathophysiologies. HLH is difficult to diagnose and can be part of inflammatory syndromes. Here, we identify a novel hematological/autoinflammatory condition (NOCARH syndrome) in four unrelated patients with superimposable features, including neonatal-onset cytopenia with dyshematopoiesis, autoinflammation, rash, and HLH. Patients shared the same de novo *CDC42* mutation (Chr1:22417990C>T, p.R186C) and altered hematopoietic compartment, immune dysregulation, and inflammation. *CDC42* mutations had been associated with syndromic neurodevelopmental disorders. In vitro and in vivo assays documented unique effects of p.R186C on CDC42 localization and function, correlating with the distinctiveness of the trait. Emapalumab was critical to the survival of one patient, who underwent successful bone marrow transplantation. Early recognition of the disorder and establishment of treatment followed by bone marrow transplant are important to survival.

[1]Department of Pediatrics, Baylor College of Medicine, Houston, TX;   [2]Department of Pediatrics, Columbia University, Irving Medical Center, New York, NY;   [3]National Center for Rare Diseases, Istituto Superiore di Sanità, Rome, Italy;   [4]Institute of Biochemistry and Molecular Biology II, Medical Faculty of the Heinrich-Heine University, Düsseldorf, Germany;   [5]Immunology Research Division, Ospedale Pediatrico Bambino Gesù, Istituto di Ricovero e Cura a Carattere Scientifico, Rome, Italy;   [6]Academic Department of Pediatrics, Ospedale Pediatrico Bambino Gesù, Istituto di Ricovero e Cura a Carattere Scientifico, Rome, Italy;   [7]Department of Systems Medicine, University of Rome Tor Vergata, Rome, Italy;   [8]San Raffaele Telethon Institute for Gene Therapy, Istituto di Ricovero e Cura a Carattere Scientifico San Raffaele Scientific Institute, Milan, Italy;   [9]Department of Oncology and Molecular Medicine, Istituto Superiore di Sanità, Rome, Italy;   [10]Department of Cellular Biotechnology and Haematology, Sapienza University of Rome, Rome, Italy;   [11]Genetics and Rare Diseases Research Division, Ospedale Pediatrico Bambino Gesù, Istituto di Ricovero e Cura a Carattere Scientifico, Rome, Italy;   [12]Department of Bioengineering, Rice University, Houston, TX;   [13]Department of Pediatric Hematology and Oncology, Ospedale Pediatrico Bambino Gesù, Istituto di Ricovero e Cura a Carattere Scientifico, Rome, Italy;   [14]Core Facilities, Italian National Institute of Health, Rome, Italy;   [15]Baylor-Hopkins Center for Mendelian Genomics, Houston, TX;   [16]Department of Molecular and Human Genetics, Baylor College of Medicine, Houston, TX;   [17]Human Genome Sequencing Center of Baylor College of Medicine, Houston, TX;   [18]Department of Chemical Biology, Max-Planck Institute of Molecular Physiology, Dortmund, Germany;   [19]Norwegian National Unit for Newborn Screening, Department of Pediatric and Adolescent Medicine, Oslo University Hospital, Oslo, Norway;   [20]Institute of Clinical Medicine, University of Oslo, Oslo, Norway;   [21]Department of Pediatric and Adolescent Medicine, Oslo University Hospital, Oslo, Norway;   [22]Pediatric Rheumatology, Astrid Lindgren Children's Hospital, Karolinska University Hospital, Stockholm, Sweden;   [23]Department of Women's and Children's Health, Karolinska Institutet, Karolinska University Hospital Solna, Stockholm, Sweden;   [24]Department of Medicine, Karolinska Institutet, Karolinska University Hospital Huddinge, Stockholm, Sweden;   [25]Broegelmann Research Laboratory, Institute of Clinical Sciences, University of Bergen, Bergen, Norway.;   [26]Pediatric Hematology, Immunology and HCT Section, Astrid Lindgren Children's Hospital, Karolinska University Hospital, Stockholm, Sweden;   [27]Center for Myelofibrosis, Fondazione Istituto di Ricovero e Cura a Carattere Scientifico Policlinico San Matteo, Pavia, Italy;   [28]Department of Pediatrics, Sapienza University of Rome, Italy;   [29]Division of Pediatric Immunology, Allergy, Rheumatology, Department of Pediatrics, Baylor College of Medicine, Houston, TX;   [30]Pediatric Immunohematology, San Raffaele Scientific Institute, Milan, Italy;   [31]Vita Salute San Raffaele University, Milan, Italy;   [32]Medical Scientist Training Program and Translational Biology and Molecular Medicine Graduate Program, Baylor College of Medicine, Houston, TX.

*M.T. Lam, S. Coppola, O.H.F. Krumbach, G. Prencipe, and A. Insalaco contributed equally to this paper;   **M.R. Ahmadian, J.S. Orange, F. De Benedetti, and M. Tartaglia contributed equally to this paper;   Correspondence to Marco Tartaglia: marco.tartaglia@opbg.net;   Mohammad R. Ahmadian: reza.ahmadian@hhu.de;   Jordan S. Orange: jso2121@cumc.columbia.edu;   Fabrizio De Benedetti: fabrizio.debenedetti@opbg.net.

Introduction

The diagnosis and delineation of novel genetic syndromes is often difficult given the limited availability of patients, genetic heterogeneity, and clinical variability. Hemophagocytic lymphohistiocytosis (HLH) has recently been characterized as a clinical syndrome with hyperinflammation driven by excessive activation and expansion of macrophages and CD8^{+} T lymphocytes (Jordan et al., 2011; Rosado and Kim, 2013). Typical features include persistent high fever, liver involvement, splenomegaly, intravascular activation of coagulation associated with pancytopenia, and usually an increase in ferritin. Although this syndrome is clinically unique, the mechanisms underlying this disorder are diverse (Sepulveda and de Saint Basile, 2017; Chinn et al., 2018). Mutations leading to defective cytotoxicity by natural killer (NK) and CD8^{+} T lymphocytes are the typical cause of monogenic HLH, typically termed primary HLH. However, a markedly higher number of patients present with HLH in the absence of genetically defective cytotoxicity in the context of infections, rheumatic inflammatory diseases and malignancy. HLH in its various forms, both in children and adults, is invariably fatal if untreated.

Cell division cycle 42 (CDC42) is a member of the Ras-homologous (Rho) GTPase family functioning as a signaling node controlling a number of cellular processes, including adhesion, migration, polarity, cell cycle, and proliferation (Zhou et al., 2013; Baschieri et al., 2014). CDC42 functions as a molecular switch by cycling between a guanosine 5′-triphosphate (GTP)–bound (active) and a guanosine diphosphate (GDP)–bound (inactive) state. Two CDC42 isoforms have been characterized. While isoform 1 is ubiquitously expressed, isoform 2 is primarily found in the brain. CDC42 function is controlled by three different classes of regulators: guanine nucleotide exchange factors (GEFs), GTPase-activating proteins (GAPs), and guanine nucleotide dissociation inhibitors (Dvorsky and Ahmadian, 2004). The GTPase primarily acts through its spatial and temporal localized interaction with multiple downstream effectors, such as IQGAP1, p21-activated kinase (PAK), and Wiskott–Aldrich syndrome protein (WASP). Reversible localization of CDC42 at the cytoplasmic leaflet of the plasma membrane and other intracellular membranes is regulated by Rho GDP-dissociation inhibitor (RhoGDI) and IQGAP1. The former controls the dynamic membrane–cytoplasm shuttling of the GTPase (Gibson and Wilson-Delfosse, 2001; Gibson et al., 2004), while the latter promotes CDC42 translocation from the Golgi apparatus to the plasma membrane (Swart-Mataraza et al., 2002). These regulatory events play a crucial role in controlling CDC42 function, cytoskeletal rearrangement, cell polarity, and migration. Notably, altered binding of CDC42 to IQGAP1 induces multiple leading edge formation and aberrant multipolarized morphology (Fukata et al., 2002). Actin rearrangements and cell migration are also promoted by CDC42 interaction with its effector, WASP, a critical actin regulator and mediator of NK cell cytotoxicity (Orange et al., 2002; Ridley et al., 2003). Finally, CDC42 function requires posttranslational processing at the C-terminus, including prenylation at Cys[188] (geranyl-geranylation, most commonly) followed by proteolytic cleavage of the last three residues and carboxyl-methylation (Aicart-Ramos et al., 2011).

We and others recently identified germline heterozygous mutations in *CDC42* as the event underlying a remarkably heterogeneous collection of neurodevelopmental phenotypes (Takenouchi et al., 2015; Martinelli et al., 2018). Core clinical features of these traits include variable growth dysregulation; facial dysmorphism; intellectual disability; cardiac defects; immunological, hematological, and lymphatic abnormalities; and brain malformations. Mutations were found to variably disrupt CDC42 function by altering the switch between the active and inactive states of the GTPase and/or affecting its interaction with effectors (Martinelli et al., 2018). As a result, multiple cellular and developmental processes were differentially perturbed. Remarkably, the biochemical and functional characterization of mutations allowed the identification of genotype–phenotype relationships, suggesting a link between the specific impact of individual mutation class and its phenotypic expression (Martinelli et al., 2018). Mutations were documented to behave either as activating or inactivating, with the latter specifically associated with thrombocytopenia. Multisystem/organ involvement occurred in all groups.

Using whole-exome sequencing/whole-genome sequencing (WES/WGS) coupled to biochemical and functional validation, we describe a novel hematological and autoinflammatory phenotype in four unrelated patients caused by the same de novo missense mutation of *CDC42* (NM_001791, c.556C>T, p.R186C). The disease differs considerably from those previously associated with *CDC42* mutations and is characterized by neonatal onset of pancytopenia, autoinflammation, rash, and episodes of HLH (NOCARH). Through in silico, in vitro, and in vivo analyses, we describe the mechanism by which this specific amino acid change affects CDC42 function, intracellular signaling, and cellular and developmental processes. Finally, we provide a clinical delineation of this disorder and document the clinical response to IFN-γ and IL-1β neutralization and hematopoietic stem cell transplantation (HSCT).

Results

Clinical features of patients

The four unrelated patients included in the study showed a superimposable previously unrecognized multisystem disease characterized by neonatal onset of pancytopenia, persistent fever, skin rash, hepatosplenomegaly, and persistently elevated inflammatory markers in the absence of any evidence of neurodevelopmental involvement (Tables 1, S1, and S2; and Fig. 1 A). A suspicion of neonatal-onset multisystem inflammatory disease in three of the four patients led to treatment with IL-1 inhibitors with incomplete improvement of fever and rash, but not cytopenia. In all cases, high chronic doses of glucocorticoids were required to treat inflammation. All patients developed HLH, which was fatal in three subjects. Based on the shared features, we propose the term of NOCARH syndrome for this trait. A detailed description of the patients' clinical history is provided in the Materials and methods.

Lam et al.
Novel syndrome caused by aberrant CDC42 function

Journal of Experimental Medicine   2
https://doi.org/10.1084/jem.20190147

77

Table 1. Features of patients sharing the de novo missense *CDC42* c.556C>T (p.R186C) mutation

	Pt 1	Pt 2	Pt 3	Pt 4
Outcome and status	Alive, 6 yr	Dead, 6 mo	Dead, 1.5 yr	Dead, 4.5 mo
Fever	+	+	+	+
Skin rash	+	+	+	+
Facial dysmorphism	–	–	–	–
Failure to thrive	+	+	+	+
Hepatomegaly	+	+	+	+
Splenomegaly	+	+	+	–
CNS inflammatory disease[a]	+	–	–	–
Gastrointestinal symptoms[b]	+	+	+	+
Cardiac abnormalities	–	–	–	–
HLH[c]	+	+	+	+
Anemia[d]	+	+	+	+
Thrombocytopenia[d]	+	+	+	+
Neutropenia[e]	+	+	+	+
Monocytopenia	+	+	N/A	N/A
Acute-phase response	+	+	+	+
BM dysplasia	+	+	+	+
Other notable features	+[f]	–	–	+[g]

CNS, central nervous system; N/A, not applicable.

[a]Pt 1, three episodes at age 2 yr with generalized seizures and white and gray matter lesions in MRI; Pt 3, increased CSF protein and MRI with leptomeningitis.

[b]Pt 1, diarrhea, intestinal bleeding at age 11 mo, and intestinal infarction at age 5 yr; Pt 2, chronic diarrhea; Pt 3, small intestine inflammation; Pt 4, severe, unremitting enterocolitis from birth and diarrhea with intestinal bleedings and infarctions.

[c]Pt 1, four episodes; Pt 2, a single episode leading to death; Pt 3, died of secondary HLH after transplant; Pt 4, four episodes.

[d]Pt 1, constant transfusion requirement until age 2 yr; Pt 2, intermittent transfusion requirement during flares; Pt 3, transfusion dependent; Pt 4, transfusion dependent.

[e]Pt 1, Pt 2, and Pt 3, profound neutropenia; Pt 4, mild neutropenia.

[f]Suspected trigonocephaly.

[g]Very small thymus; arthritis.

Genetic studies

Two patients (patient 1 [Pt 1] and Pt 3) were enrolled in the Undiagnosed Disease Programs at the Ospedale Pediatrico Bambino Gesù and Baylor-Hopkins Center for Mendelian Genomics (CMG) at Baylor College of Medicine and the NK cell Evaluation and Research Program at Baylor and Columbia University. Using a trio-based WES strategy, a de novo missense *CDC42* change (NM_001791, Chr1:22417990, c.556C>T, p.R186C) affecting an isoform 1–specific exon was identified as the only candidate variant underlying the disorder in both subjects (Table S3). Occurrence of mutations in genes known to be associated with HLH or other immunological and hematologic disorders was

excluded. Similarly, there was no other rare substantively damaging variant shared by the two patients. The missense mutation had not previously been reported in the Exome Aggregation Consortium/Genome Aggregation Database (gnomAD) and was predicted to be damaging by in silico tools (Combined Annotation-Dependent Depletion [CADD] v1.3: 24.5, and Mendelian clinically applicable pathogenicity [M-CAP] v1.3: 0.0531). Based on this finding, a third patient (Pt 2) having clinical features resembling those of the two previously studied subjects underwent Sanger sequencing for the relevant *CDC42* coding portion, revealing heterozygosity for the same c.556C>T transition, which was validated to occur as a de novo event. Finally, through networking, a fourth patient (Pt 4) sharing a similar clinical phenotype, and the same de novo *CDC42* mutation was identified. In this case, the mutation was revealed by WGS using a trio-based strategy (Table S3), which excluded the occurrence of functionally and clinically relevant variants in HLH- and autoinflammation-related genes.

Biochemical and functional studies

To explore the functional consequence of the identified missense change, we initially assessed CDC42 levels in primary fibroblasts (Pt 1 and Pt 2) and HEK-293T cells transiently expressing the FLAG-tagged CDC42 mutant. In primary fibroblasts, the protein was expressed to similar levels without any apparent accelerated degradation (Fig. 1 B). Similarly, no reduction in the level of the mutant was observed in transfected cells. These data suggested that the disease-associated missense change does not significantly decrease CDC42 synthesis/stability, pointing to a specific perturbing effect on protein function.

Compared with the previously identified variants of CDC42 underlying neurodevelopmental disorders (Takenouchi et al., 2015; Martinelli et al., 2018), the p.R186C amino acid substitution occurs in a unique region at the C-terminus, within the hypervariable region (Fig. 1 C). Specifically, Arg[186] lies in proximity of Cys[188], which serves as substrate site for CDC42 prenylation. This irreversible posttranslational modification is required for proper CDC42 subcellular localization and function. To assess a possible effect of the p.R186C substitution on CDC42 prenylation, mass spectrometry (MS) analysis of the purified CDC42 mutant was performed, revealing proper C-terminal processing and lipid incorporation (Fig. 1 D), excluding the possibility of a defective or aberrant CDC42 posttranslational processing. Structural studies indicate that Arg[186] is located far from the GDP/GTP-binding pocket and major regions controlling CDC42 interaction with positive and negative regulators (switch regions I and II; Phillips et al., 2008). Consistently, fluorescence-based cell-free assays showed that replacement of Arg[186] by cysteine did not have a significant impact on either CDC42 basal and GEF-catalyzed GDP/GTP exchange activity or basal and GAP-stimulated GTPase activity of the protein (Fig. 1 E).

Arg[186] is a solvent-exposed residue located at the surface of CDC42 in one of the two major sites of binding to RhoGDI (Hoffman et al., 2000; Fig. 2 A). The residue stabilizes the geranylgeranyl-mediated CDC42–RhoGDI interaction. This interaction has a key role in the control of CDC42 function, as it

Lam et al.
Novel syndrome caused by aberrant CDC42 function

Journal of Experimental Medicine 3
https://doi.org/10.1084/jem.20190147

Lam et al.
Novel syndrome caused by aberrant CDC42 function

Journal of Experimental Medicine   4
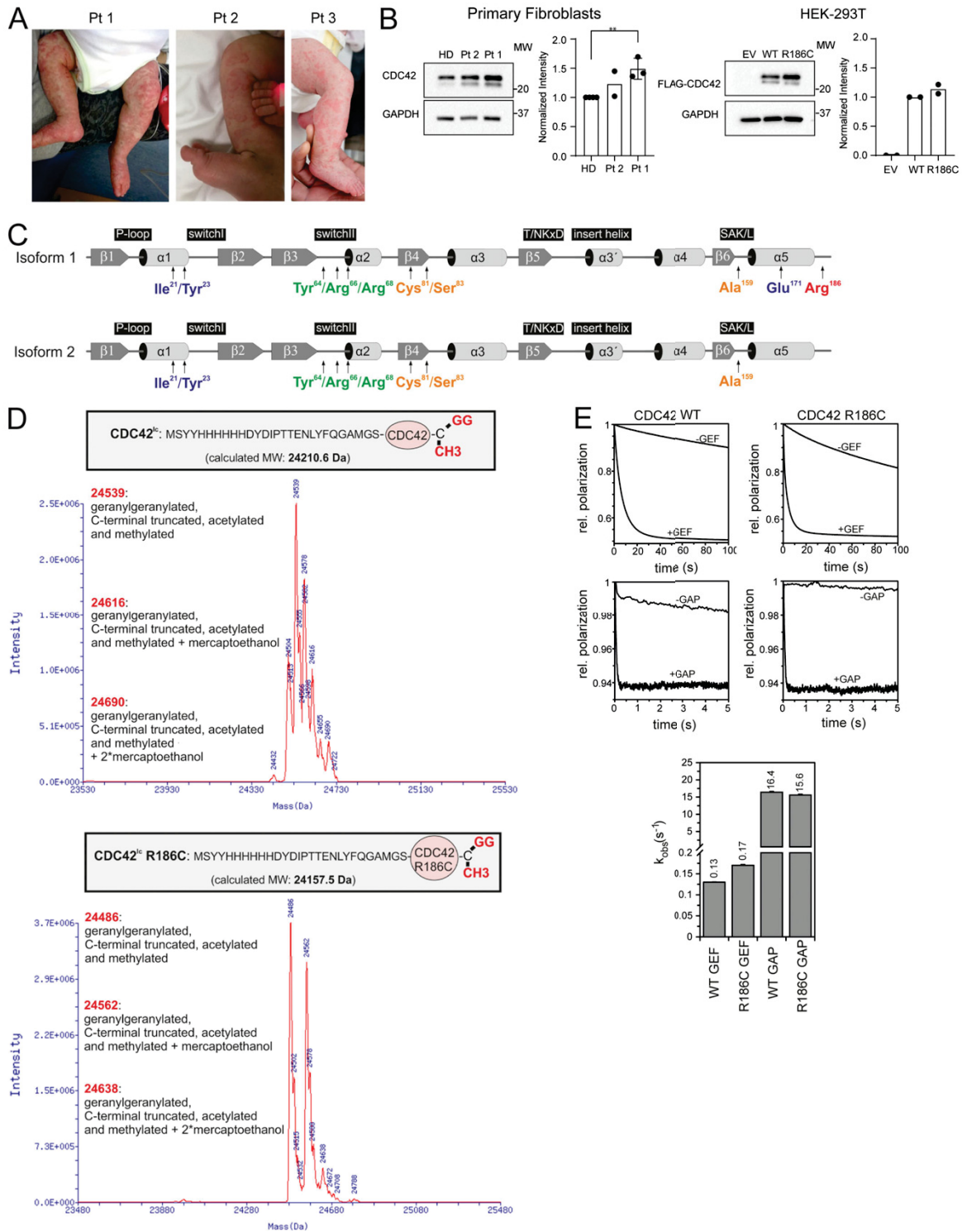https://doi.org/10.1084/jem.20190147

Figure 1. Clinical features of patients carrying the c.556C>T change (p.R186C) in *CDC42*, and biochemical profiling of the disease-causing mutant. (A) Skin findings of the affected subjects. **(B)** CDC42 levels in Pt 1 (n = 3, normalized intensity relative to HDs; **, P < 0.01, unpaired *t* test) and Pt 2 (n = 2) primary fibroblasts and HEK-293T cells (n = 2) expressing FLAG-tagged WT and mutant CDC42 or an empty vector (EV). **(C)** CDC42 domain organization indicating key functional regions and locations of residues affected by disease-causing variants. The two CDC42 isoforms are shown. Isoform 1 is ubiquitously expressed, while isoform 2 is brain restricted. The missense variants affecting E171 and R186 only affect isoform 1, while mutations affecting the other residues involve both isoforms. **(D)** p.R186C does not affect CDC42 posttranslational processing. MS analysis of WT and R186C CDC42 proteins shows a strong peak at 24,539 daltons and 24,486 daltons, respectively, indicating that CDC42^{R186C} is properly processed at the C-terminus. Da, daltons. **(E)** p.R186C does not affect CDC42 GTPase activity and nucleotide exchange behavior. GTPase activity and nucleotide exchange reaction in CDC42^{R186C} (right) are compared with WT CDC42 (left). k_{obs} values (observed dissociation constant) are reported (bottom). Representative polarization curves are shown (n = 4–6). MW, molecular weight; SAK/L, serine-alanine-lysine/leucine motif.

negatively regulates stable binding of the GTPase to the cytoplasmic leaflet of membranes and modulates CDC42 trafficking (Gibson and Wilson-Delfosse, 2001; Gibson et al., 2004). Based on the predicted disruptive effect of the Arg-to-Cys substitution on RhoGDI binding (Fig. 2 A), pull-down assays were performed to confirm defective interaction between the CDC42 mutant and RhoGDI (Fig. 2 B). The impaired binding of prenylated CDC42^{R186C} protein to RhoGDI was also demonstrated by surface plasmon resonance (SPR) analysis (Fig. 2 C). These data strongly suggest a perturbation of proper subcellular localization and trafficking of CDC42 as a major event contributing to pathogenesis. Notably, since other residues previously reported to be mutated in CDC42-related neurodevelopmental disorders are located at the interacting surface of the second major site of the GTPase mediating binding to RhoGDI, with a subset of them directly involved in RhoGDI binding (Fig. 2 A), the defective binding of CDC42 to RhoGDI likely does not represent a distinctive impairment of the CDC42^{R186C} mutant. This was confirmed by pull-down assays using a panel of bacterially expressed mutants to assess the impact of amino acid substitutions in regions far from the C-terminal tail on RhoGDI binding, which consistently with the structural data suggest that other missense changes variably impact CDC42 binding to RhoGDI (data not shown).

GTP-bound CDC42 activates multiple downstream signaling pathways by interacting with a variety of effectors (Dvorsky and Ahmadian, 2004; Nouri et al., 2017). We assessed the capability of the CDC42^{R186C} mutant to transduce signals by measuring its direct binding to major effectors, including WASP, PAK1, and IQGAP1. Glutathione S-transferase (GST) pull-down assays coupled to immunoblotting demonstrated a decreased effector binding of the mutant protein compared with WT CDC42, with a significantly diminished binding to WASP and a dramatically reduced interaction with IQGAP1 (Fig. 2 D). Given the established role of RhoGDI and IQGAP1 in the control of the dynamic redistribution of CDC42 within cells, we analyzed the possible disruption of the subcellular localization of the CDC42^{R186C} protein by using complementary cellular models. Depending on the cellular context and stimuli, CDC42 localizes to the cytoplasmic leaflet of multiple compartments, vesicles, and plasma membrane and partly the cytoplasm (Valdés-Mora and Lacal, 2011). Surprisingly, a constitutive cis/medial-Golgi–restricted localization of CDC42^{R186C} was observed in the totality of COS-1 cells ectopically expressing the mutant protein (Fig. 3 A). On the other hand, a similar Golgi-specific targeting was not observed for a representative panel of previously identified

disease-associated CDC42 mutants (e.g., p.Y23C, p.R68Q, p.S83P, p.A159V, and p.E171K; Martinelli et al., 2018), supporting the unique consequence of the p.R186C change on CDC42 subcellular distribution. This distinctive localization was observed in a disease-relevant cellular model, the YTS NK cell line, generated by CRISPR/Cas9 technology to express the mutant allele in the homozygous state (Fig. 3 B). Consistent with these findings, an enriched Golgi localization was also observed in the heterozygous primary fibroblasts obtained from Pt 1 (Fig. 3 C).

We investigated the consequences of altered CDC42 localization and function on major cellular processes controlled by CDC42, including proliferation, polarized migration, and cytoskeletal rearrangement. In vitro proliferation of CD34+ cells from Pt 1 assessed in response to KIT ligand (KITLG) or a growth factor mixture (KITLG, FLT3L, thrombopoietin, and IL3) revealed a specific unresponsiveness to KITLG, suggesting a selective hematopoietic proliferation signaling defect (Fig. 4 A). Defective proliferation was also observed in fibroblasts derived from Pt 1 and Pt 2, and NIH-3T3 cells transiently transfected to overexpress the CDC42 mutant (Fig. 4 B). Notably, Pt 1 fibroblasts and NIH-3T3 cells overexpressing the mutant protein also showed reduced polarized migration (Fig. 4 C). Consistently, defective chemotaxis toward C-X-C motif chemokine 12 (CXCL12) was observed in Pt 1 purified bone marrow (BM) CD34+ cells, peripheral blood mononuclear cells (PBMCs), as well as in the homozygous CDC42^{R186C} YTS NK cell line (Fig. 4 C). CDC42 is critical for cytoskeletal rearrangement primarily through the formation of filopodia, an F-actin–based structure contributing to cell adhesion, polarization, and migration (Etienne-Manneville, 2004; Mattila and Lappalainen, 2008; Jacquemet et al., 2015). Thus, imaging of filopodial pattern and cell polarization was performed in serum-stimulated fibroblasts from Pt 1. A higher number of cells with filopodia and an aberrantly polarized morphology compared with control cells was observed. In particular, aberrant polarization consisted of multiple lateral F-actin flat protruding edges (multipolar cells), in contrast with the front-rear canonical polarization (Fig. 4 D). Interestingly, in a cytolytic immunological synapse model on glass surface utilizing higher resolution imaging, a lower number of filopodia was detected in the mutant YTS cells, with a higher proportion of these cells retracting when activated on a CD18/28 surface (Fig. 4 E). Together, these data documented a variable perturbation of diverse cell-specific processes mediated by remodeling of the actin architecture, including cell polarity and migration.
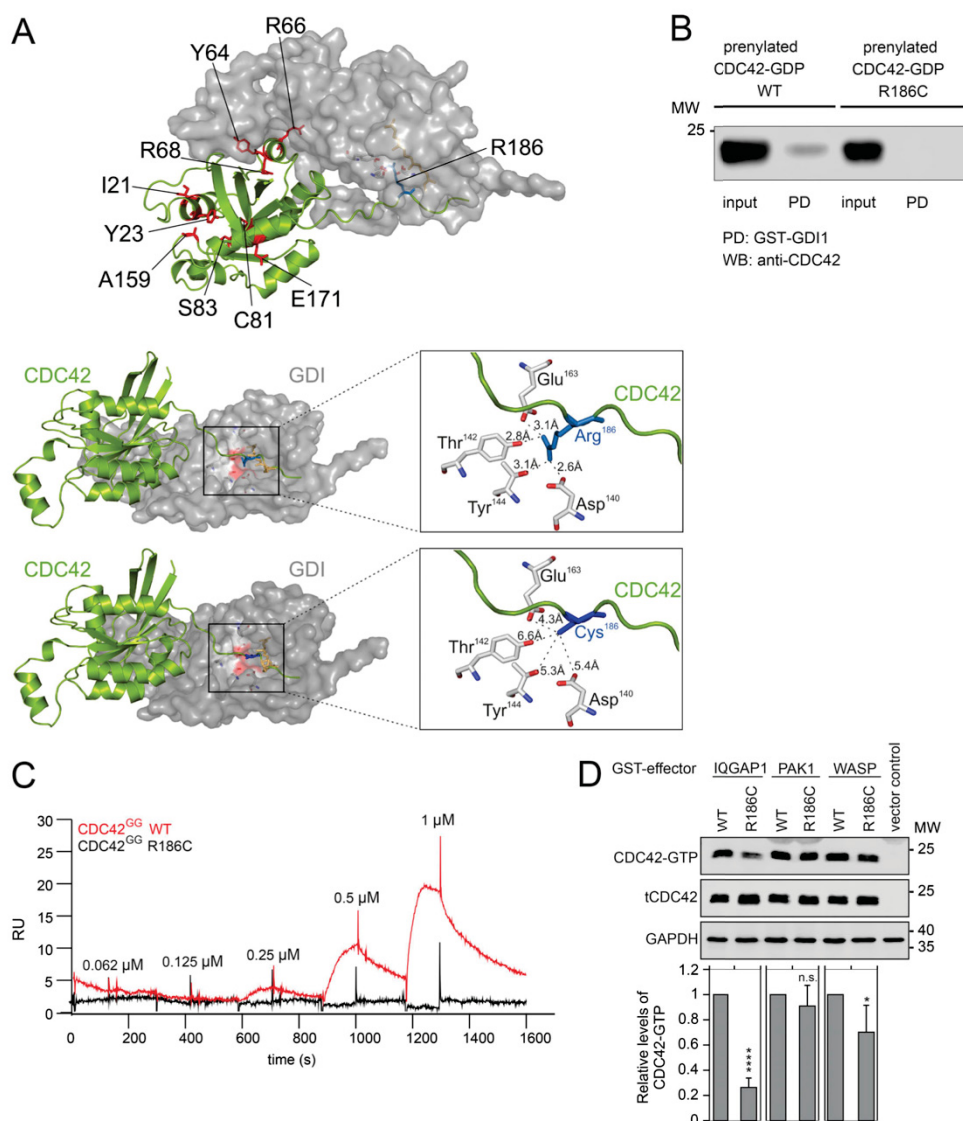
Lam et al.
Novel syndrome caused by aberrant CDC42 function

Journal of Experimental Medicine 5
https://doi.org/10.1084/jem.20190147

Figure 2. **p.R186C affects CDC42 binding to RhoGDI, IQGAP1, and WASP. (A)** Structure of CDC42 complexed with RhoGDI. Visualization of residues affected in human disease (left). Arg[186] has a unique localization within the hypervariable region. Arg[186] is surrounded by Asp[140], Thr[142], Tyr[144], and Glu[163] of RhoGDI (within 4 Å; right middle panel). p.R186C is predicted to disrupt the interaction between the hypervariable region of CDC42 and RhoGDI (right lower panel). **(B)** Pull-down (PD) assays showing RhoGDI interaction of prenylated WT and mutant CDC42. Binding of GST-fused RhoGDI to CDC42 proteins was analyzed by WB documenting defective CDC42[R186C] binding. A representative image is shown ($n = 2$). **(C)** SPR analysis of the RhoGDI–CDC42 interaction. Immobilized GST-tagged RhoGDI was titrated with increasing concentrations of WT (red) and R186C (black) CDC42[GG] proteins. No binding for the mutant protein was observed. RU, response unit ($n = 1$). **(D)** Representative WB visualizing pull-down of overexpressed FLAG-tagged WT and R186C CDC42 from COS-7 cell lysates by GST-fused effector proteins IQGAP1, PAK1, and WASP. The same amount of cell lysate was used as a loading control (tCDC42). Bar charts indicate the relative levels of GTP-bound WT and R186C CDC42 normalized to the levels of total CDC42. A strongly reduced and decreased binding of CDC42[R186C] to IQGAP1 and WASP was documented, respectively (mean ± SD, $n = 3$ independent experiments; *, $P < 0.05$; ****, $P < 0.0001$, one-way ANOVA with Sidak's multiple comparison test). n.s., not significant; MW, molecular weight.

HLH occurring in infants and young children is generally associated with defects in immune regulation, including function of NK cells (Henter et al., 2007). We observed a slightly to markedly reduced NK cell activity in Pt 2 and Pt 3 through clinical assessments of immune cell function (Fig. 5 A). The homozygous CDC42[R186C] YTS cell line was used as an immune cell model to directly study the impact of the mutant on NK cytotoxicity. Chromium release assay against MHC class
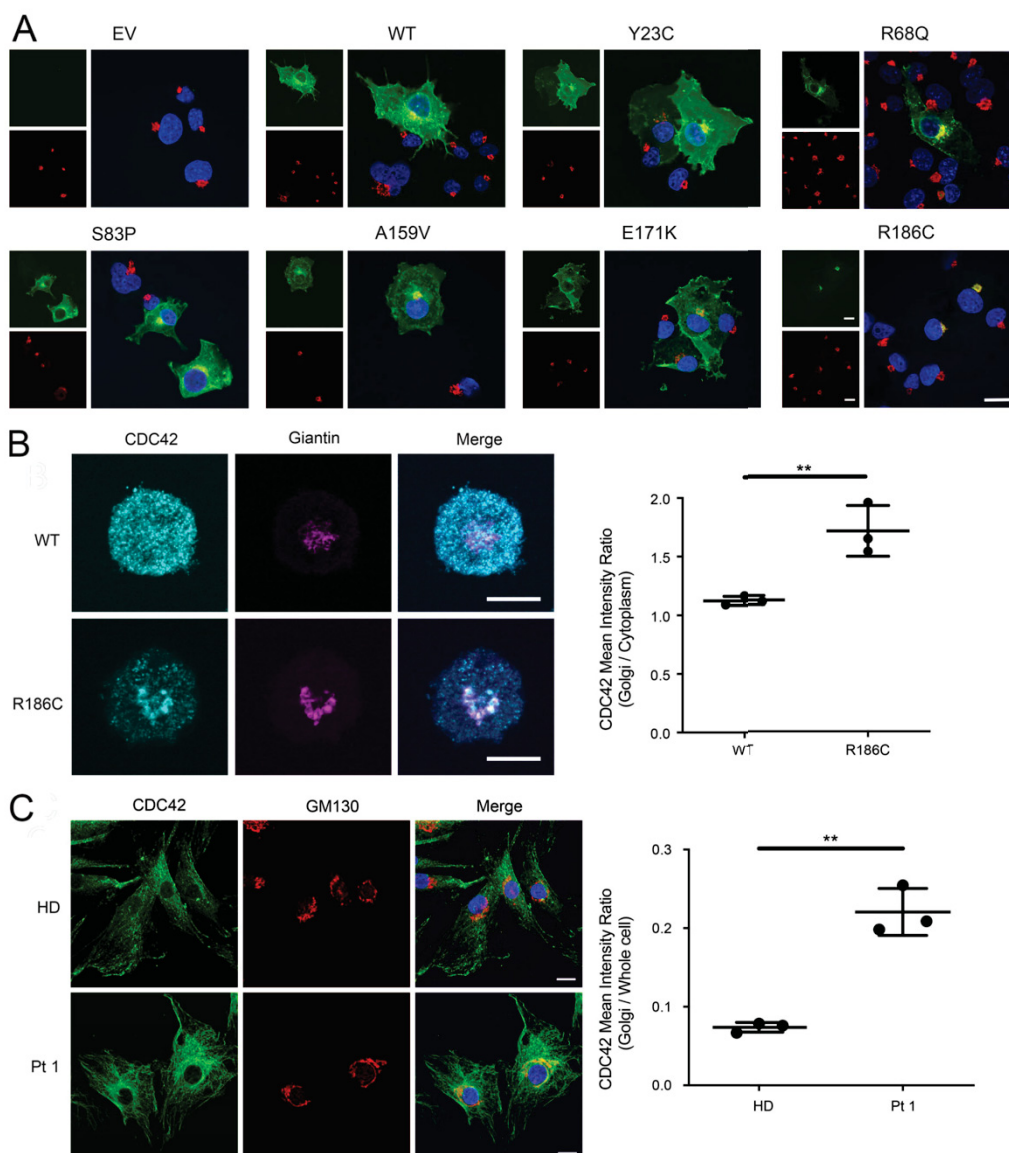
Lam et al.
Novel syndrome caused by aberrant CDC42 function

Journal of Experimental Medicine   6
https://doi.org/10.1084/jem.20190147

81

Figure 3. **p.R186C leads to aberrant subcellular localization of CDC42. (A)** CDC42^{R186C} shows a Golgi apparatus–restricted localization. Immunofluorescence staining of FLAG-tagged CDC42 proteins (green) and GM130 (red), a marker of cis/medial-Golgi apparatus, in COS1 cells transiently transfected with mock DNA (empty vector [EV]), WT CDC42, or mutant alleles carrying different disease-causing mutations (Y23C, R68Q, S83P, A159V, E171K, and R186C). Composite colocalization images are shown in the right panels with nuclei in blue. At least 200 FLAG-tagged CDC42-expressing cells were analyzed for each sample. Representative image of three independent repeats. Scale bar, 20 μm (applicable to all other images shown). **(B)** Subcellular localization of CDC42 in YTS NK cell lines homozygous for the p.R186C mutation. CDC42^{R186C} was found to be predominantly localized to the Golgi apparatus with reduced cytoplasmic signal. CDC42 signal intensity within the Golgi apparatus was quantified using giantin as a Golgi-specific marker relative to the cytoplasm and presented as a ratio. Representative images of three independent repeats are shown. The graph shows the mean + SD of three independent experiments with n = 38 cells for WT and n = 35 cells for R186C; **, P ≤ 0.01, unpaired two-tailed t test. Scale bar, 10 μm (applicable to all images shown). **(C)** Immunofluorescence staining of CDC42 (green), GM130 (red), and nuclei (blue) in primary fibroblasts expressing WT CDC42 (HD) or heterozygous for p.R186C (Pt 1). Visual composite colocalization images are shown in the merge panels. Colocalization (orange/yellow overlay) of CDC42 and cis-Golgi is detected in mutant CDC42–expressing cells. Images refer to representative pictures of three independent experiments. Using GM130 as a mask for cis/medial-Golgi, CDC42 fluorescence intensity was quantified as the ratio of Golgi to whole-cell staining using ImageJ software (mean ± SD, n = 3; **, P < 0.01, unpaired two-tailed t test). Scale bar, 20 μm (applicable to all images shown).

Lam et al.
Novel syndrome caused by aberrant CDC42 function

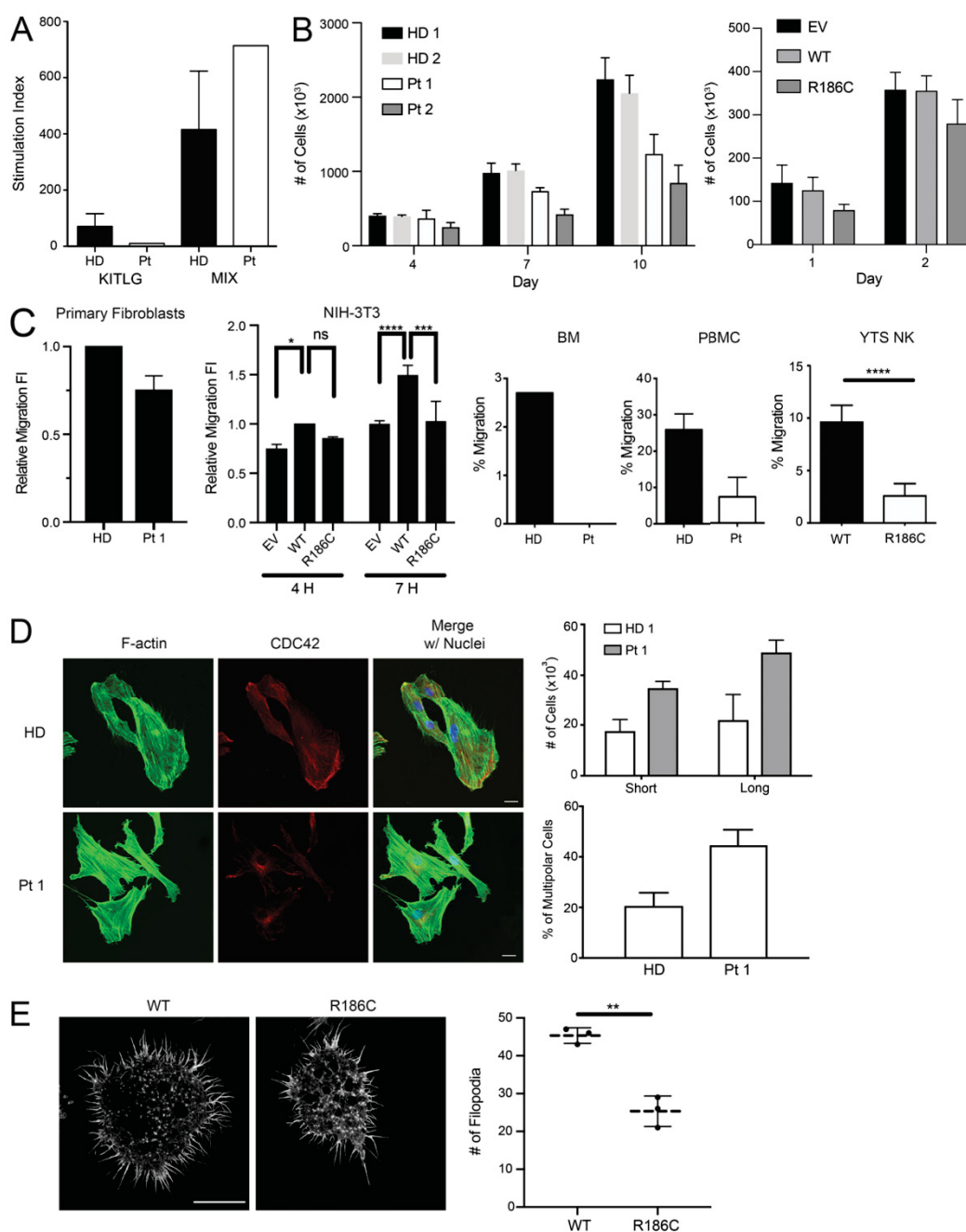Journal of Experimental Medicine   7
https://doi.org/10.1084/jem.20190147

Figure 4.   **p.R186C is associated with defects in proliferation, migration, and formation of actin-based structures. (A)** Proliferation of BM CD34$^+$ cells from Pt 1 in response to stem cell factor (SCF/KITLG) or a cytokine mixture (MIX; n = 1). **(B)** Proliferation of primary fibroblasts from Pt 1 (n = 3) and Pt 2 (n = 3) at indicated time points of culture, and NIH-3T3 cells transiently expressing WT or mutant CDC42 or an empty vector (EV). **(C)** Migration assays of primary fibroblasts from Pt 1 (n = 3), transfected NIH-3T3 cells (n = 3; *, P < 0.05; **, P < 0.01; ****, P < 0.0001, two-way ANOVA with Sidak's multiple comparisons), purified BM CD34$^+$ sorted cells (n = 1), PBMCs (n = 2), and a YTS CRISPR/Cas9-modified cell line (n = 3; ****, P < 0.0001, unpaired two-tailed t test; mean ± SEM for CD34$^+$/PBMCs and mean ± SD for NK cells, NIH-3T3 cell line, and primary fibroblasts). Migration was assayed using a wound-healing assay on primary fibroblasts and transfected NIH-3T3 cells and directed migration toward chemoattractant CXCL12 in BM CD34$^+$ cells, PBMCs, and YTS NK cells. Decreased directed migration of all tested cell types was observed. FI, fold increase of migratory cells. **(D)** Cytoskeletal rearrangements of cells expressing CDC42^{R186C}. Multipolarization and filopodia in primary fibroblasts from Pt 1 (n = 3) compared with fibroblasts from an HD. Immunofluorescence staining of CDC42 (red),

83

F-actin (green), and nuclei (blue) in cells stimulated 3 h with 20% serum. In HD fibroblasts, CDC42 localizes to the front leading edge, whereas in Pt 1 fibroblasts, the protein mostly localizes to the perinuclear area. On the right of the panel, quantification of multipolar cells and number of cells with short and long filopodia length are shown. Cells bearing multiple F-actin flat protruding edges (butterfly shaped) were considered multipolar. While HD fibroblasts polarize showing a front (leading edge), a large proportion of Pt 1 fibroblasts show multiple protruding edges. Filopodia twofold longer than nuclei diameter were considered long filopodia. Filopodial length and number were notably increased in fibroblasts, suggesting a disruption of CDC42-dependent actin architecture. Scale bar, 20 μm (applicable to all images shown). **(E)** Filopodia dynamics of the YTS cells on an activating CD18/CD28 surface. Filopodia were imaged using SIM-TIRF microscopy with representative images showing decreased filopodia count (mean ± SD, $n = 3$; **, $P < 0.01$, unpaired two-tailed t test with Welch's correction) in cells expressing CDC42R186C. Scale bar, 10 μm (applicable to all images shown). n.s., not significant.

I–negative 721.221 target cells demonstrated reduced cytotoxic function in the mutant cell line through a cell-intrinsic defect (Fig. 5 B). The reduction in cytotoxic function was in part due to a reduction in the ability to form conjugates with target cells (Fig. 5 C) and impaired migration (Fig. 4 C). Consistent with the observed altered filopodia structure and number, these findings suggest that immune dysfunction in the patients is likely linked to actin dysregulation (Sinai et al., 2010).

The unique behavior of the CDC42R186C mutant was also validated in vivo. In *Caenorhabditis elegans*, CDC-42 controls a number of developmental programs, including vulval development (Reiner and Lundquist, 2018). Our previous studies documented that *CDC42* mutations differentially perturb vulval induction and morphogenesis, with some amino acid changes up-regulating multiple signaling pathways, including those mediated by LET-60/rat sarcoma (RAS), and others behaving as hypomorphic mutations on WSP-1/WASP-dependent signaling

(Martinelli et al., 2018). In particular, overexpression of WT *cdc-42* at early/mid larval stage 3 (L3) was shown to induce the formation of a single protrusion at the site of the vulva (protruding vulva [Pvl] phenotype) in a WSP-1–dependent manner. Ectopic expression of the WT protein also elicited a low penetrant multivulva (Muv) phenotype and partially rescued the vulvaless (Vul) phenotype of nematodes carrying a hypomorphic *let-23/EGFR* allele, demonstrating hyperactivation of signal flow through LET-60 and the MAPK cascade. Compared with WT CDC-42, the K186C (homologue of R186C) mutant induced a less penetrant Pvl phenotype and less efficiently rescued the Vul phenotype, indicating a hypomorphic effect of this mutation on both LET-60/RAS and WSP-1/WASP signaling pathways (Fig. 6, A and B; and Table S4).

Collectively, the in vitro and in vivo biochemical and functional data consistently indicate a unique impact of the identified disease-causing p.R186C change on CDC42 subcellular
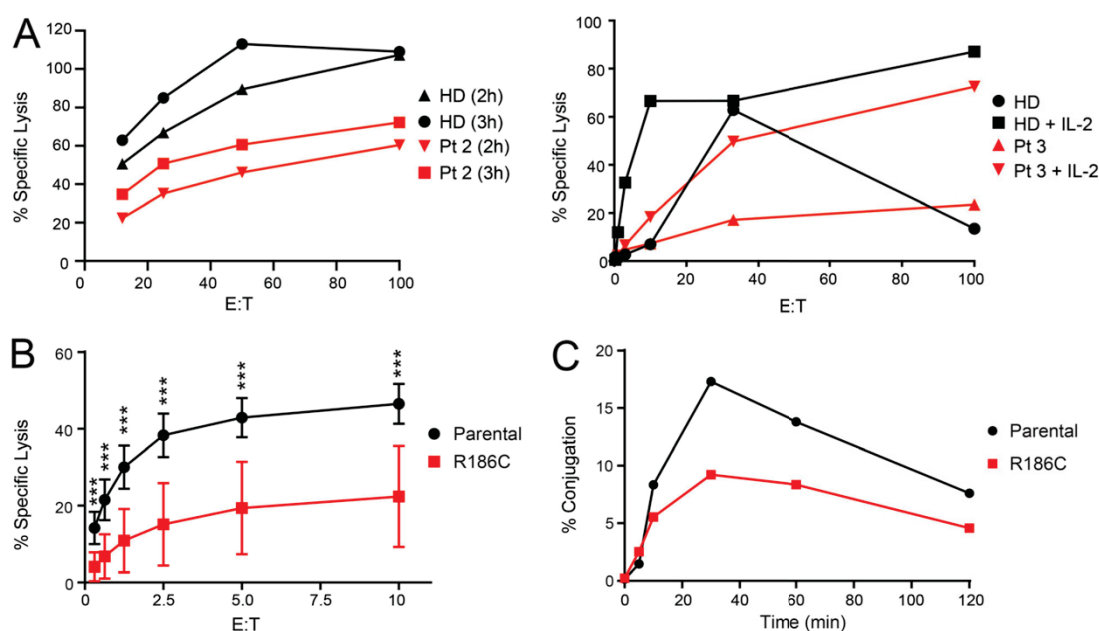

Figure 5. **p.R186C is associated with impaired NK cell cytotoxic function. (A)** Assessment of NK cell cytotoxicity in Pt 2 and 3. Using NK cell cytotoxicity assays, Pt 2 at diagnosis had a decreased cytotoxic function compared with an HD at the shown E/T ratios at time points 2 h and 3 h. For Pt 3 at diagnosis, NK cells were stimulated with IL-2, and cytotoxicity was also decreased. **(B)** Functional characterization of YTS NK cell model. Standard Cr-51 release assay of YTS NK cell lines against 721.221 target cells. The mutant cell line showed a significant decrease in cytotoxicity (pooled mean ± SD, $n = 3$ independent repeats each with triplicates; ***, $P < 0.001$, Mann–Whitney U test). **(C)** Co-culture conjugation assay of YTS NK cell lines against 721.221 target cells. Compared with parental YTS NK cells, a reduced ability of the YTS NK cells expressing the mutant allele to form conjugates with 721.221 target cells was also observed. A representative figure is shown ($n = 4$).
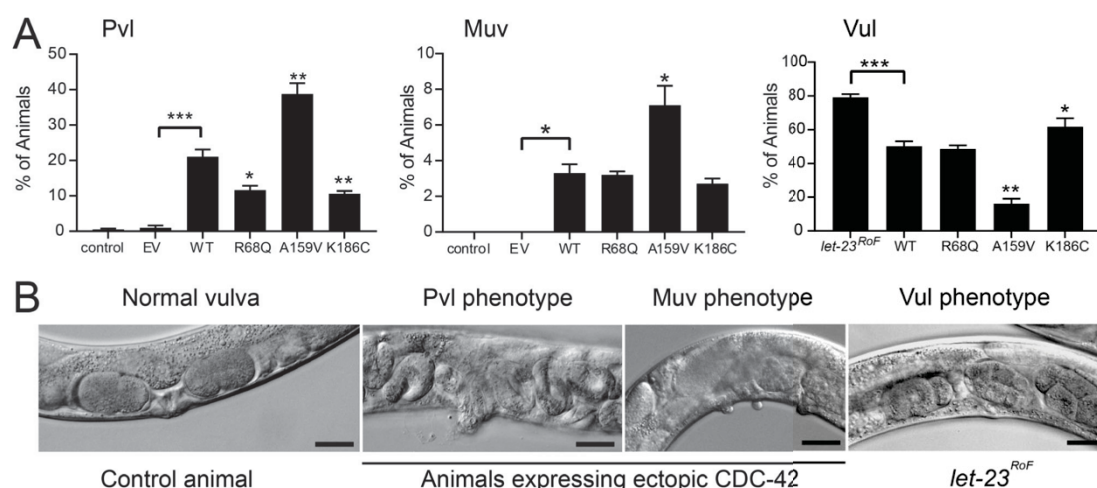
Lam et al.
Novel syndrome caused by aberrant CDC42 function

Journal of Experimental Medicine   9
https://doi.org/10.1084/jem.20190147

84

Figure 6. **p.R186C affects *C. elegans* vulval development. (A)** Hypomorphic effect of the mutation on pathways controlling *C. elegans* vulval development. Compared with WT CDC-42, the K186C mutant induces a less penetrant Pvl phenotype and less efficiently rescues the Vul phenotype of animals carrying a hypomorphic *let-23/EGFR* allele, indicating a hypomorphic behavior on multiple signaling pathways. The R68Q and A159V mutants, representative of group I (substitutions characterized by impaired binding to regulators and effectors) and group II (gain-of-function changes) mutations, respectively, are shown for comparison. Error bars indicate SEM of three independent experiments. Asterisks specify significant differences between animals expressing WT CDC-42 and those expressing the empty vector (EV) or the *let-23(sy1)* allele (*, P < 0.05; ***, P < 1.2e-6; two-tailed Fisher's exact test), and between animals expressing WT and mutant CDC-42 (*, P < 0.05 [Muv] or P < 0.005 [Pvl and Vul]; **, P < 0.00002 [Pvl] or P < 3.2e-6 [Vul]). Number of animals are reported in Table S4. **(B)** Representative images of *C. elegans* phenotypes. Scale bars, 20 μm.

localization and function, which likely underlies the distinctiveness of the trait.

Clinical profiling of NOCARH syndrome

The four unrelated patients sharing the same de novo missense *CDC42* mutation (p.R186C) showed a similar multisystem inflammatory disease characterized by pancytopenia, fever, skin rash, hepatosplenomegaly, and persistently elevated inflammatory markers. Differently from what had previously been reported for other *CDC42* mutations (Martinelli et al., 2018), no neurodevelopmental involvement was observed. In these patients, Wiskott–Aldrich syndrome, idiopathic myelofibrosis, dyskeratosis congenita, and classical immunodeficiency were rapidly excluded based on established clinical, biochemical, and genetic diagnostic criteria. Treatment with IL-1 inhibitors partially improved fever and rash, and high chronic doses of glucocorticoids were required to treat inflammation. Fatal HLH developed in three cases.

Trilineage dyshematopoiesis was observed in BM with prevalence of early differentiation elements, and decreased clonogenic progenitor content having altered clonogenicity was documented (Fig. 7 and Table S5). This indicates that the p.R186C substitution in CDC42 affects hematopoiesis, ultimately altering BM composition.

Since typical autoinflammatory features were present, we investigated IL-1β production. Increased IL-1β secretion was measured via ex vivo spontaneous IL-1β release from unstimulated BM mononuclear cells as well as high levels of IL-1β in BM supernatants and plasma (Fig. 8, A and B). This finding demonstrates that IL-1β overproduction is likely responsible for

part of the phenotype, particularly the observed features typically associated with IL-1β–driven inflammasopathies (i.e., fever, rash and elevated acute phase proteins; Harapas et al., 2018). Remarkably, patients showed strikingly increased production of IL-18. This was demonstrated by a 300-fold higher ex vivo spontaneous IL-18 release from unstimulated BM mononuclear cells and by levels of IL-18 in BM supernatant and plasma that were ~1,000-fold higher than those of healthy donors (HDs; Fig. 8, A and B). Stimulation of BM mononuclear cells with LPS or LPS plus ATP did not increase further IL-18 production as compared with unstimulated cells, suggesting the presence of constitutive maximal activation of IL-18 processing and release in the patient's marrow. In contrast, no ex vivo spontaneous IL-6 release from unstimulated BM mononuclear cells was observed (Fig. 8 A), and circulating IL-6 levels in Pt 1 and Pt 2 were comparable to those observed in healthy subjects (data not shown). Importantly, IL-18 is a potent costimulator of IFN-γ production (Okamura et al., 1995), and IFN-γ appears to be a common mediator of all forms of HLH (Grom et al., 2016). Consistently, IFN-γ levels were increased in patients, particularly during HLH episodes. In multiple samples available from Pt 1, we observed that elevated IFN-γ levels were strictly correlated (r = 0.82) with elevated levels of CXCL9 (Fig. 8 C), a chemokine specifically induced by IFN-γ that has been proposed as biomarker of HLH (Bracaglia et al., 2017). CXCL9 levels were strictly correlated with levels of ferritin (r = 0.82), which is the most typical marker of HLH activity. In line with the finding that IL-18 alone is not sufficient to induce IFN-γ, we did not find a significant correlation between IL-18 and IFN-γ or ferritin levels (Fig. 8 C). Accordingly, in Pt 2, high IFN-γ levels were also
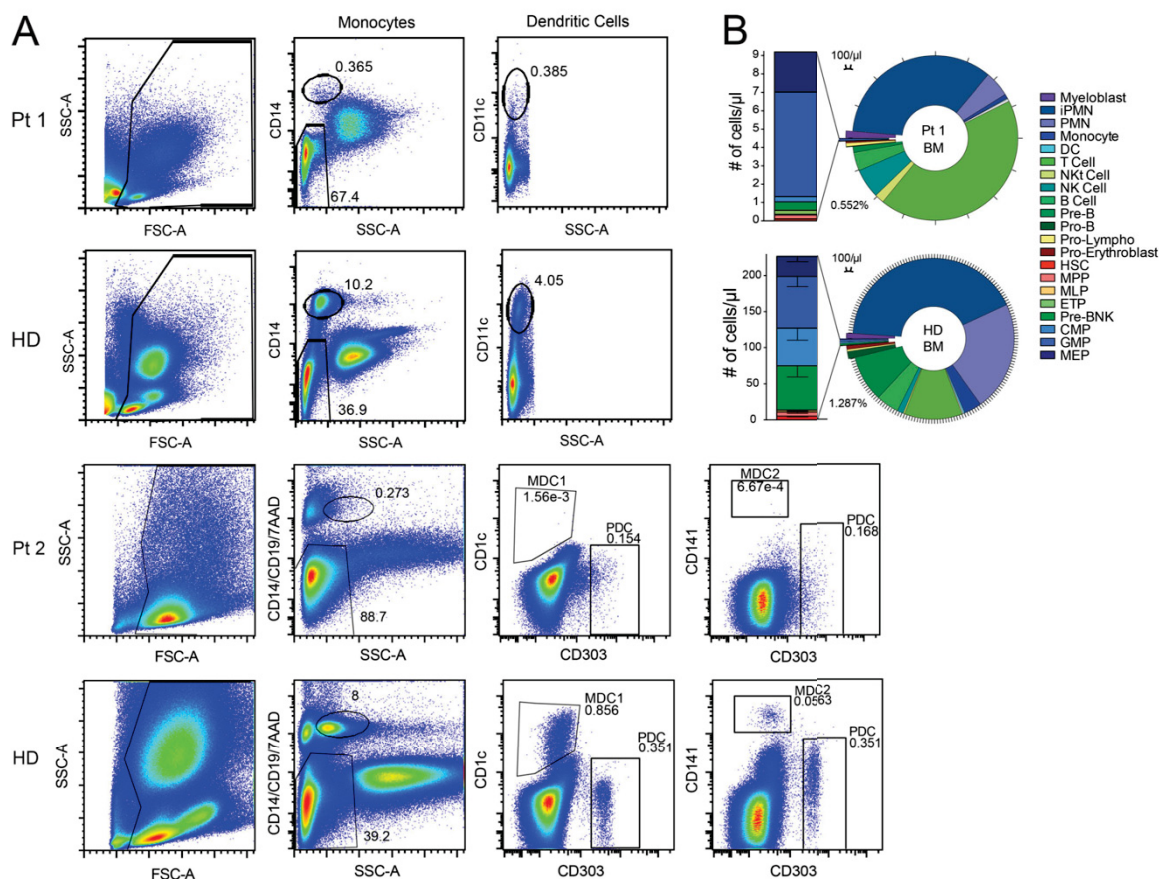
Lam et al.
Novel syndrome caused by aberrant CDC42 function

Journal of Experimental Medicine   10
https://doi.org/10.1084/jem.20190147

Figure 7. **p.R186C leads to disruption of certain hematopoietic compartments. (A)** Flow cytometric analysis of monocyte and dendritic cell (DC) immunophenotype on whole lysed peripheral blood of Pt 1 ($n = 1$) and Pt 2 ($n = 1$) showing a severe reduction of monocytes and myeloid dendritic cells. Upper plots (Pt 1 and Pt 2) from left to right: after elimination of debris, we gated on CD14 or CD14, CD19, 7AAD SSC^{low} cells to identify monocytes. In the CD14$^-$ SSC^{low} population, we gated on CD11c$^+$ cells for dendritic cell identification in Pt 1. In the CD14$^-$CD19$^-$7AAD$^-$ SSC^{low} population, we gated on CD1c, CD141, or CD303 to distinct the dendritic cell major subtypes (MDC1, type 1 myeloid dendritic cell; MDC2, type 2 myeloid dendritic cell; PDC, plasmacytoid dendritic cell) in Pt 2. Numbers within the plots show the frequency of monocytes and dendritic cells in the total events displayed. SSC-A, SSC-area; FSC-A, FSC-area. **(B)** The ring chart shows absolute counts of distinct hematopoietic subpopulations on total CD45$^+$ cells (indicated in the legend) in BM of pediatric HDs ($n = 6$) and Pt 1. The stacked bar graph on the left is a zoom on the absolute count of hematopoietic stem and progenitor cell subtypes within the LIN$^-$CD34$^+$ compartment. PreB/NK, B and NK cell progenitor; CMP, common myeloid progenitor; ETP, early T progenitor; GMP, granulocyte/monocyte progenitor; iPMN, immature polymorphonucleated cell; MEP, megakaryocyte/erythrocyte progenitor; MLP multi-lymphoid progenitor; MPP, multi-potent progenitor; NKt, NK T cell; PMN, polymorphonucleated cell.

associated with high CXCL9 and ferritin levels (Table S1). In addition, serum IL-6 levels were measured, and persistent elevation was not detected (Fig. 8 A). Notably, in Pt 1, the last severe HLH episode not responding to repeated glucocorticoid pulses, cyclosporine A, and high-dose anakinra (10 mg/kg/d) was successfully treated with emapalumab, a monoclonal antibody targeting IFN-γ. Altogether, these data show that the R186C change in CDC42 leads eventually to activation of the IFN-γ pathway through overproduction of IL-18, which has been demonstrated to be associated with secondary HLH development in the context of autoinflammatory diseases (Canna et al., 2014; Weiss et al., 2018).

The surviving patient (Pt 1) underwent allogeneic HSCT from his HLA-haploidentical father after selective depletion of αβ T cells and CD19$^+$ cells from the graft for preventing occurrence of graft-versus-host disease and Epstein-barr virus–related posttransplant lymphoproliferative disease, respectively (Locatelli et al., 2017). The conditioning regimen used treosulfan, thiotepa, and fludarabine. To avoid HLH flares, the patient was given emapalumab and anakinra until days +28 and +100 after HSCT, respectively. Neutrophil and platelet recovery occurred on days +18 and +12 after HSCT; successful engraftment of donor hematopoiesis was associated with normalization of IL-1β and IL-18 production (Fig. 8 B). No inflammatory or HLH flare has been observed up to day +210.
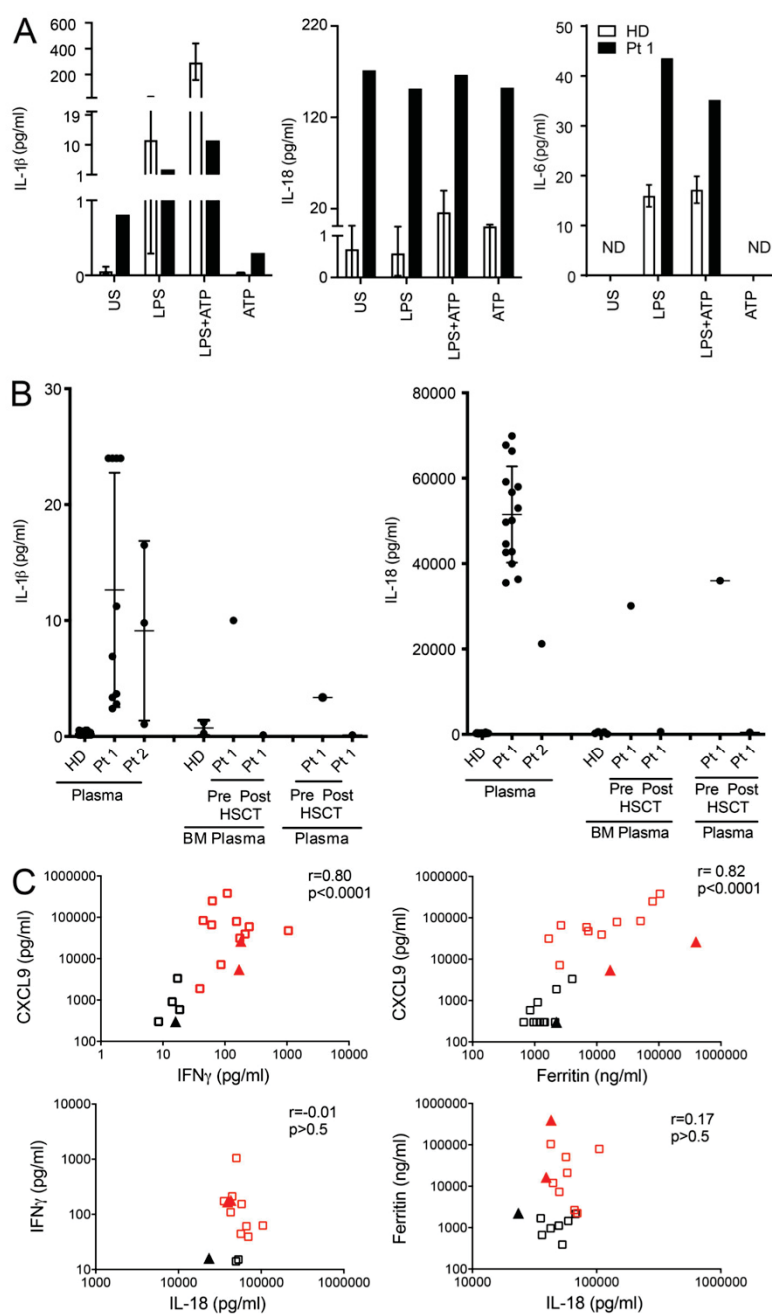
Lam et al.
Novel syndrome caused by aberrant CDC42 function

Journal of Experimental Medicine   11
https://doi.org/10.1084/jem.20190147

86

Figure 8. **p.R186C is associated with high production of inflammasome-related cytokines IL-1β and IL-18 in vivo and ex vivo. (A)** HD ($n = 3$) and Pt 1 BM mononuclear cells were left unstimulated (US) or stimulated with LPS (10 μg/ml) for 5 h, with or without ATP (1 mM) for an additional 1 h. Compared with unstimulated HD cells, unstimulated Pt 1 cells release high levels of IL-1β and IL-18. In LPS-primed HD cells, ATP addition caused a marked increase in IL-1β and IL-18 release, while this is not observed in LPS-primed Pt 1 cells. IL-6 levels released in supernatants were also measured; no spontaneous release was observed. ND, not detectable. Secreted cytokines were measured by ELISA, and results obtained were normalized by the absolute number of monocytes per milliliter BM. **(B)** IL-1β and IL-18 levels were measured in plasma samples collected from Pt 1 and Pt 2 at different time points over the course of the disease. IL-1β and IL-18 levels were also measured in BM, and plasma samples were obtained from Pt 1 30 d before and after HSCT. For HDs, plasma $n = 24$ and BM $n = 5$. For Pt 1 and Pt 2, $n = 1$. Mean ± SD is indicated. **(C)** Plasma levels of IFN-γ, CXCL9, and IL-18 were measured in Pt 1 (squares) and Pt 2 (triangles) and correlated with ferritin levels, a typical marker of HLH activity. IFN-γ and CXCL9 levels, but not IL-18 levels, are significantly correlated with ferritin levels. Red squares and triangles indicate samples collected when Pt 1 and Pt 2 fulfilled at least five criteria required for HLH diagnosis.

Discussion

Here, we characterize a previously unrecognized and distinctive hematological/autoinflammatory disorder due to a specific missense mutation of *CDC42* (p.R186C). By using complementary biochemical and functional analyses, we provide evidence that the disease-causing amino acid substitution has unique consequences on CDC42 function,

leading to a perturbation of hematopoiesis, immune function, and inflammatory response. We also provide a first characterization of the clinical profile of the associated phenotype and propose the acronym of NOCARH syndrome to highlight the major features of the condition, including neonatal onset of cytopenia, autoinflammation, rash, and episodes of HLH.

CDC42 codes for a small GTPase of the Rho family controlling multiple signaling pathways regulating cell polarity and migration, endocytosis, and cell cycle progression by cycling between an active (GTP-bound) and an inactive (GDP-bound) state (Etienne-Manneville and Hall, 2002; Etienne-Manneville, 2004). Recently, a number of missense mutations in this gene have been associated with developmental traits characterized by an unusually broad spectrum of anomalies, with core clinical features including defective growth, intellectual disability, brain malformations, facial dysmorphism, hearing/vision problems, cardiac malformations, and immune and hematologic and lymphatic defects (Takenouchi et al., 2015; Martinelli et al., 2018). Genotype–phenotype correlations were identified and linked to a variable functional impact of mutations, suggesting specific consequences of individual mutations on cellular processes controlling development. In contrast to those phenotypes, NOCARH syndrome is a hematological and autoinflammatory condition with no major involvement of other systems, which is in line with the documented peculiar functional consequences of the p.R186C change on protein function.

Our immunophenotype and clonogenic data are consistent with previous findings showing that controlled inactivation of CDC42 in BM cells results in altered frequency and distribution of hematopoietic stem cells, decreased abundance of long-term hematopoietic stem cells, and occurrence of myeloid and erythroid developmental defects, as well as functional defects in engraftment, migration, and BM retention (Yang et al., 2007a,b). Notably, present findings confirm the key role of the GTPase in controlling processes implicated in hematopoietic stem and progenitor cell fate and behavior.

Based on structural modeling and biochemical and cellular testing, we predicted and confirmed the mutated protein to have impaired interaction with known regulators and effectors, including RhoGDI, IQGAP1, and WASP, leading to aberrant subcellular localization, actin cytoskeleton rearrangement, and reduced migration. CDC42 mislocalization data are consistent with the physiological role played by RhoGDI and IQGAP1, key mediators of membrane cycling of CDC42 (Gibson and Wilson-Delfosse, 2001; Swart-Mataraza et al., 2002; Gibson et al., 2004). The observation that cells expressing the p.R186C variant undergo deep cytoskeletal rearrangements leading to multiple leading edges is congruous to findings by Fukata et al. (2002) showing that cells expressing IQGAP1 mutants defective in CDC42 binding display aberrant multipolar morphology. This supports the notion that the IQGAP1–CDC42 interaction is crucial to cell polarization and migration. Notably, the finding that CDC42 aberrant localization and trafficking is coupled to altered polarization and migration is in line with the relevant role played by CDC42 at the Golgi and the leading edge in the control of cell polarity (Baschieri et al., 2014). Compositional and functional assessment revealed impaired proliferation and polarized migration, further emphasizing the requirement of proper CDC42 function in these processes (Martinelli et al., 2018). Notably, although we were unable to identify a specific CDC42 functional perturbation associated with the p.R186C change as causally linked to the complex phenotype of NOCARH syndrome, this mutant seems unique in its mislocalization, which

suggests this is a key factor in the pathogenesis for this uniquely presenting disease.

Our findings indicate that aberrant CDC42 function can involve components of hyperinflammation and immune impairment in NK cells, contributing to the HLH phenotype observed in NOCARH. The underlying pathogenetic mechanism of the p.R186C mutation in the context of anemia and thrombocytopenia has yet to be determined, suggesting a context-dependent effect on specific blood cell compartments. Future studies involving murine models carrying the heterozygous mutation would be needed to assess the effect on hematopoiesis in a similar context to that of our patients.

Several mutations in genes with a role in actin cytoskeleton remodeling of immune cells have been demonstrated to be involved in the pathogenesis of hematological/autoinflammatory diseases, underlining the importance of the actin cytoskeleton in modulating inflammatory responses. Indeed, mutations in the actin-binding protein cofilin (CFL1; Seeland et al., 2018), WAS (Li et al., 2017), DOCK8 (Dasouki et al., 2011), and ARPC1B (Brigida et al., 2018), as well as in RAC2, a Rho GTPase structurally and functionally related to CDC42 (Caye et al., 2015; Hsu et al., 2019), cause abnormal migration, proliferation, and/or differentiation of lymphoid and/or myeloid cells and are associated with features of autoinflammation. Moreover, aberrant actin depolymerization due to an inactivating mutation of the actin-depolymerizing cofactor Wdr1 has been demonstrated to cause in mice an autoinflammatory disease characterized by spontaneous autoinflammation, thrombocytopenia, and neutrophilia (Kim et al., 2015). In these mice, the autoinflammatory phenotype is IL-18, but not IL-1β, dependent and is driven by activation of the pyrin inflammasome. In our study, we could not investigate the exact molecular mechanism involved in the overproduction of IL-18 and the role of CDC42 in inflammasome regulation. However, the spontaneous release of IL-18 by BM mononuclear cells, associated with high IL-18 circulating levels, has been exclusively described in patients carrying mutations in the NLRC4 protein (Canna et al., 2014) who present with recurrent episodes of HLH. Moreover, it is well known that inactivation of RhoA GTPases by many bacterial toxins is sensed by the inflammasome (Jamilloux et al., 2018). Interestingly, IQGAP1 has also been described as a novel regulator of caspase-1 in macrophages infected with *Yersinia pestis* (Chung et al., 2014). Based on the above-mentioned observations regarding the connection between the actin cytoskeleton and inflammation, we propose the term "inflammatory actinopathies" to group these diseases, including NOCARH, differently from actinopathies with neurological and myologic features.

In conclusion, NOCARH is an autoinflammatory disease at high risk for HLH, similarly to what has been observed for the disorder caused by NLRC4 gain-of-function mutations (Canna et al., 2014; Romberg et al., 2014). Given the observed autoinflammation associated with markedly elevated IL-18 levels, the mechanism is most likely associated with the role of IL-18 as a costimulus for IFN-γ production. The characteristic inflammation in two patients in conjunction with elevated IL-18 levels support IL-18 as a disease biomarker for diagnosing NOCARH and potentially related syndromes of dysregulated CDC42

Lam et al.
Novel syndrome caused by aberrant CDC42 function

Journal of Experimental Medicine   13
https://doi.org/10.1084/jem.20190147

88

function that involve inflammation. One patient survived severe HLH, and this appears to have been dependent on timely therapeutic neutralization of IL-1 and IFN-γ. Early recognition and establishment of treatment for NOCARH, based on the unique association of early-onset trilinear cytopenia and autoinflammation, are crucial to prevent multiorgan failure and subsequent death.

Materials and methods
Detailed clinical history of patients
Pt 1

Pt 1 is a 6-yr-old Caucasian girl born from healthy unrelated parents with no family history of genetic disease. At birth, she presented with persistent high fever; erythematous skin lesions of the face, trunk, and limbs; a large abdomen because of hepatosplenomegaly (spleen diameter, 6.4 cm); and suspected trigonocephaly (Table 1). Laboratory tests showed an increase in inflammatory markers and a severe trilinear cytopenia requiring frequent red blood cell and platelet transfusions during the first year of life. BM biopsy at disease onset revealed fibrosis with trilineage dyshematopoiesis (prevalence of early differentiation elements in erythroid and myeloid lineage, dysmorphic and reduced megakaryocytes, increased lymphocytes, and abundant CD68^{+} histiocytes with focal or absent phagocytosis; Tables S1 and S2). Given the partial clinical overlap with chronic infantile neurological cutaneous articular syndrome–neonatal-onset multisystem inflammatory disease (CINCA-NOMID), she was started on glucocorticoids and daily therapy with anakinra, with improvement of fever and rash, but no effect on cytopenia. Failure to thrive was present. Treatment with G-CSF was started with partial response. Recurrence of inflammatory symptoms following tapering and/or discontinuation of glucocorticoids was observed. At age of 11 mo, she presented with recurrent episodes of intestinal bleeding, associated with persistent/chronic diarrhea. Meckel's diverticulum was excluded. At 2 yr and 6 mo, she presented with three episodes of generalized seizures followed by hypotonia, hypersomnia, and transient hemiparesis requiring in one case admission to an intensive care unit. Magnetic resonance imaging (MRI) performed during the first episode showed lesions suggestive of inflammatory central nervous system involvement; during the third episode, the MRI showed one additional lesion of the brainstem. CSF was sterile, CSF white blood cells were 18/mmc, and no hemophagocytic cells were detected. All the episodes were treated with a high dose of i.v. glucocorticoid with good response; therapy with levetiracetam was started. At the age of 5 yr, because of incomplete control of the inflammatory state, anakinra was switched to canakinumab. Starting from 5 yr of age, she developed four episodes of full-blown HLH, fulfilling the HLH-2004 diagnostic criteria. All episodes were treated with high dose of i.v. glucocorticoids and cyclosporine-A with resolution in all cases except one. The last episode was severe and associated with massive intestinal ischemia and necrosis requiring surgical resection and consequent ileocolostomy. This episode was unresponsive to high-dose glucocorticoids and IL-1 inhibition. Treatment with emapalumab, an anti–IFN-γ antibody, was

added with rapid resolution of the episode. At age of 6 yr, the patient underwent allogeneic HSCT from her HLA-haploidentical father after a selective depletion of αβ T cells and CD19^{+} cells from the graft. The conditioning regimen consisted of a combination of treosulfan, thiotepa, and fludarabine. To avoid flares of HLH, the patient was given emapalumab and anakinra until days +28 and +100 after the allograft, respectively. Neutrophil and platelet recovery occurred on days +18 and +12 after HSCT. Normalization of the acute phase response and no inflammatory or HLH flare have been observed up to day +210.

Pt 2

Pt 2 was a male born from Caucasian healthy unrelated parents. Since the first day of life, he presented with persistent fever, skin rash, mild hepatosplenomegaly, failure to thrive, increase in inflammatory markers, and trilinear pancytopenia that required red blood cell and platelet transfusions. Extensive microbiological screening revealed a positive IgM titer for parvovirus B19, with B19 parvovirus PCR negative on whole blood. At age 57 d, he was first seen at one of our centers transferred from another hospital. He presented with failure to thrive (height and weight below the fifth percentile), persistent fever, skin rash, mild hepatosplenomegaly, and chronic diarrhea and positive blood stool. Inflammatory bowel disease was suspected, and temporary parenteral nutrition started. Laboratory tests showed elevated acute-phase reactants and severe trilinear cytopenia requiring recurrent red blood cells and platelet transfusions. BM biopsy revealed dyshematopoiesis and some lymphohistiocytic aggregates without significant hemophagocytosis. The disease course was characterized by a persistent inflammatory state despite several treatment attempts with glucocorticoids, antibiotics, high doses of i.v. immunoglobulins, and cyclosporine-A. Suspecting an autoinflammatory condition, treatment with anakinra was also started with only partial improvement of the clinical and laboratory parameters. At age 7 mo, he developed severe HLH with multiorgan failure that rapidly progressed to death. Extensive immunological workup showed severe monocytopenia and reduction of plasmacytoid, myeloid dendritic cells, neutropenia, increased central memory CD4^{+} cells with reduced naive and recent thymic emigrant CD31^{+} cells, increased regulatory T cells with high memory phenotype, and increased switched B cell memory cells, plasma cells, and autoreactive B cells associated with reduced transitional B cells (Table S2).

Pt 3

Pt 3 was a female born from nonconsanguineous Caucasian parents with no family history of inherited diseases. At birth, she presented with generalized rash, intermittent cytopenia (leukopenia, thrombocytopenia, and anemia requiring transfusions), and generalized lymphadenopathy. Hepatosplenomegaly, nutritional problems, and stagnant growth were also noted within the first few months after birth. The anemia was profound and required several red blood cell transfusions. At age 3 mo, the condition was thought to be CINCA-NOMID, and treatment with anakinra was started, which was temporarily

Lam et al.
Novel syndrome caused by aberrant CDC42 function

Journal of Experimental Medicine   14
https://doi.org/10.1084/jem.20190147

effective for rash and overall inflammation, but not cytopenia. Treatment was stopped due to respiratory infections and no clear effect of the treatment. 6 mo later, she started treatment per modified HLH-2004 protocol with steroids and weekly etoposide-phosphate over 8 wk. No neurological deficits were noted, but the patient declined over time, requiring increasing erythrocyte and thrombocyte transfusions. She was then transferred to another hospital, and for the first few weeks, she was stable, but she developed signs of an HLH relapse with increased hepatosplenomegaly, high ferritin, high triglycerides, bicytopenia, and a florid rash. Histologically, hemophagocytosis was not detected. She also developed breathing difficulties of unknown origin. She was commenced on a modified HLH-2004 protocol with the addition of antithymocyte globulin, infliximab, and anakinra. There was some clinical response on this treatment and a decision to opt for a stem cell transplant was made. While she was being investigated and prepared for transplant, she continuously deteriorated; she was treated with two courses of alemtuzumab in this time period. She received a CD3/CD19-depleted haploidentical transplant and died 4 d later.

Pt 4

Pt 4 was a boy born in week 34 to nonconsanguineous parents from a Christian minority originating from the Middle East with a history of thalassemia minor and familial cardiomyopathy. The patient was small for gestational age and presented at birth with bloody diarrhea, cholestasis, ascites, and a generalized rash. He had an unusually small thymus for his age. The patient also rapidly developed additional symptoms, including stiff/contracted joints, high fever, highly elevated inflammatory markers, intermittent cytopenia (thrombocytopenia and anemia requiring transfusions), hepatomegaly, and diatheses (bleeding from the mucosas; Table 1). At 2 wk of age, an extensive workup was initiated. Investigations excluded known gut, liver, and metabolic diseases. Immunological investigations slightly lowered number of T cells with prevalence of naive T cells. Results of functional tests of NK/T cells and degranulation ability were normal. Serum IL-6 and IL-18 was remarkably high on repeated occasions. An autoinflammatory condition in combination with a primary immunodeficiency was suspected. The patient was treated with high dose glucocorticoids and anakinra. Because of insufficient response tocilizumab was also added. This intensive antiinflammatory treatment was effective for some of the rash, ascites, cholestasis, as well as intermittently for overall inflammation and cytopenia. The patient needed supportive treatment in the intensive care unit on six separate occasions, four of which were due to macrophage activation syndrome–HLH episodes, likely triggered by infection.

Severe gastrointestinal symptoms and unexplained mucosal bleedings persisted. The patient continued to have watery diarrhea. Gastroduodenal endoscopy showed severe inflammation with ongoing bleeding. Biopsies of the duodenum showed acute and chronic inflammation with ulcers. In connection with colonoscopy, the patient suffered a perforation and needed surgery. Since no matched related SCT donor was available, a search for an unrelated matched donor was initiated; however,

his conditions were too unstable with no signs of remission, and HSCT was considered too risky. Because of the symptoms of agonizing pain and high levels of anxiety, and in the presence of no response to treatments, the antiinflammatory therapies were gradually stopped, and the patient was transferred to another hospital for palliative care, where he died at 4.5 mo of age.

Mutation analyses

This study was approved by the Ospedale Pediatrico Bambino Gesù and Baylor College of Medicine Ethical Committees. Clinical data and DNA specimens from the subjects included in the study were collected following procedures in accordance with the ethical standards of the declaration of Helsinki protocols and approved by the review boards of all involved institutions, with signed informed consents from the participating subjects/families (study protocol for Pt 1 and 3: "Genome Sequencing to Elucidate the Causes and Mechanisms of Mendelian Genetic Disorders" [H-29697] of Baylor College of Medicine; study protocol for Pt 1 and 2: 1702_OPBG_2018).

Pt 1

Exome capture was performed using SureSelect AllExon v5+UTR (Agilent) and sequenced on a HiSeq platform (Illumina). WES data were processed and analyzed using an in-house–implemented pipeline as previously described (Flex et al., 2016; Stray-Pedersen et al., 2017; Bauer et al., 2018). Briefly, reads were aligned to human genome build GRCh37/UCSC hg19, and variants were quality filtered according to the Genome Analysis Toolkit's 2016 best practices, annotated, and filtered against public (dbSNP150 and gnomAD V.2.0.1) and in-house (>1,300 population-matched exomes) databases to retain private and rare (unknown frequency or minor allele frequency <0.1%) variants located in exons with any effect on the coding sequence (CDS) and within splice site regions. Functional annotation of variants was performed using SnpEff v.4.3 and dbNSFP V.2.9, and functional impact was analyzed by CADD v.1.3 and M-CAP v.1.0.(Cingolani et al., 2012; Liu et al., 2013; Kircher et al., 2014; Jagadeesh et al., 2016). Average coverage was 91× and 20× for ≥86% of the target. Among 127,405 high-quality variants, 14,224 affect either the CDS or splice sites, while 338 have low or unknown frequencies according to the aforementioned frequency thresholds. For sequencing statistics, see Table S3. Relevant variants and the de novo origin of the c.556C>T change were validated by Sanger sequencing.

Pt 2

Mutation analysis was performed by Sanger sequencing using DNA obtained from circulating leukocytes. Primer pairs are available upon request.

Pt 3

Initial mutation analysis was performed by Sanger sequencing (and Baylor College of Medicine CMA v9.1), which was negative for NLRP3, IL1RN, LPIN2, NOD2, MEFV, TNFRSF1A, PSTPIP1, MVK, and PSMB8. The patient was identified in a shared CMG database at Baylor College of Medicine by searching for rare, likely damaging variants (using the Exome Aggregation Consortium and CADD) in CDC42 in a cohort of unsolved immunodeficiency

Lam et al.
Novel syndrome caused by aberrant CDC42 function

Journal of Experimental Medicine   15
https://doi.org/10.1084/jem.20190147

probands. On further study, patient had underwent trio-based WES in Norway, revealing the presence of the de novo c.556C>T change in *CDC42*, and proband-only WES was repeated at Baylor College of Medicine. Sanger sequencing of proband and parents was then performed, confirming the presence of a de novo variant (Table S3).

Pt 4

Blood samples from the patient and his parents were obtained with informed consent according to the Declaration of Helsinki. The study was approved by the Regional Ethics Review Board in Stockholm, Sweden. DNA samples were subjected to trio-based WGS with a TruSeq DNA PCR-free protocol followed by sequencing on an Illumina HiSeq X machine with an average coverage of 34×. Sequencing reads were analyzed with the pipeline SpeedSeq. In brief, reads were mapped to the human genome build GRCh37 with Burrows–Wheeler aligner, while calling of single-nucleotide and structural variants was performed, respectively, with FreeBayes and Lumpy. No mutations were identified in HLH/autoinflammation–related genes. The genomic region spanning *CDC42* was visualized with the Integrative Genomics Viewer, indicating a de novo c.556C>T mutation, which was validated by Sanger sequencing (Table S3).

MS

WT CDC42 from TNAO38 insect cells were dissolved in 50% (vol/vol) acetonitrile and 0.2% (vol/vol) formic acid at a final concentration of 2 mg/ml. Proteins were subjected to a C4 HPLC column (MassPrep Online Desalting Cartridge, dimensions 2.1 × 10 mm; Waters) equilibrated with 20% (vol/vol) acetonitrile and 0.1% (vol/vol) formic acid. For HPLC separation, the following conditions were used: HPLC-system U300 series (Agilent Technology), a flow rate of 500 µl/min; eluent A, 0.1% (vol/vol) formic acid in water; eluent B, 0.1% (vol/vol) formic acid in acetonitrile; gradient conditions, 20% B for 0.5 min, linear gradient up to 60% B in 1.5 min, linear gradient up to 90% B in 0.5 min, 90% B for 0.5 min, and reequilibration of the column. The HPLC system was coupled on-line to an ion trap mass spectrometer (VelosPro; ThermoFisher Scientific) equipped with an electrospray ionization source. Full spectra were acquired using a mass-to-charge range of 700–2,000. Obtained spectra were deconvoluted using the program package Promass (ThermoFisher Scientific). Masses obtained from the respective spectra are described with respect to calculated molecular weights (CH3, methyl group; Ic, insect cells; GG, geranylgeranyl moiety).

Constructs and proteins for biochemical analysis

pGEX vectors were used for bacterial overexpression of CDC42^{WT}, CDC42^{R186C}, RhoGDI-1, p50GAP, ITSN1, WASP (GTPase-binding domain), PAK1 (GTPase-binding domain), and IQGAP1 (863–1,657). All proteins were isolated as GST fusion proteins in *Escherichia coli* BL21 (DE3) purified after cleavage of the GST tag via gel filtration (Superdex 75 or 200; Pharmacia). Nucleotide-free and fluorescent nucleotide-bound CDC42 were prepared using alkaline phosphatase (Roche) and phosphodiesterase (Sigma-Aldrich) at 4°C as described. Fluorescent nucleotide

was methylanthraniloyl (mant-) GppNHp (guanosine 5′-β,γ-imidotriphosphate), a nonhydrolysable GTP analogue. All proteins were analyzed by SDS-PAGE and stored at −80°C. The GTPase assay and nucleotide exchange reaction were performed with a Hi-Tech Scientific (SF-61) stopped-flow instrument. The release of fluorescently labeled GDP (mantGDP) was measured basally and with the catalytic GEF domain of ITSN1. Hydrolysis of tamraGTP was measured basally and following stimulation with the catalytic GAP domain of ARHGAP1 (p50GAP). The excitation wavelengths were 543 nm and 362 nm for tamraGTP and mantGDP, respectively. Fluorescence experiments were performed in a Fluoromax 4 fluorimeter in polarization mode. Human WT and mutant *CDC42* were subcloned into pFastBacHTB vector (Invitrogen) and fused with an N-terminal hexa-histidine (6xHis) tag and transformed into DH10BAC strain for insect cell purification.

Fluorescence assays

The GTPase assay and nucleotide exchange reaction were performed with a Hi-Tech Scientific (SF-61) stopped-flow instrument. The excitation wavelengths were 543 nm and 362 nm for tamraGTP (Jena Bioscience) and mantGDP (Jena Bioscience), respectively. For the GTPase assay, equal volumes (600 µl) of 0.2 µM CDC42-tamraGTP and 10 µM of p50GAP in 30 mM Tris/HCl, pH 7.5, 10 mM K$_2$HPO$_4$/KH$_2$PO$_4$, 5 mM MgCl$_2$, and 3 mM dithiothreitol at 25°C were rapidly mixed and transferred to a fluorescence detection cell within seconds. For the nucleotide exchange reaction, 0.2 µM CDC42-mantGDP and 40 µM GDP + 10 µM ITSN1 were used.

Structural analysis

To elucidate the impact of substituted arginine to cysteine at residue 186, the protein–protein interaction between CDC42 and RhoGDI-1 (PDB: 1DOA) was analyzed. Residues in vicinity ≤4 Å were considered as part of binding interface of Arg^{186}. Analysis and illustrations were made using the PyMOL molecular viewer.

SPR

A Biacore X100 instrument (GE Healthcare) was used in a single-cycle mode to analyze the kinetics of interaction between WT or R186C CDC42^{GG} with RhoGDI. SPR experiments were performed at 25°C in HBS-P+ running buffer (10 mM HEPES pH 7.4, 0.15 M NaCl, 0.05% [vol/vol] surfactant P20; GE Healthcare). GST capturing method was used to immobilized GST antibody on the surface of CM5 chip. 4 µM GST-GDI (5 µl/min) in HBS-P buffer injects for the period of 180 s in order to immobilized GST-GDI over the chip surface. Regeneration of the chip performed using 10 mM glycine, pH 3.0, at the end of each experiment. WT and R186C CDC42^{GG} were injected in 0.06–1 µM concentrations with twofold increase in each injection step. Final curve was fitted in a 1:1 binding model.

Cell lines and cultures

Dermal mutant fibroblasts were obtained from patients, and HEK-293T, COS-1, and NIH-3T3 cell lines and primary control dermal fibroblasts were obtained from American Type Culture Collection and grown in high-glucose DMEM supplemented

Lam et al.
Novel syndrome caused by aberrant CDC42 function

Journal of Experimental Medicine   16
https://doi.org/10.1084/jem.20190147

91

with 10% FCS, 2 mM L-glutamine, and 10 U/ml penicillin/streptomycin (all from Sigma-Aldrich). YTS cells, a subclone of the YT cell line, were cultured in R10 composed of RPMI-1640 supplemented with 10% FBS (Premium; Atlanta Biologicals), 2 mM L-glutamine (ThermoFisher Scientific), 1 mM sodium pyruvate (ThermoFisher Scientific), 1% MEM nonessential amino acid (100×; ThermoFisher Scientific), 10 mM Hepes (ThermoFisher Scientific), and 1% penicillin/streptomycin (ThermoFisher Scientific).

Plasmids for CDC42 expression in HEK-293T, COS-1, and NIH-3T3 cell lines

WT human CDC42 isoform 1 (NP_001782.1) was cloned into a pcDNA3-FLAG backbone using PCR and standard cloning methods via BamHI and EcoRI digestion. Mutant constructs carrying the R186C change were generated by site-directed mutagenesis using the QuikChange XL kit (Agilent Technologies) and verified by direct sequencing. Each of the FLAG-tagged CDC42 protein expression constructs or the empty vector was transfected using Fugene 6 (Roche). 24 h after transfection, cells were assayed for cell growth or processed for wound healing assays, immunofluorescence, or immunoprecipitation analysis. Transfection efficiency was verified by Western blot (WB) analysis of the protein lysate.

Pull-down of CDC42 variants from COS-7 cell lysates

COS-7 cells were transfected with pcDNA3.1-Flag plasmids containing WT and R186C CDC42 and transiently overexpressed for 48 h. 10 μg of each plasmid was used for transfection of the COS-7 cells (900,000 cells per 10-cm Petri dish). Empty vector was used as control. 20 μl TurboFect transfection reagent (ThermoFisher Scientific) was added to the plasmids and incubated for 20 min at room temperature before adding it to the cells. Medium was changed after 4 h, and cells were incubated for 48 h. Cells were lysed in an ice-cold buffer containing 50 mM Tris/HCl, pH 7.4, 100 mM NaCl, 2 mM MgCl$_2$, 1% Igepal Ca-630, 10% glycerol, 20 mM β-glycerolphosphate, 1 mM Na$_3$VO$_4$, and one tablet EDTA-free protease inhibitor (Roche). Cell lysates were incubated with glutathione beads coupled to GST-effector proteins for 30 min at 4°C. Beads were washed five times, heated in 1× Laemmli buffer at 95°C for 10 min, and subjected to SDS-PAGE for immunoblot analysis. WB was performed using an anti-FLAG antibody (F3165, M2; Sigma-Aldrich) and anti-GAPDH antibody (21185, clone 14C10; Cell Signaling Technology).

Polarized migration

Polarized migration of primary fibroblasts and NIH-3T3 cells on fibronectin-coated wells (10 μg/ml; Sigma-Aldrich) were evaluated by wound-healing assays. Monolayers of cells were scratched with a 200-μl micropipette tip and incubated in low-serum medium (2% FBS in DMEM high glucose without Phenol red, 2 mM L-glutamine, and 1% penicillin/streptomycin; all purchased from Sigma-Aldrich) in the presence of thymidine (10 mM, T1895; Sigma-Aldrich) to inhibit cell proliferation. Images were acquired at different time points using a Nikon Eclipse TS100 microscope, a Nikon Plan Fluor 10×/0.13 objective, and a Nikon Coolpix 990 digital camera. Cells that had migrated in the wounded area were counted in four fields per well, and the fold increase of migratory cells was evaluated after scratch at the time points indicated.

Proliferation and viability

Proliferation and viability of transiently transfected NIH-3T3 cells and primary fibroblasts were quantified by manual counting using a Neubauer hemocytometer. Cell viability was detected by the exclusion of trypan blue dye (5 mg/ml in PBS, ECB4004L; Euroclone). Cells were counted at different time points by phase contrast using a Leitz Ortholux II microscope and a Leitz 10×/0.13 objective.

Immunofluorescence analysis of primary fibroblasts and COS-1 cells

Cells were washed in PBS, fixed (4% paraformaldehyde [PFA], 20 min, room temperature), washed twice, treated for free aldehydes quenching (50 mM NH$_4$Cl, 10 min at room temperature), and washed again. After 5-min permeabilization with 0.5% Triton X-100 in PBS, cells were blocked for 30 min with 2% FBS and 1% BSA in PBS. Then, cells were sequentially incubated with primary and secondary antibodies 1.5 h at 37°C, 1:500 mouse anti-FLAG (F-1804; Sigma-Aldrich) or 1:50 mouse anti-CDC42 (SC8401; Santa Cruz); 30 min at room temperature, 1:100 goat anti mouse Alexa Fluor 488 (A11017; ThermoFisher Scientific); 30 min room temperature, 1:50 rabbit anti-GM130 (PA1-077; ThermoFisher Scientific); and 30 min at room temperature, 1:100 goat anti-rabbit Alexa Fluor 568 (A11011; ThermoFisher Scientific). All antibodies were diluted in 0.5% BSA and 0.1% saponin in PBS. Unbound antibodies were removed after each incubation by three washes with washing buffer (0.2% BSA in PBS). After a 30-min incubation with phalloidin-Alexa Fluor 647 (Life Technologies), coverslips were washed and then mounted on glass slides with 5 μg/ml Hoechst33342 (Life Technologies) nuclear dye in antifade reagent (ThermoFisher Scientific) and analyzed. Imaging was performed on an Olympus FV1000 using excitation spectral laser lines at 405, 488, and 633 nm. Signals from different fluorescent probes were taken in sequential scanning mode. Images were captured using Olympus FluoView Viewer Software. Golgi localization of CDC42 in primary fibroblasts was quantitated using GM130 as a mask for cis/medial-Golgi, and CDC42 fluorescence intensity was quantified as the ratio of Golgi to whole-cell staining by using ImageJ software. Multipolar and filopodia-bearing cells were determined (blinded to sample information) by manually counting in FluoView Viewer ≥200 cells from ≥10 randomly chosen images. Cells having multiple F-actin flat protruding edges (butterfly shaped) were considered multipolar, while cells showing a front (leading edge) and a rear were considered unipolar. To calculate the average filopodial length, the distance from the cell base to the tip was determined. Actin protrusions <1 μm were not considered as filopodia. Filopodia measured as twofold longer than nuclei diameter were considered long filopodia, while the remaining filopodia were considered short.

Lam et al.
Novel syndrome caused by aberrant CDC42 function

Journal of Experimental Medicine   17
https://doi.org/10.1084/jem.20190147

CRISPR cell line production

The immortalized YTS human NK cell line was used as the model for immune function. In collaboration with the Cell Based Assay Screening Service at Baylor College of Medicine, a homozygous knock-in of the c.556C>T/p.R186C mutation was placed into chromosome 1, isoform 1 of *CDC42*. Briefly, guide RNAs were screened in 293T cells for editing efficiency. Each guide RNA was incorporated into an all-in-one vector encoding Cas9 and eGFP.

A single-stranded donor oligonucleotide template (antisense; 5′-GAATGTATTTGACGAAGCAATATTGGCTGCCCTGGAGCC TCCAGAACCGAAAAAGTCCTGCAGGTGTGTGCTGCTATGAAC ATCTCTCCAGAGCCCTTTCTGCACAGCTGGTGTCGGC-3′) was synthesized incorporating the desired mutation, a silent mutation encoding for the SbfI restriction site, and another mutation to reduce Cas9 recutting. Constructs were transfected into the parental YTS cell line (Neon electroporator, 1,400 V/10 ms/three pulses, 2.5e6 YTS cells). Cells were sorted based on eGFP 48 h later and plated by limiting dilution. Clones were screened based on genomic extraction and SbfI digestion and then sequenced using Sanger sequencing of the targeted region for verification. Clones were expanded in R10 medium and then underwent repeat Sanger sequencing for the presence of the *CDC42* mutation and for the lack of off-site mutagenesis at *GBA3*, a known pseudogene of *CDC42*. A single clone was used for all YTS experiments presented.

YTS fixed-cell immunofluorescence confocal microscopy

YTS cells were washed once with complete R10 and resuspended to a final concentration of 1e6/ml in complete R10. 200,000 cells were plated onto a poly-lysine–coated slide and incubated at 37°C for 20 min for adherence. After incubation, cells were gently washed three times with PBS and fixed and permeabilized with BD cytofix/cytoperm (554655; BD Biosciences) for 20 min at room temperature. All subsequent washes and antibody incubations are done with PBS-S (PBS + 1% BSA + 0.1% saponin). Cells were incubated with anti-CDC42 (1:300, 187643; Abcam) for 1 h at room temperature followed by goat anti-rabbit Alexa Fluor 568 (1:300, A11011; ThermoFisher Scientific) for 1 h. Lastly, cells were incubated with phalloidin-Alexa Fluor 647 (1:100, A22287; ThermoFisher Scientific) and anti-giantin Alexa Fluor 488 (1:200, #908701/Poly19087; BioLegend) for 1 h. After washing, cells were mounted with Prolong Diamond (P36970; ThermoFisher Scientific) to a #1.5 coverslip and allowed to cure for 24 h before sealing with nail varnish. Imaging was done using Metamorph on a Zeiss Axio Observer CSU-X confocal microscope with a 63×/1.4 NA objective. Colocalization was conducted in ImageJ software where a segmentation mask was created around the Golgi apparatus (using giantin thresholding) and cell membrane (using CDC42 thresholding) and average intensity signal within the Golgi and the cytoplasm were measured. The ratios between the signal within the Golgi and the cytoplasm were calculated.

SIM-TIRF microscopy and filopodial analysis

A Lab-Tek II 8-well chambered #1.5 coverglass (#155409; Nunc) was coated with 5 µg/ml anti-CD18 (IB4, single batch) and 5 µg/ml

anti-CD28.2 (LEAF anti-CD28.2, 302923; BioLegend) and incubated for ≥30 min at 37°C. YTS cells were resuspended in R10 without FBS and phenol red (imaging media) and resuspended in imaging media at ~50,000 cells/150 µl (0.33e6/ml). 50,000 YTS cells plated in 150 µl imaging media and incubated at 37°C for exactly 20 min. After, cells were immediately fixed with 4% PFA for 20 min at room temperature. Cell were then washed once with PBS and permeabilized with 0.1% Triton X-100 in PBS for 10 min at room temperature. After three additional PBS washes, cells were stained with phalloidin-Alexa Fluor 568 (1:50, A12380; ThermoFisher Scientific) for ≥1 h and cells were imaged thereafter without buffer exchange. Imaging was done on a GE DeltaVision OMX-SR microscope under structured illumination microscopy–total internal reflection fluorescence (SIM-TIRF) mode using a 60×/1.42 PlanApoN objective and a pco.edge 4.2 camera. Images were then reconstructed in GE Softworx using experimentally measured OTF files. Filopodia were manually counted for cells that spread onto the surface on ImageJ. Cells with retraction fibers and not filopodia were omitted from calculation.

Immune cytotoxicity assay for NK cell lines and Pt 2 and Pt 3

For the NK cell line, a chromium-based assay was used. For Pt 2, the DELFIA cytotoxicity assay was used as described below. For Pt 3, a flow cytometric–based cytotoxicity assay was performed similarly to that previously described (Bryceson et al., 2009; Valiathan et al., 2012). Target cells (721.221) were incubated with 100 µCi of ^{51}Cr (sodium chromate in normal saline, NEZ030005MC; PerkinElmer) for 1 h at 37°C, washed three times in complete R10, and resuspended in complete R10 at a final concentration of 10^5 cells/ml. Unlabeled effector YTS cells were washed once in complete R10 and resuspended to a final concentration of 10^6/ml. 10^5 (200 µl) effector cells were plated into the first well of a 96-well, round-bottomed polystyrene tissue culture–treated plate and serially diluted 1:2, except for the spontaneous and total lysis control wells, which contain only target cells. 10^4 ^{51}Cr signal from the LumaPlate was read using a TopCount NXT (PerkinElmer) at the conditions indicated by the manufacturer. Percent lysis is calculated as: [(TopCount measured cpm – spontaneously released cpm)/ (total cpm – spontaneously released cpm)] × 100. Total cpm was derived from a target containing well that was lysed with 1% IGEPAL (I3021; Sigma-Aldrich) in water.

The DELFIA cytotoxicity assay is based on loading cells with an acetoxymethyl ester of a fluorescence enhancing ligand. After the ligand has penetrated the cell membrane the ester bonds are hydrolyzed within the cell to form a hydrophilic ligand, which no longer passes through the membrane. After cytolysis, the released ligand is introduced to a europium solution to form a fluorescent chelate. The measured signal correlates directly with the amount of lysed cells. 100 µl of loaded target cells (5,000 cells) is pipetted into a round-bottomed sterile plate, and 100 µl effector cells of varying cell concentration is added. An E/T ratio from 6:1 to 100:1 is commonly used for NK cells. Additional wells containing only target cells are plated for detection of background, spontaneous release, and maximum release. Cells are then incubated 2 and 3 h in a humidified 5% CO_2 atmosphere at

Lam et al.
Novel syndrome caused by aberrant CDC42 function

Journal of Experimental Medicine 18
https://doi.org/10.1084/jem.20190147

93

37°C. After incubation, the plate is centrifuged for 5 min at 500 ×*g*. 20 µl the supernatant is transferred to a flat-bottomed plate with 200 µl Eu solution, the plate is shaken at 250 rpm for 15 min, and fluorescence is measured. Percent lysis is calculated as: [(TopCount measured cpm – spontaneously released cpm)/ (total cpm – spontaneously released cpm)] × 100. To measure spontaneous release, incubate the target cells (100 µl) with 100 µl of medium instead of effector cells. After centrifugation, transfer 20 µl of the supernatant to the flat-bottomed plate and add 200 µl Eu solution. Shake for 15 min and measure. To measure maximum release, incubate the target cells (100 µl) with 100 µl of medium supplemented with 10 µl of lysis buffer. After centrifugation, transfer 20 µl of the supernatant to the flat-bottomed plate and add 200 µl Eu solution. Shake for 15 min and measure.

Transwell migration assay for immune cells

A standard Boyden chamber assay was used. Corning transwell polycarbonate membrane cell culture inserts (6.5 mm, 5-µm pore polycarbonate, 3421; Corning) were coated overnight with 10 µg/ml fibronectin in PBS at 4°C. YTS cells were washed once using complete R10 and resuspended to a final concentration of 2–4e6 cells/ml. 600 µl of complete R10 supplemented with 100 ng/ml SDF1a/CXCL12 (300-28A; Peprotech) chemoattractant was plated into a 24-well tissue culture–treated plate. Fibronectin was removed from the transwell, and the transwell was placed into the wells containing CXCL12-supplemented media. 100 µl (200,000–400,000 cells) YTS cells were plated onto the upper chamber of the transwell. The cells were incubated at 37°C for 4 h. After incubation, the cells were counted by measuring the volume in the lower chamber and counting the number of events at medium speed for 1 min on an LSR Fortessa Flow Cytometer. The live events were gated for based on forward scatter (FSC) and side scatter (SSC) and used for the migration measurement. The percent migration was calculated as the number of cells that migrated into the lower chamber divided by the number of cells in a control well (input cell count) containing the same number of cells but no transwell.

Immune conjugation assay

YTS NK cells and 721.221 target cells were washed once with complete R10. YTS cells were then resuspended in PBS at 1e6/ml and incubated with efluor 450 (#65-0842-85; 1:1,000, 10 min, and 37°C; eBioscience). 721.221 cells were resuspended in PBS at 1e6/ml and incubated with Cell Trace CFSE (#C34554; 1:2,000, 10 min, and 37°C). Both labeled cells were then washed once with complete R10 and counted. Labeled YTS cells were resuspended to 1e6/ml and labeled 721.221 cells resuspended to 2e6/ml in complete R10. Cells were then combined at an E/T ratio of 1:2 (100,000 YTS cells:200,000 721.221 cells) and incubated at 37°C for 0, 5, 10, 30, and 60 min. The conjugation reaction was stopped by vortexing for 3 s and fixed with 4% PFA in PBS for ≥10 min before acquisition. Cells were then counted on a BD LSR Fortessa flow cytometer and gated based on negative and single-positive control cells. At least 20,000 live cells counted based on FSC/SSC gating. Percent conjugation was

calculated as: (double-positive cells)/(single-positive eFluor 450/YTS cells + double-positive cells) × 100.

Peripheral blood immunophenotype

All flow cytometric analyses were performed on EDTA blood samples within 24 h of venipuncture. After red blood cell lysis with ammonium chloride, lymphocytes were washed, resuspended in PBS, and stained with the following mouse anti-human antibodies to identify T and B cell subsets: CD45RA APC-H7 (clone T6D11; Miltenyi Biotec), CD3 PerCP (clone BW264/56; Miltenyi Biotec), CCR7 PE (clone 3D12; eBioscience), CD4 APC (clone OKT4; Becton Dickinson), CD8 PE-Cy7 (clone RPA-T8; Becton Dickinson), CD19 PE-CY7 (clone SJ25C1; Becton Dickinson), CD16 PE (clone 3G8), CD56 PE, CD27 FITC (clone M-T271, Becton Dickinson), TCR α-beta APC (clone T10B9; Becton Dickinson), TCR gamma-delta FITC (11F3; Miltenyi Biotec), CD21 PE (clone B-ly4; Becton Dickinson), CD24 PE (clone ML5; Becton Dickinson), IgD FITC (clone IA6-2; Becton Dickinson), Goat F(ab) 2 anti-Human IgM (µ)-Alexa Fluor 647 (Jackson Immuno-Research), and CD38 FITC (clone HIT2; Becton Dickinson). Cells were incubated with the appropriate antibody cocktail for 30 min at 4°C and then washed with PBS and resuspended in PBS for flow cytometric acquisition. At least 50,000 events were acquired within the lymphogate. Data were acquired on a FACSCanto II (Becton Dickinson) and analyzed with FlowJo software (Tree Star).

Dendritic cell flow cytometric analysis

Dendritic cell analysis was performed with the Blood Dendritic cell enumeration kit (#130-091-086; Miltenyi Biotec). This assay is based on dendritic cell–specific surface antigens CD303 (BDCA-2), CD141 (BDCA-3), and CD1c (BDCA-1). Three distinct dendritic cell subsets were identified in whole blood: plasmacytoid dendritic cells as CD303+ (FITC clone: AC144, BDCA-2), type 1 myeloid dendritic cells (MDC1s) as CD1c+ (PE clone: AD5-8E7, BDCA-1), and type 2 myeloid dendritic cells (MDC2s) as CD141+ (APC clone: Ad4-14H12, BDCA-3) surface expression. Gate exclusion for CD19, CD14, and dead cells was performed. After 10 min of incubation in ice with the mix of antibodies, red blood cells were lysed. Cells were washed with PBS, fixed with 1% PFA for 10 min, acquired with a FACSCanto II (Becton Dickinson), and analyzed with FlowJo software (Tree Star Inc.; version 8.8.6). At least 10⁶ total events were acquired.

Clinical flow cytometry for BM analysis/composition

The detailed protocol for whole BM staining has been previously reported (Basso-Ricci et al., 2017). In brief, Precision Count beads (BioLegend) were added to 100 µl of P1 BM sample to allow absolute quantification of hematopoietic cell subsets, and red blood cell lysis was performed. The lysed sample was labeled with fluorescent antibodies for CD3-BV605, CD56-PE-Cy5, CD14-BV510, CD61/41-PE-Cy7, CD135-PE, CD34-BV421, CD45RA-APC-Cy7 (BioLegend), CD33-BB515, CD66b-BB515, CD38-BUV737, CD45-BUV395, CD90-APC, CD10-BV786, CD11c-BV650, CD19-APCR700, CD7-PE-Cy5.5, and CD71-BV711 (BD Biosciences). Titration assays were performed to assess the best antibody concentration. After surface marking, the cells were incubated

Lam et al.
Novel syndrome caused by aberrant CDC42 function

Journal of Experimental Medicine   19
https://doi.org/10.1084/jem.20190147

with PI (BioLegend) to stain dead cells. All samples were acquired using a BD LSR Fortessa (BD Bioscience) flow cytometer after calibration with SPHERO rainbow calibration particles (Spherotech), and raw data were collected using BD FACSDIVA software. The data were subsequently analyzed with FlowJo software, and the graphical output was automatically generated using GraphPad Prism.

Functional characterization of proliferation and migration of CD34+ cells

Purification of CD34+ cells was performed by two steps of immunomagnetic selection (CD34+ microbeads, 130–097-047; Miltenyi Biotec). For proliferation, 10^4 BM CD34+ cells were stimulated with stem cell factor (SCF; 100 ng/ml) or a growth factor mixture (SCF 300 ng/ml, thrombopoietin 100 ng/ml, IL3 60 ng/ml). Proliferation was evaluated at day 5 of stimulation by 16 h liquid scintillation counting of ^{3}H-thymidine (Amersham Biosciences). The stimulation index was calculated as the ratio between stimulated and nonstimulated cells. For the transwell migration assay, 0.5×10^6 peripheral blood lymphocytes or 0.5×10^4 BM CD34+ cells were seeded on a transwell chambers in presence of SDF1-α/CXCL12 (100 ng/ml; Peprotech). Migration was assessed after 3 h. To evaluate clonogenic potential of CDC42− cells, 2×10^5 BM mononuclear cells as well as 10^3 BM CD34+ cells were plated in Methocult medium (H4434; Stemcell Technologies), and the number of colony-forming units per cell was scored at day 14 to determine number and type of colonies.

BM mononuclear cells stimulation and cytokine measurements

BM mononuclear cells were isolated from HD ($n = 3$) and Pt BM and were left unstimulated or stimulated with LPS (10 μg/ml) for 5 h, with or without the addition of ATP (1 mM) for an additional hour. Secreted cytokines were measured by in conditioned media. Plasma and supernatant levels of IFNγ, CXCL9, and IL-6 were assessed using enzyme-linked immunosorbent assays with human Duoset ELISA kits, and IL-1β plasma levels were measured using the high-sensitivity quantikine ELISA kit (all purchased from R&D Systems). Plasma IL-18 levels were measured using an ELISA kit obtained from MBL.

C. elegans studies

WT cdc-42 cDNA (open reading frame clone R07G3.1; Thermo-Fisher Scientific) was cloned into the pPD49.83 heat shock–inducible vector (a kind gift of Andrew Fire, Stanford University, Stanford, CA). The c.556_558AAG>TGT trinucleotide substitution (p.K186C corresponding to human p.R186C) was introduced by site-directed mutagenesis (Stratagene). Germline transformation and genetic crosses were performed using standard techniques. Constructs were injected at a concentration of 100 ng/ml. The pJM67 plasmid (pelt-2::NLS::GFP; 30 ng/ml) was used as coinjection marker. To explore vulval defects, synchronized animals from three independent lines for each construct were grown at 20°C and heat shocked (33°C, 90 min followed by 30°C, 30 min) in parallel at the early (Muv and Vul) or mid (Pvl) L3 larval stages. Adults were scored blindly at a Leica MZ10F dissecting microscope to check for the presence of Pvl phenotype,

multiple ectopic pseudovulvae (Muv phenotype) and lack of a vulva (Vul phenotype). After each cross, the genotype was confirmed by Sanger sequencing. Isogenic worms that had lost the transgene were cloned separately and used as controls. Microscopy observations were performed with a Nikon Eclipse 80i instrument equipped with Nomarski differential interference contrast optics on live animals mounted on 2% agarose pads containing 10 mM sodium azide as anesthetic. The N2 (Bristol) and PS21 (let-23(sy1), let-23/EGFR hypomorphic allele) strains were provided by the Caenorhabditis Genetics Center, which is funded by the National Institutes of Health Office of Research Infrastructure Programs (P40 OD010440).

Statistical analyses

Data are represented as means ± SD or SEM where indicated. Statistical analyses were conducted in GraphPad Prism. WB of patient CDC42 expression intensity measurements and protein localization intensity measurements were analyzed with the Student's t test. GTPase function assays were analyzed using a Student's t test. For variance analysis in pull-down assays, an ordinary one-way ANOVA was performed using the Sidak's multiple comparison test. Proliferation assays were analyzed using either a two-way ANOVA with Dunnett's multiple comparisons for patient fibroblasts. Migration assays were assessed using a Student's t test (for YTS NK cell and primary fibroblasts) or a two-way ANOVA with Tukey's multiple comparisons (for NIH-3T3 cells). Multipolarity cell counts, filopodia number, and filopodia length were assessed using a Welch's t test. NK cell cytotoxicity was assessed using the Mann–Whitney U test of three pooled replicates. NK cell conjugation was assessed using a Welch's t test. For C. elegans studies, P values were calculated using two-tailed Fisher's exact test. All remaining assays were performed with n of ≤2. Statistical significance is indicated with asterisks (*, $P < 0.05$; **, $P < 0.01$; ***, $P < 0.001$; ****, $P < 0.0001$) for all tests except two-tailed Fisher's exact test (*, $P < 0.005$; **, $P < 0.00002$, ***, $P < 1.2e^{-6}$).

Online supplemental material

Table S1 reports clinical laboratory data for Pt 1 and Pt 2. Table S2 shows the hematological and immunological profiles of Pt 1–3. Table S3 provide WES/WGS metrics and data output. Table S4 reports on the vulval phenotypes in transgenic C. elegans expressing WT CDC-42 or the K186C, R68Q, and A159V disease-causing mutants. Table S5 reports on the clonogenic assay of BM cells from Pt 1.

Lam et al.
Novel syndrome caused by aberrant CDC42 function

Journal of Experimental Medicine   20
https://doi.org/10.1084/jem.20190147

References

Aicart-Ramos, C., R.A. Valero, and I. Rodriguez-Crespo. 2011. Protein palmitoylation and subcellular trafficking. *Biochimica et Biophysica Acta (BBA) -. Biomembranes.* 1808:2981–2994. https://doi.org/10.1016/j.bbamem.2011.07.009

Baschieri, F., S. Confalonieri, G. Bertalot, P.P. Di Fiore, W. Dietmaier, M. Leist, P. Crespo, I.G. Macara, and H. Farhan. 2014. Spatial control of Cdc42 signalling by a GM130-RasGRF complex regulates polarity and tumorigenesis. *Nat. Commun.* 5:4839. https://doi.org/10.1038/ncomms5839

Basso-Ricci, L., S. Scala, R. Milani, M. Migliavacca, A. Rovelli, M.E. Bernardo, F. Ciceri, A. Aiuti, and L. Biasco. 2017. Multiparametric Whole Blood Dissection: A one-shot comprehensive picture of the human hematopoietic system. *Cytometry A.* 91:952–965. https://doi.org/10.1002/cyto.a.23148

Bauer, C.K., P. Calligari, F.C. Radio, V. Caputo, M.L. Dentici, N. Falah, F. High, F. Pantaleoni, S. Barresi, A. Ciolfi, et al. 2018. Mutations in KCNK4 that Affect Gating Cause a Recognizable Neurodevelopmental Syndrome. *Am. J. Hum. Genet.* 103:621–630. https://doi.org/10.1016/j.ajhg.2018.09.001

Bracaglia, C., K. de Graaf, D. Pires Marafon, F. Guilhot, W. Ferlin, G. Prencipe, I. Caiello, S. Daví, G. Schulert, A. Ravelli, et al. 2017. Elevated circulating levels of interferon-γ and interferon-γ–induced chemokines characterise patients with macrophage activation syndrome complicating systemic juvenile idiopathic arthritis. *Ann. Rheum. Dis.* 76:166–172. https://doi.org/10.1136/annrheumdis-2015-209020

Brigida, I., M. Zoccolillo, M.P. Cicalese, L. Pfajfer, F. Barzaghi, S. Scala, C. Oleaga-Quintas, J.A. Álvarez-Álvarez, L. Sereni, S. Giannelli, et al. 2018. T-cell defects in patients with ARPC1B germline mutations account for combined immunodeficiency. *Blood.* 132:2362–2374.

Bryceson, Y.T., C. Fauriat, J.M. Nunes, S.M. Wood, N.K. Björkström, E.O. Long, and H.-G. Ljunggren. 2009. Natural Killer Cell Protocols, Cellular and Molecular Methods. *Methods Mol. Biol.* 612:335–352. https://doi.org/10.1007/978-1-60761-362-6_23

Canna, S.W., A.A. de Jesus, S. Gouni, S.R. Brooks, B. Marrero, Y. Liu, M.A. DiMattia, K.J.M. Zaal, G.A.M. Sanchez, H. Kim, et al. 2014. An activating NLRC4 inflammasome mutation causes autoinflammation with recurrent macrophage activation syndrome. *Nat. Genet.* 46:1140–1146. https://doi.org/10.1038/ng.3089

Caye, A., M. Strullu, F. Guidez, B. Cassinat, S. Gazal, O. Fenneteau, E. Lainey, K. Nouri, S. Nakhaei-Rad, R. Dvorsky, et al. 2015. Juvenile myelomonocytic leukemia displays mutations in components of the RAS pathway and the PRC2 network. *Nat. Genet.* 47:1334–1340. https://doi.org/10.1038/ng.3420

Chinn, I.K., O.S. Eckstein, E.C. Peckham-Gregory, B.R. Goldberg, L.R. Forbes, S.K. Nicholas, E.M. Mace, T.P. Vogel, H.A. Abhyankar, M.I. Diaz, et al. 2018. Genetic and mechanistic diversity in pediatric hemophagocytic lymphohistiocytosis. *Blood.* 132:89–100. https://doi.org/10.1182/blood-2017-11-814244

Chung, L.K., N.H. Philip, V.A. Schmidt, A. Koller, T. Strowig, R.A. Flavell, I.E. Brodsky, and J.B. Bliska. 2014. IQGAP1 is important for activation of caspase-1 in macrophages and is targeted by Yersinia pestis type III effector YopM. *MBio.* 5:e01402–e01414. https://doi.org/10.1128/mBio.01402-14

Cingolani, P., A. Platts, L. Wang, M. Coon, T. Nguyen, L. Wang, S.J. Land, X. Lu, and D.M. Ruden. 2012. A program for annotating and predicting the effects of single nucleotide polymorphisms, SnpEff: SNPs in the genome of Drosophila melanogaster strain w1118; iso-2; iso-3. *Fly (Austin).* 6:80–92. https://doi.org/10.4161/fly.19695

Dasouki, M., K.C. Okonkwo, A. Ray, C.K. Folmsbeel, D. Gozales, S. Keles, J.M. Puck, and T. Chatila. 2011. Deficient T Cell Receptor Excision Circles (TRECs) in autosomal recessive hyper IgE syndrome caused by DOCK8 mutation: implications for pathogenesis and potential detection by newborn screening. *Clin. Immunol.* 141:128–132. https://doi.org/10.1016/j.clim.2011.06.003

Dvorsky, R., and M.R. Ahmadian. 2004. Always look on the bright site of Rho: structural implications for a conserved intermolecular interface. *EMBO Rep.* 5:1130–1136. https://doi.org/10.1038/sj.embor.7400293

Etienne-Manneville, S. 2004. Cdc42--the centre of polarity. *J. Cell Sci.* 117:1291–1300. https://doi.org/10.1242/jcs.01115

Etienne-Manneville, S., and A. Hall. 2002. Rho GTPases in cell biology. *Nature.* 420:629–635. https://doi.org/10.1038/nature01148

Flex, E., M. Niceta, S. Cecchetti, I. Thiffault, M.G. Au, A. Capuano, E. Piermarini, A.A. Ivanova, J.W. Francis, G. Chillemi, et al. 2016. Biallelic Mutations in TBCD, Encoding the Tubulin Folding Cofactor D, Perturb Microtubule Dynamics and Cause Early-Onset Encephalopathy. *Am. J. Hum. Genet.* 99:962–973. https://doi.org/10.1016/j.ajhg.2016.08.003

Fukata, M., T. Watanabe, J. Noritake, M. Nakagawa, M. Yamaga, S. Kuroda, Y. Matsuura, A. Iwamatsu, F. Perez, and K. Kaibuchi. 2002. Rac1 and Cdc42 capture microtubules through IQGAP1 and CLIP-170. *Cell.* 109:873–885. https://doi.org/10.1016/S0092-8674(02)00800-0

Gibson, R.M., and A.L. Wilson-Delfosse. 2001. RhoGDI-binding-defective mutant of Cdc42Hs targets to membranes and activates filopodia formation but does not cycle with the cytosol of mammalian cells. *Biochem. J.* 359:285–294. https://doi.org/10.1042/bj3590285

Gibson, R.M., P.N. Gandhi, X. Tong, J. Miyoshi, Y. Takai, M. Konieczkowski, J.R. Sedor, and A.L. Wilson-Delfosse. 2004. An activating mutant of Cdc42 that fails to interact with Rho GDP-dissociation inhibitor localizes to the plasma membrane and mediates actin reorganization. *Exp. Cell Res.* 301:211–222. https://doi.org/10.1016/j.yexcr.2004.07.033

Grom, A.A., A. Horne, and F. De Benedetti. 2016. Macrophage activation syndrome in the era of biologic therapy. *Nat. Rev. Rheumatol.* 12:259–268. https://doi.org/10.1038/nrrheum.2015.179

Harapas, C.R., A. Steiner, S. Davidson, and S.L. Masters. 2018. An Update on Autoinflammatory Diseases: Inflammasomopathies. *Curr. Rheumatol. Rep.* 20:40. https://doi.org/10.1007/s11926-018-0750-4

Henter, J.I., A. Horne, M. Aricó, R.M. Egeler, A.H. Filipovich, S. Imashuku, S. Ladisch, K. McClain, D. Webb, J. Winiarski, and G. Janka. 2007. HLH-

Lam et al.
Novel syndrome caused by aberrant CDC42 function

Journal of Experimental Medicine   21
https://doi.org/10.1084/jem.20190147

96

2004: Diagnostic and therapeutic guidelines for hemophagocytic lymphohistiocytosis. *Pediatr. Blood Cancer.* 48:124–131. https://doi.org/10.1002/pbc.21039

Hoffman, G.R., N. Nassar, and R.A. Cerione. 2000. Structure of the Rho family GTP-binding protein Cdc42 in complex with the multifunctional regulator RhoGDI. *Cell.* 100:345–356. https://doi.org/10.1016/S0092-8674(00)80670-4

Hsu, A.P., A. Donkó, M.E. Arrington, M. Swamydas, D. Fink, A. Das, O. Escobedo, V. Bonagura, P. Szabolcs, H.N. Steinberg, et al. 2019. Dominant activating RAC2 mutation with lymphopenia, immunodeficiency, and cytoskeletal defects. *Blood.* 133:1977–1988. https://doi.org/10.1182/blood-2018-11-886028

Jacquemet, G., H. Hamidi, and J. Ivaska. 2015. Filopodia in cell adhesion, 3D migration and cancer cell invasion. *Curr. Opin. Cell Biol.* 36:23–31. https://doi.org/10.1016/j.ceb.2015.06.007

Jagadeesh, K.A., A.M. Wenger, M.J. Berger, H. Guturu, P.D. Stenson, D.N. Cooper, J.A. Bernstein, and G. Bejerano. 2016. M-CAP eliminates a majority of variants of uncertain significance in clinical exomes at high sensitivity. *Nat. Genet.* 48:1581–1586. https://doi.org/10.1038/ng.3703

Jamilloux, Y., F. Magnotti, A. Belot, and T. Henry. 2018. The pyrin inflammasome: from sensing RhoA GTPases-inhibiting toxins to triggering autoinflammatory syndromes. *Pathog. Dis.* 76:fty020. https://doi.org/10.1093/femspd/fty020

Jordan, M.B., C.E. Allen, S. Weitzman, A.H. Filipovich, and K.L. McClain. 2011. How I treat hemophagocytic lymphohistiocytosis. *Blood.* 118:4041–4052. https://doi.org/10.1182/blood-2011-03-278127

Kim, M.L., J.J. Chae, Y.H. Park, D. De Nardo, R.A. Stirzaker, H.-J. Ko, H. Tye, L. Cengia, L. DiRago, D. Metcalf, et al. 2015. Aberrant actin depolymerization triggers the pyrin inflammasome and autoinflammatory disease that is dependent on IL-18, not IL-1β. *J. Exp. Med.* 212:927–938. https://doi.org/10.1084/jem.20142384

Kircher, M., D.M. Witten, P. Jain, B.J. O'Roak, G.M. Cooper, and J. Shendure. 2014. A general framework for estimating the relative pathogenicity of human genetic variants. *Nat. Genet.* 46:310–315. https://doi.org/10.1038/ng.2892

Li, W., X. Sun, J. Wang, Q. Zhao, R. Dai, Y. Wang, L. Zhou, L. Westerberg, Y. Ding, X. Zhao, and C. Liu. 2017. Defective thymic output in WAS patients is associated with abnormal actin organization. *Sci. Rep.* 7:11978. https://doi.org/10.1038/s41598-017-12345-z

Liu, X., X. Jian, and E. Boerwinkle. 2013. dbNSFP v2.0: a database of human non-synonymous SNVs and their functional predictions and annotations. *Hum. Mutat.* 34:E2393–E2402. https://doi.org/10.1002/humu.22376

Locatelli, F., P. Merli, D. Pagliara, G. Li Pira, M. Falco, D. Pende, R. Rondelli, B. Lucarelli, L.P. Brescia, R. Masetti, et al. 2017. Outcome of children with acute leukemia given HLA-haploidentical HSCT after αβ T-cell and B-cell depletion. *Blood.* 130:677–685. https://doi.org/10.1182/blood-2017-04-779769

Martinelli, S., O.H.F. Krumbach, F. Pantaleoni, S. Coppola, E. Amin, L. Pannone, K. Nouri, L. Farina, R. Dvorsky, F. Lepri, et al. University of Washington Center for Mendelian Genomics. 2018. Functional Dysregulation of CDC42 Causes Diverse Developmental Phenotypes. *Am. J. Hum. Genet.* 102:309–320. https://doi.org/10.1016/j.ajhg.2017.12.015

Mattila, P.K., and P. Lappalainen. 2008. Filopodia: molecular architecture and cellular functions. *Nat. Rev. Mol. Cell Biol.* 9:446–454. https://doi.org/10.1038/nrm2406

Nouri, K., D.J. Timson, and M.R. Ahmadian. 2017. New model for the interaction of IQGAP1 with CDC42 and RAC1. *Small GTPases.*:1–7. https://doi.org/10.1080/21541248.2017.1321169

Okamura, H., H. Tsutsi, T. Komatsu, M. Yutsudo, A. Hakura, T. Tanimoto, K. Torigoe, T. Okura, Y. Nukada, K. Hattori, et al. 1995. Cloning of a new cytokine that induces IFN-γ production by T cells. *Nature.* 378:88–91. https://doi.org/10.1038/378088a0

Orange, J.S., N. Ramesh, E. Remold-O'Donnell, Y. Sasahara, L. Koopman, M. Byrne, F.A. Bonilla, F.S. Rosen, R.S. Geha, and J.L. Strominger. 2002. Wiskott-Aldrich syndrome protein is required for NK cell cytotoxicity and colocalizes with actin to NK cell-activating immunologic synapses.

Proc. Natl. Acad. Sci. USA. 99:11351–11356. https://doi.org/10.1073/pnas.162376099

Phillips, M.J., G. Calero, B. Chan, S. Ramachandran, and R.A. Cerione. 2008. Effector proteins exert an important influence on the signaling-active state of the small GTPase Cdc42. *J. Biol. Chem.* 283:14153–14164. https://doi.org/10.1074/jbc.M706271200

Reiner, D.J., and E.A. Lundquist. 2018. Small GTPases. *WormBook.* 2018:1–65. https://doi.org/10.1895/wormbook.1.67.2

Ridley, A.J., M.A. Schwartz, K. Burridge, R.A. Firtel, M.H. Ginsberg, G. Borisy, J.T. Parsons, and A.R. Horwitz. 2003. Cell migration: integrating signals from front to back. *Science.* 302:1704–1709. https://doi.org/10.1126/science.1092053

Romberg, N., K. Al Moussawi, C. Nelson-Williams, A.L. Stiegler, E. Loring, M. Choi, J. Overton, E. Meffre, M.K. Khokha, A.J. Huttner, et al. 2014. Mutation of NLRC4 causes a syndrome of enterocolitis and autoinflammation. *Nat. Genet.* 46:1135–1139. https://doi.org/10.1038/ng.3066

Rosado, F.G.N., and A.S. Kim. 2013. Hemophagocytic lymphohistiocytosis: an update on diagnosis and pathogenesis. *Am. J. Clin. Pathol.* 139:713–727. https://doi.org/10.1309/AJCP4ZDKJ4ICOUAT

Seeland, I., Y. Xiong, C. Orlik, D. Deibel, S. Prokosch, G. Küblbeck, B. Jahraus, D. De Stefano, S. Moos, F.C. Kurschus, et al. 2018. The actin remodeling protein cofilin is crucial for thymic αβ but not γδ T-cell development. *PLoS Biol.* 16:e2005380. https://doi.org/10.1371/journal.pbio.2005380

Sepulveda, F.E., and G. de Saint Basile. 2017. Hemophagocytic syndrome: primary forms and predisposing conditions. *Curr. Opin. Immunol.* 49: 20–26. https://doi.org/10.1016/j.coi.2017.08.004

Sinai, P., C. Nguyen, J.D. Schatzle, and C. Wülfing. 2010. Transience in polarization of cytolytic effectors is required for efficient killing and controlled by Cdc42. *Proc. Natl. Acad. Sci. USA.* 107:11912–11917. https://doi.org/10.1073/pnas.0913422107

Stray-Pedersen, A., H.S. Sorte, P. Samarakoon, T. Gambin, I.K. Chinn, Z.H. Coban Akdemir, H.C. Erichsen, L.R. Forbes, S. Gu, B. Yuan, et al. 2017. Primary immunodeficiency diseases: Genomic approaches delineate human Mendelian disorders. *J. Allergy Clin. Immunol.* 139: 232–245. https://doi.org/10.1016/j.jaci.2016.05.042

Swart-Mataraza, J.M., Z. Li, and D.B. Sacks. 2002. IQGAP1 is a component of Cdc42 signaling to the cytoskeleton. *J. Biol. Chem.* 277:24753–24763. https://doi.org/10.1074/jbc.M111165200

Takenouchi, T., R. Kosaki, T. Niizuma, K. Hata, and K. Kosaki. 2015. Macrothrombocytopenia and developmental delay with a de novo CDC42 mutation: Yet another locus for thrombocytopenia and developmental delay. *Am. J. Med. Genet. A.* 167A:2822–2825. https://doi.org/10.1002/ajmg.a.37275

Valdés-Mora, F., and J.C. Lacal. 2011. CDC42 (cell division cycle 42 (GTP binding protein, 25kDa)). *Atlas Genet. Cytogenet. Oncol. Haematol.* (11). https://doi.org/10.4267/2042/44606

Valiathan, R., J.E. Lewis, A.B. Melillo, S. Leonard, K.H. Ali, and D. Asthana. 2012. Evaluation of a flow cytometry-based assay for natural killer cell activity in clinical settings. *Scand. J. Immunol.* 75:455–462. https://doi.org/10.1111/j.1365-3083.2011.02667.x

Weiss, E.S., C. Girard-Guyonvarc'h, D. Holzinger, A.A. de Jesus, Z. Tariq, J. Picarsic, E.J. Schiffrin, D. Foell, A.A. Grom, S. Ammann, et al. 2018. Interleukin-18 diagnostically distinguishes and pathogenically promotes human and murine macrophage activation syndrome. *Blood.* 131: 1442–1455. https://doi.org/10.1182/blood-2017-12-820852

Yang, L., L. Wang, H. Geiger, J.A. Cancelas, J. Mo, and Y. Zheng. 2007a. Rho GTPase Cdc42 coordinates hematopoietic stem cell quiescence and niche interaction in the bone marrow. *Proc. Natl. Acad. Sci. USA.* 104: 5091–5096. https://doi.org/10.1073/pnas.0610819104

Yang, L., L. Wang, T.A. Kalfa, J.A. Cancelas, X. Shang, S. Pushkaran, J. Mo, D.A. Williams, and Y. Zheng. 2007b. Cdc42 critically regulates the balance between myelopoiesis and erythropoiesis. *Blood.* 110:3853–3861. https://doi.org/10.1182/blood-2007-03-079582

Zhou, Y., J.L. Johnson, R.A. Cerione, and J.W. Erickson. 2013. Prenylation and membrane localization of Cdc42 are essential for activation by DOCK7. *Biochemistry.* 52:4354–4363. https://doi.org/10.1021/bi301688g

Chapter VI

The Pseudo Natural Product Rhonin Targets RHOGDI1

Graphical abstract
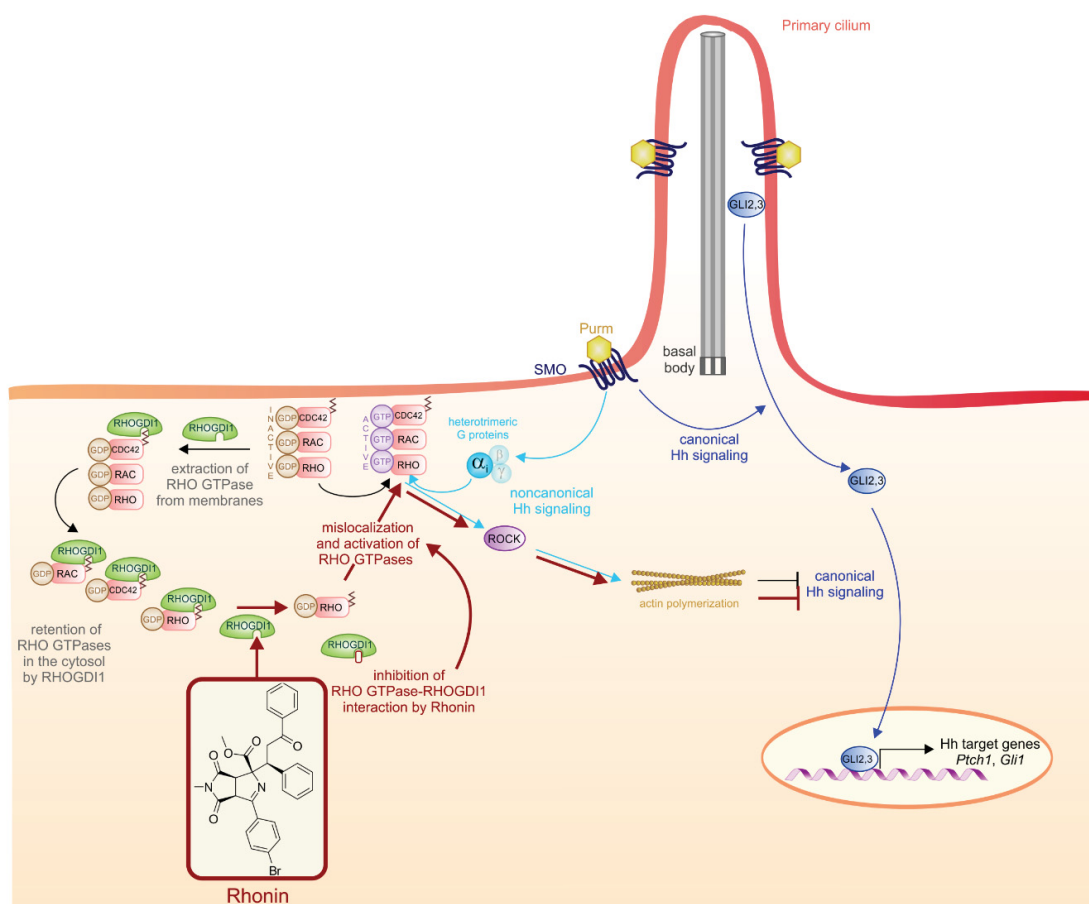
Status:	Under Revision in Nature Chemical Biology
Impact factor:	10.51
Own proportion to this work:	10 %
	Cell culture, expression and purification of RAC effectors, RAC GTP pull down assays, discussion, writing the manuscript.

The Pseudo Natural Product Rhonin Targets RHOGDI1

Sumersing Patil,[1] Erchang Shang,[1] Mohammad Akbarzadeh,[2] Marcel Buchholzer,[2] Neda S. Kazemein Jasemi,[2] Marco Potowski,[3] Rishikesh Narayan,[1,4] Hacer Karatas,[1] George Karageorgis,[1,5] Christopher Golz,[3] Carsten Strohmann,[3] Andrey P. Antonchick,[1] Petra Janning,[1] Mohammad Reza Ahmadian,[2] Slava Ziegler,[1] Herbert Waldmann[1,3*]

Affiliations

[1] Department of Chemical Biology, Max-Planck-Institute of Molecular Physiology, Otto-Hahn-Straße 11, 44227 Dortmund, Germany

[2] Institute of Biochemistry and Molecular Biology II, Medical Faculty, Heinrich-Heine-University, Düsseldorf 40225, Germany

[3] Faculty of Chemistry and Chemical Biology, Technical University Dortmund, Otto-Hahn-Straße 6, 44221 Dortmund, Germany

[4] School of Chemical and Biological Sciences (SCBS), IIT Goa, Farmagudi, Ponda, Goa-403401, India

[5] School of Chemistry, University of Leeds, LS2 9JT, Leeds, U.K

*Correspondence: herbert.waldmann@mpi-dortmund.mpg.de

Abstract

For the discovery of novel chemical matter, *in general* endowed with bioactivity strategies may be particularly efficient that combine previous insight about biological relevance, *e.g.* natural product (NP) structure, with methods that enable efficient coverage of chemical space, such as fragment based design. We describe the *de novo* combination of different 5-membered NP-derived N-heteroatom fragments to structurally unprecedented "*pseudo natural products*" in an efficient complexity-generating and enantioselective one-pot synthesis sequence. The pseudo NPs inherit characteristic elements of NP structure but occupy areas of chemical space not covered by NP-derived chemotypes, and may have novel biological targets. Investigation of the pseudo-NPs in unbiased phenotypic assays and target identification led to the discovery of the first small-molecule ligand of the RHO GDP-dissociation inhibitor1 (RHOGDI1), termed Rhonin. Rhonin inhibits binding of the RHOGDI1 chaperone to GDP-bound Rho GTPases, induces activation of the GTPases and inhibits signal transduction through a non-canonical Hedgehog (Hh) pathway.

Introduction

The discovery of novel chemical matter, *in general* endowed with bioactivity and biological relevance is at the heart of chemical biology. Such compound classes may have new biological targets and modes of action, and, therefore, their bioactivity will best be evaluated in unbiased target-agnostic phenotypic assays, followed by target identification and validation.[1-3]

Strategies for the design of such novel compound classes can draw from previous insight about biological relevance of compound classes as for instance gained by Biology Oriented Synthesis (BIOS). In BIOS, complex natural product (NP) scaffolds are reduced to less complex, synthetically better accessible structures retaining the characteristic properties of the guiding NPs.[4] However, BIOS covers only a small fraction of natural product-like chemical space and arrives at compound classes that often retain the kind of bioactivity of the guiding NPs. These limitations can be overcome by the design and synthesis of "pseudo-natural products".[5] In pseudo-NPs natural product fragments that represent NP structure and properties[6] are combined *de novo* to unprecedented NP-inspired compound classes not accessible by known biosynthesis pathways. Pseudo-NPs inherit characteristic NP structure and properties but go beyond the chemical space explored by nature and, therefore, promise to have unexpected bioactivity and targets.

Five-membered N-heterocycles are defining structural units of numerous natural products with diverse bioactivity. Thus, succinimides occur for instance in the haterumaimides, which have antitumor activity[7], and the fungal metabolite hirsutellone, which is active against *Mycobacterium tuberculosis* (Figure 1a).[8] Pyrrolines are characteristic structural elements of eudistomin alkaloids with calmodulin antagonist activity (Figure 1a)[9] and the tobacco alkaloid myosmine[10] (Figure 1a). Pyrrolidines occur as isolated scaffolds in various structurally simple alkaloids like nicotine or fused to other scaffolds in structurally more complex alkaloids, such as dendrobine (Figure 1a). In addition, in the nicotin receptor agonist epibatidine two pyrrolidines are fused in a bicyclic [2.2.1] arrangement (Figure 1a).

In light of this diverse occurrence of five-membered N-heterocycles in NPs we designed and synthesized a pseudo-NP collection which combines these fragments in novel, different connectivities. Phenotypic investigation of bioactivity and target identification led to the discovery of the novel Hedgehog pathway inhibitor Rhonin. Rhonin is the first small-molecule ligand of the RHO GDP-dissociation inhibitor1 (RHOGDI1), and inhibits binding of this chaperone to GDP-bound Rho GTPases. Its discovery establishes a link between RHOGDI1 and the Hh pathway.

Results

Establishment of a tandem catalysis sequence

For the synthesis of a pseudo-NP collection we considered to combine 5-membered N-heterocycle fragments in a complexity-generating manner and by different connectivities (Figure 1b), i.e. such that (i) the fragments do not share atoms and are linked via one bond (monopodal connection; green bonds, Figure 1b), (ii) they share two atoms linked via a common bond (edge fusion; red bonds, Figure 1b) or they may be linked in a bicyclic arrangement sharing three atoms and two bonds (bridge fusion; magenta bonds, Figure 1b). Thereby related but different pseudo-NPs could be synthesized based on a limited set of fragments.

It was planned to initially construct pyrrolidines by means of an enantioselective dipolar cycloaddition of azomethine ylides with maleimides. This would yield an edge-fused pyrrolidine-succinimide pseudo-NP class, i. e. 3. Subsequent oxidation of the pyrrolidine to an imine would give rise to a succinimide-pyrroline combination 4 which can undergo further transformations. The imine could be converted to a new azomethine ylide which might react with maleimides in a second 1,3-dipolar cycloaddition to yield a double fused pseudo-NP class 5 combining two succinimides with a bicyclic azabicyclo[2.2.1] scaffold characteristic for epibatidine. Nucleophilic addition to maleimides will generate a pseudo-NP class 6 containing two fragments linked by an edge fusion to a second succinimide fragment via a monopodal connection. Finally, conjugate addition to different α,β-unsaturated electrophiles would yield pseudo-NPs 7 in which a succinimide and a pyrrolidine are combined. The side chain may contain additional natural product fragments.

By means of this divergent synthesis approach several different pseudo-NP types would be accessible efficiently making use of a unified strategy. This synthesis strategy offers several attractive features. The metal-catalyzed 1,3-dipolar cycloaddition and the subsequent regio- and chemoselective oxidation could potentially be coupled in a novel tandem catalytic approach in which the metal catalyst used for the cycloaddition could be employed in combination with an oxidizing agent. Such tandem catalysis sequences combining two or more mechanistically distinct chemical reactions are considered to be particularly attractive, since they enable expedient generation of molecular complexity and efficiency of the reaction sequence.[11] Hitherto Δ^1-pyrrolines have been synthesized by means of cycloaddition of Münchnones to electron-deficient alkenes.[12,13] Thus, the tandem catalysis strategy outlined in Figure 1b also represents a novel method for the synthesis of this compound class.

In order to identify suitable reaction conditions for the tandem catalysis sequence, azomethine ylide 2a (Figure 2a; R^2 = 4-Br) was reacted with N-methylmaleimide 1a (R^1 = Me) in CH_2Cl_2 in the presence of $Cu(CH_3CN)_4PF_6$ as catalyst and (R)-Fesulphos [(R_p)-2-(tert-butylthio)-1-(diphenylphosphino)ferrocene)] as chiral ligand for the 1,3-dipolar cycloaddition.[14],[15] Subsequent

addition of TBHP as terminal oxidant for the Cu(I) catalyzed oxidation gratifyingly yielded the desired pyrroline 4a (Figure 1b; R^1 = Me, R^2 = 4-Br) in good yield (82%) and with complete regio- and chemoselectivity. Combination of these two steps with the envisaged additional cycloaddition and conjugate addition required careful optimization of the reaction conditions (see Supplementary Information for details). After substantial experimentation, use of 1.5 equivalents of each Et_3N and maleimide in CH_2Cl_2 was best for the formation of Michael addition products 6. The double cycloaddition to tricyclic products 5 proceeded best in the presence of 0.5 equiv of DBU in THF. In CH_2Cl_2 and in the presence of DBU, instead nucleophilic addition to acyclic Michael acceptors occurred and products 7 were obtained (see Supplementary Information for details).

Synthesis of a pseudo-NP collection.

The successful identification of conditions for the selective formation of the three envisaged compound classes enabled the assembly of a pseudo-NP collection. In the synthesis of double cycloadducts 5 (Figure 2a, conditions A) the aromatic ring of the azomethine ylides 2 can be varied (Figure 2a, 5a-5d). Electron-donating and -accepting substituents on the phenyl ring were well tolerated and gave the cycloadducts 5a-d in good yields and with generally excellent enantioselectivity (see Figure 2a). In addition, both aryl and alkyl maleimides could be successfully employed in the reaction in different order and combination (Figure 2a, 5e, 5f).

Under the conditions identified for the Michael addition to unsaturated cyclic electrophiles a variety of azomethine ylide precursors embodying electron-donating or –withdrawing substituents gave the corresponding products 6 in excellent yield and with high diastereo- and enantioselectivity (Figure 2a, 6a-6e) and independent of the electronic nature and the position of the substituents on the phenyl ring in the dipole. Acyclic electrophiles like chalcone and different vinyl- and ethynyl ketones gave the corresponding products 7 in good yields and with high *ee* (Figure 2a, 7a-7h). Notably, in the case of styrylvinylketone, a single regioisomer 7d was obtained in 72% yield. Ethynyl-phenyl ketone yielded the *E*-isomer 7f in 71% yield.

The relative configuration of the cycloadducts was unambiguouly assigned by means of a crystal structure obtained for *rac*-6a. By means of VCD spectroscopy, the absolute configuration of the major diastereomer of 7a was determined as (*S*)-7a. For 7h a crystal structure analysis established the *E*-configuration (see the Supplementary Information for details). Since the diastereoselectivity of the last functionalization is determined by the two stereocenters established in the first cycloaddition, the absolute configuration of all other compounds was assigned by analogy. For a mechanistic proposal to rationalize the observed direction and level of stereochemical induction see Supplementary Scheme S1.

These results demonstrate that the synthesis strategy efficiently yields a pseudo NP collection including the formation of three stereocenters and a tetrasubstituted carbon atom, in a highly efficient one pot reaction.

Cheminformatic analysis

The chemical space occupied by the new pseudo-NPs was analyzed by employing the natural-product score (NP-score) distribution[16] as measure. Since the majority of the collection is defined by pyrrolines fused to succinimides, the NP-score was calculated for the sub-library defined by this scaffold and compared with both the score calculated for NPs in ChEMBL[17] and the score calculated for marketed and experimental drugs listed in DrugBank.[18] The pyrroline-derived pseudo-NPs display a narrow distribution in a region of the NP-Score graph which is sparsely covered by NPs (Figure 2b). The fact that the combination of NP-derived fragments yields compounds with properties diverging from NPs may be counterintuitive. However, the fragment combination generated here is not encountered in nature, such that the NP-score distribution of these pseudo-NPs should be different to NPs themselves. Comparison to the set of compounds in DrugBank which represent approved and experimental drugs, demonstrates that the pseudo-NPs display NP-scores in an area populated by synthetically accessible biologically relevant molecules. However, an additional analysis of the principal moments of inertia (PMI)[19], used as a measure of molecular shape, revealed that the pseudo-NPs described here have a high degree of three-dimensionality (Figure 2c) compared to typical synthetically accessible compound collections.[20] Further analysis using "Lipinski-Ro5" criteria showed that only 42 % of the newly synthesized collection is included within the limits of drug-like space (Figure 2d), indicating that *de novo* combinations of NP-derived fragments may result in compound collections with enhanced biological relevance even when deviating from established metrics.

The analysis indicates that the succinimide-pyrroline pseudo-NPs may occupy a previously not accessible fraction of NP-inspired chemical space, reflecting the fact that they are not obtainable via current biosynthetic pathways. This novel scaffold may be endowed by design with advantageous physiochemical properties, as the pseudo-NP collection displays a NP-score distribution closer to the region occupied by approved drugs, even if the majority of the collection falls outside the limits of "Lipinski-Ro5" space.

Biological evaluation of the pseudo NP collection

Investigation of biological activity of the pseudo NP collection in several cell-based assays monitoring modulation of autophagy, Wnt signaling, reactive oxygen species (ROS) induction, Notch signaling, and Hedgehog (Hh) signaling revealed that the pyrroline-derived compounds are potent and

selective inhibitors of Hh pathway-dependent osteogenesis in pluripotent mouse mesenchymal C3H/10T1/2 cells (see Supplementary Table S6). Despite the limited number of compounds, trends for structure-activity correlation became apparent. Thus, extension of the ketone part of the most potent hit 7a, e. g. by introduction of an extra methylene group and by a fluorine in to the phenyl ring (Figure 2a, compare 7a and 7c) or introduction of a *para*-Br substituent into the aryl ketone part of 7a (to yield 7i; Supplementary Table S6, compare data for 7a and 7i) abolished activity. A phenyl group is not required in the electrophile for activity, since methyl-vinyl ketone yielded active compound 7b (Figure 2a and Supplementary Table S6, 7b). However, in the presence of a phenyl group derived either from the aryl ketone part or the aryl-vinyl part of the electrophile, activity is higher (compare 7b to 7a, 7f and 7d). All active cycloadducts were derived from N-methyl maleimide. If the methyl group was replaced by a phenyl substituent, activity was lost (compare 7b and 7e). The configuration of the stereocenter generated in the final conjugate addition to yield 7a has only minor impact on the bioactivity (Supplementary Table S6, compare 7a, 7a-epi2). The most potent compound 7a (Figure 3a; ultimately termed Rhonin, see below) showed an IC_{50} value of 1.60 ± 0.15 µM in the orthogonal GLI-dependent reporter gene assay in Sonic hedgehog (Shh)-LIGHT2 cells (see Supplementary Table S6 and Figure 3b) and was selected for in-depth biological characterization. Rhonin dose dependently suppressed the expression of the Hh target genes *Ptch1* and *Gli1* to approx. 20 % (Figure 3c), thus confirming Hh pathway inhibition.

Most Hh pathway inhibitors target the seven pass transmembrane protein Smoothened (SMO) and often affect SMO ciliary localization[21]. However, Rhonin did not displace the SMO binder BODIPY-cyclopamine from SMO (Figure 3d and Supplementary Figure S1). In addition, Rhonin did not affect localization of SMO to cilia as indicated by the co-localization of acetylated tubulin (as a ciliary marker) and SMO (Figure 3e). These findings indicate that Rhonin acts downstream of SMO.

Rhonin targets RHOGDI1

For target identification, affinity probes 8 and 9 (Figure 4a) were synthesized based on the structure-activity relationship. The corresponding Boc protected analogue of 8 retained significant Hh pathway inhibiting activity (S10a, IC_{50} = 12.0 ± 1.2 µM, Supplementary Table S6), whereas the Boc-protected analogue of 9 was inactive (S10b, Supplementary Table S6). After immobilization of the probes and affinity-based target enrichment (pulldown), label-free quantification of proteins that selectively bound to the active probe 8 as compared to the control probe 9 indicated RHO GDP-dissociation inhibitor 1 (RHOGDI1), Filamin-B and Filamin-C as potential targets (Supplementary Table S7). Subsequent immunoblotting after the pulldown confirmed the selective enrichment of RHOGDI1 but not of Filamin-B and Filamin-C (Figures 4b and 4c and Supplementary Figure S2) such that RHOGDI1 was further evaluated as target.

RHOGDI1 is a chaperone for geranylgeranylated (GerGer) proteins, in particular the RHO GTPases.[22] The major fraction (90 - 95%) of prenylated RHO GTPases are maintained in stable soluble state in the cytosol by RHOGDI1 [23]. Rhonin directly binds to RHOGDI1 as demonstrated for the fluorescent Rhonin derivative 10 which displays a dissociation constant (K_d) of 7.2 μM (Figures 4d and 4e). RHOGDI1 can extract GDP-bound inactive RHO GTPases from membranes and sequesters them in the cytosol. In an *in vitro* liposome sedimentation assay,[24] addition of RHOGDI1 to liposomes loaded with prenylated GDP-bound RAC1 resulted in extraction of RAC1, i.e., RAC1 was detected in the soluble fraction (Figure 4f). However, in the presence of Rhonin and RHOGDI1, RAC1 remained bound to the liposomes, i.e., RAC1 was detected in the insoluble fraction. This finding indicates that Rhonin inhibits the extraction of RAC1 by RHOGDI1. The structurally similar Rhonin analog 7c (Figure 2a), which did not inhibit Hh signaling, also did not inhibit extraction of RAC1 from liposomes (Figure 4f). Similar results were obtained in a liposome flotation assay[25] (Supplementary Figures S3a and S3b). In addition to RAC1, Rhonin also inhibited the RHOGDI1-mediated extraction of RHOA and CDC42 (Figure 4f). Rhonin slowed down the extraction of geranylgeranylated RAC1 by RHOGDI1 in an surface plasmon resonance (SPR) setup using immobilized synthetic PI(4,5)P$_2$-rich liposomes loaded with geranylgeranylated GDP-bound RAC1, whereas the inactive derivative 7c did not. (Supplementary Figures S3c-S3e). These results suggest that Rhonin may directly modulate the RHOGDI1-RAC1 interaction. Whereas non-prenylated TAMRA-GDP-RAC1 bound to RHOGDI1 with a K_d of 14 μM, which is in agreement with previous reports,[26] in the presence of Rhonin the K_d value for the RHOGDI1-RAC1 interaction increased to 134 μM, which indicates that Rhonin does interfere with RHOGDI1-RAC1-GDP complex formation (Supplementary Figures S3f and S3g).

To gain insight into the binding site for Rhonin on RHOGDI1, competition between fluorescent derivative 10 and prenylated RAC1 was monitored. Addition of prenylated RAC1 to a pre-formed 10-RHOGDI1 complex reduced fluorescence polarization, indicating displacement of 10 from RHOGDI1 (Figure 4g). However, non-prenylated RAC1 could not displace the ligand. Moreover, Rhonin failed to compete with fluorescein-labelled atorvastatin for binding to the prenyl-binding pocket of PDEδ, indicating a specificity of Rhonin towards RHOGDI1 (Supplementary Figure S3h). These results show that Hh-pathway inhibitor 7a targets RHOGDI1 and inhibits its RHO GTPase binding activity most likely by binding to the geranylgeranyl binding site of RHOGDI1. Hence, the compound was termed Rhonin.

RHOGDI is a negative regulator of Hh signaling

To examine the role of RHOGDI1 in Hh signaling we depleted RHOGDI1. Knockdown of RHOGDI1 by two different small interfering RNAs (knockdown efficiency siRNA-1:88 %; siRNA-2: 64 %, (Figure 5a))

and simultaneous activation of the Hh pathway increased Hh pathway activity and the levels of the Hh target genes *Ptch1* and *Gli1* (Figure 5b). By analogy, purmorphamine-mediated osteoblast differentiation was increased upon RHOGDI1 depletion (Figure 5c and Supplementary Figure S4a). Conversely, RHOGDI1 overexpression decreased Hh pathway activity (Figure 5d and Supplementary Figure S4b). These results indicate that, in principle, RHOGDI1 is a negative regulator of Hh signaling.

Graded RHOGDI1 depletion by siRNA-1 and siRNA-2 also led to graded loss of Hh inhibitory activity of Rhonin, since the compound had no (for siRNA-1) or only a weaker (for siRNA-2) influence on Hh target gene expression (Figure 5b and Supplementary Figure S5). This graded loss in Rhonin activity correlates with the knockdown levels reached by the employed siRNAs and is a strong evidence that Rhonin inhibits Hh signaling by targeting RHOGDI1.

Rhonin activates RHO GTPases by inhibiting RHOGDI1

Since RHOGDI1 is a negative regulator of RHO GTPases, it is to be expected that an inhibitor of RHOGDI1 should positively affect the activity of RHO GTPases. Depletion of RHOGDI1 lowered the total level of RHOA and increased the level of RHOA-GTP by two fold (Figure 6a and 6b), which is in agreement with previous reports.[23] Stimulation of Hh signaling with purmorphamine slightly increased the RHOA-GTP level. Notably, in the presence or absence of purmorphamine, treatment with Rhonin led to increased levels of GTP-bound RHOA. This finding indicates that RHOGDI1 inhibition by Rhonin phenocopies RHOGDI1 depletion. A similar trend was observed for knock down of RAC1 and CDC42 (Figure 6b).

RHO GTPases regulate formation of the actin cytoskeleton in fibroblasts and endothelial cells.[27] Serum starvation inhibits RHO GTPases and leads to disruption of the actin cytoskeleton (Figure 6c).[28,29] Treatment of serum-starved cells with Rhonin for 24 h resulted in a dense network of actin stress fibers. The onset of stress fiber formation was observed as early as 2 h after treatment with Rhonin, indicating activation of RHOA (and most likely RHO associated kinase, ROCK). Interference with RHOGDI1 function should alter the subcellular localization of RHO GTPases.[23] Indeed, treatment with Rhonin led to a shift of the three RHO GTPases from the cytosolic to the heavy membrane fraction with the strongest influence on RHOA (Figure 6d and 6e and Supplementary Figure S6). The heavy membrane fraction contains the plasma membrane and the rough endoplasmic reticulum (rER). Thus, upon treatment with Rhonin the amount of RHO GTPases at the plasma membrane increases, i.e. the site of RHO-GTPase activation. Alternatively, the GTPases are mislocalized and trapped at the rER, thus preventing their activation. These findings show that Rhonin leads to activation and change in the subcellular localization of RHO GTPases.

Discussion

Efficient strategies for the discovery of new bioactive compounds with novel chemotypes may best build on established biological relevance of compound classes and their underlying scaffolds. In particular, natural product (NP) structure and activity have provided inspiration [4] for strategies like Biology Oriented Synthesis [30,31] and natural product ring-distortion and modification [32,33]. However, NP-related compound collections usually represent only focused areas of chemical space, and, most likely also of biological target space. Thus, strategies that enable efficient and wider coverage of biologically relevant, NP-related chemical space, like fragment-based design, are highly desirable and in high demand.

Application of fragment-based design to the synthesis of NP-inspired compound collections, calls for *de novo* combinations of NP fragments.[6] The resulting novel compound classes will inherit characteristic NP-structure, properties and relevance but go beyond the chemical space explored by nature because they will not be accessible by known biosynthesis pathways. Thus, they may be regarded as "pseudo natural products".[5] This term has been previously used by Suga *et al*., [34,35] to describe cyclopeptides synthesized *in vitro,* as well as by Oshima *et al*. [36,37] to characterize hybrid compounds obtained by biosynthetic pathway interception. Due to the unprecedented combination of NP fragments pseudo-NPs may have unexpected and novel targets which may not be related to the bioactivity of the guiding NPs. Hence their bioactivity should be analyzed in unbiased, target-agnostic phenotypic assays to widely cover biological target space.

We validate the "pseudo natural product" concept by the design, synthesis and evaluation of a compound collection that combines five-membered N-heterocycles (i.e. pyrrolidines, pyrrolines and succinimides) characteristic for NP classes with different structure and different biosynthetic origin, in novel arrangements and with different connectivities.

Cheminformatic analysis, employing the NP-score as measure for NP-likeness, indicated that the pyrroline-derived pseudo-NPs occupy an area of chemical space previously not accessible to and, therefore, only sparsely covered by NPs. Rather the pseudo-NPs display NP scores characteristic for drug-like compound classes, such that they may be endowed by design with advantageous physiochemical properties.

The novel pseudo-NP Rhonin proved to be an inhibitor of Hh signaling. The Hh signaling pathway is vital for organ development and body patterning during embryogenesis and its inappropriate activation is linked to several types of cancers. SMO is the most druggable target in Hh signaling, however, there is a need to impinge the pathway downstream of SMO due to recently discovered drug-resistant mutations in SMO.[38] In addition, there are SMO-dependent and –independent non-canonical Hh-pathways for which small molecule modulators have rarely been developed.[39,40] We

demonstrate that Rhonin binds to RHOGDI1, which translates to displacement of RHOGDI1-bound RHO GTPases results in enrichment of GTP-bound RHO GTPases in membranes and establishes a link between RHOGDI1 and Hh signalling. The compound most likely directly binds into the prenyl binding pocket. Efficient depletion of RHOGDI1 completely abolished the pathway inhibitory activity of Rhonin and validates RHOGDI1 as the target protein with regard to Hh pathway inhibition. To the best of our knowledge, no direct RHOGDI1 inhibitor has been described to date. The only reported small molecule related to RHOGDI1 function is secramine A, which inhibits CDC42-mediated actin polymerization in a RHOGDI1-dependent manner.[41] However, direct interaction between secramine A and RHOGDI1has not been shown.

RHOGDI1 is a chaperone and negative regulator of the geranylgeranylated RHO GTPases RHOA, RAC1 and CDC42[42] which regulate the actin cytoskeleton and, thus, processes like cell adhesion, establishment of cell polarity and cell migration.[42] RHOGDI1 binds and buries the membrane-anchoring geranylgeranyl moiety of the GTPases in a hydrophobic pocket and, thereby, increases their solubility in the cytosol.[22] It extracts RHO GTPases from membranes and sequesters them in the cytosol, thus preventing their activation at the target membrane.[22] In the absence of RHOGDI, the cytosolic pool of the geranylgeranylated RHO GTPases, constituting 90-95% of total RHO GTPases, is rapidly degraded by the proteasome, while the levels of membrane-bound GTP-bound RHO GTPases increase.[43,44] However, these activated RHO GTPases may fail to properly localize to their target membranes and accumulate at the endoplasmic reticulum , thus effectors may not be activated.[23] As opposed to activation of all GTPases, in $RHOGDI1^{-/-}$ mice activation of only RHOA but not RAC1 and CDC42 was observed along with hyper-phosphorylation of myosin light chain.[45] Activation of only RHOA was also evident in the detection of stress fiber formation upon RHOGDI knockdown in HUVEC cells.[45] Interestingly, Rhonin increases the level of GTP-bound RHOA and induces stress fiber formation, which is in line with increased activity of RHOA.[46]

Direct involvement of RHOGDI1 in Hh pathway regulation has not been reported before. However, RHO GTPases have been linked to Smo-dependent, non-canonical Hh signaling[39,40] (Supplementary Figure S7a). SMO can signal through $G\alpha_i$ to activate RHOA and RAC1 and modulate the actin cytoskeleton in a non-canonical fashion.[47-50] In addition, RHOA has been linked to GLI-mediated transcription, however, the signal to RHOA was transmitted via by $G\alpha_{12}$ or $G\alpha_{13}$ and did not include SMO or SHH.[51,52] In hematopoietic stem cells, a constitutively active mutant of RAC1 induced higher expression of GLI-2 and SHH. Conversely, dominant negative RAC1 decreased the expression of GLI-2 and SHH, therefore suggesting a GLI-dependent regulation of Hh signaling by RHO GTPases.[53] Furthermore, *IFT80* (Intraflagellar transport protein 80) deletion causes cilia defects and leads to suppression of Hh-GLI signaling and osteoblast differentiation while increasing Hh-SMO-$G\alpha_i$-RHOA-stress fiber signaling.[54] The resulting RHOA activation and its suppressive influence on Hh-induced

osteogenesis was partially or fully reverted by RHOA or ROCK inhibition or by disrupting the actin cytoskeleton.[54] Inhibition of actin assembly positively influences ciliogenesis,[54,55] and RHO GTPases have also been linked to ciliogenesis, i.e. CDC42 restricts the frequency of ciliated cells and axoneme length by recruiting the regulators of actin dynamics.[56] However, although depletion of CDC42 increases axoneme length and ciliation, it suppresses canonical Hh signaling.[56] Thus, an intricate interplay between RHO GTPases and GLI-mediated transcription exists and genetic or pharmacological modulation of RHOGDI1 is expected to have a pleiotropic influence with not readily predictable outcome with regard to osteogenesis and Hh-SMO-GLI signaling.

The non-canonical SMO-RHOA pathway suppresses the SMO-GLI pathway[54], and RHOGDI1 knockdown should positively modulate the SMO-GLI axis because the amount of GTP-bound RHO GTPases will increase but downstream effectors may not be activated. Indeed, we observed increased Hh-mediated osteogenesis upon depletion of RHOGDI1. However, knockdown of RHOGDI1 should also impair CDC42-controlled ciliation that may negatively influence Hh-GLI-related processes. The $G\alpha_{12}/G\alpha_{13}$-RHOA-GLI axis, if active during osteogenesis in the employed cell line, would likewise be inhibited by RHOGDI1 depletion. We observe, most likely as net sum of all effects on RHO GTPases, an increase in osteogenesis upon RHOGDI1 knockdown. Pathway perturbation and RHOGDI1 inhibition by Rhonin have effects on Hh signaling opposite to RHOGDI1 depletion. Such divergence between chemical and genetic perturbations has been observed before and, actually, may differentiate a chemical-biological analysis form a genetic investigation.[57,58] Genetic knockout or knockdown remove or reduce the target protein, whereas small molecules modulate individual binding sites or functions. RHOGDI1 recognizes its target GTPases via two binding sites. While Rhonin affects binding to the prenyl binding pocket, RHOGDI1 knockdown abolishes binding to both sites.

Our findings suggest that Rhonin influences canonical Hh signaling via a non-canonical route. They are in agreement with a mode of action in which Rhonin binds to RHOGDI1, prevents the extraction of RHO GTPases from membranes and, thereby, leads to increased pools of active, GTP-bound RHO GTPases. Whether all three GTPases are activated or not, would depend on the employed system since activity of RHO GTPases will depend on different factors, i.e. phosphorylation, ubiquitination, GEFs and GAPs etc.[42]. Our data indicate that, in contrast to RHOGDI1 depletion, inhibition of RHOGDI1 with Rhonin increases RHOA activity, thus causing stress fiber formation. Increased actin polymerization has been linked to impaired cilia-related function[54,59] and may be the causal link between RHOA activity and Hh-GLI pathway inhibition.

Acknowledgments

Author contributions

S.P. carried out biological experiments, affinity probe synthesis, target identification and genetic validations. E.S. and R.N. synthesized the pseudo-NP compound library. M.A., M.B. and N.J. performed biological experiments, M.P. and H.K. synthesized chemical probes. G.K. performed chemoinformatic analysis. C.G. and C.S. analyzed crystallography data. P.J. carried out the MS-proteomics analysis. H.W., S.Z. and M.R.A. designed research. S.P., E.S., S.Z, and H.W. wrote the manuscript. All authors discussed the results and commented on the manuscript.

References

1. Ursu, A.; Waldmann, H. Hide and seek: Identification and confirmation of small molecule protein targets. *Bioorganic & medicinal chemistry letters* **2015**, *25*, 3079-3086, doi:10.1016/j.bmcl.2015.06.023.
2. Wagner, B.K.; Schreiber, S.L. The Power of Sophisticated Phenotypic Screening and Modern Mechanism-of-Action Methods. *Cell chemical biology* **2016**, *23*, 3-9, doi:10.1016/j.chembiol.2015.11.008.
3. Vincent, F.; Loria, P.; Pregel, M.; Stanton, R.; Kitching, L.; Nocka, K.; Doyonnas, R.; Steppan, C.; Gilbert, A.; Schroeter, T., et al. Developing predictive assays: the phenotypic screening "rule of 3". *Science translational medicine* **2015**, *7*, 293ps215, doi:10.1126/scitranslmed.aab1201.
4. van Hattum, H.; Waldmann, H. Biology-oriented synthesis: harnessing the power of evolution. *Journal of the American Chemical Society* **2014**, *136*, 11853-11859, doi:10.1021/ja505861d.
5. Karageorgis, G.; Reckzeh, E.S.; Ceballos, J.; Schwalfenberg, M.; Sievers, S.; Ostermann, C.; Pahl, A.; Ziegler, S.; Waldmann, H. Chromopynones are pseudo natural product glucose uptake inhibitors targeting glucose transporters GLUT-1 and -3. *Nature Chemistry* **2018**, 10.1038/s41557-018-0132-6, doi:10.1038/s41557-018-0132-6.
6. Over, B.; Wetzel, S.; Grutter, C.; Nakai, Y.; Renner, S.; Rauh, D.; Waldmann, H. Natural-product-derived fragments for fragment-based ligand discovery. *Nat Chem* **2013**, *5*, 21-28, doi:10.1038/nchem.1506.

7.   Uddin, M.J.; Kokubo, S.; Ueda, K.; Suenaga, K.; Uemura, D. Haterumaimides F–I, Four New Cytotoxic Diterpene Alkaloids from an Ascidian Lissoclinum Species. *Journal of Natural Products* **2001**, *64*, 1169-1173, doi:10.1021/np010066n.

8.   Isaka, M.; Rugseree, N.; Maithip, P.; Kongsaeree, P.; Prabpai, S.; Thebtaranonth, Y. Hirsutellones A–E, antimycobacterial alkaloids from the insect pathogenic fungus Hirsutella nivea BCC 2594. *Tetrahedron* **2005**, *61*, 5577-5583, doi:10.1016/j.tet.2005.03.099.

9.   Kobayashi, J.i.; Nakamura, H.; Ohizumi, Y.; Hirata, Y. Eudistomidin-A, a novel calmodulin antagonist from the okinawan tunicate eudistoma glaucus. *Tetrahedron Letters* **1986**, *27*, 1191-1194, doi:https://doi.org/10.1016/S0040-4039(00)84213-6.

10.   Tyroller, S.; Zwickenpflug, W.; Richter, E. New Sources of Dietary Myosmine Uptake from Cereals, Fruits, Vegetables, and Milk. *Journal of Agricultural and Food Chemistry* **2002**, *50*, 4909-4915, doi:10.1021/jf020281p.

11.   Lohr, T.L.; Marks, T.J. Orthogonal tandem catalysis. *Nat Chem* **2015**, *7*, 477-482, doi:10.1038/nchem.2262.

12.   Melhado, A.D.; Amarante, G.W.; Wang, Z.J.; Luparia, M.; Toste, F.D. Gold(I)-Catalyzed Diastereo- and Enantioselective 1,3-Dipolar Cycloaddition and Mannich Reactions of Azlactones. *Journal of the American Chemical Society* **2011**, *133*, 3517-3527, doi:10.1021/ja1095045.

13.   Sun, W.; Zhu, G.; Wu, C.; Li, G.; Hong, L.; Wang, R. Organocatalytic Diastereo- and Enantioselective 1,3-Dipolar Cycloaddition of Azlactones and Methyleneindolinones. **2013**, *52*, 8633-8637, doi:doi:10.1002/anie.201302831.

14.   Antonchick, A.P.; Gerding-Reimers, C.; Catarinella, M.; Schürmann, M.; Preut, H.; Ziegler, S.; Rauh, D.; Waldmann, H. Highly enantioselective synthesis and cellular evaluation of spirooxindoles inspired by natural products. *Nature Chemistry* **2010**, *2*, 735, doi:10.1038/nchem.730
https://www.nature.com/articles/nchem.730#supplementary-information.

15.   Narayan, R.; Potowski, M.; Jia, Z.-J.; Antonchick, A.P.; Waldmann, H. Catalytic Enantioselective 1,3-Dipolar Cycloadditions of Azomethine Ylides for Biology-Oriented Synthesis. *Accounts of Chemical Research* **2014**, *47*, 1296-1310, doi:10.1021/ar400286b.

16.   Ertl, P.; Roggo, S.; Schuffenhauer, A. Natural Product-likeness Score and Its Application for Prioritization of Compound Libraries. *Journal of Chemical Information and Modeling* **2008**, *48*, 68-74, doi:10.1021/ci700286x.

17.   Bento, A.P.; Gaulton, A.; Hersey, A.; Bellis, L.J.; Chambers, J.; Davies, M.; Krüger, F.A.; Light, Y.; Mak, L.; McGlinchey, S., et al. The ChEMBL bioactivity database: an update. *Nucleic Acids Research* **2014**, *42*, D1083-D1090, doi:10.1093/nar/gkt1031.

18.   Law, V.; Knox, C.; Djoumbou, Y.; Jewison, T.; Guo, A.C.; Liu, Y.; Maciejewski, A.; Arndt, D.; Wilson, M.; Neveu, V., et al. DrugBank 4.0: shedding new light on drug metabolism. *Nucleic Acids Research* **2014**, *42*, D1091-D1097, doi:10.1093/nar/gkt1068.

19.   Sauer, W.H.B.; Schwarz, M.K. Molecular Shape Diversity of Combinatorial Libraries: A Prerequisite for Broad Bioactivity. *Journal of Chemical Information and Computer Sciences* **2003**, *43*, 987-1003, doi:10.1021/ci025599w.

20.   Colomer, I.; Empson, C.J.; Craven, P.; Owen, Z.; Doveston, R.G.; Churcher, I.; Marsden, S.P.; Nelson, A. A divergent synthetic approach to diverse molecular scaffolds: assessment of lead-likeness using LLAMA, an open-access computational tool. *Chemical Communications* **2016**, *52*, 7209-7212, doi:10.1039/C6CC03244C.

21.   Lin, T.L.; Matsui, W. Hedgehog pathway as a drug target: Smoothened inhibitors in development. *OncoTargets and therapy* **2012**, *5*, 47-58, doi:10.2147/OTT.S21957.

22.   Garcia-Mata, R.; Boulter, E.; Burridge, K. The 'invisible hand': regulation of RHO GTPases by RHOGDIs. *Nature reviews. Molecular cell biology* **2011**, *12*, 493-504, doi:10.1038/nrm3153.

23.   Boulter, E.; Garcia-Mata, R.; Guilluy, C.; Dubash, A.; Rossi, G.; Brennwald, P.J.; Burridge, K. Regulation of Rho GTPase crosstalk, degradation and activity by RhoGDI1. *Nature cell biology* **2010**, *12*, 477-483, doi:10.1038/ncb2049.

24. Zhang, S.-C.; Gremer, L.; Heise, H.; Janning, P.; Shymanets, A.; Cirstea, I.C.; Krause, E.; Nürnberg, B.; Ahmadian, M.R. Liposome Reconstitution and Modulation of Recombinant Prenylated Human Rac1 by GEFs, GDI1 and Pak1. *PLOS ONE* **2014**, *9*, e102425, doi:10.1371/journal.pone.0102425.

25. Bigay, J.; Casella, J.F.; Drin, G.; Mesmin, B.; Antonny, B. ArfGAP1 responds to membrane curvature through the folding of a lipid packing sensor motif. *The EMBO journal* **2005**, *24*, 2244-2253, doi:10.1038/sj.emboj.7600714.

26. Newcombe, A.R.; Stockley, R.W.; Hunter, J.L.; Webb, M.R. The Interaction between Rac1 and Its Guanine Nucleotide Dissociation Inhibitor (GDI), Monitored by a Single Fluorescent Coumarin Attached to GDI. *Biochemistry* **1999**, *38*, 6879-6886, doi:10.1021/bi9829837.

27. Guilluy, C.; Garcia-Mata, R.; Burridge, K. Rho protein crosstalk: another social network? *Trends in cell biology* **2011**, *21*, 718-726, doi:10.1016/j.tcb.2011.08.002.

28. Ridley, A.J.; Hall, A. The small GTP-binding protein rho regulates the assembly of focal adhesions and actin stress fibers in response to growth factors. *Cell* **1992**, *70*, 389-399.

29. Ridley, A.J.; Paterson, H.F.; Johnston, C.L.; Diekmann, D.; Hall, A. The small GTP-binding protein rac regulates growth factor-induced membrane ruffling. *Cell* **1992**, *70*, 401-410.

30. Bon, R.S.; Waldmann, H. Bioactivity-guided navigation of chemical space. *Acc Chem Res* **2010**, *43*, 1103-1114, doi:10.1021/ar100014h.

31. Wetzel, S.; Bon, R.S.; Kumar, K.; Waldmann, H. Biology-oriented synthesis. *Angewandte Chemie (International ed. in English)* **2011**, *50*, 10800-10826, doi:10.1002/anie.201007004.

32. Huigens, R.W.; Morrison, K.C.; Hicklin, R.W.; Flood, T.A.; Richter, M.F.; Hergenrother, P.J. A ring-distortion strategy to construct stereochemically complex and structurally diverse compounds from natural products. *Nature Chemistry* **2013**, *5*, 195-202, doi:10.1038/Nchem.1549.

33. Rafferty, R.J.; Hicklin, R.W.; Maloof, K.A.; Hergenrother, P.J. Synthesis of Complex and Diverse Compounds through Ring Distortion of Abietic Acid. *Angew Chem Int Edit* **2014**, *53*, 220-224, doi:10.1002/anie.201308743.

34. Goto, Y.; Ito, Y.; Kato, Y.; Tsunoda, S.; Suga, H. One-Pot Synthesis of Azoline-Containing Peptides in a Cell-free Translation System Integrated with a Posttranslational Cyclodehydratase. *Chem Biol* **2014**, *21*, 766-774, doi:10.1016/j.chembiol.2014.04.008.

35. Ozaki, T.; Yamashita, K.; Goto, Y.; Shimomura, M.; Hayashi, S.; Asamizu, S.; Sugai, Y.; Ikeda, H.; Suga, H.; Onaka, H. Dissection of goadsporin biosynthesis by in vitro reconstitution leading to designer analogues expressed in vivo. *Nat Commun* **2017**, *8*, doi:ARTN 14207 10.1038/ncomms14207.

36. Asai, T.; Tsukada, K.; Ise, S.; Shirata, N.; Hashimoto, M.; Fujii, I.; Gomi, K.; Nakagawara, K.; Kodama, E.N.; Oshima, Y. Use of a biosynthetic intermediate to explore the chemical diversity of pseudo-natural fungal polyketides. *Nature Chemistry* **2015**, *7*, 737-743, doi:10.1038/Nchem.2308.

37. Kikuchi, H.; Ichinohe, K.; Kida, S.; Murase, S.; Yamada, O.; Oshima, Y. Monoterpene Indole Alkaloid-Like Compounds Based on Diversity-Enhanced Extracts of Iridoid-Containing Plants and Their Immune Checkpoint Inhibitory Activity. *Org Lett* **2016**, *18*, 5948-5951, doi:10.1021/acs.orglett.6b03057.

38. Cook, D.R.; Rossman, K.L.; Der, C.J. Rho guanine nucleotide exchange factors: regulators of Rho GTPase activity in development and disease. *Oncogene* **2014**, *33*, 4021-4035, doi:10.1038/onc.2013.362.

39. Teperino, R.; Aberger, F.; Esterbauer, H.; Riobo, N.; Pospisilik, J.A. Canonical and non-canonical Hedgehog signalling and the control of metabolism. *Semin Cell Dev Biol* **2014**, *33*, 81-92, doi:10.1016/j.semcdb.2014.05.007.

40. Robbins, D.J.; Fei, D.L.; Riobo, N.A. The Hedgehog signal transduction network. *Sci Signal* **2012**, *5*, re6, doi:10.1126/scisignal.2002906.

41. Pelish, H.E.; Peterson, J.R.; Salvarezza, S.B.; Rodriguez-Boulan, E.; Chen, J.-L.; Stamnes, M.; Macia, E.; Feng, Y.; Shair, M.D.; Kirchhausen, T. Secramine inhibits Cdc42-dependent functions

in cells and Cdc42 activation in vitro. *Nature Chemical Biology* **2005**, *2*, 39, doi:10.1038/nchembio751

https://www.nature.com/articles/nchembio751z#supplementary-information.

42.   Hodge, R.G.; Ridley, A.J. Regulating Rho GTPases and their regulators. *Nature Reviews Molecular Cell Biology* **2016**, *17*, 496-510, doi:10.1038/nrm.2016.67.

43.   Arnst, J.L.; Hein, A.L.; Taylor, M.A.; Palermo, N.Y.; Contreras, J.I.; Sonawane, Y.A.; Wahl, A.O.; Ouellette, M.M.; Natarajan, A.; Yan, Y. Discovery and characterization of small molecule Rac1 inhibitors. *Oncotarget* **2017**, *8*, 34586-34600, doi:10.18632/oncotarget.16656.

44.   Hong, L.; Kenney, S.R.; Phillips, G.K.; Simpson, D.; Schroeder, C.E.; Noth, J.; Romero, E.; Swanson, S.; Waller, A.; Strouse, J.J., et al. Characterization of a Cdc42 protein inhibitor and its use as a molecular probe. *The Journal of biological chemistry* **2013**, *288*, 8531-8543, doi:10.1074/jbc.M112.435941.

45.   Gorovoy, M.; Neamu, R.; Niu, J.; Vogel, S.; Predescu, D.; Miyoshi, J.; Takai, Y.; Kini, V.; Mehta, D.; Malik, A.B., et al. RhoGDI-1 modulation of the activity of monomeric RhoGTPase RhoA regulates endothelial barrier function in mouse lungs. *Circ Res* **2007**, *101*, 50-58, doi:10.1161/Circresaha.106.145847.

46.   Schaefer, A.; Reinhard, N.R.; Hordijk, P.L. Toward understanding RhoGTPase specificity: structure, function and local activation. *Small GTPases* **2014**, *5*, 6, doi:10.4161/21541248.2014.968004.

47.   Carballo, G.B.; Honorato, J.R.; de Lopes, G.P.F.; Spohr, T.C.L.D.E. A highlight on Sonic hedgehog pathway. *Cell Commun Signal* **2018**, *16*, doi:ARTN 11
10.1186/s12964-018-0220-7.

48.   Pandit, T.; Ogden, S.K. Contributions of Noncanonical Smoothened Signaling During Embryonic Development. *J Dev Biol* **2017**, *5*, doi:ARTN 11
10.3390/jdb5040011.

49.   Chinchilla, P.; Xiao, L.; Kazanietz, M.G.; Riobo, N.A. Hedgehog proteins activate pro-angiogenic responses in endothelial cells through non-canonical signaling pathways. *Cell cycle (Georgetown, Tex.)* **2010**, *9*, 570-579, doi:10.4161/cc.9.3.10591.

50.   Polizio, A.H.; Chinchilla, P.; Chen, X.L.; Kim, S.; Manning, D.R.; Riobo, N.A. Heterotrimeric G(i) Proteins Link Hedgehog Signaling to Activation of Rho Small GTPases to Promote Fibroblast Migration. *Journal of Biological Chemistry* **2011**, *286*, 19589-19596, doi:10.1074/jbc.M110.197111.

51.   Kasai, K.; Takahashi, M.; Osumi, N.; Sinnarajah, S.; Takeo, T.; Ikeda, H.; Kehrl, J.H.; Itoh, G.; Arnheiter, H. The G12 family of heterotrimeric G proteins and Rho GTPase mediate Sonic hedgehog signalling. *Genes to cells : devoted to molecular & cellular mechanisms* **2004**, *9*, 49-58.

52.   Douglas, A.E.; Heim, J.A.; Shen, F.; Almada, L.L.; Riobo, N.A.; Fernandez-Zapico, M.E.; Manning, D.R. The alpha Subunit of the G Protein G(13) Regulates Activity of One or More Gli Transcription Factors Independently of Smoothened. *Journal of Biological Chemistry* **2011**, *286*, 30714-30722, doi:10.1074/jbc.M111.219279.

53.   Choi, S.S.; Witek, R.P.; Yang, L.; Omenetti, A.; Syn, W.K.; Moylan, C.A.; Jung, Y.; Karaca, G.F.; Teaberry, V.S.; Pereira, T.A., et al. Activation of Rac1 promotes hedgehog-mediated acquisition of the myofibroblastic phenotype in rat and human hepatic stellate cells. *Hepatology (Baltimore, Md.)* **2010**, *52*, 278-290, doi:10.1002/hep.23649.

54.   Yuan, X.; Cao, J.; He, X.N.; Serra, R.; Qu, J.; Cao, X.; Yang, S.Y. Ciliary IFT80 balances canonical versus non-canonical hedgehog signalling for osteoblast differentiation. *Nat Commun* **2016**, *7*, doi:10.1038/ncomms11024.

55.   Kim, J.; Lee, J.E.; Heynen-Genel, S.; Suyama, E.; Ono, K.; Lee, K.; Ideker, T.; Aza-Blanc, P.; Gleeson, J.G. Functional genomic screen for modulators of ciliogenesis and cilium length. *Nature* **2010**, *464*, 1048-U1114, doi:10.1038/nature08895.

56.   Drummond, M.L.; Li, M.; Tarapore, E.; Nguyen, T.T.L.; Barouni, B.J.; Cruz, S.; Tan, K.C.; Oro, A.E.; Atwood, S.X. Actin polymerization controls cilia-mediated signaling. *J Cell Biol* **2018**, *217*, 3255-3266, doi:10.1083/jcb.201703196.

57.   Knight, Z.A.; Shokat, K.M. Chemical genetics: Where genetics and pharmacology meet. *Cell* **2007**, *128*, 425-430, doi:10.1016/j.cell.2007.01.021.

58.   Weiss, W.A.; Taylor, S.S.; Shokat, K.M. Recognizing and exploiting differences between RNAi and small-molecule inhibitors. *Nature Chemical Biology* **2007**, *3*, 739-744, doi:10.1038/nchembio1207-739.

59.   Mirvis, M.; Stearns, T.; Nelson, W.J. Cilium structure, assembly, and disassembly regulated by the cytoskeleton. *Biochem J* **2018**, *475*, 2329-2353, doi:10.1042/Bcj20170453.

60.   Herbrand, U.; Ahmadian, M.R. p190-RhoGAP as an integral component of the Tiam1/Rac1-induced downregulation of Rho. *Biol Chem* **2006**, *387*, 311-317, doi:10.1515/BC.2006.041.

61.   Zhang, S.C.; Gremer, L.; Heise, H.; Janning, P.; Shymanets, A.; Cirstea, I.C.; Krause, E.; Nurnberg, B.; Ahmadian, M.R. Liposome reconstitution and modulation of recombinant prenylated human Rac1 by GEFs, GDI1 and Pak1. *PLoS One* **2014**, *9*, e102425, doi:10.1371/journal.pone.0102425.

62.   Taha, M.S.; Nouri, K.; Milroy, L.G.; Moll, J.M.; Herrmann, C.; Brunsveld, L.; Piekorz, R.P.; Ahmadian, M.R. Subcellular fractionation and localization studies reveal a direct interaction of the fragile X mental retardation protein (FMRP) with nucleolin. *PLoS One* **2014**, *9*, e91465, doi:10.1371/journal.pone.0091465.
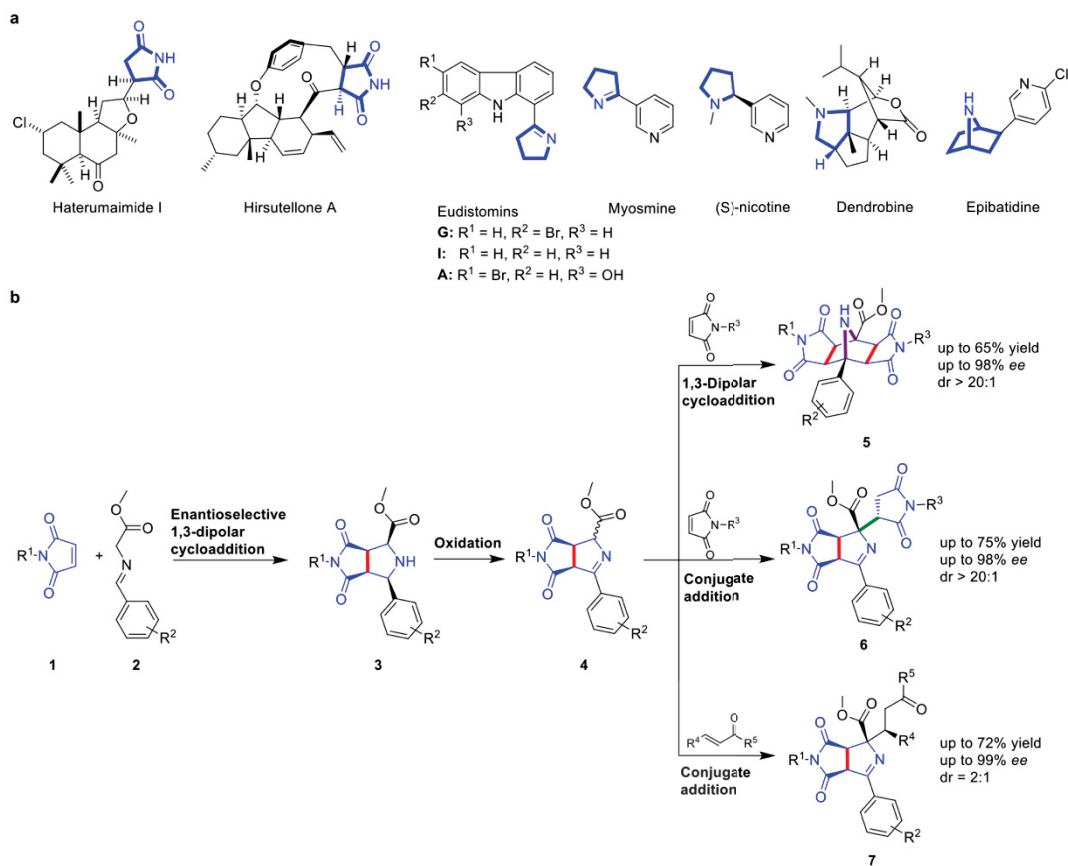
Figure 1. Design of a pseudo-NP collection (**a**) Representative natural products embodying 5-membered N-heterocycles; (**b**) Tandem catalysis sequence for the synthesis of a pseudo-NP collection containing 5-membered N-heterocycles in different connectivities.

a

	R[1]	R[2]	R[3]	Yield (%)	ee (%)	ODA	RGA
5a	Me	4-Br	Ph	48	96	n.a	n.a
5b	Me	4-Me	Ph	44	98	n.a	n.a
5c	Me	4-CO$_2$Me	Ph	65	98	n.a	n.a
5d	Me	4-Cl	Ph	55	96	n.a	n.a
5e	Ph	4-Br	n-Pr	46	98	n.a	n.a
5f	Cy	4-Br	Ph	43	96	n.a	n.a

	R[1]	R[2]	R[3]	Yield (%)	ee (%)	ODA	RGA
6a	Me	4-Br	Ph	69	97	n.a	n.a
6b	Me	4-CF3	Ph	57	98	n.a	n.a
6c	Me	4-F	Ph	72	97	n.a	n.a
6d	Me	4-tert-butyl	Ph	75	95	n.a	n.a
6e	Me	3-OMe	Ph	72	95	n.a	n.a

7a, 35%,
98% ee, dr 2:1
ODA IC$_{50}$: 1.50 μM
RGA IC$_{50}$: 1.60 μM

7b, 60%
97% ee
ODA IC$_{50}$: 6.2 μM
RGA IC$_{50}$: 8.0 μM

7c, 60%
98% ee
ODA IC$_{50}$: n.a
RGA IC$_{50}$: n.a

7d, 72%,
97% ee
ODA IC$_{50}$: 2.81 μM
RGA IC$_{50}$: 4.24 μM

7e, 51%
97% ee
ODA IC$_{50}$: n.a
RGA IC$_{50}$: n.a

7f, 71%
99% ee
ODA IC$_{50}$: 3.13 μM
RGA IC$_{50}$: 6.15 μM

7g, 64%,
98% ee E/Z 3:1
ODA IC$_{50}$: n.a
RGA IC$_{50}$: n.a

7h, 69%
96% ee E/Z 3:1
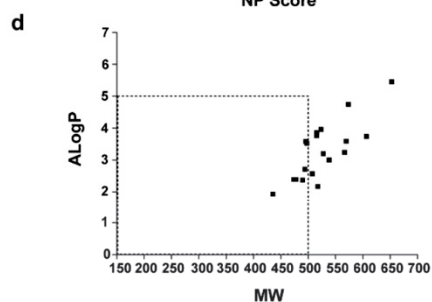ODA IC$_{50}$: n.a
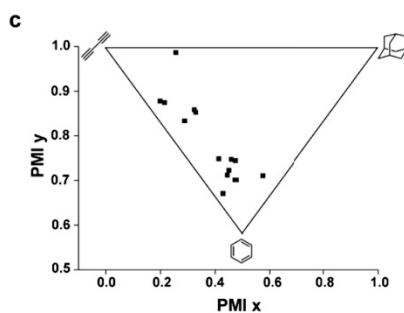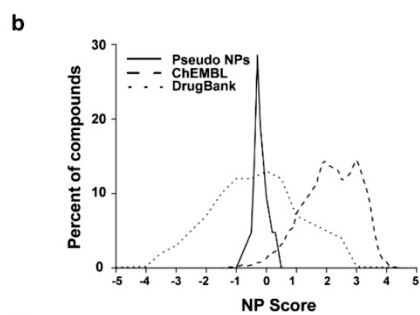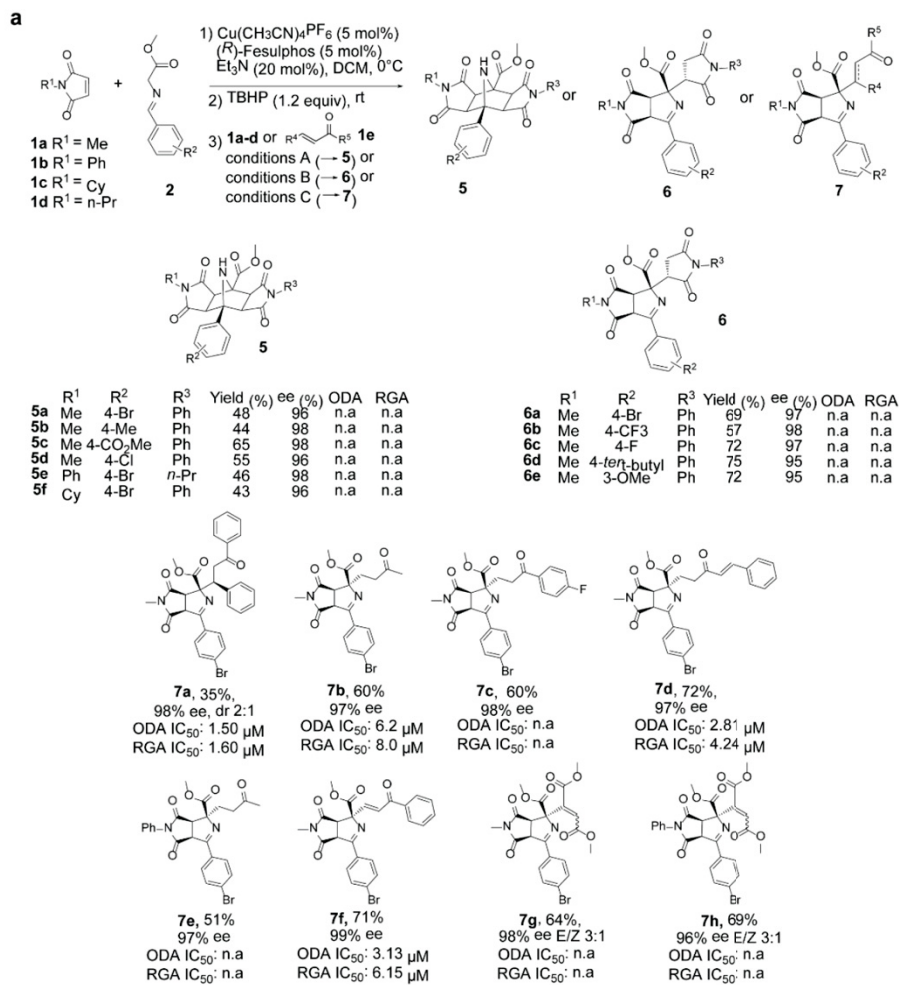RGA IC$_{50}$: n.a

b

c

d

Figure 2. Synthesis of a pseudo-NPs that occupy a distinct portion of chemical space. (a) Reaction conditions: A) **1a-d** (3 equiv), DBU (0.5 equiv), THF, rt; B) **1a-d** (1.5 equiv), Et$_3$N (1.5 equiv), DCM, rt; C) **1e** (1.5 equiv), DBU (0.5 equiv), DCM, rt. ODA: Osteoblast differentiation assay. RGA: Reporter gene assay. All ODA and RGA data are mean values of three independent experiments (n = 3) ± s.d. **(b)** NP-likeness score comparison of NPs represented in ChEMBL (dashed curve), Drugbank (dotted curve) and succinimide-pyrroline pseudo NPs (solid curve). **(c)** PMI plot for succinimide-pyrroline pseudo-NPs. **(d)** ALogP vs MW plot of succinimide-pyrroline pseudo NPs.
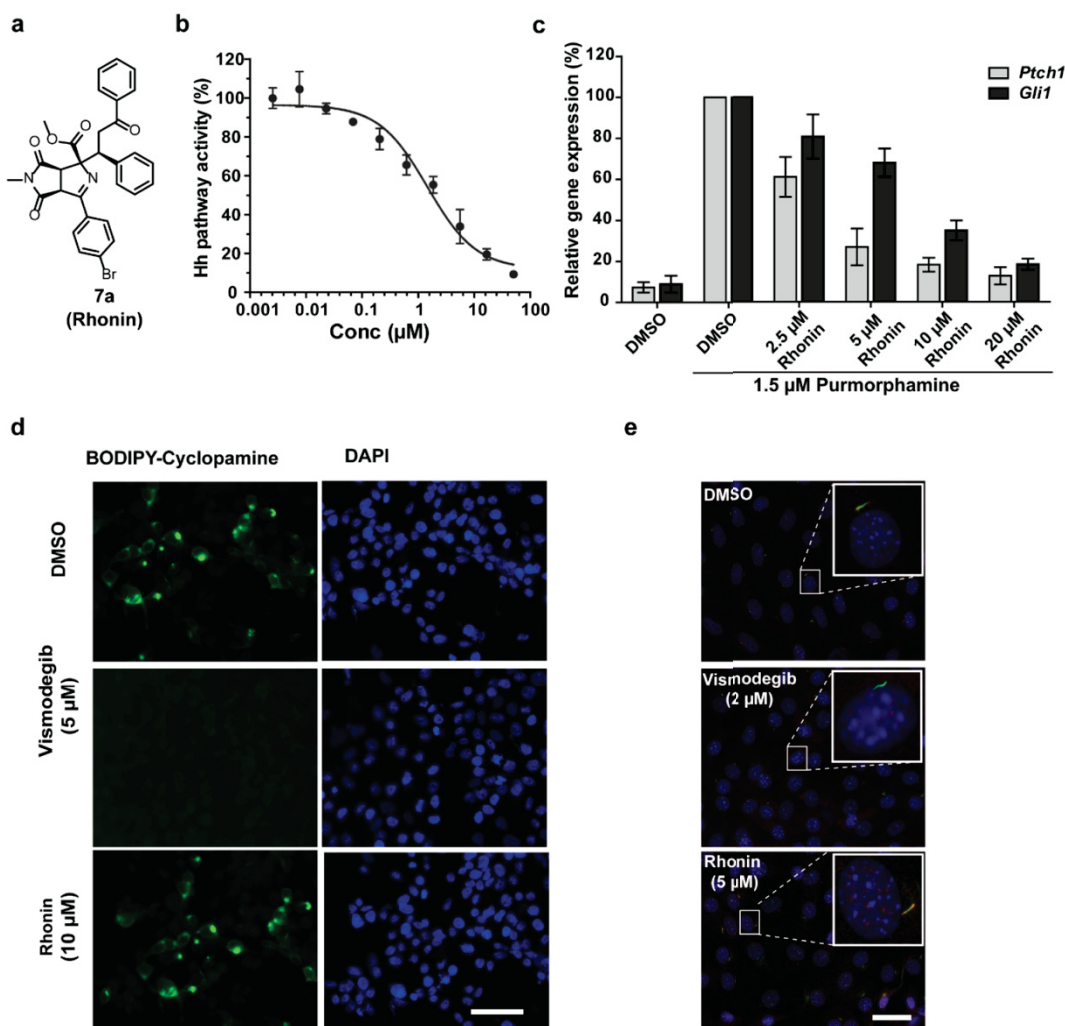
Figure 3. Rhonin inhibits GLI-dependent Hh signaling and acts downstream of SMO. (a) Structure of Rhonin (**7a**). **(b)** Rhonin inhibits GLI-dependent reporter gene expression in Shh-LIGHT2 cells. Cells were treated with 1.5 μM purmorphamine and different concentrations of the compound for 48 h. Firefly (fluc) and *Renilla* luciferase (rluc) activities were determined and ratios of fluc/rluc signals were calculated as a measure of Hh pathway activity. Nonlinear regression analysis was performed using a four parameter fit. All data are mean values of three independent experiments (n = 3) ± s.d. **(c)** C3H/10T1/2 cells were treated with purmorphamine (1.5 μM) and different concentrations of Rhonin or DMSO as a control for 48 h prior to isolation of total RNA. Following cDNA preparation, the relative expression levels of *Ptch1*, *Gli1* and *Gapdh* were determined by means of RT-qPCR. Expression levels of *Ptch1* and *Gli1* were normalized to the levels of *Gapdh* and were related to the value of purmorphamine-treated cells (set to 100 %). Data are mean values of three independent experiments (n = 3) ± s.d. **(d)** HEK293T cells were transiently transfected with SMO expressing plasmid or empty vector. 48 h later cells were treated with BODIPY-cyclopamine (5 nM, green) followed by addition of

10 μM of Rhonin or 5 μM vismodegib and DMSO as controls and incubation for 1 h. Cells were then fixed and stained with DAPI to visualize the nuclei (blue). Scale bar: 20 μm. (**e**) NIH/3T3 cells were serum starved to induce ciliation and treated with 1.5 μM purmorphamine for 2 h followed by addition of 2 μM vismodegib or 5 μM Rhonin, and further incubation for 12 h. Cells were then fixed and stained with DAPI to visualize the nuclei (blue), SMO was stained with an anti-SMO antibody (red) and cilia stained with an antibody against acetylated tubulin (Ac-tubulin, green). Insets: representative single cilia. Scale bar: 10 μm.
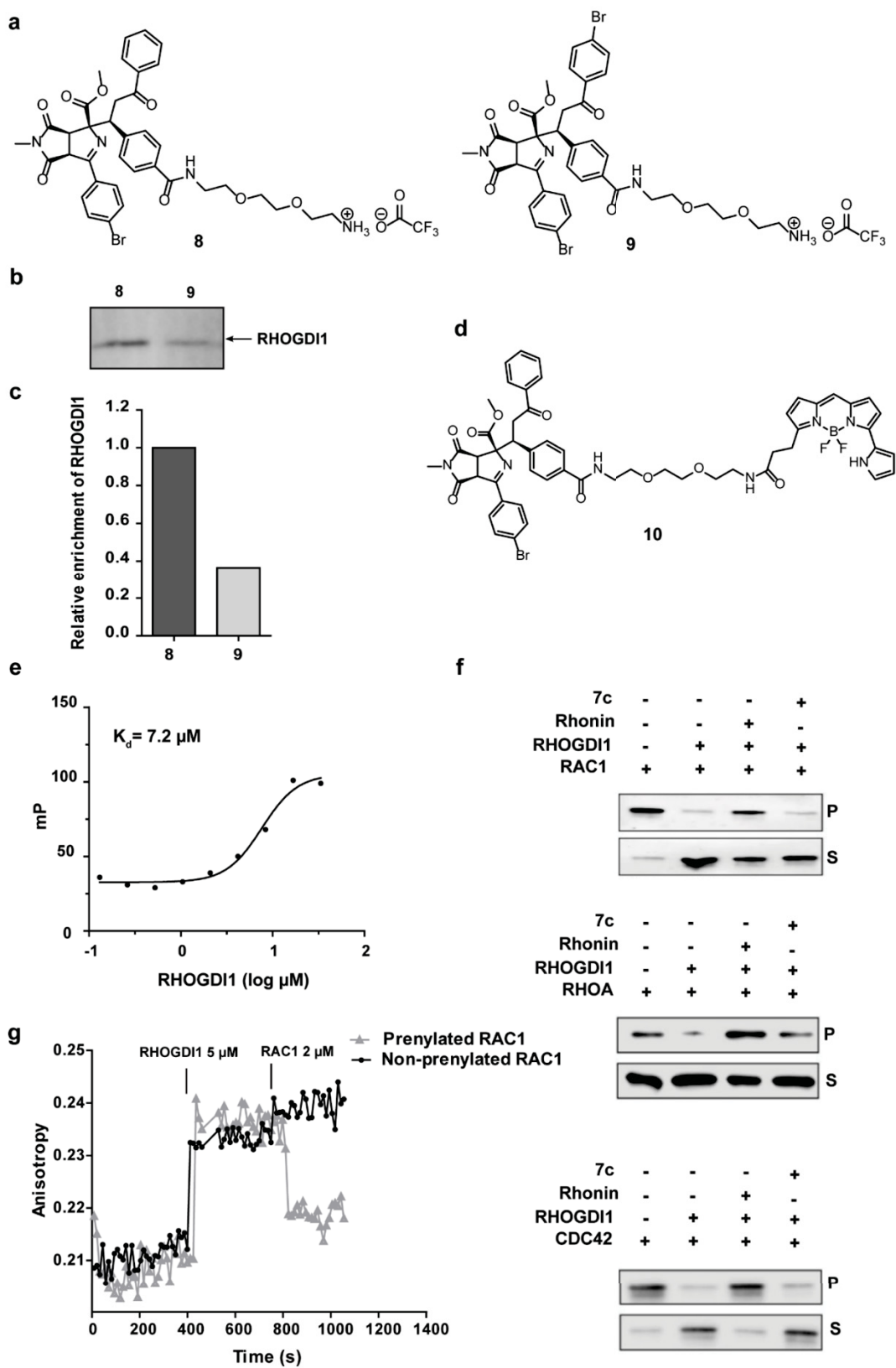
Figure 4. Rhonin is a RHOGDI1 inhibitor. (a) Structure of the affinity probes **8** and **9**. **(b)** Affinity-based enrichment of RHOGDI1 by probe **8** as compared to probe **9**. Active probe **8** and inactive probe **9** were immobilized on NHS ester magnetic beads and exposed to NIH/3T3 lysates. Bound proteins were eluted and analyzed by immunoblotting using a RHOGDI1-specific antibody. **(c)** Densitometric analysis of **(b)** for quantification of RHOGDI1 enrichment. Data is representative for three biological replicates. **(d)** Structure of the fluorescent Rhonin derivative **10**. **(e)** Binding of the Rhonin derivative **10** to RHOGDI1. Fluorescence polarization measurements were performed using **10** and titrating increasing concentrations of RHOGDI1. Data is representative of three independent experiments. **(f)** Displacement of prenylated GDP-bound RHO GTPases (RHOA, RAC1 and CDC42) from synthetic liposomes by GST-RHOGDI1 in the presence or absence of 50 μM Rhonin or inactive derivative **7c** was determined using a liposome sedimentation assay. Data is representative of three independent experiments. P: pellet; S: supernatant. **(g)** Competition of the Rhonin derivative **10** with RAC1. Fluorescence polarization measurements were performed by adding 2 μM prenylated RAC1 or non-prenylated RAC1 into a mixture of **10** and 5 μM RHOGDI1. Data is representative of three independent experiments.
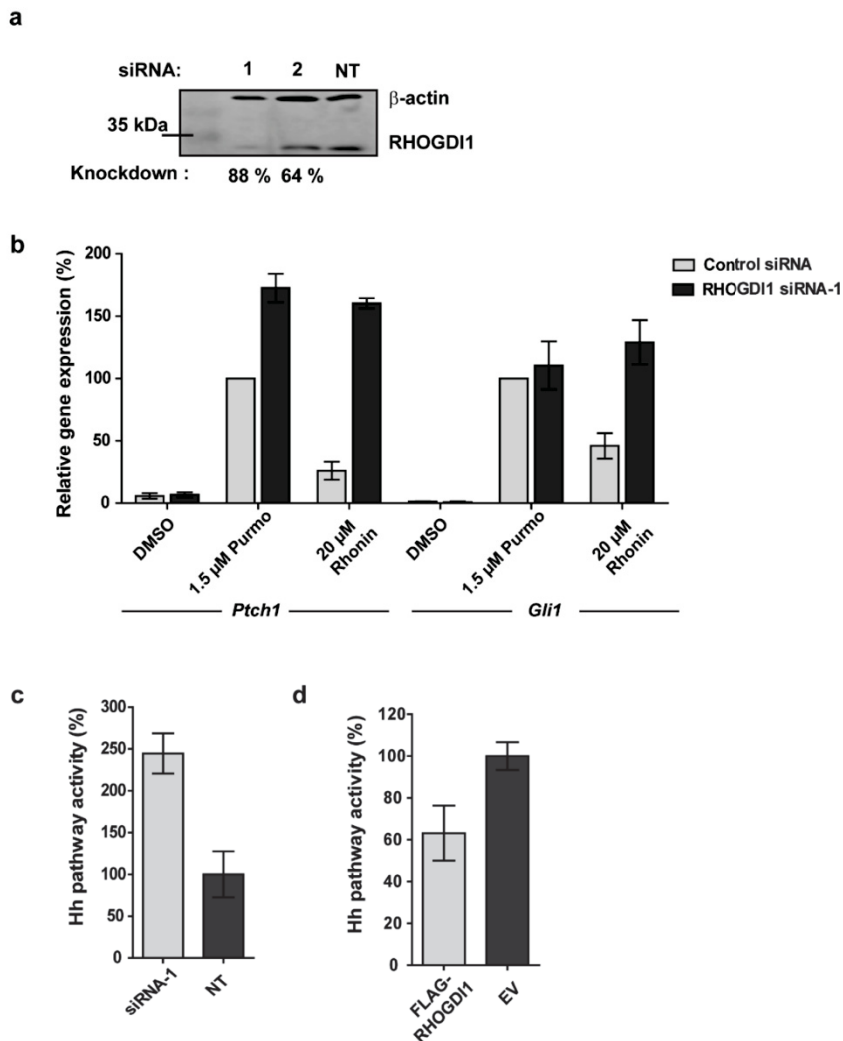
Figure 5. RHOGDI1 is a negative regulator of Hh signaling. (a) RHOGDI1 knockdown efficiency for siRNA-1 and siRNA-2 as used in **b** and Supplementary Figure S4**. (b)** NIH/3T3 cells were transfected with RHOGDI1 siRNA-1 or control siRNA. After 48 h cells were treated with purmorphamine (1.5 µM) and different concentrations of Rhonin or DMSO as a control for 48 h before isolation of total RNA. Following cDNA preparation, the relative expression levels of *Ptch1*, *Gli1* and *Gapdh* were determined by means of RT-qPCR. Expression levels of *Ptch1* and *Gli1* were normalized to the levels of *Gapdh* and are depicted as percentage of gene expression in cells activated with purmorphamine (100 %). All data are mean values of three independent experiments (n = 3) ± s.d. **(c)** C3H/10T1/2 cells were transfected with RHOGDI1 siRNA-1 and control siRNA. After 48 h the cells were treated with 1.5 µM purmorphamine and DMSO and osteoblast differentiation was monitored after 96 h. The Hh pathway activity in cells treated with purmorphamine and control siRNA was set to 100%. All data are mean values of three independent experiments (n = 3) ± s.d. See also Supplementary Figure 4a. **(d)**

C3H/10T1/2 cells were transfected with 800 ng FLAG-RHOGDI1 plasmid or empty vector. After 24 h the cells were treated with 1.5 µM purmorphamine and DMSO and osteoblast differentiation was monitored after 72 h. The Hh pathway activity in cells that were transfected with the empty vector and treated with purmorphamine was set to 100%. All data are mean values of three independent experiments (n = 3) ± s.d. See also Supplementary Figure 4b.
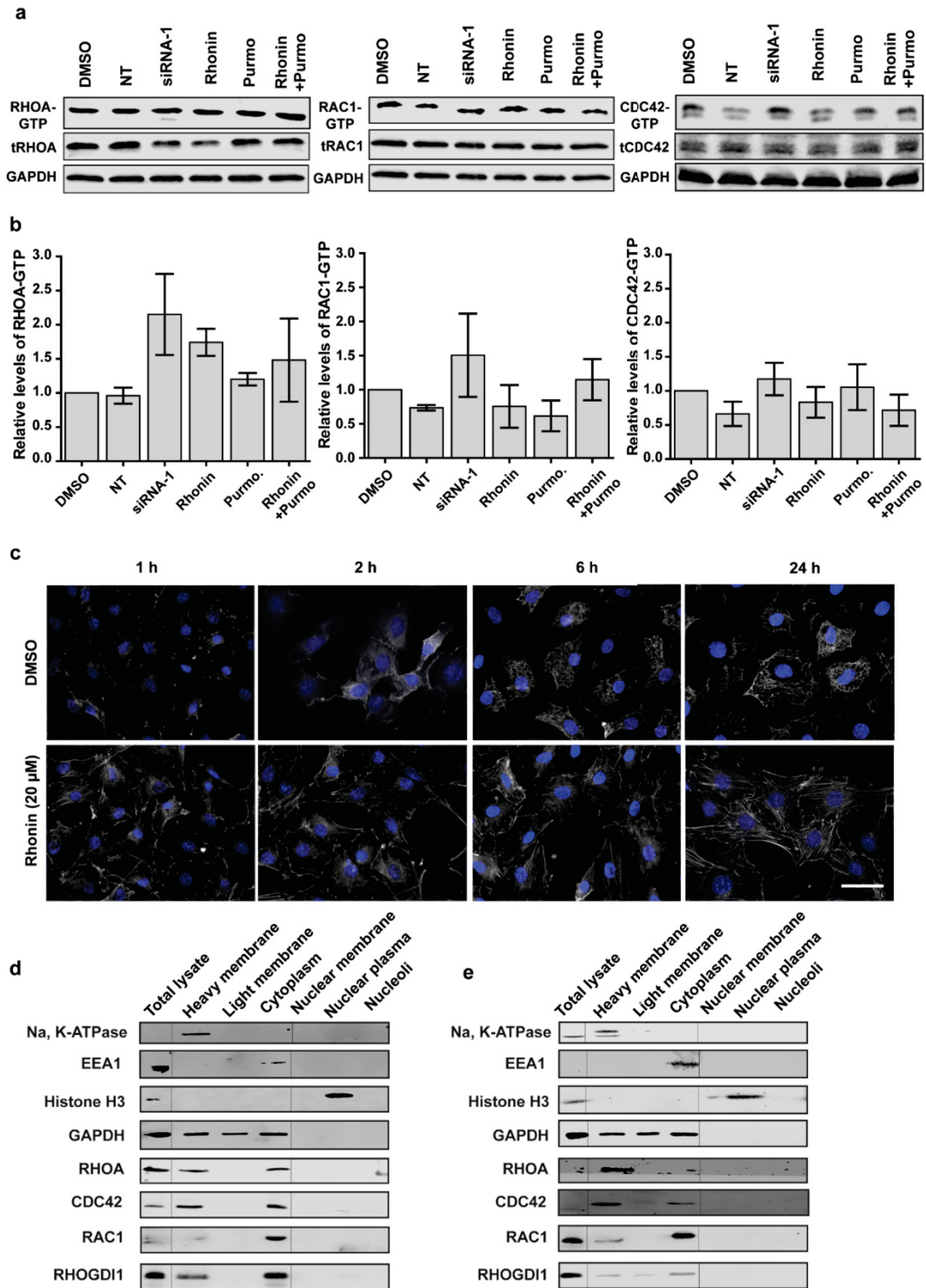
Figure 6. Influence of Rhonin on RHO GTPases in cells. (a) GST pull-down of GTP-bound RHOA, RAC1 and CDC42 by GST-fused effector proteins. GST-fused effector proteins of RHOA (Rhotekin) or RAC1 and CDC42 (PAK) were employed to enrich the GTP-bound GTPases in NIH/3T3 cells after RHOGDI1 knockdown by siRNA-1 and non-targeting siRNA (NT) or treatment with DMSO, Rhonin or purmorphamine. Proteins were detected by means of immunoblotting using specific antibodies for RHOA, RAC1 and CDC42. Data is representative of three independent experiments. **(b)** Densitometric quantification of the relative levels of RHOA-GTP, RAC1-GTP and CDC42-GTP after normalization to the total levels (t) of each GTPase and as compared to DMSO (set to 1). Data are mean values of three independent experiments (n = 3) ± s.d. **(c)** NIH/3T3 cells were serum starved for 48 h to inactivate RHO GTPases. Cells were then treated with DMSO or Rhonin for 24 h. Cells were fixed and stained with DAPI and phalloidin-rhodamine to visualize the nuclei (blue) and actin filaments (grey), respectively. Images are representative of three biological replicates. Scale bar: 10 μm. **(d** and **e)** NIH/3T3 cells were treated with DMSO (**d**) or Rhonin (**e**) and fractionated into six distinct fractions using ultracentrifugation. The fractions were analyzed using antibodies for RHOA, RAC1, CDC42 and for specific markers of each fraction including Na+/K+-ATPase (plasma membrane), EEA1 (endosomes), GAPDH (cytoplasm) and histone H3 (nuclear fraction). Data are representative of three independent experiments.

Online Methods

Chemistry

General information

Unless otherwise noted, all commercially available compounds were used as provided without further purifications. Dry solvents (THF, toluene) were used as commercially available; CH_2Cl_2 was purified by the Solvent Purification System *M-BRAUN Glovebox Technology SPS-800*. Solvents for chromatography were technical grade.

Analytical thin-layer chromatography (TLC) was performed on *Merck silica gel aluminium plates* with F-254 indicator. Compounds were visualized by irradiation with UV light or potassium permanganate staining. Column chromatography was performed using *silica gel Merck 60* (particle size 0.040-0.063 mm). Solvent mixtures are understood as volume/volume.

^{1}H-NMR and ^{13}C-NMR were recorded on a *Bruker DRX400* (400 MHz), *Bruker DRX500* (500 MHz) and *INOVA500* (500 MHz) using $CDCl_3$ or $(CD_3)_2SO$ as solvent. Data are reported in the following order: chemical shift (δ) values are reported in ppm with the solvent resonance as internal standard (CDCl3: δ = 7.26 ppm for ^{1}H, δ = 77.16 ppm for ^{13}C; $(CD_3)_2SO$: δ = 3.30 ppm for ^{1}H, δ = 39.52 ppm for ^{13}C); multiplicities are indicated br s (broadened singlet), s (singlet), d (doublet), t (triplet), q (quartet) m (multiplet); coupling constants (J) are given in Hertz (Hz).

High resolution mass spectra were recorded on a *LTQ Orbitrap* mass spectrometer coupled to an *Acceka HPLC*-System (HPLC column: *Hypersyl GOLD*, 50 mm x 1 mm, particle size 1.9 μm, ionization method: electron spray ionization). Fourier transform infrared spectroscopy (FT-IR) spectra were obtained with a *Bruker Tensor 27* spectrometer (ATR, neat) and are reported in terms of frequency of absorption (cm^{-1}). Optical rotations were measured in a *Schmidt + Haensch Polartronic HH8* polarimeter. The enantiomeric excesses were determined by HPLC analysis using a chiral stationary phase column (column: CHIRALCEL IC, eluent: (DCM/EtOH = 100/2) / *iso*-hexane). The chiral HPLC methods were calibrated with the corresponding racemic mixtures. The ratio of diastereomers was determined by 1H-NMR analysis. Chemical yields refer to pure isolated substances. Yields, enantiomeric excesses, and diastereoselectivity are given in the tables.

The chemicals and solvents were purchased from the companies Sigma-Aldrich, Acros Organics, ABCR and Alfa Aesar. (*Rp*)-2-(*tert*-Butylthio)-1-(diphenyl-phosphino)ferrocene (purity: 98%), Tetrakis(acetonitrile)copper(I) hexafluorophosphate (purity; 97%) and Tetrakis(acetonitrile)copper(I) tetrafluoroborate (purity: 97%) were purchased from Sigma-Aldrich.

General procedures

GP-1: General Optimized Procedure for the formation for double cycloaddition product 5:

Cu(CH$_3$CN)$_4$PF$_6$ (5 mol%) and (*R*)-Fesulphos (5 mol%) was transferred to a dry reaction vial with a stir bar and 0.5 mL of dry CH$_2$Cl$_2$ was added and stirred for 10 mins at rt. Then, first maleimide **1** (1 equiv) and azomethine ylide **2** (1.05 equiv) was successively added followed by the addition of Et$_3$N (20 mol%). The reaction mixture was left to stir at 0°C till the completion (0.5 – 1h) as monitored by TLC. After the completion of the cycloaddition, TBHP (70% aq. soln) (1.2 equiv) was added to the reaction mixture and left to stir at rt till completion (monitored by TLC). Then, all the volatiles were removed in vacuo and THF (1mL/0.1 mmol) was added to the reaction vial. To this solution, DBU (0.5 equiv) was added and finally, *N*-phenylmaleimide (3 equiv as solution in 0.5 mL THF) was added dropwise and stirred at rt till completion. The crude reaction mixture was directly put on the column and separated using EA/PE (40-80%) mixture. The products **5** are very weakly UV active but can be visualized using KMnO$_4$ stain.

GP-2: General Optimized Procedure for the formation for Michael Addition product 6 and 7:

Cu(CH$_3$CN)$_4$PF$_6$ (5 mol%) and (*R*)-Fesulphos (5 mol%) was transferred to a dry reaction vial with a stir bar and 0.5 mL of dry CH$_2$Cl$_2$ was added and stirred for 10 mins at rt. Then, maleimide **1** (1 equiv) and azomethine ylide **2** (1.05 equiv) was successively added followed by the addition of Et$_3$N (20 mol%). The reaction mixture was left to stir at 0°C till the completion (0.5 – 1h) as monitored by TLC. After the completion of the cycloaddition, TBHP (70% aq. soln) (1.2 equiv) was added to the reaction mixture and left to stir at rt till completion (monitored by TLC). Finally to this solution, base and *electrophile* **1'** was added and stirred at rt till completion. The crude reaction mixture was directly put on the column and separated using EA/PE (30-60%) mixture. The products **6/7** are UV active and can be visualized under standard UV lamp.

Biology

Materials

Dulbecco's Modified Eagle's medium (DMEM), **L**-glutamine, sodium pyruvate, penicillin/streptomycin, fetal bovine serum (FBS) and fetal calf serum (FCS) were obtained from PAN Biotech, Germany. The chemiluminescent substrate CDP-Star was purchased from Roche, Switzerland. Dual-Luciferase Reporter Assay System was obtained from Promega, USA. Anti-SMO rabbit Ab (#ab38686) and anti-β-actin rabbit polyclonal Ab (#ab8227) were purchased from Abcam, USA. Anti-N-acetylated tubulin mouse Ab (#T6793) was purchased from Sigma Aldrich, Germany. Anti-RHOGDI-1 mouse Ab (#sc-373724) was purchased from Santa Cruz Biotechnology, USA. Anti-Filamin-B polyclonal Ab (# PA5-21345) and anti-Filamin-C polyclonal Ab (# PA5-45573) were purchased from Thermo Fisher Scientific, Germany. Phalloidin coupled to TRITC was obtained from Sigma, Germany. Anti-rabbit-Alexa594 goat Ab (#A11012) and anti-mouse-Alexa488 donkey (#A21202) were purchased from Invitrogen, Germany. Anti-mouse-IR800 donkey Ab (#926-32212) and anti-rabbit-IR680 onkey (#926-68072) antibodies were obtained from LI-COR, Biosciences, USA. Anti Histone H3 rabbit Ab (#9715), anti RhoA (67B9) Rabbit Ab (#2117), EEA1 rabbit Ab (#2411), and Anti GAPDH (14C10) Rabbit Ab (#2118 S) were purchased from Cell Signaling Technologies. Anti-CDC42 Clone 44/CDC42 (RUO) mouse (# 610929) was purchased from Bioscience. Anti-Rac1 mouse Ab, clone 23A8 (# 05-389), and Anti-Na+/K+ ATPase (α Subunit) mouse Ab (#A276) was purchased from Merk.

pGEN-mSMO, was a gift from Philip Beachy, Addgene plasmid # 37673, Addgene, USA.[1] pCMV3-N-FLAG-mArhgdia (MG52485-NF) and pCMV3-N-Flag-NCV (CV016) were purchased from Sino Biologicals, Beijing, China. pGEX-4T1-Rhotekin-HR1 (aa. 1-89) and pGEX-2TK-PAK1-RBD (aa 57-141) were used as previously described [60]. siRNA duplexes (mouse Arhgdia (192662) siRNA 1 – CGACUGACCUUGGUAUGCA, J-064240-05-0002; mouse Arhgdia (192662) siRNA 2 – UCAAGUCGCGCUUCACAGA, J-064240-06-0002; non-targeting siRNA - UGGUUUACAUGUCGACUAA , D-001810-01-05) were purchased from GE Healthcare Europe GmbH, Germany.

Cell lines

NIH/3T3 cells were obtained from DSMZ, Germany (DSMZ ACC 59) and were cultured in DMEM (high glucose) supplemented with 10% heat-inactivated FCS, 2 mM L-glutamine and 1 mM sodium pyruvate. Shh-LIGHT2 cells (NIH/3T3 cells stably transfected with a Gli-responsive firefly luciferase reporter plasmid and a pRL-TK constituitive Renilla luciferase expression vector)[1] were cultured in the same culturing medium supplemented with 400 μg ml^{-1} G418 and 150 μg ml^{-1} Zeocin as selecting agents. The murine osteoblasts C3H/10T1/2 (ATCC CCL-226) were obtained from ATCC, USA and were cultured in DMEM (high glucose) supplemented with 10% heat-inactivated FCS, 6 mM L-glutamine, 1 mM sodium pyruvate. HEK293T cells (ATCC, England) were grown in DMEM containing 10% FBS,

100 U ml^{-1} penicillin and 0.1 mg ml^{-1} streptomycin. All cell lines were maintained at 37 °C and 5% CO_2 in a humidified atmosphere. All the cell lines were regularly assayed for mycoplasma and were confirmed to be mycoplasma-free. Transfection of DNA constructs and siRNAs were performed using Fugene HD (Promega), Lipofectamine® LTX (Invitrogen) and DharmaFECT™ (GE Healthcare) transfection reagent according to the manufacturer's directions.

Osteoblast differentiation assay

The osteoblast differentiation assay was performed by the Compound Management and Screening Center (COMAS) in Dortmund, Germany. C3H/10T1/2 cells were seeded (800 per well) in white 384-well plates. After incubation for 16 h, compounds or DMSO were added to a final concentration of 10 µM using the acoustic nanoliter dispenser ECHO 520 (Labcyte). One hour later, osteogenesis was induced with 1.5 µM purmorphamine. Plates were incubated for 96 h at 37 °C and 5% CO_2. Alkaline phosphatase activity was measured by replacing the medium with 35 µL osteogenesis-lysis buffer (lysis buffer: 100 mM Tris pH 9.5, 250 mM NaCl, 25 mM $MgCl_2$, 1% Triton X-100, sterile filtered) containing 1:100 chemiluminescent substrate CDP-Star® (Promega) for one hour in the dark at 25 °C. The luminescence was monitored using the Paradigm plate reader (Molecular Devices, USA). Dose-response analyses were performed for all hit compounds using a three-fold dilution series starting from a concentration of 30 µM. Half-maximal inhibitory concentrations (IC_{50}) were calculated using the Quattro software suite (Quattro Research, Planegg, Germany).

The effect of test compounds on the viability of C3H/10T1/2 cells was determined by CellTiter-Glo Luminescence cell viability assay (Promega). Cells were treated as described for the osteogenesis assay prior to addition of the CellTiter-Glo® reagent according to manufacturer's protocol. Compounds causing at least a 50% reduction in the osteogenesis assay and retaining cell viability of at least 80% were considered as hits. Dose-response analyses were performed for all hit compounds using a three-fold dilution series starting from a concentration of 30 µM. Half-maximal inhibitory concentrations (IC_{50}) were calculated using the Quattro software suite (Quattro Research GmbH).

GLI-dependent reporter gene assay

Shh-LIGHT2 cells were seeded (2.5×10^4 per well) in 96-well plates. After incubation for 16 h, medium was replaced by low serum-containing medium (0.5% FCS) supplemented with 1.5 µM purmorphamine. One hour later, various concentrations of the compounds or DMSO as a control were added and cells were further incubated for 48 h. Firefly and *Renilla* luciferase activities were determined by means of the Dual-Luciferase® Reporter Assay System (Promega) according to the manufacturer's protocol and luminescence was measured using the Infinite® M200 plate reader (Tecan, Austria).

SMO binding assay

HEK293T cells were seeded (1.5×10^4 per well) on poly-D-lysine-coated coverslips placed in a 24-well plate. 16 h later cells were transfected with the SMO expressing plasmid (pGEN-mSMO) using Fugene HD (Promega) according to the manufacturer's protocol. After 48 h of incubation at 37 °C, cells were washed once with PBS and incubated further in fresh DMEM medium containing 0.5% FBS, 5 nM BODIPY-cyclopamine and various concentrations of the test compounds or DMSO as a control. One hour later cells were washed twice with PBS and fixed with 3% paraformaldehyde for 10 min at room temperature and subsequently permeabilized with 0.1% (v/v) triton X-100 in PBS for 5 min at room temperature. Cells were then stained with 1 µg/ml DAPI for 10 min and were mounted on glass slides using Aqua Polymount (Polysciences Inc). Images were acquired on an Axiovert Observer Z1 microscope (Carl Zeiss, Germany) using a Plan-Apochromat 63x/1.40 Oil DIC M27 objective.

Additionally, SMO binding was confirmed by flow cytometry. HEK293T cells were seeded (3×10^5 per well) in 6-well plate and transfected with the SMO expressing plasmid pGEN-mSMO as described above. After 48 h of incubation the medium was replaced by DMEM containing 0.5% FBS, 5 nM BODIPY-cyclopamine and various concentrations of the test compounds or DMSO as a control. Following incubation for 5 h cells were washed once with PBS, detached using trypsin/EDTA (0.05/0.02% (v/v) in PBS), and collected by centrifugation at 250 x g for 5 min at room temperature. Cells were washed twice and then suspended in ice-cold PBS. Cell suspensions were subjected to flow cytometry analysis employing the BD LSR II Flow Cytometer (laser line: 488 nm, emission filter: 530/30) to detect the presence of BODIPY. Data analysis was performed using the FlowJo software, version 7.6.5 (Tree Star Inc., USA).

Immunofluorescence

To detect ciliary localization of SMO, NIH/3T3 cells (3×10^4 per well) were seeded on coverslis in 24-well plates and cultured for 16 h. Cells were then incubated for 12 h in DMEM containing 0.5% FCS to induce ciliation followed by treatment with 1.5 µM purmorphamine and various concentrations of the test compounds or DMSO as a control. 12 h later cells were washed with PBS followed by fixation in 4% ice-cold paraformaldehyde for 10 min. Permeabilization and blocking was performed with a solution containing 0.1% Triton X-100 and 1% heat-inactivated horse serum in PBS for 30 min at room temperature. Samples were then incubated with mouse anti-N-acetylated tubulin antibody (dilution 1:5000) as a marker for cilia and rabbit anti-SMO antibody (dilution 1:200) overnight at 4 °C followed by washing and subsequent incubation with Alexa Fluor 594-conjugated goat anti-rabbit and Alexa Fluor 488-conjugated donkey anti-mouse antibodies (1:500 dilutions) and DAPI (0.1 µg/mL) for 45 min at room temperature. Coverslips were washed and mounted using Aqua Polymount (Polysciences Inc).

Images were acquired with Axiovert Observer microscope Z1 (Carl Zeiss, Germany) using a Plan-Apochromat 63x/1.40 Oil DIC M27 objective.

For stress fiber staining, NIH/3T3 cells were cultivated in medium containing 0.5 % FCS for 24 h. Cells were then serum-starved for 24 h in serum-free medium to inactivate RHO GTPases. Cells were then treated with DMSO or 20 μM Rhonin for 24 h and incubated at 37 °C. Cells were washed and fixed with 3% paraformaldehyde for 10 min at room temperature and subsequently permeabilized with 0.1% (v/v) triton X-100 in PBS in 1x PBS for 5 min at room temperature. Cells were stained with 0.5μg/mL Phalloidin-TRITC and 1 μg/mL DAPI for 30 min and were mounted on glass slides using Aqua Polymount (Polysciences Inc). Images were acquired on an Axiovert Observer Z1 microscope (Carl Zeiss, Germany) using a Plan-Apochromat 63x/1.40 Oil DIC M27 objective.

Reverse transcription- quantitative PCR (RT-qPCR)

C3H10T1/2 cells were seeded (2×10^4 per well) in 24-well plates. 16 h later cells were treated with 1.5 μM purmorphamine and the test compounds or DMSO for 48 h. Total RNA was isolated using the RNeasy mini kit (Qiagen) according to the manufacturer's protocol. The concentration of purified RNA was determined by means of the Nanodrop 2000. 500 ng total RNA was used to prepare complementary DNA (cDNA) using QuantiTect Reverse Transcription Kit (Qiagen) according to the manufacturer's protocol. The expression of Hh target genes *Ptch1* and *Gli1* and the reference gene *Gapdh* was determined by means of quantitative PCR using the QuantiFast SYBR Green PCR Kit (Qiagen) and iQ 5 Real-Time PCR Detection System (Bio-Rad) and the following oligonucleotides: *Ptch1*: 5'-CTCTGGAGCAGATTTCCAAGG-3' and 5'-TGCCGCAGTTCTTTTGAATG-3', *Gli1*: 5'-GGAAGTCCTATTCACGCCTTGA-3' and 5'-CAACCTTCTTGCTCACACATGTAAG-3', *Gapdh*: 5'-AGCCTCGTCCCGTAGACAAAAT-3' and 5'-CCGTGAGTGGAGTCATACTGGA-3'. The expression levels of *Ptch1* and *Gli1* were determined using the $2^{-\Delta\Delta Ct}$ method.[2]

Knockdown of RHOGDI1

Which cells were transiently transfected with RHOGDI1 siRNA-1 or siRNA-2 and non-targeting siRNA using DharmaFECT™ reagent by employing the manufacturer's protocol. Briefly, NIH/3T3 cells were seeded in T25 cell culture flask. Upon reaching ca. 70 % confluence, cells were transiently transfected with DharmaFECT™ transfection reagent. For the transfection, siRNAs and DharmaFECT™ transfection reagent were independently mixed with Opti-MEM® serum-free media in low-binding tubes and incubated for 5 min at room temperature. Subsequently, the lipid solution was added to the siRNA solution in the ratio 1:1 and incubated for 20 min at room temperature. The corresponding lipid:siRNA solution was diluted 1:5 with the respective cell culture medium and was added to cells , which were seeded on the previous day, by replacing the old medium and incubated for 48 h at 37 °C. Cells were detached and reseeded at 20,000 cells per well in 24-well plate for determining the target gene

expression upon RHOGDI1 knockdown. Knockdown efficiency was determined by immunoblotting using anti-RHOGDI1 specific antibodies.

Immunoblotting

Unless otherwise mentioned, the cells were lysed in 1X SDS buffer without bromophenol blue. The resulting lysates were analyzed by DC Assay (Bio-Rad) for protein concentrations determination. The cell lysates were then supplemented with bromophenol blue and boiled at 95 °C for 10 min. The cooked proteins were loaded on 10% polyacrylamide gels and run at a constant voltage of 80 V for 15 min followed by 120 V for approximately 1.5 h. Protein were transferred on PVDF membrane using semi-dry transfer at 25 V for 45 min. Membranes were washed and blocked in LI-COR blocking buffer for 1 h at room temperature. The blocking buffer was replaced with fresh LI-COR blocking buffer containing primary antibodies and incubated overnight at 4 °C. Membranes were washed with TBS-T (3 x 5 min) and incubated with the secondary antibody in blocking buffer for one hour at room temperature. Signals were visualized using Odyssey Fc imaging system (LI-COR Biosciences). Quantification of band intensities was performed by densitometry of scanned signals with the aid of image studio software (Version 4.0.21, LI-COR Biosciences, ©2014).

RHOGDI1 overexpression

C3H10T1/2 cells were transiently transfected with pCMV3-N-FLAG-mArhgdia or pCMV3-N-Flag-NCV using Lipofectamine® LTX & PLUS ™ reagent according to manufacturer's protocol. Briefly, C3H10T1/2 cells were seeded in a T25 cell culture flask and incubated overnight at 37 °C and 5% CO_2. For the transfection, plasmid DNA and PLUS reagent were diluted in Opti-MEM® medium and incubated for 5 min at room temperature. Lipofectamine® LTX reagent was directly added to this mixture and incubated for 30 min at room temperature. The DNA-lipid complex was added dropwise to the cells in the flask and incubated for 24 h. Cell were then detached and reseeded at 5,000 cells per well in 96-well plate for determining the effect of RHOGDI1 overexpression on osteoblast differentiation as described above.

Cell lysate preparation for chemical proteomics

NIH/3T3 cells were grown to 90-95% confluence and were then detached using cell dissociation solution for 5 min at 37 °C and 5% CO_2. Cells were suspended in cell culture medium and pelleted by centrifugation at 250 x g, 5 min at 4 °C. Cell pellets were then washed thrice with ice-cold PBS and lysed in lysis buffer containing 50 mM PIPES, 50 mM NaCl, 5 mM $MgCl_2$, 5 mM EGTA, 0.1 % NP40, 0.1 % Triton X-100, 0.1 % Tween®20, with freshly added 1 mM DTT, EDTA-free protease inhibitors (Complete EDTA-free, Roche) and phosphatase inhibitors (PhosphoSTOP, Roche). To assure complete cell lysis, the suspension was passed through 0.9 μm and 0.45 μm cannula 10 times each and incubated on ice for 40 min with intermittent vortexing every five minutes until a homogeneous mixture was

obtained. The resulting homogenate was centrifuged at 18,000 x g for 30 min at 4 °C and the supernatant was subsequently snap frozen in liquid nitrogen and stored at -80 °C. Total protein content was determined by DC protein assay (Bio-Rad, Germany).

Affinity chromatography enrichment of compound-bound proteins

25 µL N-hydroxysuccinimide magnetic beads (GE Healthcare) were activated with 500 µL 1 mM HCl for 1 min. HCl was replaced by 500 µL coupling buffer (0.15 M triethanolamine, 0.5 M NaCl, pH 8.3) containing 10 µM of free amine affinity probes (S11a and S11b) and incubated for 2 h at room temperature with overhead rotation. The residual active groups of N-hydroxysuccinimide magnetic were quenched by alternating incubation with 500 µL block A buffer (0.5 M ethanolamine, 0.5 M NaCl, pH 8.3) and block B buffer (0.1 M sodium aceate, 0.5 M NaCl, pH 4.0) for 5 min three times each. For protein binding, the magnetic beads were equilibrated with 500 µL lysis buffer followed by incubation with 500 µL lysate (protein concentration: 2 mg/mL) 2 h at 4 °C with overhead rotation. In order to wash out non-specifically bound proteins, the beads were first washed with 500 µL lysis buffer containing 25 mM MgCl$_2$ followed by three times washing with 500 µL PBS. Tryptic digestion of bead-bound proteins was carried out in two stages. First, bound proteins were reduced by incubating the beads with 50 µL reducing buffer (1 mM DTT, 8 M urea in 50 mM Tris (pH 7.5)) at 30 °C for 30 min with shaking. Later, the reduced proteins were alkylated by addition of 5.5 µL alkylating solution (1 mM DTT, 50 mM chloroacetamide, 8 M urea in 50 mM Tris pH 7.5) and further incubation in the dark at 30 °C for 30 min while shaking at 350 rpm. The reduced and alkylated proteins were digested by adding 1 µg LysC at 37 °C for 1 h while shaking at 350 rpm. The supernatant was transferred to a new tube and the beads were further incubated with 50 mM Tris-HCl (pH 7.5) containing 1 µg trypsin at 37 °C for 1 h while shaking at 350 rpm. Both supernatants were combined together and further digested by adding 2 µg trypsin for 16 h at 37 °C with continuous shaking. The enzymatic digestion was stopped by addition of 2 µL proteomics grade trifluoroacetic acid (TFA). In order to purify the resulting peptides, STAGE tips were prepared by loading the 200 µL microtips with two layers of C18 (octadecyl) disks. The tips with C18 disks were activated by addition of 100 µL methanol. Furthermore, the tips were calibrated by washing with 100 µL Buffer B (20% H$_2$O / 80% acetonitrile with 0.1% formic acid) and 100 µL Buffer A (H$_2$O with 0.1% formic acid). The peptide purification was achieved by passing the digestion solution over the activated STAGE tips. Bound peptides were eluted twice using 20 µL Buffer B and the solvent was evaporated by means of rotary speed vacuum evaporator.

Mass spectrometry and data evaluation

In order to analyse the tryptic peptides, the samples were purified by UltiMate™ 3000 RSLC nano system (Dionex, Germany) and MS/MS analysis was carried out using Q Exactive™ HF Hybrid Quadrupole-Orbitrap Mass Spectrometer equipped with a nano-spray source (Nanospray Flex Ion

Source, Thermo Scientific). Briefly, the tryptic peptides were solubilized in 20 µL 0.1% (v/v) TFA in water and 3 µL were injected onto a pre-column cartridge (5 µm, 100 Å, 300 µm ID * 5 mm, Dionex, Germany) using 0.1% (v/v) TFA in water as eluent with a flow rate of 30 µL/min. Desalting was performed for 5 min with eluent flow through followed by back-flushing of the sample during the whole analysis from the pre-column to the PepMap100 RSLC C18 nano-HPLC column (2 µm, 100 Å, 75 µm ID × 50 cm, nanoViper, Dionex, Germany) using a linear gradient starting with 95% water containing 0.1% (v/v) formic acid / 5% (v/v) acetonitrile containing 0.1% (v/v) formic acid and increasing to 70% water containing 0.1% (v/v) formic acid / 30% (v/v) acetonitrile containing 0.1% (v/v) formic acid after 95 min using a flow rate of 300 nL/min. The nano-HPLC was coupled to the Quadrupole-Orbitrap Mass Spectrometer using a standard coated SilicaTip (ID 20 µm, Tip-ID 10 µM, New Objective, Woburn, MA, USA), mass range of m/z 300 to 1650 was acquired with a resolution of 60000 for a full scan, followed by up to ten high energy collision dissociation (HCD) MS/MS scans of the most intense at least doubly charged ions with a resolution of 15000.

Data evaluation was performed using MaxQuant software[3] (v.1.5.3.30) including the Andromeda search algorithm and searching the mouse reference proteome of the Uniprot database. Briefly, the search was performed for full enzymatic trypsin cleavages allowing two miscleavages. For protein modifications carbamidomethylation was chosen as fixed and oxidation of methionine and acetylation of the N-terminus as variable modifications. The mass accuracy for full mass spectra was set to 20 ppm for the first and 4.5 ppm for the second search. The mass accuracy for MS/MS spectra was set to 20 ppm. The false discovery rates for peptide and protein identification were set to 1%. Relative quantification of proteins was carried out using the label-free quantification algorithm implemented in MaxQuant. Further data evaluation was performed using Perseus software[4] (v. 1.5.2.6). Proteins not identified with at least two peptides in at least one of the samples and known contamination were filtered off. Samples resulting from pulldown using the active probe were grouped together and those from the pulldown using the inactive one as well. Label-free quantification (LFQ) intensities were logarithmized (log2) and proteins, which were not three times quantified in at least one of the groups, were filtered off. Missing values were imputed using small normal distributed values (width 0.3, down shift 1.8) and a two sided t-test (s0 = 1, FDR 0.05) was performed. Proteins which were statistically significant enriched by the active probe compared to the inactive one were considered as hits.

Fluorescence polarization

The binding to Rhonin to RHOGDI1 was confirmed by fluorescence polarization experiments. RHOGDI1 was titrated against 5 µM of the fluorescent Rhonin derivative **10** in buffer containing 20 mM Hepes, pH 7.4, 150 mM NaCl, 5 mM MgCl$_2$, 3 mM DTT and incubated for 1 h. The change in fluorescence polarization was monitored at an excitation / emission wavelength of 535 nm and 593

nm, respectively. To understand the impact of geranylgeranyl moiety on the interaction of RHOGDI and RAC1, 5 μM RHOGDI was added to 2 μM fluorescent Rhonin in buffer containing 20 mM HEPES, pH 7.4, 150 mM NaCl, 5 mM MgCl₂, 3 mM DTT, led to increase in anisotropy signal. 2 μM of prenylated/ or non-prenylated RAC1 were added in two independent experiments. Geranygeranylated RAC1 (GerGer-RAC1) was dissolved in a buffer containing 1% CHAPS and 0.5% sodium cholate.

To determine the effect of Rhonin on the binding of RHOGDI1 to non-prenylated RAC1-GDP, fluorescence polarization measurements were performed by titrating 1 μM TAMRA-GDP-bound RAC1 with increasing concentrations of RHOGDI1 in the presence and absence of 50 μM Rhonin in buffer containing 30 mM Tris-HCl, pH 7.5, 150 mM NaCl, 5 mM MgCl₂, 1% DMSO. The change in the fluorescence polarization was monitored at an excitation and emission wavelengths of 557 nm and 583 nm, respectively.

Competition-based fluorescence polarization were performed by titrating Rhonin with 30 nM fluorescein-labelled atorvastatin and 60 nM His6-tagged PDEδ in PBS buffer containing 0.05% CHAPS,1% DMSO.

Liposome sedimentation assay

Liposomes were prepared by self-assembly of the lipids (500 μg) containing 20% (w/w) phosphatidylethanolamine, 45% (w/w) phosphatidylcholine, 20% (w/w) phosphatidylserine, 10% (w/w) cholesterol, and 5% (w/w) phosphatidylinositol 4,5-bisphosphate. 1 μM. Liposome assays were performed by mixing, sonicating (20 s with minimal power, 50% off and 50% on) and extruding (0.2 μM filter) the lipids in 300 μl of a buffer, containing 20 mM HEPES-NaOH pH 7.4, 50 mM NaCl, 3 mM DTT, 5 mM MgCl₂. GerGer-RAC1-GDP was added to the liposomes and incubated for 20 min on ice. 1.5 μM GST-RHOGDI-1 and the compounds or DMSO were added to the liposome-GerGer-RAC1-GDP complex prior to incubation on ice for 30 min. The samples were centrifuged at 20,000 x g for 30 min at 4 °C. The resulting pellet and supernatant fractions were collected and analyzed by immunoblotting. 10 μl of each sample leaded on a SDS-PAGE gel for Western blotting. Specific antibodies were used to visualize RAC1, CDC42 and RHOA.

Liposome flotation assay

10 μM of GerGer-RAC1-GDP was added to liposomes suspended in flotation assay buffer containing 20 mM HEPES-NaOH pH 7.4, 50 mM NaCl, 3 mM DTT, 5 mM MgCl2, and incubated for 20 min on ice. The liposomes were prepared by using self-assembling the lipids (500 μg), containing 15% (w/w) phosphatidylethanolamine, 0.5% (w/w) NBD-PE (N-(7-nitrobenz-2-oxa-1,3-diazol-4-yl)-1,2-dihexadecanoyl-sn-glycero-3-phosphoethanolamine, triethylammonium salt), 45% (w/w)

phosphatidylcholine, 20% (w/w) phosphatidylserine, 10% (w/w)cholesterol, and 5% (w/w) phosphatidylinositol 4,5-bisphosphate. 15 μM of GST-RHOGDI-1 and compounds or DMSO was added to liposome-GerGer-RAC1-GDP complex and samples were further incubated on ice for 30 min. The samples were added to 30% (w/v) sucrose solution. The resulting suspension was overlaid with protein buffer containing 25% (w/v) sucrose and finally with 50 μl of buffer without sucrose. The resulting samples were centrifuged at 140000 x g for 1 h at 4 °C. The upper liposome-containing phase (detected by fluorescent NDB-PE) was collected and analyzed by immunoblotting.

Surface plasmon resonance (SPR)

Biacore® X100 instrument (Biacore, now GE Healthcare) was used to analyze the effect of Rhonin on the GerGer-RAC1-GDP and RHOGDI-1 interaction. Liposomes suspended in SPR buffer (20 mM HEPES, pH 7.4, 50 mM NaCl, 5 mM MgCl2, 3 mM DTT) were immobilized by injecting 0.5 mM liposomes with flowrate of 5 μL/min on the surface of a Pioneer® L1 sensor chip (GE Healthcare) for the period of 900 s, as indicated by a constant signal. Unbound liposomes were removed by passing the buffer and 10 mM NaOH with flowrate of 5 μL/min for 30 s over the sensor chip. Buffer containing 15 μM GerGer-RAC1-GDP was passed with flowrate of 5 μL/min over the immobilized liposomes to facilitate the loading of GerGer-RAC1-GDP on to the liposomes. The effect of compounds on the association of GerGer-RAC1-GDP with liposomes and the resulting dissociation of GerGer-RAC1 upon passing 25 μM of RHOGDI-1 was monitored by the change in the response unit signal.

Protein expression and purification

Human Rhotekin HR1 (aa. 1-89) and human PAK1-RBD (aa. 57-141) encoded on pGEX vectors were expressed over night as GST fusion proteins in E. coli BL21 (DE) after induction of 0.2 mM IPTG. These RHO effectors were extracted by cell lysis performed by sonication of the cells. After centrifugation of the cellular debris the supernatant was used to attach the GST-fused effector proteins to the GSH Sepharose beads [60].

Insect cell purification system was used for expression and purification of prenylated proteins based on an established protocol [61]. *Sf*9/or *TNAO*38 insect cells were grown to the level of 1.5×10^6 cells/ml before they were transduced with Baculoviruses encoding genes related to the RHO GTPases. Cells were resuspended in lysis buffer, containing 20 mM HEPES-NaOH pH 7.4, 150 mM NaCl, 2 mM β-mercaptoethanol, 5 mM MgCl₂, 0.1 mM GDP, 10 mM imidazole and the optimized detergents including 1% CHAPS and 0.5% sodium cholate [61]. Cells were lysed by sonication in ice. After centrifugation for 20 min in 20000 x g, supernatants were collected and loaded on a Ni-NTA column (Qiagen, Hilden, Germany). The protein was eluted by passing a buffer containing 300 mM imidazole into the Ni-NTA column. The eluted solution was further purified on an analytical Superdex 75 column (10/300 GL, GE-Healthcare, Uppsala, Sweden) using 20 mM HEPES-NaOH pH 7.4, 150 mM NaCl, 3 mM DTT, 5 mM

MgCl$_2$ and 0.5% (w/v) Na-cholate as buffer system. Non-prenylated RAC1 and human RHOGDI1 were prepared from *E. coli* as a GST recombinant protein as described previously [61].

Pull down of active RHO GTPases

Pull-down of active (i.e., GTP-bound) RHO GTPases was performed by using GSH sepharose beads (GE Healthcare, UK) from NIH/3T3 total cell lysates. NIH/3T3 cells were treated with DMSO, purmorphamine and/or, Rhonin for 24 h or transfected with RHOGDI1 siRNA-1 or non-targeting siRNA. RHO GTPases were obtained by lysis of 15 cm cell dishes with 500 µl Fish buffer (50 mM Tris/HCl pH 7.4, 100 mM NaCl, 2 mM MgCl$_2$, 1% Igepal Ca-630, 10% glycerol, 20 mM beta-glyceolphosphate, 1 mM sodium orthovanadate, cOmplete™, EDTA-free Protease Inhibitor Cocktail (Roche, Basel, Switzerland)). GSH Sepharose beads were washed three times with 1 ml Fish buffer. Equal amounts of bacterial lysates containing GST (negative control) or GST-fused effector proteins were added to the GSH Sepharose beads and incubated at 4°C for 1 h followed by another three times washing with 1 ml of Fish buffer. Thereafter, the total cell lysate obtained from one 15-cm dish was added to the GST beads and incubated for 30 min at 4°C. Samples were washed three times with 1 ml Fish buffer. Laemmli buffer was added into the samples before heat denaturation for 10 min at 95°C. The protein-protein interaction was analyzed by SDS-PAGE and immunoblotting. Data were evaluated using GraphPad Prism 6 software. For variance analysis ordinary one-way analysis of variance test was performed using the Dunnett's multiple comparison test. Results were considered significant with $p < 0.05$. (*($p < 0.05$), ** ($p < 0.01$), *** ($p < 0.001$), **** ($p < 0.0001$).

Sub-cellular fractionation

NIH/3T3 cells were treated with 10 µM Rhonin or DMSO for 24 h. The cells were collected from the culture dishes by trypsinization and scraping out the cells. After centrifugation step, the pellet was washed three times with PBS and was resuspended in a detergent-free lysis buffer containing 10 mM Tris/HCl (pH 7.4), 10 mM NaCl, 0.5 mM MgCl$_2$, and EDTA-free protease inhibitor. The total cell lysate was centrifuged at 1200 x g for 5 min at 4 °C after homogenization by using an insulin syringe. The supernatant was collected and further subjected to a 16,000 x g centrifugation to isolate the heavy membrane pellet and cytoplasm and light membrane in the supernatant. The cytosolic supernatant was divided into Light membrane and cytoplasm by applying 130,000 x g centrifugation for 90 minutes. The nuclear pellet was resuspended in 250 mM sucrose solution containing 10 mM MgCl$_2$ which were layered on top of an 880 mM sucrose cushion containing 0.5 mM MgCl2. Nuclear fraction was centrifuged at 1,200 x g for 10 minutes to obtain the intact nuclear. The intact nuclear was homogenized using a Balch homogenizer (clearance of 8 mm) and 8-10 up-and-down strokes and later were separated to nucleoli and nucleoplasm fractions [62]. The nucleoplasm and nuclear membrane were separated by centrifugation of nuclear fraction at 130,000 x g for 90 minutes. The resulting pellet

contained the nuclear membrane and the supernatant contained the nucleoplasm fraction. All subcellular fractionation steps were carried out at 4°C. Protein concentrations of all fractions were determined by the Bradford assay and all fractions were mixed with 5x SDS-PAGE loading buffer. The separated fractions were analyzed by specific marker for each fraction and the protein localization was analyzed by applying immunoblotting.

Chapter VII

Inhibition of the Dbl-Family Member Vav3 by the Small Molecule IODVA1 Impedes Rac Signaling and Overcomes Resistance to Tyrosine Kinase Inhibition in Lymphoblastic Leukemia

Graphical abstract
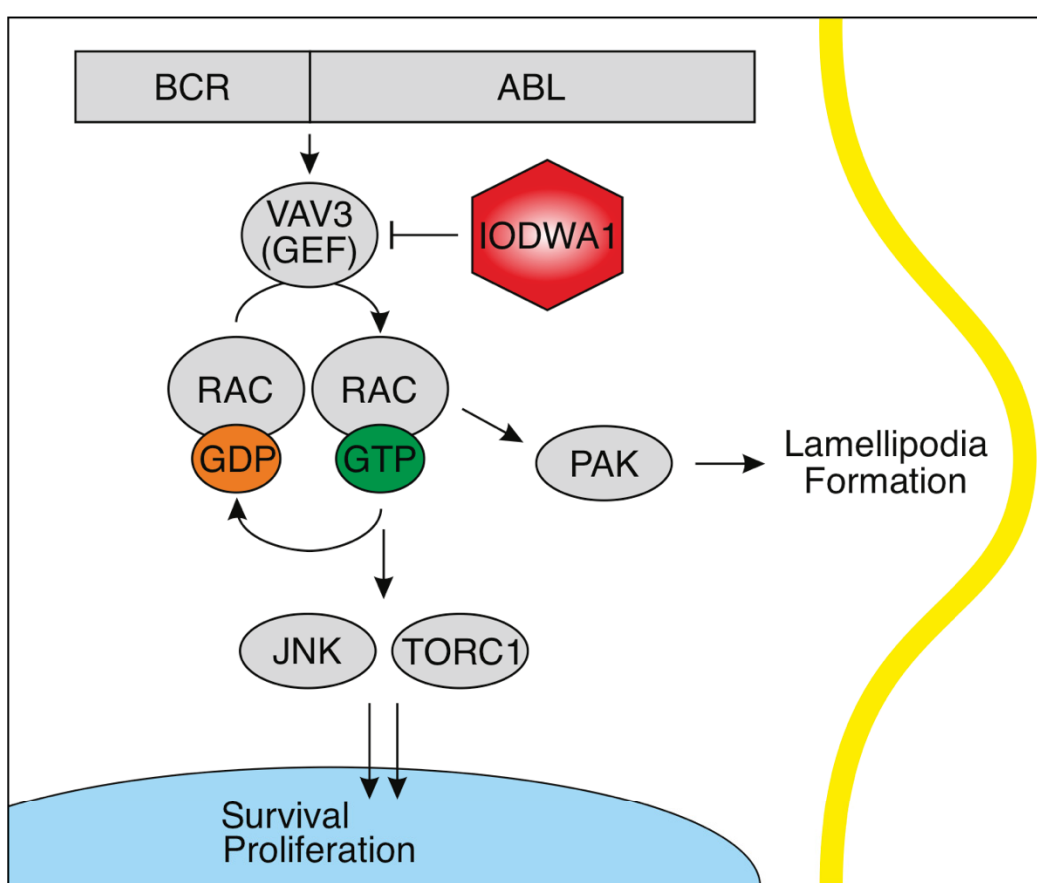
Status:	In preparation
Impact factor:	none
Own proportion to this work:	10 %

Expression and purification of RAC1 effectors, RAC1 GTP pull down assays, writing the manuscript.

Inhibition of the Dbl-Family Member Vav3 by the Small Molecule IODVA1 Impedes Rac Signaling and Overcomes Resistance to Tyrosine Kinase Inhibition in Lymphoblastic Leukemia

Shailaja Hegde [1,2], Anjelika Gasilina [1], Mark Wunderlich [1], Yuan Lin [1], Gurdat Premnauth [3], Edward Merino [3], Marcel Buchholzer [4], Oliver H.F. Krumbach [4], Mohammad Akbarzadeh [4], Mohammad Reza Ahmadian [4], William Seibel [5], Yi Zheng [1,6], Benjamin Mizukawa [1], Lisa Privette Vinnedge [5,6], José A. Cancelas [1,2,6], and Nicolas N. Nassar [1,6*]

[1]: Division of Experimental Hematology and Cancer Biology, Children's Hospital Research foundation, 3333 Burnet Ave, Cincinnati, OH 45229

[2]: Hoxworth Blood Center, University of Cincinnati Academic Health Center, OH, USA

[3]: Department of Chemistry, University of Cincinnati, 404 Crosley Tower, Cincinnati, Ohio 45221

[4]: Institute of Biochemistry and Molecular Biology II, Medical Faculty, Heinrich-Heine-University, Düsseldorf 40225, Germany

[5]: Division of Oncology, Cincinnati Children's Hospital Medical Center, Cancer and Blood Diseases Institute, 3333 Burnet Ave, Cincinnati, OH 45229

[6]: Department of Pediatrics, University of Cincinnati College of Medicine, 3230 Eden Ave, Cincinnati, OH 45267

*: To whom correspondence should be addressed at nicolas.nassar@cchmc.org

Summary

Aberrant activation of Rho guanine nucleotide exchange factors (RhoGEFs) is a chief mechanism driving abnormal activation of their RhoGTPase targets in transformation and tumorigenesis. Consequently, small molecule inhibitor of RhoGEF activities can be used as an anti-cancer drug. Here, we used cellular, mouse, and humanized models of Rac-dependent BCR-ABL1-driven leukemia to identify Vav3, the tyrosine phosphorylation–dependent RacGEF as the target of the small molecule IODVA1. We show that IODVA1 binds tightly to Vav3, inhibits Rac activation and signaling, and increases pro-apoptotic activity in BCR-ABL expressing cells only. Consistent with this mechanism of action, Vav3-deficient leukemic cells and mouse models of BCR-ABL leukemia do not respond to IODVA1. Importantly, IODVA1 eradicates leukemic propagating activity of TKI-resistant BCR-ABL1(T315I) B-ALL cells after treatment withdrawal by decreasing Rac signaling in vivo. Cells representing pediatric ALL patients are highly sensitive to IODVA1 ex vivo. IODVA1 thus spearheads a novel class of drugs that inhibits a RacGEF and holds promise as an anti-tumor therapeutic agent.

Keywords: Rac, RacGEF, Vav3, Philadelphia chromosome positive (Ph+), Ph-like, TKI-resistance, drug discovery, small molecule inhibitor, Ras-driven cancer, leukemia, BCR-ABL, pediatric ALL.

Introduction

RacGTPases (Rac1, Rac2, Rac3, and RhoG) are tightly regulated signaling switches that mediate inputs from various receptors and oncogenes to regulate growth, apoptosis, cell-cell and cell-matrix interactions in response to growth factors such as EGF, PDGF, and HGF. Regulation of the actin cytoskeleton, which plays a key role in cell shape, polarity, division, migration and metastasis, is a major target of Rac, as it promotes membrane ruffling and formation of lamellipodia and circular dorsal ruffles [1-6]. Rac also controls cell cycle progression and cell survival, integrin-mediated adhesion, and is required for Ras transformation [7-11]. Furthermore, Rac is pivotal in most aggressive types of leukemias [12-19]. Thus, Rac has been associated with pro-tumorigenic functions and linked to the development of cancer. Moreover, it is characteristic of resistance to chemo-, radio-, and targeted-therapies and associated with persistence of leukemic stem cell [2,20-27].

Reducing Rac activity specifically in cancer cells is desirable and is an active area of research. Unfortunately, no small molecule inhibitor of Rac signaling is in clinical use despite the many efforts. Rac activity is regulated by an intricate and well-orchestrated set of proteins comprised of guanine nucleotide exchange factors (GEFs), GTPase-activating proteins (GAPs), and guanine dissociation inhibitors (GDIs). RacGEFs activate Rac by exchanging the bound GDP to GTP to initiate signaling while GAPs deactivate Rac by increasing the rate of GTP hydrolysis to arrest signaling. GDIs extract Rac from membranes, thereby preventing it from signaling. When active, Rac binds to and activates downstream effectors such as the p21-activated kinases (PAKs), which in turn activate pro-survival pathways and actin-regulating proteins. Rac regulators and effectors are themselves subject to tight regulation. For example, Vav proteins (Vav1, Vav2, and Vav3) are multi-domain tyrosine phosphorylation–dependent RacGEFs. Phosphorylation of specific tyrosine residues releases an N-terminal autoinhibition mechanism allowing Rac to access the Dbl-homology (DH) domain necessary for the GTP-exchange reaction. Therefore, finding a small molecule inhibitor of Rac itself or its activator, such as the Vav proteins, will provide an effective new strategy for treatment of malignancies with aberrant Rac signaling.

In this study, we reveal the mechanism of action (MoA) of IODVA1, a 2-guanidinobenimidazole derivative we identified as the active ingredient in NSC124205. Initial characterization of IODVA1 showed that it is not a kinase inhibitor but that it prevents lamellipodia and circular dorsal ruffle formation at low concentrations and within minutes of cell exposure. It also decreases cell-cell and cell-extra cellular matrix interactions and reduces growth of Ras-driven tumors [28]. These properties and the specificity of IODVA1 to oncogene expressing cells hinted that it targets Rac activation. We used in vitro and in vivo leukemic models of the chimeric BCR-ABL1 oncoprotein B-cell acute lymphoblastic leukemia (Ph+ B-ALL) to study the MoA of IODVA1. BCR-ABL1 B-ALL models are well-

suited for our endeavor for several reasons. First, BCR-ABL B-ALL is a single-driver genetic model. Expression of BCR-ABL, which has constitutive kinase activity is sufficient to promote the growth advantage of leukemic cells. When expressed, BCR-ABL1 activates a variety of pathways including the Ras-mitogen-activated kinase (MAPK) leading to abnormal cell proliferation, the Janus-activated kinase (JAK)-STAT pathway leading to impaired transcriptional activity, and the phosphoinositide 3-kinase (PI-3K)/AKT pathway resulting in prolonged survival [29]. In addition, expression of p190- or p210-BCR-ABL activates Rac signaling pathways to regulate leukemogenesis [16,30-32] and deleting Rac2 or the combination of Rac1 and Rac2, impairs myeloid leukemogenesis induced by p210-BCR-ABL expression in the hematopoietic stem and progenitor cell compartment [12,15]. Second, seemingly complex pathways activated by BCR-ABL all depend on the deregulated kinase activity of BCR-ABL [33] and ABL1-tyrosine kinase inhibitors (ABL1-TKIs), e.g. imatinib, are used as first-line therapy. Thus, imatinib can be used as positive control to assess the efficacy of IODVA1. Third, despite their tremendous success in treating B-ALL in the clinic, appearance of mechanisms of TKI-dependent and -independent resistance limited their efficacy [34,35]. Thus, there is an unmet need for novel treatments of patients with TKI-resistant leukemia and treatments that prevent leukemic-cell persistence.

Here, we show that IODVA1 binds tightly and inhibits Vav3, consequently leading to the deactivation of Rac and of its downstream signaling and to the induction of apoptosis in BCR-ABL expressing cells only in vivo and in vitro. Further, we show that IODVA1 prolongates the survival of a mouse model of TKI-resistance and reduces its leukemic burden long after treatment was withdrawn. We also show that IODVA1 is effective in decreasing proliferation and survival of relapsed and de novo primary patient-derived cells. To the best of our knowledge, IODVA1 is the first inhibitor of a RhoGEF with in vivo activity against xenograft mouse models of cancer. Our findings have direct implications for overcoming TKI-resistance in the clinic and for treating cancers where Vav3 is a target, including Ras-driven cancers.

Results

IODVA1 specifically targets BCR-ABL B-ALL cells in vitro.

To confirm that IODVA1 is specific for oncogene-expressing cells, we tested its efficacy on the proliferation and survival of CD34$^+$ human peripheral blood mononuclear cells transduced with retroviral bicistronic p190-BCR-ABL or Mieg3 empty vector [36]. As expected, expression of BCR-ABL increased cell proliferation (**Fig. 1a**). Treatment with IODVA1 (IO1, 1 μM) decreased proliferation of BCR-ABL- transformed cells, while proliferation of Mieg3 transduced cells was not affected. We then assessed survival of p190-BCR-ABL-transformed CD34$^+$ cells in the presence of IODVA1 by trypan blue exclusion. The survival of p190-BCR-ABL expressing cells decreased in a dose-dependent manner to 60

$\pm$ 16% (SD, N = 3) at 1 μM on day 5 and to 1 $\pm$ 0.2% (SD, N = 3) at 3 μM on day 3 (Fig. 1b). Survival of Mieg3 expressing cells was not affected by IODVA1. IODVA1 irreversibly inhibits survival of p190- and p210-BCR-ABL but not Mieg3 expressing Ba/F3 cells with a half maximal effective concentration (EC50) of 0.8 M and inhibits the clonogenic ability of BCR-ABL expressing Ba/F3 cells in methylcellulose (Supplementary Fig. S1a-S1c). Together, these results indicate that IODVA1 specifically targets proliferation and survival of BCR-ABL-transformed cells and are consistent with our previous report that IODVA1 is more specific to oncogene expressing cells [28].

IODVA1 prevents leukemia-related death and significantly decreases the leukemia burden in BCR-ABL-induced leukemic murine model

To test if IODVA1's potency on cells can be recapitulated in vivo, we probed its efficacy on a murine model of p190-BCR-ABL induced B-ALL and compared it to imatinib, an ABL1-TKI with well-characterized MoA in mouse models of Ph[+] B-ALL used as first-line therapy in Ph[+]-induced malignancies in the clinic. C57Bl/6 mice were used as donors and/or recipients of transduction/transplantation model. Mouse low-density bone marrow (LDBM) cells were transduced with a MSCV-driven bicistronic retroviral vector (MSCV-IRES-EGFP) encoding p190-BCR-ABL. Transduced LDBM cells (1×10^6) were intravenously transplanted into lethally irradiated C57Bl/6 mice. Mice were bled post 23 days and GFP^{+} cells were analyzed by flow cytometry. All mice had developed leukemia by day 28. Leukemic mice were stratified into 5 groups (7 per group) and administered either PBS control vehicle, 0.25 or 0.5 mM IODVA1, 0.5 mM imatinib, or the combination 0.25 mM IODVA1 + 0.5 mM imatinib. Vehicle control group had the same DMSO amount (0.1%) as the other groups. Drugs were administered subcutaneously in osmotic pumps for continuous slow release for 4 weeks. Mice survival plot shows that while the control group had died within 7 to 10 days post administration of the PBS vehicle, the low IODVA1 dose (0.25 mM) increased survival by an average of 10 days. Mice treated with imatinib or 0.5 mM IODVA1 or the combination were alive for the 4-week duration of the therapy (Fig. 1c). Significantly, IODVA1 decreased the residual p190-BCR-ABL expressing leukemic progenitor B-cells (EGFP[+]/B220[+]) from peripheral blood (PB) of treated mice (Supplementary data and Supplemental Fig. S1d).

IODVA1 eradicates leukemic propagating activity assessed by serial transplantation

Despite its significant clinical success, imatinib and, more generally, TKIs do not eliminate leukemic stem/progenitor cells in the bone marrow (BM), which can lead to residual disease, appearance of mechanisms of resistance, and ultimately relapse [37,38]. To determine if IODVA1 eradicates progenitor B-cells with ability to propagate tumors as a functional surrogate of minimal residual disease capable of leukemia relapse, BM cells from vehicle-control and treated mice from Fig. 1c

(without the 0.25 mM IODVA1-treated mice) were transplanted into lethally irradiated secondary C57BL/6 mice in a limiting dilution series of 1×10^6, 0.3×10^6, and 0.1×10^6 cell doses and analyzed for leukemia development and survival in the absence of any additional therapy. Kaplan-Meier survival plots for the 10^6-cell dilution transplant indicate that administration of IODVA1 alone or in combination with imatinib resulted in survival of p190-BCR-ABL chimeric mice beyond the 70-day endpoint analysis (Fig. 1d). Mice transplanted with BM cells from primary recipient mice treated with imatinib alone died by day 40 post-transplantation. Analysis at week 5 post transplantation of the leukemic progenitor cells (EGFP$^+$/B220$^+$) from the peripheral blood of secondary transplanted mice (Supplemental data, Fig. S1e) indicate that IODVA1 is superior than imatinib at eradicating leukemic cell burden. Poisson's distribution analysis of the lower cell dose transplantations (Fig. S1f-S1i) indicates >10-fold depletion of tumor propagating activity in grafts from IODVA1- or IODVA1+imatinib-treated leukemic mice compared with imatinib-treated leukemic mice.

IODVA1 eradicates TKI-resistant BCR-ABL B-ALL

We have previously reported that IODVA1 has no inhibitory activity against major wild-type kinases including ABL1 and SRC-like kinases. Thus, the anti-proliferative activity of IODVA1 towards in vitro and in vivo BCR-ABL B-ALL models and its ability to eradicate residual disease cannot be explained by ABL1 inhibition. To further test this idea, we evaluated the ability of IODVA1 to increase the survival of mice harboring p210-BCR-ABL(T315I). We chose this ABL1 mutant because it is one of the most frequent mutations arising in CML patients on imatinib therapy [39-43]. Mice were treated for 4 weeks with two rounds of pumps containing vehicle control, imatinib, or IODVA1. At the end of the 4-week treatment, surviving mice were kept in their cages without any additional treatment. As expected, p210(T315I) mice did not respond to the TKI as all imatinib-treated mice died by day 22, before the end of the treatment (Fig. 2a). 80% of IODVA1-treated mice survived until day 65, 37 days post last treatment. 60% of IODVA1-treated mice survived till day 80, 52 days post last treatment (Fig. 2a). Counts of leukemic progenitor cells EGFP$^+$/B220$^+$ from the T315I-leukemic mice PB indicated that IODVA1 significantly decreased leukemic progenitor levels by 24% by week two, by 84% by week 5, and by 91% by week 10 (Fig. 2b).

To assess signaling pathways affected by IODVA1 by pharmacodynamics, LDBM cells were isolated from two-week treated p210(T315I) mice and sorted for EGFP$^+$/B220$^+$. Sorted cells were fixed and stained with phospho-antibodies against the pro-proliferative Rac-dependent effectors JNK, PAK, 4EBP, and S6 and the Rac-independent effectors ERK1/2, STAT3, STAT5, p38, and AKT and analyzed by flow cytometry. IODVA1 resulted in significant decrease in pJNK, pPAK, p4EBP, and pS6 by 55% (p = 0.0029), 56% (p = 0.0016), 20.3% (p = 0.037), and 17.8% (p = 0.0012), respectively (Fig. 2c). Phosphorylation levels of p38, ERK, STAT3, STAT5, and AKT were not affected by IODVA1. Interestingly,

imatinib had the opposite effect, it decreased the levels of pERK, pSTAT3, and pAKT but did not affect the phosphorylation levels of the Rac-dependent effectors. Taken together, IODVA1 not only overcomes TKI-resistance but also eliminates TKI-resistant leukemic stem/progenitor cells likely by acting on imatinib-independent growth signaling pathways that involve Rac effectors.

IODVA1 decreases Rac activity and downstream signaling

We have previously shown that IODVA1 prevents formation of F-actin suprastructures, such as lamellipodia and circular dorsal ruffles, within minutes of cell incubation [28]. Rac is a major regulator of lamellipodia formation and of JNK and TORC1 activities [44,45] and is required for circular dorsal ruffles formation and is also activated downstream of BCR-ABL. We thus tested if IODVA1 inhibits Rac activation and measured levels of RacGTP during treatment using PAK GBD (GTPase-binding domain). A 70% decrease in the levels of active Rac occurs post 10-15 minutes incubation of p190-BCR-ABL Ba/F3 cells with IODVA1 (3 μM, Fig. 3a). Interestingly, this 10-minute time point is consistent with the IODVA1-driven decrease in lamellipodia formation in MDA-MB-231 breast cancer cells [28]. IODVA1 is specific to Rac (IC50 = 2 μM) and is less effective on Cdc42 and not on RhoA (Supplemental data, Fig. S3a & S3c).

To test if the decrease in Rac activation is translated into a decrease in its downstream signaling in vitro as was observed with xenograft-derived TKI-resistant cells (Fig. 2c), we analyzed vehicle- and IODVA1-treated p190-BCR-ABL- or Mieg3-expressing Ba/F3 cells by phosphor-flow. Fig. 3b shows that the phosphorylation levels of JNK, S6, 4EBP, PAK, and AKT were increased by more than 2.5 times in the BCR-ABL- than in the Mieg3-expressing cells. IODVA1 decreases the phosphorylation levels of JNK, S6, 4EBP, and PAK by 1.8 (p = 0.015), 1.5 (p = 0.05), 3.0 (p = 0.009), and 6.1 (p = 0.004) fold, respectively. Importantly, the decrease in effectors phosphorylation levels induced by IODVA1 treatment is specific to BCR-ABL- but not Mieg3-expressing cells. IODVA1 did not affect the phosphorylation levels of AKT regardless of the oncogene BCR-ABL status (Fig. 3b). The decrease in JNK, S6, and 4EBP activity in IODVA1-treated Ba/F3 cells mirrors the decrease observed in LDBM cells from IODVA1-treated p210-T315I mice in pharmacodynamics studies (Fig. 2c). Together, our in vitro and in vivo data are consistent with IODVA1 targeting activation of Rac and its downstream signaling.

Significantly, IODVA1 decreases Rac downstream pro-survival PAK and increases pro-apoptotic BAD activities within minutes of cell exposure (Supplemental data, Fig. S3B). The decrease in PAK and BAD phosphorylation suggests that IODVA1 promotes reduction in survival and induction of apoptosis. To further test this hypothesis, we analyzed the cell cycle of murine p190-BCR-ABL leukemic progenitor cells (EGFP$^+$/B220^{dim}) incubated with vehicle control or IODVA1 (1-10 μM) for 20 h, followed by in vitro BrdU incorporation and flow cytometry analysis. If IODVA1 did not affect the G0+G1 phase, it significantly affected the distribution of the G2+M, S and apoptotic phases. It increased the percentage

of cells in the G2+M phases from $7 \pm 1\%$ (SD, N = 3) in the presence of vehicle control to 22 ± 6.6, 32 ± 3, and $36 \pm 7\%$ (SD, N = 3) at 1, 3, and 10 µM, respectively (Fig. 3e). It reduced the S-phase 8-fold (p = 0.0002) and increased apoptosis by at least 5.3-times (p = 0.007).

To confirm that IODVA1 targets Rac-dependent pathways, we assessed its effects in Rac2-null background. $Rac1^{\Delta/\Delta}+Rac2^{-/-}$ murine leukemic cells show severe reduction in Rac1 expression and are deficient in Rac2 (Fig. S3H). $Rac1^{\Delta/\Delta}+Rac2^{-/-}$ or wild-type murine leukemic cells expressing p190-BCR-ABL [30] were tested for clonogenic ability in the presence of IODVA1 (Fig. 3d). $Rac1^{\Delta/\Delta}+Rac2^{-/-}$ leukemic cells formed 3.8-times less colonies than wild-type leukemic cells (p = 0.0003). IODVA1 did not alter the number of colonies formed by $Rac1^{\Delta/\Delta}+Rac2^{-/-}$ cells, suggesting these that cells are insensitive to IODVA1. Interestingly, $Rac1^{\Delta/\Delta}+Rac2^{-/-}$ leukemic cells treated with vehicle or IODVA1 formed 2.4-times more colonies than wild-type cells treated with IODVA1 (p = 0.0091). Combined with the biochemical data, these data support the idea that IODVA1 targets Rac activity and thus, inhibits its downstream pro-survival signals, promotes apoptosis signals within minutes of cell exposure resulting in increase in cells accumulating in the G2+M phase or undergoing apoptosis and decrease in cells undergoing DNA-synthesis.

IODVA1 is an inhibitor of the RacGEF Vav3

Rac activity and signaling is regulated by GAPs, GDIs, and RacGEFs. We argued that the decrease in Rac activity might be caused by IODVA1 targeting one Rac regulator. Using biochemical assays, we show that IODVA1 does not stimulate the activity of the Rac negative regulators p50GAP and RhoGDI1 (Supplemental data, Fig. S3E-S3G). We next turned to GEFs and posited that IODVA1 inhibits one Rac-specific GEF leading to its inactivation. While several RacGEFs have been associated with leukemogenesis [46-52], Vav3 was shown to play an important role in leukemogenesis [53]. We thus focused on Vav3 and tested if IODVA1 inhibits Vav3 binding to Rac. Ba/F3 cells expressing either p190-BCR-ABL or Mieg3 empty vector were incubated with IODVA1 (3 µM) or vehicle control for 30 min and subjected to GST-Rac pull-down. The pull-down protein complex was separated on SDS-PAGE and immunoblotted for pVav3 and Vav3 and quantified (Fig. 4A & S4A). There was no significant change in Vav3 or pVav3 bound to Rac in empty vector expressing Ba/F3 cells treated with IODVA1 or vehicle control (Fig. 4A, lanes 1 & 2) suggesting that IODVA1 did not affect Vav3 binding to Rac in cells expressing the empty vector. Strong pVav3 and Vav3 bands appeared in cells expressing the p190-BCR-ABL oncogene and treated with vehicle (Fig. 4A, lane 3) implying strong binding between active Vav3 and Rac. The 5-fold increase in the pVav3 intensity is consistent with similar observation that BCR-ABL increases Vav3 activation [53]. The intensity of this band is decreased 8-times in cells treated with IODVA1 (Fig. 4A, lane 4) suggesting that IODVA1 inhibited Vav3 binding to Rac in BCR-ABL expressing cells. This inhibition is likely due to the overall decrease in pVav3 levels in IODVA1 treated cells (Fig. 4,

input pVav3 band, lanes 3 & 4). Taken together, our data suggest that IODVA1 interferes with Vav3 activation and binding to Rac thus preventing the activation of the latter.

The previous observation suggests that IODVA1 binds to Vav3. To test this hypothesis, we measured its binding affinity (k_d) to recombinant Vav3 and Rac1 using microscale thermophoresis (MST); the catalytic domain (DH/PH) of the RhoGEF LARG served as negative control. We used LARG for two reasons. First, we reasoned that if Rho-activation is not affected by IODVA1 (Fig. S3A), we should not detect any binding between LARG and IODVA1. Second, like Vav3, LARG contains a DH/PH domain responsible for the exchange activity such that any non-specific binding should be detected. The MST signal for Vav3 reaches saturation at 10 μM IODVA1 and beyond (Fig. S4B). The MST signal for Rac1 and LARG showed no saturation at the highest IODVA1 concentration tested. Fitting of the MST titration data shows that one molecule of IODVA1 binds to Vav3 with a k_d of 0.4 μM. The best estimate for the k_d for Rac and LARG is 35.5 and 7.7 μM, respectively. Thus, IODVA1 binds tightly and specifically to Vav3.

Vav3-deficient leukemic cells do not respond to IODVA1 in vitro and in vivo

To further validate Vav3 as IODVA1's target, we studied the effects of IODVA1 on leukemic cells from the Vav3-KO mice we published previously [12,30,53]. We argued that if IODVA1 targets Vav3, then Vav3-deficient cells should be insensitive to its action. Wild-type or Vav3$^{-/-}$ murine BM leukemic cells expressing p190-BCR-ABL (EGFP$^+$/B220$^+$) were tested in colony formation assay in the presence of IODVA1 (Fig. 4B), as in Fig. 3D. The number of colonies formed by leukemic cells expressing Vav3 decreased on average by 3- and 7-folds in the presence of 1 and 3 μM IODVA1, respectively. Vav3$^{-/-}$ cells on the other hand formed similar number of colonies when grown in the presence of vehicle control or IODVA1 suggesting they lost sensitivity to our drug. Interestingly, the difference in the number of colonies formed by Vav3-deficient leukemic cells and by IODVA1-treated wild-type leukemic cells is not statistically significant (p = 0.13). Similarly, cell cycle analysis shows that Vav3$^{-/-}$ cells expressing p190-BCR-ABL were not affected by IODVA1 (Supplementary data, Fig. S4C). Taken together, our data suggest that while wild-type leukemic cells respond to IODVA1, Vav3$^{-/-}$ leukemic cells are irresponsive and mimic IODVA1-treated wild-type leukemic cells.

Next, we tested if the lack of response to IODVA1 by Vav3$^{-/-}$ cells holds in vivo. We transplanted wild-type or Vav3-KO LDBM cells transduced with p190-BCR-ABL retrovirus into lethally irradiated C57BL/6 mice (N = 5 per group), waited 21 days for the leukemia to develop, and treated the mice with either vehicle control or IODVA1 administered through osmotic pumps as before (Fig. 4C). Because the mice died shortly post leukemia transplantation, only one pump was used in all mice groups, e.g. all treatments started at day 21 and ended by day 35. Kaplan-Meier survival plots show that, as expected, mice transplanted with wild-type leukemia and treated with vehicle control die between days 33 and

38. Mice treated with IODVA1 survive until day 60, i.e. 25 days after treatment has ended. Compared to mice receiving vehicle control where leukemic progenitors constituted 23.8% of peripheral blood cells, mice treated with IODVA1 showed drastic reduction of levels of leukemic progenitors to 5% and 2% after one week and two weeks of IODVA1 treatment, respectively (Fig. 4D). These in vivo data are consistent with Fig. S1E and with the hypothesis that IODVA1 eliminates leukemic progenitor cells responsible for disease propagation. Mice transplanted with Vav3$^{-/-}$ leukemia and treated with vehicle control or IODVA1 die between days 34 and 42 and days 40 and 44, respectively. Thus, IODVA1 had no significant effect on Vav3$^{-/-}$ leukemic mice (p = 0.41). Vav3-KO leukemic mice seem to have increased survival over the wild-type leukemic mice, but analysis showed weak statistical significance (p = 0.1). This can also be seen in the level of peripheral blood leukemic progenitor cells that kept increasing in Vav3-KO mice treated with IODVA1 or vehicle control (Fig. 4D).

The observation that mice engrafted with Vav3-KO leukemia die by day 44 while mice engrafted with normal leukemia and treated with IODVA1 survive until day 60 suggests that Vav3-KO leukemia relies on Vav3- and IODVA1-independent pathways for survival. To test this hypothesis, we tested by phospho-flow cytometry the activity of several effectors in BM cells from one-week treated mice. The phosphorylation levels of the Vav3/Rac effectors JNK and PAK are severely reduced in IODVA1-treated mice (Fig. 4E). The levels of pJNK and pPAK in Vav3$^{-/-}$ leukemia are not affected by IODVA1 and are similar to IODVA1-treated wild-type leukemia. Interestingly, the phosphorylation levels of the non-Vav3/Rac effectors AKT and STAT3 are not only unaffected by IODVA1 in wild-type leukemia as seen before in Fig. 2C & 3B but significantly increased in Vav3-deficient leukemia. This observation suggests that in vivo, Vav3$^{-/-}$ leukemic cells are not only unresponsive to IODVA1 but rely on AKT and STAT3 signaling for survival.

Taken together, our data show that Vav3-deficient leukemia progenitor cells do not respond to IODVA1 in cellular and in vivo assays consistent with the idea that Vav3 is IODVA1's target in vivo and in vitro. The persistency of leukemia in vivo in Vav3$^{-/-}$ mice suggests that Vav3$^{-/-}$ BCR-ABL leukemia has evolved mechanisms of escape relying, among others, on AKT and STAT3 signaling.

IODVA1 targets Vav3 in MDA-MB-231 cells and xenograft tumors

Next, we tested if IODVA1 is effective in another model of Vav3-dependent cancer. We chose MDA-MB-231 triple negative breast cancer cells because these cells express high endogenous levels of Vav3 [54] and because Vav3 is an acknowledged target in breast cancer [54-58]. In addition, we have previously shown that these cells are sensitive to IODVA1 and that IODVA1 halts tumor growth and induces apoptosis in MDA-MB-231 xenograft mice [28]. First, we showed that reduction in Vav3 expression levels by targeting shRNA severely reduces proliferation of MDA-MB-231 cells. If IODVA1 (0.1 – 1 μM) reduces in a dose-dependent manner the viability and proliferation of scrambled MDA-

MB-231, it has no effect on the shVav3 expressing cells (Fig. 5A). Second, we incubated MDA-MB-231 cells with IODVA1 (3 μM) for 15 min and analyzed the levels of phosphorylated Vav3 (pY173) by immunoblotting. Fig. 5B shows that IODVA1 treatment results in significant decrease in pY173 signal. Since phosphorylation of this Tyr173 is indicative of Vav3 activation, we conclude that IODVA1 inhibits Vav3 activity shortly after exposure.

To test if IODVA1 inhibits Vav3 in vivo, we took advantage of the MDA-MB-231 xenograft tumors we generated [28] and stained them by immunohistochemistry for pVav3. Comparison of pVav3 stained tumor sections treated with vehicle control and with IODVA1 shows significant decrease in pVav3 staining for cells treated with IODVA1 than with vehicle control (Fig. 5C). Thus, IODVA1 inhibits Vav3 in vitro and vivo in solid tumor models and in a cell-independent manner.

IODVA1 decreases survival of patient-derived leukemia cells

Consistent with our findings with peripheral CD34+ BCR-ABL cells (Fig. 1A-1B), cells from PDX models representing pediatric Ph+ B-ALL patients were found to be highly sensitive to IODVA1 ex vivo (Table 1, Fig. 6).

Cells from relapsed patient #2018-136 with Ph+ (BCR-ABL1) were treated with ABL-TKI dasatinib, JAK-inhibitor ruxolitinib, dasatinib and ruxolitinib combination (das + rux), CDK-inhibitor abemaciclib, and IODVA1. Dasatinib (20 nM) reduced the proliferation of #2018-136 cells by 56%; ruxolitinib or abemaciclib (1 μM) had no effect. The das+rux combination resulted in 63% decrease in proliferation, which is likely due to dasatinib's inhibitory action. IODVA1 (0.5 μM) reduced the proliferation of these cells by 78%. When tested in the colony formation assay, IODVA1 (1 μM) reduced the number of colonies by 60% (p = 0.001) (Fig. 6A).

Cells from patient #2017-58 with a dual Ph+ (BCR-ABL1) and Ph-like (P2RY8-CRLF2) rearrangement were similarly treated. These cells clearly responded to dasatinib, ruxolitinib, and the combination. IODVA1 was not as potent as it decreased their proliferation by only 40% at 1 μM and had no effect at 0.2 μM (Fig. 6B). Original CD19+ cells from patient #2017-129 with Ph+ B-ALL (BCR-ABL1; T315I) who relapsed after initial treatment were treated with vehicle control, dasatinib, ruxolitinib, (das + rux), and IODVA1. As expected dasatinib, ruxolitinib, or the combination had no effect on proliferation of the CD19+ cells (Fig. 6C, left panel). In contrast, IODVA1 at 1 μM but not at 0.2 μM reduced the CD19+ B-ALL cell counts by 80%. Additionally, we confirmed that IODVA1 does not exert toxic effects to cells of normal stroma (Fig. 6C, right panel arrows). Thus, IODVA1 decreases the proliferation of Ph+ B-ALL (BCR-ABL1) primary cells including cells expressing the TKI-resistant T315I mutant consistent with our findings that Ph+ B-ALL (BCR-ABL1) model cells express high-levels of Vav3. The fact that #2017-58 cells did not respond to IODVA1 is probably due to the existence of other genetic mutations (e.g. P2RY8-CRLF2) that promote cell growth independently of Vav3.

Our cohort of samples also contained numerous cases of Ph-like disease with a diverse series of genetic aberrations and a few cases of MLL-rearranged B-ALL. These patient cells generally responded positively to IODVA1 (Supplementary data, Fig. S6A-S6H).

Discussion

Vav3 is a multi-domain tyrosine phosphorylation–dependent RacGEF that functions downstream of several different signaling molecules including immune response receptors, G-protein-coupled receptors (GPCRs), protein tyrosine kinases and integrins [59-65] and a critical component of BCR-ABL induced Rac activation [53]. Thus far, no small molecule inhibitor of a Vav family-member has been reported. Small molecule inhibitors of the RhoGEFs LARG, AKAP13, DOCK2, and DOCK5 [66-70] have been identified in in vitro and cellular assays however, these molecules work at high concentrations and their mechanism of action of and their potential drug-likeness is questionable [71].

This study in cellular and murine models of the chimeric BCR-ABL1 oncoprotein demonstrates that inhibitor of oncogene-driven Vav3 activation, IODVA1 binds tightly to Vav3 (K_d = 400 nM, Fig. S4B), prevents its activation, and the activation of Rac in vitro and in vivo. In accordance with this MoA, IODVA1 significantly decreased the levels of active-Vav3 in xenograft tumors of triple negative breast cancer mouse model (Fig. 5C) suggesting that IODVA1 inhibition of Vav3 is not specific to leukemia models. One can argue that IODVA1 inhibits the transmembrane or cytosolic protein tyrosine kinases such as Syk, Janus, Tec, Abl, and Src family kinases responsible for Vav3 phosphorylation [62,72] however, this is unlikely since IODVA1 is not a kinase inhibitor. IODVA1 binding to Vav3 seems specific as it doesn't bind Rac or LARG and does not interfere with the actions of p50GAP or RhoGDI1. The possibility that IODVA1 binds to the homologous Vav1/2 exists but based on the loss of IODVA1's efficacy in vitro and in vivo in Vav3$^{-/-}$ models (Fig. 4B & 4C), this binding is unlikely. Significantly, IODVA1 has no effect on Vav3-deficient murine bone marrow leukemic cells and does not affect the survival of a mouse model of Vav3-deficient p190-BCR-ABL-induced leukemia. In addition, IODVA1 has no effect on Rac1$^{\Delta/\Delta}$+Rac2$^{-/-}$ leukemic cells (Fig. 3D). These in vivo and in vitro results are relevant because if IODVA1 had off-targets with a contribution to BCR-ABL-driven leukemia, an increase in mouse survival and in cell proliferation would have been detected, which is not the case.

Our in vitro cell cycle and colony formation data indicate that IODVA1's pharmacological action on leukemic cells mimics the genetic deletion of Vav3 (Fig. 4B & Fig. S4C). The IODVA1-triggered increase in BAD activity was also observed in Vav3$^{-/-}$ leukemic cells [53]. Results from the colony formation assays with the Rac1$^{\Delta/\Delta}$+Rac2$^{-/-}$ leukemic cells (Fig. 3D) and from viability of shVav3 MDA-MB-231 cells (Fig. 5A) are also consistent with this idea. We noticed however, that the Rac1$^{\Delta/\Delta}$+Rac2$^{-/-}$ leukemic cells resulted in higher number of colonies than cells treated with IODVA1. This can be explained by residual Rac1, which is pro cell-proliferation or by the Rac-independent pathways regulated by Vav3 that are

inhibited by IODVA1. Likewise, there is a noticeable difference between IODVA1's pharmacological action, which increases survival of leukemic mice and Vav3 genetic deletion, which results in premature leukemic mice death (Fig. 4C). Our phosphor-flow data show however, that in the background of Vav3$^{-/-}$, BCR-ABL leukemic cells increase signaling through the pro-survival and Vav3/Rac-independent effectors AKT and STAT3. This mechanism of adaptation is likely responsible for the proliferation of LSCs and the death of Vav3-KO leukemic mice (see also [53]).

IODVA1 decreases Rac activation and the activity of several of its downstream effectors such as PAK, JNK, S6, and 4EBP in vitro and in vivo. The decrease in PAK activity leads to dephosphorylation and therefore activation of BAD [73]. BAD activation prevents its association with Bcl2/Bcl-xL and promotes cell apoptosis. IODVA1's induction of apoptosis of BCR-ABL expressing cells is supported by our cell cycle analysis in vitro and in vivo (Fig. 3C & S4C). Most relevant to this MoA is the decrease in levels of pJNK, pPAK, pS6, and p4EBP following IODVA1 administration to TKI-resistant BCR-ABL(T315I) leukemia model and the associated decrease in leukemic burden (Fig. 2).

The expression of BCR-ABL in B-ALL confers a much poorer prognosis compared to other cytogenetic or molecular abnormalities [74]. Treatment with the imatinib and second-generation ABL-TKI inhibitors (e.g. dasatinib/ponatinib) has proven to be only partly effective in Ph$^+$ B-ALL patients. The relative failure of TKI therapy in these types of ALL is due among others to the development of resistance-inducing mutations such as ABL1-T315I [39,75] and primary resistance of leukemic stem cells to TKI therapy [76]. In studies of patients with high-risk B-cell ALL that were resistant to conventional treatment, a high frequency of recurrent somatic alterations was found in key signaling pathways such as the Ras/ERK, PI3K/AKT, B-cell development and differentiation, Rac/PAK, and Janus kinases [77-79]. An emerging concept to overcome TKI-shortcomings is to target leukemic stem cells (LSCs), which are responsible for disease initiation and propagation. Whereas imatinib alone does not eradicate LSCs in vivo, deletion of Rac2 in p210-BCR-ABL–transduced hematopoietic cells prolonged the survival of leukemic mice [12,15,16,30]. Similarly, genetic deficiency of Vav3 but not of Vav1/Vav2 delays leukemogenesis by p190-BCR-ABL and phenocopies the effect of Rac2 deficiency [53] suggesting that Vav3 and Rac GTPases are targets in BCR-ABL LSCs. IODVA1 eliminates residual leukemic stem/progenitor cells responsible for BCR-ABL B-ALL disease relapse in secondary transplant mice (Fig. 1D) better than imatinib and overcomes resistance to ABL1-TKI (Fig. 2). It reduces the viability of primary cells from pediatric patients with Ph$^+$ B-ALL including TKI-resistant BCR-ABL1(T315I), Ph-like, and MLL with superior potency than currently administered therapies. The specificity of IODVA1 to the oncoprotein expressing cells (Fig. 1A & 6C) explains its low toxicity in vivo. IODVA1 is thus well-suited to treat Ph$^+$ leukemias with a superior outcome.

If our data are consistent with IODVA1 binding to Vav3, they do not reveal where it binds. Vav3 is a multidomain signaling protein that can be roughly divided into two halves: (1) a catalytic N-terminal half responsible for Rac binding and activation and (2) an adaptor C-terminal half involved in protein-protein interactions. The nucleotide exchange activity of Vav3 is subject to tight regulation. It is accepted that upon cell stimulation, phosphorylation of conserved Tyr-residues (e.g. Tyr173) releases an autoinhibitory mechanism by the N-terminus Calponin-homology CH-domain and the acidic stretch (Ac) and the C-terminal SH3 domain, thus allowing GTPase access to the DH domain [80-84]. Based on our biochemical data (Fig. 4A & 5B), we argue that IODVA1 inhibits Vav3 phosphorylation by preventing the access of tyrosine residues in the Ac-stretch to Src-kinases. We postulate that IODVA1 likely locks Vav3 into the autoinhibitory state, thus preventing Rac from accessing the DH domain for activation. Dissection of the exact binding site is currently underway.

In conclusion, we have shown that pharmacological inhibition of Vav3 by IODVA1 is an attractive therapeutic strategy to treat TKI-resistant BCR-ABL B-ALL. This strategy should benefit other malignancies where Vav3 is a target [53-57,85-98]. We thus expect IODVA1 to have a broader therapeutic application. In addition, IODVA1 constitutes an exceptional tool to dissect the Vav3/Rac signaling axis. Broadly, RhoGEFs are multi-domain proteins that are regulated by an autoinhibition mechanism [99-102]. Consequently, small molecules that stabilize the autoinhibited conformation of RhoGEFs and inhibit their activity could be developed into drug to treat human cancer.

Acknowledgement

References

1. Etienne-Manneville, S.; Hall, A. Rho GTPases in cell biology. *Nature* **2002**, *420*, 629-635.
2. Jaffe, A.B.; Hall, A. Rho GTPases: biochemistry and biology. *Annu Rev Cell Dev Biol* **2005**, *21*, 247-269, doi:10.1146/annurev.cellbio.21.020604.150721.
3. Bustelo, X.R. RHO GTPases in cancer: known facts, open questions, and therapeutic challenges. *Biochemical Society transactions* **2018**, *46*, 741-760, doi:10.1042/BST20170531.
4. Ridley, A.J. Rho GTPase signalling in cell migration. *Current opinion in cell biology* **2015**, *36*, 103-112, doi:10.1016/j.ceb.2015.08.005.
5. Ridley, A.J.; Paterson, H.F.; Johnston, C.L.; Diekmann, D.; Hall, A. The small GTP-binding protein rac regulates growth factor-induced membrane ruffling. *Cell* **1992**, *70*, 401-410.
6. Steffen, A.; Ladwein, M.; Dimchev, G.A.; Hein, A.; Schwenkmezger, L.; Arens, S.; Ladwein, K.I.; Margit Holleboom, J.; Schur, F.; Victor Small, J., et al. Rac function is crucial for cell migration but is not required for spreading and focal adhesion formation. *J Cell Sci* **2013**, *126*, 4572-4588, doi:10.1242/jcs.118232.
7. Coleman, M.L.; Marshall, C.J.; Olson, M.F. RAS and RHO GTPases in G1-phase cell-cycle regulation. *Nat Rev Mol Cell Biol* **2004**, *5*, 355-366, doi:10.1038/nrm1365.
8. Kiosses, W.B.; Shattil, S.J.; Pampori, N.; Schwartz, M.A. Rac recruits high-affinity integrin alphavbeta3 to lamellipodia in endothelial cell migration. *Nat Cell Biol* **2001**, *3*, 316-320, doi:10.1038/35060120.
9. Sundaresan, M.; Yu, Z.X.; Ferrans, V.J.; Sulciner, D.J.; Gutkind, J.S.; Irani, K.; Goldschmidt-Clermont, P.J.; Finkel, T. Regulation of reactive-oxygen-species generation in fibroblasts by Rac1. *Biochem J* **1996**, *318 (Pt 2)*, 379-382.
10. Mack, N.A.; Whalley, H.J.; Castillo-Lluva, S.; Malliri, A. The diverse roles of Rac signaling in tumorigenesis. *Cell Cycle* **2011**, *10*, 1571-1581, doi:10.4161/cc.10.10.15612.
11. Qiu, R.G.; Chen, J.; Kirn, D.; McCormick, F.; Symons, M. An essential role for Rac in Ras transformation. *Nature* **1995**, *374*, 457-459, doi:10.1038/374457a0.
12. Thomas, E.K.; Cancelas, J.A.; Chae, H.D.; Cox, A.D.; Keller, P.J.; Perrotti, D.; Neviani, P.; Druker, B.J.; Setchell, K.D.; Zheng, Y., et al. Rac guanosine triphosphatases represent integrating molecular therapeutic targets for BCR-ABL-induced myeloproliferative disease. *Cancer Cell* **2007**, *12*, 467-478, doi:10.1016/j.ccr.2007.10.015.
13. Somervaille, T.C.; Cleary, M.L. Identification and characterization of leukemia stem cells in murine MLL-AF9 acute myeloid leukemia. *Cancer Cell* **2006**, *10*, 257-268, doi:10.1016/j.ccr.2006.08.020.
14. Wei, J.; Wunderlich, M.; Fox, C.; Alvarez, S.; Cigudosa, J.C.; Wilhelm, J.S.; Zheng, Y.; Cancelas, J.A.; Gu, Y.; Jansen, M., et al. Microenvironment determines lineage fate in a human model of MLL-AF9 leukemia. *Cancer Cell* **2008**, *13*, 483-495, doi:10.1016/j.ccr.2008.04.020.
15. Sengupta, A.; Arnett, J.; Dunn, S.; Williams, D.A.; Cancelas, J.A. Rac2 GTPase deficiency depletes BCR-ABL+ leukemic stem cells and progenitors in vivo. *Blood* **2010**, *116*, 81-84, doi:10.1182/blood-2009-10-247437.
16. Skorski, T.; Wlodarski, P.; Daheron, L.; Salomoni, P.; Nieborowska-Skorska, M.; Majewski, M.; Wasik, M.; Calabretta, B. BCR/ABL-mediated leukemogenesis requires the activity of the small GTP-binding protein Rac. *Proc Natl Acad Sci U S A* **1998**, *95*, 11858-11862.
17. Mizukawa, B.; Wei, J.; Shrestha, M.; Wunderlich, M.; Chou, F.S.; Griesinger, A.; Harris, C.E.; Kumar, A.R.; Zheng, Y.; Williams, D.A., et al. Inhibition of Rac GTPase signaling and downstream prosurvival Bcl-2 proteins as combination targeted therapy in MLL-AF9 leukemia. *Blood* **2011**, *118*, 5235-5245, doi:10.1182/blood-2011-04-351817.
18. Bassermann, F.; Jahn, T.; Miething, C.; Seipel, P.; Bai, R.Y.; Coutinho, S.; Tybulewicz, V.L.; Peschel, C.; Duyster, J. Association of Bcr-Abl with the proto-oncogene Vav is implicated in activation of the Rac-1 pathway. *J Biol Chem* **2002**, *277*, 12437-12445, doi:10.1074/jbc.M112397200.
19. Nieborowska-Skorska, M.; Kopinski, P.K.; Ray, R.; Hoser, G.; Ngaba, D.; Flis, S.; Cramer, K.; Reddy, M.M.; Koptyra, M.; Penserga, T., et al. Rac2-MRC-cIII-generated ROS cause genomic

instability in chronic myeloid leukemia stem cells and primitive progenitors. *Blood* **2012**, *119*, 4253-4263, doi:10.1182/blood-2011-10-385658.

20. Loirand, G.; Pacaud, P. The role of Rho protein signaling in hypertension. *Nat Rev Cardiol* **2010**, *7*, 637-647, doi:10.1038/nrcardio.2010.136.

21. Mulloy, J.C.; Cancelas, J.A.; Filippi, M.D.; Kalfa, T.A.; Guo, F.; Zheng, Y. Rho GTPases in hematopoiesis and hemopathies. *Blood* **2010**, *115*, 936-947, doi:10.1182/blood-2009-09-198127.

22. Newey, S.E.; Velamoor, V.; Govek, E.E.; Van Aelst, L. Rho GTPases, dendritic structure, and mental retardation. *J Neurobiol* **2005**, *64*, 58-74, doi:10.1002/neu.20153.

23. Sahai, E.; Marshall, C.J. RHO-GTPases and cancer. *Nat Rev Cancer* **2002**, *2*, 133-142, doi:10.1038/nrc725.

24. Vigil, D.; Cherfils, J.; Rossman, K.L.; Der, C.J. Ras superfamily GEFs and GAPs: validated and tractable targets for cancer therapy? *Nat Rev Cancer* **2010**, *10*, 842-857, doi:10.1038/nrc2960.

25. Porter, A.P.; Papaioannou, A.; Malliri, A. Deregulation of Rho GTPases in cancer. *Small GTPases* **2016**, *7*, 123-138, doi:10.1080/21541248.2016.1173767.

26. Zandvakili, I.; Lin, Y.; Morris, J.C.; Zheng, Y. Rho GTPases: Anti- or pro-neoplastic targets? *Oncogene* **2017**, *36*, 3213-3222, doi:10.1038/onc.2016.473.

27. Cardama, G.A.; Alonso, D.F.; Gonzalez, N.; Maggio, J.; Gomez, D.E.; Rolfo, C.; Menna, P.L. Relevance of small GTPase Rac1 pathway in drug and radio-resistance mechanisms: Opportunities in cancer therapeutics. *Crit Rev Oncol Hematol* **2018**, *124*, 29-36, doi:10.1016/j.critrevonc.2018.01.012.

28. Gasilina, A.; Premnauth, G.; Gurjar, P.; Biesiada, J.; Hegde, S.; Milewski, D.; Ma, G.; Kalin, T.V.; Merino, E.; Meller, J., et al. IODVA1, a guanidinobenzimidazole derivative, targets Rac activity and Ras-driven cancer models. *PLoS One* **2020**, *15*, e0229801, doi:10.1371/journal.pone.0229801.

29. Cilloni, D.; Saglio, G. Molecular pathways: BCR-ABL. *Clin Cancer Res* **2012**, *18*, 930-937, doi:10.1158/1078-0432.CCR-10-1613.

30. Thomas, E.K.; Cancelas, J.A.; Zheng, Y.; Williams, D.A. Rac GTPases as key regulators of p210-BCR-ABL-dependent leukemogenesis. *Leukemia* **2008**, *22*, 898-904, doi:10.1038/leu.2008.71.

31. Harnois, T.; Constantin, B.; Rioux, A.; Grenioux, E.; Kitzis, A.; Bourmeyster, N. Differential interaction and activation of Rho family GTPases by p210bcr-abl and p190bcr-abl. *Oncogene* **2003**, *22*, 6445-6454, doi:10.1038/sj.onc.1206626.

32. Sahay, S.; Pannucci, N.L.; Mahon, G.M.; Rodriguez, P.L.; Megjugorac, N.J.; Kostenko, E.V.; Ozer, H.L.; Whitehead, I.P. The RhoGEF domain of p210 Bcr-Abl activates RhoA and is required for transformation. *Oncogene* **2008**, *27*, 2064-2071, doi:10.1038/sj.onc.1210841.

33. Lugo, T.G.; Pendergast, A.M.; Muller, A.J.; Witte, O.N. Tyrosine kinase activity and transformation potency of bcr-abl oncogene products. *Science* **1990**, *247*, 1079-1082, doi:10.1126/science.2408149.

34. Arrigoni, E.; Del Re, M.; Galimberti, S.; Restante, G.; Rofi, E.; Crucitta, S.; Barate, C.; Petrini, M.; Danesi, R.; Di Paolo, A. Concise Review: Chronic Myeloid Leukemia: Stem Cell Niche and Response to Pharmacologic Treatment. *Stem Cells Transl Med* **2018**, *7*, 305-314, doi:10.1002/sctm.17-0175.

35. Hamilton, A.; Helgason, G.V.; Schemionek, M.; Zhang, B.; Myssina, S.; Allan, E.K.; Nicolini, F.E.; Muller-Tidow, C.; Bhatia, R.; Brunton, V.G., et al. Chronic myeloid leukemia stem cells are not dependent on Bcr-Abl kinase activity for their survival. *Blood* **2012**, *119*, 1501-1510, doi:10.1182/blood-2010-12-326843.

36. Williams, D.A.; Tao, W.; Yang, F.; Kim, C.; Gu, Y.; Mansfield, P.; Levine, J.E.; Petryniak, B.; Derrow, C.W.; Harris, C., et al. Dominant negative mutation of the hematopoietic-specific Rho GTPase, Rac2, is associated with a human phagocyte immunodeficiency. *Blood* **2000**, *96*, 1646-1654.

37. Milojkovic, D.; Apperley, J. Mechanisms of Resistance to Imatinib and Second-Generation Tyrosine Inhibitors in Chronic Myeloid Leukemia. *Clin Cancer Res* **2009**, *15*, 7519-7527, doi:10.1158/1078-0432.CCR-09-1068.

38. Bixby, D.; Talpaz, M. Mechanisms of resistance to tyrosine kinase inhibitors in chronic myeloid leukemia and recent therapeutic strategies to overcome resistance. *Hematology Am Soc Hematol Educ Program* **2009**, 10.1182/asheducation-2009.1.461, 461-476, doi:10.1182/asheducation-2009.1.461.

39. Gorre, M.E.; Mohammed, M.; Ellwood, K.; Hsu, N.; Paquette, R.; Rao, P.N.; Sawyers, C.L. Clinical resistance to STI-571 cancer therapy caused by BCR-ABL gene mutation or amplification. *Science* **2001**, *293*, 876-880, doi:10.1126/science.1062538.

40. Azam, M.; Latek, R.R.; Daley, G.Q. Mechanisms of autoinhibition and STI-571/imatinib resistance revealed by mutagenesis of BCR-ABL. *Cell* **2003**, *112*, 831-843.

41. Jabbour, E.; Kantarjian, H.; Jones, D.; Talpaz, M.; Bekele, N.; O'Brien, S.; Zhou, X.; Luthra, R.; Garcia-Manero, G.; Giles, F., et al. Frequency and clinical significance of BCR-ABL mutations in patients with chronic myeloid leukemia treated with imatinib mesylate. *Leukemia* **2006**, *20*, 1767-1773, doi:10.1038/sj.leu.2404318.

42. Nicolini, F.E.; Corm, S.; Le, Q.H.; Sorel, N.; Hayette, S.; Bories, D.; Leguay, T.; Roy, L.; Giraudier, S.; Tulliez, M., et al. Mutation status and clinical outcome of 89 imatinib mesylate-resistant chronic myelogenous leukemia patients: a retrospective analysis from the French intergroup of CML (Fi(phi)-LMC GROUP). *Leukemia* **2006**, *20*, 1061-1066, doi:10.1038/sj.leu.2404236.

43. Jabbour, E.; Kantarjian, H.; Jones, D.; Breeden, M.; Garcia-Manero, G.; O'Brien, S.; Ravandi, F.; Borthakur, G.; Cortes, J. Characteristics and outcomes of patients with chronic myeloid leukemia and T315I mutation following failure of imatinib mesylate therapy. *Blood* **2008**, *112*, 53-55, doi:10.1182/blood-2007-11-123950.

44. Minden, A.; Lin, A.; Claret, F.X.; Abo, A.; Karin, M. Selective activation of the JNK signaling cascade and c-Jun transcriptional activity by the small GTPases Rac and Cdc42Hs. *Cell* **1995**, *81*, 1147-1157, doi:10.1016/s0092-8674(05)80019-4.

45. Saci, A.; Cantley, L.C.; Carpenter, C.L. Rac1 regulates the activity of mTORC1 and mTORC2 and controls cellular size. *Mol Cell* **2011**, *42*, 50-61, doi:10.1016/j.molcel.2011.03.017.

46. Biswas, M.; Chatterjee, S.S.; Boila, L.D.; Chakraborty, S.; Banerjee, D.; Sengupta, A. MBD3/NuRD loss participates with KDM6A program to promote DOCK5/8 expression and Rac GTPase activation in human acute myeloid leukemia. *FASEB J* **2019**, *33*, 5268-5286, doi:10.1096/fj.201801035R.

47. Chatterjee, S.S.; Biswas, M.; Boila, L.D.; Banerjee, D.; Sengupta, A. SMARCB1 Deficiency Integrates Epigenetic Signals to Oncogenic Gene Expression Program Maintenance in Human Acute Myeloid Leukemia. *Mol Cancer Res* **2018**, *16*, 791-804, doi:10.1158/1541-7786.MCR-17-0493.

48. Martin, H.; Mali, R.S.; Ma, P.; Chatterjee, A.; Ramdas, B.; Sims, E.; Munugalavadla, V.; Ghosh, J.; Mattingly, R.R.; Visconte, V., et al. Pak and Rac GTPases promote oncogenic KIT-induced neoplasms. *J Clin Invest* **2013**, *123*, 4449-4463, doi:10.1172/JCI67509.

49. Lyons, R.; Williams, O.; Morrow, M.; Sebire, N.; Hubank, M.; Anderson, J. The RAC specific guanine nucleotide exchange factor Asef functions downstream from TEL-AML1 to promote leukaemic transformation. *Leuk Res* **2010**, *34*, 109-115, doi:10.1016/j.leukres.2009.06.032.

50. Reuther, G.W.; Lambert, Q.T.; Booden, M.A.; Wennerberg, K.; Becknell, B.; Marcucci, G.; Sondek, J.; Caligiuri, M.A.; Der, C.J. Leukemia-associated Rho guanine nucleotide exchange factor, a Dbl family protein found mutated in leukemia, causes transformation by activation of RhoA. *J Biol Chem* **2001**, *276*, 27145-27151, doi:10.1074/jbc.M103565200.

51. Rouard, H.; Tamasdan, S.; Fridman, W.H.; Teillaud, J.L. Vav and SLP-76 recruitment by cross-linking of FcgammaRIIa1 in promyelocytic HL-60 cells. *Immunol Lett* **1999**, *68*, 347-353.

52. Bourgoin, S.; Harbour, D.; Desmarais, Y.; Takai, Y.; Beaulieu, A. Low molecular weight GTP-binding proteins in HL-60 granulocytes. Assessment of the role of ARF and of a 50-kDa cytosolic protein in phospholipase D activation. *J Biol Chem* **1995**, *270*, 3172-3178, doi:10.1074/jbc.270.7.3172.

53. Chang, K.H.; Sanchez-Aguilera, A.; Shen, S.; Sengupta, A.; Madhu, M.N.; Ficker, A.M.; Dunn, S.K.; Kuenzi, A.M.; Arnett, J.L.; Santho, R.A., et al. Vav3 collaborates with p190-BCR-ABL in

lymphoid progenitor leukemogenesis, proliferation, and survival. *Blood* **2012**, *120*, 800-811, doi:10.1182/blood-2011-06-361709.

54. Chen, X.; Chen, S.I.; Liu, X.A.; Zhou, W.B.; Ma, R.R.; Chen, L. Vav3 oncogene is upregulated and a poor prognostic factor in breast cancer patients. *Oncol Lett* **2015**, *9*, 2143-2148, doi:10.3892/ol.2015.3004.

55. Lee, K.; Liu, Y.; Mo, J.Q.; Zhang, J.; Dong, Z.; Lu, S. Vav3 oncogene activates estrogen receptor and its overexpression may be involved in human breast cancer. *BMC Cancer* **2008**, *8*, 158, doi:10.1186/1471-2407-8-158.

56. Aguilar, H.; Urruticoechea, A.; Halonen, P.; Kiyotani, K.; Mushiroda, T.; Barril, X.; Serra-Musach, J.; Islam, A.; Caizzi, L.; Di Croce, L., et al. VAV3 mediates resistance to breast cancer endocrine therapy. *Breast Cancer Res* **2014**, *16*, R53, doi:10.1186/bcr3664.

57. Citterio, C.; Menacho-Marquez, M.; Garcia-Escudero, R.; Larive, R.M.; Barreiro, O.; Sanchez-Madrid, F.; Paramio, J.M.; Bustelo, X.R. The rho exchange factors vav2 and vav3 control a lung metastasis-specific transcriptional program in breast cancer cells. *Sci Signal* **2012**, *5*, ra71, doi:10.1126/scisignal.2002962.

58. Lorenzo-Martin, L.F.; Citterio, C.; Menacho-Marquez, M.; Conde, J.; Larive, R.M.; Rodriguez-Fdez, S.; Garcia-Escudero, R.; Robles-Valero, J.; Cuadrado, M.; Fernandez-Pisonero, I., et al. Vav proteins maintain epithelial traits in breast cancer cells using miR-200c-dependent and independent mechanisms. *Oncogene* **2019**, *38*, 209-227, doi:10.1038/s41388-018-0433-7.

59. Bustelo, X.R.; Barbacid, M. Tyrosine phosphorylation of the vav proto-oncogene product in activated B cells. *Science* **1992**, *256*, 1196-1199.

60. Bustelo, X.R.; Ledbetter, J.A.; Barbacid, M. Product of vav proto-oncogene defines a new class of tyrosine protein kinase substrates. *Nature* **1992**, *356*, 68-71, doi:10.1038/356068a0.

61. Turner, M.; Billadeau, D.D. VAV proteins as signal integrators for multi-subunit immune-recognition receptors. *Nat Rev Immunol* **2002**, *2*, 476-486, doi:10.1038/nri840.

62. Bustelo, X.R. Regulatory and signaling properties of the Vav family. *Mol Cell Biol* **2000**, *20*, 1461-1477.

63. Schuebel, K.E.; Movilla, N.; Rosa, J.L.; Bustelo, X.R. Phosphorylation-dependent and constitutive activation of Rho proteins by wild-type and oncogenic Vav-2. *Embo J* **1998**, *17*, 6608-6621, doi:10.1093/emboj/17.22.6608.

64. Movilla, N.; Bustelo, X.R. Biological and regulatory properties of Vav-3, a new member of the Vav family of oncoproteins. *Mol Cell Biol* **1999**, *19*, 7870-7885.

65. Crespo, P.; Schuebel, K.E.; Ostrom, A.A.; Gutkind, J.S.; Bustelo, X.R. Phosphotyrosine-dependent activation of Rac-1 GDP/GTP exchange by the vav proto-oncogene product. *Nature* **1997**, *385*, 169-172, doi:10.1038/385169a0.

66. Shang, X.; Marchioni, F.; Evelyn, C.R.; Sipes, N.; Zhou, X.; Seibel, W.; Wortman, M.; Zheng, Y. Small-molecule inhibitors targeting G-protein-coupled Rho guanine nucleotide exchange factors. *Proc Natl Acad Sci U S A* **2013**, *110*, 3155-3160, doi:10.1073/pnas.1212324110.

67. Diviani, D.; Raimondi, F.; Del Vescovo, C.D.; Dreyer, E.; Reggi, E.; Osman, H.; Ruggieri, L.; Gonano, C.; Cavin, S.; Box, C.L., et al. Small-Molecule Protein-Protein Interaction Inhibitor of Oncogenic Rho Signaling. *Cell Chem Biol* **2016**, *23*, 1135-1146, doi:10.1016/j.chembiol.2016.07.015.

68. Nishikimi, A.; Uruno, T.; Duan, X.; Cao, Q.; Okamura, Y.; Saitoh, T.; Saito, N.; Sakaoka, S.; Du, Y.; Suenaga, A., et al. Blockade of inflammatory responses by a small-molecule inhibitor of the Rac activator DOCK2. *Chem Biol* **2012**, *19*, 488-497, doi:10.1016/j.chembiol.2012.03.008.

69. Vives, V.; Laurin, M.; Cres, G.; Larrousse, P.; Morichaud, Z.; Noel, D.; Cote, J.F.; Blangy, A. The Rac1 exchange factor Dock5 is essential for bone resorption by osteoclasts. *J Bone Miner Res* **2011**, *26*, 1099-1110, doi:10.1002/jbmr.282.

70. Bouquier, N.; Vignal, E.; Charrasse, S.; Weill, M.; Schmidt, S.; Leonetti, J.P.; Blangy, A.; Fort, P. A cell active chemical GEF inhibitor selectively targets the Trio/RhoG/Rac1 signaling pathway. *Chem Biol* **2009**, *16*, 657-666, doi:10.1016/j.chembiol.2009.04.012.

71.   Gray, J.L.; von Delft, F.; Brennan, P. Targeting the Small GTPase Superfamily through their Regulatory Proteins. *Angew Chem Int Ed Engl* **2019**, 10.1002/anie.201900585, doi:10.1002/anie.201900585.

72.   Bustelo, X.R. Vav family exchange factors: an integrated regulatory and functional view. *Small GTPases* **2014**, *5*, 9, doi:10.4161/21541248.2014.973757.

73.   Schurmann, A.; Mooney, A.F.; Sanders, L.C.; Sells, M.A.; Wang, H.G.; Reed, J.C.; Bokoch, G.M. p21-activated kinase 1 phosphorylates the death agonist bad and protects cells from apoptosis. *Mol Cell Biol* **2000**, *20*, 453-461.

74.   Arico, M.; Valsecchi, M.G.; Camitta, B.; Schrappe, M.; Chessells, J.; Baruchel, A.; Gaynon, P.; Silverman, L.; Janka-Schaub, G.; Kamps, W., et al. Outcome of treatment in children with Philadelphia chromosome-positive acute lymphoblastic leukemia. *N Engl J Med* **2000**, *342*, 998-1006, doi:10.1056/NEJM200004063421402.

75.   Azam, M.; Seeliger, M.A.; Gray, N.S.; Kuriyan, J.; Daley, G.Q. Activation of tyrosine kinases by mutation of the gatekeeper threonine. *Nat Struct Mol Biol* **2008**, *15*, 1109-1118, doi:10.1038/nsmb.1486.

76.   Corbin, A.S.; Agarwal, A.; Loriaux, M.; Cortes, J.; Deininger, M.W.; Druker, B.J. Human chronic myeloid leukemia stem cells are insensitive to imatinib despite inhibition of BCR-ABL activity. *J Clin Invest* **2011**, *121*, 396-409, doi:10.1172/JCI35721.

77.   Hunger, S.P.; Mulligan, C.G. Redefining ALL classification: toward detecting high-risk ALL and implementing precision medicine. *Blood* **2015**, *125*, 3977-3987, doi:10.1182/blood-2015-02-580043.

78.   Roberts, K.G.; Li, Y.; Payne-Turner, D.; Harvey, R.C.; Yang, Y.L.; Pei, D.; McCastlain, K.; Ding, L.; Lu, C.; Song, G., et al. Targetable kinase-activating lesions in Ph-like acute lymphoblastic leukemia. *N Engl J Med* **2014**, *371*, 1005-1015, doi:10.1056/NEJMoa1403088.

79.   Zhang, J.; Mullighan, C.G.; Harvey, R.C.; Wu, G.; Chen, X.; Edmonson, M.; Buetow, K.H.; Carroll, W.L.; Chen, I.M.; Devidas, M., et al. Key pathways are frequently mutated in high-risk childhood acute lymphoblastic leukemia: a report from the Children's Oncology Group. *Blood* **2011**, *118*, 3080-3087, doi:10.1182/blood-2011-03-341412.

80.   Llorca, O.; Arias-Palomo, E.; Zugaza, J.L.; Bustelo, X.R. Global conformational rearrangements during the activation of the GDP/GTP exchange factor Vav3. *Embo J* **2005**, *24*, 1330-1340, doi:10.1038/sj.emboj.7600617.

81.   Yu, B.; Martins, I.R.; Li, P.; Amarasinghe, G.K.; Umetani, J.; Fernandez-Zapico, M.E.; Billadeau, D.D.; Machius, M.; Tomchick, D.R.; Rosen, M.K. Structural and energetic mechanisms of cooperative autoinhibition and activation of Vav1. *Cell* **2010**, *140*, 246-256, doi:10.1016/j.cell.2009.12.033.

82.   Aghazadeh, B.; Lowry, W.E.; Huang, X.Y.; Rosen, M.K. Structural basis for relief of autoinhibition of the Dbl homology domain of proto-oncogene Vav by tyrosine phosphorylation. *Cell* **2000**, *102*, 625-633.

83.   Rapley, J.; Tybulewicz, V.L.; Rittinger, K. Crucial structural role for the PH and C1 domains of the Vav1 exchange factor. *EMBO Rep* **2008**, *9*, 655-661, doi:10.1038/embor.2008.80.

84.   Chrencik, J.E.; Brooun, A.; Zhang, H.; Mathews, II; Hura, G.L.; Foster, S.A.; Perry, J.J.; Streiff, M.; Ramage, P.; Widmer, H., et al. Structural basis of guanine nucleotide exchange mediated by the T-cell essential Vav1. *J Mol Biol* **2008**, *380*, 828-843, doi:10.1016/j.jmb.2008.05.024.

85.   Katzav, S.; Martin-Zanca, D.; Barbacid, M. vav, a novel human oncogene derived from a locus ubiquitously expressed in hematopoietic cells. *Embo J* **1989**, *8*, 2283-2290.

86.   Fernandez-Zapico, M.E.; Gonzalez-Paz, N.C.; Weiss, E.; Savoy, D.N.; Molina, J.R.; Fonseca, R.; Smyrk, T.C.; Chari, S.T.; Urrutia, R.; Billadeau, D.D. Ectopic expression of VAV1 reveals an unexpected role in pancreatic cancer tumorigenesis. *Cancer Cell* **2005**, *7*, 39-49, doi:10.1016/j.ccr.2004.11.024.

87.   Menacho-Marquez, M.; Garcia-Escudero, R.; Ojeda, V.; Abad, A.; Delgado, P.; Costa, C.; Ruiz, S.; Alarcon, B.; Paramio, J.M.; Bustelo, X.R. The Rho exchange factors Vav2 and Vav3 favor skin tumor initiation and promotion by engaging extracellular signaling loops. *PLoS Biol* **2013**, *11*, e1001615, doi:10.1371/journal.pbio.1001615.

88.   Liu, Y.; Wu, X.; Dong, Z.; Lu, S. The molecular mechanism of Vav3 oncogene on upregulation of androgen receptor activity in prostate cancer cells. *Int J Oncol* **2010**, *36*, 623-633.

89.   Dong, Z.; Liu, Y.; Levin, L.; Oleksowicz, L.; Wang, J.; Lu, S. Vav3 oncogene is involved in regulation of secretory phospholipase A2-IIa expression in prostate cancer. *Oncol Rep* **2011**, *25*, 1511-1516, doi:10.3892/or.2011.1237.

90.   Liu, Y.; Mo, J.Q.; Hu, Q.; Boivin, G.; Levin, L.; Lu, S.; Yang, D.; Dong, Z.; Lu, S. Targeted overexpression of vav3 oncogene in prostatic epithelium induces nonbacterial prostatitis and prostate cancer. *Cancer Res* **2008**, *68*, 6396-6406, doi:10.1158/0008-5472.CAN-08-0645.

91.   Dong, Z.; Liu, Y.; Lu, S.; Wang, A.; Lee, K.; Wang, L.H.; Revelo, M.; Lu, S. Vav3 oncogene is overexpressed and regulates cell growth and androgen receptor activity in human prostate cancer. *Mol Endocrinol* **2006**, *20*, 2315-2325, doi:10.1210/me.2006-0048.

92.   Lyons, L.S.; Burnstein, K.L. Vav3, a Rho GTPase guanine nucleotide exchange factor, increases during progression to androgen independence in prostate cancer cells and potentiates androgen receptor transcriptional activity. *Mol Endocrinol* **2006**, *20*, 1061-1072, doi:10.1210/me.2005-0346.

93.   Lin, K.T.; Gong, J.; Li, C.F.; Jang, T.H.; Chen, W.L.; Chen, H.J.; Wang, L.H. Vav3-rac1 signaling regulates prostate cancer metastasis with elevated Vav3 expression correlating with prostate cancer progression and posttreatment recurrence. *Cancer Res* **2012**, *72*, 3000-3009, doi:10.1158/0008-5472.CAN-11-2502.

94.   Lin, K.Y.; Wang, L.H.; Hseu, Y.C.; Fang, C.L.; Yang, H.L.; Kumar, K.J.; Tai, C.; Uen, Y.H. Clinical significance of increased guanine nucleotide exchange factor Vav3 expression in human gastric cancer. *Mol Cancer Res* **2012**, *10*, 750-759, doi:10.1158/1541-7786.MCR-11-0598-T.

95.   Tan, B.B.; Zhang, M.M.; Li, Y.; Zhao, Q.; Fan, L.Q.; Liu, Y.; Wang, D. Inhibition of Vav3 gene can promote apoptosis of human gastric cancer cell line MGC803 by regulating ERK pathway. *Tumour Biol* **2016**, *37*, 7823-7833, doi:10.1007/s13277-015-4505-9.

96.   Tan, B.; Li, Y.; Wang, C.; Tan, M.; Fan, L.; Zhao, Q.; Wang, D.; Jia, N. The clinical value of Vav3 in peripheral blood for predicting lymphatic metastasis of gastric cancer. *Br J Biomed Sci* **2017**, *74*, 133-137, doi:10.1080/09674845.2017.1278889.

97.   Salhia, B.; Tran, N.L.; Chan, A.; Wolf, A.; Nakada, M.; Rutka, F.; Ennis, M.; McDonough, W.S.; Berens, M.E.; Symons, M., et al. The guanine nucleotide exchange factors trio, Ect2, and Vav3 mediate the invasive behavior of glioblastoma. *The American journal of pathology* **2008**, *173*, 1828-1838, doi:10.2353/ajpath.2008.080043.

98.   Liu, J.K.; Lubelski, D.; Schonberg, D.L.; Wu, Q.; Hale, J.S.; Flavahan, W.A.; Mulkearns-Hubert, E.E.; Man, J.; Hjelmeland, A.B.; Yu, J., et al. Phage display discovery of novel molecular targets in glioblastoma-initiating cells. *Cell Death Differ* **2014**, *21*, 1325-1339, doi:10.1038/cdd.2014.65.

99.   Zheng, Y. Dbl family guanine nucleotide exchange factors. *Trends in biochemical sciences* **2001**, *26*, 724-732.

100.   Rossman, K.L.; Der, C.J.; Sondek, J. GEF means go: turning on RHO GTPases with guanine nucleotide-exchange factors. *Nat Rev Mol Cell Biol* **2005**, *6*, 167-180.

101.   Hoffman, G.R.; Cerione, R.A. Signaling to the Rho GTPases: networking with the DH domain. *FEBS Lett* **2002**, *513*, 85-91.

102.   Schmidt, A.; Hall, A. Guanine nucleotide exchange factors for Rho GTPases: turning on the switch. *Genes Dev* **2002**, *16*, 1587-1609, doi:10.1101/gad.1003302.

103.   Lee, L.H.; Gasilina, A.; Roychoudhury, J.; Clark, J.; McCormack, F.X.; Pressey, J.; Grimley, M.S.; Lorsbach, R.; Ali, S.; Bailey, M., et al. Real-time genomic profiling of histiocytoses identifies early-kinase domain BRAF alterations while improving treatment outcomes. *JCI Insight* **2017**, *2*, e89473, doi:10.1172/jci.insight.89473.

104.   Zhang, S.C.; Gremer, L.; Heise, H.; Janning, P.; Shymanets, A.; Cirstea, I.C.; Krause, E.; Nurnberg, B.; Ahmadian, M.R. Liposome reconstition and modulation of recombinant prenylated human Rac1 by GEFs, GDI1 and Pak1. *PLoS One* **2014**, *9*, e102425, doi:10.1371/journal.pone.0102425.

105. Studier, F.W. Protein production by auto-induction in high density shaking cultures. *Protein Expr Purif* **2005**, *41*, 207-234.

106. Jerabek-Willemsen, M.; Wienken, C.J.; Braun, D.; Baaske, P.; Duhr, S. Molecular interaction studies using microscale thermophoresis. *Assay Drug Dev Technol* **2011**, *9*, 342-353, doi:10.1089/adt.2011.0380.

107. Nouri, K.; Fansa, E.K.; Amin, E.; Dvorsky, R.; Gremer, L.; Willbold, D.; Schmitt, L.; Timson, D.J.; Ahmadian, M.R. IQGAP1 Interaction with RHO Family Proteins Revisited: KINETIC AND EQUILIBRIUM EVIDENCE FOR MULTIPLE DISTINCT BINDING SITES. *J Biol Chem* **2016**, *291*, 26364-26376, doi:10.1074/jbc.M116.752121.

108. Fujikawa, K.; Miletic, A.V.; Alt, F.W.; Faccio, R.; Brown, T.; Hoog, J.; Fredericks, J.; Nishi, S.; Mildiner, S.; Moores, S.L., et al. Vav1/2/3-null mice define an essential role for Vav family proteins in lymphocyte development and activation but a differential requirement in MAPK signaling in T and B cells. *J Exp Med* **2003**, *198*, 1595-1608, doi:10.1084/jem.20030874.

109. Wunderlich, M.; Brooks, R.A.; Panchal, R.; Rhyasen, G.W.; Danet-Desnoyers, G.; Mulloy, J.C. OKT3 prevents xenogeneic GVHD and allows reliable xenograft initiation from unfractionated human hematopoietic tissues. *Blood* **2014**, *123*, e134-144, doi:10.1182/blood-2014-02-556340.

Experimental Methods

Plasmids, Cell Lines, and Reagents

Plasmid set for purification of fixed-arm carrier fusions pMalX (A-E) was a kind gift from Dr. Lars C. Pedersen (NIEHS), pET28b-N_9-MBP-mOrange plasmid was from Addgene (#29748), chaperone co-expression plasmid set was from TaKaRa (cat #3340). Primers were from Integrated DNA Technologies (IDT, Inc.). Primer and construct design were performed with NEBuilder Tool. Restriction enzymes, polymerases, cloning assembly kits and competent cells were from New England Biolabs and Invitrogen.

MDA-MB-231 cells were maintained in IMEM (Invitrogen) supplemented with 10% FBS, 1% penicillin/streptomycin, and 1% amphotericin B. Ba/F3 cells were cultured in RPMI (GIBCO) supplemented with 10% FBS and IL-3 (10 ng/ml). HEK293T cells were maintained with DMEM supplemented with 10% FBS and 1% penicillin/streptomycin. All cell lines were cultured at 37°C in a 5% CO_2 humidified incubator. Cell viability was assessed by trypan blue exclusion assay as previously described (Gasilina et al., 2019). Cytokines were from Peprotech.

The following antibodies were used: GAPDH (#627408, GeneTex), pERK1/2 (#4370), pAKT (#9271 and #9018), Cdc42 (#2462), RhoA (#2117), pPAK1 (#9018S), pS6 (#48515), PAK1/3 (#2602S), pBAD (#4366), and BAD (#9292), anti-mouse HRP (#7076), anti-rabbit HRP (#7074) were from Cell Signaling Technologies, pVav3(Y173) (#ab109544) and total Vav3 (#ab203315) were from Abcam, pJNK (Alexa Fluor 647 conjugated, #562481), p-p38 (PE-conjugated, #612565), Rac2 (#610850), pStat3 (#55385), and pStat5 (Alexa Fluor 647 conjugated, #612599), and B220 APC-Cy7 antibody (#552094) were from BD Bioscience, p4EBP1 (PE-conjugated, #12-9107-42) was form Thermofisher Scientific.

Lipids (Phosphatidylserine (PS), Phosphatidylcholine (PC), phosphatidylethanolamine (PE) and sphingomyelin (SM), and phosphatidylinositol 4,5-bisphosphate (PIP_2) for membrane displacement assays were from Avanti.

IODVA1 was synthesized from 2-guanidinobenzimidazole and purified as described [28]. Imatinib (#SML1027) was from SIGMA-Aldrich, dasatinib (#S1021), and ruxolitinib (#S1378) from Selleck.

Retroviral and Lentiviral Particle Production, Transduction and Transplantation of Transduced Leukemic cells

Production of lentivirus and retrovirus for stable transduction of murine and human cells were done as described previously [103]. Scrambled and Vav3-specific shRNAs (Sigma-Aldrich MISSION shRNA) were obtained from Cincinnati Children's Lenti-shRNA Library Core. Retroviral and lentiviral vectors, viral transduction of cell lines and mouse LDBM, and transplantation of transduced leukemic cells were previously described [53].

SDS-PAGE, Pull-down Assays and Immunoblotting

Exponentially growing (6 x 10^6) p190-BCR-ABL Ba/F3 cells were treated with either vehicle or IODVA1 at indicated concentrations and time points. Active GTPase pulldown was done according to the manufacturer's instructions using GST-PAK1 PBD or GST-Rhotekin (Thermofisher, #16118 and #16116). Protein complexes was separated on SDS-PAGE and immunoblotted with anti-Rac1, anti-Cdc42 and anti-RhoA antibodies.

For analysis of expression, cells were lysed in RIPA buffer, supplemented with phosphatase and protease inhibitors, separated on SDS-PAGE, transferred on PVDF or nitrocellulose membrane and blotted with appropriate primary and secondary antibodies, as described previously (Lee LH et al., 2016, Chang KH et al., 2012).

Relative signals were normalized to the unstimulated conditions after normalization to the total protein amount. Quantification was performed using Licor Image Studio.

Cloning

Human *Rac1* (GenBank accession n° NM_006908.4) was subcloned into pFastBacHTB vector (Invitrogen) and fused with an N-terminal His_6-tag.

For pMalX(E)-based expression, full-length Vav3 was amplified with primers overlapping NotI restriction site of pMalX(E) vector with N-terminal linkers AAAA, AAAASEF or AAAASEFGS linkers. The finalized construct encoded MBPX(E)-linker-Vav3. For His_6-MBP-N_9-TEV-Vav3 construct, full-length Vav3 cDNA with a stop codon at the end of the coding sequence was amplified by PCR with primers overlapping pET28a-MBP-N_9TEV-mOrange vector at the SspI site. The resulting construct encoded MBP-N_9-Vav3-His_6. All constructs were verified using Sanger sequencing using CCHCM DNA Core. To minimize aggregation and improve on quality of purified protein, the expression clones were tested with chaperone plasmids according to the manufacturer's protocol.

Protein Expression and Purification

For membrane displacement assays, full-length human Rac1 was purified from baculovirus. pFastBacHTB-Rac1 was transformed into DH10 cells. The resulting bacmid was used to generate baculovirus in Sf9 cells. Rac1 was produced in TNAO38 insect cells and purified using Ni-IMAC chromatography [104].

For production of recombinant Vav3, plasmids were co-transformed with chaperone plasmid Gro7 groEL-groES in BL21 (DE3) or T7 Express. Cultures were grown in LB, supplemented with metal mix [105]. Protein was purified using Ni-IMAC chromatography, dialyzed and further purified using size-exclusion gel filtration (HiLoad Superdex 200 16/60). Fractions were analyzed by SDS-PAGE and protein

fractions containing Vav3 were pooled, concentrated to ~10 mg/mL and flash frozen in liquid nitrogen. Final yields for MBP-N9-Vav3 and MBPXE-Vav3 were 5 mg and 20 mg per 6 L of culture, respectively.

Recombinant LARG (DH/PH) was purified as a MBP-fusion protein as described previously (Kristelly R. et al., 2003).

RhoGDI extracting prenylated Rac1 from liposomes

Displacement of prenylated-Rac1-GDP and Rac1-GPPNHP from synthetic liposomes by GST-RhoGDI1 in the presence and absence of IODVA1 was studied using liposome sedimentation assay as in [104]. Briefly, liposomes were generated by using a defined composition of lipids (194 μg) containing 39% w/w phosphatidylethanolamine, 16% w/w phosphatidylcholine, 36% w/w phosphatidylserine, 4% sphingomyelin, and 5 % w/w phosphatidylinositol 4,5-bisphosphate. All lipids were obtained from Avanti (Germany). Prenylated Rac1GDP or Rac1GppNHp (1 μM) was added to liposomes suspended in protein buffer (20 mM Hepes, pH 7.4, 150 mM NaCl, 3 mM DTT) and incubated for 20 min on ice. GST-RHOGDI1 (2 μM) in the absence or presence of IODVA1 was added to the liposome/prenylated Rac1 and further incubated on ice for 30 min. The samples were then centrifuged at 20,000 x g for 20 min at 4 °C. Pellet and supernatant fractions were collected, separated on SDS-PAGE and immunoblotted for Rac1.

Microscale Thermophoresis (MST)

Purified Vav3, LARG or Rac (1 uM) were incubated with the indicated concentrations of IODVA1 at room temperature for 30 min. Samples were loaded into Zero Background MST Premium Coated capillaries and binding events were measured on Monolith NT.LabelFree (NanoTemper Technologies). Binding data were analyzed using Thermophoresis or Thermophoresis with Temperature Jump analysis as described previously [106]. Data were normalized using fraction-bound binding. The 95% confidence interval for K_d values was 0.27 to 0.98 μM for Vav3, 5.9 to 10.37 μM for LARG, and 19.6 to 105.8 μM for Rac.

Stopped-flow spectrometry

GTPase assay and nucleotide exchange reaction were performed with a Hi- Tech Scientific (SF-61) stopped-flow instrument as described [107] The excitation wavelengths were 543 nm and 362 nm for tamraGTP and mantGppNHp, respectively. For GTPase assay, equal volumes (600 μl) of 0.2 μM RAC1-tamraGTP and 10 μM of p50GAP were used. GTPase assay as well the protein-protein interaction were performed in presence of 5% DMSO.

Animals and in vivo Drug Administration

Vav3-deficient mice [108] and Rac1$^{\Delta/\Delta}$+Rac2-deficient [12] mice have been described previously. C57Bl/6 mice were commercially obtained (The Jackson Laboratory and Harlan Laboratories) and used as donors and/or recipients of transduction/transplantation models under a protocol approved by The Cincinnati Children's Hospital Medical Center Institutional Animal Care and Use Committee. For in vivo drug administration, Alzet implantable osmotic pumps (Model 2002, Durect) were used according to the manufacturer's protocol and implantation was done as described previously [12].

CFU-proB assay

B-cell lineage colony-forming units (CFU-proB) were quantified post 9-day culture of leukemic BM cells or sorted for p190-BCR-ABL–expressing B-cell progenitors in M3134 methylcellulose (StemCell Technologies) supplemented with 30% FBS (for mouse B lymphoid colony forming cells; StemCell Technologies), 2 mM L-glutamine (Invitrogen), 1% penicillin-streptomycin (Invitrogen), 100 µM β-mercaptoethanol (Fisher-Scientific), 1% BSA (Sigma-Aldrich), 20 ng/mL of recombinant mouse IL-7 (PeproTech), and 100 ng/mL of recombinant mouse SCF (PeproTech).

Cell cycle analysis

Cell cycle was analyzed by using in vitro incorporation of 5-Bromo-2-deoxyuridine using Brdu Flow kit (BD Pharmingen, Cat# 552598). Briefly, mice leukemic progenitors were incubated with 1 mM BrdU solution for 45 minutes, cells were further fixed and permeabilized. DNAse treatment was done according to the instructions and stained with anti BrdU and apoptosis was analyzed by 7-AAD staining through flow cytometry analysis.

Flow cytometry analysis

Peripheral blood flow cytometry analysis was done by lysing the RBCs using BD pharma lyse (BD bioscience, Cat# 555899). Cells were washed once with PBS then stained with anti-B220 APC-Cy7 antibody. Stained cells were washed once and analyzed by flow cytometry.

Primary PDX ex vivo drug treatments

Primary patient specimens were obtained from patients at CCHMC according to Institutional Review Board Approved protocols (#2008-0021 and #2008-0658). Samples were subjected to RBC lysis and the isolated WBCs were mixed with OKT3 anti-CD3 antibody to eliminate the potential for xenogenic Graft Versus Host Disease before injection into busulfan conditioned NSG or NRG mice [109]. Spleen preparations from mice successfully engrafted with B-ALL were co-cultured with MS-5 or OP9 stroma in MEMα media supplemented with 20% FBS and 10 ng/mL recombinant human SCF (Kit-L), Flt3L, and IL-7 (KF7). IODVA1 was added 24 h after initial seeding. Co-cultures were collected by trypsinization

after 7 days and cell counts were performed with trypan blue. Flow cytometry was performed with mCD45-APC-Cy7 (BD), hCD45-FITC (BD), hCD19-VioBlue (Miltenyi Biotech), and 7-AAd (for viability) to determine percentage of human ALL in the cultures. Total absolute ALL cell numbers were determined by multiplying cell counts by percentage human ALL cells.
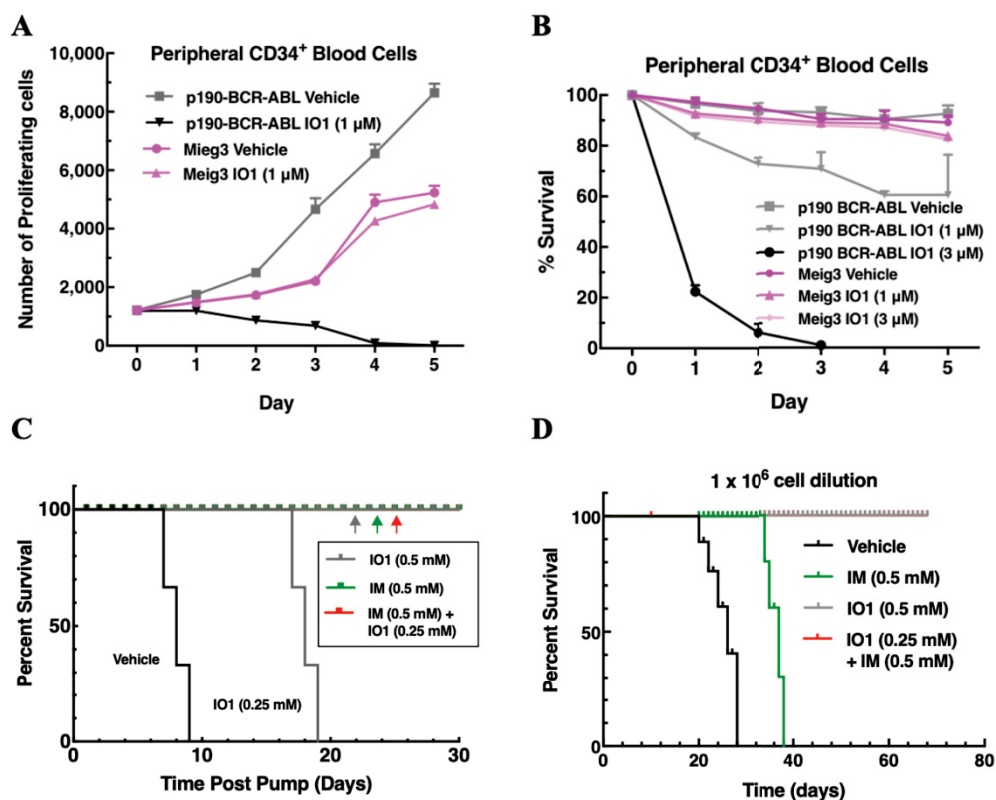
Figure 1: IODVA1 inhibits the proliferation and survival of BCR-ABL expressing cells in vitro and in vivo and eradicates leukemia propagating cells in secondary transplants. (A) Human peripheral CD34^{+} blood cells transduced with p190-BCR-ABL (grey line, squares, and black line, inverted triangles) or Mieg3 vector control (lilac lines, circles and triangles) virus were co-cultured on OP-9 stromal cells and incubated with either vehicle or IODVA1 (IO1, 1 μM). Cell proliferation was assessed by flow cytometry. (B) Cell were transduced and cultured as in (A) but incubated with either vehicle or IODVA1 (IO1, 1 or 3 μM) and survival (%) was determined by trypan blue exclusion. (C) Kaplan-Meier plot showing survival of p190-BCR-ABL leukemic mice post treatment with vehicle control, IDOVA1 (IO1), imatinib (IM), or the combination at the indicated concentrations in the pump. LDBM cells were transduced with bicistronic p190-BCR-ABL/EGFP retrovirus and transplanted into recipient mice. After initial assessment of leukemic burden, drugs were delivered in subcutaneously implanted osmotic pumps, each lasting two weeks. (D) Kaplan-Meier survival plot of secondary mice transplants. Bone marrow cells from mice treated with vehicle, imatinib, IODVA1 or the combination at the indicated concentrations were transplanted into secondary recipients. Results for the 10[6] cell-dilution are shown.
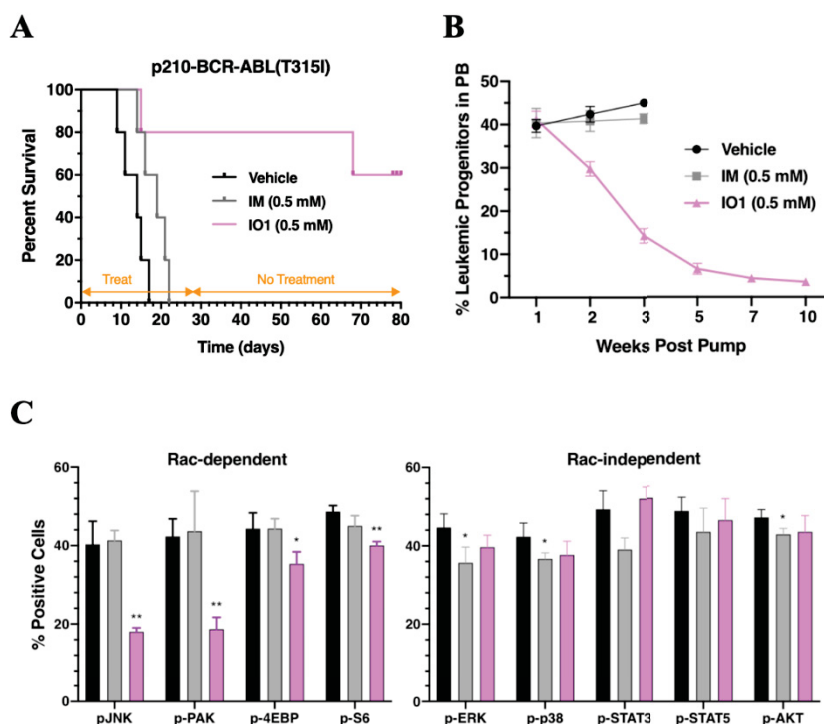
Figure 2: IODVA1 but not imatinib increases the survival of a mouse model of TKI-resistant B-ALL. LDBM cells were transduced with TKI-resistant (gate-keeper) p210-BCR-ABL(T315I) and transplanted into recipient mice as in Fig. 1. Pumps were surgically introduced into mice (N = 5 per treatment group) and treatment lasted 28 days or two rounds of pumps. After 28 days, mice were monitored without any additional treatment. (A) Kaplan-Meier survival plot of imatinib-resistant mice. Pumps either carried vehicle control (black line), 0.5 mM imatinib (IM, grey line), or 0.5 mM IODVA1 (IO1, lilac line). (B) Flow cytometric analysis of leukemic progenitor (EGFP⁺) B-cells in peripheral blood at the indicated week. Only IODVA1-treated mice remained alive for analysis at weeks 5, 7, and 10. (C) Pharmacodynamic assessment of leukemic progenitor cells (%) from the 2-week treated mice with vehicle control (black), imatinib (grey), or IODVA1 (lilac) using phospho-flow analysis of the indicated Rac-dependent and -independent effectors (* $p \leq 0.05$; ** $p \leq 0.01$).
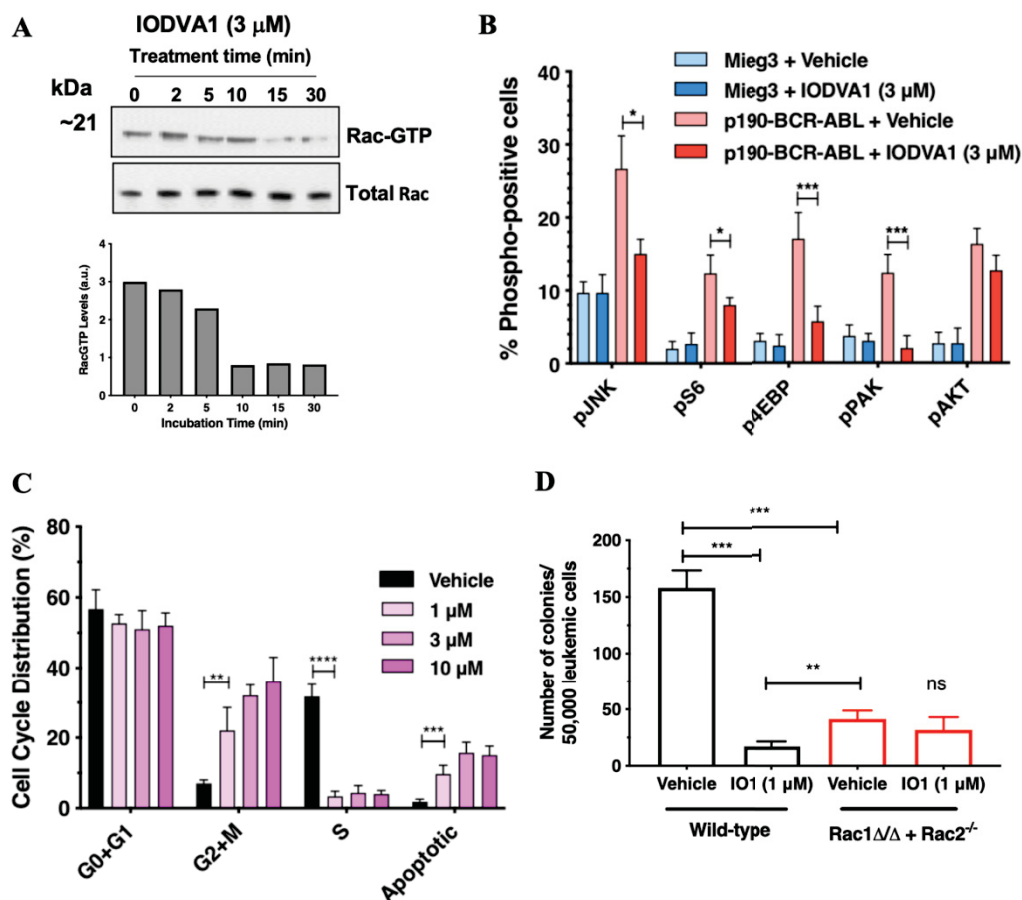
Figure 3: **IODVA1 decreases Rac activation and signaling**. (A) Ba/F3 cells expressing p190-BCR-ABL were treated with IODVA1 (3 µM) as indicated and levels of active Rac (RacGTP) were assessed by pull-down using GST-PAK-PBD, followed by immunoblotting and densitometric quantification. Upper panel: Immunoblot showing levels of RacGTP from cells treated at the indicated time points, lower panel: quantification of levels of active Rac. (B) Flow-cytometry analysis of pJNK, pS6, p4EBP, pPAK, and pAKT of Ba/F3 cells expressing Mieg3 empty vector (light and dark blue) or p190-BCR-ABL (light and dark salmon) and treated with vehicle control or IODVA1 (3 µM) for 30 min. (C) Representative histogram data of the cell cycle analysis of Ba/F3 cells expressing p190-BCR-ABL and treated with vehicle control or IODVA1 (1, 3, and 10 µM) for 20 h. (D) Quantification of the average number of colonies of bone marrow wild-type (black) and $Rac1^{\Delta/\Delta}+Rac2^{-/-}$ (red) p190-BCR-ABL leukemic cells treated with vehicle control or IODVA1 (IO1, 1 µM) (** $p \leq 0.01$; *** $p \leq 0.001$).
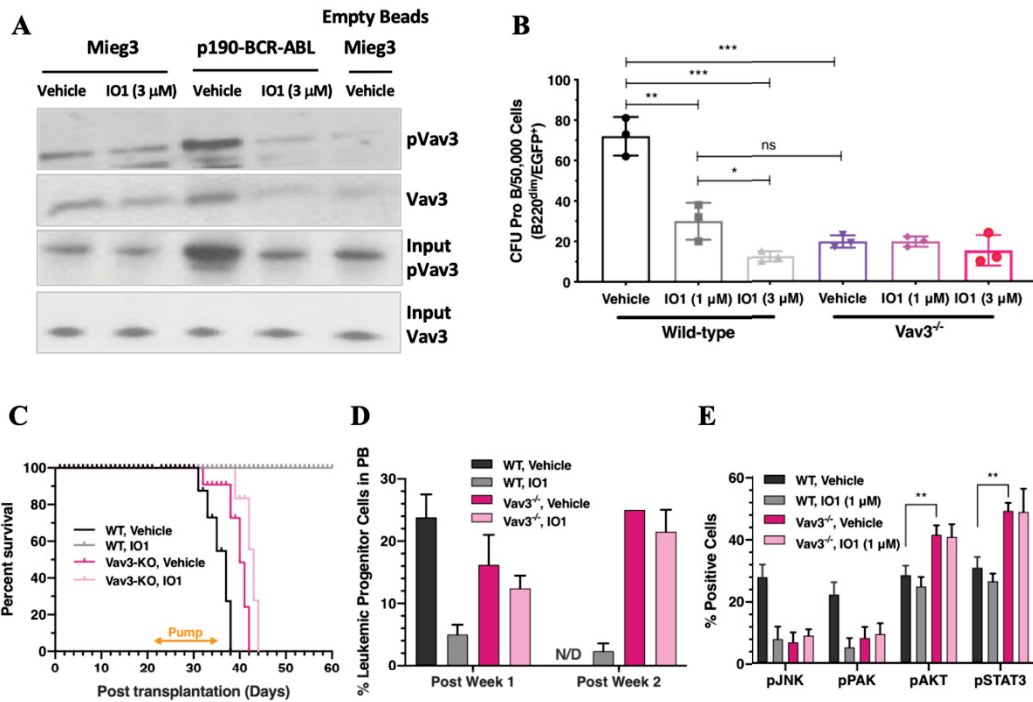
Figure 4: IODVA1 targets Vav3 in vitro and in vivo. (A) Ba/F3 cells expressing Mieg3 or p190-BCR-ABL were treated with vehicle control or IODVA1 (IO1, 3 μM) for 30 min and incubated with GST-Rac and glutathione beads. Beads were washed and the protein complex separated on SDS-PAGE and immunoblotted for pVav3. Input Vav3 was used as control. (B) Quantification of the average number of colonies made by bone marrow wild-type (black) and Vav3$^{-/-}$ (lilac) p190-BCR-ABL leukemic cells treated with vehicle control or IODVA1 (IO1, 1 and 3 M) (* $p \leq 0.05$; ** $p \leq 0.01$; *** $p \leq 0.001$; ns non-significant). (C) Kaplan-Meier plot showing survival of wild-type or Vav3$^{-/-}$ p190-BCR-ABL leukemic mice post treatment with osmotic pumps implanted subcutaneously and carrying vehicle control or IDOVA1 (IO1, 1 mM). (D) Count (% leukemic progenitors in peripheral blood) of residual leukemic (EGFP$^+$-BCR-ABL) cells at week 1 and 2 post treatment for the mice from (C). (E) Pharmacodynamic assessment of leukemic progenitor cells (%) from the mice transduced with wild-type or Vav3$^{-/-}$ p190-BCR-ABL leukemia and treated with vehicle control (blue and green) or IODVA1 (IO1, red and purple) following 2-week treatment using phospho-flow analysis of the indicated effectors (* $p \leq 0.05$; ** $p \leq 0.01$).
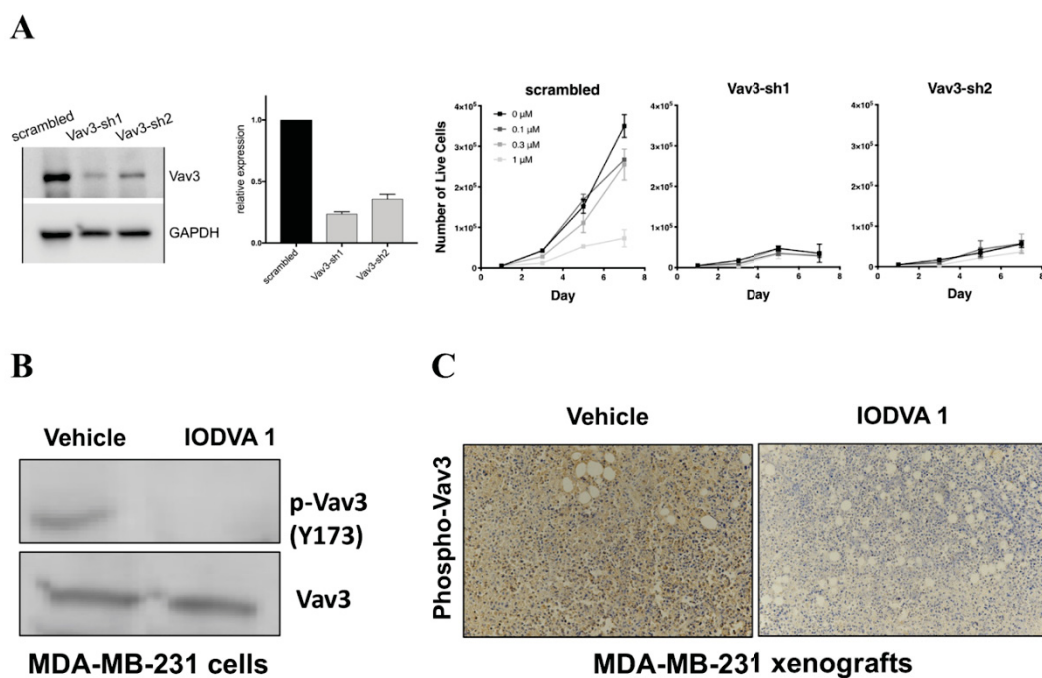
A

B

MDA-MB-231 cells

C

MDA-MB-231 xenografts

Figure 5: IODVA1 decreases levels of pVav3 in in vitro and in vivo models of triple negative breast cancer. (**A**) Immunoblot and quantification of Vav3 protein in lysates of MDA-MB-231 triple negative breast cancer cells stably expressing scrambled or Vav3-targeting shRNAs. Viability of the MDA-MB-231 cells stably expressing shVav3 in the presence of IODVA1 (0 - 1 μM). Cells were grown in the presence of IODVA1 and counted by trypan blue exclusion at the indicated time points. (**B**) MDA-MB-231 cells were incubated with IODVA1 (3 μM) for 15 min and the levels of phosphorylated Vav3 (pY173) were assessed by immunoblotting. (**C**) Immunohistochemical analysis of the levels of phosphorylated Vav3 in tissue derived from MDA-MB-231 xenografts treated with vehicle control or IODVA1.
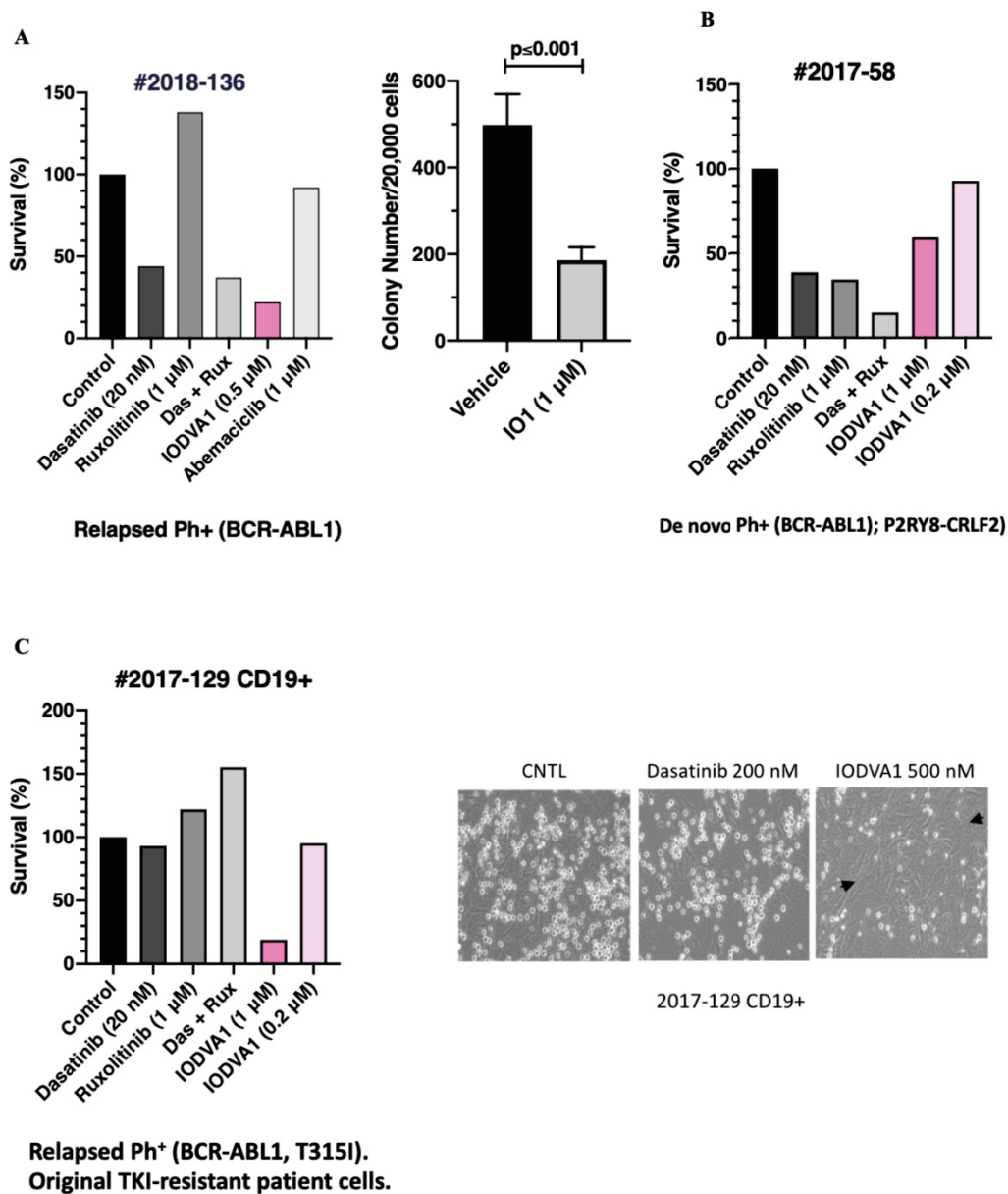
Figure 6: IODVA1 reduces survival of relapsed and de novo pediatric patient derived Ph+ leukemia cells. Patient derived xenograft (PDX) cells were co-cultured ex vivo on MS-5 or OP-9 stromal cells and treated with dasatinib (Das, ABL1-inhibitor), ruxolitinib (Rux, JAK-inhibitor), combination of dasarinib and ruxolitinib (Das + Rux), abemaciclib (CDK inhibitor), or IODVA1 and assessed for survival. **(A)** Representative survival of patient #2018-136 treated cells and of colony number in the presence of IODVA1 (IO1). **(B)** Representative survival of patient #2017-58 and **(C)** patient #2017-129 treated cells. Note lack of toxicity of IODVA1 to normal stromal cells (black arrows) in the accompanying image.

Chapter VIII

Rho inhibition by lovastatin affects apoptosis and DSB repair of primary human lung cells in vitro and lung tissue in vivo following fractionated irradiation

Graphical abstract
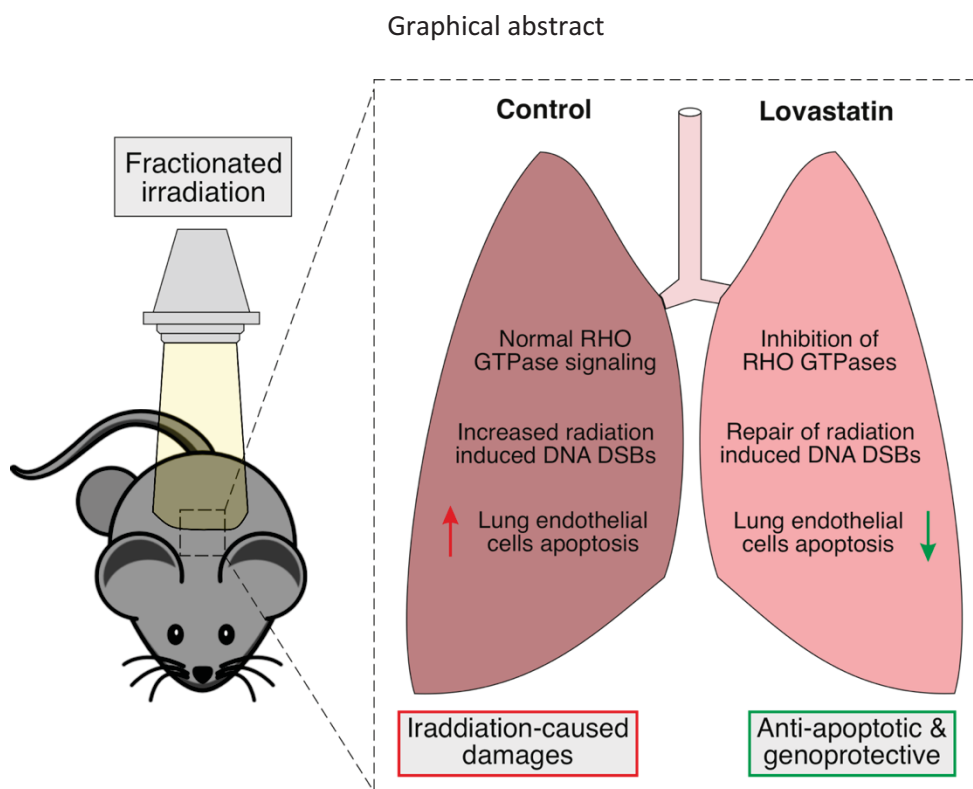
Status:	Published in Cell Death & Disease, August 10th 2017
Impact factor:	5.702
Own proportion to this work:	10 %
	Expression and purification of RHO GTPase effectors, RAC GTP pull down assays, writing the manuscript, discussion.

OPEN

Rho inhibition by lovastatin affects apoptosis and DSB repair of primary human lung cells *in vitro* and lung tissue *in vivo* following fractionated irradiation

Verena Ziegler[1], Christian Henninger[1], Ioannis Simiantonakis[2], Marcel Buchholzer[3], Mohammad Reza Ahmadian[3], Wilfried Budach[2] and Gerhard Fritz*,[1]

Thoracic radiotherapy causes damage of normal lung tissue, which limits the cumulative radiation dose and, hence, confines the anticancer efficacy of radiotherapy and impacts the quality of life of tumor patients. Ras-homologous (Rho) small GTPases regulate multiple stress responses and cell death. Therefore, we investigated whether pharmacological targeting of Rho signaling by the HMG-CoA-reductase inhibitor lovastatin influences ionizing radiation (IR)-induced toxicity in primary human lung fibroblasts, lung epithelial and lung microvascular endothelial cells *in vitro* and subchronic mouse lung tissue damage following hypo-fractionated irradiation (4x4 Gy). The statin improved the repair of radiation-induced DNA double-strand breaks (DSBs) in all cell types and, moreover, protected lung endothelial cells from IR-induced caspase-dependent apoptosis, likely involving p53-regulated mechanisms. Under the *in vivo* situation, treatment with lovastatin or the Rac1-specific small molecule inhibitor EHT1864 attenuated the IR-induced increase in breathing frequency and reduced the percentage of γH2AX and 53BP1-positive cells. This indicates that inhibition of Rac1 signaling lowers IR-induced residual DNA damage by promoting DNA repair. Moreover, lovastatin and EHT1864 protected lung tissue from IR-triggered apoptosis and mitigated the IR-stimulated increase in regenerative proliferation. Our data document beneficial anti-apoptotic and genoprotective effects of pharmacological targeting of Rho signaling following hypo-fractionated irradiation of lung cells *in vitro* and *in vivo*. Rac1-targeting drugs might be particular useful for supportive care in radiation oncology and, moreover, applicable to improve the anticancer efficacy of radiotherapy by widening the therapeutic window of thoracic radiation exposure.
Cell Death and Disease (2017) **8,** e2978; doi:10.1038/cddis.2017.372; published online 10 August 2017

Radiation therapy (RT) is a frequently used treatment modality for thoracic malignancies. However, its therapeutic efficacy is limited because of adverse effects on normal lung tissue, resulting in radiation-induced lung injury (RILI). RILI manifests as lung inflammation or fibrosis weeks to years after RT. More sophisticated RT techniques (e.g., conformal RT or intensity-modulated RT) allow better tumor control whilst sparing normal tissue.[1] In addition, pharmacological strategies to prevent RILI are preferential because they would allow the application of higher cumulative radiation doses, thereby further improving local tumor control and, moreover, improving the quality of life of cancer patients. In view of clinical translation of preclinical data in a timely manner, off-label use of already approved drugs appears desirable.

Statins are such promising class of drugs because they are frequently used for lipid-lowering purpose and are well tolerated. All statins have in common that they interfere with the rate-limiting step in the synthesis of cholesterol by inhibiting the conversion of 3-hydroxy-3-methylglutaryl coenzyme A (HMG-CoA) by the HMG-CoA reductase. In consequence, the cellular pool of isoprene moieties (i.e., geranyl- and farnesylpyrophosphate) is depleted. In addition to cholesterol biosynthesis, isoprene residues are also required for C-terminal prenylation and membrane localization of regulatory proteins, notably Ras-homologous small GTPases (Rho-GTPases). Therefore, the pleiotropic effects of statins are believed to mainly result from the inhibition of Rho-GTPases,[2,3] in particular RhoA[4] and Rac1.[5,6] Apart from exhibiting anticancer effects *in vitro* and *in vivo*[7–9] statins also mitigate normal tissue damage evoked by anticancer therapeutics and irradiation. For instance, lovastatin protects cardiomyocytes from the anthracycline derivative doxorubicin.[6,10–12] Moreover, statins are radio-protective *in vitro*[13] and *in vivo*.[14–16] However, in most of these studies, the impact of statins on anticancer therapy-induced normal tissue damage was investigated in acute models, that is, after single treatment with high doses and analysis at early time points after exposure. The influence of statins on adverse late responses resulting from fractionated irradiation of the lung is unknown. Moreover, it is unclear which cell type of the lung is particularly sensitive to fractionated irradiation and, hence, might be of major relevance for the pathophysiology of RILI and, correspondingly, could be targeted for radioprotection.

In the present study we investigated (i) the effects of lovastatin on different types of confluent (non-growing)

[1]Institute of Toxicology, Medical Faculty, Heinrich Heine University Duesseldorf, Moorenstrasse 5, Duesseldorf, Germany; [2]Department of Radiotherapy and Radiation Oncology, University Hospital Duesseldorf, Moorenstraße 5, Duesseldorf, Germany and [3]Institute of Biochemistry and Molecular Biology II, Medical Faculty, Heinrich Heine University, Duesseldorf, Germany
*Corresponding author: G Fritz, Institute of Toxicology, Heinrich Heine University Duesseldorf, Moorenstrasse 5, 40225 Düsseldorf, Germany. Tel: +49 221 81 13022; Fax: +49 221 81 13013; E-mail: fritz@uni-duesseldorf.de
Received 16.3.17; revised 22.6.17; accepted 02.7.17; Edited by A Stephanou

2

primary human lung cells following fractionated irradiation *in vitro* and (ii) the impact of lovastatin and the Rac1-specific small molecule inhibitor EHT1864 on RILI analyzed four weeks after fractionated lung irradiation *in vivo*. EHT1864 was included to figure out the specific relevance of Rac1-regulated signaling mechanisms for statin-mediated effects.

Results

Analysis of radioprotective effects of lovastatin in primary human lung cells. So far radioprotective effects of statins were mostly investigated under acute settings, applying single and high radiation doses. This poorly mimics the clinical relevant situation of radiotherapy. Here, we applied a hypo-fractionated irradiation protocol and analyzed delayed lung toxicity *in vitro* (Figure 1a) and *in vivo* (Figure 4b). Regarding the *in vitro* analyses, we used different types of primary human lung cells and performed the experiments at cell confluency as confirmed by microscopy (Figure 1d)

and measurement of mitotic index (Figures 1b and c). Upon fractionated irradiation (4 × 4 Gy, every 24 h) of microvascular endothelial cells of the lung (HMVEC-L), pulmonary fibroblasts (HPF) or small airway epithelial cells (HSAEpC) we observed significant cytotoxicity only in HMVEC-L as shown by microscopical analysis (Figure 1d) and analysis of apoptosis by Annexin V-based method (Figures 1e–g). We assume that pulmonary fibroblasts and epithelial cells preferentially activate mechanisms of senescence following radiation.[17,18] Co-treatment with low doses of lovastatin completely prevented apoptosis induction in HMVEC-L (Figure 1e). Fractionated irradiation decreased the protein level of pro-caspase 3, increased the levels of cleaved caspases 3 and 7 and promoted PARP-1 cleavage (Figure 2a). Lovastatin mitigated activation of caspases and PARP cleavage (Figure 2a). Protein expression of Bax, Bcl-2 and XIAP remained unchanged in all experimental groups (Figure 2a). Fractionated irradiation-induced apoptosis of HMVEC-L was accompanied by slightly increased mRNA expression of *Bax* and substantial increase in Fas receptor
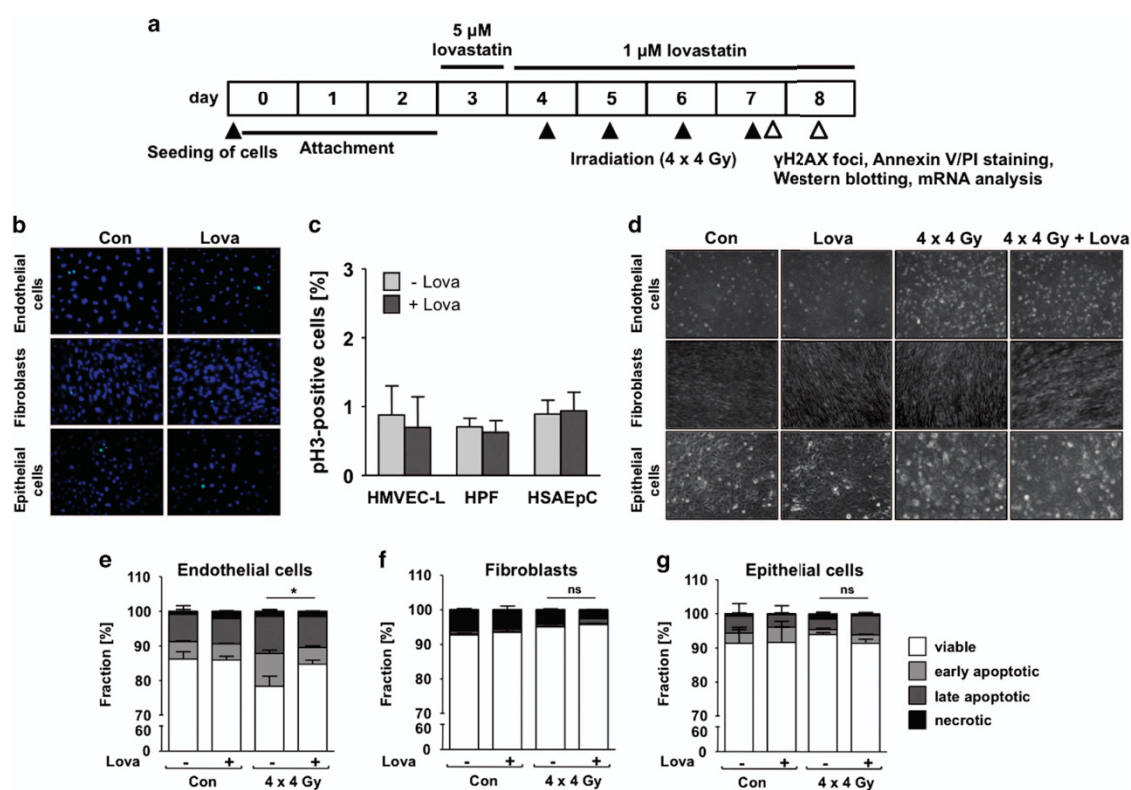

Figure 1 Fractionated irradiation does not induce apoptosis in confluent primary human lung epithelial cells or lung fibroblasts, but leads to apoptotic cell death in lung endothelial cells, which is prevented by lovastatin. Human microvascular endothelial cells of the lung (HMVEC-L), human pulmonary fibroblasts (HPF) and human small airway epithelial cells (HSAEpC) were seeded in high density and grown to confluency before lovastatin (Lova) (5 μM) pretreatment. After incubation period of 24 h, lovastatin concentration was reduced (1 μM) and irradiation was performed (4 × 4 Gy) as described in methods. Control cells were vehicle-treated and subjected to sham irradiation. (**a**) Treatment scheme. (**b,c**) pH3 staining (= mitotic index) after 24 h pre-incubation with lovastatin (5 μM) to verify cell confluency. Shown are representative images (**b**) and quantitative data (**c**). (**d**) Analysis of cell morphology 24 h after the last irradiation. (**e–g**) Apoptosis was measured by Annexin V/PI staining 24 h after the last irradiation. Data show the mean ± S.D. from $n = 2$–3 independent experiments. Annexin V positive/PI-negative cells are considered as early apoptotic, Annexin V negative/PI-positive cells as necrotic. Two-way ANOVA with Bonferroni *post hoc* test. *$P \leq 0.05$ IR *versus* IR+Lova
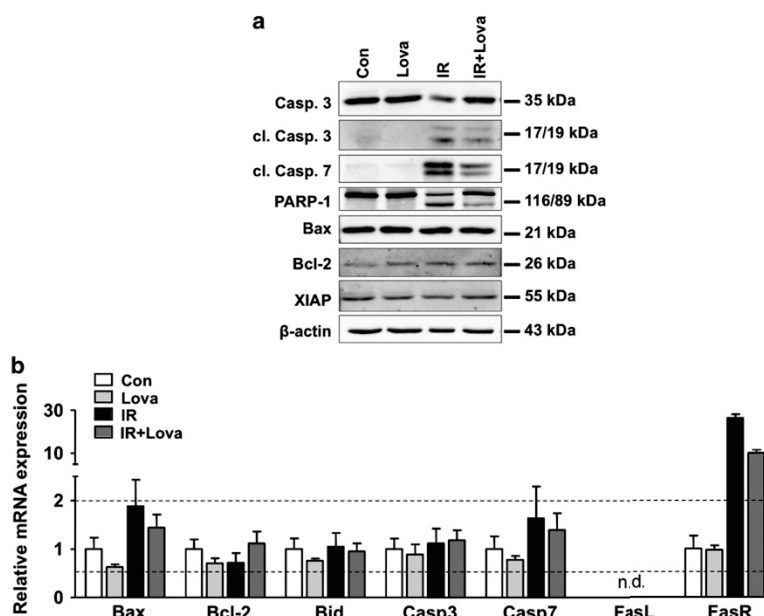
Figure 2 Fractionated irradiation causes activation of caspases in human lung endothelial cells, which is attenuated by lovastatin. Human microvascular endothelial cells of the lung (HMVEC-L) were seeded in high density and grown to confluency before lovastatin (Lova) (5 μM) pretreatment. After incubation period of 24 h, lovastatin concentration was reduced (1 μM) and irradiation was performed (4x4 Gy) as described in methods. Control cells were vehicle-treated and subjected to sham irradiation. (**a**) Protein extracts were harvested 24 h after the last irradiation and analyzed for the expression of pro-caspase 3 (Casp. 3), cleaved caspase 3 (cl. Casp. 3), cleaved caspase 7 (cl. Casp. 7), Poly (ADP-ribose)-polymerase 1 (PARP-1) as well as of Bax, Bcl-2 and XIAP. Expression of β-actin was used as loading control. (**b**) mRNA levels of Bax, Bcl-2, Bid, caspases 3 (Casp3) and 7 (Casp7) as well as of Fas ligand (FasL) and Fas receptor (FasR) were analyzed six hours after the last irradiation using quantitative real-time PCR. Results are shown as mean ± S.D. of a representative experiment performed in triplicates. mRNA expression of ≥ 2 and ≤ 0.5 as compared with control (set to 1.0) are marked with dashed lines. n.d., not detectable

(*FasR*) expression (Figure 2b), which again was partially reduced by lovastatin (Figure 2b). Overall, the data indicate that fractionated irradiation triggers caspase-dependent and lovastatin-sensitive death pathways preferentially in lung endothelial cells.

Lovastatin protects lung cells from DNA damage induced by fractionated irradiation. DNA double-strand breaks (DSBs) are major cytotoxic lesions induced by IR and effectively trigger apoptosis or senescence.[19,20] Nuclear γH2AX (Ser139 phosphorylated histone H2AX) foci are commonly used surrogate markers of DSBs.[21] All lung cell types revealed a similar initial number of γH2AX foci (Figures 3a, b, d and f), which was unaffected by the statin. Hence, we hypothesize that lung cells form identical levels of initial DSBs but differ from each other regarding complex DNA damage-triggered pro-apoptotic signaling mechanisms.[22] After post-incubation period of 24 h, significantly lower DSB levels were found in the lovastatin co-treated groups (Figures 3c, e and g), showing that the statin accelerates the repair of DSBs. The number of residual γH2AX foci in the absence of lovastatin was 2–3-fold higher in epithelial cells as compared with endothelial cells and fibroblasts (Figures 3c, e and g), indicating that epithelial cells have the lowest DSBs repair capacity. Apparently, lovastatin favors the repair of IR-induced potentially lethal damage especially in lung endothelial cells.

Lovastatin did not reduce the radiation-stimulated increase in pATM protein, a key regulator of the DNA damage response (DDR), and its substrate pKap1 (Figure 3h). Protein levels of pp53, which were also increased following IR treatment, were lower in statin-treated lung fibroblasts and epithelial cells, but were largely unaffected in endothelial cells (Figure 3h), supporting the view of cell type-specific effects of fractionated irradiation and statins on lung cells.

Response of HUVEC and MRC-5 cells to fractionated irradiation. Including primary human umbilical vein endothelial cells (HUVEC) and human fetal lung fibroblasts (MRC-5 cells) in our study, similar results were obtained as with primary lung cells. Whereas HUVEC revealed a substantially elevated frequency of apoptotic cells following fractionated irradiation, which was reduced by lovastatin (Supplementary Figure 1A), apoptosis was not triggered in MRC-5 cells (Supplementary Figure 2A). However, both cell types showed accelerated repair of DSBs if lovastatin was present (Supplementary Figures 1B and 2B). Moreover, IR-stimulated DDR was affected by lovastatin in both cell types, as detectable on the levels of pKap1 and pp53 (Supplementary Figures 1C and 2C). The data demonstrate that the response of confluent primary human cells to hypo-fractionated irradiation is cell type-specific: a substantial apoptotic response occurs in lung microvascular endothelial
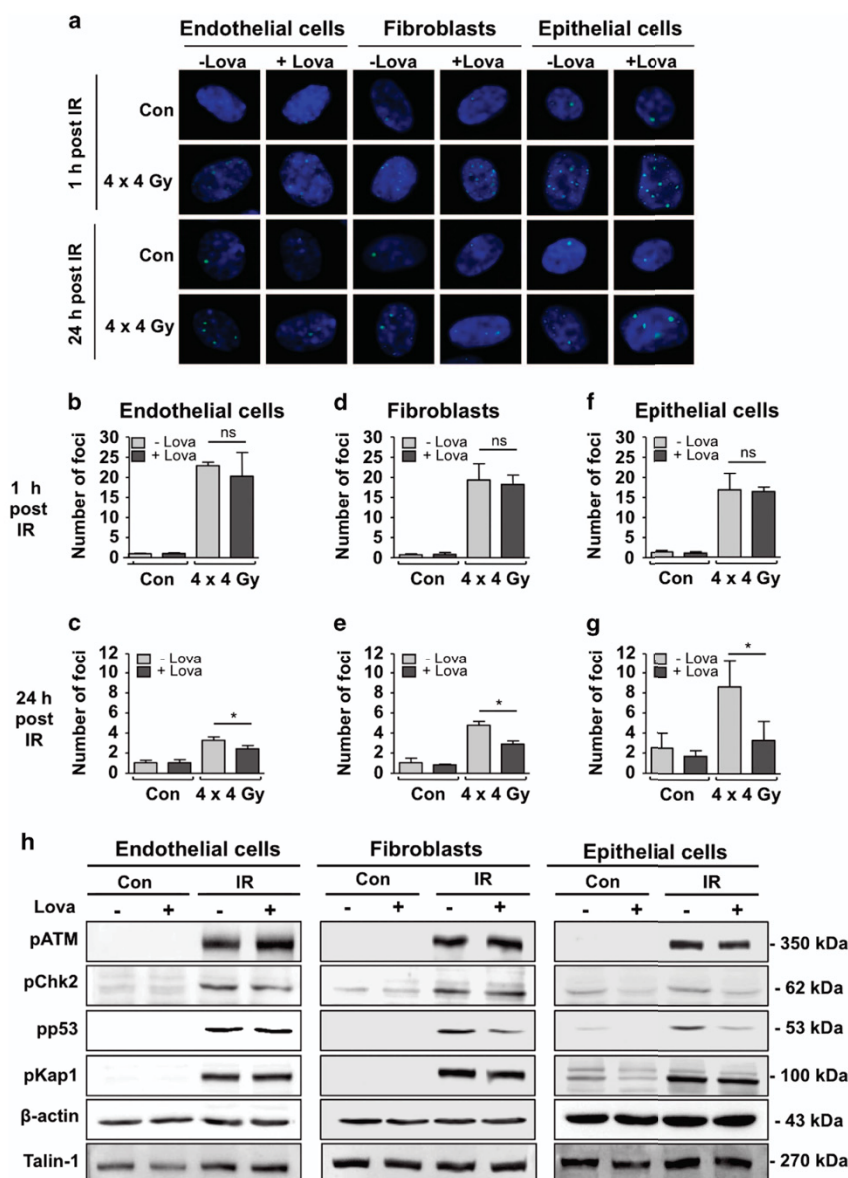
Figure 3 Lovastatin has no influence on initial DNA double-strand break (DSB) formation following fractionated irradiation. However, it lowers the amount of residual DNA DSBs and impacts mechanisms of the DDR in primary human lung cells. Non-growing HMVEC-L, HPF and HSAEpC were treated as described before (Figure 1a). The number of nuclear γH2AX foci was analyzed by immunocytochemical staining. (**a**) Representative images. green, γH2AX foci; blue, DAPI. (**b–g**) Number of γH2AX foci detectable 1 h (**b**, **d**, **f**) and 24 h (**c**, **e**, **g**) after the last irradiation. Shown are the mean $\pm$ S.D. from $n = 2$–3 independent experiments. Two-way ANOVA with Bonferroni *post hoc* test. *$P \leq 0.05$ IR *versus* IR+Lova. (**h**) One hour after the last irradiation the activation status of a subset of key proteins of the DNA damage response was investigated by Western blot analysis. Shown are the protein levels of Ser1981 phosphorylated ATM (pATM), Thr68 phosphorylated checkpoint kinase-2 (pChk2), Ser15 phosphorylated protein 53 (pp53), Ser824 phosphorylated KRAB-associated protein-1 (pKap1). Expression of β-actin and Talin-1 were used as loading controls

and umbilical vein endothelial cells but not in lung fibroblasts or lung epithelial cells. However, independent of the cell type, lovastatin accelerates the repair of radiation-induced DSBs.

Fractionated lung irradiation *in vivo*: effects on body weight and breathing frequency. To address the question

whether lovastatin is radioprotective *in vivo,* we aimed to selectively irradiate the right lung of mice without profuse concomitant irradiation of the left lung or other non-target organs. We established an irradiation device (Figure 4a) that is shielding other tissues (i.e., left lung, heart, liver) using CT-based 3D modeling. One hour after single irradiation
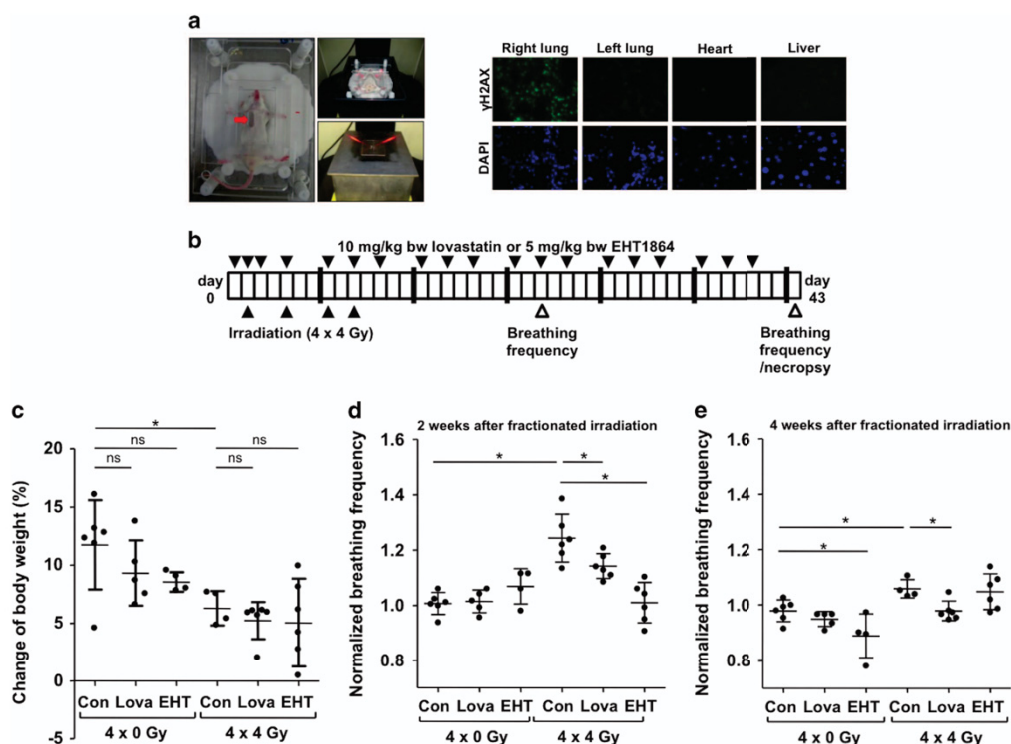
Figure 4 Fractionated irradiation of the lung leads to a reduced gain of body weight and an increased breathing frequency two weeks after irradiation. Lovastatin and EHT1864 treatment have no effect on body weight, but decrease IR-mediated increase in breathing frequency. (**a**) Selective irradiation of the right mouse lung was achieved using a metal-free device, which is adjustable in *x*-, *y*- and *z*-direction. 6 mm lead shielding prevents irradiation of other tissue. The red arrow marks the radiation field. One hour after single irradiation (4 Gy) of the right lung of anesthesized BALB/c mice, different tissues (lung, heart, liver) were analyzed for the presence of γH2AX foci, which are indicative of DSBs. Nuclei were counterstained with DAPI. Shown are representative photographs. (**b**) Treatment scheme. As based on previous *in vivo* studies[6,14,66,67] male BALB/c mice were treated three times per week with lovastatin (10 mg/kg BW) or the Rac1-specific small molecule inhibitor EHT18641 (5 mg/kg BW) during a total period of six weeks. In the course of the first two weeks the right lung of the animals was irradiated four times with each 4 Gy (4 × 4 Gy), resulting in a cumulative dose of 16 Gy. Control animals were not irradiated (4 × 0 Gy). (**c**) Body weight was recorded three times per week. Data shown are changes in percent of body weight between the start and end of the experiment. Shown are the mean ± S.D. of $n = 4–6$ animals per experimental group. Two-way ANOVA with Bonferroni *post hoc* test, $*P \leq 0.05$. ns, not significant. (**d,e**) Breathing frequency, which is indicative of radiation pneumonitis,[24,25,68] was determined two weeks (**d**) and four weeks (**e**) after the end of the fractionated irradiation. Breathing frequency of control animals was set to 1. Mean ± S.D. of $n = 4–6$ animals per experimental group. Two-way ANOVA with Bonferroni *post hoc* test, $*P \leq 0.05$

(4 Gy) the frequency of γH2AX-positive cells was specifically increased in the right lung but not in other adjacent tissues (Figure 4a), demonstrating the accuracy of our radiation device.

To investigate delayed radiation-induced lung injury, the right lung of male BALB/c mice was subjected to hypo-fractionated irradiation in the presence or absence of lovastatin or the Rac-specific inhibitor EHT1864[23] (Figure 4b). Irradiation slightly slowed down the gain of body weight during the evaluation period (Figure 4c), which was not affected by lovastatin and EHT1864. The moderate radiation effect on body weight is indicative of a low general radiotoxicity. Breathing frequency, which is widely used as indication of lung function (e.g., radiation-induced pneumonitis),[24–26] was elevated by ~20% in the irradiated group two weeks after the last irradiation (Figure 4d). While lovastatin reduced the breathing frequency only slightly, inhibition of Rac1 by EHT1864 caused a more pronounced normalization of

breathing frequency (Figure 4d). Four weeks after the last irradiation, breathing frequency was only marginally elevated in the irradiated group (Figure 4e).

Fractionated lung irradiation (4x4 Gy) does not cause sustained inflammation or oxidative stress. Lung sections stained with hematoxylin/eosin or Sirius Red showed no obvious inflammatory cell infiltrates or fibrotic lesions, respectively (Supplementary Figures 3A and B), indicating that fractionated irradiation does not cause sustained inflammatory or fibrotic processes. qRT-PCR-based mRNA expression analyses showed similar results (Supplementary Figure 4). Only IL-1α, MMP2 and MPO exhibited a slight mRNA upregulation in the irradiated group as compared with sham-treated controls (Supplementary Figure 4). Lovastatin and EHT1864 had no effect. A 2–3-fold increase in the number of CD68-positive cells (i.e., alveolar macrophages[27]) was observed in the irradiated group (Supplementary Figures

3C and D), which was neither influenced by lovastatin nor EHT1864 (Supplementary Figure 3D). As irradiation also triggers the generation of reactive oxygen species (ROS), we investigated oxidative stress by measuring the expression of major factors of the antioxidative defense system, which is majorly regulated by the transcription factor Nuclear Factor (erythroid-derived 2)-like 2 (Nrf2).[28] Immunohistological staining of Nrf2 in irradiated animals did not reveal any increase in protein level (Supplementary Figure 5A). Likewise, the mRNA expression of prototypical Nrf2 target genes such as glutathione peroxidase-1 (GPX1), heme oxygenase-1 (HO-1) and glutathion-S transferase (GSTM1) remained unchanged in irradiated lung tissue (Supplementary Figure 5B). Protein and mRNA expression of manganese superoxide dismutase (MnSOD), which is radioprotective in lung,[29–31] was also not influenced by our irradiation protocol (Supplementary Figures 5B and C). Noteworthy yet, GPX1 and HO-1 mRNA expression were upregulated in human lung endothelial cells (HMVEC-L) following fractionated irradiation *in vitro* (Supplementary Figure 5D). Lovastatin reduced the irradiation-induced upregulation of both genes in HMVEC-L. Thus, although it appears questionable that ROS is a major trigger of chronic lung toxicity following fractionated irradiation, its contribution to lung damage cannot be ruled out.

Lovastatin and EHT1864 reduce IR-induced cell death of lung cells *in vivo*. Apoptosis of lung cells is a hallmark of RILI.[27] Fractionated irradiation caused a 6-fold increase in the number of apoptotic (i.e., TUNEL positive) cells in the irradiated group (Figures 5a and b), which was mitigated by lovastatin and EHT1864 (Figure 5b). On protein level, no radiation-induced increase in the cleavage of caspases or PARP-1 was observed (Supplementary Figure 6B). Only the mRNA expression of *Bax* and *caspase 7* was slightly increased in irradiated animals, which was attenuated by lovastatin and EHT1864 co-treatment (Figure 5g). Fractionated lung irradiation raised the mitotic index (= frequency of phospho-histone H3 (Ser10) positive cells), which is indicative of regenerative proliferation, in the lung (Figures 5c and d). Again, both lovastatin and EHT1864 largely prevented this radiation effect. Analyzing the expression of proliferating cell nuclear antigen (PCNA), another surrogate marker of proliferation, identical results were obtained (Figures 5e and f).

Lovastatin and EHT1864 lower IR-induced residual DNA damage in lung tissue. IR-induced DNA double-strand breaks (DSBs) are vastly detrimental DNA lesions and effectively trigger cell death.[32] Following fractionated lung irradiation an about 8-fold increased frequency of γH2AX foci-positive cells was found (Figures 6a and b). Lovastatin reduced the IR-induced DNA damage by about 30%. This radioprotective effect was even more pronounced (~ 50%) by EHT1864. Identical results were obtained upon analysis of nuclear 53BP1 foci (Figures 6c and d), another surrogate marker of DSBs. The non-irradiated left lung showed no elevated number of γH2AX foci expressing cells (Supplementary Figure 7), ruling out the possibility of delayed DNA damaging effects in non-irradiated adjacent tissue. In conclusion, lovastatin and EHT1864 lower the number of lung cells with residual DSBs resulting from fractionated irradiation.

Influence of lovastatin and EHT1864 on IR-activated DDR *in vivo*. Cells respond to the induction of DSBs with the activation of the ATM (Ataxia telangiectasia mutated) protein kinase, a key regulator of the DDR that coordinates DNA repair and apoptosis.[33–35] The protein levels of phosphorylated ATM and its prototypical substrates p53 and the heterochromatin protein Kap-1 were elevated in total lung tissue extracts of irradiated animals as compared with non-irradiated controls (Figure 7). Protein expression of activated ATR (pATR) and checkpoint kinase 1 (pChk1), which are key players in the regulation of replicative stress responses, was not detectable under our experimental conditions (data not shown). Phosphorylation of DDR factors in the irradiated mice remained largely unaffected by lovastatin and EHT1864 (Figures 7a and b). Only the IR-induced increase in pATM was significantly reduced by EHT1864 (Figure 7b). Regarding pp53 levels, the statin and EHT caused a slight reduction (Figure 7b). Summarizing, fractionated irradiation results in a sustained activation of DDR factors in lung tissue, which is partially affected by lovastatin or EHT1864.

Discussion

HMG-CoA reductase inhibitors (statins) have multiple cholesterol-independent effects by interfering with Rho-GTPases.[2] Inhibition of Rho signaling by statins is radioprotective in umbilical vein endothelial cells *in vitro*[13] and in an acute rat model of radiation enteritis,[15,16] with Rho-associated kinase (ROCK) being involved. Cytoprotective properties of statins on acute lung injury have been demonstrated using intratracheal instillation of the radiomimetic bleomycin,[36,37] single high-dose thorax irradiation[14,38] or total body irradiation.[39] Here, we investigated delayed radiotoxicity resulting from fractionated irradiation employing both *in vitro* and *in vivo* model systems. We found that human lung microvascular endothelial cells are characterized by a higher frequency of radiation-induced caspase-mediated apoptosis as compared with lung fibroblasts or lung epithelial cells, indicating that especially injury of endothelial cell-related functions contributes to RILI. Since radiation-induced damage to endothelial cells is also mitigated by atorvastatin[40] and pravastatin,[41] we hypothesize that radiation triggered caspase-mediated death and its prevention by statins is particularly relevant for endothelial cells. By contrast, lung fibroblasts and lung epithelial cells might preferentially undergo senescence upon irradiation.[17,18] As fractionated irradiation-stimulated apoptosis in lung endothelial cells was accompanied by ATM-dependent activation of p53 as well as upregulation of the p53-regulated *FasR* gene, we hypothesize that p53 is involved in this process.

Lovastatin accelerated the removal of radiation-induced DSBs in all three types of lung cells, suggesting that it stimulates DSB repair. Noteworthy, lovastatin also promotes DSB repair in human keratinocytes *in vitro*.[42] Moreover, pravastatin improves the repair of radiation-induced DSBs in fibroblasts obtained from Huntington's disease patient's[43] and atorvastatin accelerates the repair of oxidative DNA damage in smooth muscle cells.[44] Additionally, lovastatin prevents DSB formation following treatment with topoisomerase type II poisons.[11,45] Apparently, statins are genoprotective *in vitro*, which is at least partially due an improved DNA repair and/or
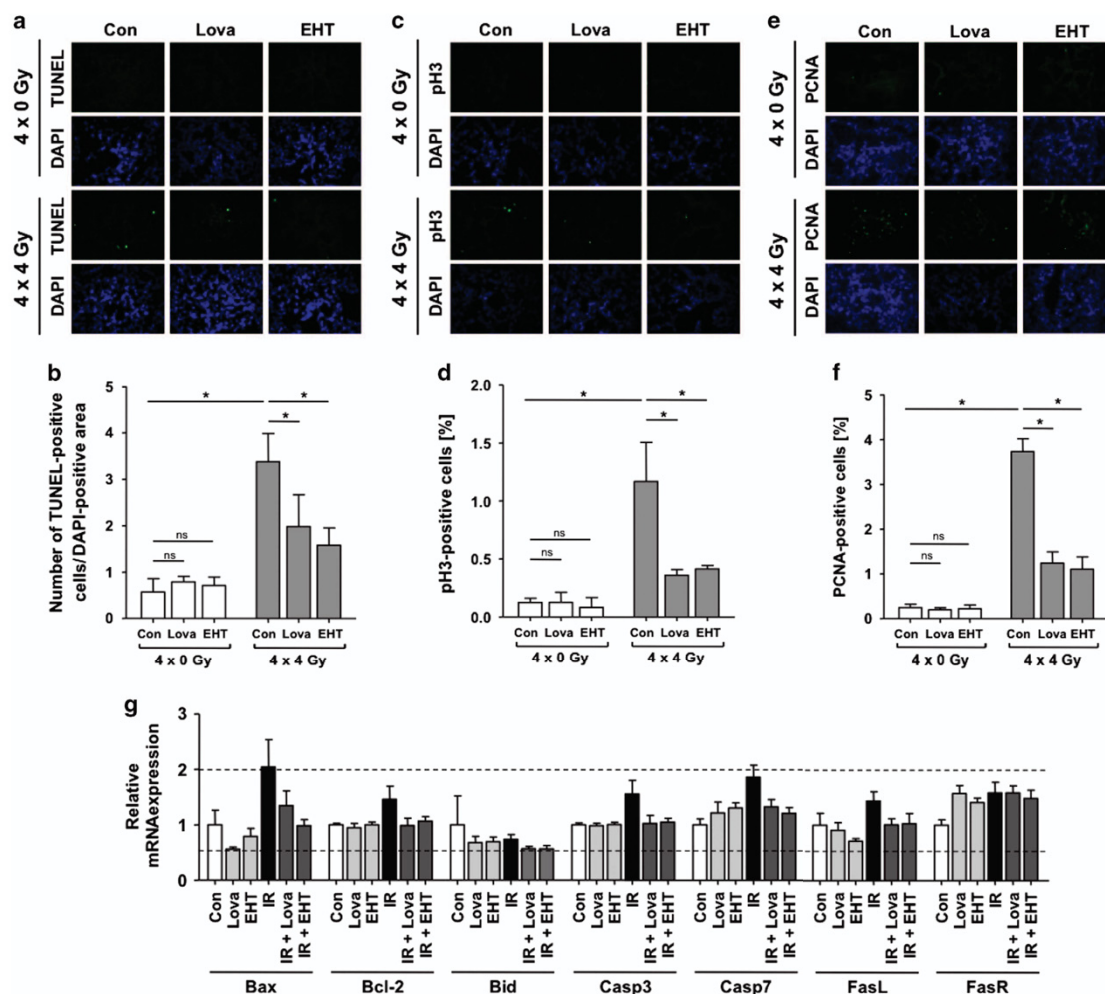
Figure 5 Lovastatin and EHT1864 attenuate IR-induced apoptosis and regenerative proliferation following fractionated irradiation of the lung. Male BALB/c mice were treated according to Figure 4b. Four weeks after the last irradiation the frequency of apoptotic cells (TUNEL), mitotic index (pH3) and cell proliferation (PCNA) were analyzed in the right lung. (**a**,**b**) Apoptotic frequency was determined using the TUNEL assay. (**a**) Representative image. Nuclei are stained by DAPI (blue). (**b**) Quantitative data are shown as the mean$\pm$S.D. from $n = 4$–6 animals per experimental group. Two-way ANOVA with Bonferroni *post hoc* test, *$P \leq 0.05$. ns, not significant. (**c**,**d**) Mitotic index was investigated by detection of cells expressing Ser10 phosphorylated histone H3 (pH3). (**c**) Representative image. Nuclei are stained by DAPI (blue). (**d**) Quantitative data are shown as the mean$\pm$S.D. from $n = 4$–6 animals per experimental group. Two-way ANOVA with Bonferroni *post hoc* test, *$P \leq 0.05$. ns, not significant. (**e**,**f**) Cell proliferation was investigated by immunohistochemistry-based staining of proliferating cell nuclear antigen (PCNA). (**e**) Representative images are shown. Nuclei are stained with DAPI (blue). (**f**) Quantitative data are shown as the mean+S.D. from $n = 3$ animals per experimental group. Two-way ANOVA with Bonferroni *post hoc* test, *$P \leq 0.05$. ns, not significant. (**g**) mRNA levels of Bax, Bcl-2, Bid, caspases 3 (Casp3) and 7 (Casp7) as well as of Fas ligand (FasL) and Fas receptor (FasR) were analyzed using quantitative real-time PCR. Relative mRNA expression in non-irradiated animals was set to 1.0. mRNA expression of ≥ 2 and ≤ 0.5 as compared with control are marked with dashed lines. Shown are the mean $\pm$ S.D. from pooled samples of $n = 4$-6 animals per group ($N = 3$).

protection from DNA damage formation. Since Rac1 is a relevant target of statins[5] and, moreover, is present in the nucleus,[46] we speculate that it interferes with the ATM/ATR-regulated DDR.[47] Accordingly, pharmacological inhibition of Rac1 blocks IR-stimulated ATM/Chk2 and ATR/Chk1 activity in pancreatic carcinoma cells.[48,49] Interestingly, zoledronic acid, which inhibits farnesylpyrophosphate (FPP) synthesis, also promotes the repair of IR-induced DSBs in mesenchymal stem cells.[50]

To scrutinize the *in vivo* relevance of our *in vitro* data, we established a mouse model that enables a local and fractionated irradiation of the right lung and analyzed RILI at late time points (i.e., 4 weeks) after irradiation. Using this clinical designed protocol we found that inhibition of Rac1 signaling might mitigate acute radiation pneumonitis as observed two weeks after irradiation. At later time point, clear signs of persisting inflammation or sustained oxidative stress, as reflected by Nrf2-regulated activation of antioxidative
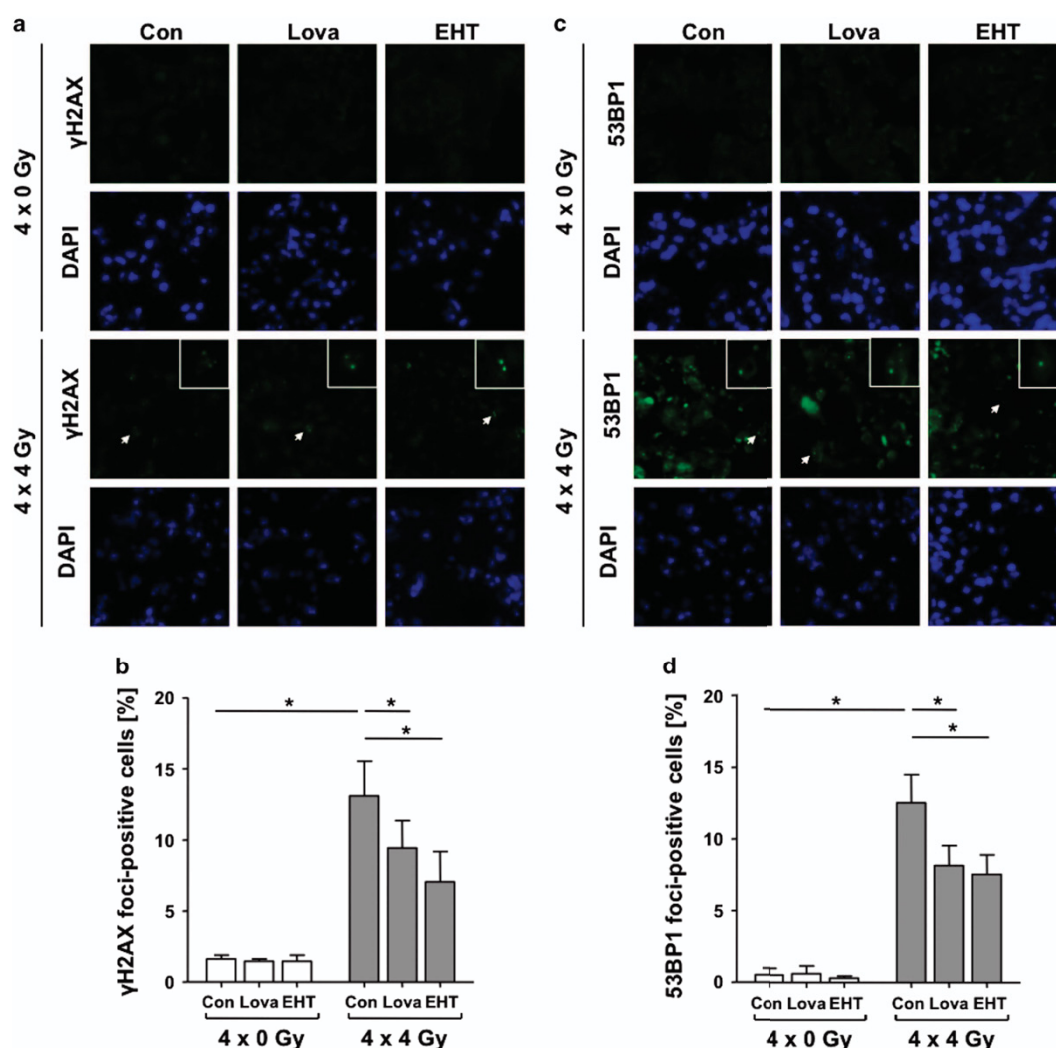
Figure 6 Lovastatin and EHT1864 attenuate the level of IR-induced residual DNA damage in lung tissue as reflected on the level of γH2AX-positive and 53BP1-positive cells. Male BALB/c mice were treated according to Figure 4b. Four weeks after the last irradiation nuclear γH2AX foci (**a,b**) and 53BP1 foci (**c,d**) were analyzed as surrogate markers of DSBs in the right lung. (**a**) Representative images. Nuclei were stained by DAPI (blue). Arrow points to a representative γH2AX-positive cell (enlarged in the image detail). (**b**) Quantification of γH2AX-positive cells in tissue of the right lung. Data shown are the mean $\pm$ S.D. from $n = 4$-6 mice per experimental group. Two-way ANOVA with Bonferroni *post hoc* test, *$P \leq 0.05$. (**c**) Representative images are shown. Nuclei were stained by DAPI (blue). Arrow points to a representative 53BP1-positive cell (this area is enlarged in the image detail). (**d**) Quantification of 53BP1-positive cells in tissue of the right lung. Data shown are the mean $\pm$ S.D. from $n = 3$ mice per experimental group. Two-way ANOVA with Bonferroni *post hoc* test, *$P \leq 0.05$

defense mechanisms, were not detectable anymore. Notably, statins are known to attenuate pro-fibrotic radiation responses after single high-dose irradiation[4,15,16,51,52] and to reduce vascular leakage and leucocyte infiltration in a model of acute RILI.[14] Thus, our data, together with these reports, further support the hypothesis of beneficial effects of statins on RILI.

The primary cytotoxic DNA damage induced by ionizing radiation are DSBs, which stimulate DDR mechanisms regulating cell cycle checkpoints, DNA repair, cell death and senescence.[20,33] The interplay between mechanisms of DNA repair, DDR and apoptosis or senescence is rather complex,[22]

with p53 being a major determinant of cell fate decision, and, moreover, mechanisms of resistance are manifold.[53] Therefore, alterations in DNA repair do not necessarily go along with proportional changes in apoptosis. This might explain the cell type-specific diverse effects of lovastatin on IR-induced apoptosis and DSB repair. We hypothesize that pharmacological interference with (early) primary stress responses resulting from radiation-induced DNA damage is more effective regarding tissue protection than abrogation of (late) secondary responses. Consequently, acceleration of DSB repair or blockage of pro-apoptotic DDR is considered
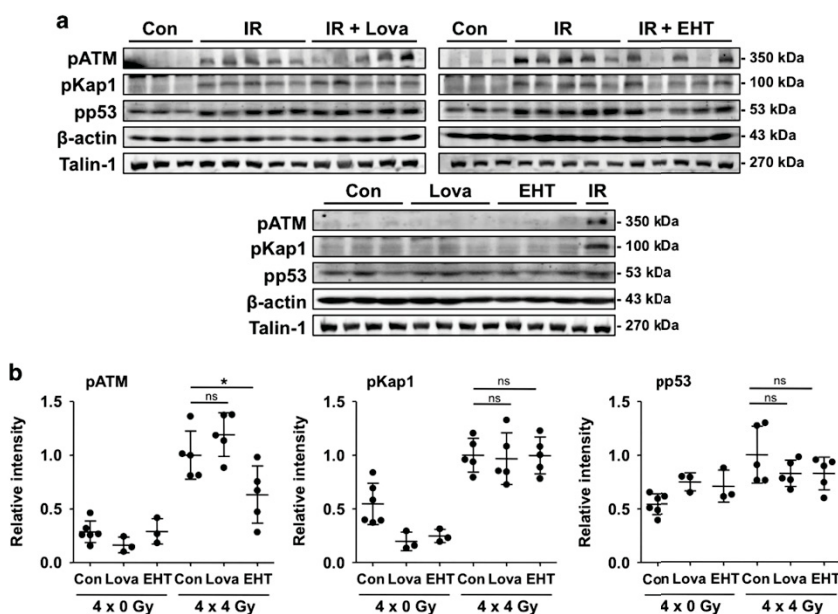
Figure 7 Fractionated irradiation causes a persistent activation of the DDR-related factors ATM, p53 and Kap-1 in lung tissue four weeks after the last irradiation. EHT1864 treatment significantly reduces the level of activated ATM. Male BALB/c mice were treated according to Figure 4b. Four weeks after the last irradiation the activation status of key proteins of the DNA damage response was analyzed in the right lung by western blot analysis. (**a**) Shown are the protein levels of Ser1981 phosphorylated (activated) ATM (pATM), Ser15 phosphorylated protein 53 (pp53) and Ser824 phosphorylated KRAB-associated protein-1 (pKap1). Results obtained from $n = 3$–5 animals per group are presented. Expression of β-actin and Talin-1 were used as loading controls. (**b**) Densitometrical analysis of alterations in the protein levels of DDR factors. Relative expression in irradiated animals was set to 1.0. Data shown are obtained from $n = 3$–6 animals per experimental group. Two-way ANOVA with Bonferroni *post hoc* test, *$P \leq 0.05$ (IR *versus* IR+Lova or IR *versus* IR+EHT). ns, not significant

as particular radioprotective. Noteworthy, lovastatin and EHT1864 significantly reduced the number of residual DSBs in lung tissue as detectable 4 weeks after the end of the fractionated irradiation. Because lovastatin does not affect the initial level of DSBs following irradiation,[13,39] we assume that the statin and the Rac1 inhibitor accelerate the repair of IR-induced DSBs. In consequence, a mitigated pro-apoptotic DDR and a diminished need for regenerative processes is anticipated. Indeed, we observed both a lower frequency of apoptotic cells and a reduced mitotic index in irradiated animals if Rac1 signaling was pharmacologically inhibited. Because targeting of Rho/Rac1 signaling also prevents the formation of DSBs following topoisomerase II poisoning,[11,45] we hypothesize that Rac1 interferes with both DNA damage induction and DNA repair, thereby eventually shutting down the primary stimulus (i.e., DNA damage) that triggers death-related DDR pathways. This hypothesis gains support by a recent report showing that epidermal Rac1 regulates DDR and repair following UV exposure, thereby protecting keratinocytes from apoptotic death.[54]

Taking into consideration the use of statins to alleviate adverse effects of radiotherapy, protection of tumor cells from DNA damage-triggered killing responses should be excluded. Fortunately, lovastatin did not attenuate IR-induced apoptosis in human breast cancer cells (MCF-7), which is a relevant cell type in the context of thoracic radiotherapy (Supplementary Figure 8). Additionally, statins augment the efficacy of various antitumor therapeutics in different tumor entities.[55,56]

Noteworthy, pitavastatin acts as a radiosensitizer for multiple tumor cell types including lung tumor cells[57–59] and, furthermore, radiosensitization of breast carcinoma cells[60] and head and neck squamous cell carcinoma (HNSCC) cells[61] is achievable by Rac1 inhibition. The molecular basis for radiosensitization of tumor cells and concomitant radio-protection of normal cells by statins and/or Rac1 inhibition remains obscure. The fact that Rho-GTPases, including Rac1, are often overexpressed in malignant tissue as compared with the corresponding normal tissue[62] might contribute to a different response of tumor versus normal cells. In extension to data that give preference to Rho/ROCK-regulated functions for radioprotection conferred by statins,[4,16,51] we provide additional evidence that inhibition of Rac1 signaling contri-butes to the radioprotective effects of statins on subchronic lung damage following fractionated radiotherapy. While statin-mediated inhibition of Rho/ROCK pathway impacts the late outcome of radiation injury (i.e., fibrosis),[15,16,51] our data further indicate that statins also interfere with preceding radiotoxic effects (i.e., DNA damage and caspase-mediated apoptosis) by targeting Rac1 signaling. Lovastatin treatment of human endothelial cells largely reduced the level of GTP-bound active Rac1 (Supplementary Figure 9), supporting the hypothesis of Rac1 as a major target of statin-mediated effects. Collectively, the data available support the view of multiple radioprotective effects of statins on normal tissue that might be useful in the clinic to widen the therapeutic window of radiotherapy. Although animals were given higher doses of

lovastatin (30 mg/kg bw/week) than used for the treatment of hypercholesterolemic patients (~5 mg/kg bw/week), even much higher statin doses (>150 mg/kg bw/week) are well tolerated in humans and do not provoke substantial adverse effects even under situation of long-term treatment.[63–65]

In conclusion, our study provides novel evidence of a radioprotective potency of lovastatin on normal primary human lung cells and rodent lung tissue under situation of hypo-fractionated irradiation, which is at least partially due to inhibition of Rac1 signaling. The data indicate that micro-vascular lung endothelial cells are particularly relevant for fractionated irradiation-induced lung damage and that lovastatin mediates protection from RILI. Further studies are preferential to investigate the impact of statins on chronic radiation-induced lung fibrosis. Moreover, the data encourage (i) retrospective or prospective clinical studies addressing the usefulness of statins in supportive care in radiotherapy and (ii) the development and preclinical analysis of novel Rac1-specific inhibitory drugs for radioprotection.

Materials and Methods

Cell culture conditions and treatment of human cells. HMVEC-L were obtained from Lonza (Basel, Switzerland) and cultured in EGM-2MV medium. HPF and HSAEpC were purchased from PromoCell (Heidelberg, Germany) and cultured in Fibroblast Growth Medium 2 and Small Airway Epithelial Cell Growth Medium obtained from the provider, respectively. The cells were directly obtained from the aforementioned providers at passage P2 and were cultured in our laboratory for less than 6 months and <15 population doublings. HMVEC-L were authenticated by the provider by monitoring the expression of von Willebrand Factor VIII and PECAM as well as the uptake of acetylated low density lipoprotein. Also HSAEpC and HPF authentication was performed by the provider. Here, cell morphology and FACS-based analysis of cytokeratin (HSAEpC) and CD90 (HPF) expression were monitored. Human umbilical vein endothelial cells (HUVEC) and human breast cancer cells (MCF-7) originate from PromoCell and and the German Tissue Culture Collection (DSMZ, Braunschweig, Germany), respectively, and were cultured in Endothelial Cell Growth Medium 2 and Dulbecco's modified Eagle medium (Sigma, Steinheim, Germany), respectively. Human lung fibroblasts (MRC-5) cells were purchased from CLS Cell Lines Service (Heidelberg, Germany) and cultivated in Dulbecco's modified Eagle medium:Ham's F12 (1:1) (Biochrom, Berlin, Germany). Cells were kept at 37 °C in a humidified atmosphere containing 5% CO_2. They were seeded in high density and grown for 72 h to ensure confluency before pretreatment with 5 μM lovastatin (Sigma). The experiments were done at cell confluency because this reflects the *in vivo* situation. 24 h later medium was changed and lovastatin concentration was reduced to 1 μM and cells were irradiated on four days in a row with 4 Gy (^{137}Cs source (Gammacell 3000, Nordion, Ottawa, Canada)). This experimental setup was chosen to analyze the ability of lovastatin to favor the repair of potentially lethal damage (PLD) induced by fractionated irradiation.

Analysis of nuclear γH2AX foci formation and determination of mitotic index. The formation of Ser139 phosphorylated histone 2AX nuclear foci (γH2AX foci) was measured as surrogate marker of ionizing radiation (IR)-induced DNA double-strand breaks (DSBs) by immunofluorescence. Ser10 phosphorylation of histone H3 is a commonly used marker of mitotic index. Cells were fixed with 4% formaldehyde followed by overnight incubation with methanol (-20 °C). After blockage (5% BSA in 0.3% Triton X-100/PBS), cells were incubated with anti-Ser139 phosphorylated histone 2AX (γH2AX) antibody (1:500, 16 h, 4 °C) (Millipore, Billerica, MA, USA) or anti-Ser10 phosphorylated histone 3 antibody (pH3) (1:200, 16 h, 4 °C) (Thermo Fisher Scientific, Waltham, MA, USA). After washing, Alexa Fluor 488 goat anti-mouse IgG antibody (Rockland, Limerick, PA, USA) was added (90 min, RT). Cell nuclei were counterstained with DAPI-containing Vectashield (Vector Laboratories, Burlingame, CA, USA) and γH2AX foci or pH3 positive cells were detected using Olympus BX43 microscope (Olympus, Hamburg, Germany).

Measurement of apoptotic cell death by Annexin V/PI staining. Apoptosis was analyzed by flow cytometer-based Annexin V/PI method. To this end, cells were resuspended in Annexin binding buffer (10 mM HEPES, 140 mM NaCl, 2.5 mM calcium chloride) and 10^5 cells were incubated with 5 μl Fluorescein-conjugated Annexin V (Life Technologies, Carlsbad, CA, USA) (15 min, on ice). 10 μl propidium iodide solution (50 μg/ml) and 200 μl Annexin binding buffer were added before samples were analyzed by BD Accuri™ C6 flow cytometer (BD, Franklin Lakes, NJ, USA) (530/30 nm and 585/40 nm filters). Cell morphology was monitored via light microscopy (Axiovert 40 CFL ((Zeiss, Jena, Germany)).

Animal experiments. Male BALB/c mice (12–16 weeks old, 20–30 g) were kept in the local animal housing facility of the University Hospital Düsseldorf (Germany). All animal experiments were approved by the local authorities (i.e., State Agency for Nature, Environment and Consumer protection, North Rhine-Westfalia, Germany; Reference number: 84-02.04.2013.A062) and performed according to the relevant guidelines and regulations. A total of six animals were randomized to each group. In line with previous studies[6,14,66,67] animals were treated three times per week with lovastatin (10 mg/kg bw, p.o) (Betapharm Arzneimittel GmbH, Augsburg, Germany) or the Rac1 small molecule inhibitor EHT1864 (5 mg/kg bw, i.p.) (Tocris Bioscience, Bristol, UK) starting two days before the first irradiation dose and continuing till the end of the experiment (Figure 4b). Vehicle-treated animals were used as control. Body weights were recorded three times per week. Fractionated local irradiation of the right lung was performed four times with each 4 Gy (cumulative dose: 16 Gy; biological effective dose (BED): 37.3 Gy) within two weeks. Before irradiation mice were anesthetized with ketamine (100 mg/kg bw) and xylazin (5 mg/kg bw). As irradiation device a Gulmay RS 225 (15 mA, 200 kV) was used. For the selective irradiation of the right lung, mice were adjusted into an irradiation device that allows selective irradiation of the right lung (Figure 4a) (radiation field: 1.26 cm^2). Control mice were subjected to sham irradiation.

Analysis of breathing frequency. Breathing frequency was monitored two and four weeks after the last irradiation. To this end, mice were anesthetized as described above and breathing frequency was determined 15 min later by two independent investigators (recording for one minute and calculation of mean values).

Histological and immunohistochemical analyses. Formaldehyde-fixed paraffin-embedded lung tissue samples were cut into 4 μm sections. Paraffin removal and tissue rehydration was performed according to standard procedures. To evaluate inflammation and fibrosis, sections were stained with hematoxylin/eosin (HE) (Sigma–Aldrich, Steinheim, Germany) and Sirius Red (Waldeck, Münster, Germany), respectively. For Nrf2 staining sections were incubated in 3% H_2O_2 for 20 min, boiled in Target Retrieval Solution (DAKO, Hamburg, Germany) for 30 min and blocked in TNB buffer (PerkinElmer, Waltham, MA, USA) for 30 min. Afterwards, samples were incubated with 0.001% avidin and 0.001% biotin (15 min each) before rabbit anti-Nrf2 antibody (1:1000; Santa Cruz, CA, USA) was added (4 °C overnight). After washing, sections were incubated with biotinylated donkey anti-rabbit IgG (Santa Cruz, CA, USA) (1:200, 45 min at RT). Afterwards TSA Biotin Kit (PerkinElmer) was used according to the manufacturer's instructions and sections were incubated with ABC reagent (Vectastain Elite ABC HRP Kit, Vector Laboratories, Burlingame, CA, USA) and stained with 3,3'-diaminobenzidine (DAB Peroxidase Substrate Kit (Vector Laboratories)) for 90 s. Sections were counter-stained with hematoxylin, mounted in Entellan and evaluated using Olympus BX43 microscope. For immunofluorescent stainings epitopes were demasked by incubation with Target Retrieval Solution (DAKO, Hamburg, Germany) in a steam boiler (1 h) before blocking in Protein Block (DAKO, Hamburg, Germany) (1 h). Incubation with primary antibody was performed overnight (4 °C, wet chamber). The following antibodies were used: rabbit anti-Ser139 phosphorylated histone 2AX (1:400 Abcam, Cambridge, MA, USA) and anti-53BP1 (1:400, Cell Signaling, Beverly, MA, USA) to detect DNA damage; rabbit anti-Ser10 phosphorylated histone 3 (1:250, Thermo Fisher Scientific) to monitor mitotic index; mouse anti-proliferating cell nuclear antigen (PCNA) (Millipore) to analyze proliferation, rabbit anti-CD68 (1:100, Abcam) to detect macrophages. After washing (PBS/0.1% Tween 20 (3×5 min)) Alexa Fluor 488-coupled goat anti-rabbit secondary antibody (Invitrogen, Darmstadt, Germany) was used. Sections were mounted in DAPI-containing Vectashield and evaluated with Olympus BX43 microscope.

Analysis of apoptosis by TUNEL assay. Apoptotic cells were detected by the *In Situ* Cell Death Detection Kit Fluorescein (Roche, Mannheim, Germany)

according to the manufacturer's instructions. Protein digestion was performed with 20 μg/ml Proteinase K (Qiagen, Hilden, Germany). As positive control treatment with 150 U/ml DNase (Qiagen) was performed. Nuclei were counterstained with DAPI-containing Vectashield and analyzed with Olympus BX43 microscope.

Total RNA purification, cDNA synthesis and qRT-PCR analysis. Total RNA from 10–20 mg lung tissue or 1–5 × 10⁶ cells was isolated using the RNeasy Mini Kit (Qiagen). RNA yield and purity were determined with NanoVue Plus Spectrophotometer (GE Healthcare, Freiburg, Germany). RNA was isolated from $n = 4$–6 animals per experimental group and pooled in equal amounts for cDNA synthesis using High-Capacity cDNA Reverse Transcription Kit (Applied Biosystems, Darmstadt, Germany). For each cDNA synthesis reaction 1000–2000 ng of total RNA was used. Quantitative real-time PCR analysis (triplicate determinations) was accomplished with 20 ng cDNA using CFX96 Touch Real-Time PCR Detection System (Bio-Rad Laboratories, Hercules, CA, USA). A semi-customized PCR-array (Sigma–Aldrich) containing 29 selected genes (Supplementary Table 1) involved in inflammation and fibrosis was used for quantitative mRNA analyses. Moreover, primers for selected oxidative stress and apoptosis-related genes were synthesized by Eurofins (Ebersberg, Germany). mRNA levels of target genes were normalized to that of the housekeeping genes glyceraldehyde 3-phosphate dehydrogenase (GAPDH), beta actin (β-actin) and ribosomal protein L32 (RPL32). 45 amplification cycles were performed (each cycle: 95 °C – 15 s; 55 °C – 15 s; 72 °C – 17 s). Following each run a melt curve analysis was included to ensure product specificity. PCR products with threshold cycles of $\geq$ 36 were omitted. Gene expression of control animals was set to 1. Data analysis was performed with the CFX Manager Software (Bio-Rad Laboratories). Alterations in mRNA expression of $\geq$ 2 and $\leq$ 0.5 as compared with untreated control animals (set to 1.0) are considered as particularly relevant and are marked with dashed lines.

Preparation of protein extracts and western blot analysis. To prepare total protein extracts 10–20 mg lung tissue was homogenized (lysis buffer: 50 mM Tris HCl, 150 mM NaCl, 2 mM EDTA, 1% NP 40, 0.1% sodium dodecyl sulfate, 1% sodium desoxycholate, 1 mM sodium orthovanadate, 1 mM phenyl-methylsulfonyl fluoride, 50 mM sodium fluoride and 1 x Protease inhibitor cocktail (Cell Signaling)) with Tissue Lyzer II (Qiagen) and sonicated on ice before centrifugation (10 min at 10.000 × g, 4 °C). Protein concentration of the supernatant was determined with the DC Protein Assay (Bio-Rad Laboratories). Protein samples were diluted with Roti-Load 1 (Roth, Karlsruhe, Germany) and heated (95 °C, 5 min). 30–100 μg of total protein was separated by SDS-PAGE (6–15% gels) and transferred onto nitrocellulose membranes (GE Healthcare, Freiburg, Germany) using Mini-PROTEAN electrophoresis chamber (Bio-Rad Laboratories). After blocking of membranes (5% dry milk in TBS/0.1% Tween 20, 2 h), incubation with primary antibody (1:1000) was performed (overnight, 4 °C). After incubation with HRP-conjugated secondary antibodies (1:2000, Rockland Immunochemicals Inc., Limerick, Pam USA) (2 h, RT), bound antibodies were visualized by chemiluminescence using the Fusion FX7 imaging system (Vilber Lourmat, Eberhardzell, Germany) or ChemiDoc Imaging System (Bio-Rad Laboratories). The following primary antibodies were used: anti-Ser15 phosphorylated protein 53 (pp53), anti-Ser345 phosphorylated checkpoint kinase 1 (pChk1) anti-caspase 3, anti-activated caspase 3 and 7, Talin-1 (Cell Signaling), anti-Ser824 phosphorylated KRAB-associated protein-1 (pKap1) (Bethyl Laboratories Inc., Montgomery, TX, USA), anti-Ser1981 phosphorylated Ataxia telangiectasia mutated (pATM), anti-Thr68 phosphorylated checkpoint kinase-2 (pChk2), (Abcam), anti-Bax, anti-Bcl-2, anti-XIAP, anti-β-actin and anti-Poly(ADP-ribose)-polymerase 1 (PARP-1) antibodies (Santa Cruz).

Active Rac1 pull-down assay. The level of active Rac1 was analyzed by Rac1 pull-down assay, which measures the binding of GTP-bound (active) Rac1 to its effector protein p21-associated protein kinase 1 (PAK1). To this end, GST-fused PAK1-GTPase-binding domain, which was isolated after recombinant expression in *Escherichia coli*, was used. GSH sepharose beads (GE Healthcare, Little Chalfont, UK) were washed three times with 1 ml Fish buffer (50 mM Tris/HCl pH 7.4, 100 mM NaCl, 2 mM MgCl₂, 1% Igepal Ca-630, 10% glycerol, 20 mM beta-glycerophosphate, 1 mM sodium orthovanadate Na₃VO₄, 1 tablet complete, EDTA-free Protease Inhibitor Cocktail (Roche, Basel, Switzerland)) and equal amounts of bacterial lysates containing GST (negative control) or GST-fused PAK1-GTPase-binding domain were added to the beads and incubated for 1 h at 4 °C, followed by another three times washing with Fish buffer. HUVEC total cell lysate was obtained from two confluent 10 cm dishes, added to the GST or GST-PAK1-bound sepharose

beads and incubated for 30 min at 4 °C. The samples were washed three times with Fish buffer and Roti-Load 1 (Roth, Karlsruhe, Germany) was added to the samples before heat denaturation for 10 min at 95 °C was performed. Samples were analyzed by SDS-PAGE and immunoblotting as described above. Mouse anti-Rac1 antibody (1:2500) from Millipore was used for the detection of Rac1.

Statistical analysis. Results are expressed as mean $\pm$ S.D. For statistical analysis, experimental groups were compared by two-way analysis of variance (ANOVA) with Bonferroni *post hoc* test using GraphPad Prism 5 (GraphPad Software Inc., La Jolla, CA, USA). A P-value of $P \leq 0.05$ was defined as level of significance.

Conflict of Interest

The authors declare no conflict of interest.

Publisher's Note

Springer Nature remains neutral with regard to jurisdictional claims in published maps and institutional affiliations.

1. Benveniste MF, Welsh J, Godoy MC, Betancourt SL, Mawlawi OR, Munden RF. New era of radiotherapy: an update in radiation-induced lung disease. *Clin Radiol* 2013; **68**: e275–e290.
2. Liao JK, Laufs U. Pleiotropic effects of statins. *Annu Rev Pharmacol Toxicol* 2005; **45**: 89–118.
3. Zhou Q, Liao JK. Pleiotropic effects of statins. - Basic research and clinical perspectives. *Circ J* 2010; **74**: 818–826.
4. Haydont V, Bourgier C, Vozenin-Brotons MC. Rho/ROCK pathway as a molecular target for modulation of intestinal radiation-induced toxicity. *Br J Radiol* 2007; **80**: 32–40.
5. Rashid M, Tawara S, Fukumoto Y, Seto M, Yano K, Shimokawa H. Importance of Rac1 signaling pathway inhibition in the pleiotropic effects of HMG-CoA reductase inhibitors. *Circ J* 2009; **73**: 361–370.
6. Huelsenbeck J, Henninger C, Schad A, Lackner KJ, Kaina B, Fritz G. Inhibition of Rac1 signaling by lovastatin protects against anthracycline-induced cardiac toxicity. *Cell Death Dis* 2011; **2**: e190.
7. Fritz G, Kaina B. Rho GTPases: promising cellular targets for novel anticancer drugs. *Curr Cancer Drug Targets* 2006; **6**: 1–14.
8. Graaf MR, Richel DJ, van Noorden CJ, Guchelaar HJ. Effects of statins and farnesyltransferase inhibitors on the development and progression of cancer. *Cancer Treat Rev* 2004; **30**: 609–641.
9. Chan KK, Oza AM, Siu LL. The statins as anticancer agents. *Clin Cancer Res* 2003; **9**: 10–19.
10. Riad A, Bien S, Westermann D, Becher PM, Loya K, Landmesser U *et al.* Pretreatment with statin attenuates the cardiotoxicity of Doxorubicin in mice. *Cancer Res* 2009; **69**: 695–699.
11. Huelsenbeck SC, Schorr A, Roos WP, Huelsenbeck J, Henninger C, Kaina B *et al.* Rac1 protein signaling is required for DNA damage response stimulated by topoisomerase II poisons. *J Biol Chem* 2012; **287**: 38590–38599.
12. Damrot J, Nubel T, Epe B, Roos WP, Kaina B, Fritz G. Lovastatin protects human endothelial cells from the genotoxic and cytotoxic effects of the anticancer drugs doxorubicin and etoposide. *Br J Pharmacol* 2006; **149**: 988–997.
13. Nubel T, Damrot J, Roos WP, Kaina B, Fritz G. Lovastatin protects human endothelial cells from killing by ionizing radiation without impairing induction and repair of DNA double-strand breaks. *Clin Cancer Res* 2006; **12**: 933–939.
14. Mathew B, Huang Y, Jacobson JR, Berdyshev E, Gerhold LM, Wang T *et al.* Simvastatin attenuates radiation-induced murine lung injury and dysregulated lung gene expression. *Am J Respir Cell Mol Biol* 2011; **44**: 415–422.
15. Haydont V, Gilliot O, Rivera S, Bourgier C, Francois A, Aigueperse J *et al.* Successful mitigation of delayed intestinal radiation injury using pravastatin is not associated with acute injury improvement or tumor protection. *Int J Radiat Oncol Biol Phys* 2007; **68**: 1471–1482.
16. Haydont V, Bourgier C, Pocard M, Lusinchi A, Aigueperse J, Mathe D *et al.* Pravastatin Inhibits the Rho/CCN2/extracellular matrix cascade in human fibrosis explants and improves radiation-induced intestinal fibrosis in rats. *Clin Cancer Res* 2007; **13**: 5331–5340.
17. Wang Y, Scheiber MN, Neumann C, Calin GA, Zhou D. MicroRNA regulation of ionizing radiation-induced premature senescence. *Int J Radiat Oncol Biol Phys* 2011; **81**: 839–848.
18. Citrin DE, Shankavaram U, Horton JA, Shield W 3rd, Zhao S, Asano H *et al.* Role of type II pneumocyte senescence in radiation-induced lung fibrosis. *J Natl Cancer Inst* 2013; **105**: 1474–1484.

19. Roos WP, Kaina B. DNA damage-induced cell death by apoptosis. *Trends Mol Med* 2006; **12**: 440–450.

20. Roos WP, Kaina B. DNA damage-induced cell death: from specific DNA lesions to the DNA damage response and apoptosis. *Cancer Lett* 2013; **332**: 237–248.

21. Olive PL. Detection of DNA damage in individual cells by analysis of histone H2AX phosphorylation. *Methods Cell Biol* 2004; **75**: 355–373.

22. Roos WP, Thomas AD, Kaina B. DNA damage and the balance between survival and death in cancer biology. *Nat Rev Cancer* 2016; **16**: 20–33.

23. Shutes A, Onesto C, Picard V, Leblond B, Schweighoffer F, Der CJ. Specificity and mechanism of action of EHT 1864, a novel small molecule inhibitor of Rac family small GTPases. *J Biol Chem* 2007; **282**: 35666–35678.

24. Liao ZX, Travis EL, Tucker SL. Damage and morbidity from pneumonitis after irradiation of partial volumes of mouse lung. *Int J Radiat Oncol Biol Phys* 1995; **32**: 1359–1370.

25. Para AE, Bezjak A, Yeung IW, Van Dyk J, Hill RP. Effects of genistein following fractionated lung irradiation in mice. *Radiother Oncol* 2009; **92**: 500–510.

26. Eldh T, Heinzelmann F, Velalakan A, Budach W, Belka C, Jendrossek V. Radiation-induced changes in breathing frequency and lung histology of C57BL/6 J mice are time- and dose-dependent. *Strahlenther Onkol* 2012; **188**: 274–281.

27. Ding NH, Li JJ, Sun LQ. Molecular mechanisms and treatment of radiation-induced lung fibrosis. *Curr Drug Targets* 2013; **14**: 1347–1356.

28. Singh S, Vrishni S, Singh BK, Rahman I, Kakkar P. Nrf2-ARE stress response mechanism: a control point in oxidative stress-mediated dysfunctions and chronic inflammatory diseases. *Free Radic Res* 2010; **44**: 1267–1288.

29. Epperly M, Bray J, Kraeger S, Zwacka R, Engelhardt J, Travis E *et al*. Prevention of late effects of irradiation lung damage by manganese superoxide dismutase gene therapy. *Gene Ther* 1998; **5**: 196–208.

30. Kang SK, Rabbani ZN, Folz RJ, Golson ML, Huang H, Yu D *et al*. Overexpression of extracellular superoxide dismutase protects mice from radiation-induced lung injury. *Int J Radiat Oncol Biol Phys* 2003; **57**: 1056–1066.

31. Antonic V, Rabbani ZN, Jackson IL, Vujaskovic Z. Subcutaneous administration of bovine superoxide dismutase protects lungs from radiation-induced lung injury. *Free Radic Res* 2015; **49**: 1259–1268.

32. Jeggo P, Lavin MF. Cellular radiosensitivity: how much better do we understand it? *Int J Radiat Biol* 2009; **85**: 1061–1081.

33. Harper JW, Elledge SJ. The DNA damage response: ten years after. *Mol Cell* 2007; **28**: 739–745.

34. Zhou BB, Elledge SJ. The DNA damage response: putting checkpoints in perspective. *Nature* 2000; **408**: 433–439.

35. Shiloh Y. ATM and ATR: networking cellular responses to DNA damage. *Curr Opin Genet Dev* 2001; **11**: 71–77.

36. Kim JW, Rhee CK, Kim TJ, Kim YH, Lee SH, Yoon HK *et al*. Effect of pravastatin on bleomycin-induced acute lung injury and pulmonary fibrosis. *Clin Exp Pharmacol Physiol* 2010; **37**: 1055–1063.

37. Zhu B, Ma AQ, Yang L, Dang XM. Atorvastatin attenuates bleomycin-induced pulmonary fibrosis via suppressing iNOS expression and the CTGF (CCN2)/ERK signaling pathway. *Int J Mol Sci* 2013; **14**: 24476–24491.

38. Monceau V, Pasinetti N, Schupp C, Pouzoulet F, Opolon P, Vozenin MC. Modulation of the Rho/ROCK pathway in heart and lung after thorax irradiation reveals targets to improve normal tissue toxicity. *Curr Drug Targets* 2010; **11**: 1395–1404.

39. Ostrau C, Hulsenbeck J, Herzog M, Schad A, Torzewski M, Lackner KJ *et al*. Lovastatin attenuates ionizing radiation-induced normal tissue damage *in vivo*. *Radiother Oncol* 2009; **92**: 492–499.

40. Ran XZ, Ran X, Zong ZW, Liu DQ, Xiang GM, Su YP *et al*. Protective effect of atorvastatin on radiation-induced vascular endothelial cell injury *in vitro*. *J Radiat Res* 2010; **51**: 527–533.

41. Gaugler MH, Vereycken-Holler V, Squiban C, Vandamme M, Vozenin-Brotons MC, Benderitter M. Pravastatin limits endothelial activation after irradiation and decreases the resulting inflammatory and thrombotic responses. *Radiat Res* 2005; **163**: 479–487.

42. Ziegler V, Albers A, Fritz G. Lovastatin protects keratinocytes from DNA damage-related pro-apoptotic stress responses stimulated by anticancer therapeutics. *Biochim Biophys Acta* 2016; **1863**: 1082–1092.

43. Ferlazzo ML, Sonzogni L, Granzotto A, Bodgi L, Lartin O, Devic C *et al*. Mutations of the Huntington's disease protein impact on the ATM-dependent signaling and repair pathways of the radiation-induced DNA double-strand breaks: corrective effect of statins and bisphosphonates. *Mol Neurobiol* 2014; **49**: 1200–1211.

44. Mahmoudi M, Gorenne I, Mercer J, Figg N, Littlewood T, Bennett M. Statins use a novel Nijmegen breakage syndrome-1-dependent pathway to accelerate DNA repair in vascular smooth muscle cells. *Circ Res* 2008; **103**: 717–725.

45. Wartlick F, Bopp A, Henninger C, Fritz G. DNA damage response (DDR) induced by topoisomerase II poisons requires nuclear function of the small GTPase Rac. *Biochim Biophys Acta* 2013; **1833**: 3093–3103.

46. Sandrock B, Bielek H, Schradi K, Schmidt G, Klugbauer N. The nuclear import of the small GTPase Rac1 is mediated by the direct interaction with karyopherin alpha2. *Traffic* 2010; **11**: 198–209.

47. Fritz G, Henninger C. Rho GTPases: novel players in the regulation of the DNA damage response? *Biomolecules* 2015; **5**: 2417–2434.

48. Yan Y, Hein AL, Etekpo A, Burchett KM, Lin C, Enke CA *et al*. Inhibition of RAC1 GTPase sensitizes pancreatic cancer cells to gamma-irradiation. *Oncotarget* 2014; **5**: 10251–10270.

49. Yan Y, Greer PM, Cao PT, Kolb RH, Cowan KH. RAC1 GTPase plays an important role in gamma-irradiation induced G2/M checkpoint activation. *Breast Cancer Res* 2012; **14**: R60.

50. Misra J, Mohanty ST, Madan S, Fernandes JA, Hal Ebetino F, Russell RG *et al*. Zoledronate attenuates accumulation of DNA damage in mesenchymal stem cells and protects their function. *Stem Cells* 2016; **34**: 756–767.

51. Bourgier C, Haydont V, Milliat F, Francois A, Holler V, Lasser P *et al*. Inhibition of Rho kinase modulates radiation induced fibrogenic phenotype in intestinal smooth muscle cells through alteration of the cytoskeleton and connective tissue growth factor expression. *Gut* 2005; **54**: 336–343.

52. Haydont V, Mathe D, Bourgier C, Abdelali J, Aigueperse J, Bourhis J *et al*. Induction of CTGF by TGF-beta1 in normal and radiation enteritis human smooth muscle cells: Smad/Rho balance and therapeutic perspectives. *Radiother Oncol* 2005; **76**: 219–225.

53. Galluzzi L, Senovilla L, Vitale I, Michels J, Martins I, Kepp O *et al*. Molecular mechanisms of cisplatin resistance. *Oncogene* 2012; **31**: 1869–1883.

54. Deshmukh J, Pofahl R, Haase I. Epidermal Rac1 regulates the DNA damage response and protects from UV-light-induced keratinocyte apoptosis and skin carcinogenesis. *Cell Death Dis* 2017; **8**: e2664.

55. Osmak M. Statins and cancer: current and future prospects. *Cancer Lett* 2012; **324**: 1–12.

56. Fritz G. HMG-CoA reductase inhibitors (statins) as anticancer drugs (review). *Int J Oncol* 2005; **27**: 1401–1409.

57. He Z, Mangala LS, Theriot CA, Rohde LH, Wu H, Zhang Y. Cell killing and radiosensitizing effects of atorvastatin in PC3 prostate cancer cells. *Journal of radiation research* 2012; **53**: 225–233.

58. Tsuboi Y, Kurimoto M, Nagai S, Hayakawa Y, Kamiyama H, Hayashi N *et al*. Induction of autophagic cell death and radiosensitization by the pharmacological inhibition of nuclear factor-kappa B activation in human glioma cell lines. *J Neurosurg* 2009; **110**: 594–604.

59. Sanli T, Liu C, Rashid A, Hopmans SN, Tsiani E, Schultz C *et al*. Lovastatin sensitizes lung cancer cells to ionizing radiation: modulation of molecular pathways of radioresistance and tumor suppression. *J Thorac Oncol* 2011; **6**: 439–450.

60. Hein AL, Post CM, Sheinin YM, Lakshmanan I, Natarajan A, Enke CA *et al*. RAC1 GTPase promotes the survival of breast cancer cells in response to hyper-fractionated radiation treatment. *Oncogene* 2016; **35**: 6319–6329.

61. Skvortsov S, Dudas J, Eichberger P, Witsch-Baumgartner M, Loeffler-Ragg J, Pritz C *et al*. Rac1 as a potential therapeutic target for chemo-radioresistant head and neck squamous cell carcinomas (HNSCC). *Br J Cancer* 2014; **110**: 2677–2687.

62. Fritz G, Just I, Kaina B. Rho GTPases are over-expressed in human tumors. *Int J Cancer* 1999; **81**: 682–687.

63. Thibault A, Samid D, Tompkins AC, Figg WD, Cooper MR, Hohl RJ *et al*. Phase I study of lovastatin, an inhibitor of the mevalonate pathway, in patients with cancer. *Clin Cancer Res* 1996; **2**: 483–491.

64. Armitage J. The safety of statins in clinical practice. *Lancet* 2007; **370**: 1781–1790.

65. Holstein SA, Knapp HR, Clamon GH, Murry DJ, Hohl RJ. Pharmacodynamic effects of high dose lovastatin in subjects with advanced malignancies. *Cancer Chemother Pharmacol* 2006; **57**: 155–164.

66. Henninger C, Huelsenbeck J, Huelsenbeck S, Grosch S, Schad A, Lackner KJ *et al*. The lipid lowering drug lovastatin protects against doxorubicin-induced hepatotoxicity. *Toxicol Appl Pharmacol* 2012; **261**: 66–73.

67. Henninger C, Huelsenbeck S, Wenzel P, Brand M, Huelsenbeck J, Schad A *et al*. Chronic heart damage following doxorubicin treatment is alleviated by lovastatin. *Pharmacol Res* 2015; **91**: 47–56.

68. Heinzelmann F, Jendrossek V, Lauber K, Nowak K, Eldh T, Boras R *et al*. Irradiation-induced pneumonitis mediated by the CD95/CD95-ligand system. *J Natl Cancer Inst* 2006; **98**: 1248–1251.

Supplementary Information accompanies this paper on Cell Death and Disease website (http://www.nature.com/cddis)

Chapter IX

General discussion

8   Discussion

The members of the RAS superfamily and their downstream effectors are involved in nearly every aspect of cellular events. In their natural function, GTPases control incoming signals and mediate them to regulate the output of their effectors. A spatial and temporal organization of the signaling components is required to achieve this highly specialized procedure. Therefore, dysregulation of these components, is frequently associated with the manifestation of human diseases [233]. The variety of pathogenic phenotypes resulting from mutations in genes encoding proteins of the RAS/MAPK pathway reaches from a diverse subset of developmental diseases (*e.g.* RASopathies) but also includes multiple types of cancer [192,234]. Therefore, extensive studies of abnormal signal transduction are necessary to understand the molecular mechanism of the individual pathologies and develop specific strategies to treat the occurring diseases.

Chapter I gives a general introduction about the topics that are reported and discussed in this doctoral thesis. Chapter II describes the regulatory mechanism of RAF paralogues with a special focus on their dysregulation in human disease and points out the importance of investigating their mechanism. Chapter III elucidates the advantages of iPSC-derived cardiomyocytes for the characterization of human genetically-caused cardiac diseases. Therefore, iPSCs, originated from dermal fibroblasts of NS patients with HCM were differentiated into cardiomyocytes to investigate the underlying RAF1^{S257L} mutation. This technique enabled a detailed analysis of the mechanistic basis of RAF1^{S257L}- induced HCM. Chapter IV and Chapter V collectively focus on the influence of missense mutations in *CDC42*, a gene encoding a small GTPase, which underlie a clinically heterogeneous group of phenotypes characterized by NS-like properties. These missense mutations did not only result in manifestation of the known developmental disorders but furthermore, in the discovery of a not yet described pathological phenotype involving dyshematopoiesis, inflammation, and hemophagocytic lymphohistiocytosis. Chapter VI deals with the discovery of a novel "*pseudo natural product"*, which in unbiased phenotypic assays and target identification led to the discovery of the first small-molecule ligand of the RHO GDP-dissociation inhibitor-1 (RHO GDI1), termed Rhonin. This compound inhibits RHO GDI1-binding to GDP-bound RHO GTPases, thereby inducing activation of GTPases and inhibiting signal transduction through a non-canonical Hedgehog pathway. Finally, Chapter VII and Chapter VIII deal with the positive aspects of RHO protein signaling inhibition. Chapter VII describes the design of small molecule inhibitor of RHO GEFs which can be used as an anti-cancer drug. IODVA1, a synthetic compound, inhibits RAC activation and signaling, and increases pro-apoptotic activity in BCR-ABL expressing cells. Chapter VIII describes reduced IR-induced residual DNA damage following promoted DNA repair due to Rac1 signaling inhibition. The individual chapters will be further discussed in three main discussion sections.

8.1 Molecular mechanism of RAF1[S257L]-caused hypertrophic cardiomyopathy

One aim of this thesis was the investigation of the mechanistic basis of RAF1[S257L]-induced hypertrophic cardiomyopathy. To achieve this goal, a protocol for the differentiation of highly pure and contractile iPSC-derived ventricular 3D cardiac bodies was established.

In comparison with previous studies [196,235] we investigated the impact of the RAF1 mutation on the best-known terminal downstream target ERK. As expected, RAF1[S257L] resulted in higher RAF activity, and in turn, in increased phosphorylation of ERK (pERK). Inhibition of MEK, the linking kinase between RAF1 and ERK, showed in turn drastically reduced levels of pERK in the mutant cells with even lower levels than in the untreated WT control cells. These results served as a proof-of-principle for the expected mutation-mediated alterations RAF signaling. Although the canonical RAS-RAF-MEK-ERK pathway was not shown to be crucial for regular heart development, its activation is known to regulate cardiac transcription factors, like GATA4, whose DNA binding capacity is thereby enhanced. GATA4 has been shown to regulate the transcription of several genes that are essential in a hypertrophic response [236-238]. It has moreover been shown that the disruption of the sarcomeric ERK-GATA4 complex resulted in the rescue of phenylephrine-induced cardiomyocyte hypertrophy [239]. Consequently, the RAF-MAPK-GATA4 axis could be one critical mediator in the occurrence of HCM, caused by hyperactive MAPK signaling.

An abnormal calcium handling is, among other disfunctions, described as a consequence of maladaptive hypertrophy [240]. Contractile analysis of the RAF1[S257L] CBs revealed a slower contraction rate compared to the control which was almost restored after MEKi treatment from day 12 until day 40. Correlating with this phenotype, we were able to obtain a switch in the expression of MYH6 to MYH7 upon mutation induction, that was also rescued after long-termed MEK inhibition. MYH7 is known to be rather expressed as a result of hypertrophic signaling and is further known as the slower contracting isoform [241]. Moreover, MYH7 is known to be expressed upon activation of GATA4 consequently to increased MAPK signaling induced by RAF1 [242]. However, the impaired contraction might result from changes in calcium transients. Oscillating levels of cytosolic calcium are crucial for proper cardiomyocytes contraction [243]. The observed reduction in calcium transients in RAF1[S257L] CBs was already described earlier in association with occurring *BRAF* and *MRAS* mutations, all affecting the activity of the canonical MAPK pathway [244,245]. Impaired calcium transients do not only play a major role on the physiological aspects of RAF[S257L] cells, but also on the activity of intracellular calcium-dependent kinase pathways. The activation of NFAT, a transcriptional regulator of hypertrophic signals, is directly mediated by calcineurin, which is a calcium binding protein [246]. Our data showed that RAF1[S257L] regulates the prominent NFAT target gene NPPB, whereas RAF1[S257L] CB treated with MEK inhibitor had 10-fold lower NPPB levels. Previous studies have shown that hypertrophy induction *via*

calcineurin-NFAT can be attenuated by ERK inhibitors [247]. Besides NFAT and GATA4, a huge variety of ERK substrates such as RSK3, ELK1, MSK1, c-MYC and NFkB, are activated by ERK1/2 in cardiomyocytes [248-250]. Therefore, the observed expression changes of NPPB, MYH7, MLY2, cTnI, SERCA2 and LTCC may be due to the co-occupation of the hypertrophy response gene promotors *via* the regulated transcription factors GATA4, AP1, MEF2, NFAT and NFkB [251].
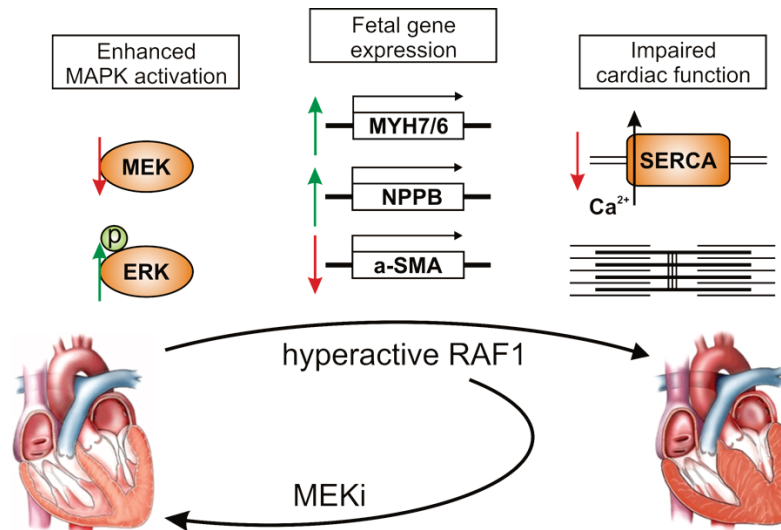

Figure 7: Schematic illustration of the main findings in the investigation of a heterozygous RAF1[S257L] mutation in iPSC-derived cardiac bodies.
The investigation of RAF1[S257L] mutation demonstrated a role for hyperactive RAF1 in the manifestation of HCM through an enhanced activation of the canonical MAPK pathway. This resulted in a switch to the fetal gene expression program and a reduction of the expression of Ca^{2+} channels and transporters. Furthermore, we obtained structural changes on the level of the sarcomeric units, e.g. the lack of the I-band. MEK inhibition partially rescued most of the obtained alterations.

One of the main findings of this study is the impaired I-band formation that was not only found in the heterozygous RAF1[S257L] mutated iPSC-derived CBs but also in the heart biopsy of the corresponding patient. The I-band is characterized as the sarcomeric unit lacking myosin and only contains actin ehih acts as a molecular spring upon sarcomere stretching [15]. Strikingly, impaired I-band formation was completely reverted after a long-term treatment with MEKi. The MAPK pathway was found to be aligned in the N2B region of titin in the I-band, scaffolded by the protein four-and-a-half LIM domain 1 (FHL-1) [252]. Phosphorylation of the N2B region regulates titin stiffness and thus, pressure overload-mediated cardiac hypertrophy [253].

In this work, we showed that also alternative RAF1-dependent pathways were altered in the RAF1[S257L] CBs. We obtained for example a higher phosphorylation of YAP. RAF1 interacts with MST1/2 and therefore inhibits MST1/2 interaction with LATS1/2, a kinase that is responsible for YAP phosphorylation. As a consequence, unphosphorylated YAP can enter the nucleus and act as a transcriptional co-activator by association with TEAD, which results in the transcription of mitogenic factors such as CTGF, miR-206, c-MYC, and NOTCH2 [254]. The activation of YAP was even considered

to be necessary for the development of a cardiac hypertrophy induced by hyperactive RAF1 [214]. Furthermore, expression of miR206 regulates hypertrophy and survival of cardiomyocytes through upregulation of the fetal genes MYH7, NPPB and NPPA [255].

Collectively, this thesis provided new insights into an aberrant RAF1 function in iPSC-derived cardiomyocytes which resemble the observed phenotype of the corresponding patient. The Ser257Leu mutation in RAF1-CBs modulates RAF1-dependent signaling network as well as cardiac-specific proteins and functions, such as re-activation of the fetal gene program, contraction rate, calcium transients and the sarcomeric structures.

8.2 CDC42 dysregulation results in a clinically heterogeneous group of developmental phenotypes

Mutations affecting the same gene but resulting in substantial phenotypic differences is a very well-known phenomenon. The wide use of exome sequencing has led to the recognition that this event occurs much more common than previously predicted [256]. Although many genetic alterations result in the same pathogenicity, the underlying mechanisms can vary according to differential impact on protein function. Here, we gained new insights into the genetic alterations of *CDC42*, a gene encoding a member of the RHO family of GTPases, underlying a clinically heterogeneous group of developmental phenotypes. In Chapter IV and Chapter V, we identified ten different missense mutations that are distributed over the entire CDC42 sequence which are classified in four different groups based on their molecular mechanism.

Group I contains the residues Tyr64, Arg66, and Arg68, which are located in the switch II region of CDC42, mediating the binding to effectors and regulators [257]. Whereas Tyr64 and Arg66 are located at the protein surface of CDC42, and therefore directly participate in the interaction of regulators and effectors, Arg68 is embedded inside the protein and stabilizes the conformation of the switch II region *via* intramolecular interactions with multiple residues. This results in slightly different effects of the mutations. Whereas CDC42[Y64C] and CDC42[R68Q] exhibited a robust GAP insensitivity, CDC42[R66G] results only in a mild decreased GAP-stimulated GTP hydrolysis. In contrast to alterations in residue Arg66 and Arg68, CDC42[Y64C] resulted in a nearly abolished GEF interaction. Due to their localization within the switch II region these mutations also resulted in a drastically lowered binding affinities zo the tested effectors PAK1, WASP, IQGAP1, and FMNL2.

Group II contains the aa residues Ala159, Cys81 and Ser83 which are located within or in close proximity to the nucleotide-binding pocket. Whereas CDC42[S83P] only slightly increased WASP binding, CDC42[A159V] promoted a fast GDP/GTP cycling comparable to what has been reported in RAS proteins [56].

Group III contains the aa residue Ile21, Tyr23, and Glu171 which are exposed residues and predicted to affect interactions with effectors containing a CDC42/RAC-interacting binding (CRIB) motif [258]. Interestingly, exchanging Glu at residue 171 into Lys does also change the electrostatic potential of this interaction site from a negative charge to a positive charge. Prior experiments have shown that electrostatics play a major role in defining the mechanisms of molecular recognition and complex formation. Results from our group showed that this so-called electrostatic steering is a critical step in the initiation of CDC42-mediated activation of WASP [259]. CDC42^{Y23C} showed an impaired interaction to all tested effectors.

Unlike to the prior introduced mutations, we characterized in Chapter V a previously unrecognized and distinctive hematological/autoinflammatory disorder due to Arg186Cys mutation of CDC42. The disease pattern considerably differs from that of previously described CDC42 mutations and is characterized by <u>n</u>eonatal <u>o</u>nset of pan<u>c</u>ytopenia, <u>a</u>utoinflammation, <u>r</u>ash, and episodes of <u>H</u>LH, therefore named as NOCARH syndrome. Based on structural modeling and the biochemical cell-free and cellular studies, we were able to elucidate an impaired interaction with known regulators and effectors, including RHO GDI, IQGAP1, and WASP. This resulted in atypical subcellular localization, actin cytoskeleton rearrangement, and reduced migration. Especially CDC42 mislocalization is consistent with the physiological role played by RHO GDI [260,261] Alignments between the C-terminal aa sequence of CDC42^{R186C} with those of other members of the RAS superfamily revealed that the Arg186Cys mutation introduces a cysteine prior to the CAAX box that is palmitoylated in HRAS [262]. Based on this, a further study showed that CDC42^{R186C} resulted in an aberrant addition of a palmitate which directly interfered with GDI1 binding, therefore inhibiting its extraction from the Golgi membrane [263,264]. Previous studies showed that cells expressing IQGAP1 mutants, defective in CDC42 binding, displayed an aberrant multipolar morphology, compared to the morphology seen in this study [265]. Together with the data presented in our study, this supports the notion that a proper IQGAP1-CDC42 interaction is crucial for cell polarization and migration. The role of actin cytoskeleton remodeling of immune cells has been demonstrated to be involved in the pathogenesis of hematological, autoinflammatory diseases. Not only alterations in RHO GTPases like RAC2, but also in actin-binding proteins cause abnormal migration, proliferation, and/or differentiation of myeloid cells and are associated with features of autoinflammation [266,267].

8.3   Reduction of RAC1 activity supports the anticancer efficacy in particular tumors

The last part of this thesis deals with the positive effect of RAC1 signal suppression in a tumor relevant surrounding. In Chapter VII we discovered the first small molecule inhibitor against the RAC GEF, VAV3, which is a critical component of BCR-ABL-induced RAC activation [268]. The <u>i</u>nhibitor of <u>o</u>ncogene <u>d</u>riven <u>V</u>av3 <u>a</u>ctivation, named IODVA1, was shown to bind VAV3 tightly (K_d = 400 nM) *in*

vitro and *in vivo* and consequently prevents RAC activation. Furthermore, IODVA1 did not interfere with transmembrane or cytosolic protein tyrosine kinases [269]. Cellular assays show that the specific IODVA1 interaction triggered an increased apoptosis similar to those observed in Vav3$^{-/-}$ models [268]. Interestingly, inhibition of VAV3 in BCR-ABL leukemic cells increased signaling through the pro-survival and VAV3/RAC-independent effectors AKT and STAT3 but decreased-RAC dependent activation of its downstream effectors such as PAK, JNK, S6, and 4EBP. The decrease in PAK activation consequently resulted in activation of BAD, promoting cellular apoptosis in BCR-ABL expressing cells. Most strikingly, IODVA1 administration to tyrosine kinase inhibitor resistant BCR-ABL (T315I) leukemia models resulted in a significant decrease of pJNK, pPAK, pS6, and p4EBP levels and therefore in their leukemic burden. This makes IODVA1 a suitable drug for malignancies in which VAV can be targeted [270-272].

Finally, in Chapter VIII we provided novel evidence that inhibition of RAC signaling by lovastatin resulted in a radioprotective potency on primary lung cells and rodent lung tissue under situation of hypo-fractionated irradiation. Statins act as β-hydroxy β-methylglutaryl-CoA (HMG-CoA) reductase inhibitors and were shown to have multiple cholesterol-independent effects by interfering with RHO GTPases [273]. Lovastatin consequently accelerated the removal of radiation-induced double stand breaks (DBS) which was already observed before in keratinocytes [274]. One possible mechanism might be an interference of inhibited RAC1 with the DNA damage response originating from DSB-initiated ATM/ATR signaling [275]. Furthermore, inhibition of RAC1 *in vivo* was able to mitigate acute radiation pneumonitis in mice two weeks after irradiation, which was not detectable in later time points. However, it is noteworthy that lovastatin significantly reduced the number of residual DSBs in lung tissue detectable 4 weeks after concluded fractionated irradiation. Whereas it was already shown that statin-mediated inhibition of the RHO/ROCK axis impacts the late fate of radiation injury (*i.e.*, fibrosis) [276,277], our data further indicates that statins can interfere with preceding radiotoxic effects (*i.e.*, DNA damage and caspase-mediated apoptosis) by targeting RAC1 signaling. Collectively, Chapter VIII emphasizes radioprotective effects of statins on normal tissue what might be useful in the clinic to widen the therapeutic window of radiotherapy.

9 References

1. Stephenson, A.; Adams, J.W.; Vaccarezza, M. The vertebrate heart: an evolutionary perspective. *J Anat* **2017**, *231*, 787-797, doi:10.1111/joa.12687.

2. Standring, S. The Anatomical Basis of Clinical Practice, 41st edn. *Elsevier Health Science* **2015**.

3. Betts, J.G.; Desaix, P.; Johnson, J.E.; Korol, O.; Kruse, D.; Poe, B.; Wise, J.A.; Womble, M.; Young, K.A. Anatomy & physiology. *OpenStax* **2013**, 787–846.

4. Camm, A.J.; Lüscher, T.F.; Serruys, P.W.; European Society of, C. *The ESC textbook of cardiovascular medicine*; Oxford University Press: Oxford; New York, 2009.

5. Paradis, A.N.; Gay, M.S.; Zhang, L. Binucleation of cardiomyocytes: the transition from a proliferative to a terminally differentiated state. *Drug Discov Today* **2014**, *19*, 602-609, doi:10.1016/j.drudis.2013.10.019.

6. Soonpaa, M.H.; Kim, K.K.; Pajak, L.; Franklin, M.; Field, L.J. Cardiomyocyte DNA synthesis and binucleation during murine development. *Am J Physiol* **1996**, *271*, H2183-2189, doi:10.1152/ajpheart.1996.271.5.H2183.

7. Gunthel, M.; Barnett, P.; Christoffels, V.M. Development, Proliferation, and Growth of the Mammalian Heart. *Mol Ther* **2018**, *26*, 1599-1609, doi:10.1016/j.ymthe.2018.05.022.

8. Mollova, M.; Bersell, K.; Walsh, S.; Savla, J.; Das, L.T.; Park, S.Y.; Silberstein, L.E.; Dos Remedios, C.G.; Graham, D.; Colan, S., et al. Cardiomyocyte proliferation contributes to heart growth in young humans. *Proc Natl Acad Sci U S A* **2013**, *110*, 1446-1451, doi:10.1073/pnas.1214608110.

9. Foglia, M.J.; Poss, K.D. Building and re-building the heart by cardiomyocyte proliferation. *Development (Cambridge, England)* **2016**, *143*, 729-740, doi:10.1242/dev.132910.

10. Shimizu, I.; Minamino, T. Physiological and pathological cardiac hypertrophy. *J Mol Cell Cardiol* **2016**, *97*, 245-262, doi:10.1016/j.yjmcc.2016.06.001.

11. Severs, N.J. Chapter 21 - Functional Morphology of the Cardiac Myocyte. In *Muscle and Exercise Physiology*, Zoladz, J.A., Ed. Academic Press: 2019; pp. 459-466.

12. Woodcock, E.A.; Matkovich, S.J. Cardiomyocytes structure, function and associated pathologies. *The international journal of biochemistry & cell biology* **2005**, *37*, 1746-1751, doi:10.1016/j.biocel.2005.04.011.

13. Spiro, D. The ultrastructure of striated muscle at various sarcomere lengths. *J Biophys Biochem Cytol* **1956**, *2*, 157-162, doi:10.1083/jcb.2.4.157.

14. Baskin, K.K.; Makarewich, C.A.; DeLeon, S.M.; Ye, W.; Chen, B.; Beetz, N.; Schrewe, H.; Bassel-Duby, R.; Olson, E.N. MED12 regulates a transcriptional network of calcium-handling genes in the heart. *JCI Insight* **2017**, *2*, doi:10.1172/jci.insight.91920.

15. Kruger, M.; Linke, W.A. The giant protein titin: a regulatory node that integrates myocyte signaling pathways. *J Biol Chem* **2011**, *286*, 9905-9912, doi:10.1074/jbc.R110.173260.

16. Huxley, A.F.; Niedergerke, R. Structural changes in muscle during contraction; interference microscopy of living muscle fibres. *Nature* **1954**, *173*, 971-973, doi:10.1038/173971a0.

17. Cooper, G.M. *The cell : a molecular approach*; ASM Press ; Sinauer Associates: Washington, D.C.; Sunderland, Mass., 2000.

18. Hodge, A.J.; Huxley, H.E.; Spiro, D. Electron microscope studies on ultrathin sections of muscle. *J Exp Med* **1954**, *99*, 201-206, doi:10.1084/jem.99.2.201.

19. Hynes, T.R.; Block, S.M.; White, B.T.; Spudich, J.A. Movement of myosin fragments in vitro: domains involved in force production. *Cell* **1987**, *48*, 953-963, doi:10.1016/0092-8674(87)90704-5.

20. Lehman, W.; Craig, R.; Vibert, P. Ca(2+)-induced tropomyosin movement in Limulus thin filaments revealed by three-dimensional reconstruction. *Nature* **1994**, *368*, 65-67, doi:10.1038/368065a0.

21. Schmitt, J.P.; Kamisago, M.; Asahi, M.; Li, G.H.; Ahmad, F.; Mende, U.; Kranias, E.G.; MacLennan, D.H.; Seidman, J.G.; Seidman, C.E. Dilated cardiomyopathy and heart failure

caused by a mutation in phospholamban. *Science* **2003**, *299*, 1410-1413, doi:10.1126/science.1081578.

22. Hilgemann, D.W. New insights into the molecular and cellular workings of the cardiac Na+/Ca2+ exchanger. *Am J Physiol Cell Physiol* **2004**, *287*, C1167-1172, doi:10.1152/ajpcell.00288.2004.

23. Kolios, G.; Moodley, Y. Introduction to stem cells and regenerative medicine. *Respiration* **2013**, *85*, 3-10, doi:10.1159/000345615.

24. Kleinsmith, L.J.; Pierce, G.B., Jr. Multipotentiality of Single Embryonal Carcinoma Cells. *Cancer Res* **1964**, *24*, 1544-1551.

25. Thomson, J.A.; Itskovitz-Eldor, J.; Shapiro, S.S.; Waknitz, M.A.; Swiergiel, J.J.; Marshall, V.S.; Jones, J.M. Embryonic stem cell lines derived from human blastocysts. *Science* **1998**, *282*, 1145-1147, doi:10.1126/science.282.5391.1145.

26. Romito, A.; Cobellis, G. Pluripotent Stem Cells: Current Understanding and Future Directions. *Stem Cells Int* **2016**, *2016*, 9451492, doi:10.1155/2016/9451492.

27. Weissman, I.L. Stem cells: units of development, units of regeneration, and units in evolution. *Cell* **2000**, *100*, 157-168, doi:10.1016/s0092-8674(00)81692-x.

28. Singh, V.K.; Saini, A.; Kalsan, M.; Kumar, N.; Chandra, R. Describing the Stem Cell Potency: The Various Methods of Functional Assessment and In silico Diagnostics. *Front Cell Dev Biol* **2016**, *4*, 134, doi:10.3389/fcell.2016.00134.

29. Zhang, F.; Citra, F.; Wang, D.A. Prospects of induced pluripotent stem cell technology in regenerative medicine. *Tissue Eng Part B Rev* **2011**, *17*, 115-124, doi:10.1089/ten.TEB.2010.0549.

30. Takahashi, K.; Tanabe, K.; Ohnuki, M.; Narita, M.; Ichisaka, T.; Tomoda, K.; Yamanaka, S. Induction of pluripotent stem cells from adult human fibroblasts by defined factors. *Cell* **2007**, *131*, 861-872, doi:10.1016/j.cell.2007.11.019.

31. Zuk, P.A.; Zhu, M.; Ashjian, P.; De Ugarte, D.A.; Huang, J.I.; Mizuno, H.; Alfonso, Z.C.; Fraser, J.K.; Benhaim, P.; Hedrick, M.H. Human adipose tissue is a source of multipotent stem cells. *Molecular biology of the cell* **2002**, *13*, 4279-4295, doi:10.1091/mbc.e02-02-0105.

32. Haghighi, F.; Dahlmann, J.; Nakhaei-Rad, S.; Lang, A.; Kutschka, I.; Zenker, M.; Kensah, G.; Piekorz, R.P.; Ahmadian, M.R. bFGF-mediated pluripotency maintenance in human induced pluripotent stem cells is associated with NRAS-MAPK signaling. *Cell Commun Signal* **2018**, *16*, 96, doi:10.1186/s12964-018-0307-1.

33. Wang, F.; Kong, J.; Cui, Y.Y.; Liu, P.; Wen, J.Y. Is Human-induced Pluripotent Stem Cell the Best Optimal? *Chin Med J (Engl)* **2018**, *131*, 852-856, doi:10.4103/0366-6999.228231.

34. Chin, M.H.; Mason, M.J.; Xie, W.; Volinia, S.; Singer, M.; Peterson, C.; Ambartsumyan, G.; Aimiuwu, O.; Richter, L.; Zhang, J., et al. Induced pluripotent stem cells and embryonic stem cells are distinguished by gene expression signatures. *Cell Stem Cell* **2009**, *5*, 111-123, doi:10.1016/j.stem.2009.06.008.

35. Rojas, S.V.; Kensah, G.; Rotaermel, A.; Baraki, H.; Kutschka, I.; Zweigerdt, R.; Martin, U.; Haverich, A.; Gruh, I.; Martens, A. Transplantation of purified iPSC-derived cardiomyocytes in myocardial infarction. *PLoS One* **2017**, *12*, e0173222, doi:10.1371/journal.pone.0173222.

36. Dahlmann, J.; Kensah, G.; Kempf, H.; Skvorc, D.; Gawol, A.; Elliott, D.A.; Drager, G.; Zweigerdt, R.; Martin, U.; Gruh, I. The use of agarose microwells for scalable embryoid body formation and cardiac differentiation of human and murine pluripotent stem cells. *Biomaterials* **2013**, *34*, 2463-2471, doi:10.1016/j.biomaterials.2012.12.024.

37. Kimbrel, E.A.; Lanza, R. Current status of pluripotent stem cells: moving the first therapies to the clinic. *Nat Rev Drug Discov* **2015**, *14*, 681-692, doi:10.1038/nrd4738.

38. Li, N.; Huang, R.; Zhang, X.; Xin, Y.; Li, J.; Huang, Y.; Cui, W.; Stoltz, J.F.; Zhou, Y.; Kong, Q. Stem cells cardiac patch from decellularized umbilical artery improved heart function after myocardium infarction. *Biomed Mater Eng* **2017**, *28*, S87-S94, doi:10.3233/BME-171628.

39. Widmann, C.; Gibson, S.; Jarpe, M.B.; Johnson, G.L. Mitogen-activated protein kinase: conservation of a three-kinase module from yeast to human. *Physiol Rev* **1999**, *79*, 143-180, doi:10.1152/physrev.1999.79.1.143.

40. Shaul, Y.D.; Seger, R. The MEK/ERK cascade: from signaling specificity to diverse functions. *Biochim Biophys Acta* **2007**, *1773*, 1213-1226, doi:10.1016/j.bbamcr.2006.10.005.

41. Zheng, C.F.; Guan, K.L. Activation of MEK family kinases requires phosphorylation of two conserved Ser/Thr residues. *EMBO J* **1994**, *13*, 1123-1131.

42. Sun, Y.; Liu, W.Z.; Liu, T.; Feng, X.; Yang, N.; Zhou, H.F. Signaling pathway of MAPK/ERK in cell proliferation, differentiation, migration, senescence and apoptosis. *J Recept Signal Transduct Res* **2015**, *35*, 600-604, doi:10.3109/10799893.2015.1030412.

43. Harvey, J.J. An Unidentified Virus Which Causes the Rapid Production of Tumours in Mice. *Nature* **1964**, *204*, 1104-1105, doi:10.1038/2041104b0.

44. Kirsten, W.H.; Schauf, V.; McCoy, J. Properties of a murine sarcoma virus. *Bibl Haematol* **1970**, 10.1159/000391714, 246-249, doi:10.1159/000391714.

45. Ellis, R.W.; Defeo, D.; Shih, T.Y.; Gonda, M.A.; Young, H.A.; Tsuchida, N.; Lowy, D.R.; Scolnick, E.M. The p21 src genes of Harvey and Kirsten sarcoma viruses originate from divergent members of a family of normal vertebrate genes. *Nature* **1981**, *292*, 506-511, doi:10.1038/292506a0.

46. Shih, C.; Weinberg, R.A. Isolation of a transforming sequence from a human bladder carcinoma cell line. *Cell* **1982**, *29*, 161-169, doi:10.1016/0092-8674(82)90100-3.

47. Pulciani, S.; Santos, E.; Lauver, A.V.; Long, L.K.; Robbins, K.C.; Barbacid, M. Oncogenes in human tumor cell lines: molecular cloning of a transforming gene from human bladder carcinoma cells. *Proc Natl Acad Sci U S A* **1982**, *79*, 2845-2849, doi:10.1073/pnas.79.9.2845.

48. Wittinghofer, A.; Vetter, I.R. Structure-function relationships of the G domain, a canonical switch motif. *Annu Rev Biochem* **2011**, *80*, 943-971, doi:10.1146/annurev-biochem-062708-134043.

49. Vetter, I.R.; Wittinghofer, A. The guanine nucleotide-binding switch in three dimensions. *Science* **2001**, *294*, 1299-1304, doi:10.1126/science.1062023.

50. Konstantinopoulos, P.A.; Karamouzis, M.V.; Papavassiliou, A.G. Post-translational modifications and regulation of the RAS superfamily of GTPases as anticancer targets. *Nat Rev Drug Discov* **2007**, *6*, 541-555, doi:10.1038/nrd2221.

51. Wennerberg, K.; Rossman, K.L.; Der, C.J. The Ras superfamily at a glance. *Journal of cell science* **2005**, *118*, 843-846, doi:10.1242/jcs.01660.

52. Rojas, A.M.; Fuentes, G.; Rausell, A.; Valencia, A. The Ras protein superfamily: evolutionary tree and role of conserved amino acids. *The Journal of cell biology* **2012**, *196*, 189-201, doi:10.1083/jcb.201103008.

53. Amin, E.; Dubey, B.N.; Zhang, S.C.; Gremer, L.; Dvorsky, R.; Moll, J.M.; Taha, M.S.; Nagel-Steger, L.; Piekorz, R.P.; Somlyo, A.V., et al. Rho-kinase: regulation, (dys)function, and inhibition. *Biol Chem* **2013**, *394*, 1399-1410, doi:10.1515/hsz-2013-0181.

54. Coleman, M.L.; Marshall, C.J.; Olson, M.F. RAS and RHO GTPases in G1-phase cell-cycle regulation. *Nat Rev Mol Cell Biol* **2004**, *5*, 355-366, doi:10.1038/nrm1365.

55. Sorkin, A.; von Zastrow, M. Endocytosis and signalling: intertwining molecular networks. *Nat Rev Mol Cell Biol* **2009**, *10*, 609-622, doi:10.1038/nrm2748.

56. Gremer, L.; Merbitz-Zahradnik, T.; Dvorsky, R.; Cirstea, I.C.; Kratz, C.P.; Zenker, M.; Wittinghofer, A.; Ahmadian, M.R. Germline KRAS mutations cause aberrant biochemical and physical properties leading to developmental disorders. *Hum Mutat* **2011**, *32*, 33-43, doi:10.1002/humu.21377.

57. Cirstea, I.C.; Gremer, L.; Dvorsky, R.; Zhang, S.C.; Piekorz, R.P.; Zenker, M.; Ahmadian, M.R. Diverging gain-of-function mechanisms of two novel KRAS mutations associated with Noonan and cardio-facio-cutaneous syndromes. *Hum Mol Genet* **2013**, *22*, 262-270, doi:10.1093/hmg/dds426.

58.   Tidyman, W.E.; Rauen, K.A. The RASopathies: developmental syndromes of Ras/MAPK pathway dysregulation. *Curr Opin Genet Dev* **2009**, *19*, 230-236, doi:10.1016/j.gde.2009.04.001.

59.   Gelb, B.D.; Tartaglia, M. Noonan syndrome and related disorders: dysregulated RAS-mitogen activated protein kinase signal transduction. *Hum Mol Genet* **2006**, *15 Spec No 2*, R220-226, doi:10.1093/hmg/ddl197.

60.   Colicelli, J. Human RAS superfamily proteins and related GTPases. *Sci STKE* **2004**, *2004*, RE13, doi:10.1126/stke.2502004re13.

61.   Nakhaei-Rad, S.; Haghighi, F.; Nouri, P.; Rezaei Adariani, S.; Lissy, J.; Kazemein Jasemi, N.S.; Dvorsky, R.; Ahmadian, M.R. Structural fingerprints, interactions, and signaling networks of RAS family proteins beyond RAS isoforms. *Crit Rev Biochem Mol Biol* **2018**, *53*, 130-156, doi:10.1080/10409238.2018.1431605.

62.   Via, A.; Ferre, F.; Brannetti, B.; Valencia, A.; Helmer-Citterich, M. Three-dimensional view of the surface motif associated with the P-loop structure: cis and trans cases of convergent evolution. *J Mol Biol* **2000**, *303*, 455-465, doi:10.1006/jmbi.2000.4151.

63.   Bos, J.L. ras oncogenes in human cancer: a review. *Cancer Res* **1989**, *49*, 4682-4689.

64.   Herrmann, C. Ras-effector interactions: after one decade. *Curr Opin Struct Biol* **2003**, *13*, 122-129, doi:10.1016/s0959-440x(02)00007-6.

65.   Malumbres, M.; Barbacid, M. RAS oncogenes: the first 30 years. *Nat Rev Cancer* **2003**, *3*, 459-465, doi:10.1038/nrc1097.

66.   Schmidt, M.; Bienek, C.; Rumenapp, U.; Zhang, C.; Lummen, G.; Jakobs, K.H.; Just, I.; Aktories, K.; Moos, M.; von Eichel-Streiber, C. A role for Rho in receptor- and G protein-stimulated phospholipase C. Reduction in phosphatidylinositol 4,5-bisphosphate by Clostridium difficile toxin B. *Naunyn Schmiedebergs Arch Pharmacol* **1996**, *354*, 87-94, doi:10.1007/bf00178707.

67.   Nussinov, R.; Tsai, C.J.; Chakrabarti, M.; Jang, H. A New View of Ras Isoforms in Cancers. *Cancer Res* **2016**, *76*, 18-23, doi:10.1158/0008-5472.CAN-15-1536.

68.   Wright, L.P.; Philips, M.R. Thematic review series: lipid posttranslational modifications. CAAX modification and membrane targeting of Ras. *J Lipid Res* **2006**, *47*, 883-891, doi:10.1194/jlr.R600004-JLR200.

69.   Lane, K.T.; Beese, L.S. Thematic review series: lipid posttranslational modifications. Structural biology of protein farnesyltransferase and geranylgeranyltransferase type I. *J Lipid Res* **2006**, *47*, 681-699, doi:10.1194/jlr.R600002-JLR200.

70.   Winter-Vann, A.M.; Casey, P.J. Post-prenylation-processing enzymes as new targets in oncogenesis. *Nat Rev Cancer* **2005**, *5*, 405-412, doi:10.1038/nrc1612.

71.   Brossier, N.M.; Prechtl, A.M.; Longo, J.F.; Barnes, S.; Wilson, L.S.; Byer, S.J.; Brosius, S.N.; Carroll, S.L. Classic Ras Proteins Promote Proliferation and Survival via Distinct Phosphoproteome Alterations in Neurofibromin-Null Malignant Peripheral Nerve Sheath Tumor Cells. *J Neuropathol Exp Neurol* **2015**, *74*, 568-586, doi:10.1097/NEN.0000000000000201.

72.   Nakhaei-Rad, S.; Nakhaeizadeh, H.; Gotze, S.; Kordes, C.; Sawitza, I.; Hoffmann, M.J.; Franke, M.; Schulz, W.A.; Scheller, J.; Piekorz, R.P., et al. The Role of Embryonic Stem Cell-expressed RAS (ERAS) in the Maintenance of Quiescent Hepatic Stellate Cells. *J Biol Chem* **2016**, *291*, 8399-8413, doi:10.1074/jbc.M115.700088.

73.   Repasky, G.A.; Chenette, E.J.; Der, C.J. Renewing the conspiracy theory debate: does Raf function alone to mediate Ras oncogenesis? *Trends Cell Biol* **2004**, *14*, 639-647, doi:10.1016/j.tcb.2004.09.014.

74.   Cardama, G.A.; Gonzalez, N.; Maggio, J.; Menna, P.L.; Gomez, D.E. Rho GTPases as therapeutic targets in cancer (Review). *Int J Oncol* **2017**, *51*, 1025-1034, doi:10.3892/ijo.2017.4093.

75.   Etienne-Manneville, S.; Hall, A. Rho GTPases in cell biology. *Nature* **2002**, *420*, 629-635, doi:10.1038/nature01148.

76.   Raftopoulou, M.; Hall, A. Cell migration: Rho GTPases lead the way. *Dev Biol* **2004**, *265*, 23-32, doi:10.1016/j.ydbio.2003.06.003.

77.   Lawson, C.D.; Burridge, K. The on-off relationship of Rho and Rac during integrin-mediated adhesion and cell migration. *Small GTPases* **2014**, *5*, e27958, doi:10.4161/sgtp.27958.

78.   Amin, E.; Jaiswal, M.; Derewenda, U.; Reis, K.; Nouri, K.; Koessmeier, K.T.; Aspenstrom, P.; Somlyo, A.V.; Dvorsky, R.; Ahmadian, M.R. Deciphering the Molecular and Functional Basis of RHOGAP Family Proteins: A SYSTEMATIC APPROACH TOWARD SELECTIVE INACTIVATION OF RHO FAMILY PROTEINS. *J Biol Chem* **2016**, *291*, 20353-20371, doi:10.1074/jbc.M116.736967.

79.   Jaiswal, M.; Dvorsky, R.; Ahmadian, M.R. Deciphering the molecular and functional basis of Dbl family proteins: a novel systematic approach toward classification of selective activation of the Rho family proteins. *J Biol Chem* **2013**, *288*, 4486-4500, doi:10.1074/jbc.M112.429746.

80.   Garcia-Mata, R.; Boulter, E.; Burridge, K. The 'invisible hand': regulation of RHO GTPases by RHOGDIs. *Nat Rev Mol Cell Biol* **2011**, *12*, 493-504, doi:10.1038/nrm3153.

81.   Dovas, A.; Couchman, J.R. RhoGDI: multiple functions in the regulation of Rho family GTPase activities. *Biochem J* **2005**, *390*, 1-9, doi:10.1042/BJ20050104.

82.   Scheffzek, K.; Ahmadian, M.R.; Wittinghofer, A. GTPase-activating proteins: helping hands to complement an active site. *Trends Biochem Sci* **1998**, *23*, 257-262, doi:10.1016/s0968-0004(98)01224-9.

83.   Csepanyi-Komi, R.; Levay, M.; Ligeti, E. Rho/RacGAPs: embarras de richesse? *Small GTPases* **2012**, *3*, 178-182, doi:10.4161/sgtp.20040.

84.   Guo, Z.; Ahmadian, M.R.; Goody, R.S. Guanine nucleotide exchange factors operate by a simple allosteric competitive mechanism. *Biochemistry* **2005**, *44*, 15423-15429, doi:10.1021/bi0518601.

85.   Vojtek, A.B.; Der, C.J. Increasing complexity of the Ras signaling pathway. *J Biol Chem* **1998**, *273*, 19925-19928.

86.   van Buul, J.D.; Geerts, D.; Huveneers, S. Rho GAPs and GEFs: controling switches in endothelial cell adhesion. *Cell Adh Migr* **2014**, *8*, 108-124.

87.   Xie, F.; Shao, S.; Aziz, A.U.R.; Zhang, B.; Wang, H.; Liu, B. Role of Rho-specific guanine nucleotide dissociation inhibitor alpha regulation in cell migration. *Acta Histochem* **2017**, *119*, 183-189, doi:10.1016/j.acthis.2017.01.008.

88.   Griner, E.M.; Theodorescu, D. The faces and friends of RhoGDI2. *Cancer Metastasis Rev* **2012**, *31*, 519-528, doi:10.1007/s10555-012-9376-6.

89.   de Leon-Bautista, M.P.; Cardenas-Aguayo, M.D.; Casique-Aguirre, D.; Almaraz-Salinas, M.; Parraguirre-Martinez, S.; Olivo-Diaz, A.; Thompson-Bonilla, M.D.; Vargas, M. Immunological and Functional Characterization of RhoGDI3 and Its Molecular Targets RhoG and RhoB in Human Pancreatic Cancerous and Normal Cells. *PLoS One* **2016**, *11*, e0166370, doi:10.1371/journal.pone.0166370.

90.   Robbe, K.; Otto-Bruc, A.; Chardin, P.; Antonny, B. Dissociation of GDP dissociation inhibitor and membrane translocation are required for efficient activation of Rac by the Dbl homology-pleckstrin homology region of Tiam. *J Biol Chem* **2003**, *278*, 4756-4762, doi:DOI 10.1074/jbc.M210412200.

91.   Zhang, S.C.; Gremer, L.; Heise, H.; Janning, P.; Shymanets, A.; Cirstea, I.C.; Krause, E.; Nurnberg, B.; Ahmadian, M.R. Liposome reconstitution and modulation of recombinant prenylated human Rac1 by GEFs, GDI1 and Pak1. *PLoS One* **2014**, *9*, e102425, doi:10.1371/journal.pone.0102425.

92.   Yoon, S.; Seger, R. The extracellular signal-regulated kinase: multiple substrates regulate diverse cellular functions. *Growth Factors* **2006**, *24*, 21-44, doi:10.1080/02699050500284218.

93.   Rapp, U.R.; Goldsborough, M.D.; Mark, G.E.; Bonner, T.I.; Groffen, J.; Reynolds, F.H., Jr.; Stephenson, J.R. Structure and biological activity of v-raf, a unique oncogene transduced by a retrovirus. *Proc Natl Acad Sci U S A* **1983**, *80*, 4218-4222.

94. Bonner, T.I.; Kerby, S.B.; Sutrave, P.; Gunnell, M.A.; Mark, G.; Rapp, U.R. Structure and biological activity of human homologs of the raf/mil oncogene. *Mol Cell Biol* **1985**, *5*, 1400-1407.

95. Kozak, C.; Gunnell, M.A.; Rapp, U.R. A new oncogene, c-raf, is located on mouse chromosome 6. *J Virol* **1984**, *49*, 297-299.

96. Huleihel, M.; Goldsborough, M.; Cleveland, J.; Gunnell, M.; Bonner, T.; Rapp, U.R. Characterization of murine A-raf, a new oncogene related to the v-raf oncogene. *Mol Cell Biol* **1986**, *6*, 2655-2662.

97. Ikawa, S.; Fukui, M.; Ueyama, Y.; Tamaoki, N.; Yamamoto, T.; Toyoshima, K. B-raf, a new member of the raf family, is activated by DNA rearrangement. *Mol Cell Biol* **1988**, *8*, 2651-2654.

98. Zhang, X.F.; Settleman, J.; Kyriakis, J.M.; Takeuchi-Suzuki, E.; Elledge, S.J.; Marshall, M.S.; Bruder, J.T.; Rapp, U.R.; Avruch, J. Normal and oncogenic p21ras proteins bind to the amino-terminal regulatory domain of c-Raf-1. *Nature* **1993**, *364*, 308-313, doi:10.1038/364308a0.

99. Vojtek, A.B.; Hollenberg, S.M.; Cooper, J.A. Mammalian Ras interacts directly with the serine/threonine kinase Raf. *Cell* **1993**, *74*, 205-214.

100. Warne, P.H.; Viciana, P.R.; Downward, J. Direct interaction of Ras and the amino-terminal region of Raf-1 in vitro. *Nature* **1993**, *364*, 352-355, doi:10.1038/364352a0.

101. Kyriakis, J.M.; App, H.; Zhang, X.F.; Banerjee, P.; Brautigan, D.L.; Rapp, U.R.; Avruch, J. Raf-1 activates MAP kinase-kinase. *Nature* **1992**, *358*, 417-421, doi:10.1038/358417a0.

102. Vandamme, D.; Herrero, A.; Al-Mulla, F.; Kolch, W. Regulation of the MAPK pathway by raf kinase inhibitory protein. *Crit Rev Oncog* **2014**, *19*, 405-415.

103. Dhillon, A.S.; Hagan, S.; Rath, O.; Kolch, W. MAP kinase signalling pathways in cancer. *Oncogene* **2007**, *26*, 3279-3290, doi:10.1038/sj.onc.1210421.

104. Wu, X.; Simpson, J.; Hong, J.H.; Kim, K.H.; Thavarajah, N.K.; Backx, P.H.; Neel, B.G.; Araki, T. MEK-ERK pathway modulation ameliorates disease phenotypes in a mouse model of Noonan syndrome associated with the Raf1(L613V) mutation. *J Clin Invest* **2011**, *121*, 1009-1025, doi:10.1172/JCI44929.

105. Urosevic, J.; Sauzeau, V.; Soto-Montenegro, M.L.; Reig, S.; Desco, M.; Wright, E.M.; Canamero, M.; Mulero, F.; Ortega, S.; Bustelo, X.R., et al. Constitutive activation of B-Raf in the mouse germ line provides a model for human cardio-facio-cutaneous syndrome. *Proc Natl Acad Sci U S A* **2011**, *108*, 5015-5020, doi:10.1073/pnas.1016933108.

106. Gelb, B.D.; Roberts, A.E.; Tartaglia, M. Cardiomyopathies in Noonan syndrome and the other RASopathies. *Prog Pediatr Cardiol* **2015**, *39*, 13-19, doi:10.1016/j.ppedcard.2015.01.002.

107. Leicht, D.T.; Balan, V.; Kaplun, A.; Singh-Gupta, V.; Kaplun, L.; Dobson, M.; Tzivion, G. Raf kinases: function, regulation and role in human cancer. *Biochim Biophys Acta* **2007**, *1773*, 1196-1212, doi:10.1016/j.bbamcr.2007.05.001.

108. Maurer, G.; Tarkowski, B.; Baccarini, M. Raf kinases in cancer-roles and therapeutic opportunities. *Oncogene* **2011**, *30*, 3477-3488, doi:10.1038/onc.2011.160.

109. Desideri, E.; Cavallo, A.L.; Baccarini, M. Alike but Different: RAF Paralogs and Their Signaling Outputs. *Cell* **2015**, *161*, 967-970, doi:10.1016/j.cell.2015.04.045.

110. Lavoie, H.; Therrien, M. Regulation of RAF protein kinases in ERK signalling. *Nat Rev Mol Cell Biol* **2015**, *16*, 281-298, doi:10.1038/nrm3979.

111. Mott, H.R.; Owen, D. Structures of Ras superfamily effector complexes: What have we learnt in two decades? *Crit Rev Biochem Mol Biol* **2015**, *50*, 85-133, doi:10.3109/10409238.2014.999191.

112. Fetics, S.K.; Guterres, H.; Kearney, B.M.; Buhrman, G.; Ma, B.; Nussinov, R.; Mattos, C. Allosteric effects of the oncogenic RasQ61L mutant on Raf-RBD. *Structure* **2015**, *23*, 505-516, doi:10.1016/j.str.2014.12.017.

113. Patel, M.; Cote, J.F. Ras GTPases' interaction with effector domains: Breaking the families' barrier. *Commun Integr Biol* **2013**, *6*, e24298, doi:10.4161/cib.24298.

114. Rezaei Adariani, S.; Buchholzer, M.; Akbarzadeh, M.; Nakhaei-Rad, S.; Dvorsky, R.; Ahmadian, M.R. Structural snapshots of RAF kinase interactions. *Biochem Soc Trans* **2018**, *46*, 1393-1406, doi:10.1042/BST20170528.

115. Erijman, A.; Shifman, J.M. RAS/Effector Interactions from Structural and Biophysical Perspective. *Mini Rev Med Chem* **2016**, *16*, 370-375.

116. Block, C.; Janknecht, R.; Herrmann, C.; Nassar, N.; Wittinghofer, A. Quantitative structure-activity analysis correlating Ras/Raf interaction in vitro to Raf activation in vivo. *Nat Struct Biol* **1996**, *3*, 244-251.

117. Fridman, M.; Maruta, H.; Gonez, J.; Walker, F.; Treutlein, H.; Zeng, J.; Burgess, A. Point mutants of c-raf-1 RBD with elevated binding to v-Ha-Ras. *J Biol Chem* **2000**, *275*, 30363-30371, doi:10.1074/jbc.M003193200.

118. Zehir, A.; Benayed, R.; Shah, R.H.; Syed, A.; Middha, S.; Kim, H.R.; Srinivasan, P.; Gao, J.; Chakravarty, D.; Devlin, S.M., et al. Mutational landscape of metastatic cancer revealed from prospective clinical sequencing of 10,000 patients. *Nature medicine* **2017**, *23*, 703-713, doi:10.1038/nm.4333.

119. Zeng, J.; Fridman, M.; Maruta, H.; Treutlein, H.R.; Simonson, T. Protein-protein recognition: an experimental and computational study of the R89K mutation in Raf and its effect on Ras binding. *Protein Sci* **1999**, *8*, 50-64, doi:10.1110/ps.8.1.50.

120. Giannakis, M.; Mu, X.J.; Shukla, S.A.; Qian, Z.R.; Cohen, O.; Nishihara, R.; Bahl, S.; Cao, Y.; Amin-Mansour, A.; Yamauchi, M., et al. Genomic Correlates of Immune-Cell Infiltrates in Colorectal Carcinoma. *Cell Rep* **2016**, *17*, 1206, doi:10.1016/j.celrep.2016.10.009.

121. George, J.; Lim, J.S.; Jang, S.J.; Cun, Y.; Ozretic, L.; Kong, G.; Leenders, F.; Lu, X.; Fernandez-Cuesta, L.; Bosco, G., et al. Comprehensive genomic profiles of small cell lung cancer. *Nature* **2015**, *524*, 47-53, doi:10.1038/nature14664.

122. Mouradov, D.; Sloggett, C.; Jorissen, R.N.; Love, C.G.; Li, S.; Burgess, A.W.; Arango, D.; Strausberg, R.L.; Buchanan, D.; Wormald, S., et al. Colorectal cancer cell lines are representative models of the main molecular subtypes of primary cancer. *Cancer Res* **2014**, *74*, 3238-3247, doi:10.1158/0008-5472.CAN-14-0013.

123. Li, Z.L.; Prakash, P.; Buck, M. A "Tug of War" Maintains a Dynamic Protein-Membrane Complex: Molecular Dynamics Simulations of C-Raf RBD-CRD Bound to K-Ras4B at an Anionic Membrane. *ACS Cent Sci* **2018**, *4*, 298-305, doi:10.1021/acscentsci.7b00593.

124. Ghosh, S.; Xie, W.Q.; Quest, A.F.; Mabrouk, G.M.; Strum, J.C.; Bell, R.M. The cysteine-rich region of raf-1 kinase contains zinc, translocates to liposomes, and is adjacent to a segment that binds GTP-ras. *J Biol Chem* **1994**, *269*, 10000-10007.

125. Ghosh, S.; Strum, J.C.; Sciorra, V.A.; Daniel, L.; Bell, R.M. Raf-1 kinase possesses distinct binding domains for phosphatidylserine and phosphatidic acid. Phosphatidic acid regulates the translocation of Raf-1 in 12-O-tetradecanoylphorbol-13-acetate-stimulated Madin-Darby canine kidney cells. *J Biol Chem* **1996**, *271*, 8472-8480.

126. Li, S.; Jang, H.; Zhang, J.; Nussinov, R. Raf-1 Cysteine-Rich Domain Increases the Affinity of K-Ras/Raf at the Membrane, Promoting MAPK Signaling. *Structure* **2018**, *26*, 513-525 e512, doi:10.1016/j.str.2018.01.011.

127. Brtva, T.R.; Drugan, J.K.; Ghosh, S.; Terrell, R.S.; Campbell-Burk, S.; Bell, R.M.; Der, C.J. Two distinct Raf domains mediate interaction with Ras. *J Biol Chem* **1995**, *270*, 9809-9812.

128. Daub, M.; Jockel, J.; Quack, T.; Weber, C.K.; Schmitz, F.; Rapp, U.R.; Wittinghofer, A.; Block, C. The RafC1 cysteine-rich domain contains multiple distinct regulatory epitopes which control Ras-dependent Raf activation. *Mol Cell Biol* **1998**, *18*, 6698-6710.

129. Hibino, K.; Shibata, T.; Yanagida, T.; Sako, Y. Activation kinetics of RAF protein in the ternary complex of RAF, RAS-GTP, and kinase on the plasma membrane of living cells: single-molecule imaging analysis. *J Biol Chem* **2011**, *286*, 36460-36468, doi:10.1074/jbc.M111.262675.

130. Zang, M.; Waelde, C.A.; Xiang, X.; Rana, A.; Wen, R.; Luo, Z. Microtubule integrity regulates Pak leading to Ras-independent activation of Raf-1. insights into mechanisms of Raf-1 activation. *J Biol Chem* **2001**, *276*, 25157-25165, doi:10.1074/jbc.M100152200.

131. Improta-Brears, T.; Ghosh, S.; Bell, R.M. Mutational analysis of Raf-1 cysteine rich domain: requirement for a cluster of basic aminoacids for interaction with phosphatidylserine. *Mol Cell Biochem* **1999**, *198*, 171-178.

132. Morrison, D.K.; Heidecker, G.; Rapp, U.R.; Copeland, T.D. Identification of the major phosphorylation sites of the Raf-1 kinase. *J Biol Chem* **1993**, *268*, 17309-17316.

133. Kolch, W.; Heidecker, G.; Kochs, G.; Hummel, R.; Vahidi, H.; Mischak, H.; Finkenzeller, G.; Marme, D.; Rapp, U.R. Protein kinase C alpha activates RAF-1 by direct phosphorylation. *Nature* **1993**, *364*, 249-252, doi:10.1038/364249a0.

134. Nussinov, R.; Jang, H.; Tsai, C.J.; Liao, T.J.; Li, S.; Fushman, D.; Zhang, J. Intrinsic protein disorder in oncogenic KRAS signaling. *Cell Mol Life Sci* **2017**, *74*, 3245-3261, doi:10.1007/s00018-017-2564-3.

135. Alessi, D.R.; Saito, Y.; Campbell, D.G.; Cohen, P.; Sithanandam, G.; Rapp, U.; Ashworth, A.; Marshall, C.J.; Cowley, S. Identification of the sites in MAP kinase kinase-1 phosphorylated by p74raf-1. *EMBO J* **1994**, *13*, 1610-1619.

136. Daum, G.; Eisenmann-Tappe, I.; Fries, H.W.; Troppmair, J.; Rapp, U.R. The ins and outs of Raf kinases. *Trends Biochem Sci* **1994**, *19*, 474-480.

137. Roskoski, R., Jr. MEK1/2 dual-specificity protein kinases: structure and regulation. *Biochem Biophys Res Commun* **2012**, *417*, 5-10, doi:10.1016/j.bbrc.2011.11.145.

138. Baljuls, A.; Kholodenko, B.N.; Kolch, W. It takes two to tango--signalling by dimeric Raf kinases. *Mol Biosyst* **2013**, *9*, 551-558, doi:10.1039/c2mb25393c.

139. Rushworth, L.K.; Hindley, A.D.; O'Neill, E.; Kolch, W. Regulation and role of Raf-1/B-Raf heterodimerization. *Mol Cell Biol* **2006**, *26*, 2262-2272, doi:10.1128/MCB.26.6.2262-2272.2006.

140. Lavoie, H.; Sahmi, M.; Maisonneuve, P.; Marullo, S.A.; Thevakumaran, N.; Jin, T.; Kurinov, I.; Sicheri, F.; Therrien, M. MEK drives BRAF activation through allosteric control of KSR proteins. *Nature* **2018**, *554*, 549-553, doi:10.1038/nature25478.

141. Nan, X.; Collisson, E.A.; Lewis, S.; Huang, J.; Tamguney, T.M.; Liphardt, J.T.; McCormick, F.; Gray, J.W.; Chu, S. Single-molecule superresolution imaging allows quantitative analysis of RAF multimer formation and signaling. *Proc Natl Acad Sci U S A* **2013**, *110*, 18519-18524, doi:10.1073/pnas.1318188110.

142. Tran, N.H.; Frost, J.A. Phosphorylation of Raf-1 by p21-activated kinase 1 and Src regulates Raf-1 autoinhibition. *J Biol Chem* **2003**, *278*, 11221-11226, doi:10.1074/jbc.M210318200.

143. Dhillon, A.S.; Meikle, S.; Yazici, Z.; Eulitz, M.; Kolch, W. Regulation of Raf-1 activation and signalling by dephosphorylation. *EMBO J* **2002**, *21*, 64-71.

144. Thorson, J.A.; Yu, L.W.; Hsu, A.L.; Shih, N.Y.; Graves, P.R.; Tanner, J.W.; Allen, P.M.; Piwnica-Worms, H.; Shaw, A.S. 14-3-3 proteins are required for maintenance of Raf-1 phosphorylation and kinase activity. *Mol Cell Biol* **1998**, *18*, 5229-5238.

145. Michaud, N.R.; Fabian, J.R.; Mathes, K.D.; Morrison, D.K. 14-3-3 is not essential for Raf-1 function: identification of Raf-1 proteins that are biologically activated in a 14-3-3- and Ras-independent manner. *Mol Cell Biol* **1995**, *15*, 3390-3397.

146. Tzivion, G.; Luo, Z.; Avruch, J. A dimeric 14-3-3 protein is an essential cofactor for Raf kinase activity. *Nature* **1998**, *394*, 88-92, doi:10.1038/27938.

147. Fischer, A.; Baljuls, A.; Reinders, J.; Nekhoroshkova, E.; Sibilski, C.; Metz, R.; Albert, S.; Rajalingam, K.; Hekman, M.; Rapp, U.R. Regulation of RAF activity by 14-3-3 proteins: RAF kinases associate functionally with both homo- and heterodimeric forms of 14-3-3 proteins. *J Biol Chem* **2009**, *284*, 3183-3194, doi:10.1074/jbc.M804795200.

148. Clark, G.J.; Drugan, J.K.; Rossman, K.L.; Carpenter, J.W.; Rogers-Graham, K.; Fu, H.; Der, C.J.; Campbell, S.L. 14-3-3 zeta negatively regulates raf-1 activity by interactions with the Raf-1 cysteine-rich domain. *J Biol Chem* **1997**, *272*, 20990-20993.

149. Freed, E.; Symons, M.; Macdonald, S.G.; McCormick, F.; Ruggieri, R. Binding of 14-3-3 proteins to the protein kinase Raf and effects on its activation. *Science* **1994**, *265*, 1713-1716.

150. Fu, H.; Xia, K.; Pallas, D.C.; Cui, C.; Conroy, K.; Narsimhan, R.P.; Mamon, H.; Collier, R.J.; Roberts, T.M. Interaction of the protein kinase Raf-1 with 14-3-3 proteins. *Science* **1994**, *266*, 126-129.

151. Bondeva, T.; Balla, A.; Varnai, P.; Balla, T. Structural determinants of Ras-Raf interaction analyzed in live cells. *Molecular biology of the cell* **2002**, *13*, 2323-2333, doi:10.1091/mbc.e02-01-0019.

152. Leonard, T.A.; Hurley, J.H. Regulation of protein kinases by lipids. *Curr Opin Struct Biol* **2011**, *21*, 785-791, doi:10.1016/j.sbi.2011.07.006.

153. Prakash, P.; Hancock, J.F.; Gorfe, A.A. Three distinct regions of cRaf kinase domain interact with membrane. *Sci Rep* **2019**, *9*, 2057, doi:10.1038/s41598-019-38770-w.

154. Okada, T.; Hu, C.D.; Jin, T.G.; Kariya, K.; Yamawaki-Kataoka, Y.; Kataoka, T. The strength of interaction at the Raf cysteine-rich domain is a critical determinant of response of Raf to Ras family small GTPases. *Mol Cell Biol* **1999**, *19*, 6057-6064.

155. Takahashi, M.; Li, Y.; Dillon, T.J.; Stork, P.J. Phosphorylation of Rap1 by cAMP-dependent Protein Kinase (PKA) Creates a Binding Site for KSR to Sustain ERK Activation by cAMP. *J Biol Chem* **2017**, *292*, 1449-1461, doi:10.1074/jbc.M116.768986.

156. Rommel, C.; Radziwill, G.; Lovric, J.; Noeldeke, J.; Heinicke, T.; Jones, D.; Aitken, A.; Moelling, K. Activated Ras displaces 14-3-3 protein from the amino terminus of c-Raf-1. *Oncogene* **1996**, *12*, 609-619.

157. Kubicek, M.; Pacher, M.; Abraham, D.; Podar, K.; Eulitz, M.; Baccarini, M. Dephosphorylation of Ser-259 regulates Raf-1 membrane association. *J Biol Chem* **2002**, *277*, 7913-7919, doi:10.1074/jbc.M108733200.

158. Ory, S.; Zhou, M.; Conrads, T.P.; Veenstra, T.D.; Morrison, D.K. Protein phosphatase 2A positively regulates Ras signaling by dephosphorylating KSR1 and Raf-1 on critical 14-3-3 binding sites. *Curr Biol* **2003**, *13*, 1356-1364.

159. Eisenhardt, A.E.; Sprenger, A.; Roring, M.; Herr, R.; Weinberg, F.; Kohler, M.; Braun, S.; Orth, J.; Diedrich, B.; Lanner, U., et al. Phospho-proteomic analyses of B-Raf protein complexes reveal new regulatory principles. *Oncotarget* **2016**, *7*, 26628-26652, doi:10.18632/oncotarget.8427.

160. Huang, Y.; Guo, X.X.; Han, B.; Zhang, X.M.; An, S.; Zhang, X.Y.; Yang, Y.; Liu, Y.; Hao, Q.; Xu, T.R. Decoding the full picture of Raf1 function based on its interacting proteins. *Oncotarget* **2017**, *8*, 68329-68337, doi:10.18632/oncotarget.19353.

161. Boned Del Rio, I.; Young, L.C.; Sari, S.; Jones, G.G.; Ringham-Terry, B.; Hartig, N.; Rejnowicz, E.; Lei, W.; Bhamra, A.; Surinova, S., et al. SHOC2 complex-driven RAF dimerization selectively contributes to ERK pathway dynamics. *Proc Natl Acad Sci U S A* **2019**, 10.1073/pnas.1902658116, doi:10.1073/pnas.1902658116.

162. Rodriguez-Viciana, P.; Oses-Prieto, J.; Burlingame, A.; Fried, M.; McCormick, F. A phosphatase holoenzyme comprised of Shoc2/Sur8 and the catalytic subunit of PP1 functions as an M-Ras effector to modulate Raf activity. *Mol Cell* **2006**, *22*, 217-230, doi:10.1016/j.molcel.2006.03.027.

163. Young, L.C.; Hartig, N.; Boned Del Rio, I.; Sari, S.; Ringham-Terry, B.; Wainwright, J.R.; Jones, G.G.; McCormick, F.; Rodriguez-Viciana, P. SHOC2-MRAS-PP1 complex positively regulates RAF activity and contributes to Noonan syndrome pathogenesis. *Proc Natl Acad Sci U S A* **2018**, *115*, E10576-E10585, doi:10.1073/pnas.1720352115.

164. Mason, C.S.; Springer, C.J.; Cooper, R.G.; Superti-Furga, G.; Marshall, C.J.; Marais, R. Serine and tyrosine phosphorylations cooperate in Raf-1, but not B-Raf activation. *EMBO J* **1999**, *18*, 2137-2148, doi:10.1093/emboj/18.8.2137.

165. Tran, N.H.; Wu, X.; Frost, J.A. B-Raf and Raf-1 are regulated by distinct autoregulatory mechanisms. *J Biol Chem* **2005**, *280*, 16244-16253, doi:10.1074/jbc.M501185200.

166. Fabian, J.R.; Daar, I.O.; Morrison, D.K. Critical tyrosine residues regulate the enzymatic and biological activity of Raf-1 kinase. *Mol Cell Biol* **1993**, *13*, 7170-7179, doi:10.1128/mcb.13.11.7170.

167. Diaz, B.; Barnard, D.; Filson, A.; MacDonald, S.; King, A.; Marshall, M. Phosphorylation of Raf-1 serine 338-serine 339 is an essential regulatory event for Ras-dependent activation and biological signaling. *Mol Cell Biol* **1997**, *17*, 4509-4516, doi:10.1128/mcb.17.8.4509.

168. Baljuls, A.; Schmitz, W.; Mueller, T.; Zahedi, R.P.; Sickmann, A.; Hekman, M.; Rapp, U.R. Positive regulation of A-RAF by phosphorylation of isoform-specific hinge segment and identification of novel phosphorylation sites. *J Biol Chem* **2008**, *283*, 27239-27254, doi:10.1074/jbc.M801782200.

169. Zhang, B.H.; Guan, K.L. Activation of B-Raf kinase requires phosphorylation of the conserved residues Thr598 and Ser601. *EMBO J* **2000**, *19*, 5429-5439, doi:10.1093/emboj/19.20.5429.

170. Shin, S.Y.; Rath, O.; Choo, S.M.; Fee, F.; McFerran, B.; Kolch, W.; Cho, K.H. Positive- and negative-feedback regulations coordinate the dynamic behavior of the Ras-Raf-MEK-ERK signal transduction pathway. *Journal of cell science* **2009**, *122*, 425-435, doi:10.1242/jcs.036319.

171. Marais, R.; Light, Y.; Paterson, H.F.; Mason, C.S.; Marshall, C.J. Differential regulation of Raf-1, A-Raf, and B-Raf by oncogenic ras and tyrosine kinases. *J Biol Chem* **1997**, *272*, 4378-4383, doi:10.1074/jbc.272.7.4378.

172. Chong, H.; Lee, J.; Guan, K.L. Positive and negative regulation of Raf kinase activity and function by phosphorylation. *EMBO J* **2001**, *20*, 3716-3727, doi:10.1093/emboj/20.14.3716.

173. Takahashi, M.; Li, Y.; Dillon, T.J.; Kariya, Y.; Stork, P.J.S. Phosphorylation of the C-Raf N-region promotes Raf dimerization. *Mol Cell Biol* **2017**, 10.1128/MCB.00132-17, doi:10.1128/MCB.00132-17.

174. Matallanas, D.; Birtwistle, M.; Romano, D.; Zebisch, A.; Rauch, J.; von Kriegsheim, A.; Kolch, W. Raf family kinases: old dogs have learned new tricks. *Genes Cancer* **2011**, *2*, 232-260, doi:10.1177/1947601911407323.

175. Rajakulendran, T.; Sahmi, M.; Lefrancois, M.; Sicheri, F.; Therrien, M. A dimerization-dependent mechanism drives RAF catalytic activation. *Nature* **2009**, *461*, 542-545, doi:10.1038/nature08314.

176. Brennan, D.F.; Dar, A.C.; Hertz, N.T.; Chao, W.C.; Burlingame, A.L.; Shokat, K.M.; Barford, D. A Raf-induced allosteric transition of KSR stimulates phosphorylation of MEK. *Nature* **2011**, *472*, 366-369, doi:10.1038/nature09860.

177. Nussinov, R.; Zhang, M.; Tsai, C.J.; Liao, T.J.; Fushman, D.; Jang, H. Autoinhibition in Ras effectors Raf, PI3Kalpha, and RASSF5: a comprehensive review underscoring the challenges in pharmacological intervention. *Biophys Rev* **2018**, 10.1007/s12551-018-0461-0, doi:10.1007/s12551-018-0461-0.

178. Tian, T.; Harding, A.; Inder, K.; Plowman, S.; Parton, R.G.; Hancock, J.F. Plasma membrane nanoswitches generate high-fidelity Ras signal transduction. *Nat Cell Biol* **2007**, *9*, 905-914, doi:10.1038/ncb1615.

179. Cseh, B.; Doma, E.; Baccarini, M. "RAF" neighborhood: protein-protein interaction in the Raf/Mek/Erk pathway. *FEBS Lett* **2014**, *588*, 2398-2406, doi:10.1016/j.febslet.2014.06.025.

180. Ohren, J.F.; Chen, H.; Pavlovsky, A.; Whitehead, C.; Zhang, E.; Kuffa, P.; Yan, C.; McConnell, P.; Spessard, C.; Banotai, C., et al. Structures of human MAP kinase kinase 1 (MEK1) and MEK2 describe novel noncompetitive kinase inhibition. *Nature structural & molecular biology* **2004**, *11*, 1192-1197, doi:10.1038/nsmb859.

181. Wilsbacher, J.L.; Juang, Y.C.; Khokhlatchev, A.V.; Gallagher, E.; Binns, D.; Goldsmith, E.J.; Cobb, M.H. Characterization of mitogen-activated protein kinase (MAPK) dimers. *Biochemistry* **2006**, *45*, 13175-13182, doi:10.1021/bi061041w.

182.   von Kriegsheim, A.; Pitt, A.; Grindlay, G.J.; Kolch, W.; Dhillon, A.S. Regulation of the Raf-MEK-ERK pathway by protein phosphatase 5. *Nat Cell Biol* **2006**, *8*, 1011-1016, doi:10.1038/ncb1465.

183.   Park, S.; Rath, O.; Beach, S.; Xiang, X.; Kelly, S.M.; Luo, Z.; Kolch, W.; Yeung, K.C. Regulation of RKIP binding to the N-region of the Raf-1 kinase. *FEBS Lett* **2006**, *580*, 6405-6412, doi:10.1016/j.febslet.2006.10.054.

184.   Dougherty, M.K.; Muller, J.; Ritt, D.A.; Zhou, M.; Zhou, X.Z.; Copeland, T.D.; Conrads, T.P.; Veenstra, T.D.; Lu, K.P.; Morrison, D.K. Regulation of Raf-1 by direct feedback phosphorylation. *Mol Cell* **2005**, *17*, 215-224, doi:10.1016/j.molcel.2004.11.055.

185.   Hekman, M.; Fischer, A.; Wennogle, L.P.; Wang, Y.K.; Campbell, S.L.; Rapp, U.R. Novel C-Raf phosphorylation sites: serine 296 and 301 participate in Raf regulation. *FEBS Lett* **2005**, *579*, 464-468, doi:10.1016/j.febslet.2004.11.105.

186.   Dhillon, A.S.; Pollock, C.; Steen, H.; Shaw, P.E.; Mischak, H.; Kolch, W. Cyclic AMP-dependent kinase regulates Raf-1 kinase mainly by phosphorylation of serine 259. *Mol Cell Biol* **2002**, *22*, 3237-3246.

187.   Zimmermann, S.; Moelling, K. Phosphorylation and regulation of Raf by Akt (protein kinase B). *Science* **1999**, *286*, 1741-1744.

188.   Rommel, C.; Clarke, B.A.; Zimmermann, S.; Nunez, L.; Rossman, R.; Reid, K.; Moelling, K.; Yancopoulos, G.D.; Glass, D.J. Differentiation stage-specific inhibition of the Raf-MEK-ERK pathway by Akt. *Science* **1999**, *286*, 1738-1741.

189.   Romano, D.; Nguyen, L.K.; Matallanas, D.; Halasz, M.; Doherty, C.; Kholodenko, B.N.; Kolch, W. Protein interaction switches coordinate Raf-1 and MST2/Hippo signalling. *Nat Cell Biol* **2014**, *16*, 673-684, doi:10.1038/ncb2986.

190.   Tartaglia, M.; Gelb, B.D. Disorders of dysregulated signal traffic through the RAS-MAPK pathway: phenotypic spectrum and molecular mechanisms. *Ann N Y Acad Sci* **2010**, *1214*, 99-121, doi:10.1111/j.1749-6632.2010.05790.x.

191.   Kim, E.K.; Choi, E.J. Pathological roles of MAPK signaling pathways in human diseases. *Biochim Biophys Acta* **2010**, *1802*, 396-405, doi:10.1016/j.bbadis.2009.12.009.

192.   Rauen, K.A. The RASopathies. *Annu Rev Genomics Hum Genet* **2013**, *14*, 355-369, doi:10.1146/annurev-genom-091212-153523.

193.   Williams, V.C.; Lucas, J.; Babcock, M.A.; Gutmann, D.H.; Korf, B.; Maria, B.L. Neurofibromatosis type 1 revisited. *Pediatrics* **2009**, *123*, 124-133, doi:10.1542/peds.2007-3204.

194.   Romano, A.A.; Allanson, J.E.; Dahlgren, J.; Gelb, B.D.; Hall, B.; Pierpont, M.E.; Roberts, A.E.; Robinson, W.; Takemoto, C.M.; Noonan, J.A. Noonan syndrome: clinical features, diagnosis, and management guidelines. *Pediatrics* **2010**, *126*, 746-759, doi:10.1542/peds.2009-3207.

195.   Digilio, M.C.; Conti, E.; Sarkozy, A.; Mingarelli, R.; Dottorini, T.; Marino, B.; Pizzuti, A.; Dallapiccola, B. Grouping of multiple-lentigines/LEOPARD and Noonan syndromes on the PTPN11 gene. *Am J Hum Genet* **2002**, *71*, 389-394, doi:10.1086/341528.

196.   Pandit, B.; Sarkozy, A.; Pennacchio, L.A.; Carta, C.; Oishi, K.; Martinelli, S.; Pogna, E.A.; Schackwitz, W.; Ustaszewska, A.; Landstrom, A., et al. Gain-of-function RAF1 mutations cause Noonan and LEOPARD syndromes with hypertrophic cardiomyopathy. *Nat Genet* **2007**, *39*, 1007-1012, doi:10.1038/ng2073.

197.   Boon, L.M.; Mulliken, J.B.; Vikkula, M. RASA1: variable phenotype with capillary and arteriovenous malformations. *Curr Opin Genet Dev* **2005**, *15*, 265-269, doi:10.1016/j.gde.2005.03.004.

198.   Rauen, K.A. HRAS and the Costello syndrome. *Clin Genet* **2007**, *71*, 101-108, doi:10.1111/j.1399-0004.2007.00743.x.

199.   Rodriguez-Viciana, P.; Tetsu, O.; Tidyman, W.E.; Estep, A.L.; Conger, B.A.; Cruz, M.S.; McCormick, F.; Rauen, K.A. Germline mutations in genes within the MAPK pathway cause cardio-facio-cutaneous syndrome. *Science* **2006**, *311*, 1287-1290, doi:10.1126/science.1124642.

200. Brems, H.; Chmara, M.; Sahbatou, M.; Denayer, E.; Taniguchi, K.; Kato, R.; Somers, R.; Messiaen, L.; De Schepper, S.; Fryns, J.P., et al. Germline loss-of-function mutations in SPRED1 cause a neurofibromatosis 1-like phenotype. *Nat Genet* **2007**, *39*, 1120-1126, doi:10.1038/ng2113.

201. Mendez, H.M.; Opitz, J.M. Noonan syndrome: a review. *Am J Med Genet* **1985**, *21*, 493-506, doi:10.1002/ajmg.1320210312.

202. Roberts, A.E.; Allanson, J.E.; Tartaglia, M.; Gelb, B.D. Noonan syndrome. *Lancet* **2013**, *381*, 333-342, doi:10.1016/S0140-6736(12)61023-X.

203. Tartaglia, M.; Gelb, B.D.; Zenker, M. Noonan syndrome and clinically related disorders. *Best Pract Res Clin Endocrinol Metab* **2011**, *25*, 161-179, doi:10.1016/j.beem.2010.09.002.

204. Capri, Y.; Flex, E.; Krumbach, O.H.F.; Carpentieri, G.; Cecchetti, S.; Lissewski, C.; Rezaei Adariani, S.; Schanze, D.; Brinkmann, J.; Piard, J., et al. Activating Mutations of RRAS2 Are a Rare Cause of Noonan Syndrome. *Am J Hum Genet* **2019**, *104*, 1223-1232, doi:10.1016/j.ajhg.2019.04.013.

205. Gripp, K.W.; Aldinger, K.A.; Bennett, J.T.; Baker, L.; Tusi, J.; Powell-Hamilton, N.; Stabley, D.; Sol-Church, K.; Timms, A.E.; Dobyns, W.B. A novel rasopathy caused by recurrent de novo missense mutations in PPP1CB closely resembles Noonan syndrome with loose anagen hair. *Am J Med Genet A* **2016**, *170*, 2237-2247, doi:10.1002/ajmg.a.37781.

206. Motta, M.; Fidan, M.; Bellacchio, E.; Pantaleoni, F.; Schneider-Heieck, K.; Coppola, S.; Borck, G.; Salviati, L.; Zenker, M.; Cirstea, I.C., et al. Dominant Noonan syndrome-causing LZTR1 mutations specifically affect the Kelch domain substrate-recognition surface and enhance RAS-MAPK signaling. *Hum Mol Genet* **2019**, *28*, 1007-1022, doi:10.1093/hmg/ddy412.

207. Roberts, A.E.; Araki, T.; Swanson, K.D.; Montgomery, K.T.; Schiripo, T.A.; Joshi, V.A.; Li, L.; Yassin, Y.; Tamburino, A.M.; Neel, B.G., et al. Germline gain-of-function mutations in SOS1 cause Noonan syndrome. *Nat Genet* **2007**, *39*, 70-74, doi:10.1038/ng1926.

208. Tartaglia, M.; Pennacchio, L.A.; Zhao, C.; Yadav, K.K.; Fodale, V.; Sarkozy, A.; Pandit, B.; Oishi, K.; Martinelli, S.; Schackwitz, W., et al. Gain-of-function SOS1 mutations cause a distinctive form of Noonan syndrome. *Nat Genet* **2007**, *39*, 75-79, doi:10.1038/ng1939.

209. Cirstea, I.C.; Kutsche, K.; Dvorsky, R.; Gremer, L.; Carta, C.; Horn, D.; Roberts, A.E.; Lepri, F.; Merbitz-Zahradnik, T.; Konig, R., et al. A restricted spectrum of NRAS mutations causes Noonan syndrome. *Nat Genet* **2010**, *42*, 27-29, doi:10.1038/ng.497.

210. Schubbert, S.; Bollag, G.; Lyubynska, N.; Nguyen, H.; Kratz, C.P.; Zenker, M.; Niemeyer, C.M.; Molven, A.; Shannon, K. Biochemical and functional characterization of germ line KRAS mutations. *Mol Cell Biol* **2007**, *27*, 7765-7770, doi:10.1128/MCB.00965-07.

211. Razzaque, M.A.; Nishizawa, T.; Komoike, Y.; Yagi, H.; Furutani, M.; Amo, R.; Kamisago, M.; Momma, K.; Katayama, H.; Nakagawa, M., et al. Germline gain-of-function mutations in RAF1 cause Noonan syndrome. *Nat Genet* **2007**, *39*, 1013-1017, doi:10.1038/ng2078.

212. Calcagni, G.; Adorisio, R.; Martinelli, S.; Grutter, G.; Baban, A.; Versacci, P.; Digilio, M.C.; Drago, F.; Gelb, B.D.; Tartaglia, M., et al. Clinical Presentation and Natural History of Hypertrophic Cardiomyopathy in RASopathies. *Heart Fail Clin* **2018**, *14*, 225-235, doi:10.1016/j.hfc.2017.12.005.

213. Jaffre, F.; Miller, C.L.; Schanzer, A.; Evans, T.; Roberts, A.E.; Hahn, A.; Kontaridis, M.I. iPSC-Derived Cardiomyocytes Reveal Aberrant ERK5 and MEK1/2 Signaling Concomitantly Promote Hypertrophic Cardiomyopathy in RAF1-Associated Noonan Syndrome. *Circulation* **2019**, 10.1161/CIRCULATIONAHA.118.037227, doi:10.1161/CIRCULATIONAHA.118.037227.

214. Yu, L.; Daniels, J.P.; Wu, H.; Wolf, M.J. Cardiac hypertrophy induced by active Raf depends on Yorkie-mediated transcription. *Sci Signal* **2015**, *8*, ra13, doi:10.1126/scisignal.2005719.

215. Maron, B.J. Hypertrophic cardiomyopathy: an important global disease. *Am J Med* **2004**, *116*, 63-65, doi:10.1016/j.amjmed.2003.10.012.

216. Wigle, E.D.; Rakowski, H.; Kimball, B.P.; Williams, W.G. Hypertrophic cardiomyopathy. Clinical spectrum and treatment. *Circulation* **1995**, *92*, 1680-1692, doi:10.1161/01.cir.92.7.1680.

217. Frey, N.; Luedde, M.; Katus, H.A. Mechanisms of disease: hypertrophic cardiomyopathy. *Nat Rev Cardiol* **2011**, *9*, 91-100, doi:10.1038/nrcardio.2011.159.

218. Shah, M. Hypertrophic cardiomyopathy. *Cardiol Young* **2017**, *27*, S25-S30, doi:10.1017/S1047951116002195.

219. Aoki, Y.; Niihori, T.; Banjo, T.; Okamoto, N.; Mizuno, S.; Kurosawa, K.; Ogata, T.; Takada, F.; Yano, M.; Ando, T., et al. Gain-of-function mutations in RIT1 cause Noonan syndrome, a RAS/MAPK pathway syndrome. *Am J Hum Genet* **2013**, *93*, 173-180, doi:10.1016/j.ajhg.2013.05.021.

220. Hickey, E.J.; Mehta, R.; Elmi, M.; Asoh, K.; McCrindle, B.W.; Williams, W.G.; Manlhiot, C.; Benson, L. Survival implications: hypertrophic cardiomyopathy in Noonan syndrome. *Congenit Heart Dis* **2011**, *6*, 41-47, doi:10.1111/j.1747-0803.2010.00465.x.

221. Heineke, J.; Molkentin, J.D. Regulation of cardiac hypertrophy by intracellular signalling pathways. *Nat Rev Mol Cell Biol* **2006**, *7*, 589-600, doi:10.1038/nrm1983.

222. Selvetella, G.; Lembo, G. Mechanisms of cardiac hypertrophy. *Heart Fail Clin* **2005**, *1*, 263-273, doi:10.1016/j.hfc.2005.03.006.

223. Rockman, H.A.; Koch, W.J.; Lefkowitz, R.J. Seven-transmembrane-spanning receptors and heart function. *Nature* **2002**, *415*, 206-212, doi:10.1038/415206a.

224. Wilkins, B.J.; Molkentin, J.D. Calcium-calcineurin signaling in the regulation of cardiac hypertrophy. *Biochem Biophys Res Commun* **2004**, *322*, 1178-1191, doi:10.1016/j.bbrc.2004.07.121.

225. Wu, X.; Zhang, T.; Bossuyt, J.; Li, X.; McKinsey, T.A.; Dedman, J.R.; Olson, E.N.; Chen, J.; Brown, J.H.; Bers, D.M. Local InsP3-dependent perinuclear Ca2+ signaling in cardiac myocyte excitation-transcription coupling. *J Clin Invest* **2006**, *116*, 675-682, doi:10.1172/JCI27374.

226. Mondry, A.; Swynghedauw, B. Biological adaptation of the myocardium to chronic mechanical overload. Molecular determinants of the autonomic nervous system. *Eur Heart J* **1995**, *16 Suppl I*, 64-73, doi:10.1093/eurheartj/16.suppl_i.64.

227. Ross, R.S.; Borg, T.K. Integrins and the myocardium. *Circ Res* **2001**, *88*, 1112-1119, doi:10.1161/hh1101.091862.

228. Knoll, R.; Hoshijima, M.; Hoffman, H.M.; Person, V.; Lorenzen-Schmidt, I.; Bang, M.L.; Hayashi, T.; Shiga, N.; Yasukawa, H.; Schaper, W., et al. The cardiac mechanical stretch sensor machinery involves a Z disc complex that is defective in a subset of human dilated cardiomyopathy. *Cell* **2002**, *111*, 943-955, doi:10.1016/s0092-8674(02)01226-6.

229. Heineke, J.; Ruetten, H.; Willenbockel, C.; Gross, S.C.; Naguib, M.; Schaefer, A.; Kempf, T.; Hilfiker-Kleiner, D.; Caroni, P.; Kraft, T., et al. Attenuation of cardiac remodeling after myocardial infarction by muscle LIM protein-calcineurin signaling at the sarcomeric Z-disc. *Proc Natl Acad Sci U S A* **2005**, *102*, 1655-1660, doi:10.1073/pnas.0405488102.

230. Lorell, B.H.; Carabello, B.A. Left ventricular hypertrophy: pathogenesis, detection, and prognosis. *Circulation* **2000**, *102*, 470-479, doi:10.1161/01.cir.102.4.470.

231. Kaab, S.; Dixon, J.; Duc, J.; Ashen, D.; Nabauer, M.; Beuckelmann, D.J.; Steinbeck, G.; McKinnon, D.; Tomaselli, G.F. Molecular basis of transient outward potassium current downregulation in human heart failure: a decrease in Kv4.3 mRNA correlates with a reduction in current density. *Circulation* **1998**, *98*, 1383-1393, doi:10.1161/01.cir.98.14.1383.

232. Ostman-Smith, I. Beta-Blockers in Pediatric Hypertrophic Cardiomyopathies. *Rev Recent Clin Trials* **2014**, *9*, 82-85, doi:10.2174/1574887109666140908125158.

233. Simanshu, D.K.; Nissley, D.V.; McCormick, F. RAS Proteins and Their Regulators in Human Disease. *Cell* **2017**, *170*, 17-33, doi:10.1016/j.cell.2017.06.009.

234. Fernandez-Medarde, A.; Santos, E. Ras in cancer and developmental diseases. *Genes Cancer* **2011**, *2*, 344-358, doi:10.1177/1947601911411084.

235. Dhandapany, P.S.; Razzaque, M.A.; Muthusami, U.; Kunnoth, S.; Edwards, J.J.; Mulero-Navarro, S.; Riess, I.; Pardo, S.; Sheng, J.; Rani, D.S., et al. RAF1 mutations in childhood-onset dilated cardiomyopathy. *Nat Genet* **2014**, *46*, 635-639, doi:10.1038/ng.2963.

236. Liang, Q.; Wiese, R.J.; Bueno, O.F.; Dai, Y.S.; Markham, B.E.; Molkentin, J.D. The transcription factor GATA4 is activated by extracellular signal-regulated kinase 1- and 2-mediated phosphorylation of serine 105 in cardiomyocytes. *Mol Cell Biol* **2001**, *21*, 7460-7469, doi:10.1128/MCB.21.21.7460-7469.2001.

237. van Berlo, J.H.; Elrod, J.W.; Aronow, B.J.; Pu, W.T.; Molkentin, J.D. Serine 105 phosphorylation of transcription factor GATA4 is necessary for stress-induced cardiac hypertrophy in vivo. *Proc Natl Acad Sci U S A* **2011**, *108*, 12331-12336, doi:10.1073/pnas.1104499108.

238. Bueno, O.F.; De Windt, L.J.; Tymitz, K.M.; Witt, S.A.; Kimball, T.R.; Klevitsky, R.; Hewett, T.E.; Jones, S.P.; Lefer, D.J.; Peng, C.F., et al. The MEK1-ERK1/2 signaling pathway promotes compensated cardiac hypertrophy in transgenic mice. *EMBO J* **2000**, *19*, 6341-6350, doi:10.1093/emboj/19.23.6341.

239. Zhong, L.; Chiusa, M.; Cadar, A.G.; Lin, A.; Samaras, S.; Davidson, J.M.; Lim, C.C. Targeted inhibition of ANKRD1 disrupts sarcomeric ERK-GATA4 signal transduction and abrogates phenylephrine-induced cardiomyocyte hypertrophy. *Cardiovasc Res* **2015**, *106*, 261-271, doi:10.1093/cvr/cvv108.

240. Lan, F.; Lee, A.S.; Liang, P.; Sanchez-Freire, V.; Nguyen, P.K.; Wang, L.; Han, L.; Yen, M.; Wang, Y.; Sun, N., et al. Abnormal calcium handling properties underlie familial hypertrophic cardiomyopathy pathology in patient-specific induced pluripotent stem cells. *Cell Stem Cell* **2013**, *12*, 101-113, doi:10.1016/j.stem.2012.10.010.

241. Gupta, M.P. Factors controlling cardiac myosin-isoform shift during hypertrophy and heart failure. *J Mol Cell Cardiol* **2007**, *43*, 388-403, doi:10.1016/j.yjmcc.2007.07.045.

242. Oka, T.; Maillet, M.; Watt, A.J.; Schwartz, R.J.; Aronow, B.J.; Duncan, S.A.; Molkentin, J.D. Cardiac-specific deletion of Gata4 reveals its requirement for hypertrophy, compensation, and myocyte viability. *Circ Res* **2006**, *98*, 837-845, doi:10.1161/01.RES.0000215985.18538.c4.

243. Fearnley, C.J.; Roderick, H.L.; Bootman, M.D. Calcium signaling in cardiac myocytes. *Cold Spring Harb Perspect Biol* **2011**, *3*, a004242, doi:10.1101/cshperspect.a004242.

244. Higgins, E.M.; Bos, J.M.; Dotzler, S.M.; John Kim, C.S.; Ackerman, M.J. MRAS Variants Cause Cardiomyocyte Hypertrophy in Patient-Specific Induced Pluripotent Stem Cell-Derived Cardiomyocytes: Additional Evidence for MRAS as a Definitive Noonan Syndrome-Susceptibility Gene. *Circ Genom Precis Med* **2019**, *12*, e002648, doi:10.1161/CIRCGEN.119.002648.

245. Josowitz, R.; Mulero-Navarro, S.; Rodriguez, N.A.; Falce, C.; Cohen, N.; Ullian, E.M.; Weiss, L.A.; Rauen, K.A.; Sobie, E.A.; Gelb, B.D. Autonomous and Non-autonomous Defects Underlie Hypertrophic Cardiomyopathy in BRAF-Mutant hiPSC-Derived Cardiomyocytes. *Stem Cell Reports* **2016**, *7*, 355-369, doi:10.1016/j.stemcr.2016.07.018.

246. Sanna, B.; Bueno, O.F.; Dai, Y.S.; Wilkins, B.J.; Molkentin, J.D. Direct and indirect interactions between calcineurin-NFAT and MEK1-extracellular signal-regulated kinase 1/2 signaling pathways regulate cardiac gene expression and cellular growth. *Mol Cell Biol* **2005**, *25*, 865-878, doi:10.1128/MCB.25.3.865-878.2005.

247. Liu, Y.L.; Huang, C.C.; Chang, C.C.; Chou, C.Y.; Lin, S.Y.; Wang, I.K.; Hsieh, D.J.; Jong, G.P.; Huang, C.Y.; Wang, C.M. Hyperphosphate-Induced Myocardial Hypertrophy through the GATA-4/NFAT-3 Signaling Pathway Is Attenuated by ERK Inhibitor Treatment. *Cardiorenal Med* **2015**, *5*, 79-88, doi:10.1159/000371454.

248. Passariello, C.L.; Martinez, E.C.; Thakur, H.; Cesareo, M.; Li, J.; Kapiloff, M.S. RSK3 is required for concentric myocyte hypertrophy in an activated Raf1 model for Noonan syndrome. *J Mol Cell Cardiol* **2016**, *93*, 98-105, doi:10.1016/j.yjmcc.2016.02.020.

249. Markou, T.; Hadzopoulou-Cladaras, M.; Lazou, A. Phenylephrine induces activation of CREB in adult rat cardiac myocytes through MSK1 and PKA signaling pathways. *J Mol Cell Cardiol* **2004**, *37*, 1001-1011, doi:10.1016/j.yjmcc.2004.08.002.

250. Zhong, W.; Mao, S.; Tobis, S.; Angelis, E.; Jordan, M.C.; Roos, K.P.; Fishbein, M.C.; de Alboran, I.M.; MacLellan, W.R. Hypertrophic growth in cardiac myocytes is mediated by Myc through a Cyclin D2-dependent pathway. *EMBO J* **2006**, *25*, 3869-3879, doi:10.1038/sj.emboj.7601252.

251. He, A.; Kong, S.W.; Ma, Q.; Pu, W.T. Co-occupancy by multiple cardiac transcription factors identifies transcriptional enhancers active in heart. *Proc Natl Acad Sci U S A* **2011**, *108*, 5632-5637, doi:10.1073/pnas.1016959108.

252. Sheikh, F.; Raskin, A.; Chu, P.H.; Lange, S.; Domenighetti, A.A.; Zheng, M.; Liang, X.; Zhang, T.; Yajima, T.; Gu, Y., et al. An FHL1-containing complex within the cardiomyocyte sarcomere mediates hypertrophic biomechanical stress responses in mice. *J Clin Invest* **2008**, *118*, 3870-3880, doi:10.1172/JCI34472.

253. Liang, Y.; Bradford, W.H.; Zhang, J.; Sheikh, F. Four and a half LIM domain protein signaling and cardiomyopathy. *Biophys Rev* **2018**, *10*, 1073-1085, doi:10.1007/s12551-018-0434-3.

254. Romano, D.; Matallanas, D.; Weitsman, G.; Preisinger, C.; Ng, T.; Kolch, W. Proapoptotic kinase MST2 coordinates signaling crosstalk between RASSF1A, Raf-1, and Akt. *Cancer Res* **2010**, *70*, 1195-1203, doi:10.1158/0008-5472.CAN-09-3147.

255. Yang, Y.; Del Re, D.P.; Nakano, N.; Sciarretta, S.; Zhai, P.; Park, J.; Sayed, D.; Shirakabe, A.; Matsushima, S.; Park, Y., et al. miR-206 Mediates YAP-Induced Cardiac Hypertrophy and Survival. *Circ Res* **2015**, *117*, 891-904, doi:10.1161/CIRCRESAHA.115.306624.

256. Chong, J.X.; Buckingham, K.J.; Jhangiani, S.N.; Boehm, C.; Sobreira, N.; Smith, J.D.; Harrell, T.M.; McMillin, M.J.; Wiszniewski, W.; Gambin, T., et al. The Genetic Basis of Mendelian Phenotypes: Discoveries, Challenges, and Opportunities. *Am J Hum Genet* **2015**, *97*, 199-215, doi:10.1016/j.ajhg.2015.06.009.

257. Dvorsky, R.; Ahmadian, M.R. Always look on the bright site of Rho: structural implications for a conserved intermolecular interface. *EMBO reports* **2004**, *5*, 1130-1136, doi:10.1038/sj.embor.7400293.

258. Pirone, D.M.; Carter, D.E.; Burbelo, P.D. Evolutionary expansion of CRIB-containing Cdc42 effector proteins. *Trends Genet* **2001**, *17*, 370-373, doi:10.1016/s0168-9525(01)02311-3.

259. Hemsath, L.; Dvorsky, R.; Fiegen, D.; Carlier, M.F.; Ahmadian, M.R. An electrostatic steering mechanism of Cdc42 recognition by Wiskott-Aldrich syndrome proteins. *Mol Cell* **2005**, *20*, 313-324, doi:10.1016/j.molcel.2005.08.036.

260. Gibson, R.M.; Wilson-Delfosse, A.L. RhoGDI-binding-defective mutant of Cdc42Hs targets to membranes and activates filopodia formation but does not cycle with the cytosol of mammalian cells. *Biochem J* **2001**, *359*, 285-294, doi:10.1042/0264-6021:3590285.

261. Gibson, R.M.; Gandhi, P.N.; Tong, X.; Miyoshi, J.; Takai, Y.; Konieczkowski, M.; Sedor, J.R.; Wilson-Delfosse, A.L. An activating mutant of Cdc42 that fails to interact with Rho GDP-dissociation inhibitor localizes to the plasma membrane and mediates actin reorganization. *Exp Cell Res* **2004**, *301*, 211-222, doi:10.1016/j.yexcr.2004.07.033.

262. Roberts, P.J.; Mitin, N.; Keller, P.J.; Chenette, E.J.; Madigan, J.P.; Currin, R.O.; Cox, A.D.; Wilson, O.; Kirschmeier, P.; Der, C.J. Rho Family GTPase modification and dependence on CAAX motif-signaled posttranslational modification. *J Biol Chem* **2008**, *283*, 25150-25163, doi:10.1074/jbc.M800882200.

263. Bekhouche, B.; Tourville, A.; Ravichandran, Y.; Tacine, R.; Abrami, L.; Dussiot, M.; Khau-Dancasius, A.; Boccara, O.; Khirat, M.; Mangeney, M., et al. A toxic palmitoylation on Cdc42 drives a severe autoinflammatory syndrome. *bioRxiv* **2019**, 10.1101/808782, 808782, doi:10.1101/808782.

264. Baschieri, F.; Confalonieri, S.; Bertalot, G.; Di Fiore, P.P.; Dietmaier, W.; Leist, M.; Crespo, P.; Macara, I.G.; Farhan, H. Spatial control of Cdc42 signalling by a GM130-RasGRF complex regulates polarity and tumorigenesis. *Nat Commun* **2014**, *5*, 4839, doi:10.1038/ncomms5839.

265. Fukata, M.; Watanabe, T.; Noritake, J.; Nakagawa, M.; Yamaga, M.; Kuroda, S.; Matsuura, Y.; Iwamatsu, A.; Perez, F.; Kaibuchi, K. Rac1 and Cdc42 capture microtubules through IQGAP1 and CLIP-170. *Cell* **2002**, *109*, 873-885, doi:10.1016/s0092-8674(02)00800-0.

266. Caye, A.; Strullu, M.; Guidez, F.; Cassinat, B.; Gazal, S.; Fenneteau, O.; Lainey, E.; Nouri, K.; Nakhaei-Rad, S.; Dvorsky, R., et al. Juvenile myelomonocytic leukemia displays mutations in components of the RAS pathway and the PRC2 network. *Nat Genet* **2015**, *47*, 1334-1340, doi:10.1038/ng.3420.

267. Seeland, I.; Xiong, Y.; Orlik, C.; Deibel, D.; Prokosch, S.; Kublbeck, G.; Jahraus, B.; De Stefano, D.; Moos, S.; Kurschus, F.C., et al. The actin remodeling protein cofilin is crucial for thymic alphabeta but not gammadelta T-cell development. *PLoS Biol* **2018**, *16*, e2005380, doi:10.1371/journal.pbio.2005380.

268. Chang, K.H.; Sanchez-Aguilera, A.; Shen, S.; Sengupta, A.; Madhu, M.N.; Ficker, A.M.; Dunn, S.K.; Kuenzi, A.M.; Arnett, J.L.; Santho, R.A., et al. Vav3 collaborates with p190-BCR-ABL in lymphoid progenitor leukemogenesis, proliferation, and survival. *Blood* **2012**, *120*, 800-811, doi:10.1182/blood-2011-06-361709.

269. Gasilina, A.; Premnauth, G.; Gurjar, P.; Biesiada, J.; Hegde, S.; Milewski, D.; Ma, G.; Kalin, T.V.; Merino, E.; Meller, J., et al. IODVA1, a guanidinobenzimidazole derivative, targets Rac activity and Ras-driven cancer models. *PLoS One* **2020**, *15*, e0229801, doi:10.1371/journal.pone.0229801.

270. Katzav, S.; Martin-Zanca, D.; Barbacid, M. vav, a novel human oncogene derived from a locus ubiquitously expressed in hematopoietic cells. *EMBO J* **1989**, *8*, 2283-2290.

271. Menacho-Marquez, M.; Garcia-Escudero, R.; Ojeda, V.; Abad, A.; Delgado, P.; Costa, C.; Ruiz, S.; Alarcon, B.; Paramio, J.M.; Bustelo, X.R. The Rho exchange factors Vav2 and Vav3 favor skin tumor initiation and promotion by engaging extracellular signaling loops. *PLoS Biol* **2013**, *11*, e1001615, doi:10.1371/journal.pbio.1001615.

272. Liu, Y.; Mo, J.Q.; Hu, Q.; Boivin, G.; Levin, L.; Lu, S.; Yang, D.; Dong, Z.; Lu, S. Targeted overexpression of vav3 oncogene in prostatic epithelium induces nonbacterial prostatitis and prostate cancer. *Cancer Res* **2008**, *68*, 6396-6406, doi:10.1158/0008-5472.CAN-08-0645.

273. Liao, J.K.; Laufs, U. Pleiotropic effects of statins. *Annu Rev Pharmacol Toxicol* **2005**, *45*, 89-118, doi:10.1146/annurev.pharmtox.45.120403.095748.

274. Ziegler, V.; Albers, A.; Fritz, G. Lovastatin protects keratinocytes from DNA damage-related pro-apoptotic stress responses stimulated by anticancer therapeutics. *Biochim Biophys Acta* **2016**, *1863*, 1082-1092, doi:10.1016/j.bbamcr.2016.02.009.

275. Fritz, G.; Henninger, C. Rho GTPases: Novel Players in the Regulation of the DNA Damage Response? *Biomolecules* **2015**, *5*, 2417-2434, doi:10.3390/biom5042417.

276. Haydont, V.; Bourgier, C.; Pocard, M.; Lusinchi, A.; Aigueperse, J.; Mathe, D.; Bourhis, J.; Vozenin-Brotons, M.C. Pravastatin Inhibits the Rho/CCN2/extracellular matrix cascade in human fibrosis explants and improves radiation-induced intestinal fibrosis in rats. *Clinical cancer research : an official journal of the American Association for Cancer Research* **2007**, *13*, 5331-5340, doi:10.1158/1078-0432.CCR-07-0625.

277. Bourgier, C.; Haydont, V.; Milliat, F.; Francois, A.; Holler, V.; Lasser, P.; Bourhis, J.; Mathe, D.; Vozenin-Brotons, M.C. Inhibition of Rho kinase modulates radiation induced fibrogenic phenotype in intestinal smooth muscle cells through alteration of the cytoskeleton and connective tissue growth factor expression. *Gut* **2005**, *54*, 336-343, doi:10.1136/gut.2004.051169.

Acknowledgement

First, I would like to deeply thank my advisor Reza Ahmadian who managed to work with me since I was doing my bachelors thesis. You gave me a continuous support in my entire academic time so far and made it always possible to motivate me and help me with your knowledge and guidance. You encouraged me to stay critical and to question every of my decisions. I deeply hope that you will find your missing keys in the unlit town one day!

A special thanks goes to Axel Gödecke who was not only my co-supervisor but also the head of my graduate school and most important, a mentor on my scientific path. Your commitment in the IRTG 1902 made it possible for me to benefit from all that amazing advantages of the graduate school. I hope that you get the chance to continue your efforts in another IRTG!

I also want to thank Roland Piekorz for always helping me out when I was lost in my data once again. Discussing with you had always inspired me for new experiments and ideas and you always helped me in situations where others were not able to help. All the best for your future!

Thanks to Jürgen Scheller for the way you manage the whole institute and kept us together like a wired family. I furthermore want to thank you for all your scientific assistance and of course also for all the nice parties we had together!

I would like to express my thanks to all present and former members of the institute of Biochemistry and Molecular Biology II, that were all beside me during my Ph.D. You people really rock and made my days so much easier!

A very special thanks goes to my group members which whom I had special and memorable time. Thank you for the stimulating discussions, working together, and for all the fun we have had in the last years. Your camaraderie was essential for me to reach my scientific goals!

Dann gibt es da noch eine Hand voll besonderer Menschen an der medizinischen Fakultät, die ein dementsprechend besonderen Dank verdienen. Petra Opree, Fereshteh Kamrani, Ilse Meyer und Sandra Berger, ohne euch wäre die Welt eine schlechtere. Danke!

Wer so viele wunderbare Menschen um sich herum Freunde nennen darf, hat das große Glück auf so Reisen, wie dieser hier, niemals allein und unbeobachtet zu sein. Daher einen riesen Dank an alle meine Freunde, dass ihr auf mich aufpasst!

Dann ist da noch Oliver, mit dem ich mein ganzes akademisches Leben bis jetzt zusammen durchgemacht habe. Dank auch für alle Momente die wir während unserer Doktorarbeit zusammen gerockt haben. Ich hoffe, dass wir irgendwann mal wieder ein Büro teilen. Bis dahin, halt die Ohren steif Großer!

Meiner Familie gebührt ein ganz besonderer Dank für ihre kontinuierliche Unterstützung! Zu sehen, wie stolz ihr auf mich seid, ist verrückt! Ich kann mir für meine Vergangenheit, die Gegenwart und meine Zukunft keine besseren Menschen um mich wünschen!

Miriam! Na ja, was soll ich sagen… Du bist einfach alles für mich! Es gibt keine Person, die mich mehr unterstützt hat und sich so viel meines Gejammers anhören musste. Gleichzeitig gibt es auch keine Person außer dir, mit der ich diese Zeit zusammen durchleben wollte. Mit dir an meiner Seite könnte ich noch 100 mal promovieren!

Eidesstattliche Erklärung

Ich versichere an Eides Statt, dass die Dissertation von mir selbstständig und ohne unzulässige fremde Hilfe unter Beachtung der „Grundsätze zur Sicherung guter wissenschaftlicher Praxis an der Heinrich-Heine-Universität Düsseldorf" erstellt worden ist.

Es wurden keinerlei andere Quellen und Hilfsmittel, außer den angegebenen, benutzt. Zitate aus anderen Arbeiten wurden kenntlich gemacht. Diese Dissertation wurde in der vorgelegten oder einer ähnlichen Form noch bei keiner anderen Institution eingereicht und es wurden bisher keine erfolglosen Promotionsversuche von mir unternommen.

Marcel Buchholzer   Düsseldorf, den